Physics of the Solid State, Vol. 43, No. 6, 2001, pp. 1001–1006. Translated from Fizika Tverdogo Tela, Vol. 43, No. 6, 2001, pp. 968–973.
Original Russian Text Copyright © 2001 by Chashchin.

METALS AND SUPERCONDUCTORS

Viscous Flow of Magnetic Vortices and Rapid Relaxation of Magnetization in YBaCuO Ceramics

V. S. Chashchin

Konstantinov Institute of Nuclear Physics, Russian Academy of Sciences, Gatchina, Leningrad oblast, 188350 Russia

Received November 13, 2000

Abstract—The viscous flow of magnetic vortices in granular YBaCuO ceramics of various granule sizes is investigated using the microwave absorption method ($f = 80$ MHz) in the range of varying magnetic fields $H = \pm 1500$ Oe and of temperatures $T = 77$ to 95 K. The conditions for the formation and melting of the vortex lattice, as well as the transition of the high-temperature superconductor (HTSC) state from the irreversibility region to the region of the viscous flow of magnetic vortices, are considered. The rapid magnetic relaxation times in the range $\tau = 72$ to 111 ms are determined from the magnetization relaxation in the HTSC materials under investigation depending on the granule size d, which varies from 1 to 30 μm. The experimental results on the variation of the relaxation time τ from 77 to 120 ms in a ceramic exposed to fast neutrons with various fluences ($\Phi = 10^{16}$ to 10^{19} cm^{-2}) are considered. The depinning process is analyzed; it occurs in the form of a thermally assisted flux flow in the range of low activation energies. *© 2001 MAIK “Nauka/Interperiodica”.*

1. INTRODUCTION

High-temperature superconductors (HTSC), which are type II superconductors with the Ginzburg–Landau parameter $K = \lambda/\xi > 1/\sqrt{2}$ (λ is the magnetic-field penetration depth in the sample and ξ is the coherence length), demonstrate a variety of magnetic effects owing to the existence of the Meissner effect and the presence of two magnetic subsystems in the form of Abrikosov (*A* subsystem) and Josephson (*J* subsystem) magnetic vortices. The layered structures of HTSC materials and strong anisotropy give rise to a large set of magnetic interactions between the vortices in the subsystems, as well as between the vortices of the *A* and *J* subsystems. Abrikosov found a two-dimensional periodic solution of the Ginzburg–Landau equations for $K \gg 1/\sqrt{2}$, which can be interpreted as the emergence of a regular lattice of vortices, each of which carries a magnetic field quantum $\Phi_0 = h/2e = 2.07 \times 10^{-15}$ T m^2. The layered structure of superconductors with clearly manifested anisotropy of their properties, which is determined by the quasi-two-dimensional nature of their electronic structure, plays a significant role in the behavior of the vortex lattice. In real superconductors, the formed vortices are fixed at various pinning centers, such as defects in the crystal lattice structure in the form of dislocations and vacancies, grain boundaries, surface inhomogeneities, and inclusions of various phases and impurities. The dynamics of the behavior of vortices is reflected in the variation of magnetization with time. Depending on the potential of pinning centers, various magnetization relaxation patterns are observed in superconductors [1]. In the presence of strong pinning centers (when the activation energy $u \gg kT$), a slow (logarithmic) magnetic relaxation takes place and the magnetic flux creep is observed [2–4]. In the presence of weak pinning centers (with an activation energy $u \leq kT$), rapid magnetic relaxation is observed, which is determined by the thermal excitation of the magnetic flux flow [5–7]. In actual practice, superconductors can contain both weak and strong pinning centers whose manifestations depend on the external magnetic field and temperature. Additional defects can appear in the structure of a superconductor as a result of bombardment by fast neutrons. Analyzing the behavior of magnetization of HTSC materials, one can establish the presence of the pinning centers responsible for the slow and rapid components of magnetic relaxation and, hence, determine the type of defects present: extended defects (in the form of disordered regions) or point defects (in the form of dislocations and vacancies in the crystal lattice structure). Study of the magnetic properties of HTSC materials at various values of temperature and magnetic flux and at different rates of its variation provides new information on the depinning processes involved and the transition of the superconductor to the region of viscous flow of magnetic vortices. We chose for the object of investigation a HTSC ceramic YBaCuO with granules of various sizes; the layered structure and the small coherence length of the granules are responsible for the clearly manifested quasi-two-dimensional (2*D*) anisotropy.

2. STRUCTURE, INTERACTION, AND FLOW OF VORTICES IN HTSC

An important feature of type II superconductors is the formation of Josephson vortices (along weak links) in these materials when the external magnetic field attains the lower critical field value:

$$B_{c1(J)}(T) = \Phi_0/(4\pi\lambda_L\lambda_J)\ln(\lambda_J/d). \quad (1)$$

When the value

$$B_{c1(A)}(T) = \Phi_0/(4\pi\lambda_L\lambda_J)\ln(\lambda_L/\xi) \quad (2)$$

is attained, Arbikosov vortices are formed and start penetrating into granules, thus forming a periodic triangular lattice with the period

$$a = (\Phi_0/B)^{1/2} \quad (3)$$

and sizes of vortices equal to the core radius

$$r_c = \sqrt{2}\xi, \quad (4)$$

where λ_L and λ_J are the London and Josephson penetration depths, respectively; and ξ and d are the coherence length and the mean size of granules, respectively.

The vector interaction potential between vortices separated by the distance $r = |\mathbf{r}_\mu - \mathbf{r}_\nu|$ is defined as [8]

$$\mathbf{V} = [\Phi_0^2\exp(-r/\lambda)/(8\pi\mu_0\lambda^2 r)]d\mathbf{r}_\mu d\mathbf{r}_\nu. \quad (5)$$

In anisotropic superconductors, vortices attract one another along the main direction of the applied magnetic field due to the energy of interaction, thus forming extended chains. If the coherence length [9] $\xi_c = \xi_{ab}\lambda_{ab}/\lambda_c < \xi_{ab}$ ($\lambda_c/\lambda_{ab} \cong 5$ in the case of YBaCuO) along the c axis is smaller than the separation r_s between the CuO planes, we can assume that the layers of the superconductor are weakly coupled with one another. In this case, the magnetic interactions between vortices in the layers can be described using the Ginzburg–Landau quasi-two-dimensional (2*D*) anisotropic theory. A periodic triangular lattice, formed in the *ab* plane of the superconductor with a period defined by relation (3), exists until the thermal energy kT becomes as high as the binding energy between the vortices. Then, the periodic structure is destroyed; i.e., the melting of the 2*D* lattice takes place [10]: magnetic vortices become independent [11, 12]. The melting point of the vortex lattice is determined from the relation

$$kT = \Phi_0^2 r_s/(8\pi\mu_0\lambda_{ab}^2). \quad (6)$$

As the current flows through the superconductor, free vortices become involved in the flow with velocity v, which leads to energy dissipation due to the ohmic resistivity ρ_{FF} in the vortex core region. This resistivity increases with the magnetic field, attaining the normal-metal value ρ_n when the field becomes as strong as the upper critical field $B_{c2}(T)$; i.e.,

$$\rho_{\text{FF}} \approx \rho_n B/B_{c2}(T). \quad (7)$$

Real superconductors contain various inhomogeneities in their material, which play the role of pinning centers for vortices. Under certain conditions, pinned vortices can be separated and can participate in the flow. In accordance with the Anderson–Kim theory [13], thermally assisted depinning is observed in a wide temperature range below T_c, which causes magnetic-flux creep. For a state of the sample close to the critical state ($j \approx j_c$ and $u \gg kT$), the decrease in the induced currents

$$j(t > t_0) \approx j(t_0) - j_{c0}\ln(t/t_0)kT/u \quad (8)$$

and in the magnetization of the superconducting sample

$$|M(t) - M(0)| \sim A\ln(t/t_0) \quad (9)$$

occurs according to a logarithmic law (t_0 is an arbitrary instant, j_{c0} is the critical current density in the absence of flux creep, and u is the binding energy between vortex lines and pinning centers).

The magnetic relaxation rate

$$A = dM/d\ln t \quad (10)$$

can be determined in terms of the binding energy between vortex lines and strong pinning centers:

$$1/M_0 dM/d\ln t = kT/u. \quad (11)$$

If we analyze the state of a sample far from the critical state ($j \ll j_c$ and $u \le kT$), the change in magnetization over a wide time interval is closely approximated [14–16] by the exponential dependence

$$|M(t) - M(0)| \approx \exp[(-t/\tau)^p], \quad (12)$$

where τ is the magnetic relaxation constant and the exponent is $p \approx 0.6$. In the given case, since the activation energy is comparable with the thermal energy kT, a thermally assisted viscous magnetic flux flow takes place; this is typical of weak pinning. The magnetic-vortex depinning due to thermal fluctuations leads to the emergence of an electric field [15, 17, 18]:

$$E(j) = E_0\exp(-u/kT)\sinh(ju/(j_{c0}kT)), \quad (13)$$

where $E_0 = 2\rho j_{c0}$, ρ is the resistivity for $j = j_{c0}$, and j_{c0} is the critical current density in the absence of flux creep at $T = 0$ K.

Knowing the magnitude of the electric field, we determine the resistivity $\rho = E/j$ offered to the flow of vortices along the sample for a thermally assisted flux flow (TAFF, $j \ll j_c$), a flux creep (FC, $j \approx j_c$), and a flux flow (FF, $j > j_c$) at very low temperatures:

$$\rho_{\text{TAFF}} = \rho_c(2u/kT)\exp(-u/kT), \quad (14)$$

$$\rho_{\text{FC}} = \rho_c\exp(j/j_1)\exp(-u/kT), \quad (15)$$

$$\rho_{\text{FF}} = \rho_c(1-(j_{c0}/j)^2)^{1/2} \approx \rho_n B/B_{c2}(T), \quad (16)$$

where $j_1 = j_{c0}u/kT$.

The relations derived determine the viscosity of the vortex flow and energy dissipation.

The viscosity of a thermally assisted vortex flow in the case of weak pinning appears due to the ohmic resistance in Eq. (14). The resistance emerges as a result of melting of the vortex lattice and flux depinning, which transform the system of vortices into the "liquid state." This indicates the suppression of the interaction between vortices in superconducting CuO layers and the disappearance of the correlation with vortices of other closely spaced layers, since the interaction energy is lower than kT [10, 19]. The thermal activation of depinning occurs due to large local fluctuations in the vortex positions. We assume that the vortex lattice melting occurs when the standard deviation of the vortex positions satisfies the Lindemann criterion $\langle x^2\rangle^{1/2}/a = 0.1$ to 0.2. It is important that the depinning activation process occurs in the magnetization reversibility region. If we consider the B–T phase diagram for an HTSC material, it has an "irreversibility line" $B_{\mathrm{irr}}(T)$ [15], which can also be referred to as the "depinning line" [20, 21]. Below this line, the magnetic flux creep takes place and the magnetization hysteresis is observed, which leads to slow (logarithmic) relaxation. Above $B_{\mathrm{irr}}(T)$, a viscous diffusion flow of vortices is observed with the reversible magnetization typical of rapid (exponential) magnetic relaxation.

3. EXPERIMENTAL STUDY OF MAGNETIZATION RELAXATION AND VISCOUS FLOW OF MAGNETIC VORTICES

We studied the magnetization relaxation on an experimental setup intended for complex investigations of HTSC materials on the basis of the contactless microwave method, which makes it possible to analyze the temperature and field dependences of the basic critical parameters of an HTSC (H_{c1}, j_{c1}, λ, and ξ), the magnetization hysteresis, relaxation phenomena, and nonlinear and anisotropic properties. The rapid component of magnetization relaxation was studied by using the technique described in [16]. The experiments were made at the temperature $T = 77$ K. Samples $2 \times 2 \times 5$ mm in size placed in the induction coil of an oscillatory circuit ($f = 80$ MHz) were brought into the magnetic field of a solenoid (the magnetic field strength could be varied in the range $H = \pm 1500$ Oe). The resultant field applied to the sample was determined by the sum of fields

$$H = H_0 + H_m + h, \qquad (17)$$

where H_0 is a constant magnetic bias field, H_m is the (pulsed, linear, or periodic) modulating field, and h is the probing radio-frequency (rf) field.

In our experiments, we detected the $P(t)$ signal determined by the rf absorption, which is proportional to the magnetic susceptibility $\chi^{\parallel}$ (and, hence, to the magnetization of the YBaCuO ceramic). The observed relaxation of $P(t)$ after the action of the magnetic field $H_0 \approx 100$ Oe is characterized by three essentially different regions: one with a rapid exponential relaxation ($t < t_1$), one with a slow logarithmic relaxation ($t > t_2$), and one with an intermediate relaxation ($t_1 < t < t_2$) that is determined by the superposition of the rapid and slow components. Rapid relaxation is observed at the initial stage up to $t_1 \approx 2$ s and obeys the exponential law in Eq. (12). It is determined by weak pinning and is characterized by a rapid relaxation time τ, which is a function of resistivity in Eq. (14). The slow relaxation observed for strong pinning after $t_2 \approx 30$ s is governed by the logarithmic law in Eq. (9) and is manifested in the form of a flux creep with the rate in Eq. (10). Intermediate relaxation exists in the presence of weak pinning centers. In this region, the relaxation rate variation considerably deviates from the logarithmic dependence and there is no clearly manifested exponential time dependence of the magnetic moment. The measurement of the field dependences $P(H)$ for samples subjected to zero field cooling (ZFC) revealed that the $P(H)$ curves describing the magnetization strongly depend on the rate of variation of the applied magnetic field. The general form of the normalized hysteresis curves recorded for various amplitudes of magnetic field scanning is presented in Fig. 1. A considerable delay of the rf absorption signal relative to the magnetic

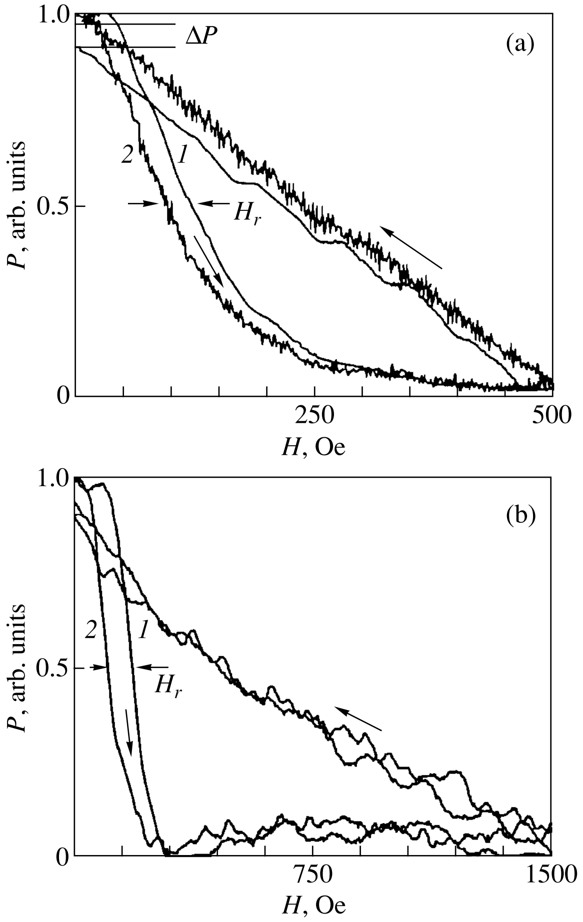

Fig. 1. Field dependence of rf absorption for various amplitudes and magnetic field scanning times: (a) $H_a = 500$ Oe, $t_{\mathrm{sc}1} = 2$ s (*1*), $t_{\mathrm{sc}2} = 35$ s (*2*), $H_r = 25$ Oe; and (b) $H_a = 1500$ Oe, $t_{\mathrm{sc}1} = 2$ s (*1*), $t_{\mathrm{sc}2} = 5$ s (*2*), $H_r = 75$ Oe. $T = 77$ K. Arrows on the curves indicate the direction of variation of the magnetic field.

field is observed for rapid scanning. Figure 1a shows the hysteresis curves obtained during the scanning times $t_{sc1} = 2$ s and $t_{sc2} = 35$ s for the amplitude $H_a = 500$ Oe of the linearly varying magnetic field. It can be seen that the rf absorption at a level of 0.5 of the initial value is attained at different values of the magnetic field ($H_r = 25$ Oe). This difference in the behavior of $P(H, t)$ can be attributed to the viscous flow of vortices penetrating into the sample: the vortices are retarded at a higher rate of variation of the magnetic field. Proceeding from the shift H_r of the hysteresis loop, we can easily obtain the retardation time $t_r = (dH/dt)^{-1}H_r$, which is equal to 0.05 s at a constant scanning rate $dH/dt = H_a/t_{sc}$ ($H_a = 500$ Oe, $t_{sc} = t_{sc1}/2$ is the time of scanning in the forward direction). The same value ($t_r = 0.05$ s) is obtained for $H_a = 1500$ Oe and $H_r = 75$ Oe (Fig. 1b). The ratio H_a/H_r for the two cases considered above (see Fig. 1) is found to be 20, indicating a linear relation between H_a and H_r. With increasing scanning time, the straight branch of the hysteresis loop is displaced monotonically towards low values of the magnetic field, attaining an extreme value for $t_{sc2} = 35$ s (see Fig. 1a). A further increase in t_{sc} only leads to an insignificant variation of this position. In the given case, the signal $P(H, t)$, which is a function of magnetization, closely follows the variation of the magnetic field and the vortex flow is not retarded. When the magnetic field decreases to zero, residual magnetization is observed ($\Delta P = P_1 - P_2$), which decreases to zero with time due to the creep (P_1 and P_2 are the values of signals for the forward and backward hysteresis branches, respectively, for $H = 0$). The dynamics of the variation of $P(H, t)$ and, hence, of the magnetization typical of strong pinning centers with the logarithmic relaxation law in Eq. (9) allow us to determine the pinning potential from Eq. (11). The value of the pinning potential (calculated according to the technique proposed in [22] and using the logarithmic time scale) for samples with a granule size $d = 1$ μm amounts to $u \approx 25$ meV, while the value obtained for $d = 20$ μm is $u \approx 15$ meV. During the scanning time $t_{sc2} = 35$ s, the residual rf absorption ΔP vanishes almost completely.

Thus, the processes occurring in YBaCuO ceramics are determined by rapid, as well as slow, magnetization relaxation. As the state of the superconductor approaches the B–T boundary between the superconducting and the normal phase, the magnetization curve becomes virtually reversible and the behavior of $P(H, t)$ becomes typical of weak pinning with a viscous vortex flow. Let us estimate the value of the rapid magnetization component by proceeding from the magnetic relaxation constant τ in the low-field region. For this purpose, we employ the frequency method [16] involving comparison of the phase of the slowly periodic reference field $H(t)$ with amplitude $H_a \approx 20$ Oe, which is applied to the sample, with the phase of the recorded signal $P(H, t)$. In order to overcome the diamagnetic expulsion, a small magnetic bias field $H_0 \approx 1$ to 5 Oe is applied to the sample. At the frequency $f_s = 0.5$ Hz of the magnetic field variation, the $P(H, t)$ curve is shifted virtually by half the period (which is a consequence of the law of electromagnetic induction). With increasing frequency, a considerable retardation takes place due to the effect of viscosity on the motion of vortices and a noticeable phase shift between the signals under investigation is observed. At a certain frequency $f_s = f_0$, the shift is as large as half the period. It is the value of this frequency that determines the relaxation time [16]:

$$\tau = 1/(2f_0). \tag{18}$$

For a sample with $d = 20$ μm, we have $\tau = 110$ ms.

Let us analyze the relaxation times for a viscous flow of vortices in YBaCuO ceramic samples with different sizes d of their granules. For this purpose, we will use the above method of determining the relaxation constant for samples in varying magnetic fields. It was proved by us earlier that the rapid relaxation of magnetization over the initial time interval is associated with a viscous vortex flow and is determined by the resistivity ρ_{TAFF} in Eq. (14). In this case, the screening currents of fine superconducting circuits obey the equation [1]

$$Ldj/dt = -\rho_{\mathrm{TAFF}}(j - j_c), \tag{19}$$

where L is the inductance of a vortex circuit. This equation leads to the following exponential dependence of the magnetization (rf absorption) signal:

$$P(t) = P(0)\exp(-t/\tau) \tag{20}$$

with the relaxation time

$$\tau = \rho_{\mathrm{TAFF}}/L. \tag{21}$$

With increasing granule size d, the ohmic component of the impedance of the superconducting circuit formed by weak links in the Josephson medium increases linearly. The resistance increases due to an increase in the length of the circuit. Accordingly, the relaxation time constant τ in Eq. (21) also increases linearly. The experimental dependence of the relaxation constant on the mean size of granules is presented in Fig. 2. The obtained graph confirms the linear form of the $\tau(d)$ dependence.

Let us compare the experimental data obtained for YBaCuO ceramic samples, having various mean granule sizes d, with the experimental results on the variation of magnetic relaxation in a similar ceramic material (with the granule size $d = 1$ μm) exposed to bombardment by fast neutrons with various fluences Φ. The dependence $\tau(\Phi)$ of the relaxation time on the neutron fluence is presented in Fig. 3. It was found that the observed range of variation of the relaxation time constant $\tau = 77$ to 120 ms in the neutron fluence range $\Phi = 10^{16}$–10^{19} cm^{-2} is very close to the range $\tau = 72$ to 111 ms obtained for samples with various granule sizes ($d = 1$ to 30 μm). This suggests that an increase in the fluence of neutrons leads to an increase in the concen-

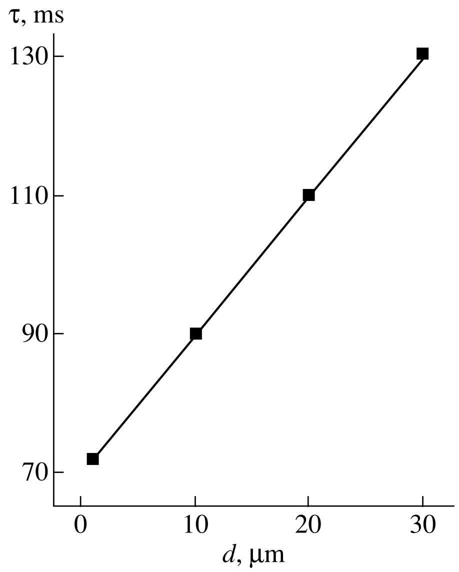

Fig. 2. Fast magnetization relaxation time as a function of the granule size in $YBa_2Cu_3O_{7-x}$ ceramic samples at $T = 77$ K.

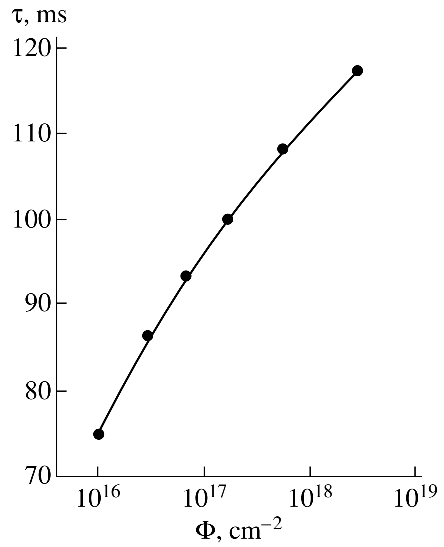

Fig. 3. Fast magnetization relaxation time as a function of the neutron fluence in $YBa_2Cu_3O_{7-x}$ ceramic samples at $T = 77$ K.

tration of defects that are centers of weak pinning. The wide time scale of the relaxation constant indicates a large spread in the effective pinning potentials with low activation energies. The presence of these defects leads to the diffusion type of vortex flow in the intergranular medium and to an increase in its viscosity. This leads to an increase in the resistivity component in Eq. (14). On the other hand, it was noted that the increase in the resistance of ceramic samples with various granule sizes is determined by the increase in size of the superconducting current loop formed by weak links. The changes in the resistance leading to an increase in the viscosity of the intergranular medium in the cases under investigation turned out to be comparable with the range of variation of the rapid magnetization relaxation times (Figs. 2, 3).

4. CONCLUSIONS

Thus, we have obtained the following results.

The method of microwave absorption is used for studying the magnetization relaxation; the regions of rapid (exponential) relaxation associated with the viscous flow of vortices, as well as the slow (logarithmic) relaxation typical of the thermally assisted creep of the flow, were determined.

We considered the conditions for the formation and melting of a vortex lattice, the depinning process, and the transition of the superconductor state from the irreversibility region (with clearly manifested hysteresis phenomena) to the region of viscous flow of magnetic vortices.

The reasons behind the dissipation of the energy of vortices involved in the flow due to the ohmic component of resistivity under various conditions are indicated, and the conditions under which the sample magnetization is retarded relative to the variation of the applied magnetic field are determined.

For the region of slow (logarithmic) relaxation, the pinning potential is calculated. Its value is found to be $u \approx 25$ meV for YBaCuO ceramic samples with granular size $d = 1$ μm and $u \approx 15$ meV for $d = 20$ μm.

The times of rapid magnetic relaxation are measured in the range $\tau = 72$ to 111 ms depending on the granule size $d = 1$ to 30 μm. The magnetization relaxation times $\tau = 77$ to 120 ms are obtained for YBaCuO ceramics ($d = 1$ μm) bombarded by fast neutrons with fluences $\Phi = 10^{16}$–10^{19} cm^{-2}. It is shown that the relaxation time increases with increasing viscosity of the intergranular medium as a result of an increase in the concentration of weak pinning centers under neutron bombardment.

ACKNOWLEDGMENTS

This work was carried out under the State Scientific and Technological Program “Neutron Studies in Condensed Media.”

REFERENCES

1. V. V. Moshchalkov, A. A. Zhukov, and L. I. Leonyuk, Sverkhprovodimost’: Fiz., Khim., Tekh. **2** (12), 84 (1989).
2. M. Touminen, A. M. Goldman, *et al.*, Phys. Rev. B **37**, 548 (1988).
3. E. L. Venturini, J. C. Bardour, D. S. Ginley, *et al.*, Appl. Phys. Lett. **56** (24), 2456 (1990).
4. F. E. Luborsky, R. H. Arendt, R. L. Fleischer, *et al.*, J. Appl. Phys. **70** (15), 5756 (1991).

5. H. G. Schnack, R. Griessen, and J. G. Lensink, Physica C (Amsterdam) **197**, 337 (1992).
6. D. Hu, W. Paul, and J. Rhyner, Physica C (Amsterdam) **200**, 359 (1992).
7. V. A. Atsarkin, G. A. Vasneva, V. V. Demidov, and N. E. Noginova, Solid State Commun. **74** (7), 603 (1990).
8. E. H. Brandt, Phys. Rev. B **34**, 6514 (1986).
9. R. F. Konopleva and V. S. Chashchin, Preprint No. 2051, PIYaF (Institute of Nuclear Physics, Russian Academy of Sciences, St. Petersburg, 1995).
10. M. V. Feigelman, V. B. Geshkenbein, and A. I. Larkin, Physica C (Amsterdam) **167**, 177 (1990).
11. J. R. Clem, Phys. Rev. B **43**, 7837 (1991).
12. L. N. Bulayevski, S. V. Mechkov, and D. Feinberg, Phys. Rev. B **43**, 3728 (1991).
13. P. W. Anderson and Y. B. Kim, Rev. Mod. Phys. **36**, 39 (1964).
14. C. W. Hagen *et al.*, Physica C (Amsterdam) **153–154**, 322 (1988).
15. E. Z. Meĭlikhov, *Outlines on High Temperature Superconductivity* (Mezhdunar. Tsentr Nauchnoĭ i Tekhnicheskoĭ Informatsii, Moscow, 1990).
16. V. S. Chashchin and R. F. Konopleva, Fiz. Tverd. Tela (St. Petersburg) **39** (6), 977 (1997) [Phys. Solid State **39**, 877 (1997)].
17. M. Tinkham, *Introduction to Superconductivity* (McGraw-Hill, New York, 1975; Atomizdat, Moscow, 1980).
18. E. H. Brandt, Z. Phys. B **80**, 167 (1990).
19. V. M. Vinokur, P. H. Kes, and A. E. Koshelev, Physica C (Amsterdam) **168**, 29 (1990).
20. A. Gupta, P. Esquinazi, and H. F. Braun, Physica B (Amsterdam) **165–166**, 1151 (1990).
21. P. Esquinazi, Solid State Commun. **74**, 75 (1990).
22. R. F. Konopleva and V. S. Chashchin, Fiz. Tverd. Tela (St. Petersburg) **39** (1), 28 (1997) [Phys. Solid State **39**, 23 (1997)].

Translated by N. Wadhwa

Physics of the Solid State, Vol. 43, No. 6, 2001, pp. 1007–1011. Translated from Fizika Tverdogo Tela, Vol. 43, No. 6, 2001, pp. 974–978.
Original Russian Text Copyright © 2001 by Orlova, Smirnov, Laval.

METALS AND SUPERCONDUCTORS

Effect of an Electric Field on the *I–V* Curves of $DyBa_2Cu_{3-x}O_y$/1 wt % Pt HTSC Ceramics

T. S. Orlova*, B. I. Smirnov*, and J. Y. Laval**

**Ioffe Physicotechnical Institute, Russian Academy of Sciences, Politekhnicheskaya ul. 26, St. Petersburg, 194021 Russia*
e-mail: orlova.t@pop.ioffe.rssi.ru
***Laboratoire de Physique du Solide, CNRS ESPCI, 75231 Paris Cedex 05, Rue Vauquelin, France*

Received November 22, 2000

Abstract—This paper reports on an experimental study of the effect of a magnetic field, $B \leq 70$ G, and an electric field, $E = 120$ MV/m, on the critical current I_c and *I–V* curves of $DyBa_2Cu_{3-x}O_y$ HTSC ceramics ($x = 0$ and 0.2), both undoped and doped with 1 wt % Pt. It has been established that, in stoichiometric ceramics ($x = 0$) at 77 K, I_c drops sharply (by more than an order of magnitude) already at very low $B \leq 1$ G. In copper-deficient ceramics ($x = 0.2$), I_c decreases with increasing B slowly, with Pt-doped samples exhibiting [on the dropping $I_c(B)$ dependence] a peak effect, i.e., an increase rather than decrease of I_c at $B \approx 10$ G. As for the effect of an electric field on I_c and the *I–V* curves (the E effect), it is not observed in ceramics of a stoichiometric composition. $DyBa_2Cu_{2.8}O_y$ samples acted upon by an electric field reveal a substantial increase in I_c and a decrease in the resistance R for $I > I_c$. In the case of $DyBa_2Cu_{2.8}O_y$/Pt, the electric field practically does not affect I_c but R decreases for $I > I_c$. In a sample placed in a magnetic field, the magnitude of the E effect is observed to correlate with the $I_c(B)$ dependence. In particular, in Pt-doped samples, the E effect decreases with increasing magnetic field B not gradually but with a maximum appearing at $B \approx 10$ G, i.e., in the region of the peak effect in the $I_c(B)$ dependence. The data obtained suggest the conclusion that the electric-field effect in ceramics exhibiting weak links of the superconductor–insulator–superconductor (SIS) type correlates with magnetic vortex pinning. *© 2001 MAIK “Nauka/Interperiodica”.*

1. INTRODUCTION

The critical current I_c in granulated high-temperature superconductors (HTSCs) is determined to a considerable extent by the existence in them of weak links (primarily at grain boundaries), whose behavior may depend substantially on a number of factors, in particular, on the electric field.

The electric field effect on I_c and the critical temperature T_c is usually studied on thin films (see reviews [1–4]), because this effect is associated with the variation of the carrier concentration in the surface layer of a sample. At the same time, it has been found that the reversible field effect increases when large-angle grain boundaries are introduced into a perfect thin film [5], as well as that this effect is also observed in thick polycrystalline films [3, 6] and even in ceramics [7–10]. It was suggested that in the Y123 ceramics this effect is accounted for by the presence of weak links, primarily of the superconductor–insulator–superconductor (SIS) type [8, 9]. The electric-field effect was established to correlate directly with the type of weak links [11, 12]. Indeed, the electric field was shown to substantially affect the *I–V* characteristics and the critical current in the samples in which the weak grain-boundary links follow the SIS behavior. In samples with weak links of the SNS type (superconductor–metal–superconductor), no electric-field effect was observed. In silver-doped ceramics, silver segregation at the boundaries was experimentally confirmed to occur by local chemical analysis (EDX) and it is this segregation that apparently accounts for the SNS character of the weak links [13]. Nevertheless, the nature of the electric-field effect in ceramics remains unclear. It appears that it can presently be associated only with the existence and behavior of weak grain-boundary links. Therefore, investigation of this effect, combined with a study of the structure and behavior of grain boundaries, could shed light on its nature. For instance, doping ceramic systems with various elements can affect the grain-boundary structure, and therefore, studying the field effect in such samples is of particular interest.

This paper reports on a study of the effect of a strong electric field on the critical current and *I–V* curves of a platinum-doped dysprosium HTSC ceramic with a known microstructure and grain-boundary characterization.

2. EXPERIMENTAL TECHNIQUE

Pure $DyBa_2Cu_{3-x}O_y$ and platinum-doped $DyBa_2Cu_{3-x}O_y$/1 wt % Pt ceramics ($x = 0$ and 0.2) were prepared in the following way [14]. Dy_2O_3, CuO, and $BaCO_3$ powders, with and without platinum powder added, were mixed in the required ratio, ground thor-

Table 1. Some characteristics of the ceramic samples studied: ρ_{300} is the resistivity at 300 K, T_{co} is the transition temperature of a sample at which its resistivity vanishes, ρ_f is the differential resistivity at 77 K, and L is the average grain size

Sample	T_{co}, K	ρ_{300}, Ω cm	ρ_f, Ω cm	L, μm
$DyBa_2Cu_3O_y$	93.8	1.5×10^{-3}	8×10^{-5}	31
$DyBa_2Cu_3O_y$/Pt	93.5	1.3×10^{-3}	7.7×10^{-5}	33
$DyBa_2Cu_{2.8}O_y$	92	1.7×10^{-3}	7.0×10^{-4}	4–5
$DyBa_2Cu_{2.8}O_y$/Pt	91.7	1.9×10^{-3}	8.5×10^{-4}	2–3

oughly, and pressed into pellets. The pellets were annealed three times in air at 920°C for 10 h, each anneal followed by grinding and pressing to bring the chemical reactions to an end and make the material more uniform. Next, the pellets were annealed in an oxygen flow first for 62 h at 960°C and then for 5 h at 500°C, with subsequent cooling in the furnace. Additionally, in contrast to [14], the pellets were additionally annealed in an oxygen flow. First, they were heated slowly to 560°C and maintained at this temperature for 4 h, after which we cooled them slowly to room temperature, with intermediate pauses at 500 and 400°C over 4 h.

The phase composition of the samples was determined on an automatic x-ray diffractometer. The composition and microstructure were analyzed with a transmission electron microscope (TEM/Jeol 2000 FX) and a scanning electron microscope with x-ray attachments for local analysis [14, 15].

The superconducting characteristics (the *I*–*V* curves and *R* vs. *T* dependences) were measured on samples approximately $1.5 \times 2 \times 4$ mm in size, with four indium contacts deposited on their sides (2×4 mm). Before contact deposition, a layer about 0.2 mm thick was removed from the sample surface.

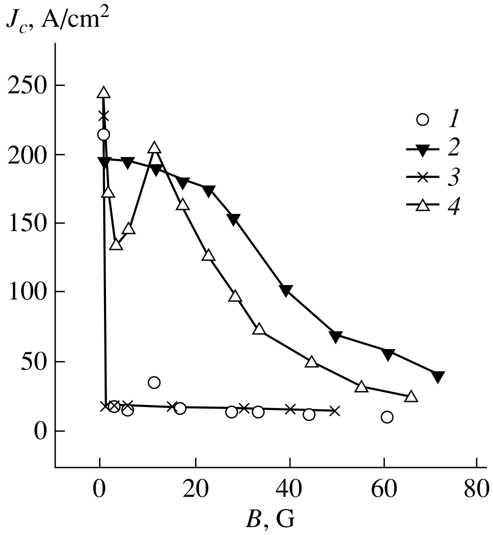

Fig. 1. Critical current density vs. magnetic field at 77 K for (*1, 2*) $DyBa_2Cu_{3-x}O_y$ and (*3, 4*) $DyBa_2Cu_{3-x}O_y$/1 wt % Pt for $x = 0$ (*1, 3*) and 0.2 (*2, 4*).

The study of the effect of an external electric field $E = U/t$ was carried out in an electrode–insulator–superconductor system at 77 K, as in [7], i.e., at $T < T_c$. A high negative voltage $U = 6$ kV was applied to a metallic electrode insulated from the sample with a teflon film $t = 50$ μm thick. The transport current I was passed through the current contacts, and the voltage V was measured across the potential contacts. The critical current was determined by a 1 μV/mm criterion.

When studying the effect of an electric field, the latter could be turned on both before the experiment and in the course of the *I*–*V* measurement at the desired value of *I*. Similar experiments could also be performed in a magnetic field $B \leq 70$ G, which was oriented parallel to the electric field and was generated by current coils.

3. EXPERIMENTAL RESULTS AND DISCUSSION

The characteristics of the ceramics studied are listed in Table 1. Deviation from a compositional stoichiometry is seen to only slightly decrease the critical temperature T_c of the ceramic. The room-temperature resistivity ρ_{300} increases somewhat, as does the differential resistivity at 77 K (ρ_f), which characterizes the effective resistance of the network of intergrain links, namely, the grain boundaries and junctions. [14, 16]. This is in accord with the observation that the grain size decreases strongly with the ceramic composition deviating from stoichiometry (Table 1), and, therefore, the total length of the boundaries increases. As for the influence of the platinum doping, it consisted in intragrain precipitation of platinum-containing secondary phases. These precipitates were of submicron size and were uniformly distributed within the 123 matrix. In the nonstoichiometric ceramics, Pt was additionally found in intergrain $BaCuO_2$ precipitates. Note that Pt did not affect the size and distribution of the 211 precipitates. Traces of Pt were observed to exist in Dy123 grains for $x = 0$ and 0.2. The Pt distribution in the matrix was nonuniform, with the maximum Pt content in the grains not exceeding 0.05 mol. No increase in the Pt concentration at the boundaries compared to that in the grains was observed.

Figure 1 shows the variation of the critical current density J_c of the samples at 77 K in an external magnetic field *B*. In stoichiometric ceramics, J_c was found to decrease strongly (by more than an order of magnitude) already at very low *B*, which apparently implies a practically total absence of magnetic vortex pinning at 77 K. At the same time, in the copper-deficient ceramics, the critical current varies smoothly, although fairly rapidly, with increasing *B*. The samples containing Pt also reveal the so-called peak effect [17, 18], in which J_c increases rather than decreases within a certain region of B on the $J_c(B)$ dependence. In this case, this peak is observed at $B_p \approx 10$ G after an abrupt drop of J_c for $B < 3$ G. The corresponding effect was also observed to occur with increasing B on the I–V curves for $I > I_c$, with beats seen on the curves in the region of the minimum (Fig. 2).

The above peak effect observed in the 123 HTSC ceramics is usually attributed to the various defects, more specifically, to twins and precipitates of other phases, as well as to clusters of oxygen vacancies and dislocations [19, 20]. In our case, the clearly pronounced peak effect in the $DyBa_2Cu_{3-x}O_y$/Pt samples originates most likely from pinning at vacancy clusters and twins, whose concentrations in doped and undoped ceramics may differ because of Pt being soluble in the matrix, although in limited amounts. Indeed, we earlier observed local regions with high twin densities in similar nonstoichiometric ceramics doped with Pt [14, 15]. A decrease in the separation between twins, which was due to Pt doping of melt-grown 123 ceramics, was also pointed out in [21, 22].

In order to estimate the type of the weak links in dysprosium ceramics, studies of the temperature dependences of J_c near T_c were carried out earlier [14, 15]. It was shown that this dependence can be approximated for all the ceramics studied by the relation

$$J_c(T) = \mathrm{const}(T_c - T),$$

which, by [23], corresponds to the SIS weak-link type. In other words, neither deviations from stoichiometry in Cu nor doping with Pt affect the weak-link type, which always remains SIS in dysprosium ceramics.

All the samples studied were checked for the existence of the electric-field effect. It was found that ceramics with a stoichiometric composition (both doped and undoped with platinum) do not exhibit the electric-field effect. Copper-deficient samples behave differently. The effect of an electric field on the I–V curves of some dysprosium ceramics is illustrated in Fig. 3. No field effect is seen in the Dy123 samples. In the $DyBa_2Cu_{2.8}O_y$/Pt samples, the electric field virtually does not affect the critical current while reducing the resistance R for $I > I_c$. In the $DyBa_2Cu_{2.8}O_y$ ceramic, the electric field increases I_c substantially and decreases R for $I > I_c$.

As for the effect of a magnetic field, it was established that in the Y123 ceramics the electric-field effect decreases with increasing B and practically disappears already at $B \approx 20$–30 G [24]. In our case, in the $DyBa_2Cu_{2.8}O_y$ samples, which did not exhibit the peak effect, the E effect also decreased with an increasing magnetic field and vanished at $B \approx 50$ G. In this connection, observation of the peak effect in the $DyBa_2Cu_{3-x}O_y$/Pt samples was of particular interest. Figure 4 shows a variation of the voltage V in the I–V curves of these samples as an electric field $E = 120$ MV/m is turned on and off for $I_c < I = \mathrm{const}$ and in various magnetic fields. One readily sees that as the magnetic field increases, the E effect (i.e., the electric-field-induced change ΔV of the voltage) first decreases, then grows in the region of B_p, decreases again for $B > B_p$, and finally vanishes altogether thereafter. Note that the I–V curves exhibit voltage oscillations (beats) at $I = \mathrm{const}$ near $B_{\min} \approx 3$ G.

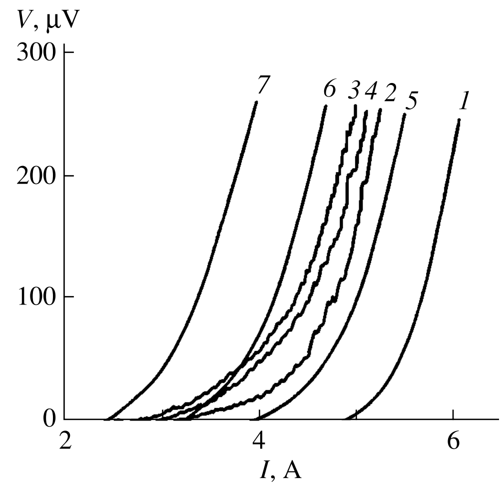

Fig. 2. I–V curves of $DyBa_2Cu_{2.8}O_y$/1 wt % Pt samples for various magnetic fields B (G): (*1*) 0, (*2*) 1, (*3*) 2.8, (*4*) 5.5, (*5*) 11, (*6*) 16.5, and (*7*) 22.

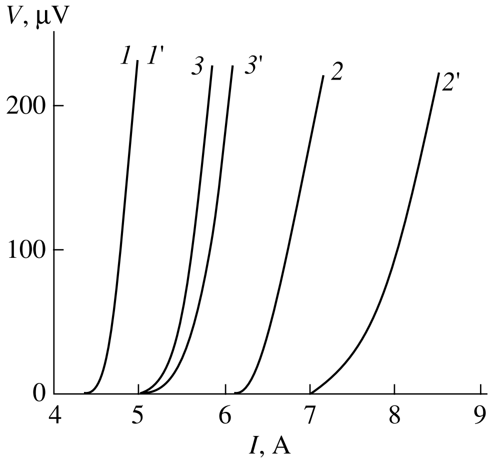

Fig. 3. I–V curves of $DyBa_2Cu_{3-x}O_y$ (*1, 1', 2, 2'*) and $DyBa_2Cu_{3-x}O_y$/1 wt % Pt (*3, 3'*) obtained for $x = 0$ (*1, 1'*) and 0.2 (*2, 2', 3, 3'*) for various values of the electric field E (MV/m): (*1–3*) 0 and (*1'–3'*) 120.

Thus, nonstoichiometric dysprosium ceramics exhibit the electric-field effect to various extents, whereas in stoichiometric ceramics it does not occur. At the same time, samples of both types, as already mentioned, have SIS-type weak links.

To reveal the nature of the electric-field effect in ceramics, we carried out a quantitative comparison of the E effect in bulk samples and in thin (single and bicrystal) films with different misorientation angles θ,

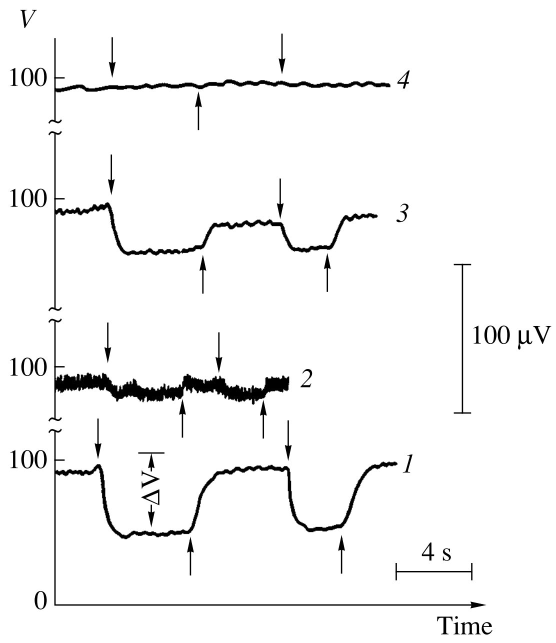

Fig. 4. Variation of voltage V in the I–V curves with the electric field E = 120 MV/m on (↓) and off (↑) measured on $DyBa_2Cu_{2.8}O_y$/1 wt % Pt samples for various magnetic fields B (G):(*1*) 0, (*2*) 5.5, (*3*) 11, and (*4*) 27.5. I = const, initial voltage $V_0 \approx 100$ µV.

which differed noticeably in thickness h. Table 2 presents experimental data, which were obtained recently on films [25] and bulk samples (in [11, 26] and in this work). One sees that in single crystals, the E effect ($\Delta I_c/I_cE$) turns out to be the same both in the films and bulk samples; in the latter case, though, the crystal contains large amounts of precipitates of the insulating phase Y211 [26]. In a film with a symmetric grain boundary, the E effect increases approximately threefold at $\theta = 24°$ and by an order of magnitude at 36.8°. An asymmetric boundary with a large misorientation angle ($\theta = 45°$) brings about a further enhancement of the effect by a factor of four. In ceramic samples, the E effect has a magnitude characteristic of the case of symmetric boundaries in films. One has, however, to bear in mind that when the E effect is studied in bicrystal films, the dielectric constant of the insulator (the $SrTiO_3$ substrate) is considerably larger than that in our experiments made with ceramics (with teflon as an insulator).

As was already mentioned, the manifestation of the E effect in the first experiments carried out on single-crystal films was associated with the electric-field-induced change in the carrier concentration in the surface layer of the sample. The enhancement of the field effect by more than an order of magnitude in bicrystals called for taking into account additional factors, such as structural properties of the grain boundaries, deviation from ideal stoichiometry, the d-symmetry effect, band structure bending at the boundary, etc. [27–29]. As a result, as was shown in [28, 29], a carrier-depleted layer (an insulator) can form at the boundary, a situation observed experimentally [30]. In terms of this model, the E effect is attributed to the influence of the external electric field on the parameters of this layer (a SIS-type weak link), in particular, on its width [27–29]. At the same time, the observed field effect in bicrystals is believed [31] to be related to the field-induced variation of the dielectric constant of the insulating substrate and it can be initiated by the large piezoelectric effect in $SrTiO_3$ at low temperatures.

Thus, the nature of the field effect in HTSCs containing grain boundaries remains open. As for the available experimental data on films and ceramics, they indicate unambiguously only the existence of a correlation of the observed E effect with the presence of SIS-type weak links in them. But while the existence of these links is apparently necessary, it is not sufficient.

In accordance with the experimental data available on the 123 ceramics, in order for the E effect to become manifest, the magnetic-vortex pinning should be strong enough. This is indicated by a correlation between the magnitude (or the presence) of the E effect and the dependence of I_c on a magnetic field, as well as by the suppression of the E effect by a magnetic field in the Y123 [24] and $DyBa_2Cu_{2.8}O_y$ samples. It is with this factor that the absence of the E effect in our experi-

Table 2. Comparative data on the electric field effect in HTSC single-crystal and bicrystal films and bulk samples

Sample	h	$\Delta I_c/I_c$, %	T, K	E, MV/m	$\Delta I_c/I_cE$, 10^{-3} m/MV	References
Y123 single crystal	15 nm	0.15	4.2	5	0.3	[25]
Y123 bicrystal:						
symmetric boundary, $\theta = 24°$	15 nm		4.2		≈0.8	[25]
symmetric boundary, $\theta = 36.8°$	15 nm	2	4.2	5	4.0	[25]
asymmetric boundary, $\theta = 45°$	15 nm	8	4.2	5	16	[25]
Y123 : 211 single crystal (35 vol%)	1.2 mm	4	77	120	0.3	[26]
$YBa_2Cu_{2.6}O_y$ ceramic	1.2 mm	7	77	120	0.6	[11]
$DyBa_2Cu_{2.8}O_y$ ceramic	1.2 mm	16	77	120	1.3	This work

ments with stoichiometric dysprosium ceramics (where a magnetic field is generated by the transport current) and the observation of the peak effect in the magnetic-field dependence of ΔV (Fig. 4) in the presence of the $I_c(B)$ peak effect (Fig. 1) in the $DyBa_2Cu_{3-x}O_y$/1 wt % Pt ceramic are associated.

Thus, the data presented in this work allow the more general conclusion that the electric field effect is correlated with the extent of the magnetic vortex pinning in ceramics with SIS-type weak links.

REFERENCES

1. J. Mannhart, Mod. Phys. Lett. B **6**, 555 (1992).
2. X. X. Xi, J. Supercond. **7**, 137 (1994).
3. V. V. Lemanov and A. L. Kholkin, Fiz. Tverd. Tela (St. Petersburg) **36**, 1537 (1994) [Phys. Solid State **36**, 841 (1994)].
4. J. Mannhart, Supercond. Sci. Technol. **9**, 49 (1996).
5. Z. G. Ivanov, E. A. Stepantsov, A. Ya. Tzalenchuk, *et al.*, IEEE Trans. Appl. Supercond. **3**, 2925 (1993).
6. V. V. Lemanov, A. L. Kholkin, and A. B. Sherman, Pis’ma Zh. Éksp. Teor. Fiz. **56**, 580 (1992) [JETP Lett. **56**, 562 (1992)].
7. B. I. Smirnov, S. V. Krishtopov, and T. S. Orlova, Fiz. Tverd. Tela (St. Petersburg) **34**, 2482 (1992) [Sov. Phys. Solid State **34**, 1331 (1992)].
8. B. I. Smirnov, T. S. Orlova, and S. V. Krishtopov, Fiz. Tverd. Tela (St. Petersburg) **35**, 2250 (1993) [Phys. Solid State **35**, 1118 (1993)].
9. T. S. Orlova and B. I. Smirnov, Supercond. Sci. Technol. **6**, 899 (1994).
10. T. S. Orlova, A. N. Kudymov, B. I. Smirnov, *et al.*, Physica C (Amsterdam) **253**, 194 (1995).
11. T. S. Orlova, B. I. Smirnov, and J.-Y. Laval, Fiz. Tverd. Tela (St. Petersburg) **40**, 1195 (1998) [Phys. Solid State **40**, 1088 (1998)].
12. T. S. Orlova, B. I. Smirnov, J. Y. Laval, and Yu. P. Stepanov, Supercond. Sci. Technol. **12**, 356 (1999).
13. T. S. Orlova, J. Y. Laval, A. Dubon, *et al.*, Supercond. Sci. Technol. **11**, 467 (1998).
14. T. S. Orlova, J. Y. Laval, C. Nguyen-van-Huong, and A. Dubon, Supercond. Sci. Technol. **12**, 1156 (1999).
15. T. S. Orlova, J. Y. Laval, and B. I. Smirnov, Mater. Phys. Mech. **1**, 39 (2000).
16. M. B. Field, D. C. Larbalestier, A. Parikh, and K. Salama, Physica C (Amsterdam) **280**, 221 (1997).
17. M. R. Koblischka, A. J. J. van Dalen, T. Higuchi, *et al.*, Phys. Rev. B **54**, R6893 (1996).
18. S. Shibata, A. K. Pradhan, and N. Koshizuka, Jpn. J. Appl. Phys. **38**, L1169 (1999).
19. H. Kupfer, Th. Wolf, C. Lessing, *et al.*, Phys. Rev. B **58**, 2886 (1998).
20. M. Ullrich, D. Muller, K. Heinemann, *et al.*, Appl. Phys. Lett. **63**, 406 (1993).
21. M. P. Delamare, M. Hervieu, J. Wang, *et al.*, Physica C (Amsterdam) **262**, 220 (1996).
22. I. Monot, K. Verbist, M. Hervieu, *et al.*, Physica C (Amsterdam) **274**, 253 (1997).
23. V. Ambegaokar and A. Baratoff, Phys. Rev. Lett. **10**, 486 (1963).
24. B. I. Smirnov, T. S. Orlova, and A. N. Kudymov, Fiz. Tverd. Tela (St. Petersburg) **36**, 1529 (1994) [Phys. Solid State **36**, 837 (1994)].
25. B. Mayer, J. Mannhart, and H. Hilgenkamp, Appl. Phys. Lett. **68**, 3031 (1996).
26. B. I. Smirnov, T. S. Orlova, S. Sengupta, and K. C. Goretta, Fiz. Tverd. Tela (St. Petersburg) **42**, 1172 (2000) [Phys. Solid State **42**, 1207 (2000)].
27. J. Mannhart and H. Hilgenkamp, Mater. Sci. Eng. B **B56**, 77 (1998).
28. H. Hilgenkamp and J. Mannhart, Appl. Phys. Lett. **73**, 265 (1998).
29. H. Hilgenkamp, C. W. Schneider, R. R. Schulz, *et al.*, Physica C (Amsterdam) **326–327**, 7 (1999).
30. N. D. Browning, P. D. Nellist, D. P. Norton, *et al.*, Physica C (Amsterdam) **294**, 183 (1998).
31. V. Windt, H. Haensel, D. Koelle, and R. Gross, Appl. Phys. Lett. **74**, 1027 (1999).

Translated by G. Skrebtsov

Physics of the Solid State, Vol. 43, No. 6, 2001, pp. 1012–1017. Translated from Fizika Tverdogo Tela, Vol. 43, No. 6, 2001, pp. 979–984.
Original Russian Text Copyright © 2001 by Andreev, Krasil'nik, Kuznetsov, Soldatkin, Bresler, Gusev, Yassievich.

SEMICONDUCTORS AND DIELECTRICS

Peculiarities of Photoluminescence of Erbium in Silicon Structures Prepared by the Sublimation Molecular-Beam Epitaxy Method

B. A. Andreev*, Z. F. Krasil'nik*, V. P. Kuznetsov*, A. O. Soldatkin*,
M. S. Bresler, O. B. Gusev**, and I. N. Yassievich****
** Institute for Physics of Microstructures, Russian Academy of Sciences, Nizhni Novgorod, 603600 Russia*
*** Ioffe Physicotechnical Institute, ul. Politekhnicheskaya 26, St. Petersburg, 194021 Russia*

Received November 9, 2000

Abstract—The photoluminescence of semiconducting structures Si : Er : O/Si grown by the molecular-beam epitaxy method is studied. The dependences of Er photoluminescence intensity on the intensity of pumping are measured at the liquid helium temperature. An analysis of the experimental results on the basis of the exciton model of excitation of Er ions in a crystalline silicon matrix reveals the significant role played by an alternative channel of free-exciton trapping (apart from the donor energy levels of erbium–oxygen complexes), as well as that played by the nonradiative channel in the recombination of excitons, bound to erbium donors, without the excitation of erbium. The ratio of the concentration of optically active centers of erbium luminescence to the total concentration of introduced erbium is estimated. © *2001 MAIK "Nauka/Interperiodica".*

1. INTRODUCTION

The new stage in the study of radiative recombination of silicon structures is associated with the attempts to obtain stimulated radiation at a wavelength of 1.54 μm under optical pumping [1, 2]. Sublimation molecular-beam epitaxy (MBE) is a promising method of creating light-emitting Si : Er/Si structures with a high photoluminescence (PL) intensity [3]. An increase in the photoluminescence efficiency is associated, among other things, with an increase in the fraction of optically active erbium centers in Si. According to estimates [4], the fraction of optically active erbium in samples obtained by ion implantation amounts to 1 to 10% of the number of implanted erbium ions. It has been proved [5, 6] that the maximum concentration of optically active erbium in implanted structures does not exceed 3×10^{17} cm^{-3} for a total concentration of introduced erbium up to 2×10^{20} cm^{-3}. The ratio of the concentration of optically active centers to the total concentration of erbium introduced in the structures grown by the SMBE method and characterized by a high PL intensity [7] has not been determined. It would also be interesting to estimate the efficiency of luminescence excitation in epitaxial structures.

The aim of the present work is to analyze the peculiarities of PL of the epitaxial Si : Er : O/Si structures grown by the SMBE method and to estimate the fraction of optically active forms of erbium in the epitaxial layers and the efficiency of their excitation.

2. EXPERIMENT

The epitaxial structures used by us were grown by the sublimation MBE method on Si:B(100) substrates [3]. According to the secondary-ion mass spectrometry (SIMS) data presented in Fig. 1, the erbium concentration was 5×10^{18} cm^{-3} (structure no. 37) and 1×10^{18} and (1 to 2) $\times 10^{17}$ cm^{-3} in structures nos. 17 and 16, respectively. The oxygen content for structure no. 37 was more than an order of magnitude higher than the erbium concentration in the epitaxial layers of structures nos. 17 and 16, while the concentration of phosphorus, boron, and aluminum impurities varied from 2×10^{16} to 7×10^{17} cm^{-3}. Structure no. 37 with a doped-layer thickness of 1.8 μm was grown at a higher temperature of the substrate (as compared to structures nos. 16 and 17). Structures 17 and 16 were annealed in hydrogen for 30 min at 800 and 900 K, respectively. The effect of annealing on the luminescence properties of epitaxial structures is described in [7]. The PL spectra were recorded on a BOMEM DA3-36 Fourier spectrometer at 4.2 and 78 K in the frequency range from 6000 to 10000 cm^{-1} with a resolution up to 0.5 cm^{-1}. The radiation of Kr$^+$ and Ar$^+$ lasers with a wavelength of 647 and 514.5 nm, respectively (the pumping radiation was up to 500 mW), as well as the radiation from a light-emitting diode with a wavelength of 640 nm and a power up to 6 mW, was used for pumping. The luminescence decay time was measured with the help of a digital oscilloscope.

1063-7834/01/4306-1012$21.00 © 2001 MAIK "Nauka/Interperiodica"

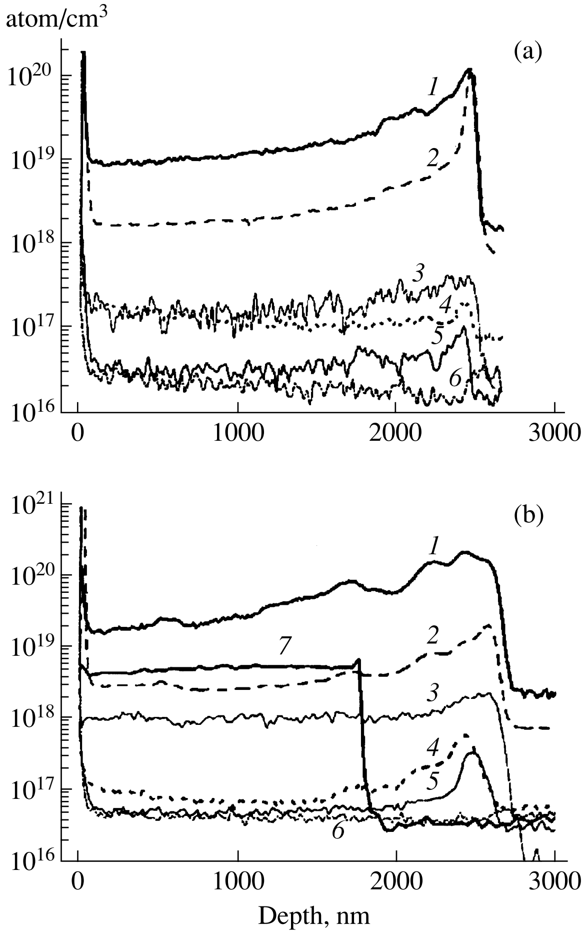

Fig. 1. Impurity concentration distribution in epitaxial layers of silicon according to the SIMS data for structures nos. (a) 16 and (b) 17: O (*1*), C (*2*), Er (*3*), Al (*4*), P (*5*), and B (*6*). Structure no. 37: Er (*7*).

3. EXPERIMENTAL RESULTS

The PL spectra of the Si : Er epitaxial layers presented in Fig. 2 correspond to the intracenter transition $^4I_{13/2} \longrightarrow {}^4I_{15/2}$ of the Er^{3+} ion and are formed by a broad (≈30 cm^{-1}) band with a peak at 6500 cm^{-1} (which, according to Jantsch *et al.* [8], can be attributed to erbium in Si–Er–O precipitates) and a series of narrow peaks (~1 cm^{-1} wide) corresponding to an isolated oxygen-containing center Er-1, which is typical of SMBE [9]. In the sequence of structures nos. 16–17–37, the total PL intensity increases abruptly due to the band of optically active erbium in the precipitates. The PL intensity of the Er-1 center in sample no. 17 is 3.5 times higher than in sample no. 16, but the fraction of radiation emitted by the Er-1 center in the total PL intensity decreases. In the high-frequency region at helium temperatures, the luminescence spectrum of excitons bound to atoms of electrically active shallow impurities is observed. The photoluminescence of free excitons, as well as excitons bound to erbium, is not observed.

The luminescence intensity for the lines emitted by the Er-1 center and the broad band of erbium in the precipitates as a function of the pumping power is presented in Fig. 3. The observed dependence can be described using the expression [10]

$$I_{\mathrm{PL}} = abP/(1+bP), \qquad (1)$$

where

$$b = Q\tau, \quad a \sim N_0^{\mathrm{Er}}\tau_d.$$

Here, P is the pumping power; Q is a factor taking into account the quantum efficiency and depending on temperature, the wavelength of exciting radiation, and geo-

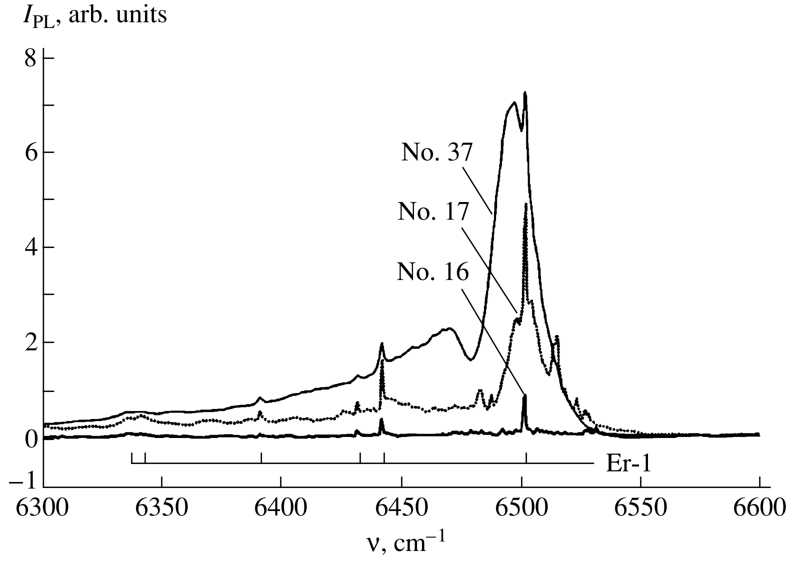

Fig. 2. Photoluminescence spectra of epitaxial structures at T = 4.2 K. The resolution is 1 cm^{-1}, and the pumping radiation power is ≈100 mW.

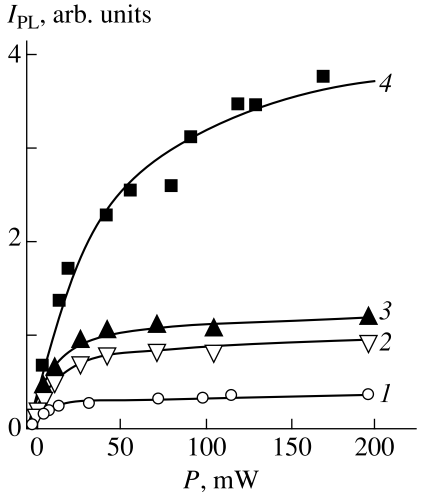

Fig. 3. Dependence of the PL intensity on the pumping power at 4.2 K. Curves *1* and *2* correspond to the lines emitted by an Er-1 center in structures nos. 16 and 17, respectively, while curves *3* and *4* correspond to the 6500-cm^{-1} band in structures nos. 17 and 37, respectively. Solid curves are calculated by Eq. (1) for structures nos. 16, 17, and 37.

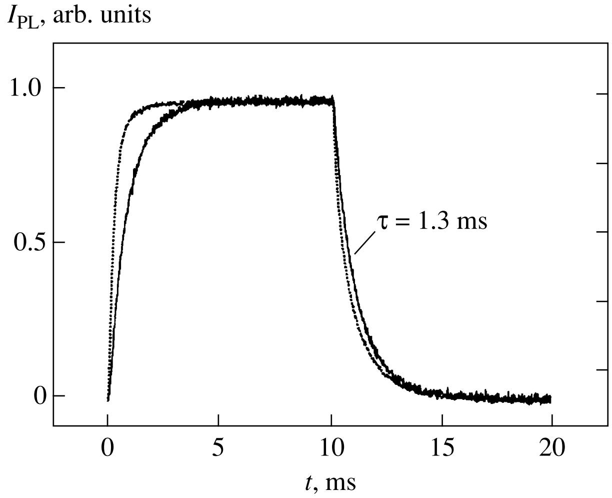

Fig. 4. Oscillograms of an erbium PL signal for structures nos. 17 (dotted curve) and 37 (solid curve) for the excitation power density $0.35\ \text{mW/mm}^2$.

metrical parameters; N_0^{Er} is the concentration of optically active Er^{3+} ions; and τ and τ_d are the total and radiative lifetimes of Er^{3+} in the excited state, respectively. The luminescence intensity is proportional to $N_{\text{Er}}^{*} w_{\text{rad}}$, where N_{Er}^{*} is the concentration of excited Er^{3+} ions and $w_{\text{rad}} = \tau_d^{-1}$ is the probability of radiative transition.

The results depicted in Fig. 3 and listed in the table show that the coefficients b characterizing the increase in the PL intensity in the region of linear dependence on the pumping level have the same value for the lines corresponding to the Er-1 center in structures nos. 16 and 17 with different concentrations N_0 of the optically active centers containing erbium ions. In the case of saturation, we have $I_{\text{PL}} = a$, and $a_1/a_2 = N_0^1/N_0^2$ for the two samples (if we assume that the lifetime τ_d does not vary with the sample type). The equality of the coefficients b for the line spectrum of the Er-1 center and for the broad PL band of Er^{3+} in the precipitates in structure no. 17 is also worth noting. Thus, the law of the increase in the number of excited Er ions (and in the PL intensity) with an increase in the power of pumping radiation for the uniformly doped structures nos. 16 and 17 does not depend on the concentration and nature of the optically active centers containing erbium. The fourfold increase in the concentration of optically active centers and in the PL intensity at saturation in structure no. 37 as compared to structure no. 17 leads to a decrease in the value of b, and the efficiency of the excitation of Er^{3+} ions decreases.

Figure 4 presents the results of measurements of the time of rise and fall of the erbium PL in structures nos. 17 and 37 at the liquid nitrogen temperature. The rise time differs from the fall time because of the nonlinear dependence of the PL intensity on pumping, which is described by Eq. (1); the effect of nonlinearity is stronger for a structure characterized by a larger value of parameter b. Indeed, the turn-on time for a pumping pulse is described by

$$I/\tau_{on} = (I + bP)/\tau,$$

which allows us to determine the lifetime of erbium in the excited state.

Parameters characterizing the dependence of PL intensity on pumping power

Structure	Emitting center	$a \times 10^{-3}$, arb. units (at $T = 4.2$ K)	b, mW^{-1} (at $T = 4.2$ K)	τ_{exp}, ms (at $T = 80$ K)
No. 16	Er-1	0.26	0.086 ± 0.020	0.01
No. 17	Er-1	0.87	0.085 ± 0.008	Not measured
No. 17	Er in precipitates, 6500-cm^{-1} band	1.1	0.087 ± 0.010	1.3
No. 37	Er in precipitates, 6500-cm^{-1} band	4.4	0.025 ± 0.004	1.3

The lifetime of the excited state of the Er^{3+} ion for structures nos. 17 and 37 is given in the table. It is measured for a PL signal in the emission band of Er in the precipitates. In structure no. 16, where the Er-1 center dominates, $\tau_{exp} = 10$ μs, which is apparently due to a rapid nonradiative Auger process of deexcitation of this center. The concentration of equilibrium charge carriers in structure no. 16 [$n \approx (2 \text{ to } 3) \times 10^{17}$ cm^{-3} at $T = 80$ K] corresponds to the measured lifetime for the known value of the coefficient $C_A = 5 \times 10^{-13}$ cm^3/s of the Auger deexcitation process. The total lifetime τ in samples nos. 17 and 37 is quite long and close to the radiative lifetime of the erbium ion. At a low temperature of 4.2 K, when the nonradiative Auger deexcitation of erbium is suppressed, the total lifetime τ for isolated Er-1 centers is also close to the radiative lifetime.

The measured lifetime of Er ions in the excited state is close to the available values for structures grown by the MBE method (e.g., $\tau = 1.8$ to 0.33 ms in [10]). At the same time, parameter b is not only determined by the efficiency of excitation (excitation cross section) of erbium ions in the given structure but also depends on the extent of focusing of the pumping radiation; i.e., its values cannot be directly compared with those from experiments made on different setups.

4. DISCUSSION OF THE MEASURED PL OF DIFFERENT STRUCTURES

For interpreting the results obtained, the existing model [11, 12] for the exciton mechanism of exciting the Er^{3+} ion in Si was supplemented with an alternative (relative to the optically active centers containing Er^{3+} with concentration N_0^E) channel for free-exciton trapping that is associated with binding an exciton to other shallow impurity centers (P, B, etc.). In addition, the possibility of recombination of an exciton bound to erbium without an energy transfer to the 4*f* shell of the erbium ion was taken into account. We denote the total concentration of exciton trapping centers in the alternative channel by N_0^P. Here and henceforth, we denote the quantities characterizing the optically active erbium by the index *E* and the quantities pertaining to the alternative channel of exciton trapping by the index *P*.

The balance equations for the concentration of electron–hole pairs, free excitons, excitons bound to erbium and to phosphorus ions, and excited erbium atoms are

$$G = \gamma np + \gamma_x np, \tag{2a}$$

$$\gamma_x np = n_x/\tau_x + c_E N_0^E n_x + c_P N_0^P n_x, \tag{2b}$$

$$c_E N_0^E n_x = n_{xb}^E/\tau_{xb}^E + n_{xb}^E(1 - N_E^*/N_0^E)/\tau^*, \tag{2c}$$

$$c_P N_0^P n_x = n_{xb}^P/\tau_{xb}^P, \tag{2d}$$

$$n_{xb}^E(1 - N_E^*/N_0^E)/\tau^* = N_E^*/\tau_d. \tag{2e}$$

Here, G is the generation rate of electron–hole pairs; n and p are the concentrations of free electrons and holes, respectively; n_x is the concentration of free excitons; n_{xb}^E and n_{xb}^P are the concentrations of excitons bound to erbium and phosphorus ions, respectively; γ is the bimolecular rate constant for free electron–hole recombination; γ_x is the rate constant for their binding into excitons; c_E and c_P are the coefficients of free exciton trapping by erbium and phosphorus levels, respectively; τ_x, τ_{xb}^E, and τ_{xb}^P are the lifetimes of free excitons and excitons bound to erbium and phosphorus, respectively; τ^* is the characteristic time of the Auger excitation process; and N_0^E and N_0^P are the concentrations of optically active erbium and phosphorus ions.

The system of balance equations is written in the low-temperature approximation, where the decay of excitons into pairs, the detrapping of bound excitons, and the deexcitation of erbium ions (i.e., all the processes are characterized by an activation energy) can be neglected.

Approximate analytical solutions of the system of balance equations for two cases (under the assumption that $\gamma \ll \gamma_x$ and that the main channel for loss of free excitons is their trapping at the donor energy levels of erbium or phosphorus) will be considered here.

(1) At $N_0^P \ll N_0^E$, the alternative channel for free-exciton trapping can be disregarded and we have

$$N^* = N_0^E G b_1/(1 + G b_1), \quad b_1 = (\tau_{xb}^E/\tau^*)\tau_d/N_0^E. \tag{3}$$

This solution is obtained in the approximation $\tau_{xb}^E \ll \tau^*$, which can be substantiated by the estimate $\tau_{xb}^E \sim 3$ ns following from review [13]; according to [12], $\tau^* \sim 0.2$ μs. Solution (3) differs insignificantly from the exact solution of the system of balance equations obtained numerically. It should be noted that for increasing pumping power, the value of N^* is determined by the concentration of optically active erbium and is independent of the concentration N_0^P. For a low power, N^* is also independent of N_0^E. The physical meaning of the latter statement is clear: the intensity is determined not by the number of centers containing Er^{3+} but by the number of generated free excitons, which is small in comparison with the number of centers of their trapping.

(2) At $N_0^P \gg N_0^E$, the alternative channel prevails and, if the generation rate is such that $G \ll N_0^P/\tau_{xb}^P$, the solution has the form

$$\begin{gathered} N^* = N_0^E G b_1/(1 + G b_1), \\ b_1 = (c_E/c_P)(\tau_{xb}^E/\tau^*)\tau_d/N_0^P. \end{gathered} \tag{4}$$

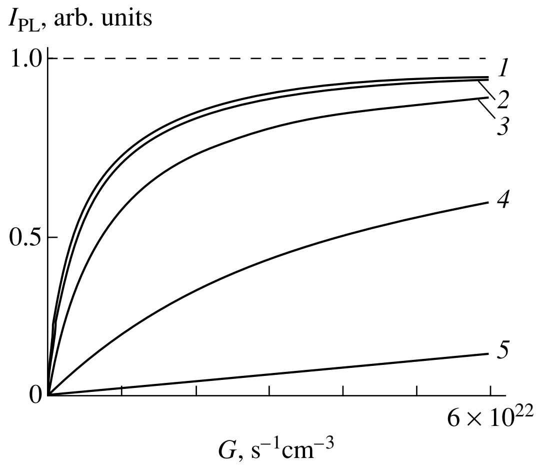

Fig. 5. Dependences of N^*/N_0^E on the pair generation rate G for various concentrations N_0^E, obtained from the numerical solution of the system of balance equations for $T = 4.2$ K and $N_0^P = 6 \times 10^{16}$ cm^{-3}. The maximum generation rate 6×10^{22} s^{-1} cm^{-3} corresponds to a pumping power of ~200 mW. N_0^E, cm^{-3}: 6×10^{14} (*1*), 6×10^{15} (*2*), 6×10^{16} (*3*), 6×10^{17} (*4*), and 6×10^{18} (*5*).

The dependence of the number of excited centers with Er on the concentration of active centers is linear. The value of b_1 (and, therefore, the law describing the increase in N^* and in the FL intensity with an increase in the pumping power) does not depend on the concentration of optically active erbium and is determined by the alternative channel characterized by the concentration N_0^P.

The theoretical dependences of N^* on G obtained above have the form of Eq. (1), and the coefficients b_{Er} corresponding to b in Eq. (1) are given by

$$b_{Er} = \beta(\tau_{xb}^E/\tau^*)\tau_d/N_0^E \quad \text{for Eq. (3),} \tag{5}$$

$$b_{Er} = \beta(c_E/c_P)(\tau_{xb}^E/\tau^*)\tau_d/N_0^P \quad \text{for Eq. (4),} \tag{6}$$

where $G = \beta P$, $\beta = 3 \times 10^{20}$ s^{-1} cm^{-3} mW^{-1} provided that G is equal to the ratio of the number of photons supplied to the sample per unit time to the volume in which laser radiation is absorbed.

Figure 5 shows the results of numerical solution of the system of balance equations describing the dependence of N^*/N_0^E on G and on N_0^E for $T = 4.2$ K and $N_0^P = 6 \times 10^{16}$ cm^{-3}. In our computations, the values of $\tau^* = 0.2$ μs, $\tau_{xb}^E = 3$ ns, and $\tau_d = 1$ ms are used. The generation rate of 6×10^{22} s^{-1} cm^{-3} corresponds to an experimental pumping power of ~200 mW. For $N_0^P \ll N_0^E$ ($N_0^E = 6 \times 10^{17}$ to 6×10^{18} cm^{-3}), the solution is described by Eq. (5) and the dependence of N^*/N_0^E on the generation rate G is determined by the concentration N_0^E of optically active erbium. Conversely, for $N_0^P \gg N_0^E$ ($N_0^E = 6 \times 10^{14}$ to 6×10^{15} cm^{-3}), the solution is described by the approximate formula (6) and the law of the increase of N^*/N_0^E with G does not depend on the concentration N_0^E of optically active erbium but is instead completely determined by the concentration N_0^P of centers in the alternative channel for exciton trapping.

5. ESTIMATION OF THE CONCENTRATION OF OPTICALLY ACTIVE CENTERS

The equality of coefficients b for erbium centers of different origins in the case when the Er concentration varies considerably and the fact that the dependence of the PL intensity of optically active Er^{3+} centers on the pumping power is correctly described by Eq. (1) indicate that the alternative (relative to optically active erbium) channel of energy dissipation for pumping radiation dominates in structures nos. 16 and 17. In the framework of the exciton model, we can conclude that the limiting case in Eq. (6) ($N_0^P \gg N_0^E$) is realized. In this case, the experimentally determined value of b can be used for determining concentration N_0^P. Using Eq. (6), the experimental data from the table, and the values of β and the lifetime reported in [11, 14–16], we obtain $N_0^P \sim 6 \times 10^{16}$ cm^{-3}. A comparison of this result with the SIMS data presented in Fig. 1 shows that the share of optically active erbium atoms in the erbium total content in structure no. 17 does not exceed 6% and that electrically active shallow impurities can make a noticeable contribution to the trapping and recombination of free excitons. Since the optically active erbium is present in sample no. 17 mainly in the form of precipitates and the ratio between the total numbers of optically active Er-1 centers in samples nos. 17 and 16 (which is determined from the intensities of the PL lines emitted by the centers at saturation) is equal to 3.5, it is clear that the fraction of optically active erbium in sample no. 16 and the fraction of optically active erbium in the form of Er-1 centers in sample no. 17 are much smaller than 6%.[1] An increase in the concentration of optically active erbium atoms (structure no. 37) does not lead to an increase in the quantum efficiency of erbium excitation; this is apparently due to

---

[1] The shape of the spectrum shows that the optically active erbium is present in sample no. 16 mainly in the form of Er-1 centers; for this reason, the share of Er-1 centers in sample no. 16 is equal to the fraction of optically active centers with erbium.

a simultaneous increase in the concentration of nonradiative recombination centers containing erbium.

Thus, the necessary condition for increasing the efficiency of the exciton excitation of erbium (by using optical pumping or a diode under direct-bias conditions) in SMBE structures characterized by a long (>1 μs) lifetime of the erbium ion in the excited state and by a high PL intensity is that the generated excitons must be bound and recombine predominantly at erbium centers with an excitation transfer to the Er^{3+} ion. If the relation $N_0^P \gg N_0^E$ takes place for the recombination channels, the saturation of erbium luminescence will be attained at a considerably higher pumping power.

ACKNOWLEDGMENTS

The authors thank Yu.A. Karpov (Institute of Chemical Problems in Microelectronics, Moscow) for providing the sources for the SMBE process.

This work was supported by the Russian Foundation for Basic Research, project nos. 98-02-16619, 98-02-18246, and 99-03-32757; MNTP “Fundamental Spectroscopy,” project no. 08.02.043; MTsFPIN, grant no. 00-2-01; and INTAS, grant no. 99-01872.

REFERENCES

1. X. Zhao, S. Komuro, H. Isshiki, *et al.*, Appl. Phys. Lett. **74** (1), 120 (1999).
2. V. I. Emel’yanov, B. V. Kamenev, P. K. Kashkarov, *et al.*, Fiz. Tverd. Tela (St. Petersburg) **42** (8), 1372 (2000) [Phys. Solid State **42**, 1410 (2000)].
3. B. A. Andreev, A. Y. Andreev, H. Ellmer, *et al.*, J. Cryst. Growth **201–202**, 534 (1999).
4. J. Michel, F. Y. G. Ren, B. Zheng, *et al.*, Mater. Sci. Forum **143–147**, 707 (1994).
5. A. Polman, G. N. van den Hoven, J. S. Custer, *et al.*, J. Appl. Phys. **77**, 1256 (1995).
6. A. Polman, J. Appl. Phys. **82**, 1 (1997).
7. A. Yu. Andreev, B. A. Andreev, M. N. Drozdov, *et al.*, Fiz. Tekh. Poluprovodn. (St. Petersburg) **33** (2), 156 (1999) [Semiconductors **33**, 131 (1999)].
8. W. Jantsch, S. Lanzerstorfer, L. Palmetshofer, *et al.*, J. Lumin. **80** (9) (1999).
9. B. A. Andreev, A. Yu. Andreev, D. M. Gaponova, *et al.*, Izv. Akad. Nauk, Ser. Fiz. **64** (2), 269 (2000).
10. R. Serna, J. H. Shin, M. Lohrmeier, *et al.*, J. Appl. Phys. **79** (5), 2658 (1996).
11. O. B. Gusev, Doctoral Dissertation (Fiz.-Tekh. Inst. Ross. Akad. Nauk, St. Petersburg, 1998).
12. M. S. Bresler, O. B. Gusev, B. P. Zakharchenya, and I. N. Yassievich, Fiz. Tverd. Tela (St. Petersburg) **38** (5), 1474 (1996) [Phys. Solid State **38**, 813 (1996)].
13. G. Davies, Phys. Rep. **176**, 83 (1989).
14. W. Schmid, Phys. Status Solidi B **84**, 529 (1977).
15. T. Steiner and M. L. W. Thewalt, Solid State Commun. **49**, 1121 (1984).
16. J. C. Merle, M. Capizzi, F. Fiorini, and A. Frova, Phys. Rev. B **17**, 4821 (1978).

Translated by N. Wadhwa

Physics of the Solid State, Vol. 43, No. 6, 2001, pp. 1018–1024. Translated from Fizika Tverdogo Tela, Vol. 43, No. 6, 2001, pp. 985–991.

SEMICONDUCTORS AND DIELECTRICS

Local-Field Effects in Reflectance Anisotropy Spectra of the (001) Surface of Gallium Arsenide

V. L. Berkovits, A. B. Gordeeva, and V. A. Kosobukin

Ioffe Physicotechnical Institute, Russian Academy of Sciences, Politekhnicheskaya ul. 26, St. Petersburg, 194021 Russia

e-mail: Vladimir.Berkovits@pop.ioffe.rssi.ru

Received November 9, 2000

Abstract—Characteristic reflectance anisotropy spectra of the naturally oxidized (001) surfaces of GaAs undoped crystals and $Ga_{0.7}Al_{0.3}As$ epitaxial films are measured in the energy range 1.5–5.7 eV. The spectra are interpreted in the framework of the microscopic model proposed for a GaAs(001)/oxide interface and the reflectance anisotropy (difference) theory developed for a multilayer medium with a monolayer of atomic dipoles located near one of the interfaces. The anisotropy of dipole polarizability and the anisotropy of the plane lattice formed by dipoles are taken into account within the unified Green function approach of classical electrodynamics. A good agreement between the measured and calculated reflectance anisotropy spectra of the oxidized GaAs(001) surfaces shows that the local field effects at the semiconductor–oxide interface make the main contribution to these spectra. *© 2001 MAIK “Nauka/Interperiodica”.*

1. INTRODUCTION

In recent years, the differential optical method, which is also referred to as reflectance anisotropy spectroscopy, has been widely used in studies of the surfaces of cubic semiconductors [1]. For normally incident light, the reflectance anisotropy spectrum as a function of the photon energy is defined by the quantity

$$\frac{\Delta R}{R} = 2\frac{R_x - R_y}{R_x + R_y}, \qquad (1)$$

where R_x and R_y are the reflectivities of linearly polarized light along the orthogonal directions x and y, respectively. For the (001) surface, the x and y directions are chosen along the $[1\bar{1}0]$ and [110] axes lying in the surface plane.

Theoretically, semiconductors with a cubic symmetry in normally incident light can be treated as optically isotropic media, and, hence, the reflectance anisotropy signal ($\Delta R/R$) from the bulk of these crystals should be equal to zero. A nonzero signal can arise only from the lowered-symmetry surface structure. Recent investigations of A_3B_5 semiconductors demonstrated that the lowering of their symmetry in a subsurface region and the related reflectance anisotropy signals can be caused by a number of factors. For example, the atomically clean (001) surfaces of gallium arsenide have a lower symmetry due to reconstructions and, hence, exhibit characteristic reflectance anisotropy spectra [2]. These spectra can contain additional lines when submonolayer chemisorption coatings are formed by foreign atoms [3]. Moreover, the reflectance anisotropy spectra of GaAs(001) surfaces can involve signals induced by the electric field of a space-charge layer [4] and signals associated with ordered features of the surface relief, such as steps, etching pits, etc. [5]. The above contributions to the reflectance anisotropy spectra of GaAs(001) were reliably measured experimentally [2, 5–7] and interpreted theoretically [5, 8, 9].

Aspnes [5] was the first to establish that a naturally oxidized GaAs(001) surface is characterized by the reflectance anisotropy spectrum with the signal magnitude $|\Delta R/R| \sim 10^{-3}$ in the energy range 1.5–6 eV (the same spectral features were observed by Acosta-Ortiz and Lastras-Martinez [4]). In our recent work [10], the characteristic reflectance anisotropy spectra in this spectral range were also measured for the oxidized (001) surfaces of the solid solutions of the $Ga_{1-x}Al_xAs$ ternary compounds. Our subsequent investigations revealed that the reflectance anisotropy spectra of the oxidized (001) surfaces of GaAs and $Ga_{1-x}Al_xAs$ cannot be explained by the aforementioned mechanisms. Observation of the reflectance anisotropy spectra for naturally oxidized (001) surfaces of GaAs and $Ga_{1-x}Al_xAs$ [4, 5, 10] is a nontrivial fact, because the low-symmetry structure formed on the oxidized (001) surfaces of A_3B_5 semiconductors due to reconstructions, evidently, should not exist. Therefore, in order to explain the reflectance anisotropy observed for oxidized surfaces of A_3B_5 semiconductors, it is necessary to elucidate the origin and the mechanism of this effect.

In this respect, the aim of the present work was to investigate experimentally and theoretically the reflectance anisotropy spectra of naturally oxidized $A_3B_5(001)$ surfaces. To accomplish this, we performed systematic investigations into the reflectance anisotropy spectra of the (001) surfaces of GaAs and $Ga_{1-x}Al_xAs$. In order to interpret these spectra, we proposed a theoretical model (in a more general form compared to the models used in earlier works [11–13]) which describes the local field effects associated with both the anisotropy of the lattice structure and the anisotropy of the dipole polarizability in surface layers. This paper is organized as follows. In Section 2, we discuss the microstructure of the oxidized GaAs(001) surface. The experimental technique and the experimental data are described in Section 3. The general theory of local field effects in reflectance anisotropy spectroscopy is presented in Section 4. In Section 5, the results obtained are applied to analyze numerically the reflectance anisotropy spectra of naturally oxidized GaAs(001) surfaces. The main conclusions are summarized in Section 6.

2. STRUCTURE OF THE NATURALLY OXIDIZED GaAs(001) SURFACE

The optical response of a material is determined by the optical dipole transitions induced by an electric field of an incident light wave. Therefore, the anisotropic optical response of cubic crystals can be caused by two main factors: (1) the symmetry of the surface *lattice* of the dipoles and (2) the anisotropy of the optical polarizability of the *dipoles* themselves. Since dipoles form a square lattice on oxidized $A_3B_5(001)$ surfaces, the reflectance anisotropy signal in A_3B_5 crystals can arise only due to the anisotropy of covalent bond polarizability.

The manifestation of dipole–dipole interactions in the optical spectra can be explained by local field effects. These effects are associated with the difference between the macroscopic field of an incident wave and the electric light field which induces dynamic dipoles on the surface. In essence, the local field effects are effects of classical electrodynamics and, as a rule, are considered in the framework of the atomic point dipole model [11–13]. As is known, surface local-field effects clearly manifest themselves in linear [12, 13] and nonlinear [14] optical spectroscopy of metals with layers of adsorbed molecules. In the case of semiconductors, the local field effects were used by Mochan and Barrera [15] in order to interpret the reflectance anisotropy spectra of Ge(110) and Si(110) clean surfaces under the assumption that atoms of the semiconductor on its surface possess anisotropic polarizability.

In A_3B_5 crystals, the fundamental optical effects induced by the dipole structure of surface layers are still not understood. For naturally oxidized surfaces, this is explained, in large measure, by the lack of reliable data on the microstructure of semiconductor–oxide interfaces. However, in the case of the GaAs(001) surface, this structure can be determined from the data on the chemical composition of the oxide film. At present, this composition has been determined in sufficient detail [16]. It is well known that the approximately 25 Å thick outer layer in this film is amorphous and consists of Ga_2O_3 and As_2O_3 oxides. According to Gerard *et al.* [16], the oxide layer and the crystal surface are separated by a layer of the so-called excess arsenic $As^{(0)}$, which is accumulated on the GaAs/oxide interface as a result of incomplete oxidation of the semiconductor material. It can be assumed that excess arsenic atoms will form bonds with atoms of the crystal surface as long as two adjacent crystal layers composed of As atoms are formed. As is known, two arsenic crystal layers are also formed during adsorption of arsenic from the vapor phase on atomically clean GaAs(001) surfaces [17].

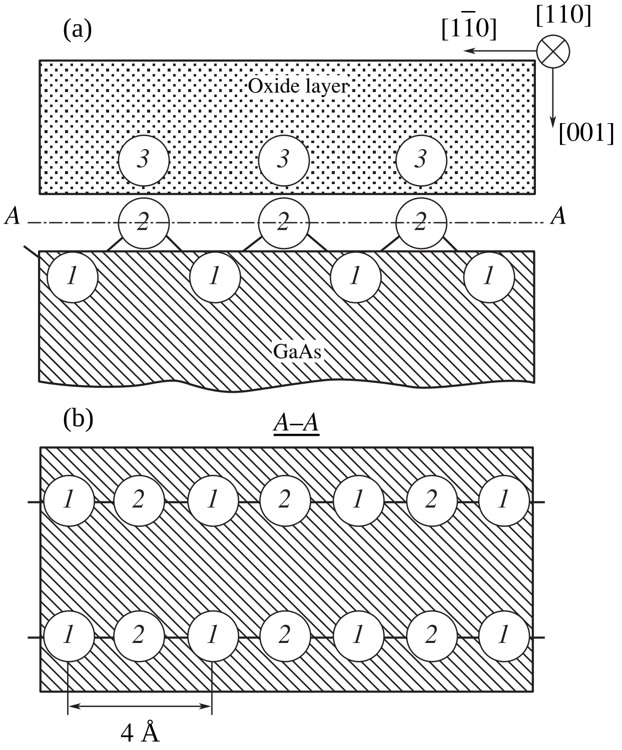

Fig. 1. A hypothetical structure of the GaAs(001)/oxide interface: (a) the vertical section and (b) the section along the horizontal plane *A–A*. Numerals indicate the As atoms located in the (*1*) GaAs crystal, (*2*) chemisorbed layer, and (*3*) amorphous layer.

In this case, the microstructure of the GaAs/oxide interface can be represented in the form depicted in Fig. 1. Crystal layer *1* of GaAs (Fig. 1a) consists of As atoms in an sp^3-hybridization. As in the (001) plane in the bulk of GaAs, the As atoms of layer *1* form a two-dimensional square lattice with a spacing of 4 Å (Fig. 1b). Layer *2* is a transition layer between the GaAs crystal and the oxide film and consists of chemisorbed As atoms. The hybridization of their bonds is unknown, but, most likely, it is intermediate between the sp^3- and sp^2-hybridizations. Atoms of layer *2* also form a two-dimensional square lattice (with a spacing of 4 Å) which is shifted by half the lattice spacing (2 Å) toward the $[1\bar{1}0]$ direction with respect to the lattice of

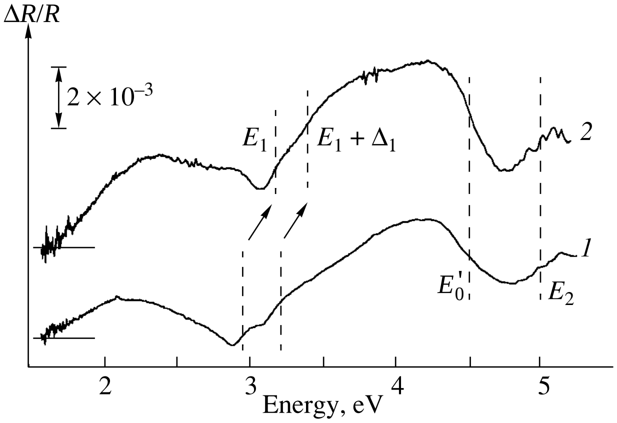

Fig. 2. Experimental reflectance anisotropy spectra $\Delta R/R$ of the oxidized (001) surfaces of (*1*) a weakly doped GaAs crystal and (*2*) an $Al_{0.3}Ga_{0.7}As$ epitaxial film. Dashed vertical lines indicate the location of bulklike optical transitions. Horizontal straight-line segments at the left of the spectra correspond to zero signals. The scale of the $\Delta R/R$ quantity is shown along the ordinate axis.

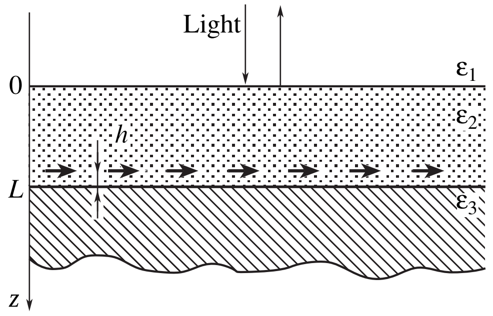

Fig. 3. A schematic representation of the three-layer dielectric medium with a layer of microscopic induced dipoles (horizontal arrows) for the description of the reflectance anisotropy.

layer *1* (Fig. 1b). Layer *3* containing arsenic and oxides of gallium and arsenic is amorphous. Consequently, each of the layers *1–3* (Fig. 1a) has an atomic configuration which, in the case of isotropic polarizability of the atomic dipoles, is characterized by the macroscopic isotropic dielectric response in the (001) plane.

The polarizabilities of atoms in surface layer *1* in the $[1\bar{1}0]$ and [110] directions are identical and equal to the polarizability of atoms in the (001) plane in the bulk of GaAs. The mean polarizability of amorphous layer *3* is also the same for all directions of the (001) plane. Hence, we assume that only the anisotropy of the atomic polarizability in layer *2* can be responsible for the reflectance anisotropy effect [4, 5, 10]. Hereafter, we will assume that the polarizability in the $[1\bar{1}0]$ direction is larger than that in the [110] direction, because chemical bonds between atoms of layers *1* and *2* have the projection only onto the $[1\bar{1}0]$ direction (Fig. 1b). Note that bonds between the atoms of layers *2* and *3* do not contribute to the anisotropy of polarizability in the surface plane.

3. EXPERIMENT

The reflectance anisotropy spectra of the (001) surfaces were measured for undoped GaAs samples with a residual impurity concentration of the order of 10^{15} cm^{-3} and undoped $Ga_{0.7}Al_{0.3}As$ epitaxial films 1 μm thick. The choice of crystals with a minimum dopant concentration makes it possible to prevent the appearance of reflectance anisotropy signals due to the near-surface electric field of a space-charge layer in the spectrum [4]. Prior to experiments, the surfaces of GaAs samples were degreased with acetone and were then slightly refreshed in a $5H_2SO_4 : 1H_2O_2 : 1H_2O$ etchant. The samples were washed with deionized water, dried, and allowed to stand in air for a day with the aim of forming the stable oxide phase. All the spectra were recorded at room temperature. The experimental setup employed for recording the reflectance anisotropy spectra was described in detail in [7]. A xenon lamp was used as a light source, which ensured the measurement of the spectra in the UV range (to approximately 5.7 eV).

The experimental reflectance anisotropy spectra of the oxidized (001) surfaces of GaAs and $Ga_{0.7}Al_{0.3}As$ samples are shown in Fig. 2. These spectra are similar in shape and consist of two broad spectral features ($\Delta R/R > 0$) separated by a boundary at about 3 eV. Both spectra exhibit a weak structure in the range of the bulklike transitions E_1 and $E_1 + \Delta_1$ and also a more intense broad minimum that covers the range between the bulklike transitions E_0' and E_2. It was found that these spectra are typical. Irrespective of the procedure of preparation of the oxidized (001) surface and the growth of GaAs crystals, their reflectance anisotropy spectra show the same characteristic features as in the spectra displayed in Fig. 2. On the other hand, the spectra shown in Fig. 2 differ radically from the relevant spectra of the atomically clean (001) surfaces of the same compounds [2, 10].

In principle, the narrow spectral features observed at energies that correspond to the bulklike optical transitions could be assigned to the disturbance of the subsurface crystal region by the electric field of a space-charge layer or by deformation. However, a similar explanation is inapplicable to the two broad features shown in Fig. 2 with maxima in the spectral ranges in which bulklike transitions are absent.

4. THEORY

In this section, according to the standard experimental scheme, we develop the reflectance anisotropy (difference) theory for a semiconductor surface covered with an oxide layer. Let us consider an electrodynamic model (Fig. 3) under the following assumptions. (1) A multilayer medium in the vicinity of one of its interfaces contains a microscopically thin layer of dipoles. (2) Dipoles possess their own anisotropic polarizability, which is constant in the optical range. (3) A lattice whose sites are occupied by dipoles is anisotropic; i.e., it has different lattice parameters along the principal axes of the polarizability tensor. Assumptions 1 and 3 essentially distinguish the proposed theory from the theories developed earlier in [11–15, 18], which dealt with surface square lattices in the vicinity of isolated surfaces.

This problem is solved by the perturbation method. As an unperturbed model, let us consider a medium formed by optically isotropic layers, which are characterized by the local permittivity tensor with the components $\varepsilon^0(z)\delta_{\alpha\beta}$, where $\delta_{\alpha\beta}$ is the Kronecker delta with the Cartesian indices α and β. According to Fig. 3, the function $\varepsilon^0(z)$ is equal to ε_1 at $z < 0$ (vacuum), ε_2 at $0 < z < L$ (oxide), and ε_3 at $z > L$ (semiconductor). A dipole layer which is considered a perturbation is located in the plane $z = z_0 = L - h$ at a microscopic distance h from the semiconductor surface ($h \ll L$).

It is assumed that the monochromatic light wave $\mathbf{E}^{(0)}(\mathbf{r}, t) = \mathbf{e}_\alpha E^{\text{inc}}\exp(-i\omega t + i\sqrt{\varepsilon_1}\,k_0 z)$ with a frequency ω ($k_0 = \omega/c$) and a linear polarization along one of the unit vectors $\mathbf{e}_x$ or $\mathbf{e}_y$ is incident normal to the crystal surface $z = 0$ from medium *1* ($z < 0$). In the surface layer, this wave induces quasi-point dipoles, which make the following contribution to the dielectric polarization:

$$P_\alpha(\mathbf{r}) = \delta(z - z_0)\sum_{\mathbf{n}}\delta(\mathbf{R} - \mathbf{R_n})\chi^{(\alpha)}E_\alpha(z_0, \mathbf{R_n}). \quad (2)$$

Here, $\mathbf{r} = (z, \mathbf{R})$, $\mathbf{R} = (x, y)$, the radius vectors $\mathbf{R_n} = \mathbf{e}_x n_1 a + \mathbf{e}_y n_2 b$ determine the sites of the two-dimensional dipole lattice with parameters $a \neq b$ (a and $b \ll k_0^{-1}$), $\mathbf{e}_\alpha$ is the unit vector of the αth Cartesian axis, $\chi^{(\alpha)}$ stands for the principal components of the anisotropic polarizability tensor, and $\mathbf{E}(z_0, \mathbf{R_n})$ is the total field acting on the $\mathbf{n}$th dipole with $\mathbf{n} = (n_1, n_2)$. The components of the unperturbed (in the absence of dipoles) electric field $E^{(0)}_\alpha$ and the tensor Green's function $G^{(0)}_{\alpha\beta}$ (the electromagnetic response of the multilayer medium to a unit point dipole located at the point $\mathbf{r}'$) are determined by the equations [19]

$$\sum_\mu\left[\sum_\nu \text{rot}_{\alpha\nu}\text{rot}_{\nu\mu} - \delta_{\alpha\mu}\varepsilon^0(z)k_0^2\right] \times \{E^{(0)}_\mu(\mathbf{r}), G^{(0)}_{\mu\beta}(\mathbf{r}, \mathbf{r}')\} = \{0, \delta_{\alpha\beta}\delta(\mathbf{r} - \mathbf{r}')\}, \quad (3)$$

where $\text{rot}_{\alpha\beta} = \sum_\gamma e_{\alpha\gamma\beta}(\partial/\partial r_\gamma)$ and $e_{\alpha\gamma\beta}$ are the components of the unit antisymmetric pseudotensor. The solutions of the differential equations (3), i.e., the electric field $\mathbf{E}^{(0)}(\mathbf{r})$ and the tensor Green's function $\hat{G}^{(0)}(\mathbf{r}, \mathbf{r}')$, meet the Maxwell boundary conditions with respect to the variable $\mathbf{r}$ and the index α at the interfaces (at $z = 0$ and L). The general solution of problem (3) was obtained in [20].

In the presence of perturbation (2), the electric field at the point $\mathbf{r}$ is determined by the integral equation

$$E_\alpha(z, \mathbf{R}) = E^{(0)}_\alpha(z, \mathbf{R}) + 4\pi k_0^2\sum_{n_1, n_2}\sum_\beta G^{(0)}_{\alpha\beta}(z_0, z_0; \mathbf{R} - \mathbf{R_n})\chi^{(\beta)}E_\beta(z_0, \mathbf{R_n}). \quad (4)$$

In our problem, the α and β indices take the values of x or y. The equation for the field acting on the $\mathbf{m}$th dipole is derived from Eq. (4) at $z = z_0$ and $\mathbf{R} = \mathbf{R_m}$. Then, the term with $\mathbf{n} = \mathbf{m}$, which corresponds to the self-action, is eliminated from the sum over $\mathbf{n}$ in Eq. (4). By definition, the second term on the right-hand side of Eq. (4) describes the local field effects. In the general case, this term is determined by the retarded interaction of the specified $\mathbf{m}$th dipole with other dipoles of the surface layer and with layers of image dipoles.

In the case when a, b, and $h \ll k_0^{-1}$, it is convenient to use a quasi-static analog of Eq. (4), which corresponds to $c \longrightarrow \infty$. Finally, at $h \ll L$, in the calculation of the quasi-static field, it is sufficient to take into account the interaction of actual dipoles with only their images associated with the interface closest to the layer ($z = L$ in Fig. 3). After these simplifications, the field [see Eq. (4)] acting on a dipole in the layer $z = z_0$ is represented in the form

$$\mathbf{E} = \mathbf{E}^{(0)} + \mathbf{E}^{(1)} + \mathbf{E}^{(2)}, \quad (5)$$

where the contributions $\mathbf{E}^{(1)}$ and $\mathbf{E}^{(2)}$ are determined by the direct interaction of dipoles in the layer and their interaction with the nearest layer of image dipoles, respectively. The $\mathbf{E}^{(1)}$ and $\mathbf{E}^{(2)}$ components for the model shown in Fig. 3 are expressed through the total field by formulas (A.1) and (A.3), which are given in the *Appendix*. The results of the self-consistent solution of Eq. (5) with due regard for formulas (A.1)–(A.4) are substituted into Eq. (1). This leads to the following relationship for the differential reflectivity:

$$\frac{R_x - R_y}{R} = \frac{16\pi\sqrt{\varepsilon_1}(\omega/c)}{ab} \times \text{Im}\left\{\Lambda(\Psi)\left[\frac{\chi^{(x)}}{1 - X\chi^{(x)}} - \frac{\chi^{(y)}}{1 - Y\chi^{(y)}}\right]\right\}. \quad (6)$$

Here, $R = (R_x + R_y)/2$, $\Psi = \exp(2i\sqrt{\varepsilon_2}\,\omega L/c)$,

$$\Lambda(\Psi) = -\frac{4\varepsilon_2}{(\sqrt{\varepsilon_1} + \sqrt{\varepsilon_2})^2(\sqrt{\varepsilon_2} + \sqrt{\varepsilon_3})^2} \times \frac{\Psi}{(r_{12} + r_{23}\Psi)(1 + r_{12}r_{23}\Psi)},$$

and $r_{kl} = (\sqrt{\varepsilon_k} - \sqrt{\varepsilon_l})/(\sqrt{\varepsilon_k} + \sqrt{\varepsilon_l})$ is the coefficient of reflection of normally incident light from the planar

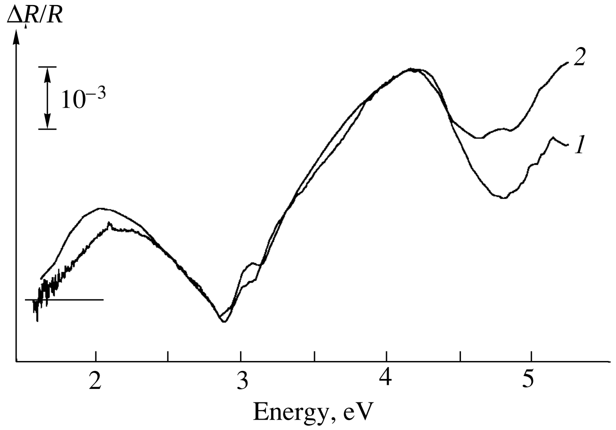

Fig. 4. (*1*) Experimental and (*2*) theoretical reflectance anisotropy spectra $\Delta R/R$ of the naturally oxidized GaAs(001) surface. The scale of the $\Delta R/R$ quantity is shown along the ordinate axis.

interface between the media k and l upon incidence from the medium k (the roots $\sqrt{\varepsilon_k}$ are calculated so that $\mathrm{Im}\sqrt{\varepsilon_k} > 0$).

In relationship (6), the quantities $X = X^{(1)} + X^{(2)}$ and $Y = Y^{(1)} + Y^{(2)}$, which are expressed in terms of the lattice sums of types (A.2) and (A.4), describe the dependence of the local field effects on the light polarization direction. For direct dipole–dipole interactions with due regard for formulas (A.2) and (A.5), we obtain

$$X^{(1)} = -\frac{1}{\varepsilon_2 a^3}\eta^3 F_1(\eta), \quad Y^{(1)} = -\frac{1}{\varepsilon_2 a^3}F_1(1/\eta), \quad (7)$$

where $\eta = a/b$,

$$F_1(\eta) = \frac{4}{\eta^3}\left[8\pi\sum_{m=1}^{\infty}\sum_{n=1}^{\infty} m^2 K_0\left(\frac{2\pi mn}{\eta}\right) - \zeta(3)\right], \quad (8)$$

$K_0(z)$ is the Macdonald function, and $\zeta(n)$ is the Riemann zeta function [$\zeta(3) = 1.202$].

Taking into account the interaction with image dipoles with the use of the lattice sums (A.4) and (A.6), we obtain

$$\begin{aligned} X^{(2)} &= -\frac{\varepsilon_2 - \varepsilon_3}{\varepsilon_2(\varepsilon_2 + \varepsilon_3)}\frac{1}{a^3}\eta^3 F_2(\eta, H), \\ Y^{(2)} &= -\frac{\varepsilon_2 - \varepsilon_3}{\varepsilon_2(\varepsilon_2 + \varepsilon_3)}\frac{1}{a^3}F_2\left(\frac{1}{\eta}, \frac{H}{\eta}\right), \end{aligned} \quad (9)$$

$$\begin{aligned} F_2(\eta, H) = \frac{8\pi^2}{\eta^3}\sum_{m=1}^{\infty}\sum_{n=-\infty}^{\infty}\frac{m^2}{\sqrt{(m/\eta)^2 + n^2}} \\ \times \exp(-2\pi H\sqrt{(m/\eta)^2 + n^2}), \end{aligned} \quad (10)$$

where $H = 2h/b$. The main convenience of series (8) and (10) lies in the fast (asymptotically exponential) decrease in magnitude of their terms in contrast with the corresponding power series (A.2) and (A.4). From expressions (7) and (9), we have $X = Y$ at $a = b$. This agrees with the results obtained in [18], which were used in analysis of the local field effects in square lattices [11–15].

5. NUMERICAL CALCULATIONS AND DISCUSSION

Relationships (6)–(10) form the basis for numerical calculations of the reflectance anisotropy spectra [see formula (1)]. The reflectance spectra of the naturally oxidized GaAs(001) surface were calculated within the model shown in Fig. 1. For atomic layer *2* with a system of induced microdipoles, we set $a = b = 4$ Å [21]. Since the electron orbitals of atoms in this layer are predominantly oriented along the $[1\bar{1}0]$ direction, we assume that $\chi^{(x)} > \chi^{(y)}$. Moreover, we suppose that the characteristic polarizabilities $|\chi^{(\alpha)}|$ are close in order of magnitude to the atomic polarizability of isolated As atoms (4.83 Å^3) [22]. Consequently, the values of $\chi^{(x)} = 8$ Å^3 and $\chi^{(y)} = 4$ Å^3 were used in the calculations. The spectral dependence of the dielectric function ε_3 (Fig. 3) for GaAs was taken from [23]. According to [24], the thickness d of the natural oxide layer on the GaAs(001) surface was chosen equal to 24 Å. Since the optical characteristics of natural oxide are unknown, the frequency-dependent dielectric function for anodic oxide on GaAs(100) was taken from [25] and used as ε_2 in our calculations. The permittivity of air ε_1 was taken to be unity.

The shape of the spectrum calculated by formula (6) is very sensitive to the distance h between the layer of dipoles and the crystal–oxide interface. The best agreement between the results of calculations (Fig. 4, curve *2*) and the experimental reflectance anisotropy spectrum of the oxidized GaAs(001) surface (Fig. 4, curve *1*) is obtained at $h = 0.582$ Å. It is reasonable to assume that $h \leqslant 0.5s$, where s is the distance between layers *1* and *2* formed by As atoms (Fig. 1a). The distance s is determined by the configuration of electron orbitals of As atoms in transition layer *2*, because the orbital configuration of atoms in layer *1* of the crystal is fixed. The value of s is maximum (1.42 Å) for the sp^3-hybridization of electron orbitals of atoms in layer *2*, and it is minimum (1.15 Å) for the sp^2-hybridization. In both cases, the As–As bond lengths that correspond to these values of s differ only slightly from twice the covalent radius of the As atom (2.4 Å). Therefore, the two aforementioned limiting values of s are permissible. Thus, the fitted value of h that provides the best agreement between the calculated and experimental spectra lies in the range $0.57 < h < 0.71$ Å, which is physically possible in terms of the hybridization of atomic orbitals.

The discrepancy between the results of calculations and the experimental data above 4.5 eV can be explained by the error in determining the permittivity of the oxide layer. In the UV range, this error strongly depends on the oxide density and the amount of amorphous arsenic at the interface [24]. The reflectance anisotropy spectrum of the oxidized surface of $Ga_{0.7}Al_{0.3}As$ (Fig. 2, curve *2*) was not quantitatively analyzed because of the lack of reliable optical characteristics for the oxide film on the surface of this compound.

6. CONCLUSIONS

The reflectance anisotropy spectra of the naturally oxidized (001) surfaces of GaAs and AlGaAs were investigated. Most attention was focused on the explanation of the two characteristic spectral features observed in the ranges 1.6–2.9 and 2.9–5 eV. Within the theory of reflectance anisotropy for layers of dipoles in multilayer media, it was demonstrated that these spectral features are associated with local field effects in a microscopically thin, dipole-polarized transition layer at the GaAs(001)/oxide interface. The atomic model of the oxidized GaAs(001) surface was proposed on the basis of data on its chemical composition. In the framework of this model, the microdipoles responsible for local field effects are attributed to the anisotropically polarizing covalent bonds of arsenic atoms that form an ordered transition layer between the crystal and the oxide. It is worth noting that, according to the model proposed, this transition layer is free from chemisorbed oxygen, which is contained only in the form of oxides in the amorphous surface film.

Good agreement between the experimental and theoretical spectra indicates the essential role played by the local field effects in the reflectance anisotropy spectroscopy of A_3B_5 semiconductors. In this respect, it should be emphasized that the acquisition of data on the interface microstructure in the case when the semiconductor surface is coated with an insulator (for example, films of oxides or passivating atoms), as a rule, involves considerable problems. Therefore, from the practical standpoint, the present work substantially extends the capabilities of reflectance anisotropy spectroscopy for obtaining specific structural data on the semiconductor surface under insulating coatings.

ACKNOWLEDGMENTS

We would like to thank V.P. Ulin for his helpful discussions and M. Losurdo (Plasma Research Center, Bari, Italy) for providing the necessary data on the oxidized surface of gallium arsenide.

This work was supported by the Russian Foundation for Basic Research (project nos. 99-02-18144 and 00-02-16924), and, in part, by the “Surface Atomic Structures” Program of the Ministry of Science and Technology of the Russian Federation (project no. 3.7.99).

APPENDIX

DIPOLE SUMS FOR A RECTANGULAR LATTICE

In the quasi-static approximation, the contribution made to field (5) by the direct interactions between the optically induced dipoles $\mathbf{p} = \sum_\alpha \chi^{(\alpha)} E_\alpha \mathbf{e}_\alpha$ in the layer, which occupy the sites $\mathbf{r}_\mathbf{n} = \mathbf{e}_x n_1 a + \mathbf{e}_y n_2 b + \mathbf{e}_z z_0$ in a plane rectangular lattice in the medium with permittivity ε_2 (Fig. 3), can be represented as

$$\mathbf{E}^{(1)} = -\frac{1}{\varepsilon_2 a^3}\left\{\eta^3\left[S_0^{(1)}(\eta) - 3S_1^{(1)}(\eta)\right]\chi^{(x)}E_x\mathbf{e}_x + \left[S_0^{(1)}\left(\frac{1}{\eta}\right) - 3S_1^{(1)}\left(\frac{1}{\eta}\right)\right]\chi^{(y)}E_y\mathbf{e}_y + \dots\right\}. \qquad (A.1)$$

This relationship contains the lattice sums (dependent on $\eta = a/b$)

$$\{S_0^{(1)}(\eta), S_1^{(1)}(\eta)\} = \sum_{n_1, n_2 = -\infty}^{\infty}{}' \frac{1}{(n_1^2\eta^2 + n_2^2)^{3/2}}\left\{1, \frac{n_1^2\eta^2}{n_1^2\eta^2 + n_2^2}\right\}, \qquad (A.2)$$

in which the terms with $n_1 = n_2 = 0$ (which correspond to the self-action) are absent.

The contribution of the induced image dipoles to field (5) has the form

$$\mathbf{E}^{(2)} = -\frac{\varepsilon_2 - \varepsilon_3}{a^3\varepsilon_2(\varepsilon_2 + \varepsilon_3)} \times \left\{\eta^3[S_0^{(2)}(\eta, H) - 3S_1^{(2)}(\eta, H)]\chi^{(x)}E_x\mathbf{e}_x + \left[S_0^{(2)}\left(\frac{1}{\eta}, \frac{H}{\eta}\right) - 3S_1^{(2)}\left(\frac{1}{\eta}, \frac{H}{\eta}\right)\right]\chi^{(y)}E_y\mathbf{e}_y + \dots\right\}, \qquad (A.3)$$

where the lattice sums dependent on η and $H = 2h/b$ are defined by the formulas

$$\{S_0^{(2)}(\eta), S_1^{(2)}(\eta)\} = \sum_{n_1, n_2 = -\infty}^{\infty} \frac{1}{(n_1^2\eta^2 + n_2^2 + H^2)^{3/2}}\left\{1, \frac{n_1^2\eta^2}{n_1^2\eta^2 + n_2^2 + H^2}\right\}. \qquad (A.4)$$

The lattice sums (A.2) and (A.4) are calculated in the same manner as in [18] with the use of the expression

$$\frac{1}{(A^2 + R^2)^z} = \frac{1}{\Gamma(z)}\int_0^\infty \exp[-t(A^2 + R^2)]t^{z-1}dt,$$

which follows from the integral representation of the gamma function $\Gamma(z)$ and the Poisson summation formula [25]. This leads to the relationships

$$S_0^{(1)}(\eta) = \frac{16\pi}{\eta^2}\sum_{n_1=1}^{\infty}\sum_{n_2=1}^{\infty}\frac{n_1}{n_2}K_1\left(\frac{2\pi}{\eta}n_1n_2\right) + \frac{4}{\eta}\zeta(2) + \frac{2}{\eta^3}\zeta(3), \qquad \text{(A.5)}$$

$$S_1^{(1)}(\eta) = -\frac{\eta}{3}\frac{dS_0^{(1)}(\eta)}{d\eta}$$

for the sums in formula (A.2) and

$$S_0^{(2)}(\eta, H) = \frac{2\pi}{\eta H}\left\{1 + 2\left(\sum_{n_1=0}^{\infty}\sum_{n_2=1}^{\infty} + \sum_{n_1=1}^{\infty}\sum_{n_2=0}^{\infty}\right) \times \exp\left[-2\pi H\sqrt{(n_1/\eta)^2 + n_2^2}\right]\right\}, \qquad \text{(A.6)}$$

$$S_1^{(2)}(\eta, H) = -\frac{\eta}{3}\frac{dS_0^{(2)}(\eta, H)}{d\eta}$$

for the sums in formula (A.4).

REFERENCES

1. P. Chiaradia and G. Charotti, in *Photonic Probes of Surfaces: Electromagnetic Waves—Recent Developments in Research*, Ed. by P. Halevi (Elsevier, Amsterdam, 1995), Vol. 2, Chap. 3, p. 99.
2. V. L. Berkovits, P. Chiaradia, D. Paget, *et al.*, Surf. Sci. **441**, 26 (1999); A. I. Shkrebtii, N. Esser, W. Richter, *et al.*, Phys. Rev. Lett. **81** (3), 721 (1998).
3. V. L. Berkovits and D. Paget, Thin Solid Films **233**, 9 (1993).
4. S. E. Acosta-Ortiz and A. Lastras-Martínez, Solid State Commun. **64** (5), 809 (1987).
5. D. E. Aspnes, J. Vac. Sci. Technol. B **3** (5), 1498 (1985).
6. D. I. Westwood, Z. Sobiesierski, C. C. Matthai, *et al.*, J. Vac. Sci. Technol. B **16** (4), 2358 (1998).
7. V. L. Berkovits, V. N. Bessolov, T. V. L'vova, *et al.*, Fiz. Tekh. Poluprovodn. (Leningrad) **25** (7), 1406 (1991) [Sov. Phys. Semicond. **25**, 847 (1991)].
8. T. Nakayama, Phys. Status Solidi B **202** (2), 741 (1997); M. Murayama, K. Shiraishi, and T. Nakayama, Jpn. J. Appl. Phys. **37** (7), 4109 (1998).
9. S. E. Acosta-Ortiz, J. Appl. Phys. **70** (6), 3239 (1991).
10. V. L. Berkovits, A. B. Gordeeva, V. M. Lantratov, and T. V. L'vova, Fiz. Tverd. Tela (St. Petersburg) **42** (5), 950 (2000) [Phys. Solid State **42**, 981 (2000)].
11. N. Kar and A. Bagchi, Solid State Commun. **33** (6), 645 (1980); A. Bagchi, R. G. Barrera, and B. B. Dasgupta, Phys. Rev. Lett. **44** (22), 1475 (1980).
12. A. Bagchi, R. G. Barrera, and R. Fuchs, Phys. Rev. B **25** (12), 7086 (1982).
13. W. L. Mochan and R. G. Barrera, Phys. Rev. Lett. **56** (20), 2221 (1986).
14. P. Ye and Y. R. Shen, Phys. Rev. B **28** (8), 4288 (1983).
15. W. L. Mochan and R. G. Barrera, Phys. Rev. Lett. **55** (11), 1192 (1985).
16. I. Gerard, C. Debiemme-Chouvy, J. Vigneron, *et al.*, Surf. Sci. **433–435**, 131 (1999).
17. W. Chen, M. Dumas, D. Mao, and A. Kahn, J. Vac. Sci. Technol. B **10** (4), 1886 (1992).
18. B. M. E. van der Hoff and G. C. Benson, Can. J. Phys. **31**, 1087 (1953); B. R. A. Nijboer and F. D. de Wette, Physica (Amsterdam) **23**, 309 (1957); **24**, 422 (1958); G. D. Mahan and A. A. Lucas, J. Chem. Phys. **68**, 1344 (1978).
19. V. A. Kosobukin, Fiz. Tverd. Tela (St. Petersburg) **36** (10), 3015 (1994) [Phys. Solid State **36**, 1605 (1994)].
20. V. A. Kosobukin, Preprint No. 1724, FTI (Ioffe Physicotechnical Institute, Russian Academy of Sciences, St. Petersburg, 1999).
21. M. Sauvage-Simkin, R. Pinchaux, J. Massies, *et al.*, Phys. Rev. Lett. **62** (5), 563 (1989).
22. I. Vasiliev, S. Ogut, and J. R. Chelikowsky, Phys. Rev. Lett. **78** (25), 4805 (1997).
23. D. E. Aspnes and A. A. Studna, Phys. Rev. B **27** (2), 985 (1983).
24. D. E. Aspnes, G. P. Schwarts, G. J. Gualtieri, *et al.*, J. Electrochem. Soc. **128** (3), 591 (1981).
25. P. M. Morse and H. Feshbach, *Methods of Theoretical Physics* (McGraw-Hill, New York, 1953; Inostrannaya Literatura, Moscow, 1958), Vol. 1.

Translated by O. Borovik-Romanova

Physics of the Solid State, Vol. 43, No. 6, 2001, pp. 1025–1029. Translated from Fizika Tverdogo Tela, Vol. 43, No. 6, 2001, pp. 992–996.

Random Acoustoelectric Oscillations of Current in Piezoelectric Semiconductors

I. K. Kamilov and V. Z. Zhokhov

Institute of Physics, Dagestan Scientific Center, Russian Academy of Sciences, ul. 26 Bakinskikh Komissarov 94, Makhachkala, 367003 Russia

e-mail: kamilov@datacom.ru

Received June 30, 2000; in final form, November 13, 2000

Abstract—The effect of the supersonic drift of charge carriers on phonon generation in tellurium crystals is studied under the conditions of the emergence of acoustic instability leading to dynamic chaos. All stages of the stochasticity evolution are traced experimentally with varying the external conditions, namely, the magnitude of the static electric field, determining the drift of charge carriers, and the magnitude and direction of the magnetic field. It is shown that with increasing electric and magnetic fields, the periodic oscillations of the current are transformed into random oscillations through the frequency-doubling and tripling bifurcations. A mathematical model in the form of phase trajectories of the dissipative dynamic system and the spectral portraits corresponding to transient processes are described. *© 2001 MAIK "Nauka/Interperiodica".*

It is well known that, when the electron drift velocity exceeds the velocity of an acoustic wave in a piezoelectric semiconductor, the latter acquires the acoustoelectric instability involving the high-intensity generation of phonons, which leads to an abrupt redistribution of the electric field. In other words, a narrow spatial region in which the electric field is quite strong and the phonon density is high (acoustoelectric domain, AED) is formed and propagates over the crystal with the velocity of sound. In spite of the fact that this phenomenon was discovered and studied more than three decades ago, a comprehensive theory of the evolution of such an instability was developed comparatively recently [1].

The experiments carried out in recent years revealed that the evolution of acoustoelectric instability may follow not only a steady-state but also a "chaotic" scenario when the period of the emerging oscillations is much smaller than the characteristic mean free time of a phonon in the crystal; additionally, the generated current oscillations are chaotic [2–6]. In early experiments on tellurium single crystals, such oscillations were detected and quite peculiar current–voltage characteristics (IVC), described in [7–9], were recorded. However, the observed effects were hypothetically attributed to the state of dynamic chaos only quite recently [2–6]. Random oscillations in systems with acoustoelectronic instability were subsequently investigated in other crystals (e.g., in indium antimonide [10–12]).

It is significant that the physical origin of this type of oscillations has already been indicated in these publications and attempts have been made to develop a theory. Tellurium crystals proved to be the most convenient object for such experiments: regular and irregular current oscillations are easily generated in them since the acoustoelectric anisotropy, in the presence of which the phase and group velocities of phonons in different directions differ significantly, is clearly manifested in these materials. The strong piezoelectric interaction and considerable electric anisotropy facilitate the enhancement of the conduction and mobility of holes in various crystallographic directions. If we also take into account the outstanding role of nonlinear effects emerging due to the large value of the electromechanical coupling constant, it becomes clear why tellurium crystals are the best object for observing stochastic acoustoelectronic processes.

Gorleĭ *et al.* [13] proved that the following anomaly is observed during the propagation of acoustic waves along the binary axis *OX* in a tellurium single crystal: the purely longitudinal mode v_3 has a phase velocity smaller than that of the transverse mode v_1, while in the *YOZ* plane, mode v_3 is purely transverse, mode v_2 is quasi-transverse, and mode v_1 is quasi-longitudinal. For phonons propagating along acoustic axes, mode v_1 is purely longitudinal, while the other two modes are transverse and degenerate. It was also noted in [13] that the electromechanical coupling coefficient for the piezoelectrically active mode v_3 attains its maximum value $K^2_{\max} = 0.11$ in the *XOY* plane, while in the *XOZ* plane, the maximum value is attained along the *X* axis. In the *XOY* and *XOZ* planes, the electromechanical coupling coefficient for mode v_2 assumes an anomalously high value (0.32).

It is well known that, among the principal crystallographic directions in a tellurium crystal, the piezoelectrically active directions are the *X* axis, along which a longitudinal wave propagates at the velocity 2.4×10^5 cm/s,

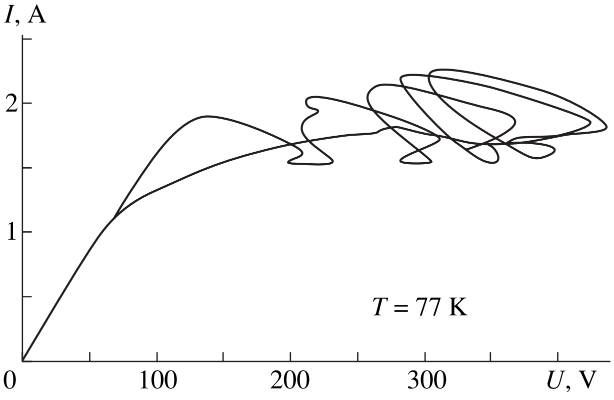

Fig. 1. IVC of a tellurium crystal: $E \parallel Y$, $L = 0.8$ cm.

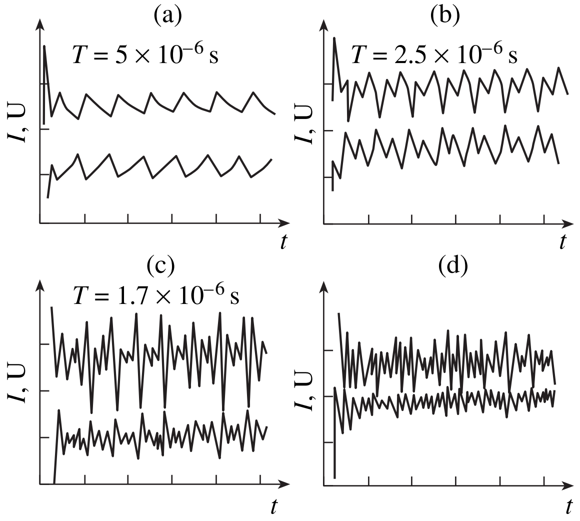

Fig. 2. Oscillograms illustrating the transition from regular to chaotic oscillations upon an increase in the electric field strength. The upper oscillograms correspond to current and lower to the voltage for $E \parallel Y$, $L = 0.8$ cm, and different values of E (V cm^{-1}): (a) 180, (b) 210, (c) 230, and (d) 250.

and the Y axis, along which a transverse wave propagates at the velocity 1.48×10^5 cm/s. Along with the axial modes, off-axis modes also exist in tellurium crystals. The velocity of propagation of off-axis phonons is approximately half the velocity of longitudinal sound. Obviously, the mechanism for the emergence of acoustoelectric instability may have more than one threshold in view of the strong anisotropy in the acoustoelectric properties.

In this work, we prove experimentally (for the evolution of acoustoelectric instability in tellurium single crystals) that the observed pattern (transition from the vibrational to the chaotic mode) fits the model of evolution of dissipative dynamic systems with a stochastic behavior [14] in nonlinear acoustoelectronic media. In the experiments, all stages of the stochasticity evolution are traced depending on the supercriticality parameters: the magnitude of the constant electric field, determination of the charge carrier drift, and the magnitude and direction of the magnetic field.

The experiments were conducted at 77 K in tellurium single crystals of $1.5 \times 0.3 \times 0.2$ cm in size at cuts [100], [010], and [001] with a charge carrier concentration ranging from 5×10^{14} to 2×10^{15} cm^{-3} and a mobility of (2 to 4) $\times 10^3$ cm^2 V^{-1} s^{-1}, in which the acoustoelectronic interaction is manifested strongly. The IVCs were recorded in the regime of solitary increasing sawtooth pulses of a duration of 10 to 100 μs. The direction of the current coincided with the direction of the piezoelectrically active crystallographic axes [100] and [010], as well as with the inactive axis [001]. The electric and magnetic fields were parallel and perpendicular to the crystallographic axes.

The results of our investigations proved that most of the samples with the above orientation and with a conductivity of ~0.3 Ω^{-1} cm^{-1} exhibit an N-shaped IVC. The current and voltage oscillations measured in these samples using rectangular pulses were shifted in phase by 180°, and the period of oscillations was comparable with the time of a single passage of an acoustic wave through the sample. For samples with a conductivity larger than ~0.6 Ω^{-1} cm^{-1}, loop-shaped IVCs were recorded (Fig. 1). In this case, the period of oscillations was smaller than the period determined by the passage of an acoustic wave through the sample and the phase shift between voltage and current oscillations was other than 180°.

Figure 1 shows the experimentally measured IVC for a tellurium sample in the simplest case of zero magnetic field. It can be seen that there is no one-to-one correspondence between the field and the current in a wide range of electric fields and currents, and the same value of the field (current) corresponds to several values of the current (field). This means that the current and the voltage applied to the crystal are not single-valued functions of each other and indicates the random nature of changes in the system that are associated with random generation of AED propagating in the crystal (the separation between domains is a random quantity).

Figures 2a–2d show the oscillograms of the time variation of the current and voltage describing the transition from Fig. 2a simple periodic oscillations of the current to Fig. 2d random oscillations through Fig. 2b frequency-doubling and Fig. 2c tripling bifurcations upon an increase in the electric field strength.

Figure 3 presents the time dependences of the current and voltage showing that the time period itself changes strongly: the initially random oscillations are transformed into regular (nearly periodic) oscillations. These experimental results indicate that bifurcation occurs in the system and its time evolution changes abruptly.

Other extrinsic parameters controlling the evolution of complex aperiodic current oscillations corresponding to the self-oscillation mode are the magnitude and direction of the magnetic field. An increase in the longitudinal magnetic field resulted in a jumpwise change in the period of current oscillations. Figure 4 shows the evolution of complex periodic and random oscillations in strong electric and magnetic fields.

The oscillogram in Fig. 4a illustrates the formation of a closed limiting cycle in the dynamic system. An external longitudinal magnetic field (Fig. 4b) does not favor the equilibrium state of the system with the formed limiting cycle, but transforms it (via a bifurcation transition) into a qualitatively new state corresponding to frequency doubling. As the magnetic field increases (Fig. 4c), three closed limiting cycles appear in the dynamic system; they are also connected through a bifurcation transition corresponding to frequency tripling. Ultimately, the system goes over to a strange attractor, i.e., the state of dynamic chaos (Fig. 4d). When the electric field was parallel to the piezoelectrically active crystallographic axis [100], current oscillations were generated in the tellurium crystal with n_0 = (5 to 7) × 10^{14} cm^{-3} within the fundamental period (the period of fundamental current oscillations coincided with the duration of the domain passage through the crystal). The number of such oscillations increased with the magnetic field, and their amplitude decreased. A further increase in the magnetic field caused a transition to the chaotic mode. The fundamental period of current oscillations remained unchanged in this case. The variation of the direction of the transverse magnetic field changes the amplitude and frequency of current oscillations within the fundamental period.

In order to obtain a mathematical description of a nonlinear acoustoelectronic system, we ran a computer experiment. A special program was composed for representing various types of oscillations in the form of phase trajectories. The mathematical model of instability of the nonlinear acoustoelectronic system constructed by us makes it possible to treat the given system as dynamic.

Figures 5–7 present the results of computer calculations of phase portraits corresponding to the oscillograms in Figs. 2a–2c. Tracing the evolution of this system from these trajectories, we can easily prove that it approaches the strange attractor. The visual observation of phase trajectories indicates the presence of a closed limiting cycle (see Fig. 5), which loses its stability as a result of frequency doubling leading to the formation of an attracting set (attractor) tending to the focus (center) of the trajectory (Fig. 6). Frequency tripling leads to a further evolution of the strange attractor (Fig. 7). A subsequent increase in the frequency of oscillations facilitates the emergence of the chaotic mode.

In order to estimate the time variation of the current oscillation frequency more exactly, we constructed spectral portraits representing the result of the Fourier analysis of these oscillations. Portraits were constructed for each oscillation period. It was proved that the maximum amplitude corresponds to the first harmonic, which determines the fundamental frequency of oscillations. As a result of the fundamental-frequency doubling, the spectrum of the oscillations changes. The predominance of the second harmonic amplitude over the amplitude of the first harmonic corresponds to the doubled frequency.

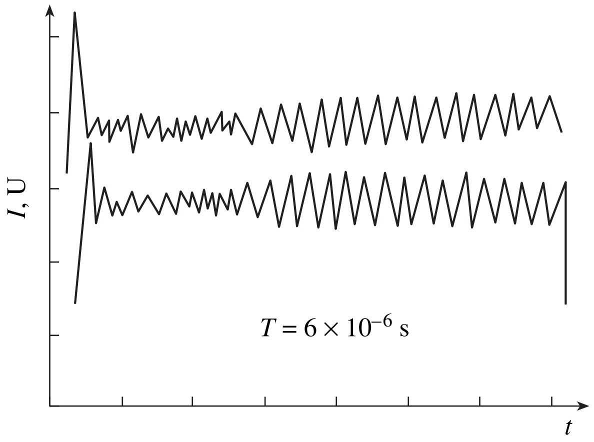

Fig. 3. Oscillograms illustrating the transition from chaos to the self-organized state of the system. The upper oscillogram corresponds to the current, and the lower, to voltage: $E \parallel Y$; L = 1.2 cm and E = 230 V cm^{-1}.

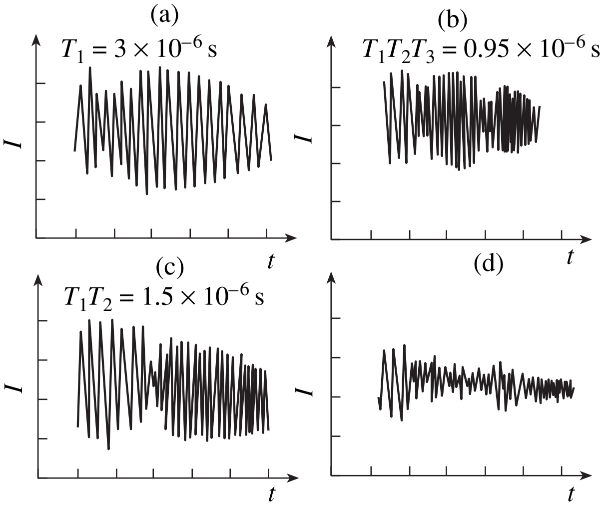

Fig. 4. Oscillograms demonstrating the transition from regular to chaotic current oscillations upon an increase in the longitudinal magnetic field for $E \parallel Y$; L = 0.6 cm, E = 100 V cm^{-1}, and different values of H (kOe): (a) 0, (b) 8, (c) 10, and (d) 12.

Frequency tripling of current oscillations also changes the spectrum of the process, and the third harmonic considerably suppresses the first and second harmonics, which confirms the quantitative, as well as qualitative, change in the state of the acoustoelectronic system.

It is well known that the threshold for the emergence of an instability is determined by the relation $v_d > v_s$

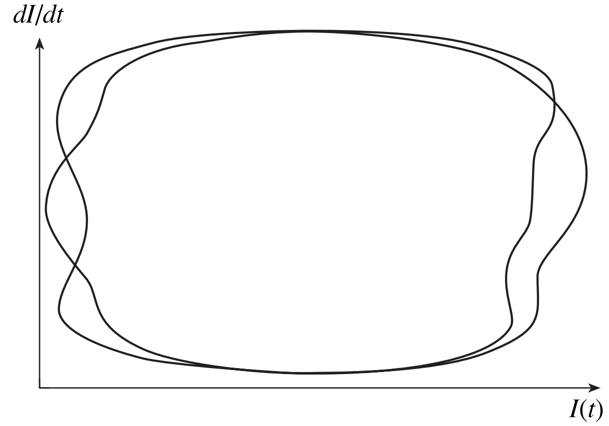

Fig. 5. Phase trajectories corresponding to regular, periodic oscillations.

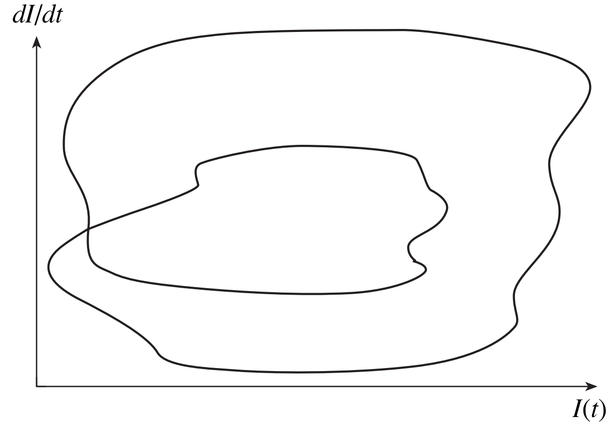

Fig. 6. Phase portrait corresponding to frequency doubling of current oscillations.

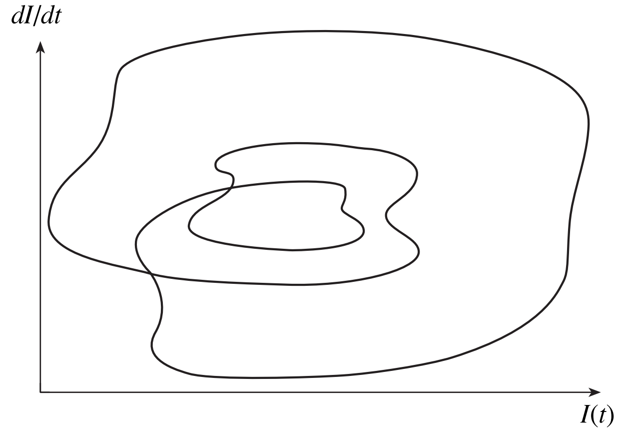

Fig. 7. Phase portrait corresponding to frequency tripling of current oscillations.

(v_d is the drift velocity of holes and v_s is the velocity of sound), indicating the acoustic origin of these oscillations. The oscillations are of the relaxation type, the increase in current with time being a very rapid process, while its decrease is relatively slow. This is explained by the fact that the spatial size of a domain is relatively small (below 10^{-3}–10^{-2} cm) and, hence, the current in the circuit increases abruptly when a domain, propagating at the velocity of sound, emerges from the crystal. The characteristic time l/v_s of this increase is of the order of 10^{-8} to 10^{-7} s, where l is the domain length. If we assume that the oscillations are uniquely connected with the propagation of domains in the crystal, an increase in the electric field leads to the situation when one, two, three, etc., AEDs are gradually formed in the crystal due to strong nonlinearity and nonlocality. In accordance with the conventional pattern of the evolution of dynamic chaos, the frequency of oscillations in this case changes jumpwise, which was observed in our numerous experiments with long samples with a concentration of 10^{15} cm^{-3}. In samples with a concentration of 10^{14} cm^{-3}, electrons are trapped in potential wells. In particular, it is well known that the superposition of two monochromatic waves gives rise to an interference pattern. In this case, the nonlinear mechanism of the emergence of acoustoelectric instability leading to dynamic chaos includes the periodic destruction and formation of AEDs due to the correlation of phases of acoustic vibrations within a domain. These vibrations with the same frequency and close wave vectors produce, as a result of dynamic interference, the resultant electric field within the domain, which either captures electrons into potential wells (when the electron velocity is equal or close to the velocity of sound) or becomes so small that electrons (holes) escape from the potential wells and the current in the circuit increases strongly. Since the number of interfering pairs of acoustic waves may be quite large, this nonlinear mechanism can significantly change the current from the value dictated by Ohm's law to a value close to saturation, i.e., $j = en_0v_s$, where n_0 is the electron concentration [6].

Such a nonlinear mechanism for the emergence of instability, which leads to dynamic chaos, is operative only in the case of a one-mode signal, but cannot form the basis of a model in which many waves with random phases are considered from the very outset without taking into account the mechanism of phase synchronization. To explain the generation of multimode acoustic noise leading to the development of chaos, we must take into account the physical reason behind the formation of AEDs due to the emergence of an AE force exerted by nonequilibrium phonons on electrons.

In the approximation which is normally used for the AE force (the so-called quasi-linear approximation), it is assumed that each mode (harmonic) generates its own partial AE force. For a multimode (wide-band) AE noise, each partial component makes an independent contribution to the AE force. For example, the AE force generated by two acoustic waves with frequencies ω_1 and ω_2 in the quasi-linear approximation is equal to the algebraic sum of the AE forces corresponding to these frequencies. If, however, there exists a correlation of waves with frequencies ω_1 and ω_2, the resultant AE force is no longer equal to the algebraic sum of the partial AE forces. This mechanism just leads to an abrupt change in the pattern of the formation or destruction of AE domains, which, in our opinion, is responsible for the dynamic chaos.

The detailed pattern of dynamic chaos obtained by us, the range of phase trajectories, and the corresponding spectral portraits of current oscillations have made it possible to substantiate the model of evolution of acoustic instability associated with dynamic chaos in acoustoelectronic systems.

ACKNOWLEDGMENTS

The authors are grateful to V.I. Pustovoĭt for fruitful discussions.

This work was supported by the Russian Foundation for Basic Research, grant no. 97-02-17623.

REFERENCES

1. Yu. V. Gulyaev and V. I. Pustovoĭt, Zh. Éksp. Teor. Fiz. **104** (4), 3457 (1993) [JETP **77**, 641 (1993)].
2. R. I. Bashirov, V. I. Pustovoĭt, V. Z. Zhokhov, *et al.*, in *Proceedings of the XIV All-Union Conference on Acoustoelectronics and Physical Acoustics of Solid, Chisinau, 1989*, Part 1, p. 12.
3. R. I. Bashirov, V. I. Pustovoit, V. Z. Zhokhov, *et al.*, in *Proceedings of the IV National Scientific Technical Conference with International Participation “Acoustoelectronics-89,” Varna, Bulgaria, 1989*, Vol. 1, p. 270.
4. I. K. Kamilov, R. I. Bashirov, V. I. Pustovoĭt, *et al.*, in *Proceedings of the XII All-Union Conference on Physics of Semiconductors* (Naukova Dumka, Kiev, 1990), Part 2, p. 160.
5. I. K. Kamilov, R. I. Bashirov, V. I. Pustovoĭt, *et al.*, in *Proceedings of the Conference “Acousto-Electronic Devices for Information Processing on Surface Acoustical Waves,” Moscow, 1990*, p. 275.
6. I. K. Kamilov, R. I. Bashirov, V. I. Pustovoĭt, *et al.*, in *Proceedings of the XI All-Union Acoustical Conference, Moscow, 1991*, p. 49.
7. V. Z. Zhokhov, A. A. Stepurenko, and M.-R. A. Magomedov, Fiz. Tekh. Poluprovodn. (Leningrad) **10** (12), 2361 (1976) [Sov. Phys. Semicond. **10**, 1398 (1976)].
8. V. Z. Zhokhov and A. A. Stepurenko, Fiz. Tekh. Poluprovodn. (Leningrad) **13** (1), 203 (1979) [Sov. Phys. Semicond. **13**, 118 (1979)].
9. A. D. Belyaev, N. N. Liberman, and A. I. Morozov, in *Proceedings of the X All-Union Conference on Quantum Acoustics and Acoustoelectronics* (FAN, Tashkent, 1978), p. 142.
10. F. Guillon, I. L. Heureux, S. L. Cyr, *et al.*, Springer Ser. Solid-State Sci. **112**, 168 (1993).
11. C. W. Skorupka, L. M. Pecora, T. L. Caroll, *et al.*, Phys. Rev. B **42** (14), 9252 (1990).
12. I. L. Heureux and F. Guillon, Phys. Rev. A **45** (8), R5366 (1992).
13. P. N. Gorleĭ, N. Ya. Kushner, and V. A. Shenderovskiĭ, Ukr. Fiz. Zh. **34** (1), 102 (1989).
14. A. P. Gaponov-Grekhov and M. I. Rabinovich, *Nonlinear Physics. Stochasticity and Structures. Physics of XX Century: Development and Outlooks* (Nauka, Moscow, 1984), p. 250.

Translated by N. Wadhwa

Physics of the Solid State, Vol. 43, No. 6, 2001, pp. 1030–1032. Translated from Fizika Tverdogo Tela, Vol. 43, No. 6, 2001, pp. 997–999.
Original Russian Text Copyright © 2001 by Kaminskiĭ, Vasil’ev, Romanova, Solov’ev.

SEMICONDUCTORS AND DIELECTRICS

The Mechanism of the Appearance of an Electromotive Force on Heating of SmS Single Crystals

V. V. Kaminskiĭ, L. N. Vasil’ev, M. V. Romanova, and S. M. Solov’ev
Ioffe Physicotechnical Institute, Russian Academy of Sciences, Politekhnicheskaya ul. 26, St. Petersburg, 194021 Russia
e-mail: Vladimir.Kaminski@shuvpop.ioffe.rssi.ru

Received November 16, 2000

Abstract—We analyze the experimental variation of the concentration of conduction electrons in semiconducting SmS single crystals with increasing temperature within a shallow-impurity model. It is shown that the appearance of an electromotive force is due to accumulation of the critical concentration of free electrons, which results in screening of the Coulomb potential of Sm^{2+} impurity ions that are responsible for the creation of donor levels with an activation energy of 0.045 eV in the band gap of SmS single crystals. *© 2001 MAIK “Nauka/Interperiodica”.*

The appearance of an electromotive force (EMF) on heating of a semiconductor material without external temperature gradients applied was discovered and investigated in [1]. The experiments were performed on single crystals of samarium sulfide (SmS). This effect has been explained by us within a model describing the mechanism of the semiconductor–metal phase transition which occurs in SmS under hydrostatic compression [2]. We suggested that, under heating, some critical concentration of electrons is reached in the conduction band, resulting in screening of the Coulomb potential of the Sm^{2+} ions located at interstitial sites of the SmS crystal lattice. These ions are responsible for the existence of impurity donor levels separated by $E_i \sim 0.045$ eV from the bottom of the conduction band. Due to the screening, the electrons located at the levels E_i are delocalized ($Sm^{2+} \longrightarrow Sm^{3+} + e^-$). Since the concentration of Sm^{2+} impurity interstitials is not uniform over the sample, this collective effect does not occur simultaneously everywhere in the sample. Because of this, a gradient of the free-electron concentration appears, which results in the EMF. However, it should be noted that no direct investigations into the behavior of the conduction electron concentration in the temperature range of the EMF effect (from 375 to 500 K) were performed in [1, 2]. The aim of the present work is to make such an investigation and to improve the model proposed in [1].

The temperature dependence of the concentration of the conduction electrons n was obtained from measurements of the Hall coefficient R_H performed in the temperature range from 290 to 475 K. The measurements were performed on a single-crystal sample of SmS $6 \times 9 \times 0.13$ mm in size cleaved along the {100} cleavage planes. At $T = 290$ K, the sample had electrical parameters typical of SmS: $n = 1.0 \times 10^{19}$ cm^{-3} and a resistivity of 0.03 Ω cm. As was shown in [3], with these parameters in SmS, the Hall factor differs from unity by no more than 4% and, therefore, the drift mobility and the actual concentration of the charge carriers are approximately equal to their Hall values. The measurements were done in the DC regime in a static magnetic field of strength 1.3×10^6 A/m. In determining R_H, correction was made for the relationship between the geometric sizes of the sample.

In Fig. 1, the temperature dependence of R_H is presented. For temperatures ranging from 290 to 400 K, the dependence exhibits an Arrhenius character with an activation energy of 0.046 eV, which agrees well with that of the shallow impurity levels E_i. For $T > 400$ K, a sharp decrease in R_H is observed, which is caused by the increase in n (Fig. 2). At the same temperatures, the EMF is observed in SmS single crystals. In Fig. 2, the

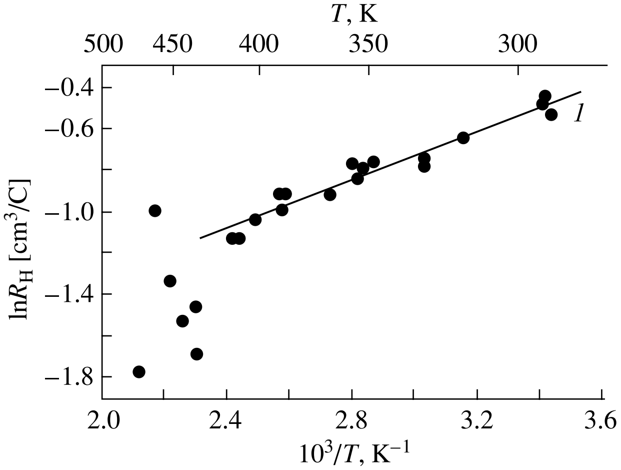

Fig. 1. Temperature dependence of the Hall coefficient of an SmS single crystal. Line *1* corresponds to the conduction electron activation energy 0.046 eV.

data from our previous work [4] and the results of the present work obtained by an analogous procedure are presented. It seems likely that the temperature dependence of the concentration of the conduction electrons reflects the following situation. As the temperature is increased from 290 to 400 K, the increase in n is mainly due to activation of the electrons from the E_i levels. At $T \sim 400$ K, the value of n becomes sufficiently large so that, with further increase in T and n, full delocalization of the electrons from the levels E_i can occur due to the screening of the Coulomb potential of these impurities in some regions of the sample. From the n values attained at $T > 400$ K, one can estimate the sizes of the regions of full delocalization of the electrons at the E_i levels. According to [5], the concentration of these levels is $N_i = (2 \pm 1) \times 10^{20}$ cm^{-3}. The maximum attained value is $n = 3.7 \times 10^{19}$ cm^{-3}. Therefore, the volume of these regions could measure from 10 to 40% of the sample volume in our experiment.

The experimental results obtained are consistent with the calculated sample temperature at which the delocalization of the electrons at the impurity levels E_i must occur. This temperature corresponds to the situation when the Coulomb potential of some samarium interstitial ions is screened by conduction electrons.

The characteristic size of the localization region of a valence electron on a shallow donor level E_i is determined by the effective Bohr radius:

$$a_{\mathrm{B}} = \frac{\varepsilon_0 \hbar^2}{m^* e^2}, \qquad (1)$$

where ε_0 is the static dielectric permittivity of SmS, which is equal to 18 [6]; $m^* \sim m_0$ is the effective mass of an electron; and e is its charge. The energy of the ground state of the impurity is derived to be $E_i = -e^4 m^*/(2\varepsilon_0^2 \hbar^2) = -0.042$ eV, which agrees well with the experimental value. This suggests that the shallow-impurity level approximation is applicable to our case [7]. It should be noted that the actual radius of the localization region of an impurity valence electron can be slightly larger than the a_{B} if there is a sufficiently large number of electrons in the conduction band.

On the other hand, the Coulomb potential of an impurity ion is subjected to electron screening by the free carriers. The space region in which a valence electron experiences the impurity potential is determined by the Debye screening length a_{D}. The Debye screening length enters into the expression for the impurity potential of type $\varphi = e\exp(-r/a_{\mathrm{D}})/(\varepsilon_0 r)$ and, by analogy with the case of electron scattering by a charged impurity in a degenerate semiconductor, has the form [8]

$$a_{\mathrm{D}} = \left[\frac{4\sqrt{2} e^2 m^{*3/2} (k_0 T)^{1/2}}{\pi \varepsilon_0 \hbar^3} F_{1/2}(\mu)\right]^{-1/2}, \qquad (2)$$

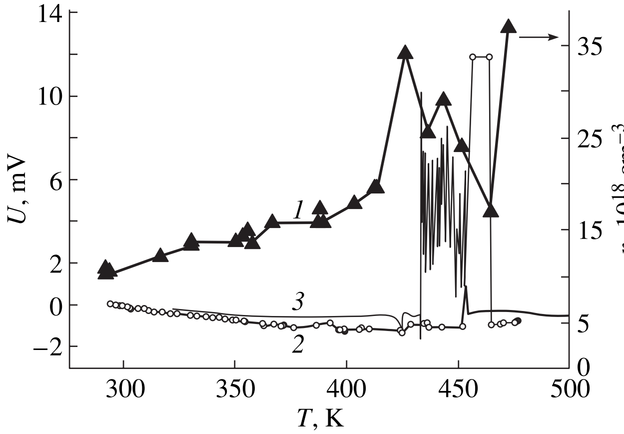

Fig. 2. Temperature dependences of (*1*) the conduction electron concentration in an SmS single crystal and the EMF appearing on heating SmS single crystals in accordance with the results obtained (*2*) in the present work and (*3*) in work [4].

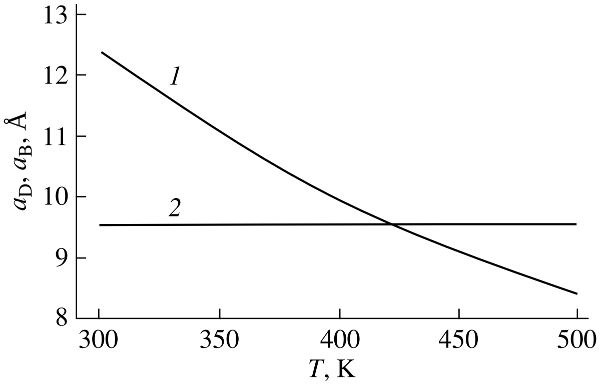

Fig. 3. Comparison between (*1*) the Debye screening length calculated for the Sm^{2+} impurity ions in SmS and (*2*) the Bohr radius of these impurities at different temperatures.

where $F_{1/2}(\mu) = \int_0^\infty (-\partial f_0/\partial x) x^{1/2} dx$, $f_0(x, \mu) = [1 + \exp(x - \mu)]^{-1}$ is the Fermi integral and μ is the reduced chemical potential. To estimate a_{D} at different temperatures, we took the values of the SmS parameters from the concentration model of piezoresistance [5]: $m^* \approx m_0$, $E_i = 0.045$ eV, the impurity concentration $N_i = 2 \times 10^{20}$ cm^{-3}, the depth of the 4f levels of Sm ions $E_f = 0.23$ eV, and their concentration $N_f = 1.8 \times 10^{22}$ cm^{-3}.

The a_{D} temperature dependence calculated numerically from Eq. (2) is presented in Fig. 3. The a_{B} value calculated from Eq. (1) is also shown in Fig. 3. The values of a_{B} and a_{D} become equal at $T \approx 420$ K. This means that, at $T \geq 420$ K, one might expect delocalization of the electrons at the E_i levels and, therefore, generation of the EMF. This result is in good agreement with the experimental data presented in Figs. 1 and 2.

In conclusion, in the present work we showed that the appearance of an EMF on heating of SmS single crystals without temperature gradients is due to screening of the Coulomb potential of the Sm^{2+} interstitial ions by conduction electrons.

ACKNOWLEDGMENTS

This work was supported by the Russian Foundation for Basic Research, project no. 00-02-16947.

REFERENCES

1. V. V. Kaminskiĭ and S. M. Solov'ev, Fiz. Tverd. Tela (St. Petersburg) **43** (3), 423 (2001) [Phys. Solid State **43**, 439 (2001)].
2. V. V. Kaminskiĭ, V. A. Kapustin, and I. A. Smirnov, Fiz. Tverd. Tela (Leningrad) **22** (12), 3568 (1980) [Sov. Phys. Solid State **22**, 2091 (1980)].
3. V. V. Kaminskiĭ, N. N. Stepanov, L. N. Vasil'ev, *et al.*, Fiz. Tverd. Tela (Leningrad) **27** (1), 77 (1985) [Sov. Phys. Solid State **27**, 44 (1985)].
4. M. M. Kazanin, V. V. Kaminskiĭ, and S. M. Solov'ev, Zh. Tekh. Fiz. **70** (5), 136 (2000) [Tech. Phys. **45**, 659 (2000)].
5. L. N. Vasil'ev and V. V. Kaminskiĭ, Fiz. Tverd. Tela (St. Petersburg) **36** (4), 1172 (1994) [Phys. Solid State **36**, 640 (1994)].
6. V. Zelezny, J. Petzelt, V. V. Kaminski, *et al.*, Solid State Commun. **72** (1), 43 (1989).
7. B. I. Shklovskiĭ and A. L. Efros, *Electronic Properties of Doped Semiconductors* (Nauka, Moscow, 1979; Springer-Verlag, New York, 1984).
8. A. I. Ansel'm, *Introduction to the Theory of Semiconductors* (Nauka, Moscow, 1978).

Translated by N. Kovaleva

Physics of the Solid State, Vol. 43, No. 6, 2001, pp. 1033–1036. Translated from Fizika Tverdogo Tela, Vol. 43, No. 6, 2001, pp. 1000–1003.
Original Russian Text Copyright © 2001 by Rogacheva, Krivul'kin.

SEMICONDUCTORS AND DIELECTRICS

Isotherms of Thermal Conductivity in PbTe–MnTe Solid Solutions

E. I. Rogacheva and I. M. Krivul'kin
Kharkov State Polytechnical University, ul. Frunze 21, Kharkov, 61002 Ukraine
e-mail: rogacheva@kpi.kharkov.ua

Received August 10, 2000; in final form, November 27, 2000

Abstract—The temperature dependences of the thermal conductivity λ of PbTe–MnTe solid solutions (0–4 mol % MnTe) are measured in the range 170–670 K. The data obtained are used in constructing the isotherms of the lattice thermal conductivity λ_l and in estimating the effective cross section for phonon scattering by Mn impurity atoms. It is found that all the isotherms exhibit an anomalous increase in λ_l in the concentration range 1.25–2.0 mol % MnTe, which disagrees with the usually observed decrease in λ_l with an increase in the impurity concentration. It is assumed that the anomalous increase in λ_l manifests itself after attainment of the percolation threshold when a continuous chain of overlapping deformation fields produced by individual atoms (an infinite cluster) is formed in the crystal. In the crystal lattice, stresses are partly compensated and phonon scattering decreases. The assumption is made that the effect observed has a universal character. *© 2001 MAIK "Nauka/Interperiodica".*

1. INTRODUCTION

Compounds of the IV–VI types and their solid solutions belong to well-known semiconductor materials that are widely used in IR technology, thermoelectricity, strain metering, etc. [1, 2]. For a number of these compounds, we revealed concentration anomalies in their properties at low impurity concentrations [3, 4]. These anomalies are associated with critical phenomena which exhibit a percolation nature and are inherent in each solid solution [5].

In the present work, we investigated PbTe-based solid solutions in the PbTe–MnTe system which crystallize in the NaCl-type structure. For these solid solutions, we earlier revealed anomalies in the concentration dependences of the Hall coefficient, the electrical conductivity, and the thermal expansion coefficient at ~1 mol % MnTe [6].

The aim of the present work was to examine temperature dependences of the thermal conductivity λ and to construct the isotherms of λ from the results obtained.

2. EXPERIMENTAL TECHNIQUE

The PbTe–MnTe alloys (0–4 mol % MnTe) were prepared by the ampule method from high-purity elements and then were subjected to homogenizing annealing at 820 K for 200 h. In order to avoid accidental errors in the course of synthesis, we prepared two series of alloys with the same compositions. The thermal conductivity λ was measured using cylindrical samples 1.5 cm in diameter and 0.5 cm in height by dynamic calorimetry under gradual heating [7] in the temperature range 170–670 K. The samples were produced by hot pressing at a temperature of 670 K and a pressure of 4000 kg/cm^2, annealed at 820 K for 200 h, and cooled in air. After the heat treatment, the PbTe-based solid solution range covered ~3 mol % MnTe. This was confirmed by the results of microstructure investigations and precision measurements of the unit cell parameter and microhardness. The temperature dependences of λ were obtained for all the studied samples. For each sample, the λ value was measured at least three times and the results obtained were averaged. The shift of the λ(T) curves for the same sample from measurement to measurement did not exceed ~5%. This can be explained by the unavoidable nonidentity in mounting of the samples in the setup. The absence of a systematic shift in the λ(T) curves upon repeated heating–cooling cycles in measurements indicates that thermocycling weakly affects λ and that the samples achieve a reasonable degree of homogeneity under the heat treatment. The resulting dependence λ(T) for each composition was constructed by averaging the data obtained for both series of alloys. The electrical conductivity σ was measured by the four-point probe method with an accuracy of no less than ~5%. The electron component λ_e of the thermal conductivity was separated according to the Wiedemann–Franz law $\lambda_e = L\sigma T$. The Lorenz number was determined from the formula for nondegenerate semiconductors $L = (r + 2)(k_0/e)^2$ (where r is the exponent in the energy dependence of the mean free path $\lambda = \varepsilon'$) [8] under the assumption that carriers are predominantly scattered by acoustic vibrations in the crystal lattice ($r = 0$).

3. RESULTS AND DISCUSSION

Figure 1 shows the dependences $\lambda(T)$ for samples of different compositions. All the curves exhibit a clear minimum at ~400–450 K.

It is known that, in the general case, heat transfer in semiconductors can occur through crystal lattice vibrations, electron gas, electromagnetic radiation, and bipolar diffusion of charge carriers [9, 10]. Therefore, the relationship for calculating the total thermal conductivity λ can be written as

$$\lambda = \lambda_l + \lambda_e + \lambda_{\mathrm{ph}} + \lambda_b, \quad (1)$$

where λ_l, λ_e, λ_{ph}, and λ_b are the lattice, electron, photon, and bipolar components of the thermal conductivity, respectively. An increase in the thermal conductivity λ above 400–450 K can be explained by the increase in electron transfer. However, the estimate of the electron component demonstrates that λ_e makes an insignificant contribution (no more than 7%) to the total thermal conductivity and cannot provide an extremal character of the $\lambda(T)$ dependence. Consequently, it can be assumed that, in our case, as in PbTe [8], we deal with the bipolar diffusion of charge carriers due to the intrinsic conductivity. The fact that the intrinsic conductivity is observed at sufficiently low temperatures is associated with a complex structure of the valence band in *p*-PbTe, whose parameters substantially depend on the temperature. According to the majority of works [1, 8], the valence band of *p*-PbTe consists of two overlapping subbands with different densities of states. These subbands are separated by the band gap ΔE, which decreases with an increase in temperature and becomes equal to zero at 450–500 K. With a further increase in the temperature, the subbands of "light" and "heavy" holes change places. Introduction of a MnTe impurity leads to an increase in the band gap; however, the valence band structures of the PbTe and PbTe–MnTe solutions remain identical [11].

Electromagnetic radiation contributes significantly to heat transfer only in the case when the absorptivity in the range of thermal radiation is small [8–10]. Since the absorption coefficient for PbTe is rather large ($\alpha \sim 200\ \mathrm{cm}^{-1}$) and the value of α for the PbTe–MnTe alloys is almost one order of magnitude higher [12], the heat transfer through electromagnetic radiation can be ignored. As follows from the estimate of the photon thermal conductivity, the contribution of λ_{ph} to the total thermal conductivity does not exceed 0.5% over the entire temperature range.

Since the contributions of λ_e and λ_{ph} are insignificant, the total thermal conductivity of the PbTe–MnTe alloys can be represented as the sum of the lattice and bipolar components: $\lambda = \lambda_l + \lambda_b$. Figure 2 displays the temperature dependences of the thermal resistance calculated in terms of the lattice and bipolar components: $W_{\mathrm{exp}} = 1/(\lambda_l + \lambda_b)$. The thermal resistance W_{exp} linearly increases in the temperature range 170–400 K and decreases above ~ 400 K.

As is known, the mean free path of phonons at $T \geq \Theta$ (where Θ is the Debye temperature) is limited by the

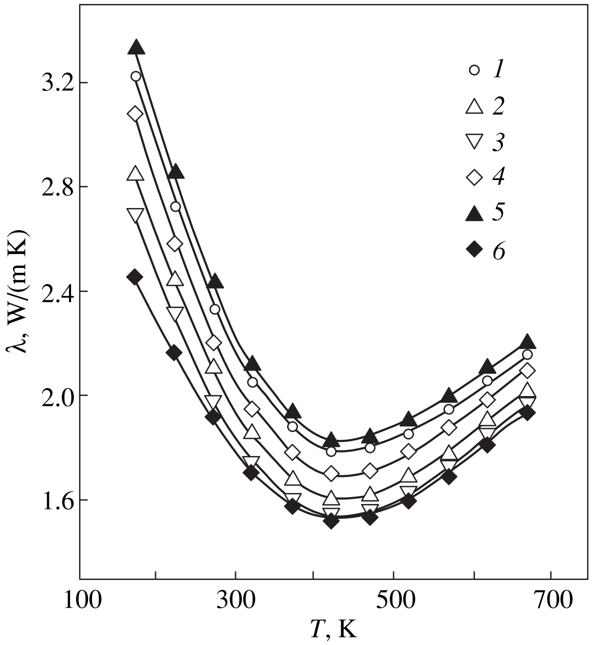

Fig. 1. Temperature dependences of the thermal conductivity in the PbTe–MnTe solid solutions. MnTe concentration (mol %): (*1*) 0, (*2*) 0.75, (*3*) 1.25, (*4*) 1.75, (*5*) 2.0, and (*6*) 4.

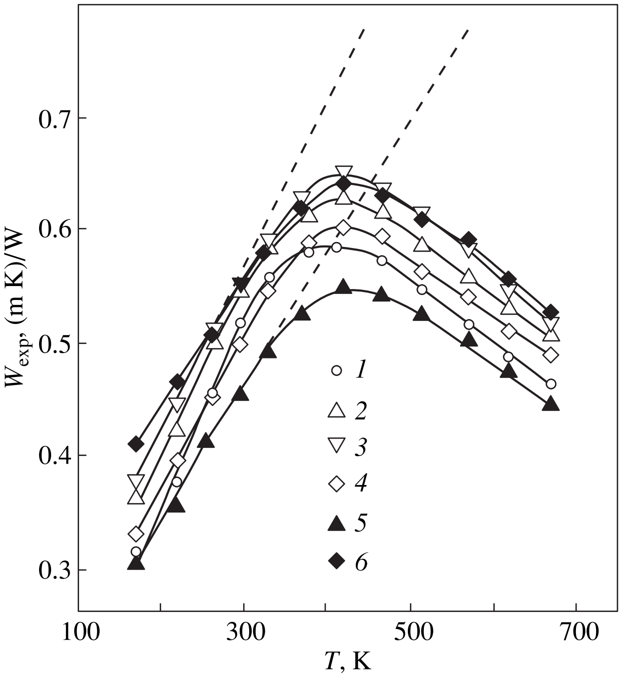

Fig. 2. Temperature dependences of the thermal resistance in the PbTe–MnTe solid solutions. MnTe concentration (mol %): (*1*) 0, (*2*) 0.75, (*3*) 1.25, (*4*) 1.75, (*5*) 2.0, and (*6*) 4.

phonon–phonon interaction with lattice defects [9, 10]. Making allowance for only three-phonon processes and scattering by defects, the thermal resistance of the lattice within the Debye–Peierls theory can be represented in the form

$$W_l = 1/\lambda_l = AT + B, \qquad (2)$$

where A is the coefficient accounting for the degree of anharmonicity of the crystal lattice vibrations and B determines the extra thermal resistance associated with lattice defects. By extrapolating the linear portion of the $W_{\text{exp}}(T)$ curve to high temperatures (dashed lines in Fig. 2), the contribution of the bipolar thermal conductivity can be determined from the distance between the dashed line and the experimental curve: $\lambda_b = 1/W_{\text{exp}} - 1/W_l$. The appropriate estimates showed that the contribution of the bipolar component is large and reaches ~60% of the total thermal conductivity at ~670 K.

Figure 3 depicts the concentration dependences of λ_l (prior to the onset of the bipolar carrier diffusion) or $(\lambda_l + \lambda_b)$ (after the onset of the bipolar carrier diffusion), which were constructed from the temperature dependences of λ and σ. As can be seen from this figure, the concentration dependences of λ_l exhibit a pronounced nonmonotonic character: an anomalous increase in the lattice thermal conductivity is observed in all the curves in the concentration range 1.25–2.0 mol % MnTe.

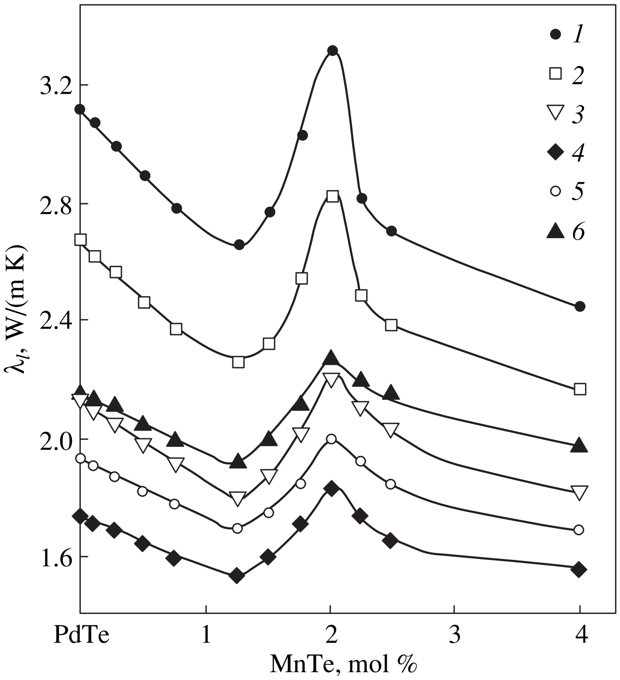

Fig. 3. Isotherms of the lattice thermal conductivity in the PbTe–MnTe solid solutions. T (K): (*1*) 170, (*2*) 220, (*3*) 295, (*4*) 420, (*5*) 570, and (*6*) 670.

As a rule, an increase in the impurity concentration in the solid solution range leads to a decrease in the lattice thermal conductivity λ_l due to phonon scattering by impurity atoms. In the framework of the Clemens theory, the decrease in λ_l in the solid solution range is determined by the difference between the masses of the impurity and base atoms in the lattice, the difference between the bonding forces in the neighborhood of the impurity atom, and the elastic stresses arising from the difference in the atomic sizes [9, 10]. In the system under investigation, λ_l decreases in the composition ranges 0–1.25 and 2.0–4.0 mol % MnTe. In our opinion, an anomalous increase in λ_l in the intermediate concentration range is associated with critical phenomena of the percolation type which occur in the impurity subsystem of the crystal [5]. Impurity atoms are the centers of local lattice distortions and the sources of internal stresses and strains that decrease inversely with distance to the third power [13]. Since noticeable atomic displacements are observed at a range equal to one or two interatomic distances, the elastic deformation field can be treated as short-range. Therefore, we can use the notion of the characteristic radius of deformation interaction R_0. At a low impurity concentration, when the separation between impurities is substantially larger than the value of R_0, the deformation fields induced by individual atoms virtually do not overlap but contribute additively to the thermal resistance of the crystal lattice, thus increasing its magnitude. As the impurity concentration increases, the elastic fields of neighboring atoms begin to overlap and the elastic stresses of the opposite sign are partly compensated. In the short-range interaction approximation with the use of the percolation theory [14] and under the assumption that impurity atoms are distributed in a random manner, we can estimate the concentration x_C (percolation threshold) from the R_0 values. This concentration corresponds to the onset of the collective interaction resulting in the formation of a single chain that consists of overlapping deformation fields and threads the whole crystal (the so-called infinite cluster). It is possible to solve the inverse problem: the R_0 radius can be determined from the critical concentration x_C. By assuming that $x_C \sim 1.25$ mol % MnTe, we obtain $R_0 \approx 1.2a_0$ (where a_0 is the unit cell parameter), which is consistent with the short-range character of deformation interaction. The crossover from the diluted to the concentrated solid solutions with the formation of an infinite cluster should be accompanied by the critical phenomena similar to second-order phase transitions [15]. Since the formation of percolation channels is attended by a partial compensation for stresses of the opposite sign and, hence, by a decrease in the total level of elastic stresses in the lattice, it is reasonable to assume that this can bring about an increase in the thermal conductivity. An increase in λ_l in the anomalous range is associated with an increase in the density of the infinite cluster. Once the process of compensating for the elastic stresses has extended over the whole crystal and the entire volume has been filled with an “impurity liquid,” further introduction of impurity atoms leads to new lattice distortions and, therefore, to a decrease in the lattice thermal conductivity. The situation can be similar to the Mott transition when the formation of percolation channels over electron shells of particular atoms gives rise to the electrical conductivity (a metal–dielectric transition). In this case, the percolation channels are formed over the deformation fields of particular impurity atoms.

The probability of the impurity atoms ordering drastically increases at critical concentrations. Simple calculations demonstrate that the solid solution composition at ~1.0 mol % MnTe is optimal for an ordered distribution of impurity atoms over sites of a primitive cubic lattice with a spacing $a = 3a_0$ (where a_0 is the unit cell parameter of the alloy). Moreover, the superstructure with a face-centered cubic lattice of impurity atoms and a spacing $a = 4a_0$ can be formed at ~1.6 mol % MnTe. A considerable increase in λ_l in the concentration range 1.25–2.0 mol % MnTe can be indirect evidence that impurity atoms undergo ordering.

Since the electron components make an insignificant contribution to the total thermal conductivity in the alloys under investigation, the observed concentration anomalies of λ_l cannot be related to the change in the Lorenz number, which can occur in the case of high doping due to the electron–electron interaction [16].

The effective cross section for phonon scattering by Mn impurity atoms was estimated from the concentration dependence of λ in the range 0–1.25 mol % MnTe according to the Ioffe formula [10]:

$$\frac{\lambda}{\lambda_0} = 1 + \Phi \frac{N}{N_0}\frac{l_0}{d}. \qquad (3)$$

Here, λ_0 and λ are the thermal conductivity coefficients for the crystal with and without impurities, respectively; N and N_0 are the numbers of impurity atoms and all atoms per unit volume, respectively; d is the interatomic distance; l_0 is the phonon mean free path in the expression for the thermal conductivity coefficient of the undoped crystal; $\lambda_0 = (1/3)l_0 C_v v_g$ (where C_v is the heat capacity per unit volume and v_g is the mean group velocity); and Φ is the coefficient in the relationship for the effective cross section for phonon scattering $S = \Phi d^2$. By substituting the values of λ_0, λ, N, N_0, and also C_v taken from [2] and v_g taken from [8], we obtain $\Phi = 1.9$ and $S = 1.9d^2 = 0.48a_0^2$ at $T = 300$ K. The obtained value of S shows that impurity atoms in the solid solution under consideration are not centers of efficient phonon scattering, as was the case in other isovalent substitutional solid solutions [10].

ACKNOWLEDGMENTS

This work was supported by the Civilian Research and Development Foundation of the United States (CRDF, grant no. UE2-2069) and the "New Compounds and Materials" Program of the Ministry of Education and Science of Ukraine.

REFERENCES

1. A. V. Lyubchenko, E. A. Sal'kov, and F. F. Sizov, *Physical Principles of Semiconductor Infrared Photoelectronics* (Naukova Dumka, Kiev, 1984).
2. N. Kh. Abrikosov and L. E. Shelimova, *Semiconductor Materials Based on IV–VI Compounds* (Nauka, Moscow, 1975).
3. E. I. Rogacheva, N. A. Sinelnik, and O. N. Nashchekina, Acta Phys. Pol. A **84** (4), 729 (1993).
4. E. I. Rogacheva, Izv. Akad. Nauk SSSR, Neorg. Mater. **25** (5), 643 (1989).
5. E. I. Rogacheva, Jpn. J. Appl. Phys. **32** (3), 775 (1993).
6. E. I. Rogacheva, I. M. Krivulkin, V. P. Popov, and T. A. Lobkovskaya, Phys. Status Solidi A **148**, K65 (1995).
7. E. S. Platunov, *Thermophysical Measurements in a Monotonic Regime* (Énergiya, Moscow, 1972).
8. Yu. I. Ravich, B. A. Efimova, and I. A. Smirnov, *Semiconducting Lead Chalcogenides* (Nauka, Moscow, 1968; Plenum, New York, 1970).
9. R. Berman, *Thermal Conduction in Solids* (Clarendon, Oxford, 1976; Mir, Moscow, 1979).
10. V. M. Mogilevskiĭ and A. F. Chudnovskiĭ, *Thermal Conductivity of Semiconductors* (Nauka, Moscow, 1972).
11. M. N. Vinogradova, N. V. Kolomoets, and L. M. Sysoeva, Fiz. Tekh. Poluprovodn. (Leningrad) **5** (2), 218 (1971) [Sov. Phys. Semicond. **5**, 186 (1971)].
12. J. Neuwirth, W. Jantsch, L. Palmetshofer, and W. Zulehner, J. Phys. C **19** (14), 2475 (1986).
13. T. Suzuki, H. Yoshinaga, and S. Takeuchi, *Dislocation Dynamics and Plasticity* (Syokabo, Tokyo, 1986; Mir, Moscow, 1989).
14. D. Stauffer and A. Aharony, *Introduction to Percolation Theory* (Taylor and Francis, London, 1992).
15. A. Z. Patashinskiĭ and V. L. Pokrovskiĭ, *Fluctuation Theory of Phase Transitions* (Nauka, Moscow, 1982, 2nd ed.; Pergamon, Oxford, 1979).
16. Kh. R. Maĭlina, Yu. A. Nikulin, L. V. Prokof'eva, and Yu. I. Ravich, Fiz. Tverd. Tela (Leningrad) **32** (2), 493 (1990) [Sov. Phys. Solid State **32**, 285 (1990)].

Translated by O. Borovik-Romanova

Physics of the Solid State, Vol. 43, No. 6, 2001, pp. 1037–1042. Translated from Fizika Tverdogo Tela, Vol. 43, No. 6, 2001, pp. 1004–1009.
Original Russian Text Copyright © 2001 by Édelman, Malakhovskiĭ, Potseluyko, Zarubina, Zamkov.

SEMICONDUCTORS AND DIELECTRICS

Intensities of *f*–*f* Transitions in Pr^{3+} and Dy^{3+} in Glasses in the Near-IR Spectral Range

I. S. Édelman*, A. V. Malakhovskiĭ, A. M. Potseluyko*, T. V. Zarubina***, and A. V. Zamkov***

** Kirenskiĭ Institute of Physics, Siberian Division, Russian Academy of Sciences, Akademgorodok,*
Krasnoyarsk, 660036 Russia
*** Bar-Ilan University, Ramat Gan, 52900 Israel*
**** Vavilov State Optical Institute, All-Russia Research Center, Birzhevaya liniya 12, St. Petersburg, 199034 Russia*
e-mail: pts@iph.krasn.ru

Received August 29, 2000

Abstract—The absorption spectra of Pr^{3+} and Dy^{3+} ions in three glass matrices (SiO_2–P_2O_5–GeO_2, Al_2O_3–B_2O_3–SiO_2, and LiB_3O_5) are thoroughly studied in the near-IR spectral range (4600–14 300 cm^{-1}). The temperature dependences of the intensity, the width, and the location of the absorption bands observed are investigated for the first time. It is shown that the *f*–*f* transitions in the studied glasses are allowed by static odd distortions in the environment of the rare-earth ions and these distortions decrease with an increase in temperature. A comparative analysis of the absorption band parameters and their temperature behavior in different materials makes it possible to determine the differences in magnitudes, symmetries, and dispersions of the distortions in the nearest environment of rare-earth ions in different glasses. *© 2001 MAIK “Nauka/Interperiodica”.*

1. INTRODUCTION

Investigations of the *f*–*f* transitions in rare-earth ions in different compounds have attracted the attention of many researchers (see [1–5] and references therein). Considerable interest in the optical properties of rare-earth materials is motivated by their diverse technical applications (for example, practical use of optical laser glasses).

The intensity of the *f*–*f* transitions is usually analyzed in terms of the Judd–Ofelt theory [6, 7], which allows one to describe all the *f*–*f* transitions in a particular ion with the use of three parameters. The majority of the *f*–*f* transitions are consistent with this theory. However, Jørgensen and Judd [8] revealed the so-called supersensitive transitions, which cannot be described by the above three parameters. These transitions turned out to be especially sensitive to the ligand environment of rare-earth ions. In free atoms, the *f*–*f* transitions are parity-forbidden in the electric dipole approximation. The *f*–*f* transitions become partly allowed in a condensed state of the material due to the static and dynamical (vibrational) odd distortions of the ligand environment. Therefore, the intensities of all *f*–*f* transitions, and not just the supersensitive transitions, should depend on the symmetry of the ligand environment and the magnitude of odd distortions. Consequently, a comparative investigation of the *f*–*f* transitions in rare-earth ions in different matrices can provide information on the environment of the rare-earth ions. This analysis was the main objective of the present work.

In this work, we investigated the temperature behavior of the *f*–*f* transitions in Pr^{3+} and Dy^{3+} ions in a number of previously unexplored glasses in the spectral range 4600–14300 cm^{-1}. Analysis of the temperature dependences of the intensities of the *f*–*f* transitions made it possible to differentiate the contributions of the static and vibronic mechanisms of allowing these transitions to the absorption intensity and to trace the evolution in certain properties of the ligand environment in glasses with a change in temperature. To our knowledge, there is only one work concerned with the investigation into the properties of the *f*–*f* transitions at different temperatures of the material [9].

2. EXPERIMENTAL TECHNIQUE

The optical absorption spectra in the near-IR range at temperatures of 78–300 K were recorded on an automated setup based on DMR-4 and MDR-12 monochromators. The instrumental resolution was equal to 20 cm^{-1}. The dynamic range of the measured optical densities was limited to 4.5. The temperature was controlled to within ±1 K. Moreover, the absorption spectra for a number of samples were measured on UVICON 943 and SF-20 spectrophotometers (at a temperature of 300 K).

We used three glass matrices: SiO_2–P_2O_5–GeO_2, Al_2O_3–B_2O_3–SiO_2, and LiB_3O_5. Praseodymium and dysprosium oxides at different concentrations were added to the melt. The procedure of glass synthesis was described in more detail in [10, 11]. The glass compositions and rare-earth ion concentrations (as-batched) are presented in Table 1.

Table 1. Glass compositions and concentrations of rare-earth ions

Sample designation	Rare-earth ion	Matrix composition	C, 10^{21} cm^{-3}	C, mol %
Pr1	Pr^{3+}	SiO_2–P_2O_5–GeO_2	5.02	20 (Pr_2O_3)
Pr2	Pr^{3+}	Al_2O_3–B_2O_3–SiO_2	2.26	15 (Pr_2O_3)
Pr3	Pr^{3+}	LiB_3O_5	1.37	6 (Pr_2O_3)
Pr4	Pr^{3+}	LiB_3O_5	3.27	13.4 (Pr_2O_3)
Dy1	Dy^{3+}	SiO_2–P_2O_5–GeO_2	3.55	15 (Dy_2O_3)
Dy2	Dy^{3+}	SiO_2–P_2O_5–GeO_2	4.52	20 (Dy_2O_3)
Dy3	Dy^{3+}	Al_2O_3–B_2O_3–SiO_2	8.60	25 (Dy_2O_3)

As follows from the magnetic susceptibility measurements, all the glasses under investigation are paramagnets in the temperature range covered.

3. RESULTS AND DISCUSSION

Figures 1 and 2 show the absorption spectra of two glasses containing praseodymium and dysprosium. The absorption bands were identified according to [12]. The ${}^6H_{15/2} \longrightarrow {}^6(F_{11/2} + H_{9/2})$ transition in Dy^{3+} and the ${}^3H_4 \longrightarrow {}^3F_2$ transition in Pr^{3+} are considered supersensitive transitions [2]. However, Hormadaly and Reisfeld [12] argued that the supersensitive transition in Pr^{3+} is the ${}^3H_4 \longrightarrow {}^3P_2$ transition. The absorption spectra of all glasses containing the same rare-earth ions are qualitatively identical. The spectra of the Dy1 and Dy2 glasses with similar glass matrices (Table 1) virtually coincide. The spectra of the Pr3 and Pr4 glasses are also identical to each other, even though the praseodymium concentrations differ substantially (Table 1). This means that the interaction between Pr^{3+} ions either is insignificant or does not affect the f–f absorption.

The absorption spectra were decomposed into Gaussian components. The Gaussian function is best suited for describing the inhomogeneously broadened absorption bands which are characteristic of glasses. Indeed, the experimental spectra are adequately represented by the spectral decomposition. As can be seen from the spectrum of Dy^{3+} (Fig. 2), whose lines are well resolved, the absorption bands are nearly symmetric at the lowest temperature studied. The number of components for the decomposition of the spectra was chosen from theoretical considerations and the observed spectral features.

The oscillator strengths of the transitions were calculated by the relationship [12]

$$f = 4.318 \times 10^{-9} \int \varepsilon(k) dk \equiv 4.318 \times 10^{-9} I, \qquad (1)$$

where $\varepsilon(k)$ is the molar extinction coefficient at a wave number k (cm^{-1}) and I is the line intensity. The oscillator strengths of the f–f transitions in the studied glasses and the experimental data available in the literature are given in Tables 2 and 3. The temperature dependences of the absorption band parameters (intensities, widths, and locations) for the praseodymium-containing glasses investigated are depicted in Figs. 3–5.

3.1. Intensities of the absorption bands. The intensity of the f–f transitions in a material in a condensed state depends on the following factors: (1) the

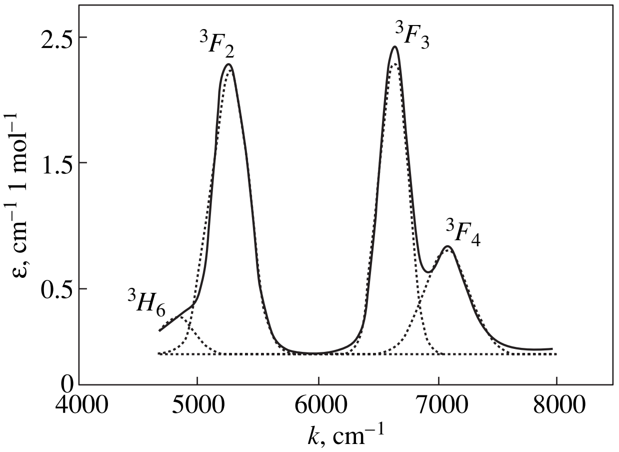

Fig. 1. Absorption spectrum of the Pr1 glass at T = 93 K. Dotted lines show the Gaussian components of the spectral decomposition.

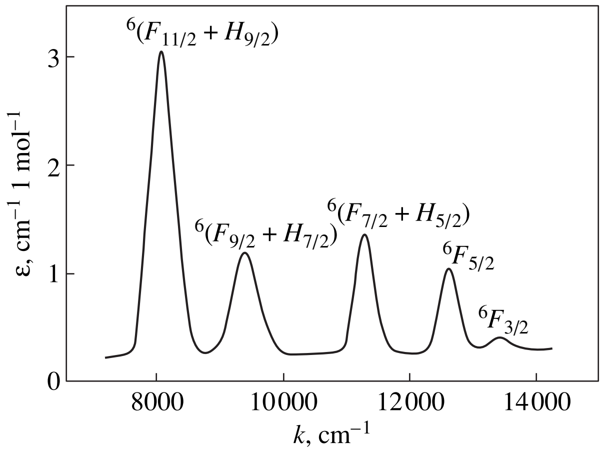

Fig. 2. Absorption spectrum of the Dy3 glass at T = 93 K.

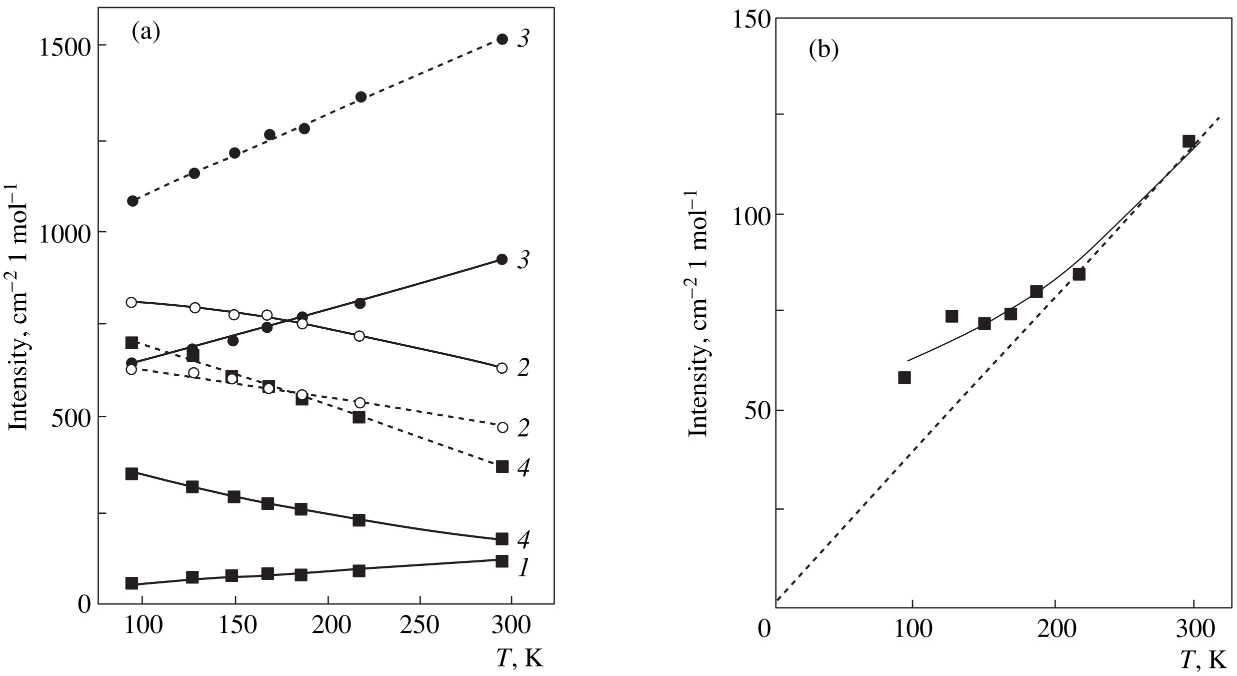

Fig. 3. (a) Temperature dependences of the absorption band intensity for (*1*) $^3H_4 \longrightarrow {}^3H_6$, (*2*) $^3H_4 \longrightarrow {}^3F_2$, (*3*) $^3H_4 \longrightarrow {}^3F_3$, and (*4*) $^3H_4 \longrightarrow {}^3F_4$ transitions in the Pr1 (solid lines) and Pr4 (dashed lines) glasses. (b) Temperature dependence of the absorption band intensity for the $^3H_4 \longrightarrow {}^3H_6$ transition in the Pr1 glass on a different scale.

symmetry and the magnitude of static and vibrational odd distortions; (2) the ligand type, i.e., the ratio between the ionic and covalent bonds of the required symmetry; and (3) the type of the transition involved.

All the Pr^{3+}-containing compounds presented in Table 2, except for those studied in [14, 16], contain the same ligands, namely, oxygen ions. Therefore, the transition intensities should depend only on the magnitude and the symmetry of distortions and the type of the transition. First and foremost, it is clearly seen that the majority of the compounds under consideration can be separated into two groups in which the total intensities of the transitions to the ^3F states differ by a factor of two. It is of interest that this intensity for a number of different glasses is equal to one-half the intensity for $Pr^{3+} : Y_3Al_5O_{12}$ garnet. Garnet is a cubic crystal, but the rare-earth ions occupy the D_2 orthorhombic sites [1]. Consequently, the magnitude of the odd distortions in the aforementioned glasses is less than that in the garnet.

The total intensity is maximum in a $Pr^{3+} : Y_2O_3$ cubic crystal (Table 2), in which the Pr^{3+} ions predominantly occupy the C_2 noncentrosymmetric sites [15]. The replacement of oxygen by fluorine as a ligand only slightly affects the intensity of *f–f* transitions, including the $^3H_4 \longrightarrow {}^3F_2$ transition (Table 2). A change in the matrix has a substantially stronger effect.

Despite the fact that, in some cases, the total intensities in particular groups of absorption bands for the studied glasses are approximately identical, the intensity ratios of individual bands can differ significantly (Table 2), which indicates different symmetries of the odd distortions. The reverse is also true: at the different total intensities, the intensity ratios of the individual bands involved in a particular group can be close to

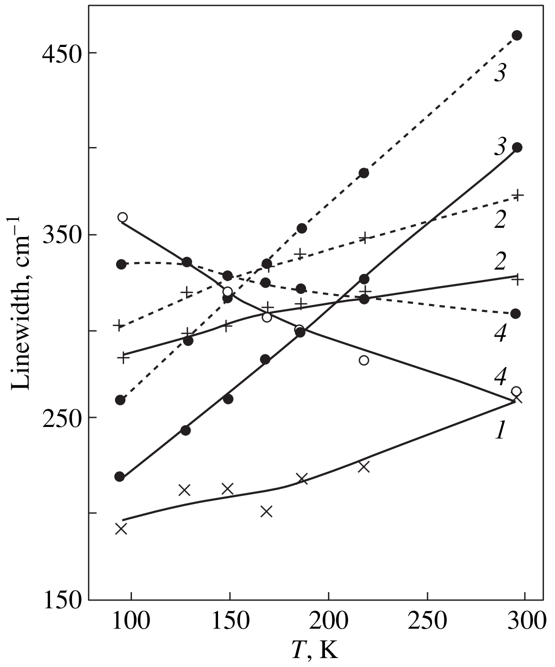

Fig. 4. Temperature dependences of the linewidth in absorption spectra for (*1*) $^3H_4 \longrightarrow {}^3H_6$, (*2*) $^3H_4 \longrightarrow {}^3F_2$, (*3*) $^3H_4 \longrightarrow {}^3F_3$, and (*4*) $^3H_4 \longrightarrow {}^3F_4$ transitions in the Pr1 (solid lines) and Pr4 (dashed lines) glasses.

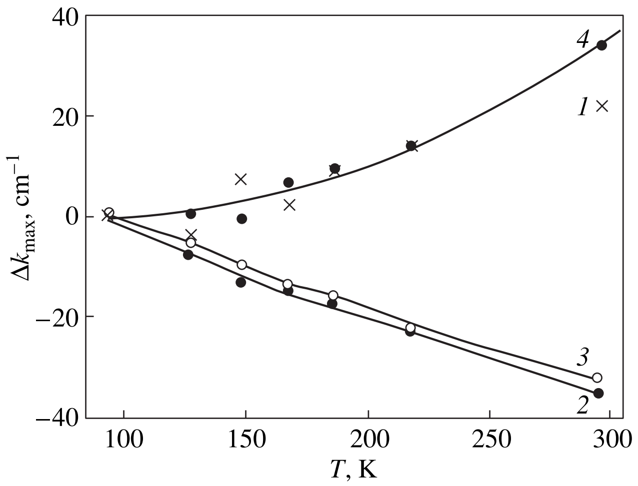

Fig. 5. Temperature dependences of the displacement of the absorption band maxima with respect to their position at T = 93 K for (*1*) $^3H_4 \longrightarrow {}^3H_6$, (*2*) $^3H_4 \longrightarrow {}^3F_2$, (*3*) $^3H_4 \longrightarrow {}^3F_3$, and (*4*) $^3H_4 \longrightarrow {}^3F_4$ transitions in the Pr1 glass.

each other. For example, the Pr1 and Pr2 glasses are virtually identical with respect to the symmetry of odd distortions, even though their matrices differ. The Pr4 (Pr3) glass essentially differs from the above glasses but is similar to the $Pr^{3+} : Y_3Al_5O_{12}$ crystal and the fluoride glass studied in [16] (Table 2). This implies that the symmetry of odd distortions in the Pr4 (Pr3) glass is similar to that in the $Pr^{3+} : Y_3Al_5O_{12}$ crystal and the fluoride glass [16], even though the total intensities of the transitions and, hence, the magnitudes of the distortions in these materials differ substantially.

The Dy^{3+}-containing compounds presented in Table 3, except for the material studied in [18], contain oxygen ions as ligands. Correspondingly, the intensity of the supersensitive transition $^6H_{15/2} \longrightarrow {}^6(F_{11/2} + H_{9/2})$ in $Dy^{3+}(aq)HClO_4$–$DClO_4$ [18] drastically differs from the intensity of this transition in these materials. As in the praseodymium-containing glasses (Table 2), the total intensity of the studied transitions is maximum in the 35ZnO–65TeO$_2$ glass. The total intensity of the transitions in the glasses studied in the present work is less by approximately half. The intensity ratios of individual bands in the Dy1 (Dy2) and Dy3 glasses with different matrices differ considerably (Table 3); i.e., the symmetries of the odd distortions of Dy sites in these matrices are also different. By contrast, the intensity ratios of individual bands in the Pr1 and Pr2 glasses (Table 2) are the same, even though their matrices are identical to those in the Dy1 and Dy3 glasses, respectively. This implies that the symmetry of odd distortions around a rare-earth ion depends not only on the matrix but also on the rare-earth ion type. Actually, the radius of Pr^{3+} ions (1.013 Å) is larger than that of Dy^{3+} ions (0.908 Å) [1]. Furthermore, the 4*f* electrons participate in the formation of bonds [19], and, hence, these bonds depend on the number of 4*f* electrons. Therefore, the ions involving 4*f* electrons can affect the shape of ligand polyhedra, the coordination numbers, and the structure-sensitive properties, including the intensity of *f*–*f* transitions.

If the static odd distortions of the environment of rare-earth ions in a material were temperature independent, the corresponding intensities of *f*–*f* transitions would also be temperature independent. In the case when an increase in the temperature leads only to a change in the magnitude of the static odd distortions (due to the thermal expansion) but not in their symmetry, the intensities of the *f*–*f* transitions should slowly decrease with an increase in the temperature. On the other hand, the intensity of the transition which is allowed only by the vibronic mechanism should increase with a rise in the temperature according to the relationship [20]

$$f = 0.5\sum f_{0s}\coth(h\nu_s/2kT). \tag{2}$$

Here, s is the number of an active odd vibration, ν_s is the frequency of the sth vibration, and f_{0s} is the oscillator strength of the electron transition which is allowed

Table 2. Oscillator strengths ($f \times 10^6$) of the transitions in Pr^{3+} in different matrices at room temperature

Transition	Pr1	Pr2	Pr4	$[12]_1$	$[12]_2$	$Pr^{3+} : Y_3Al_5O_{12}$ [13]	[14]	[16]	$Pr^{3+} : Y_2O_3$ [15]
$^3H_4 \longrightarrow {}^3F_2$	2.75	4.0	2.05	6.15	6.36	5.63	3.12	1.25	
	(1)	(1)	(1)	(1)	(1)	(1)	(1)	(1)	
$^3H_4 \longrightarrow {}^3F_3$	4.0	5.59	6.55	11.36	11.06	14.91	5.48	3.83	
	(1.45)	(1.4)	(3.2)	(1.85)	(1.74)	(2.65)	(1.76)	(3.06)	
$^3H_4 \longrightarrow {}^3F_4$	0.75	1.16	1.6	3.92	3.41	5.68	2.89	1.38	
	(0.27)	(0.29)	(0.78)	(0.64)	(0.54)	(1.01)	(0.93)	(1.1)	
$\Sigma(^3F)$	7.5	10.7	10.2	21.4	20.8	26.22	11.49	6.46	46.25

Note: $[12]_1$: 35ZnO–65TeO$_2$, $[12]_2$: 20Na$_2$O–80TeO$_2$, [14]: 60ZrF$_4$–31BaF$_2$–4YF$_3$–2PbF$_2$–2AlF$_3$–LaF$_3$, and [16]: 36InF$_3$–20ZnF$_2$–15BaF$_2$–20SrF$_2$–5CaF$_2$–2GaF$_3$–2PbF$_2$. Numbers in parentheses indicate the oscillator strength ratios for the given transition and the $^3H_4 \longrightarrow {}^3F_2$ transition.

Table 3. Oscillator strengths ($f \times 10^6$) of the transitions in Dy^{3+} in different matrices at room temperature

	Transition	Dy1	Dy3	$[12]_1$	$[12]_2$	[17]	[18]
1	$^6H_{15/2} \longrightarrow {}^6(F_{11/2} + H_{9/2})$	6.75	5.56	10.63	7.11	10.7	1.1
		(1)	(1)	(1)	(1)	(1)	
2	$^6H_{15/2} \longrightarrow {}^6(F_{9/2} + H_{7/2})$	0.94	2.31	3.27	2.59	2.57	2.97
		(0.14)	(0.41)	(0.31)	(0.36)	(0.24)	
3	$^6H_{15/2} \longrightarrow {}^6(F_{7/2} + H_{5/2})$	0.75	1.85	2.81	2.09	2.26	2.85
		(0.11)	(0.33)	(0.26)	(0.29)	(0.21)	
4	$^6H_{15/2} \longrightarrow {}^6F_{5/2}$	0.44	1.12	1.53	1.27	1.21	1.55
		(0.065)	(0.2)	(0.14)	(0.18)	(0.11)	
	Σ	8.88	10.8	18.2	13.0	16.75	8.47

Note: $[12]_1$: $35ZnO–65TeO_2$, $[12]_2$: $20Na_2O–80TeO_2$, [17]: the Dy_2O_3 solution in the $LiNO_3–KNO_3$ melt, and [18]: $Dy^{3+}(aq)HClO_4–DClO_4$. Numbers in parentheses indicate the oscillator strength ratios for the given transition and the $^6H_{15/2} \longrightarrow {}^6(F_{11/2} + H_{9/2})$ transition.

by the *s*th vibration at $T = 0$ K. The summation is carried out over all odd vibrations. At sufficiently high temperatures ($2kT > h\nu$), function (2) tends to a straight line passing through the origin of the coordinates.

The experimental temperature dependences of the intensity of *f–f* transitions are due to the competition of the aforementioned mechanisms. As the temperature increases, the transition intensity can increase or decrease depending on the ratio between the contributions of two mechanisms of the allowed transition. In particular, the intensity of the $^3H_4 \longrightarrow {}^3H_6$ transition in the Pr1 glass approximately follows relationship (2) for the vibronic mechanism (Fig. 3b). The contribution of the vibronic mechanism to the intensity of the $^3H_4 \longrightarrow {}^3F_3$ transition in Pr^{3+} is rather large for the studied glasses (Fig. 3a). The $^3H_4 \longrightarrow {}^3F_2$ transition is allowed primarily by static distortions. It should be noted that the temperature dependences of the intensities of transitions, for example, in Pr^{3+} (Fig. 3a), do not depend on the matrix type, even though the matrix strongly affects the magnitudes of these intensities. This means that the character of the temperature dependences and, hence, the ratio of the contributions to the transition intensity are essentially the features of a particular transition rather than of the glass matrix.

The intensity of the $^3H_4 \longrightarrow {}^3F_4$ transition in Pr^{3+} in the Pr1 and Pr4 (Pr3) glasses is approximately halved with an increase in the temperature from 93 K to room temperature. Similar effects were observed by Bell *et al.* [9] for the absorption bands of Pr^{3+} in the visible spectral range in the temperature range 21–360°C. The severe decrease in the intensity cannot be explained by the thermal expansion of the glass matrices. This implies that the odd distortions responsible for the intensity of a particular transition substantially decrease with an increase in the temperature. It is quite possible that the same situation, but to a smaller degree, occurs for other transitions and, hence, for other odd distortions. As is known, a decrease in the temperature often leads to the lowering of the crystal symmetry; i.e., the structural phase transition takes place. In glasses, similar phenomena can be observed at certain temperatures in microscopic regions without macroscopic phase transitions.

The temperature dependences of the intensity of the *f–f* transitions in Dy^{3+} in the studied glasses are considerably weaker than those of the praseodymium-containing glasses. No specific features of the supersensitive transition are observed. Thus, we can conclude that the odd distortions around rare-earth ions in the dysprosium-containing glasses are weakly temperature dependent as compared to those in the praseodymium-containing glasses.

3.2. Locations and widths of the absorption bands. The location of absorption bands for a material in a condensed state depends primarily on the even components of the interaction between the absorbing ion and the environment (the crystal field and covalence). These interactions vary with an increase in the temperature due to thermal expansion of the material. Hence, the observed temperature dependences of the absorption band location (Fig. 5) reflect the thermal expansion of glasses. The presumably symmetric dispersion of even distortions does not affect the location of the absorption maximum but leads to the broadening of the absorption bands. In glasses, this inhomogeneous broadening makes the main contribution to the linewidth. If the dispersion of even distortions increases with a rise in the temperature, the inhomogeneous broadening should also increase. In crystals, the shape of the *f–f* absorption bands reflects the density of states of acoustic phonons in the neighborhood of the excited ion (see, for example, [21]). An increase in the temperature results in an increase in the width of these bands due to different relaxation processes. This suggests that the widths of the observed bands should increase with a rise in the temperature. Actually, the widths of the majority of the absorption bands for the praseodymium-containing glasses (Fig. 4) and the widths of all the absorption bands for the dysprosium-containing glasses increase. The linewidths for the Dy1 (Dy2) glass are less than those for the Dy3 glass, and the linewidths for the Pr1 glass are smaller than those for the Pr4 (Pr3) glass. Consequently, the dispersion of even distortions in the Dy1 (Dy2) glass is smaller than that in the Dy3 glass, and this dispersion in the Pr1 glass is less than that in the Pr4 (Pr3) glass. In both pairs, the smaller dispersion of even distortions is observed for the SiO_2–P_5O_2–GeO_2 glass matrix.

In the Pr1 and Pr4 (Pr3) glasses, the width of the $^3H_4 \longrightarrow {}^3F_4$ (Pr^{3+}) band exhibits a specific behavior: its value decreases with an increase in the temperature. This is the same transition whose intensity drastically decreases with an increase in the temperature. However, this can be only a coincidence, because the distortions responsible for the intensity and the linewidth differ radically: these are the odd and even distortions, respectively. The observed decrease in the linewidth can be explained by the decrease in the particular even distortion and, as a consequence, by the decrease in its dispersion.

4. CONCLUSION

Thus, in the present work, it was shown that the *f–f* transitions in the studied glasses are allowed primarily by the static odd distortions, which decrease with an increase in the temperature. The temperature dependences of the intensity of the *f–f* transitions are not affected by the matrix and depend on the type of electron transitions. The intensity of the $^3H_4 \longrightarrow {}^3F_4$ transition in Pr^{3+} considerably decreases with an increase in the temperature. This indicates the severe decrease in the particular odd distortions. The same transition is characterized by the specific behavior of the linewidth: it decreases with an increase in the temperature. This effect was explained by the decrease in the particular even distortions.

The comparative analysis of the absorption band parameters for different materials made it possible to determine the differences in the magnitudes, symmetries, and dispersions of the distortions in the nearest environment of rare-earth ions in different glasses. In particular, it was proved that (i) the symmetry of odd distortions depends on the matrix and the rare-earth ion type; (ii) the symmetry of the odd distortions in the Pr4 (Pr3) glass with the LiB_3O_5 matrix is similar to that in the $Pr^{3+}:Y_3Al_5O_{12}$ crystal, but the distortions in the glass are substantially smaller; and (iii) the dispersion of the even distortions is minimum in the SiO_2–P_5O_2–GeO_2 glass matrix.

ACKNOWLEDGMENTS

We are grateful to R. Reisfeld for helpful discussions.

This work was supported by the Russian Foundation for Basic Research (project nos. 99-02-17375 and 00-02-16098) and the KAMEA Program (Israel).

REFERENCES

1. G. H. Dieke, *Spectra and Energy Levels of Rare-Earth Ions in Crystals* (Interscience, New York, 1968).
2. R. D. Peacock, Struct. Bonding (Berlin) **22**, 83 (1975).
3. R. Reisfeld, Struct. Bonding (Berlin) **22**, 123 (1975).
4. C. Görller-Walrand and K. Binnemans, *Handbook on the Physics and Chemistry of Rare Earths*, Ed. by K. A. Gschneidner and L. Eyring (North-Holland, Amsterdam, 1998), Vol. 25, p. 101.
5. S. Tanabe, T. Hanada, M. Watanabe, *et al.*, J. Am. Ceram. Soc. **78** (11), 2917 (1995).
6. B. R. Judd, Phys. Rev. **127** (3), 750 (1962).
7. G. S. Ofelt, J. Chem. Phys. **37** (3), 511 (1962).
8. C. K. Jørgensen and B. R. Judd, Mol. Phys. **8** (3), 281 (1964).
9. J. T. Bell, C. C. Thompson, and D. M. Helton, J. Phys. Chem. **73** (10), 3338 (1969).
10. G. T. Petrovskiĭ, I. S. Édelman, T. V. Zarubina, *et al.*, J. Non-Cryst. Solids **130** (40), 35 (1991).
11. I. S. Édel'man, A. M. Potseluĭko, V. N. Zabluda, *et al.*, Fiz. Khim. Stekla **26** (1), 96 (2000).
12. J. Hormadaly and R. Reisfeld, J. Non-Cryst. Solids **30** (3), 337 (1979).
13. M. Malinowski, R. Wolski, and W. Wolinski, Solid State Commun. **74** (1), 17 (1990).
14. P. Goldner and F. Auzel, J. Appl. Phys. **79** (10), 7972 (1996).
15. W. F. Krupke, Phys. Rev. **145** (1), 325 (1966).
16. J. A. Medeiros Neto, D. W. Hewak, and H. Tate, J. Non-Cryst. Solids **183** (1–2), 102 (1995).
17. W. T. Carnall, J. P. Hessler, and F. Waagner, J. Phys. Chem. **82** (20), 2152 (1978).
18. W. T. Carnall, P. R. Fields, and K. Rajnak, J. Chem. Phys. **49** (10), 4412 (1968).
19. G. A. Bandurkin, B. F. Dzhurinskiĭ, and I. V. Tananaev, *Specific Features of Crystal Chemistry of Rare-Earth Compounds* (Nauka, Moscow, 1984).
20. A. D. Liehr and C. J. Ballhausen, Phys. Rev. **106** (9), 1161 (1957).
21. M. J. L. Sangster, Phys. Rev. **6** (1), 254 (1972).

Translated by O. Borovik-Romanova

Physics of the Solid State, Vol. 43, No. 6, 2001, pp. 1043–1051. From Fizika Tverdogo Tela, Vol. 43, No. 6, 2001, pp. 1010–1017.
Original English Text Copyright © 2001 by Basun, Kaplyanskiĭ, Kutsenko, Dierolf, Tröster, Kapphan, Polgar.

SEMICONDUCTORS AND DIELECTRICS

Dominant Cr^{3+} Centers in $LiNbO_3$ under Hydrostatic Pressure[1]

S. A. Basun[1], A. A. Kaplyanskiĭ[1], A. B. Kutsenko[1, 2], V. Dierolf [2],
T. Tröster[2], S. E. Kapphan[3], and K. Polgar[4]
[1] *Ioffe Physical-Technical Institute, St.-Petersburg, 194021 Russia*
e-mail: A.Kutsenko@pop.ioffe.rssi.ru
[2] *Fachbereich Physik, Universität-GH Paderborn, D-33095, Germany*
[3] *Fachbereich Physik, Universität Osnabrück, D-49069, Germany*
[4] *Research Institute for Solid State Physics and Optics, 1121 Budapest, Hungary*

Received October 31, 2000

Abstract—Low-temperature luminescence spectra of stoichiometric Cr : $LiNbO_3$ and of congruent Cr, Mg : $LiNbO_3$ were studied. Cr^{3+} impurity ions preferentially occupy Li^+ sites (Cr_{Li}) in the $LiNbO_3$ crystal lattice, while Cr^{3+} ions substituting for Nb^{5+} ions (Cr_{Nb}) occur in addition to Cr_{Li} centers in codoped Cr, Mg : $LiNbO_3$ crystals. Application of a high hydrostatic pressure leads to a transformation of (dominant in concentration) Cr^{3+} centers from low- to high-crystal-field centers. Due to a strong pressure-induced blue shift of the $^4T_2$ state resulting in crossing with the ^2E state, the replacement of the broad band $^4T_2 \longrightarrow {}^4A_2$ emission by a narrow *R*-line emission $^2E \longrightarrow {}^4A_2$ occurs in the luminescence spectra of the samples. This effect of level crossing was observed for the dominant Cr^{3+}_{Li} and Cr^{3+}_{Nb} centers at pressures which correlated well with estimations based on the $^4T_2$–^2E energy gap (230 and 1160 cm^{-1}) and on the rate of their pressure-induced change (14.35 and 11.4 cm^{-1}/kbar, respectively). © *2001 MAIK “Nauka/Interperiodica”.*

1. INTRODUCTION

$LiNbO_3$ crystals doped with Cr^{3+} ions have been investigated intensively since 1968, and considerable progress was made recently in understanding the complicated optical spectra of this material [1–9]. In the rhombohedral (space group *R*3*c*) lattice of $LiNbO_3$, the cations Li^+ and Nb^{5+} are surrounded by 6 oxygen ions forming trigonally distorted octahedrons. The present interpretation (see, e.g., [4]) based on ESR data (see [10–12] and references therein) assumes that the “main” (dominant in concentration) Cr^{3+} centers in $LiNbO_3$ crystals correspond to Cr^{3+} ions that are substituted into regular Li^+ sites in the host lattice. The energy diagram of $Cr^{3+}_{Li}(3d^3)$ electronic states corresponds to the case of a low octahedral crystal field, where the energy of the electronic $^4T_2(t^2e)$ state is lower than that of the $^2E(t^3)$. Therefore, the broad band $^4T_2(t^2e) \longrightarrow {}^4A_2(t^3)$ transition [2, 4] dominates at low temperatures in the photoluminescence spectrum of Cr^{3+} : $LiNbO_3$. The positions of two broad absorption bands, $^4A_2 \longrightarrow {}^4T_2$ and $^4A_2 \longrightarrow {}^4T_1$, provide the green color of the Cr^{3+} : $LiNbO_3$ samples.

Most studies on Cr^{3+} in congruent $LiNbO_3$ crystals codoped with Mg (at an Mg concentration less than 4.5 mol %) show that Cr^{3+} ions also preferentially occupy Li^+ sites (Cr^{3+}_{Li}). However, with increasing the Mg concentration (higher than 4.5 mol % for congruent samples), a fraction of the Cr^{3+} ions tends to additionally occupy Nb^{5+} sites (Cr^{3+}_{Nb}) in the $LiNbO_3$ lattice, which was confirmed by ESR and ENDOR studies [13–15]. Above this Mg concentration threshold, the samples change color from green to pink due to a strong red shift of the broad band transitions $^4A_2 \longrightarrow {}^4T_2$, $^4A_2 \longrightarrow {}^4T_1$ of the Cr^{3+}_{Nb} centers relative to those of the Cr^{3+}_{Li} centers. The Cr^{3+} ions substituting for Nb^{5+} are also at low-crystal-field octahedral sites, and the emission of Cr^{3+}_{Nb} centers in Mg codoped $LiNbO_3$ samples is characterized by an intense broad band $^4T_2 \longrightarrow {}^4A_2$ transition, which exhibits a red shift relative to the $^4T_2 \longrightarrow {}^4A_2$ transition of Cr^{3+}_{Li} centers in $LiNbO_3$ [4, 15].

As was shown earlier [16], the effect of high hydrostatic pressure on the spectroscopic properties of crystals with octahedrally coordinated impurity Cr^{3+} ions is a powerful tool for studying the electronic structure of impurity centers. Indeed, the hydrostatic pressure results in a decrease in the distance *R* between impurity ions and ligands and, hence, in an increase in the crystal field strength *Dq* ($\sim 1/R^5$). According to the crystal field theory for $Cr^{3+}(3d^3)$ ions in an octahedral field, the

---

[1] This article was submitted by the authors in English.

increase of Dq strongly shifts the energies of the $^4T_2$ and $^4T_1$ states upward, while the energy of the ^2E state depends on the distance from the ligands much less [17]. Therefore, the applied pressure drastically changes the distance between the low-lying $^4T_2$ and ^2E levels of Cr^{3+}, resulting in strong effects in the luminescence properties of Cr^{3+} ions due to changes in the mixing and relative population of the $^4T_2$ and ^2E states [16]. Of special interest is the behavior of low-field sites of Cr^{3+} under pressure application when pressure-induced crossing of the lower $^4T_2$ and the higher ^2E electronic levels can be achieved. This crossing leads to the inversion of the lowest (emitting) state of Cr^{3+} from $^4T_2$ (at ambient pressure) to ^2E (at higher pressure). This manifests itself in drastic effects in the spectral and kinetic properties of the Cr^{3+} luminescence at low temperatures. Such a pressure-induced $^4T_2$, ^2E crossing was recently discovered experimentally for low-field dominant $\mathrm{Cr}_{\mathrm{Li}}^{3+}$ centers in congruent $\mathrm{LiNbO_3}$. At low temperatures, the change from broad band $^4T_2 \longrightarrow {}^4A_2$ luminescence at ambient pressure to sharp R-line emission $^2E \longrightarrow {}^4A_2$ under high hydrostatic pressure application was observed [18, 19]. As to low-field $\mathrm{Cr}_{\mathrm{Nb}}^{3+}$ centers in Mg codoped congruent $\mathrm{LiNbO_3}$, a large pressure-induced shift of the $^4T_2 \longrightarrow {}^4A_2$ band was observed, but the highest pressure value (~100 kbar) used in [18, 19] was insufficient to observe the crossing of the $^4T_2$ and $^4A_2$ levels of $\mathrm{Cr}_{\mathrm{Nb}}^{3+}$ centers.

In the present paper, the effect of high pressures, up to 300 kbar, on the luminescence spectra of low-field $\mathrm{Cr}_{\mathrm{Li}}^{3+}$ and $\mathrm{Cr}_{\mathrm{Nb}}^{3+}$ centers in $\mathrm{LiNbO_3}$ was studied experimentally at 4 K. The appearance of the R-lines emission due to pressure-induced crossing of $^4T_2$ and ^2E levels was observed for both types of Cr^{3+} centers. The energies determined for the electronic levels $^4T_2$ and ^2E, together with the data on the pressure dependence of the $^4T_2$–^2E energy gap, allowed us to estimate the values of pressure that correspond to the $^4T_2$–^2E crossing points for $\mathrm{Cr}_{\mathrm{Li}}^{3+}$ (16 kbar) and for $\mathrm{Cr}_{\mathrm{Nb}}^{3+}$ (102 kbar). These values agree well with experimentally determined ones when the $^4T_2$–^2E level crossing of these centers occurs under the pressure applied. Studies of the photoexcitation spectra (in the energy region of R lines) of the $^4T_2 \longrightarrow {}^4A_2$ broad band luminescence of $\mathrm{Cr}_{\mathrm{Li}}^{3+}$ and $\mathrm{Cr}_{\mathrm{Nb}}^{3+}$ centers at ambient pressure reveal a strong homogeneous broadening of the ^2E states due to fast nonradiative relaxation to lower ($^4T_2$) states of these low-field sites.

Perfect, close-to-stoichiometric, “green” samples of $\mathrm{Cr}^{3+}:\mathrm{LiNbO_3}$ were used to study $\mathrm{Cr}_{\mathrm{Li}}^{3+}$ centers. For a study of $\mathrm{Cr}_{\mathrm{Nb}}^{3+}$ centers, congruent codoped “red” Cr, $\mathrm{Mg}:\mathrm{LiNbO_3}$ samples were used (these samples contain both $\mathrm{Cr}_{\mathrm{Li}}^{3+}$ and $\mathrm{Cr}_{\mathrm{Nb}}^{3+}$ centers). High-hydrostatic-pressure measurements were performed using a diamond-anvil cell. A mixture of ethanol, methanol, and water was used as a pressure-transmitting medium. For pressure calibration and monitoring of the hydrostatic conditions, the R-line luminescence of ruby was used from small ruby granules (~20 μm size), which were loaded into the cell together with a probe sample (~80 μm size). The 488 nm line of an Ar-ion laser was used as an excitation source for the luminescence measurements of $\mathrm{Cr}^{3+}:\mathrm{LiNbO_3}$ and ruby. The high-pressure cell was mounted in a bath helium cryostat for measuring at 4K.

2. EFFECT OF HIGH PRESSURE ON THE LUMINESCENCE SPECTRA OF LOW-FIELD $\mathrm{Cr}_{\mathrm{Li}}^{3+}$ CENTERS IN $\mathrm{Cr}^{3+}:\mathrm{LiNbO_3}$ CRYSTALS

A close-to-stoichiometric sample of $\mathrm{Cr}^{3+}:\mathrm{LiNbO_3}$ (~0.25 mol % Cr) was prepared by the vapor phase transport equilibration (VTE) technique [5]. At ambient pressure, in the luminescence of this sample at liquid helium temperatures, only transitions from the lowest excited state $^4T_2$ of the low-field Cr^{3+} centers are observed. The broad $^4T_2 \longrightarrow {}^4A_2$ band emission with a narrow zero-phonon line at 13540 cm^{-1} is associated with “majority” (dominating in concentration) low-field $\mathrm{Cr}_{\mathrm{Li}}^{3+}$ sites [8]. Some contribution to the broad band emission $^4T_2 \longrightarrow {}^4A_2$ is also given by the “minority” low-field Cr^{3+} centers [8] with a relatively small concentration. The microscopic nature of the minority centers is not completely clear yet (these centers were attributed to Cr^{3+} ions in intrinsic octahedral voids in the $\mathrm{LiNbO_3}$ lattice [8]). The presence of minority low-field centers in the sample follows directly from the luminescence spectrum at elevated temperatures, when the appearance of $^2E \longrightarrow {}^4A_2$ transitions (R-lines) is stimulated by thermal population of the upper doublet ^2E states. Indeed, at 65 K, besides the doublet R_1 = 13772 and R_2 = 13810 cm^{-1} belonging to the majority $\mathrm{Cr}_{\mathrm{Li}}^{3+}$ centers, additional lines R_1' = 13683 and R_2' = 13747 cm^{-1} of minority low-field centers are observed in the luminescence (see also [8, Fig. 3]).

The luminescence spectra of stoichiometric $\mathrm{Cr}^{3+}:\mathrm{LiNbO_3}$ at different hydrostatic pressures are presented in Fig. 1. At ambient pressure, only the onset of the $^4T_2 \longrightarrow {}^4A_2$ broad band transition with the zero phonon line 13540 cm^{-1} of the dominant $\mathrm{Cr}_{\mathrm{Li}}^{3+}$ centers can be seen. The short wavelength region of $^2E \longrightarrow {}^4A_2$ transitions is practically empty. But already at 16 kbar, two lines R_1' and R_1 in this spectral region are clearly seen. We can attribute them to $E(^2E) \longrightarrow {}^4A_2$ transitions from the lowest sublevel (populated at 4 K) of the doublet ^2E state of the minority and majority low-field centers, respectively. Arguments in support of this assignment are given below. While at 16 kbar the intensity of R_1' exceeds that of the R_1 line, the R_1 line of the majority centers becomes dominant in the spectra at higher pressures. The pressure-induced appearance of the $E(^2E) \longrightarrow {}^4A_2$ lines is obviously due to the crossing of excited $^4T_2$ and ^2E states, when the $E(^2E)$ state becomes the lowest emitting state. In some spectra in Fig. 1, the R_2 line related to $2A(^2E) \longrightarrow {}^4A_2$ transitions from the upper sublevel of the doublet ^2E state of the majority centers also shows up in the luminescence. The reason for this is thermal population of the upper sublevel caused by local heating of a very small piece of $Cr^{3+} : LiNbO_3$ in the high-pressure cell by the excitation laser beam. It should also be noted that at very high pressures >140 kbar, the luminescence spectrum changes drastically and reveals the appearance of some additional structure of R lines. The origin of such behavior is not completely clear. It can be caused by nonhydrostatic perturbation or by the formation of different crystalline phases of $LiNbO_3$ at very high pressures.

Figure 2 displays the frequencies of the luminescence lines detected at different hydrostatic pressures. With an increase in pressure, all R lines exhibit a red shift. The linear extrapolation of experimental dependences to zero pressure gives the positions of these lines at ambient pressure. The obtained values for the R_1 and R_2 lines 13772 and 13810 cm^{-1} coincide with the R_1 and R_2 frequencies ($E(^2E) \longrightarrow {}^4A_2$, $2A(^2E) \longrightarrow {}^4A_2$ transitions) of the majority low-field centers. These lines also manifest themselves in absorption and photoexcitation spectra of $Cr^{3+} : LiNbO_3$ at ambient pressure [2–4, 20] and are interpreted as lines of dominant low-field Cr_{Li}^{3+} centers (γ centers [4]). The frequency of the R_1' line extrapolated to zero pressure is equal to 13683 cm^{-1}, which coincides well with that for the $E(^2E) \longrightarrow {}^4A_2$ transition of the minority low-field centers [8]. It follows from Fig. 2 that the energies of the ^2E states of the majority and of the minority low-field centers have slightly different sensitivity to pressure (their linear shift coefficients are 2.35 and 2.72 cm^{-1}/kbar, respectively). The weak line at the low-energy side of the spectra (Fig. 1) demonstrates the same pressure dependence of the frequency as the R_1 line and probably can be identified with a vibronic satellite of the zero-phonon R_1 line of the majority low-field Cr_{Li}^{3+} centers, with the corresponding vibration frequency being ~270 cm^{-1}.

The above explanation of the origin of pressure-induced R-line spectra of $Cr^{3+} : LiNbO_3$ as the result of the $^4T_2$–^2E level crossing of low-field majority and minority Cr^{3+} centers is also confirmed by a quantitative estimate of the applied pressure values corresponding to the $^4T_2$–^2E level crossing point for the majority

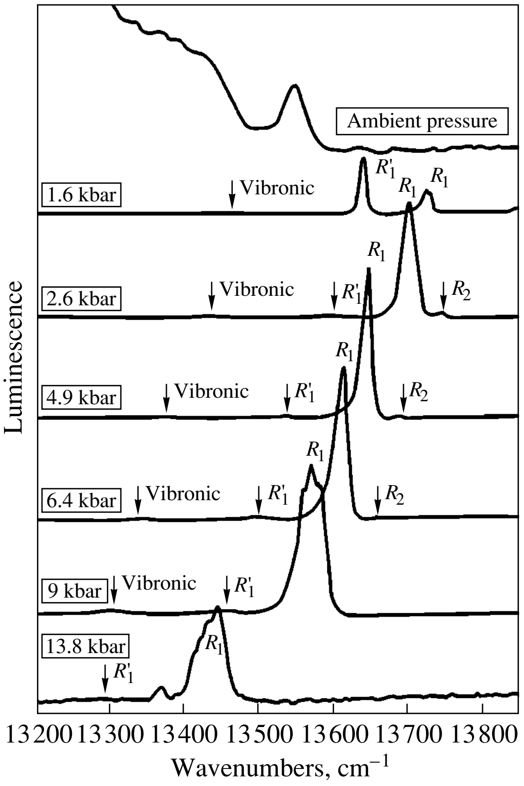

Fig. 1. Luminescence spectra of a VTE-treated sample of $Cr : LiNbO_3$ under hydrostatic pressure (T = 4 K, λ_{exc} = 488 nm).

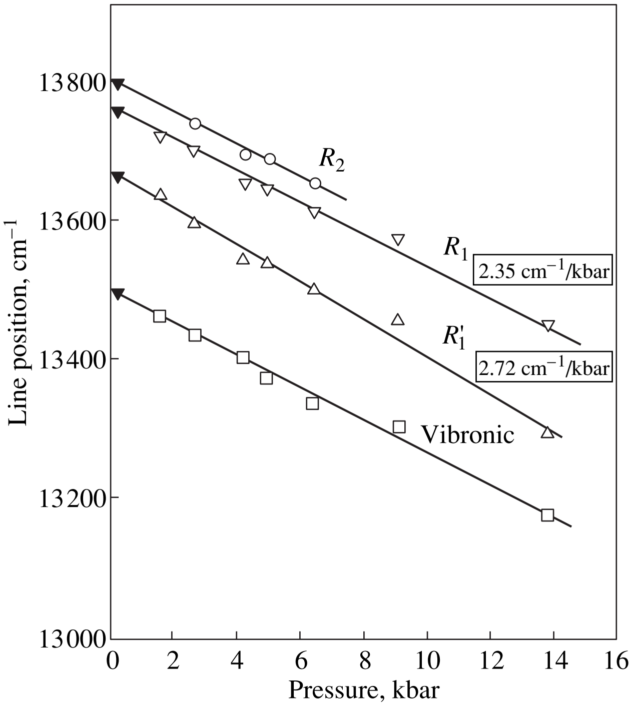

Fig. 2. Pressure dependence of the spectral position of the R lines of $Cr : LiNbO_3$.

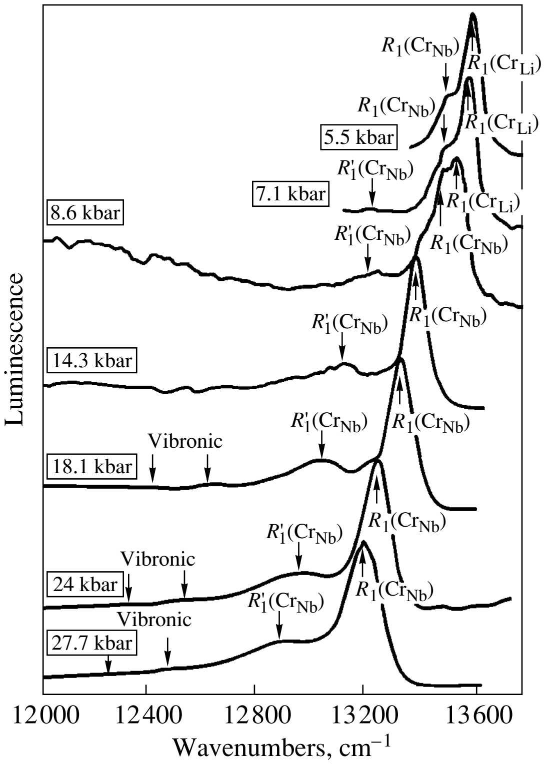

Fig. 3. Luminescence spectra of a congruent Cr, Mg : $LiNbO_3$ sample under hydrostatic pressure ($T = 4$ K, $\lambda_{exc} = 488$ nm).

and minority Cr^{3+} centers. Evidently, these pressure values depend on the $^4T_2$–^2E energy difference and on the rate of its change with applied hydrostatic pressure. The energy interval between the electronic $^4T_2$ and ^2E states of low-field centers is directly determined as the spectral distance between zero-phonon lines of the $^4T_2 \longrightarrow {}^4A_2$ broad band and of the $E(^2E) \longrightarrow {}^4A_2$ transition (R lines). The energies of the zero-phonon $^4T_2 \longrightarrow {}^4A_2$ lines for the majority and minority low-field Cr^{3+} centers are 13540 [8] and 13560 cm^{-1} [20], respectively. Using the energies of R_1 (13772 cm^{-1}) and R_1' (13683 cm^{-1}) for the majority and minority sites, we obtain the values of the $^4T_2$–$E(^2E)$ intervals for these sites as ~230 and 125 cm^{-1}, respectively. The rate of pressure-induced change of the $^4T_2$–^2E interval is determined by the algebraic difference of rates for the $^4T_2$ and ^2E levels. The rate of the pressure-induced blue shift of the $^4T_2$ level based on measurements of the shift of the $^4T_2 \longrightarrow {}^4A_2$ emission band of the $\mathrm{Cr_{Li}^{3+}}$ centers is equal to 12 ± 3 cm^{-1}/kbar [18]. The observed blue direction of the pressure-induced shift of the $^4T_2 \longrightarrow {}^4A_2$ band is consistent with the prediction of the Sugano–Tanabe theory [17]. Using the rates for red shifts of R_1 and R_1' lines (Fig. 2), 2.35 and 2.72 cm^{-1}/kbar, we obtain the rates of pressure-induced shifts of $^4T_2$–^2E intervals for the majority and minority sites as 14.35 and 14.72 cm^{-1}/kbar, respectively. The ratio of the $^4T_2$–^2E interval to the above rate gives the value of pressure at which this interval becomes zero (crossing point): 16 kbar for the majority and 8.5 kbar for the minority low-field Cr^{3+} centers. These estimations are in good agreement with the observed sequence of appearance of R_1 lines in the luminescence spectra of the crystal with increasing pressure. The R_1' line of the minority centers appears first and dominates at relatively small pressures, below ~16 kbar, while the R_1 line of the majority centers becomes dominant at higher pressures. The constant ratio of intensities of the R_1' and R_1 lines at pressures >26 kbar is consistent with the low concentration of the minority low-field Cr^{3+} centers in comparison with the concentration of the dominating $\mathrm{Cr_{Li}^{3+}}$ centers.

The R_1 and R_2 lines of the main $\mathrm{Cr_{Li}^{3+}}$ centers observed in the luminescence of Cr^{3+} : $LiNbO_3$ under hydrostatic pressure due to the high concentration of these sites are easily observed at ambient pressure in absorption and photoexcitation spectra of the broad band $^4T_2 \longrightarrow {}^4A_2$ luminescence of a Cr^{3+} : $LiNbO_3$ crystal [2–4, 20]. In the pioneering work of [2], the anomalous large linewidth 50 cm^{-1} of the R_1 and R_2 absorption lines of the dominant low-field Cr^{3+} centers in congruent $LiNbO_3$ was observed and explained by the lifetime broadening of the ^2E state due to nonradiative relaxation from the ^2E to lower excited states of the low-field Cr^{3+} centers. Recently [20], a comparison of the linewidth of R_1 and of R_2 transitions of the dominant $\mathrm{Cr_{Li}^{3+}}$ centers in samples of different stoichiometry allowed us to estimate the lifetime broadening of the ^2E state as ~10 cm^{-1}, which corresponds to a decay time of ~5×10^{-13} s.

3. THE EFFECT OF HIGH PRESSURE ON THE LUMINESCENCE SPECTRA OF LOW-FIELD $\mathrm{Cr_{Nb}^{3+}}$ CENTERS IN Cr, Mg : $LiNbO_3$ CONGRUENT SAMPLES

Congruent $LiNbO_3$ codoped with 0.25 mol % Cr and 6 mol % Mg was grown using the Czohralski method. The red color of the sample is typical for $LiNbO_3$ samples with a high (more than 4.5 mol %) concentration of Mg, where Cr^{3+} ions occupy not only Li sites but also Nb sites of the crystal lattice. At ambient pressure, the low (liquid-helium) temperature luminescence spectrum of such samples contains overlapping broad $^4T_2 \longrightarrow {}^4A_2$ bands of both low-field $\mathrm{Cr_{Li}^{3+}}$ and $\mathrm{Cr_{Nb}^{3+}}$ centers (maximum at 900 and at 1000 nm, respectively [15]). In the short wavelength region of the $^4T_2 \longrightarrow {}^4A_2$ band, inhomogeneous broadened R lines of the perturbed high-field Cr_{Li}^{3+} centers (α and β types [4]) are observed in our congruent Cr, Mg : $LiNbO_3$ sample.

Figure 3 represents the low-temperature (T = 4 K) luminescence spectra in the region of the $^2E \longrightarrow {}^4A_2$ transitions at hydrostatic pressures starting from 55 kbar. In accordance with observations on the stoichiometric sample (Fig. 1), the pressure-induced R_1 line of the main Cr_{Li}^{3+} centers dominates at 55 kbar. A further increase in pressure results in the appearance of other intensive lines in the long wavelength region of the spectra, which we attribute to the R_1 lines of Cr^{3+} ions at the Nb sites. The most intense new short-wavelength line, which dominates in the spectra at high pressures above 140 kbar, can be attributed to the R_1 line [$E(^2E) \longrightarrow {}^4A_2$ transition] of the main Cr_{Nb}^{3+} centers, which are responsible for the red-shifted $^4A_2 \longrightarrow {}^4T_2$, $^4T_1$ absorption and $^4T_2 \longrightarrow {}^4A_2$ emission bands of red colored Cr, Mg : $LiNbO_3$ samples with an Mg concentration above the 4.5 mol % threshold. A second rather intense R_1' line in the spectra indicates the presence of another Cr_{Nb}^{3+} center in the sample. As follows from Fig. 3, the relative intensity of the R_1 line of the main Cr_{Li}^{3+} centers decreases significantly at pressures above 70 kbar. The observed drastic change in relative intensity of the R_1 luminescence of the Cr_{Nb}^{3+} and Cr_{Li}^{3+} centers with increasing the pressure (compare the spectra at pressures below and above 86 kbar) is due to the difference in the site selective excitation of these centers by the Ar line (488 nm) at low and high pressures. In Fig. 4, the excitation spectra of the broad band $^4T_2 \longrightarrow {}^4A_2$ emission of congruent Cr, Mg : $LiNbO_3$ and of stoichiometric Cr : $LiNbO_3$ samples at ambient pressure are shown. Indeed, the excitation spectra are significantly different for the sample with only Cr_{Li}^{3+} centers and for the sample with both Cr_{Li}^{3+} and Cr_{Nb}^{3+} centers because of the difference in energy of the $^4A_2 \longrightarrow {}^4T_1$ absorption band of the Cr^{3+} ions at Li and Nb sites. As one can see, at ambient pressure, the 488 nm Ar-laser line is located near the maximum of the $^4A_2 \longrightarrow {}^4T_1$ band of the Cr_{Li}^{3+} centers, thus providing the preferential excitation of Cr_{Li}^{3+} centers at moderate hydrostatic pressures. Assuming the rate of a pressure-induced shift of the $^4T_1$ state to a higher energy to be approximately 12 cm^{-1}/kbar [18], we conclude that, at hydrostatic pressures above 70 kbar, the $^4A_2 \longrightarrow {}^4T_1$ band shifted to higher energies will strongly reduce the efficiency of the 488 nm photoexcitation of the Cr_{Li}^{3+} centers and increase this efficiency for the Cr_{Nb}^{3+} centers.

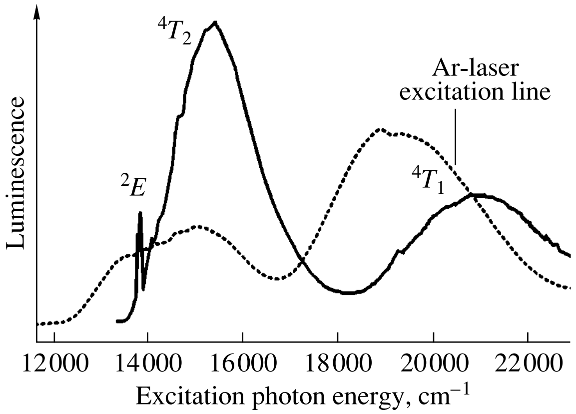

Fig. 4. Photoexcitation spectra of the $^4T_2 \longrightarrow {}^4A_2$ emission in stoichiometric Cr : $LiNbO_3$ (solid line) and congruent Cr, Mg : $LiNbO_3$ (dashed line) samples (T = 4 K). Luminescence monitored at 11200–8500 cm^{-1}.

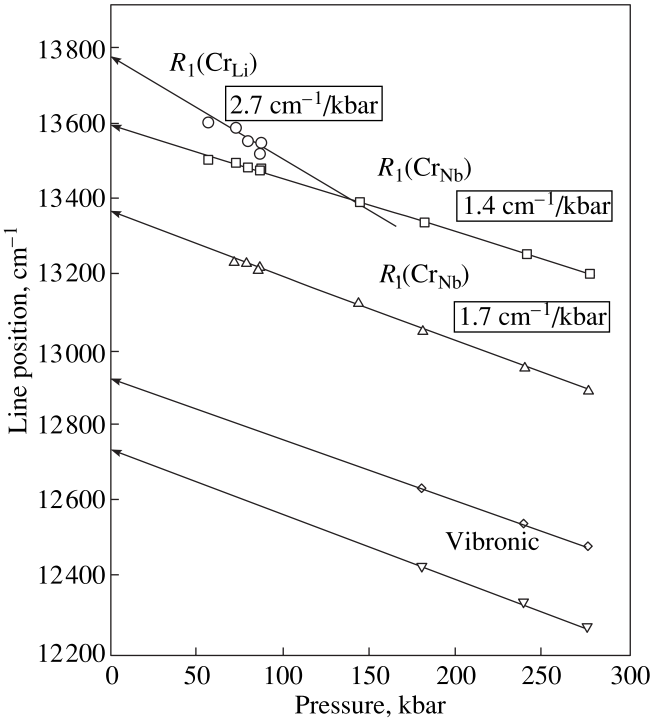

Fig. 5. Pressure dependence of the spectral position of the R lines of a Cr, Mg : $LiNbO_3$ sample.

In Fig. 5, the energies of the lines detected are plotted versus hydrostatic pressure. The linear pressure dependence of these energies is demonstrated. The slope for the R_1 position of the Cr_{Li}^{3+} centers (~2.7 cm^{-1}/kbar) coincides well with that for Cr_{Li}^{3+} centers in stoichiometric samples (Fig. 2). The R_1 and R_1' lines of the two Cr_{Nb}^{3+} centers are much less sensitive to pressure (1.4 and 1.7 cm^{-1}/kbar, respectively). The linear extrapolation to ambient pressure gives a frequency of 13595 for the R_1 and 13365 cm^{-1} for the R_1' line. The positions of two weak satellite lines detected in the low-energy region of

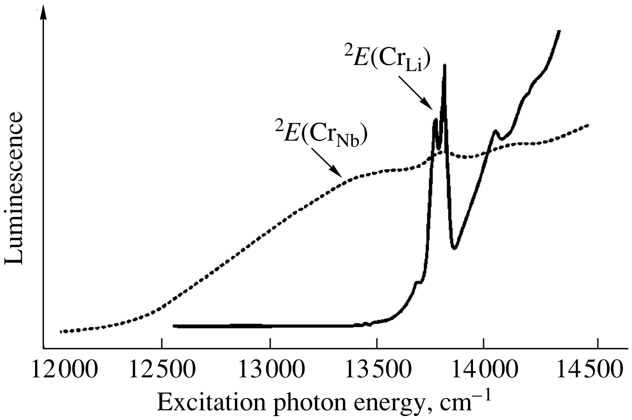

Fig. 6. Detailed photoexcitation spectra of the $^4T_2 \longrightarrow {}^4A_2$ emission in Cr : LiNbO$_3$ (solid line) and in Cr, Mg : LiNbO$_3$ (dashed line) samples in the region of $^4A_2 \longrightarrow {}^2E$ transitions (T = 4 K). Luminescence monitored at 11200–8500 cm^{-1}.

the spectra (Fig. 4) reveal the same pressure dependence (1.7 cm^{-1}/kbar) as the most intense R_1 line of Cr$^{3+}_{Nb}$ and probably can be identified with the vibronic satellites of this line. The corresponding vibration frequencies are 670 and 860 cm^{-1}.

As was mentioned above, the most intense R_1 line, which appears at high pressures only in Cr, Mg : LiNbO$_3$, should be attributed to the dominant low-field Cr$^{3+}_{Nb}$ centers responsible for the main spectroscopic features of red samples such as the $^4A_2 \longrightarrow {}^4T_2$, $^4T_1$ absorption bands and the broad $^4T_2 \longrightarrow {}^4A_2$ emission band centered at 1000 nm [15]. The hydrostatic pressure induces a blue shift of this emission band at a rate of approximately 10 cm^{-1}/kbar [18, Fig. 5]. As was observed in the present study, the broad band $^4T_2 \longrightarrow {}^4A_2$ is completely absent at a pressure of 140 kbar (Fig. 3) because of the crossing of the $^4T_2$ and ^2E states also being accompanied by the appearance of a $^2E \longrightarrow {}^4A_2$ R_1-line emission. This pressure far exceeds the pressure of 16 kbar required for the $^4T_2$–^2E level crossing in the main Cr$^{3+}_{Li}$ centers (Section 2). We assume that this difference is due to the much larger distance between the $^4T_2$ and ^2E states of the Cr$^{3+}_{Nb}$ centers in comparison with the corresponding distance (230 cm^{-1}) for the Cr$^{3+}_{Li}$ centers. The absence of the detectable zero-phonon line $^4T_2 \longrightarrow {}^4A_2$ for the Cr$^{3+}_{Nb}$ centers prevents direct determination of the position of the electronic $^4T_2$ state of these centers and does not allow one to find precisely the $^4T_2$–^2E distance for the Cr$^{3+}_{Nb}$ centers. However, the following estimation can be made. The red shift of the broad $^4T_2 \longrightarrow {}^4A_2$ emission band of the dominant Cr$^{3+}_{Nb}$ centers (maximum at 1000 nm) relative to that of the dominant Cr$^{3+}_{Li}$ centers (maximum at 900 nm) is equal to ~1100 cm^{-1} [15]. Assuming the same red shift for the zero-phonon line of the $^4T_2 \longrightarrow {}^4A_2$ band and knowing the position of the $^4T_2 \longrightarrow {}^4A_2$ zero-phonon line of the Cr$^{3+}_{Li}$ centers (13540 cm^{-1}), we find that the position of this line of Cr$^{3+}_{Nb}$ centers is 12440 cm^{-1} = 13540 – 1100 cm^{-1}, which is equal to the excitation energy of the electronic $^4T_2$ state. The value of 12440 cm^{-1} is in agreement with the position of the zero-phonon $^4A_2$–$^4T_2$ line estimated in [4] for Cr$^{3+}_{Nb}$ centers denoted as δ centers. The ($^4T_2$–^2E) energy distance of 1160 cm^{-1} is determined as the difference (13600 – 12440 cm^{-1}) between this energy and the energy of the lowest sublevel of the ^2E doublet extrapolated to the ambient pressure position of the R_1 line, 13595 cm^{-1}. Thus, the value of the $^4T_2$–^2E energy interval for the Cr$^{3+}_{Nb}$ centers (1160 cm^{-1}) exceeds the corresponding interval for the Cr$^{3+}_{Li}$ centers (230 cm^{-1}) by a factor of 5; therefore, the pressure needed for the crossing of the $^4T_2$ and ^2E levels for Cr$^{3+}_{Nb}$ centers should be much higher than that for Cr$^{3+}_{Li}$.

In order to estimate the pressure that corresponds to the crossing point of the $^4T_2$ and ^2E levels, we used data [18] on the pressure-induced shift of the broad $^4T_2 \longrightarrow {}^4A_2$ emission band of Cr$^{3+}_{Nb}$ centers in a Cr, Mg : LiNbO$_3$ crystal at an Mg concentration of ~5.5% [18, Fig. 5]. In [18, Fig. 5], a comparison of the spectra at 24 kbar (at this pressure, the $^4T_2 \longrightarrow {}^2E$ crossing in Cr$^{3+}_{Li}$ centers already occurs and only the $^4T_2 \longrightarrow {}^4A_2$ band of Cr$^{3+}_{Nb}$ centers should be seen) and at 93 kbar is made. From the observed shift of the $^4T_2 \longrightarrow {}^4A_2$ band, we determined the linear rate of its pressure-induced blue shift as ~10 cm^{-1}/kbar. Adding to this value the rate 1.4 cm^{-1}/kbar of the red shift of the R_1 line of the $^2E \longrightarrow {}^4A_2$ transition frequency (R_1 line, Fig. 5), we obtain the coefficient of the linear pressure-induced change in the $^4T_2$–^2E energy interval as 11.4 cm^{-1}/kbar. This rate provides a decrease in the $^4T_2$–^2E distance from 1160 cm^{-1} to zero (crossing point) at the pressure 102 kbar (=1160/11.4 cm^{-1}/kbar). This estimation is in good agreement with the observed (Fig. 5) value of the pressure between 86 and 143 kbar needed for the disappearance of the broad $^4T_2 \longrightarrow {}^4A_2$ band.

The optical transitions $^4A_2 \longrightarrow {}^2E$ of Cr$^{3+}_{Nb}$ centers found in the above high-pressure experiments, which are located at 13595 cm^{-1} at ambient pressure, should in principle reveal themselves in observations of the corresponding resonant R transitions in the absorption spectra and in the $^4T_2 \longrightarrow {}^4A_2$ photoexcitation spectrum of Cr, Mg: LiNbO$_3$ samples similarly to such transitions of Cr_{Li}^{3+} centers (Section 2 and [2–4, 20]). Figure 6 shows the broad $^4T_2 \longrightarrow {}^4A_2$ band of the luminescence photoexcitation spectrum of the congruent Cr, Mg : $LiNbO_3$ red sample used in high-pressure measurements in the low energy region of the $^4A_2 \longrightarrow {}^4T_2$ absorption, also including the region of $^4A_2 \longrightarrow {}^2E$ transitions. In contrast to the case of Cr_{Li}^{3+} centers in $LiNbO_3$, where the R_1 and R_2 peaks were clearly observed in the photoexcitation spectrum (Fig. 6 and also [20]), no structure in the vicinity of the position (~13600 cm^{-1}) of the $^4A_2 \longrightarrow {}^2E$ transitions of Cr_{Nb}^{3+} centers is observed in the spectrum of the congruent Cr, Mg : $LiNbO_3$ sample. We assume that the lack of a resonant $^4A_2 \longrightarrow {}^2E$ structure in the photoexcitation spectrum of Cr_{Nb}^{3+} centers is due to a very large broadening of these transitions caused by lifetime homogeneous broadening of the ^2E state, together with a very large inhomogeneous broadening of the R transitions in the congruent codoped Cr, Mg : $LiNbO_3$ sample. The latter is clearly seen in the luminescence spectra of the sample at high pressure, when these transitions appear in the luminescence due to $^4T_2$–^2E level crossing (Fig. 3). The observed spectral width of the R_1 line of the Cr_{Nb}^{3+} centers (~80 cm^{-1}) not only far exceeds the width of the corresponding line of Cr_{Li}^{3+} centers (Fig. 1) observed at high pressures in near-to-stoichiometry VTE-treated samples, but also exceeds the inhomogeneous R-line width of perturbed high-field Cr^{3+} centers in congruent Cr : $LiNbO_3$ samples at ambient pressure [21, 22]. This very large inhomogeneous broadening of R lines of Cr_{Nb}^{3+} centers can be explained by a disorder in the lattice of codoped Cr, Mg : $LiNbO_3$ due to a very high (~6 mol %) concentration of Mg ions. Figure 3 also demonstrates a prominent increase in the inhomogeneous width of the R_1 line of Cr_{Nb}^{3+} centers with an increase in pressure. This effect can possibly be attributed to different pressure-induced shifts of the transition frequencies inside the inhomogeneously broadened zero-phonon line of the impurity ion [23, 25].

4. DISCUSSION

The experimental results in Section 2 on the pressure-induced crossing of the $^4T_2$ and ^2E states of the majority Cr_{Li}^{3+} centers in VTE-treated samples of Cr : $LiNbO_3$ are in good agreement with the results of an earlier study made on congruent samples (Cr : $LiNbO_3$ codoped with a small, 2%, concentration of Mg) [18, 19]. The measured coefficient of the pressure-induced linear R_1-line shift of the majority Cr_{Li}^{3+} centers is close to the value of 3 cm^{-1}/kbar given in [18]. At the same time, our experimental results show that the pressure-induced luminescence line that appears in the low energy region of the R_1 line of the majority centers should be attributed to the R_1' line of the minority Cr^{3+} centers [8] but not to perturbed defect β centers [4] as was supposed in [18, 19]. Indeed, the β centers, whose R_1 frequency at ambient pressure accidentally coincides with that of the low-field minority Cr^{3+} centers [8], are practically absent in our close-to-stoichiometry Cr^{3+} : $LiNbO_3$ sample. Furthermore, quantitative estimations of the pressure value corresponding to the $^4T_2$–^2E level crossing point that are based on spectroscopic data on the $^4T_2$–$E(^2E)$ energy intervals at ambient pressure for majority (230 cm^{-1}) and minority (125 cm^{-1}) low-field centers, as well as on measured linear pressure-induced shifts of spectral $^4T_2 \longrightarrow {}^4A_2$ and $^2E \longrightarrow {}^4A_2$ transitions, agree well with experimental data for both low-field centers; this confirms the validity of our interpretation. It should be noted that at high pressures, when inversion of the $^4T_2$ and ^2E levels of the main Cr^{3+} centers has already occurred, the relative intensity of the R lines of high-field perturbed Cr_{Li}^{3+} centers (α, β) must always be negligible compared to the R lines of main centers, even in congruent samples, where the integrated intensity of the R-line emission of perturbed centers does not exceed ~1/1000 of the integrated emission intensity of the main Cr^{3+} centers.

The results of Section 3 concerning the pressure-induced $^4T_2$–^2E level crossing in Cr_{Nb}^{3+} centers in congruent Cr, Mg : $LiNbO_3$ samples allowed us to obtain detailed information on the energy diagram of the excited electronic $^4T_2$ and ^2E states of these low-field centers, which are studied much less than the Cr_{Li}^{3+} centers. The centers of Cr^{3+} at Nb^{5+} sites were discussed recently in [24]. It is clear now that the large broadening of the ^2E level due to fast decay into lower excited states, together with the large inhomogeneous broadening of the R lines caused by a strong disorder of the codoped congruent Cr, Mg : $LiNbO_3$ crystals, hampers any direct manifestation of narrow R lines of low-field Cr_{Nb}^{3+} centers in absorption and photoexcitation spectra at ambient pressure. Only the pressure-induced inversion of the $^4T_2$ and ^2E levels, which results in cancellation of the lifetime broadening of the ^2E state, allows us to directly observe the resonant $^2E \longrightarrow {}^4A_2$ transitions in the luminescence of congruent Cr, Mg : $LiNbO_3$ crystals. In a recently published paper [26], the appearance of the R line in the luminescence of Cr_{Nb}^{3+} centers under hydrostatic pressure was detected in “near-stoichiometric” Cr, Mg : $LiNbO_3$ samples which reveal reduced inhomogeneous broadening of R lines. The determined values of the $^4T_2$–^2E energy gaps for Cr_{Nb}^{3+} centers in the present paper (1160 cm^{-1}) and in [26] (>1000 cm^{-1}) are consistent.

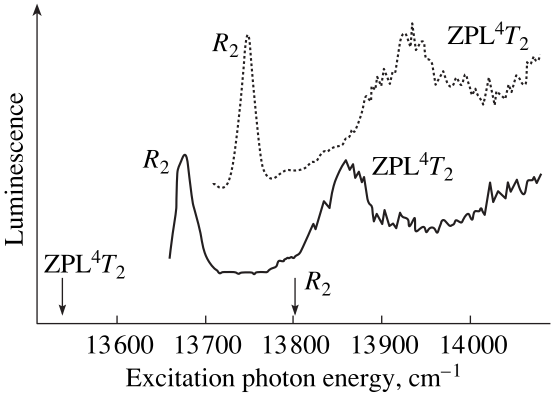

Fig. 7. Photoexcitation spectra of the $2A(^2E) \longrightarrow {}^4A_2$ emission of α centers (solid line) and β centers (dashed line) in a congruent $LiNbO_3$ sample at ambient pressure (T = 4 K). Luminescence is monitored at the $R_1(\alpha)$ and $R_1(\beta)$ lines, respectively. The arrows indicate the positions of the R_2 line and of the zero-phonon ${}^4T_2 \longrightarrow {}^4A_2$ line of unperturbed trigonal $\mathrm{Cr}_{\mathrm{Li}}^{3+}$ centers.

It is interesting to note that while the pressure-induced linear blue shifts of the ${}^4T_2 \longrightarrow {}^4A_2$ optical transitions differ slightly (~20%) for $\mathrm{Cr}_{\mathrm{Li}}^{3+}$ and $\mathrm{Cr}_{\mathrm{Nb}}^{3+}$ centers, the pressure-induced red shifts of the R lines (${}^2E \longrightarrow {}^4A_2$ transitions) for these centers differ almost by a factor of 2. As is known [17, 21], the ${}^2E$–${}^4A_2$ energy interval in Cr^{3+} ($3d^3$) ions is determined mainly by the Racah parameters B and C, which describe the Coulomb electron–electron interaction in the 3d shell in Cr^{3+} ions, and, to a smaller extent, by the crystal field strength $10Dq$. The Racah parameters of 3d ions in crystals are reduced from their free-ion values by covalency between 3d and ligand electrons, a phenomenon known as the nephelauxetic effect [21]. Similarly to the case of ruby, the pressure-induced red shift of the R lines of Cr^{3+} centers in $LiNbO_3$ can be due to a decrease in the Cr–O distance and an increase in the overlap between the 3d and ligand electrons, thus resulting in reduction of the Racah B parameter and, hence, in reduction of the ${}^4A_2 \longrightarrow {}^2E$ excitation energy. As can be seen, the pressure-induced reduction of the Racah parameter is essentially different for Cr^{3+} ions occupying the Li^+ and Nb^{5+} sites in the $LiNbO_3$ lattice. We can add that it is this change in the Racah parameter that is responsible not only for the pressure-induced red shift of the R lines of Cr^{3+} centers in $LiNbO_3$, but also for the small energy shifts of the R-line frequencies in random fields of intrinsic defects (inhomogeneous broadening of the R lines of Cr^{3+} ions in $LiNbO_3$ [21, 22]).

The existing model of the microstructure of main low-field $\mathrm{Cr}_{\mathrm{Li}}^{3+}$ and $\mathrm{Cr}_{\mathrm{Nb}}^{3+}$ centers assumes that both centers have a simple structure when Cr^{3+} ions substitute for regular Li^+ or Nb^{5+} ions in the $LiNbO_3$ lattice and are located in the trigonal (group C_3) crystal field. The perturbed $\mathrm{Cr}_{\mathrm{Li}}^{3+}$ sites (α, β) which exhibit relatively weak R lines in luminescence spectra at low temperatures belong to the high-field Cr^{3+} centers formed by $\mathrm{Cr}_{\mathrm{Li}}^{3+}$ ions with a nearby intrinsic defect in the nearest cation coordination shell [4, 22]. Hence, these are nearby point defects which are responsible for the transformation of the low-field $\mathrm{Cr}_{\mathrm{Li}}^{3+}$ center into a high-field complex center. It is important to note that this defect-induced transformation of trigonal $\mathrm{Cr}_{\mathrm{Li}}^{3+}$ centers from low-field to high-field centers has some common spectroscopic features with a similar transformation of these trigonal main centers under high pressure. Indeed, the frequencies of the ${}^4A_2 \longrightarrow {}^2E$ and ${}^4A_2 \longrightarrow {}^4T_2$ electronic transitions of both α and β centers are shifted to lower and higher energies, respectively, relative to these transitions in trigonal $\mathrm{Cr}_{\mathrm{Li}}^{3+}$ centers. The same behavior of the corresponding transitions of $\mathrm{Cr}_{\mathrm{Li}}^{3+}$ centers was observed under hydrostatic pressure. This is clearly seen in the photoexcitation spectra of the $2A(^2E) \longrightarrow {}^4A_2$ emission of α and β centers where the corresponding R_2 lines and zero-phonon lines of the ${}^4A_2 \longrightarrow {}^4T_2$ transition are shown (Fig. 7). The above-mentioned similarity indicates the role of the lattice compression around the $\mathrm{Cr}_{\mathrm{Li}}^{3+}$ ion produced by nearby defects.

ACKNOWLEDGMENTS

A.A. Kaplyanskiĭ acknowledges the support of the Alexander von Humboldt Foundation. S.A. Basun and A.B. Kutsenko are grateful for the support of the Russian Foundation for Basic Research (RFBR), project no. 99-02-18319, and of the Deutsche Forschungsgemeinschaft (DFG) for its participation in the framework of the Russian–German program “Defects in Insulators and Deep Centers in Semiconductors.” K. Polgar acknowledges the partial support of the Hungarian Science Research Foundation (OTKA), project nos. T-024092 and T-023092. The authors are grateful to A. Suchocki for his valuable remarks.

REFERENCES

1. G. Burns, D. F. O’Kane, and R. S. Title, Phys. Rev. **167** (2), 314 (1968).
2. A. M. Glass, J. Chem. Phys. **50** (4), 1501 (1969).
3. W. Jia, H. Liu, R. Knutson, and W. M. Yen, Phys. Rev. B **41** (16), 10906 (1990).
4. P. I. Macfarlane, K. Holliday, J. F. H. Nicholls, and B. Henderson, J. Phys.: Condens. Matter **7**, 9657 (1995).
5. C. Fisher, S. Kapphan, Xi-Qi Feng, and Ning Cheng, Radiat. Eff. Defects Solids **135** (1–4), 199 (1995).
6. V. Trepakov, A. Skvortsov, S. Kapphan, *et al.*, Ferroelectrics **239**, 297 (2000).
7. F. Lhomme, P. Bourson, M. D. Fontana, *et al.*, J. Phys.: Condens. Matter **10**, 1137 (1998).

8. G. M. Salley, S. A. Basun, G. F. Imbusch, *et al.*, J. Lumin. **83–84**, 423 (1999).
9. G. M. Salley, S. A. Basun, A. A. Kaplyanskii, *et al.*, J. Lumin. **87–89**, 1133 (2000).
10. G. I. Malovichko, V. G. Grachev, and S. N. Lukin, Fiz. Tverd. Tela (Leningrad) **28**, 991 (1986) [Sov. Phys. Solid State **28**, 553 (1986)].
11. G. Corradi, A. V. Chadwick, A. R. West, *et al.*, Radiat. Eff. Defects Solids **134** (1–4), 219 (1995).
12. G. Malovichko, V. Grachev, E. Kokanyan, and O. Schirmer, Phys. Rev. B **59** (14), 9113 (1999) and references therein.
13. J. Díaz-Caro, J. García-Sole, D. Bravo, *et al.*, Phys. Rev. B **54** (18), 13042 (1996).
14. G. Corradi, G. Sothe, J.-M. Spaeth, and K. Polgar, J. Phys.: Condens. Matter **3**, 1901 (1991).
15. J. Díaz-Caro, J. García-Sole, J. L. Martínez, *et al.*, Opt. Mater. **10**, 69 (1998).
16. V. Hömmerich and K. L. Bray, Phys. Rev. B **51** (13), 8595 (1995).
17. B. Henderson and G. F. Imbusch, *Optical Spectroscopy of Inorganic Solids* (Oxford Univ. Press, Oxford, 1989).
18. A. Kaminska, J. E. Dmochowski, A. Suchocki, *et al.*, Phys. Rev. B **60** (11), 7707 (1999).
19. A. Kaminska, A. Suchocki, M. Grinberg, *et al.*, J. Lumin. **87–89**, 571 (2000).
20. G. M. Salley, S. A. Basun, A. A. Kaplyanskiĭ, *et al.* (in press).
21. P. I. Macfarlane, K. Holliday, and B. Henderson, Chem. Phys. Lett. **252**, 311 (1996).
22. V. Dierolf, A. A. Kaplyanskii, S. Kapphan, and A. B. Kutsenko, in *Proceedings of the ICDIM'2000*, Radiat. Eff. Defects Solids (2001) (in press).
23. B. B. Laird and J. L. Skinner, J. Chem. Phys. **90** (6), 3274 (1989).
24. V. Grachev and G. Malovichko, Phys. Rev. B **62** (12), 7779 (2000).
25. P. Shellenberg, J. Friedrich, and J. Kikas, J. Chem. Phys. **100** (8), 5501 (1994).
26. A. Kaminska, A. Suchocki, L. Arizmendi, *et al.*, Phys. Rev. B **62** (16), 10802 (2000).

Physics of the Solid State, Vol. 43, No. 6, 2001, pp. 1052–1058. Translated from Fizika Tverdogo Tela, Vol. 43, No. 6, 2001, pp. 1018–1024.
Original Russian Text Copyright © 2001 by Fazlizhanov, Ulanov, Zaripov.

SEMICONDUCTORS AND DIELECTRICS

Local Structure of Bivalent Copper Centers in SrF_2 Crystals: An ENDOR Spectroscopic Study

I. I. Fazlizhanov, V. A. Ulanov, and M. M. Zaripov
Kazan Physicotechnical Institute, Russian Academy of Sciences, Sibirskiĭ trakt 10/7, Kazan 29, 420029 Tatarstan, Russia
e-mail: ilshat@dionis.kfti.kcn.ru

Received July 4, 2000; in final form, November 13, 2000

Abstract—Structural distortions of the SrF_2 crystal lattice near the bivalent copper impurity Jahn–Teller center are investigated by the ENDOR method ($\nu = 9.3$ GHz, $T = 4.2$ K). The approximate directions and the magnitudes of displacements of a Cu^{2+} impurity ion and its surrounding F^- ions are determined with respect to one of the anionic networks in the crystal matrix. The tensor components for the ligand hyperfine interaction (LHFI) with fluorine ions separated from the impurity by a distance $R \leq 6.2$ Å are obtained from the angular dependences of the location of the ENDOR resonance lines. It is found that the parameters of magnetic interactions between the impurity and these ligands contain the contributions determined by the covalence of bonds in the impurity complex and the polarization of electron shells of the ligands. *© 2001 MAIK “Nauka/Interperiodica”.*

1. INTRODUCTION

Since the publication of the pioneering works by Bleaney *et al.* [1], paramagnetic centers of bivalent copper in crystals of different compounds have been the center of attention of physicists concerned with the Jahn–Teller effect in solids. A large number of works devoted to the investigation into different aspects of this phenomenon were carried out in the succeeding years. In the vast majority of cases, these works dealt with Cu^{2+} centers whose ground state represents the orbital doublet (degenerate or slightly split by random deformations of the crystal lattice).

A qualitatively different situation occurs for bivalent copper impurity ions in crystals of the fluorite structure type. These ions substitute for diamagnetic cations and occupy positions at the center of a coordination cube of these cations. In this case, the orbital triplet T_{2g} becomes ground, whereas the energy of states of the orbital doublet E_g turns out to be higher by several thousand inverse centimeters. As a result, the physical properties of impurity ions appear to be very sensitive to lattice vibrations of two symmetry types (t_{2g} and e_g). Moreover, these properties are considerably affected by the spin–orbit interaction, because its operator has nonzero matrix elements between the states of the ground triplet. Note also that, compared to the octahedral crystal field, the cubic field splits the orbital levels of a paramagnetic ion to a lesser degree, all other factors being the same. Taken together, these factors are responsible for a number of specific features in the physical properties of impurity eightfold-coordinated cubic copper complexes, which essentially differ from the octahedral copper complexes. In particular, the cubic copper complexes are noncentral in a number of crystals belonging to the fluorite structure type. In $SrCl_2$ [2], SrF_2 [3], and BaF_2 [4] crystals, a Cu^{2+} impurity ion is displaced by ~1 Å from the lattice position of the substituted cation in parallel to one crystal symmetry axis (C_4). It is evident that this displacement can be explained by the relatively small ionic radius of copper, which leads to a considerable weakening of the repulsive exchange interaction between the impurity ion and its ligands. The displacement results in a decrease in the total energy of the crystal lattice. As a consequence of this displacement, the impurity ion appears to be in a crystal field with a considerable number of odd components. In turn, this should change the state of the impurity ion due to the mixing of odd wave functions of its excited configurations with even functions of the T_{2g} cubic triplet of its ground configuration $3d^9$. Therefore, in the case of noncentral Jahn–Teller ions, consideration of the vibronic interaction between impurity ions and the lattice cannot be reduced only to the states of the T_{2g} ground cubic triplet. It is necessary to take into account the possible pseudo-Jahn–Teller interaction. For example, an interaction scheme of the type $[A_{2u} + T_{2g}] \otimes (a_{1g} + e_g + t_{2g} + t_{1u})$ can be considered for Cu^{2+} ions in SrF_2 [5].

For an impurity ion with a small radius, the possible substantial displacements of its ligands from their initial positions should also be taken into account. It is known that these displacements cannot be obtained from the EPR data. In this case, we can determine only the direction and the approximate magnitude of the displacement of an impurity ion with respect to the nearest ligands (the interaction with these ligands manifests itself in the EPR spectra). However, the displacements of the ligands themselves relative to their positions in an undistorted lattice cannot be found from EPR data.

This problem is usually solved using the ENDOR method.

The main purposes of the present work were (1) to determine the parameters of the ligand hyperfine interaction (LHFI) between the electron magnetic moment of a bivalent copper impurity center and the nuclear magnetic moments of ligands in a number of its coordination spheres and (2) to evaluate the approximate magnitudes and directions of the displacements of impurity ions and their nearest ligands with respect to the corresponding positions in the undistorted lattice.

The calculations involving the determination of the structure parameters of the lattice near the impurity were performed approximately within the MO LCAO angular overlap model to the first order of the perturbation theory. These calculations will be described in detail in a separate work.

2. EXPERIMENTAL, RESULTS, AND DISCUSSION

Measurements were carried out in the 3-cm band on an E-12 Varian spectrometer equipped with a special ENDOR accessory. The main part of this accessory was a wide-band power amplifier of original design, which made it possible to examine the ENDOR spectra in the frequency range 1–50 MHz.

The ENDOR spectra were recorded at $T = 4.2$ K in the crystallographic planes (100) and (110). Figures 1 and 2 show the ENDOR spectra for the two main orientations of a sample with respect to the external magnetic field ($\mathbf{B}_0 \parallel \langle 001\rangle$ and $\mathbf{B}_0 \parallel \langle 110\rangle$). As can be seen from these figures, the entire range of the spectrum is as large as 2.5–2.6 MHz. The obtained spectra exhibit groups of isolated lines, which are apparently associated with interactions between the impurity and the nearest fluorine nuclei. The central part of the spectra contains poorly resolved lines, which, for the most part, correspond to interactions with distant nuclei. Certain of the lines labeled by numbers in the spectra will be subsequently assigned to the corresponding groups of ligands.

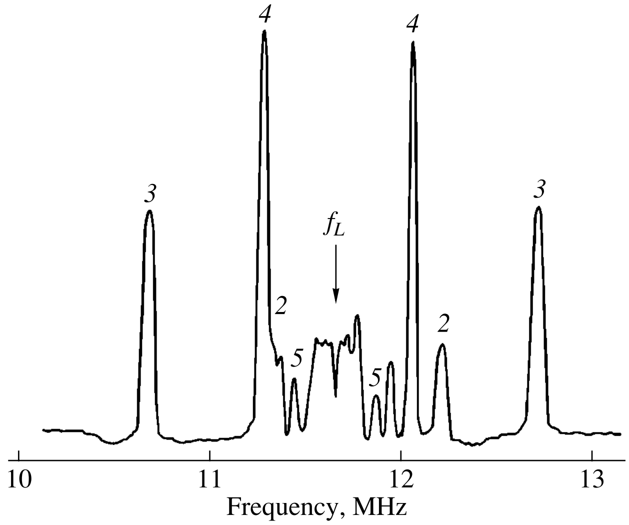

Fig. 1. ENDOR spectrum taken at the highest-field line in the EPR spectrum of copper impurity centers in the SrF_2 crystal at $T = 4.2$ K, $f = 9.3$ GHz, and $B \parallel Z$ (Z is the tetragonal axis of impurity centers, f is the operating frequency of the spectrometer, and f_L is the Larmor precession frequency of fluorine ions). Lines labeled by different numbers (*2*–*5*) correspond to particular groups of ligands.

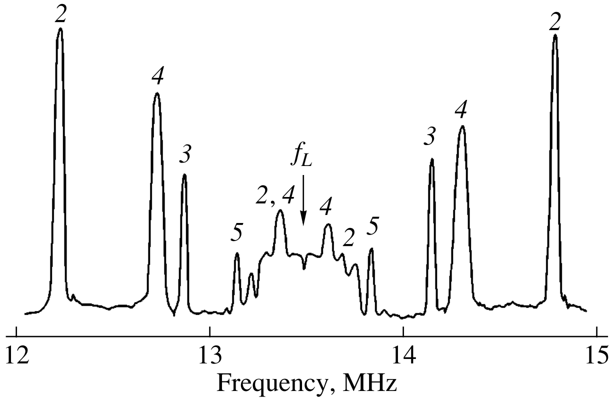

Fig. 2. ENDOR spectrum taken at the highest-field line in the EPR spectrum of copper impurity centers in the SrF_2 crystal at $T = 4.2$ K, $f = 9.3$ GHz, and $B \parallel X$ (X is the axis of the intrinsic coordinate system of the impurity center in Fig. 4). The designations are the same as in Fig. 1.

The angular dependences of the frequency of the ENDOR transitions between nuclear states of both electronic levels ($M_S = +1/2$ and $-1/2$) were obtained upon rotation of the vector $\mathbf{B}_0$ of a static external magnetic field in the (110) and (001) planes of the $SrF_2 : Cu^{2+}$ sample. The theoretical dependences and the corresponding experimental points are depicted in Figs. 3a and 3b. Figure 3a shows the graphs and the experimental points taken at the high-field line in the EPR spectrum for a group of equivalent centers that are identically oriented with respect to the $\mathbf{B}_0$ vector [i.e., the case in point is the EPR transitions between the states, conventionally, with $m_I(\mathrm{Cu}) = -3/2$ and $m_I(\mathrm{F}_i) = -1/2$ for all $i = 1$–4, where i is the number of the ligand within the given group]. Note that, in our work, particular nuclei within the group of equivalent ligands are numbered by Arabic numerals and the groups themselves are numbered by Roman numerals. The angular dependences obtained upon rotation of the $\mathbf{B}_0$ vector in the planes (110) and (001) are depicted on the left and the right of Fig. 3a, respectively. The theoretical dependences are shown by solid lines, and the points are the experimental data. Figure 3b displays the graphs and points for the low-field lines in the EPR spectrum of the same group of impurity centers [according to the above classification of states, here we are dealing with the transitions between the states with $m_I(\mathrm{Cu}) = +3/2$ and $m_I(\mathrm{F}_i) = +1/2$]. As can be seen, the angular depen-

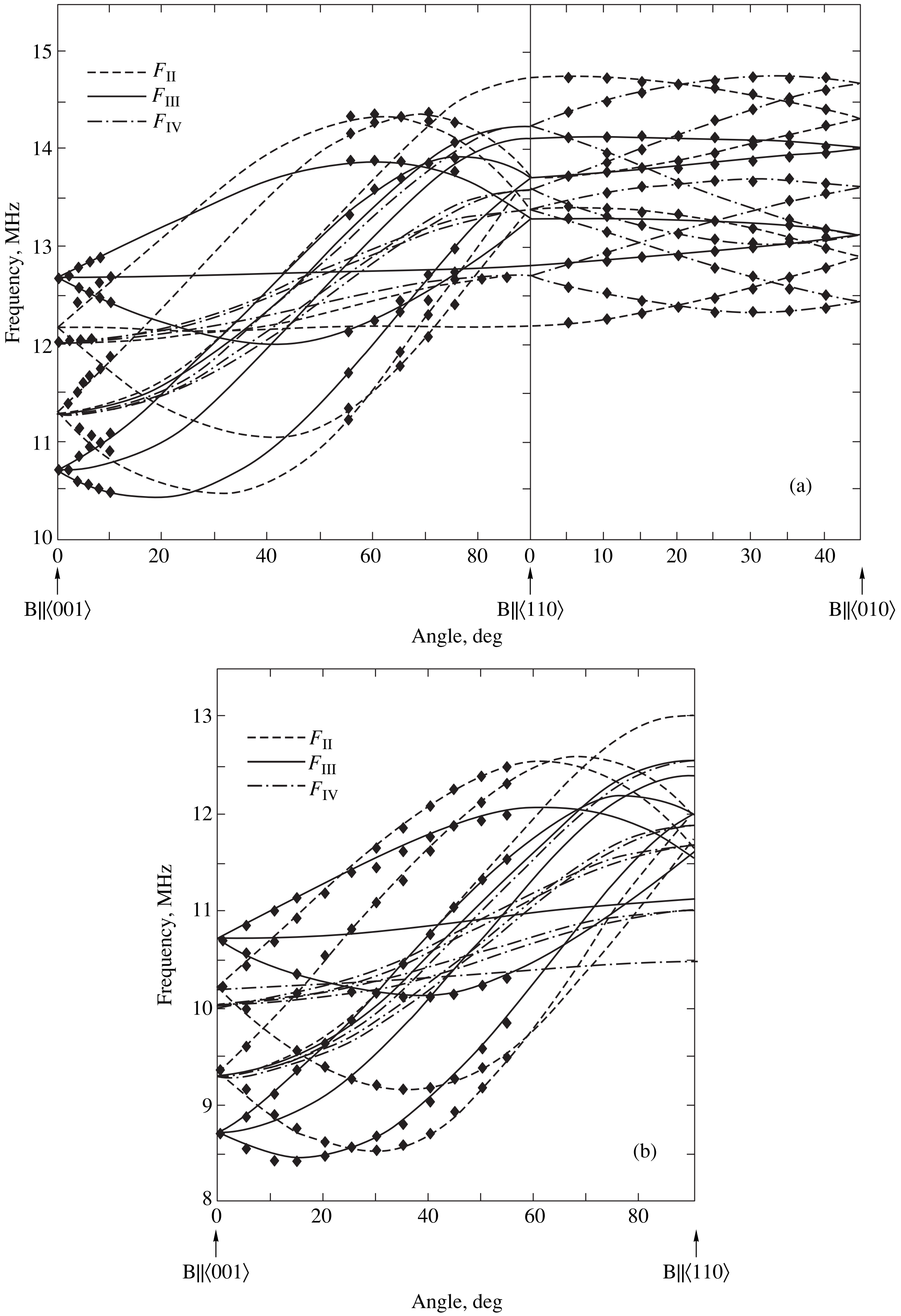

Fig. 3. Angular dependences of the ENDOR frequencies (T = 4.2 K and f = 9.3 GHz) at (a) the highest-field and (b) lowest-field lines in the EPR spectrum of a particular group of magnetically equivalent paramagnetic copper complexes upon rotation of the $\mathbf{B}_0$ vector in the *ZOX* plane of the coordinate system specified for this group of complexes in Fig. 4.

dences in Fig. 3a correspond to the hyperfine interactions with three groups of equivalent ligands. These dependences are designated by F_{II}, F_{III}, and F_{IV} (the numbering coincides with the numbering of lines in the above ENDOR spectra). To avoid the overloading of the figures by too large a number of graphs, the angular dependences for lines *5* are not shown.

For a complete identification of the graphs with the actual crystal structure in the vicinity of an impurity ion, let us consider a model for this crystal region. This model (Fig. 4) can be qualitatively constructed on the basis of the EPR data obtained for $SrF_2 : Cu^{2+}$ in [3]. In this model, the ligands of group I are the closest to the Cu^{2+} ion. The LHFI parameters for these ligands were determined by the EPR technique in [3]. As follows from these parameters, the splittings between nuclear states are equal to several hundred MHz, which is considerably larger than the operating range of our nuclear pumping oscillator. Consequently, in our case, we can expect the ENDOR transitions between the nuclear states of ligands in the second and more distant coordination spheres of the impurity ion.

The spin Hamiltonian of the studied impurity complex can be written as follows:

$$H_S = \beta_e \mathbf{B}_0 \cdot g\mathbf{S} + \mathbf{S} \cdot a\mathbf{I}^{\mathrm{Cu}} - \beta_n g_n^{\mathrm{Cu}} \mathbf{B}_0 \cdot \mathbf{I}^{\mathrm{Cu}} + \sum_{i=1}^{N} (\mathbf{S} \cdot A_i^{\mathrm{F}} \mathbf{I}_i^{\mathrm{F}} - \beta_n g_n^{\mathrm{F}} \mathbf{B}_0 \cdot \mathbf{I}_i^{\mathrm{F}}), \tag{1}$$

where $\mathbf{S}$ is the electron spin moment operator for the Cu^{2+} impurity ion ($S = 1/2$), $\mathbf{I}^{\mathrm{Cu}}$ and $\mathbf{I}^{\mathrm{F}}$ are the nuclear spin moment operators for impurity copper and its ligands ($I^{\mathrm{Cu}} = 3/2$ and $I^{\mathrm{F}} = 1/2$), a is the tensor for the hyperfine interactions of the electron and nuclear magnetic moments of the impurity center, A_i^{F} is the tensor for the hyperfine interactions of the electron magnetic moment of the impurity center with the nuclear magnetic moments of its ligands, g is the electron Zeeman interaction tensor, g_n^{Cu} and g_n^{F} are the g values for copper and fluorine, β_e and β_n are the electronic and nuclear Bohr magnetons, and N is the number of the ligands that interact with the impurity and can be observed by the ENDOR method.

The angular dependences of the ENDOR spectra are conveniently analyzed when the spin Hamiltonian (1) is represented in the coordinate system in which the electron Zeeman interaction operator has a diagonal form.

In this coordinate system, new Cartesian components of the electron spin moment operator $\mathbf{S}$ can be obtained using the transformation

$$\mathbf{S}' = L_S \mathbf{S},$$

where the transformation matrix L_S has the form

$$L_S = \begin{pmatrix} \frac{g_{\parallel}}{g}\cos\theta\cos\varphi & \frac{g_{\parallel}}{g}\cos\theta\sin\varphi & -\frac{g_{\perp}}{g}\sin\theta \\ -\sin\varphi & \cos\varphi & 0 \\ \frac{g_{\perp}}{g}\sin\theta\cos\varphi & \frac{g_{\perp}}{g}\sin\theta\sin\varphi & \frac{g_{\parallel}}{g}\cos\theta \end{pmatrix}.$$

Here, θ and φ are two Eulerian angles that determine the orientation of the external magnetic field vector $\mathbf{B}_0$ with respect to the principal magnetic axes of the paramagnetic complex (θ is the angle between the Z axis and the $\mathbf{B}_0$ vector, and φ is the angle between the X axis and the projection of this vector onto the XOY plane) and g is the effective value of the g tensor which, for the given orientation of the $\mathbf{B}_0$ vector, is defined as

$$g = \sqrt{g_{\perp}^2 \sin^2\theta + g_{\parallel}^2 \cos^2\theta}.$$

The nuclear spin moment operators $\mathbf{I}^{\mathrm{Cu}}$ and $\mathbf{I}^{\mathrm{F}}$ can be transformed in the same manner, that is,

$$\mathbf{I}' = L_I \mathbf{I},$$

where

$$L_I = \begin{pmatrix} \cos\alpha\cos\beta & \sin\alpha\sin\beta & -\sin\beta \\ -\sin\alpha & \cos\alpha & 0 \\ \cos\alpha\sin\beta & \sin\alpha\sin\beta & \cos\beta \end{pmatrix}.$$

Here, the α and β angles are chosen individually for each ligand in such a way that the Hamiltonian of the ligand hyperfine interaction with the nucleus of this ligand would be diagonal for the states of each electronic level. In this case, the main contribution to the energy of each nuclear level is determined by the first order of the perturbation theory. Therefore, formally we are dealing here with the LHFI tensor transformation which results in the "effective" interaction tensor

$$A'(g_{\parallel}, g_{\perp}, \varphi, \theta).$$

In this new representation, the LHFI operator takes the form

$$H_S' = \sum_i [\mathbf{S} \cdot (L_S A_i \tilde{L})\mathbf{I}_i - g_N \beta_N \mathbf{B}_0 \cdot \mathbf{I}_i]$$

$$= \sum_i [\mathbf{S}' \cdot A'(g_{\parallel}, g_{\perp}, \varphi, \theta)\mathbf{I}_i' - g_N \beta_N \mathbf{B}_0 \cdot \mathbf{I}_i'],$$

where the components of the transformed LHFI tensor $A_i'(g_{\parallel}, g_{\perp}, \varphi, \theta)$ appear to be functions of the polar coordinates of the $\mathbf{B}_0$ vector and the components g_{ij} of the electron Zeeman interaction tensor.

In the cases when the ENDOR spectrum does not exhibit a fine structure, the first order of the perturba-

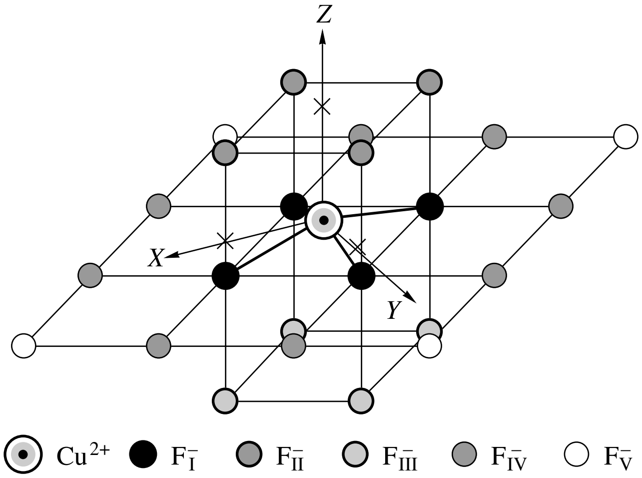

Fig. 4. A model of the Cu^{2+} impurity center in SrF_2 (the ligands of the first coordination sphere of an impurity ion and the fluorine ions involved in the interaction studied in this work are shown).

tion theory can be considered a good approximation. Otherwise, the calculations should also include the second-order contributions of the perturbation theory. As is seen from the angular dependences of the resonance frequencies of the lines in the ENDOR spectrum obtained in the present work (Figs. 3a, 3b), the fine structure of the spectra is absent. Hence, the components of the LHFI tensor were first determined within the first order of the perturbation theory. Then, the LHFI tensor components thus obtained were corrected using the exact diagonalization of the matrix of the spin Hamiltonian (1). This approach appreciably simplified the analysis of the obtained experimental results without loss of accuracy in the calculations.

The calculated components of the $A(F_i)$ LHFI tensors for the ligands of groups II–V (according to the group numbering in Fig. 4) are the important results obtained in this work. These components represented in the so-called local coordinate systems are listed in the table. The axes of these coordinate systems can be determined via a unitary transformation of the axes of the intrinsic coordinate system *XYZ* for the impurity center (Fig. 4). The matrices of these transformations have the following form:

$$\begin{pmatrix} \cos\Phi_i\cos\Theta_i & \sin\Phi_i\sin\Theta_i & -\sin\Theta_i \\ -\sin\Phi_i & \cos\Phi_i & 0 \\ \cos\Phi_i\sin\Theta_i & \sin\Phi_i\sin\Theta_i & \cos\Theta_i \end{pmatrix}, \qquad (2)$$

where Φ_i and Θ_i are two Eulerian angles determined so that the transformed tensor is diagonal and its maximum diagonal component corresponds to the Z' axis of the local coordinate system (the subscript i indicates the number of the ligand F_i under consideration). These angles (Φ_i and Θ_i) are also given in the table. Furthermore, the table presents the components of the $A^d(F_i)$ tensors, which were calculated under the assumption that the interaction between the electron magnetic moment of the impurity center and the nuclear magnetic moment of any ligand of the *j*th group (j = I–V) is

Components (MHz) of the tensors for the ligand hyperfine interaction between the electron magnetic moment of a copper impurity center and the nuclear magnetic moments of different ligand groups shown in Fig. 4

LHFI tensor components and Eulerian angles		Ligand group				
		I	II	III	IV	V
$A^d(F_i)$	A_X^d	–10.11	–2.47	–1.39	–0.94	–0.39
	A_Y^d	–8.49	–2.29	–1.32	–0.79	–0.33
	A_Z^d	17.12	5.12	3.02	1.59	0.67
	Θ_i, deg	101.2	39.4	153	95.2	93.3
	Φ_i, deg	0	0	0	26.4	0
$A(F_i)$	A_X	102 [3]	–2.74	–1.35	–0.75	–0.41
	A_Y	99 [3]	–2.53	–1.29	–0.65	–0.35
	A_Z	407 [3]	3.31	2.92	2.39	0.69
	Θ_i, deg	107	39	152	95	94
	Φ_i, deg	0	0	0	31	0

Note: The Φ_i and Θ_i Eulerian angles determine the axis in a local coordinate system of the given ligand in which the symmetric part of the LHFI tensor matrix for this ligand becomes diagonal. $A^d(F_i)$ is the LHFI tensor part accounting for the direct magnetic dipole–dipole interaction between the electron and nuclear magnetic moments. $A(F_i)$ is the LHFI tensor describing the angular dependences in the ENDOR spectra. The accuracy in the determination of the experimental tensor components $A(F_i)$ and the angles Φ_i and Θ_i corresponds to the accuracy of their representation in the table.

the direct magnetic dipole–dipole interaction without any additional contribution. Moreover, it was assumed that only the impurity ion is displaced to the noncentral position and all its surrounding ions remain in the same positions which they occupy in an impurity-free crystal. The components of the direct dipole–dipole interaction tensor $A^d(F_i)$ were evaluated with the use of the equality taken from [6]

$$A^d = \frac{g_n^F \beta_n \beta_e}{R^3} \begin{pmatrix} g_\perp(3l^2-1) & g_\perp(3lm) & g_\perp(3ln) \\ g_\perp(3lm) & g_\perp(3m^2-1) & g_\perp(3mn) \\ g_\parallel(3nl) & g_\parallel(3mn) & g_\parallel(3n^2-1) \end{pmatrix}, \quad (3)$$

where l, m, and n are the direction cosines for the vector "impurity ion–ith ligand" with respect to the axes (X, Y, and Z) of the intrinsic coordinate system for the impurity center; R is the distance between the impurity ion and the ligand; and $g_\parallel$ and $g_\perp$ are the components of the electron Zeeman interaction tensor for the impurity ion ($g_\parallel = 2.4926 \pm 0.0005$ and $g_\perp = 2.084 \pm 0.001$ [3]).

The l, m, and n direction cosines are related to the elements of the transformation matrix (2) by the requirement of the diagonalization of the $A^d(F_i)$ tensor.

It should be emphasized that, when the ligand hyperfine interaction involves only the direct magnetic dipole–dipole interaction between the electron and nuclear magnetic moments, the local axis Z' in the case of an isotropic electron Zeeman interaction precisely coincides with the impurity–ligand direction. No such precise coincidence occurs if the paramagnetic system with $S = 1/2$ is characterized by an anisotropic electron Zeeman interaction. However, in this case too, the calculations demonstrate that these vectors approximately coincide, because the angle between the Z' axis and the impurity–ligand direction turns out to be negligibly small. For this reason, the Φ_i and Θ_i angles are often used for specifying the impurity–ligand direction (i is the number of the ligand of the LHFI tensor under consideration).

However, the ligand hyperfine interaction is far from necessarily described by such a simple model. When the distance between a paramagnetic impurity ion and a diamagnetic ligand is small, the bond with the ligand cannot be considered purely ionic. In this case, the components of the LHFI tensor can contain additional contributions determined by the covalence of the bond and the nonorthogonality of the electronic wave functions for the impurity ion and ligand. Taken together, these factors lead to the fact that the actual direction of the impurity–ligand vector can very strongly differ from the direction of the local axis Z' (see, for example, [7]).

The lines in the ENDOR spectrum were assigned to ligands of particular groups on the basis of the following experimental data. First, important structural data on the nearest environment of the impurity copper ion were obtained in our earlier work [3], in which these centers were studied by the EPR technique. In this work, we determined the parameters of the ligand hyperfine interaction with nuclei of ligands of group I and found that the impurity copper ion is substantially displaced from the center of the coordination cube toward the anionic network depicted in Fig. 4. In this case, the $d_{x^2-y^2}$ function (represented in the coordinate system given in Fig. 4) is the orbital state of an unpaired electron of the copper ion. Thus, the observed ENDOR spectra should be interpreted primarily taking into account ligands of groups II–V. Second, the Φ_i and Θ_i angles determined in the present work are such (see table) that there is no doubt regarding the assignment of lines *4* and *5* to ligands of groups IV and V, respectively. As for the assignment of the ENDOR lines associated with the hyperfine interaction with ligands of groups II and III, the following factors were additionally taken into consideration. According to [3], the symmetry plane of a four-lobe electron density cloud of the unpaired electron of copper lies parallel to the plane of the anionic network displayed in Fig. 4 and is closer to ligands of group II. Therefore, the isotropic components of the LHFI tensors for ligands of this group should be somewhat larger in magnitude than those for ligands of group III. A comparison of the Θ_i angles and the isotropic LHFI constants that correspond to lines *2* and *3* makes it possible to reveal the direct relation between the Arabic (2 and 3) and Roman (II and III) numerals used in the present work for the numbering of lines and ligand groups, respectively.

Now, let us discuss the structure of the nearest environment of the impurity copper ion. It is seen from the table that the components of the LHFI tensors $A(F_i)$ for fluorine ions of the first, second, and fourth ligand groups noticeably differ from the components of the corresponding $A^d(F_i)$ tensors. Differences toward larger values for ligands of the first group are evidently associated with the contributions made to the LHFI tensor by the electron transfer from ligands to levels of the ground configuration of the impurity ion and the nonorthogonality of the wave functions for the impurity and its ligands. According to the preliminary theoretical calculations performed for ligands of the first group by the MO LCAO angular overlap method, the same reasons lead to a considerable difference between the calculated and experimental Θ_i angles (see table). As to ligands of the second group, the components of their experimental LHFI tensor appear to be less than the corresponding components of the calculated $A^d(F_{II})$ tensor. With due regard for the fact that the components of the $A^d(F_{II})$ tensor were calculated under the assumption that ligands are not displaced, the found difference can be explained by the increase in the distance between the impurity ion and ligands of the second group due to their displacement from the initial positions by approximately 0.5 Å. However, in this case, the negative isotropic contribution to the $A(F_{II})$ tensor remains unexplainable. The calculations demonstrate that, in this case, we should take into account both the displacement of ligands along the bond axis (by approximately 0.30–0.35 Å from the impurity) and the covalence of bonds between the impurity ion and ligands of this group. The negative sign of covalent contributions is explained by the effective decrease in the electron magnetic moment of the impurity center due to partial transfer of the electron spin density from the ligands to the levels of the ground and excited configurations of the impurity ion and also by the polarization of the ligand electron shell by the displaced impurity ion. However, despite the presence of covalent contributions for ligands of the second group, the Θ_i angles determined for the corresponding tensors $A(F_i)$ and $A^d(F_i)$ do not differ from each other. Therefore, this angle can be regarded as a structure parameter of the impurity complex under investigation.

The experimental LHFI tensor for ligands of the third group almost coincides with the $A^d(F_i)$ tensor calculated for these ligands. However, this does not indicate the absence of covalent contributions to this tensor. First, the displacement of the impurity ion to the noncentral position should bring about the decompensation of Coulomb forces acting on ligands when they occupy the positions of the defect-free crystal lattice. For this reason, ligands of the third group should be slightly displaced toward the impurity and the components of the $A^d(F_{III})$ tensor should noticeably differ from those presented in the table. Second, the components of the LHFI tensor for more distant ligands of the fourth group substantially differ from the corresponding components of the $A^d(F_{IV})$ tensor toward larger values (as for ligands of the first group). The last fact suggests that the cloud of the unpaired electron extends sufficiently far from the impurity and overlaps with electron shells of ligands of the first four groups. The change in the sign of covalent contributions is caused by the presence of several nodes in the wave function of the unpaired electron. This supports the assumption that states of the ground configuration of the Cu^{2+} impurity ion contain a large admixture of its excited configurations.

Finally, we consider ligands of the fifth group. Their ligand hyperfine interaction is almost completely determined by the direct magnetic dipole–dipole interaction. Therefore, the parameters of the LHFI tensors for ligands of the fifth group allow us to obtain more precisely the position of the impurity ion with respect to the anionic network involving ligands of this group. Simple geometric constructions show that the distance between the plane of this anionic network and the impurity is equal to 0.41–0.43 Å. Ligands of the third group are only slightly displaced from the positions occupied by them in the impurity-free crystal. These small displacements (approximately equal to 0.02–0.03 Å) occur along the bond toward the impurity copper ion. Ligands of the first group occupy the positions located 0.07–0.09 Å above the anionic network. It is virtually impossible to determine the distance from these ligands to the impurity copper ion, because the magnitudes of the covalence parameters used in calculations are unknown in advance and only approximate ratios between them are available. Hence, the magnitude of the impurity–ligand vector can be obtained from these calculations with a considerably lower accuracy as compared to the direction of this vector [6]. Therefore, for relative displacements of ligands of the first group, we can evaluate with some degree of certainty only the displacement components perpendicular to the impurity–ligand directions. With regard to their parallel components, we can only make assumptions. Most likely, ligands of this group are appreciably displaced toward the impurity ion. This can be associated with two factors. First, the displacement of the impurity copper toward the anionic network strongly disturbs the balance of the Coulomb forces that should act on these ligands. Second, the bonds formed between the impurity ion and ligands of the first group make the negative covalent contribution to the lattice energy. We also should restrict ourselves only to assumptions regarding the displacements of ligands of the fourth group. Since these ligands are rather far from the displaced impurity ion, it is believed that they are virtually not displaced from the positions occupied in the impurity-free crystal.

REFERENCES

1. B. Bleaney and D. I. E. Ingram, Proc. Phys. Soc. London, Sect. A **63**, 408 (1950); B. Bleaney and K. D. Bowers, Proc. R. Soc. London, Ser. A **65**, 667 (1952).
2. H. Bill, Phys. Lett. A **44** (2), 101 (1973).
3. M. M. Zaripov and V. A. Ulanov, Fiz. Tverd. Tela (Leningrad) **31** (10), 251 (1989) [Sov. Phys. Solid State **31**, 1796 (1989)].
4. M. M. Zaripov and V. A. Ulanov, Fiz. Tverd. Tela (Leningrad) **31** (10), 254 (1989) [Sov. Phys. Solid State **31**, 1798 (1989)].
5. S. K. Hoffmann and V. A. Ulanov, J. Phys.: Condens. Matter **12**, 1855 (2000).
6. J. M. Baker, E. R. Davies, and J. P. Hurrell, Proc. R. Soc. London, Ser. A **308**, 403 (1968).
7. M. V. Eremin, V. A. Ulanov, and M. M. Zaripov, Appl. Magn. Reson. **14**, 446 (1998).

Translated by O. Borovik-Romanova

Physics of the Solid State, Vol. 43, No. 6, 2001, pp. 1059–1071. Translated from Fizika Tverdogo Tela, Vol. 43, No. 6, 2001, pp. 1025–1036.
Original Russian Text Copyright © 2001 by Basun, Bursian, Razdobarin, Sochava.

Anisotropic Photoionization as a Mechanism of Axial Iron Center Alignment in $KTaO_3$

S. A. Basun, V. É. Bursian, A. G. Razdobarin, and L. S. Sochava

Ioffe Physicotechnical Institute, Russian Academy of Sciences, Politekhnicheskaya ul. 26, St. Petersburg, 194021 Russia
e-mail: Victor.Bursian@pop.ioffe.rssi.ru

Received November 14, 2000

Abstract—An EPR study has revealed light-induced recharging and optical alignment of the Fe_{Ta}^{4+}–V_O tetragonal complexes in $KTaO_3$. The data on the optical creation and destruction of this center by light of different polarizations and wavelengths are discussed together with similar results obtained for the Fe_K^{3+}–O_i center. These two centers were established to undergo mutual charge transfer, in which the electron released in the photoionization of the Fe_K^{2+}–O_i center is trapped by the Fe_{Ta}^{5+}–V_O center. Irradiation by light with a photon energy below 2.05 eV, which is the ionization threshold of Fe_K^{2+}–O_i, reverses this process. In both cases, the absorption cross section depends on the orientation of the center axis relative to the light polarization vector. As a result, the Fe_{Ta}^{4+}–V_O and Fe_K^{3+}–O_i tetragonal centers in $KTaO_3$ acted upon by polarized light undergo orientation-sensitive light-induced recharging and the defects with the *given* charge state are no longer characterized by an equally probable distribution of the orientations of their axes over the three ⟨100⟩ directions. This mechanism, which does not involve real reorientations of the Fe_{Ta}–V_O and Fe_K–O_i complexes, gives rise, nevertheless, to the alignment of the centers along (or at right angles to) the light polarization vector. *© 2001 MAIK "Nauka/Interperiodica".*

INTRODUCTION

The effect of symmetry lowering of a photoemulsion medium caused by photochemically active polarized light was discovered by Weigert in 1921 [1]. This phenomenon was known to exist in crystals (KCl, NaCl, CaF_2) as far back as the 1940s and was called the Weigert effect (see [2] and references therein). It was described within a phenomenological framework by Feofilov [2] as orientation-sensitive absorption of polarized light by low-symmetry defect centers, which results in the destruction of centers with a specific orientation and, thus, in a decrease in their concentration. Understanding the microscopic nature of this effect requires, however, additional studies.

The light-induced alignment of low-symmetry defect centers may have different origins. According to the well-known studies of Lüty [3], the alignment of F_A centers in alkali halide crystals is initiated by orientation-sensitive excitation of the centers with their subsequent reorientation in the excited state (i.e., through halogen vacancy hopping). Another alignment mechanism involving light-induced center recharging was proposed by Berney and Cowan [4] as operative for the Fe^+–V_O centers in $SrTiO_3$. Obviously enough, if a center can reside in two charge states, preferential recharging of specifically oriented centers manifests itself as alignment.

The above two, essentially different mechanisms of alignment are illustrated schematically in Fig. 1. It presents a fragment of a cubic lattice with four axial defect centers having different orientations and charge states. Shown on top are, consecutively, (i) selective absorption of polarized light; (ii) reorientation of the center in the excited state, in which the barrier can be lower; and (iii) the final state, in which the positively charged cen-

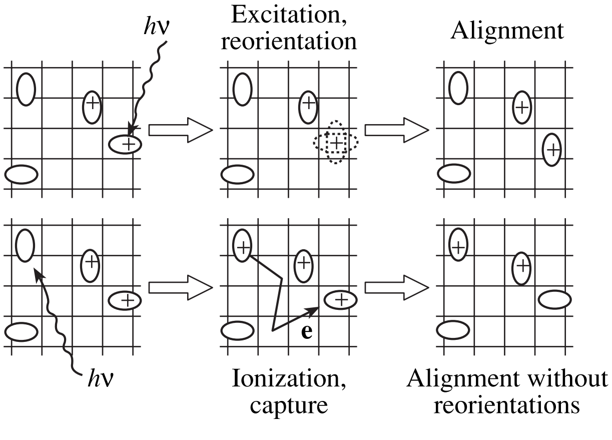

Fig. 1. Two mechanisms of axial center alignment under polarized illumination of a cubic crystal. One can see differently oriented centers in two charge states, namely, the conventionally neutral and ionized states (specified by the plus sign).

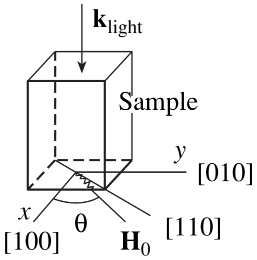

Fig. 2. Geometry of the experiment. The magnetic field $\mathbf{H}_0$ lies in the (001) plane.

ters are aligned. The lower part of the figure demonstrates the second alignment mechanism, in which selective ionization is followed by photoelectron trapping by a positively charged center. The probabilities of this trapping by differently oriented centers are usually equal. Therefore, an anisotropy in the center ionization brings about preferential destruction[1] of specifically oriented centers and, hence, alignment of the centers. Note that, in contrast to the first mechanism, the alignment does not involve any real reorientations here.[2]

In this work, we are dealing with the more complex situation of the light-induced charge transfer involving centers of different types, which reveals new, interesting manifestations of the alignment effect. At the same time, this factor provides more information on the mechanism of the phenomenon.

The potassium tantalate crystal retains a cubic perovskite-like structure down to very low temperatures. The iron impurity ion can occupy the sites of both tantalum ($\mathrm{Fe_{Ta}}$) and potassium ($\mathrm{Fe_K}$), with the deficient or excess charge being locally compensated by an oxygen vacancy (V_O) or by interstitial oxygen (O_i) to form the $\mathrm{Fe_K}$–O_i and $\mathrm{Fe_{Ta}}$–V_O complexes.

The two tetragonal iron centers studied are $\mathrm{Fe_K^{3+}}$–O_i [5, 6] and the $\mathrm{Fe_{Ta}^{4+}}$–V_O center detected recently by us [7].

An ODMR observation of optical alignment of the $\mathrm{Fe_K^{3+}}$–O_i centers was reported by Reyher *et al.* [8]. Polarized light was found to change substantially the ratio of the numbers of the above centers with different orientations; namely, the concentration of the centers with their tetragonal axis parallel to the electric vector of incident light (**e**) increased, while that of the centers with their axis perpendicular to the vector **e** decreased. This observation was interpreted [8] as a result of a redistribution of the $\mathrm{Fe_K^{3+}}$–O_i centers between different *orientational* states caused by light-induced hopping of the interstitial oxygen ion among the six possible positions. The other possible interpretation, consisting in a redistribution between different *charge* states of the $\mathrm{Fe_K}$–O_i centers because of their anisotropic light-induced recharging, was also mentioned in [8], but rejected.

The EPR investigation of the optical alignment of the $\mathrm{Fe_K^{3+}}$–O_i centers provided additional information [9], which yielded a decisive argument for establishing the actual alignment mechanism. The most interesting results were obtained on reduced samples, in which the $\mathrm{Fe_K^{3+}}$–O_i centers, while being absent in the samples at thermal equilibrium, form only after illumination as a result of light-induced recharging from $\mathrm{Fe_K^{2+}}$–O_i, the state not detectable by EPR. These data convincingly imply the existence of orientation-sensitive photoionization, which manifests itself in the experiment as alignment of the $\mathrm{Fe_K^{3+}}$–O_i centers.

The present paper reports on the observation of light-induced recharging and optical alignment of the $\mathrm{Fe_{Ta}^{4+}}$–V_O centers. The kinetics of photogeneration and photodestruction and the spectral dependence of the steady-state concentration of these centers were studied in parallel with those of the $\mathrm{Fe_K^{3+}}$–O_i centers. It was found that both types of the centers are produced in the same process, namely, in the ionization of the $\mathrm{Fe_K^{2+}}$–O_i center, followed by the trapping of the released electron by the $\mathrm{Fe_{Ta}^{5+}}$–V_O center.

1. EXPERIMENTAL TECHNIQUE

1.1. Samples

We studied $\mathrm{KTaO_3:Fe}$ single crystals grown by Dr. H. Hesse at the Physical Department of Osnabrück University, Germany, from a batch containing 1300–10000 ppm iron. The crystals were seed-pulled in air from a melt with excess $\mathrm{K_2O}$. Rectangular samples, typically ~10 mm^3 in volume, were cut from a single-crystal boule along the {100} planes and polished to optical-grade quality.

To change the equilibrium charge state of the defects, some of the samples were chemically reduced by heating them in $\mathrm{H_2}$ at $T = 1000°\mathrm{C}$ for 1–2 h. Another part of the samples was subjected to oxidizing annealing (heating in $\mathrm{O_2}$ at $T = 1000°\mathrm{C}$ for 4 h); the remaining samples were studied in the as-grown state. It was established that the samples of the last two groups did not differ from one another in all characteristics of interest to us (which was obviously due to the crystals having been grown in an oxidizing atmosphere), and therefore, these two groups are referred to subsequently as “oxidized.”

---

[1] In other words, this means the disappearance of centers in the given charge state.

[2] Significantly, in the second case, both charge states are aligned. This difference can serve as a means of establishing the true mechanism. However, the EPR method usually permits observation of only one of the two charge states. In addition, the degree of alignment of centers in one of the charge states can be substantially lower than that in the other, if the corresponding concentrations differ strongly.

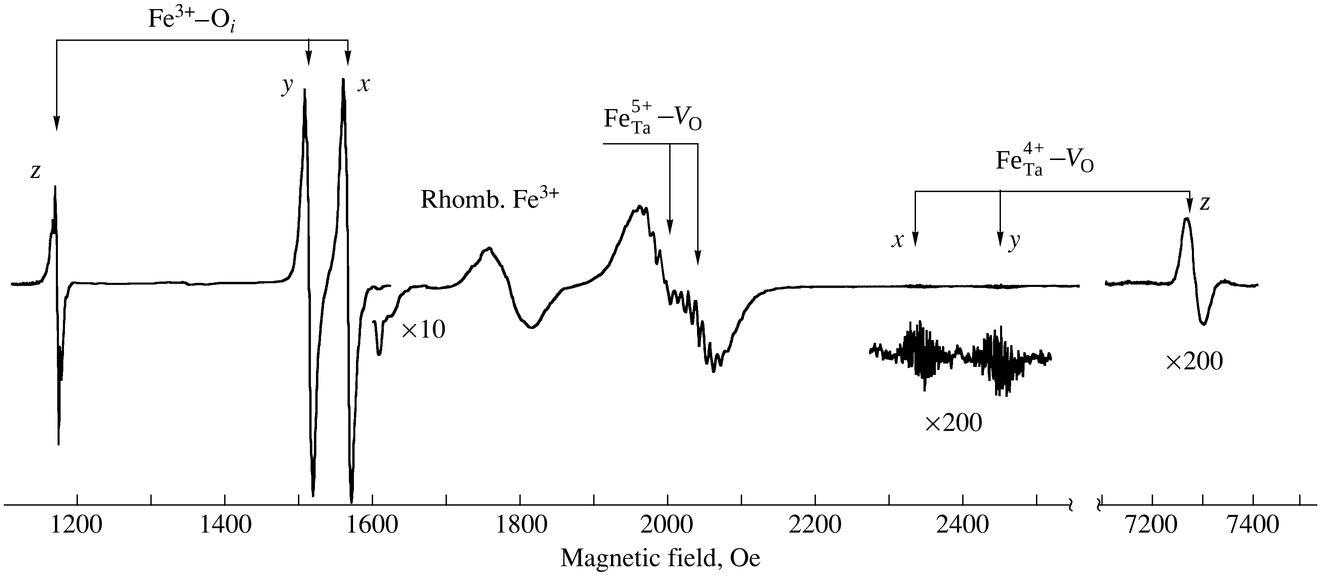

Fig. 3. Typical EPR spectrum of an oxidized sample of $KTaO_3$: Fe (10000 ppm). $T = 78$ K, $\theta = 43.5°$.

1.2. Setup

The types of the iron centers present in a sample were identified, and the light-induced changes in their concentrations were measured using a modified X-range (9.3 GHz) SE/X-2544 spectrometer.

A polaroid film and the sample were attached to the lower end face of a quartz rod (4 mm in diameter, 270 mm long, end faces being plane and polished), which served as a light guide. The light from a halogen incandescent lamp (70 W) passed through an f/1 lens and a set of cut-off and interference filters, to be focused on the upper end face of the quartz rod. Argon and helium–neon lasers were also used. The lower part of the rod with the sample was mounted in the cold finger of a nitrogen (or helium) Dewar vessel installed in the spectrometer cavity. Unpolarized light impinged on the sample from below, through the Dewar finger bottom. The orientation of the sample relative to the magnetic field $\mathbf{H}_0$ and to the light wavevector is shown in Fig. 2.

Special precautions were taken to prevent unwanted room illumination from falling on the sample (Section 3).

1.3. EPR Spectra

The EPR spectra of oxidized $KTaO_3$: Fe samples obtained at the liquid nitrogen temperature consist of a large number of lines differing in intensity. The strongest of them are due to the well-known iron centers in $KTaO_3$, namely, the rhombic centers Fe^{3+} [10] and two tetragonal centers, Fe_K^{3+}–O_i [5, 6] and Fe_{Ta}^{5+}–V_O [7, 11–13] (Fig. 3). Illumination of the oxidized samples with visible light at $T = 78$ K produces a spectrum which is much weaker than the above two and exhibits a well-resolved ligand hyperfine structure. This spectrum was obtained by us fairly recently and assigned to the Fe_{Ta}^{4+}–V_O complex [7]. Because of the large initial splitting ($|D| = 4.15$ cm^{-1}), the experiment reveals only forbidden transitions within the $|\pm1\rangle$ and $|\pm2\rangle$ doublets and this is what accounts for the weak intensity of the spectrum (Fig. 3).

The angular dependence of the fine structure permits observation of individual lines due to the tetragonal centers oriented along the [100], [010], and [001] crystal axes and investigation of the relative changes in the concentrations of differently oriented centers. The most convenient for this problem is the geometry in which the magnetic field $\mathbf{H}_0$ lies in the (001) crystal plane and is deflected by 1°–2° from the [110] direction (Fig. 2). In this case, the EPR lines corresponding to centers with the axes parallel to the [100] and [010] axes (subsequently referred to as *x* and *y* centers) are seen in magnetic fields close in magnitude and have about equal intensities (the *x* and *y* lines for the Fe_K^{3+}–O_i and Fe_{Ta}^{4+}–V_O centers in Fig. 3).[3] When extracting the center concentrations from the line intensities, small corrections for the angular dependence of the integrated line intensity were introduced.

---

[3] Note that even in this $\mathbf{H}_0$ orientation the initial intensities of the *x* and *y* lines can differ substantially. This is due to the cavity microwave field becoming strongly distorted when a $KTaO_3$ sample is introduced (for more details, see [7, Section 1.3]). In this work, we avoided such situations by properly choosing the sample shape and dimensions.

Presence of tetragonal iron centers in different samples at equilibrium and after illumination

Center	Sample	
	oxidized	reduced
Fe_K^{3+}–O_i	Yes	No, but forms on illumination
Fe_{Ta}^{3+}–V_O	No	Yes
Fe_{Ta}^{4+}–V_O	No, but forms on illumination	No
Fe_{Ta}^{5+}–V_O	Yes	No

2. CHANGES IN THE THERMODYNAMICALLY EQUILIBRIUM CHARGE STATES OF TETRAGONAL IRON CENTERS INDUCED BY A REDUCING ANNEAL

The thermodynamically equilibrium state of a crystal is attained by slow cooling in the dark from room temperature to the liquid nitrogen temperature or lower. One can then assume to a good approximation that the impurity levels lying below the Fermi level ($\mathcal{E}_F$) are filled completely and those above $\mathcal{E}_F$ are empty. As a rule, the Fermi level lies close, to within kT, to one of the impurity levels (pinned to it). This level is only partially filled. At a low temperature, a defect of a given type in thermodynamic equilibrium is in either one or two *adjacent* charge states. A reducing anneal can change the charge states of the centers in the negative sense to make the Fermi level rise.

The table presents data on the presence of various iron centers in oxidized and reduced samples after their cooling *in the dark* from room temperature to 78 K and after illumination. The illumination was performed in the blue–green region; near IR light produces the opposite effect. The spectral features of the recharging are discussed in more detail later. Note that the Fe ion in the Fe_{Ta}–V_O tetragonal complex can be in one of *three* charge states, with all of them detectable by EPR.

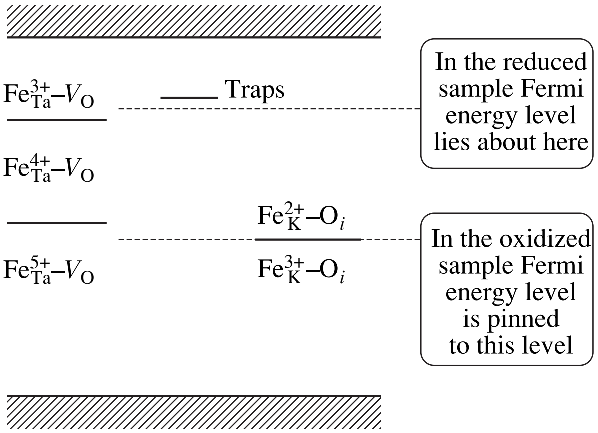

Fig. 4. Charge states of the two tetragonal complexes in $KTaO_3$ vs. Fermi level position. Dashed lines indicate the Fermi level for oxidized (bottom) and reduced (top) samples. Not drawn to scale.

An analysis of these data based on the above considerations permits one to draw a diagram of the levels associated with the tetragonal iron centers in $KTaO_3$ (Fig. 4). The solid horizontal lines here separate regions of different equilibrium charge states and, at the same time, indicate the position of the impurity levels involved in the impurity $\longleftrightarrow$ band charge-transfer transitions.

3. LIGHT-INDUCED RECHARGING OF THE Fe_{Ta}–V_O AND Fe_K–O_i TETRAGONAL COMPLEXES

As follows from the table, oxidized samples do not originally contain the Fe_{Ta}^{4+}–V_O centers, but they can be created by illumination in the blue–green spectral region. In the dark at a low temperature,[4] the concentration of the centers produced in this way remains constant indefinitely.

3.1. Independence of the Steady-State Center Concentration from the Illumination Intensity

The concentration of light-induced centers increases with time and tends to a steady-state value (Fig. 5). The growth kinetics depends only on the exposure (i.e., intensity times time). In other words, the intensity of the light generating the centers affects neither the course of the curve (Fig. 5) nor the steady-state concentration reached.

This behavior implies that the steady-state center concentration is a result of competition between the creation and destruction processes, the efficiency of each of them being proportional to the light intensity. Because the light-induced changes in the concentrations persist in the dark (at a low temperature), by creation and destruction one should understand complex processes including both the photoexcitation of the carrier and its subsequent trapping by another center. Section 6 presents rate equations describing recharging whose solutions possess the required properties.

The independence of the steady-state center concentration from the light intensity has an important methodological implication; namely, even a very weak stray illumination penetrating through slits in the microwave cavity will eventually produce the same concentration of the centers as the one created by the laser beam incident on the sample. Therefore, one has to thoroughly screen the instrument from extraneous light sources.

---

[4] Here and subsequently, by “low” we understand the liquid nitrogen or lower temperatures.

3.2. Spectral Dependence of Steady-State Concentrations

At the same time, the steady-state concentration exhibits a dependence on the light wavelength (circles in Fig. 6) with a spectral threshold of 2.05 ± 0.10 eV; light with photon energies above this threshold creates centers, otherwise it destroys them by releasing the trapped electrons.

We reported earlier [9] on a similar behavior of the Fe_K^{3+}–O_i centers in reduced $KTaO_3$: Fe samples. The creation of the Fe_K^{3+}–O_i centers was related [9] to the photoionization of the Fe_K^{2+}–O_i centers followed by electron capture by other centers representing relatively deep traps. The spectral dependence of the concentration of this center (triangles in Fig. 6) also revealed a threshold energy which was identified with the photoionization threshold of the Fe_K^{2+}–O_i centers or, in other words, with the position of the $Fe_K^{2+/3+}$–O_i impurity level relative to the conduction-band bottom.

Note the equality of the spectral thresholds for these two centers, which implies that they undergo recharging in the same process. We believe that the mechanism of creation of the Fe_{Ta}^{4+}–V_O centers in oxidized samples is in some sense opposite to that of the Fe_K^{3+}–O_i centers in reduced samples. The Fe_{Ta}^{4+}–V_O centers are created through the capture of optically excited free electrons by the Fe_{Ta}^{5+}–V_O centers. Most of the photoelectrons are produced in the ionization of the Fe_K^{2+}–O_i centers present in oxidized samples together with the Fe_K^{3+}–O_i centers. Thus, the threshold in the spectral dependence of the Fe_{Ta}^{5+}–V_O concentration is determined by the characteristic energy of another center, namely, by the photoionization energy of Fe_K^{2+}–O_i.

Studies of the iron center recharging by polarized light provide support for the above mechanisms to be operative.

3.3. Manifestation of Light-Induced Recharging in Different Samples

Recall that a strong spectral dependence of the Fe_K^{3+}–O_i steady-state concentration (open triangles in Fig. 6) is observed only in reduced samples. It is practically absent in all oxidized samples, with the changes not in excess of 10%. For a weakly reduced sample, this dependence is exemplified with diamonds in Fig. 6.

Quantitatively significant manifestations of the recharging processes can obviously be different in samples differing in the concentration ratios of defects and in their equilibrium charge states. Nevertheless, it should be stressed that in oxidized samples too, Fe_K^{2+}–O_i photoionization becomes initiated as soon as the photon energy exceeds the corresponding threshold (2.05 eV). Although this process does not change the Fe_K^{2+}–O_i and Fe_K^{3+}–O_i concentrations substantially, it can act as the main source of photoelectrons, become manifest in photocurrent excitation spectra (see Section 7), and initiate recharging in other centers (for instance, the Fe_{Ta}^{5+}–$V_O \longrightarrow Fe_{Ta}^{4+}$–$V_O$ process by electron trapping).

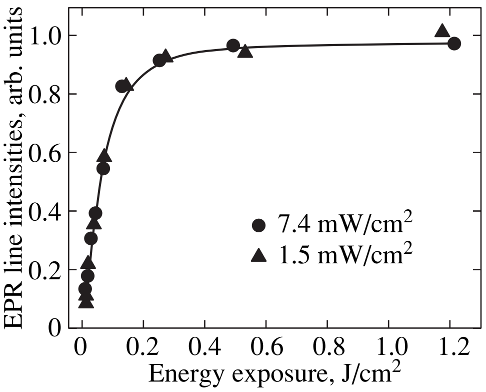

Fig. 5. Kinetics of Fe_{Ta}^{4+}–V_O creation in $KTaO_3$: Fe for two different incident light flux densities. $T = 78$ K, $\lambda = 454.5$ nm.

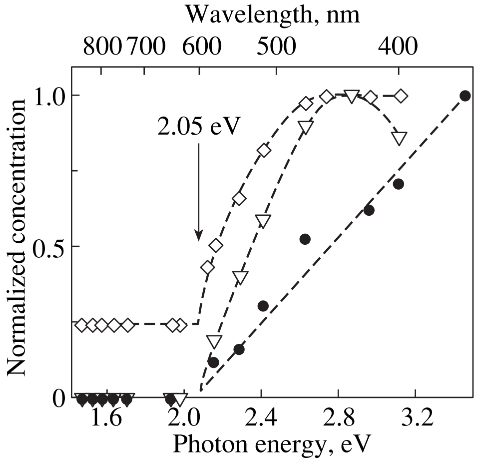

Fig. 6. Steady-state concentration of iron centers in $KTaO_3$ vs. incident wavelength. Circles are the Fe_{Ta}^{4+}–V_O concentration in oxidized samples derived from EPR spectra (with the maxima normalized to unity); triangles represent the same for Fe_K^{3+}–O_i in a reduced sample; and diamonds are the same for Fe_K^{3+}–O_i in a slightly reduced sample. $T = 78$ K. The dashed lines are drawn to aid the eye.

4. CENTER ALIGNMENT BY POLARIZED LIGHT

Illumination of the $KTaO_3$: Fe cubic crystal by unpolarized light ($\lambda = 454.5$ nm, $k \parallel [001]$, see Fig. 2) creates equal concentrations m_x and m_y of the Fe_{Ta}^{4+}–V_O

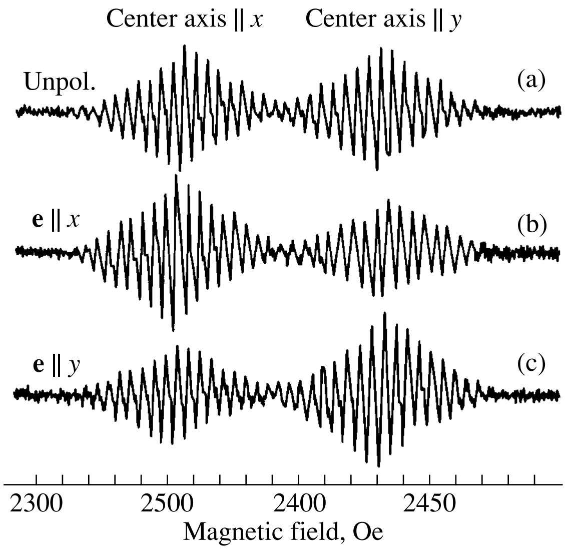

Fig. 7. Optical alignment of the $\mathrm{Fe}_{\mathrm{Ta}}^{4+}$–$V_{\mathrm{O}}$ centers in $\mathrm{KTaO_3}$. One sees a fragment of the EPR spectrum, which contains two lines (with a ligand hyperfine structure) corresponding to the $|+1\rangle \longleftrightarrow |-1\rangle$ transitions in the *x*- and *y*-oriented centers. (a) On illumination with unpolarized light; (b) on illumination with **e** || *x*; and (c), the same for **e** || *y*. $T = 78$ K, $\lambda = 454.5$ nm, and $\theta = 43.5°$.

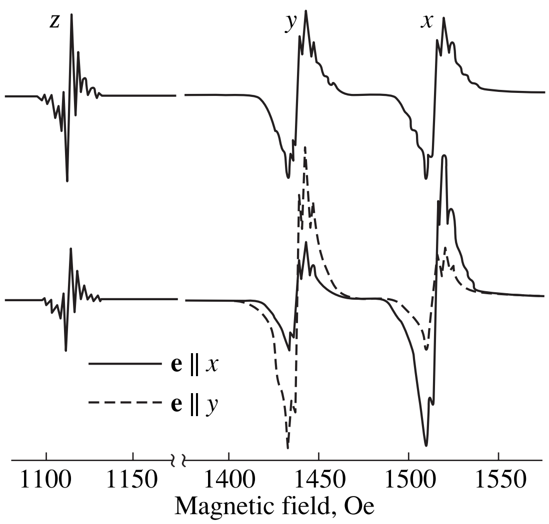

Fig. 8. Optical alignment of the $\mathrm{Fe}_{\mathrm{K}}^{3+}$–$\mathrm{O}_i$ centers in $\mathrm{KTaO_3}$. Top: EPR spectrum taken after cooling the crystal in the dark. Bottom: the spectra measured after illumination with different directions of polarization. The other conditions are the same as in Fig. 7.

centers oriented along the *x* and *y* crystal axes, respectively. However, polarized illumination brings about a substantial redistribution between m_x and m_y (Fig. 7). More specifically, if the light polarization vector is parallel to *y*, the centers become partially aligned along the same axis, $m_y > m_x = m_z$.

The alignment can conveniently be characterized by an alignment factor

$$A_m = \frac{m_y - m_x}{m_y + m_x} = \frac{I_y - I_x}{I_y + I_x},$$

where I_x and I_y are the integrated intensities of the corresponding EPR lines corrected in accordance with the transition probabilities.

For the experiment depicted in Fig. 7c, $A_m \approx 0.2$, which corresponds to the ratio $m_y/m_x \approx 1.5$.

In the same experiment, the $\mathrm{Fe}_{\mathrm{K}}^{3+}$–$\mathrm{O}_i$ centers, which were initially present in the oxidized sample, also undergo alignment (Fig. 8). For the experiment specified by the dotted line in Fig. 8, $n_y \approx 3n_x \approx 3n_z$, which corresponds to $A_n \approx 0.5$.

The alignment produced by polarized light persists in the dark indefinitely at 78 K or at a lower temperature. This effect is also observed at 4.2 K, with both the degree of alignment and the typical exposure required to reach steady-state alignment being approximately the same.

5. KINETICS OF RECHARGING AND ALIGNMENT

Studies of the light-induced recharging showed that the steady-state concentrations are determined by the dynamic equilibrium setting in between the competing processes of the creation and destruction of the observed center charge state. Hence, an anisotropy of either of these processes under polarized light illumination can produce anisotropy in the steady-state concentrations. Which of the processes is anisotropic can be determined by studying the kinetics of the alignment, provided these processes play different parts in the different kinetics stages. For instance, in the initial stage of the center creation there is no destruction, because there is nothing to be destroyed.

5.1. Creation of $\mathrm{Fe}_{\mathrm{Ta}}^{4+}$–$V_{\mathrm{O}}$ *Centers by Polarized Violet Light*

Figure 9a (filled circles and squares) presents the evolution of the concentration of *x*- and *y*-oriented $\mathrm{Fe}_{\mathrm{Ta}}^{4+}$–$V_{\mathrm{O}}$ centers created by light with **e** || *y* polarization. Before the experiment, the sample was cooled in the dark. One readily sees that the m_y/m_x ratio is close to unity for the first several points, then grows, and tends to the limit of $m_y/m_x \approx 1.5$ with $A_m \approx 0.2$ (filled triangles in Fig. 9).

This experiment gives one grounds to maintain that the $\mathrm{Fe}_{\mathrm{Ta}}^{4+}$–$V_{\mathrm{O}}$ centers are created isotropically and, most likely, are due to the capture of free photoexcited electrons by the available $\mathrm{Fe}_{\mathrm{Ta}}^{5+}$–$V_{\mathrm{O}}$ centers, whereas their alignment sets in as dynamic equilibrium is reached and is due to the anisotropy of the destruction process, which consists in the ionization of the $\mathrm{Fe}_{\mathrm{Ta}}^{4+}$–$V_{\mathrm{O}}$ centers thus created (see the diagram in Fig. 10). The ionization cross section of centers with the axis parallel to the polarization vector ($\sigma^{\parallel}$) is smaller than that for the centers whose axis is perpendicular to this vector ($\sigma^{\perp}$).

5.2. Destruction of $\mathrm{Fe}_{\mathrm{Ta}}^{4+}$–$V_{\mathrm{O}}$ *Centers by Polarized Red Light*

Another means of separating the processes consists in using red light. First, one creates equal concentrations $m_x = m_y$ of the $\mathrm{Fe}_{\mathrm{Ta}}^{4+}$–$V_{\mathrm{O}}$ centers by violet light depolarized in the (xy) plane, after which y-polarized red light is turned on. If the proposed model is correct, then the decrease in m_x and m_y should be accompanied by alignment with $m_y > m_x$ because the ionization of centers with the axis perpendicular to the polarization vector is more efficient (see diagram in Fig. 11a). The corresponding experiment shows this to indeed be the case (Fig. 12).

5.3. Kinetics of Light-Induced Recharging of $\mathrm{Fe}_{\mathrm{K}}^{3+}$–$\mathrm{O}_i$ *Centers*

Similar experiments performed on the $\mathrm{Fe}_{\mathrm{K}}^{3+}$–$\mathrm{O}_i$ centers in a reduced sample yield opposite results. Polarized destroying light does not affect the relative magnitude of n_x and n_y (Fig. 13). This difference can be accounted for by the fact that the $\mathrm{Fe}_{\mathrm{Ta}}^{4+}$–$V_{\mathrm{O}}$ centers are destroyed by photoionization, whereas the $\mathrm{Fe}_{\mathrm{K}}^{3+}$–$\mathrm{O}_i$ centers are destroyed by trapping a photoexcited carrier (see diagram in Fig. 11b).

Another difference consists in that the creation of the $\mathrm{Fe}_{\mathrm{K}}^{3+}$–$\mathrm{O}_i$ centers in a reduced sample is anisotropic, starting from the lowest exposures (Fig. 14). This is accounted for by the fact that the $\mathrm{Fe}_{\mathrm{K}}^{3+}$–$\mathrm{O}_i$ centers are created by photoionization, while the $\mathrm{Fe}_{\mathrm{Ta}}^{4+}$–$V_{\mathrm{O}}$ formation is due to the trapping of a photoexcited carrier.

The kinetics of $\mathrm{Fe}_{\mathrm{K}}^{3+}$–$\mathrm{O}_i$ production in a reduced sample has a complex character; namely, the *alignment factor reverses its sign* (Fig. 14). In oxidized samples, where the $\mathrm{Fe}_{\mathrm{K}}^{3+}$–$\mathrm{O}_i$ centers are initially present in substantial concentrations, the alignment factor increases from zero to +0.56 for $\mathbf{e} \parallel y$ without reversing its sign (open symbols in Fig. 9). These observations imply the existence of two alignment mechanisms, with one of them becoming dominant above a certain concentration of the $\mathrm{Fe}_{\mathrm{K}}^{3+}$–$\mathrm{O}_i$ centers. We believe that this occurs because of optical electron transfer from the valence band to the $\mathrm{Fe}_{\mathrm{K}}^{3+}$–$\mathrm{O}_i$ centers (Fig. 15). Both transfer processes have anisotropy of the same sign ($\sigma_1^{\perp} > \sigma_1^{\parallel}$ and

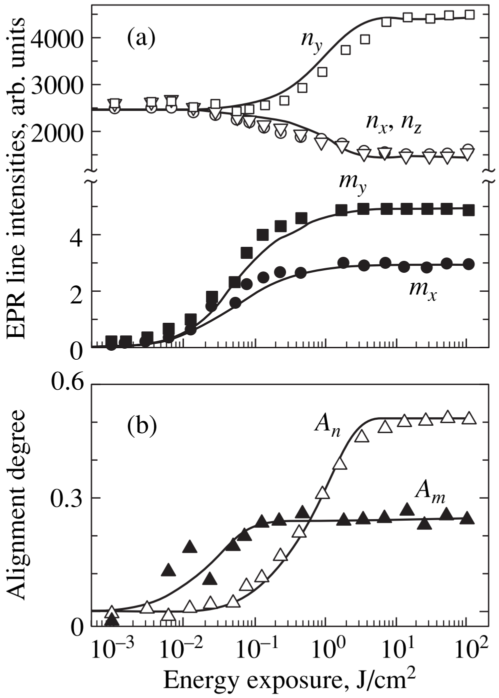

Fig. 9. (a) Evolution of the concentrations of the $\mathrm{Fe}_{\mathrm{K}}^{3+}$–$\mathrm{O}_i$ and $\mathrm{Fe}_{\mathrm{Ta}}^{4+}$–$V_{\mathrm{O}}$ centers and (b) their alignment on illumination with polarized light. $T = 78$ K, $\lambda = 454.5$ nm, and $\mathbf{e} \parallel y$. Points are the experiment, and curves are the calculation; the notation is explained in the text.

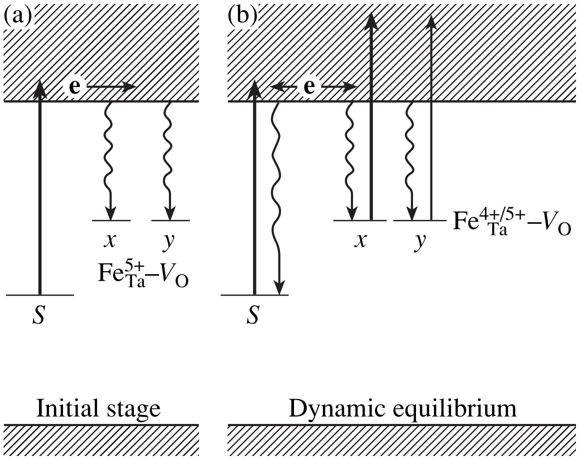

Fig. 10. Scheme of $\mathrm{Fe}_{\mathrm{Ta}}^{4+}$–$V_{\mathrm{O}}$ creation by polarized light (a) in the initial stage and (b) on reaching dynamic equilibrium. The symbol S identifies the center with an ionization threshold of 2.05 eV, which provides electrons (we believe it to be $\mathrm{Fe}_{\mathrm{K}}^{2+}$–$\mathrm{O}_i$). The thickness of the arrows illustrates the ionization cross section ratio for $\mathbf{e} \parallel y$.

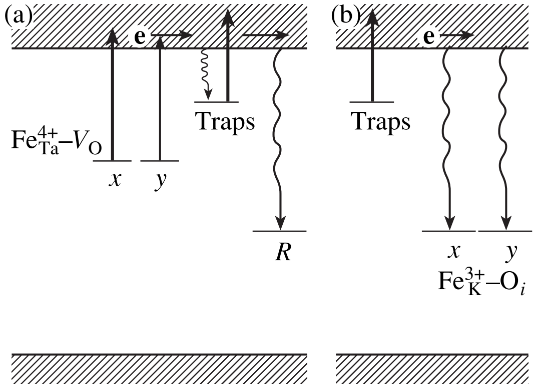

Fig. 11. Left: scheme of anisotropic destruction of the Fe^{4+}_{Ta}–V_O centers in an oxidized sample through their anisotropic photoionization by polarized red light. The *R* symbol denotes a recombination center (this may be the same defect as *S* in Fig. 10). Right: scheme of isotropic destruction of the Fe^{3+}_K–O_i centers in a reduced sample through their trapping of the electrons released from the traps.

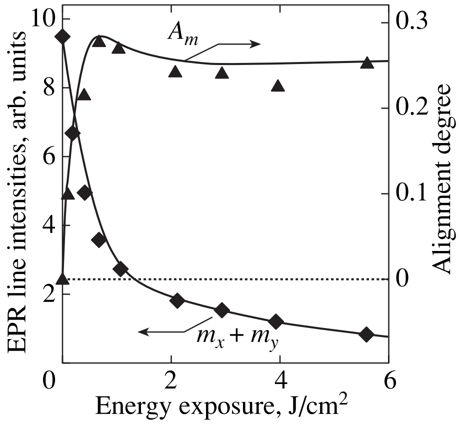

Fig. 12. Anisotropic destruction of the Fe^{4+}_{Ta}–V_O centers in $KTaO_3$ by polarized red light. $T = 78$ K, $\lambda = 632.8$ nm, and **e** ∥ *y*. Points are the experiment, and curves are the calculation.

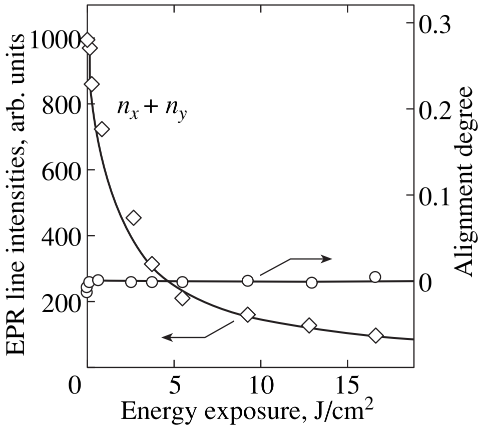

Fig. 13. Isotropic destruction of the Fe^{3+}_K–O_i centers by polarized red light. $T = 78$ K, $\lambda = 632.8$ nm, and **e** ∥ *y*. Points are the experiment, and curves are the calculation.

$\sigma_2^{\perp} > \sigma_2^{\parallel}$), but they act in the opposite sense on the Fe^{3+}_K–O_i concentration and, therefore, they produce alignments of opposite signs.

It appears appropriate to consider here the transitions between the impurity state and both electronic bands of the crystal in parallel. The point is that, in accordance with the Born–Haber thermodynamic cycle [14, 15], the sum of the threshold energies for Fe^{2+}_K–O_i photoionization (electron transfer from Fe^{2+}_K–O_i to the conduction band) and for the electron transfer from the valence band to the Fe^{3+}_K–O_i center should be exactly equal to the band-gap energy E_g. Knowing the band-gap width and one of the recharging thresholds, one can estimate the other threshold. Estimates made for $KTaO_3$ yield E_g = 3.6–3.8 eV [16, 17]. Thus, the spectral threshold for electron transfer from the valence band to Fe^{3+}_K–O_i can be estimated as 1.45–1.85 eV, and, hence, illumination with a photon energy in excess of 2.05 eV can initiate both processes.

It should be noted that any *experimental* manifestation of recharging is, in principle, possible only if the excitation energy *exceeds* the true threshold involved in the Born–Haber cycle. In particular, this also holds for the 2.05-eV threshold estimated in experiments on the photoionization of Fe^{2+}_K–O_i. Summing up, it can be maintained that the $Fe^{2+/3+}_K$–O_i level (see Fig. 15) lies very close to the band midgap in $KTaO_3$ and that both recharging processes have approximately equal spectral thresholds.

6. GENERAL SCHEME AND RATE EQUATIONS

Figure 15 proposes a general diagram of levels and transitions associated with the tetragonal iron centers in $KTaO_3$, all of whose elements have been discussed above in connection with the key experiments.

The single-electron band diagram of $KTaO_3$ shows the impurity levels of the differently oriented Fe_{Ta}–V_O and Fe_K–O_i complexes (for the sake of simplicity, the centers parallel to the *z* axis were dropped but naturally were included in the differential equations below).

For the Fe_{Ta}–V_O complex, the $Fe^{4+/5+}_{Ta}$–V_O level involved in the processes occurring in oxidized samples is shown. In reduced samples, one should instead consider the $Fe^{3+/4+}_{Ta}$–V_O level (Fig. 4). However, the Fe^{3+}_{Ta}–V_O concentration does not change under illumination, so that this complex does not apparently affect the pattern of the recharging noticeably.[5] Therefore, we

---

[5] This can occur, for instance, in the limiting case in which the $Fe^{3+/4+}_{Ta}$–V_O level is filled completely and its electron trapping coefficient is large compared to those for other centers.

neglected a part of the diagram when analyzing the recharging kinetics in reduced samples.

The diagram arbitrarily shows a trap level. We do not know its nature and depth, and it can, quite possibly, be assigned to several levels due to different centers. In that case, the photoionization cross section and the trapping coefficient are some averaged effective values.

The charge exchange kinetics in such a system is described by the coupled differential equations

$$\frac{d}{dt}n_x(t) = (\sigma_1^{\parallel}P_x + \sigma_1^{\perp}P_y)\left(\frac{N}{3} - n_x(t)\right) - \alpha_n e(t)n_x(t) - (\sigma_2^{\parallel}P_x + \sigma_2^{\perp}P_y)n_x(t) + \beta_n h(t)\left(\frac{N}{3} - n_x(t)\right), \quad (1)$$

$$\frac{d}{dt}n_y(t) = (\sigma_1^{\parallel}P_y + \sigma_1^{\perp}P_x)\left(\frac{N}{3} - n_y(t)\right) - \alpha_n e(t)n_y(t) - (\sigma_2^{\parallel}P_y + \sigma_2^{\perp}P_x)n_y(t) + \beta_n h(t)\left(\frac{N}{3} - n_y(t)\right), \quad (2)$$

$$\frac{d}{dt}n_z(t) = \sigma_1^{\perp}(P_x + P_y)\left(\frac{N}{3} - n_z(t)\right) - \alpha_n e(t)n_z(t) - \sigma_2^{\perp}(P_x + P_y)n_z(t) + \beta_n h(t)\left(\frac{N}{3} - n_z(t)\right), \quad (3)$$

$$\frac{d}{dt}m_x(t) = -(\sigma_3^{\parallel}P_x + \sigma_3^{\perp}P_y)m_x(t) + \alpha_m e(t)\left(\frac{M}{3} - m_x(t)\right), \quad (4)$$

$$\frac{d}{dt}m_y(t) = -(\sigma_3^{\parallel}P_y + \sigma_3^{\perp}P_x)m_y(t) + \alpha_m e(t)\left(\frac{M}{3} - m_y(t)\right), \quad (5)$$

$$\frac{d}{dt}m_z(t) = -\sigma_3^{\perp}(P_x + P_y)m_z(t) + \alpha_m e(t)\left(\frac{M}{3} - m_z(t)\right), \quad (6)$$

$$\frac{d}{dt}c(t) = -\sigma_c(P_x + P_y)c(t) + \alpha_c e(t)(C - c(t)), \quad (7)$$

$$\frac{d}{dt}h(t) = (\sigma_2^{\parallel}P_x + \sigma_2^{\perp}P_y)n_x(t) + (\sigma_2^{\parallel}P_y + \sigma_2^{\perp}P_x)n_y(t) + \sigma_2^{\perp}(P_x + P_y)n_z(t) - \beta_n h(t)(N - n_x(t) - n_y(t) - n_z(t)), \quad (8)$$

$$e(t) = \{n_x(t) - n_x(0) + n_y(t) - n_y(0) + n_z(t) - n_z(0)\} - \{c(t) - c(0)\} - \{m_x(t) - m_x(0) + m_y(t) - m_y(0) + m_z(t) - m_z(0)\} + h(t), \quad (9)$$

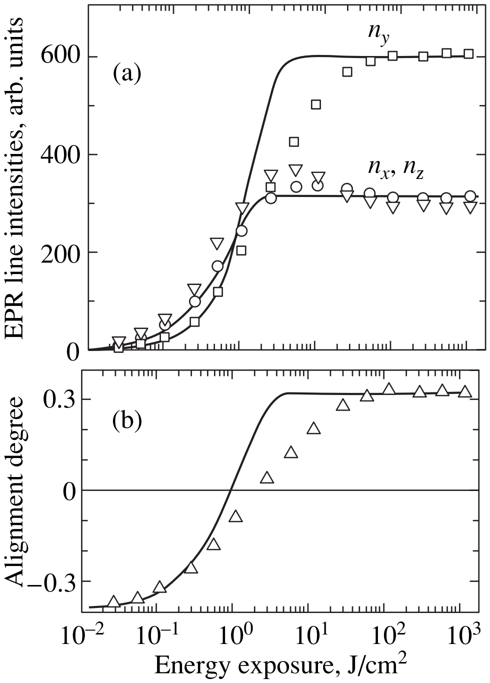

Fig. 14. Reversal of the sign of alignment in the course of $\mathrm{Fe_K^{3+}}$–O_i creation by polarized light. (a) concentrations and (b) degree of alignment. T = 78 K, λ = 454.5 nm, **e** ∥ y. Curves are the calculation, and points are the experiment.

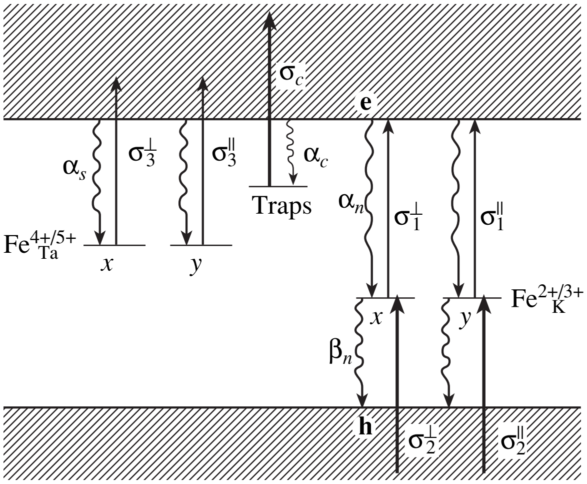

Fig. 15. Diagram of levels and transitions associated with the $\mathrm{Fe_{Ta}}$–V_O and $\mathrm{Fe_K}$–O_i tetragonal iron centers (the center notation is abbreviated). The cross sections assigned to the optical transitions refer to the case of **e** ∥ y light polarization. The arrow thickness reflects the difference between the ionization cross sections.

where $n_x(t)$, $n_y(t)$, and $n_z(t)$ are the concentrations of the $\mathrm{Fe_K^{3+}}$–O_i centers oriented along the corresponding axes; N is the total concentration of the $\mathrm{Fe_K}$–O_i complexes in both charge states; $m_x(t)$, $m_y(t)$, and $m_z(t)$ are the concentrations of the $\mathrm{Fe}^{4+}_{\mathrm{Ta}}$–$V_\mathrm{O}$ centers oriented along the corresponding axes; M is the total concentration of the $\mathrm{Fe}_{\mathrm{Ta}}$–$V_\mathrm{O}$ complexes in both charge states; $c(t)$ is the concentration of the trapped electrons; C is the total concentration of empty and filled traps; $e(t)$ and $h(t)$ are the free electron and hole concentrations, respectively; α_n, α_m, and α_c are the electron trapping coefficients by $\mathrm{Fe}^{3+}_{\mathrm{K}}$–$\mathrm{O}_i$, $\mathrm{Fe}^{5+}_{\mathrm{Ta}}$–$V_\mathrm{O}$, and by the traps, respectively; β_n is the hole trapping coefficient by $\mathrm{Fe}^{2+}_{\mathrm{K}}$–$\mathrm{O}_i$; $\sigma_i^{\parallel}$ and $\sigma_i^{\perp}$ ($i = 1, 2, 3$) are the absorption cross sections for photoionization transitions for light polarized parallel and perpendicular to the center axis, respectively; σ_c is the absorption coefficient for photoionization of a filled trap; and P_x and P_y are the flux densities of photons with polarizations along the corresponding axes. Each term in the right-hand part of Eqs. (1)–(8) corresponds to one of the transitions in the diagram of Fig. 15. Equation (9) is the charge conservation law.

The curves in Figs. 9 and 12–14 are the solutions of these coupled rate equations for the following set of parameters:

$$\begin{gathered}
\sigma_1^{\perp}/\sigma_1^{\parallel} = 2.3, \quad \sigma_2^{\perp}/\sigma_2^{\parallel} = 15, \quad \sigma_3^{\perp}/\sigma_3^{\parallel} = 1.65, \\
\sigma_1^{\perp} = 4.5 \times 10^{-20}\ \mathrm{cm}^2 \ (\text{for 455 nm}), \\
\sigma_2^{\perp} = 1.35 \times 10^{-18}\ \mathrm{cm}^2 \ (\text{for 455 nm}), \\
\sigma_3^{\perp} = 7.2 \times 10^{-17}\ \mathrm{cm}^2 \ (\text{for 455 nm}), \\
\sigma_3^{\perp} = 3.5 \times 10^{-18}\ \mathrm{cm}^2 \ (\text{for 633 nm}), \\
\sigma_c = 4.5 \times 10^{-18}\ \mathrm{cm}^2 \ (\text{for 455 nm}), \\
\sigma_c = 1.7 \times 10^{-19}\ \mathrm{cm}^2 \ (\text{for 633 nm}), \\
\alpha_c = 1.25\alpha_n, \quad \alpha_m = 8\alpha_n, \\
C = 0.4N \ (\text{for the reduced sample}), \\
C = 0.15N \ (\text{for the oxidized sample}), \\
M = 0 \ (\text{for the reduced sample}), \\
M = 0.1N \ (\text{for the oxidized sample}), \\
n_x(0) = n_y(0) = n_z(0) = 0.4(N/3) \\
(\text{for the oxidized sample} \\
\text{in thermodynamic equilibrium}).
\end{gathered} \tag{10}$$

Note that some of these values, for instance, $\sigma_1^{\perp}/\sigma_1^{\parallel} = 2.3$, follow directly from the experiment and, thus, are not fitting parameters for the inverse problem. Additionally, some parameters enter only in ratios to one another. For instance, the absolute values of the trapping coefficients do not affect the solution within a reasonable range of their variation and the values of the concentrations N, M, and C influence only the normalization of the solutions.

As can be seen from Figs. 9 and 12–14, the solution of Eqs. (1)–(9) with the parameters in Eq. (10) is in fairly good agreement with the experiment, although the model is certainly oversimplified. We do not consider, for instance, the wavelength dependence of the $\sigma_i^{\parallel}/\sigma_i^{\perp}$ anisotropy and disregard the existence of other centers; in particular, only one trap level is taken into account.

The solutions obtained suggest the independence of the steady-state center concentration from the intensity of the light that created them. Moreover, the kinetics is a function of exposure, in agreement with the experiment (see Section 3.1). By and large, such properties are observed if the recharging kinetics is described by differential equations in which all terms in the right-hand part are linear functions of P:

$$\frac{d}{dt}n(t) = A(n(t), \ldots)P + B(n(t), \ldots)P + \ldots, \tag{11}$$

where A and B depend on the running concentrations of the various centers taking part in the recharging, but do not depend on P. In this case, P does not enter steady-state solutions and the kinetics can be presented as a function of the exposure tP.

In our case, Eqs. (1)–(9) contain both terms linear in P, which describe impurity–band single-photon transitions and the P-independent terms relating to the free-carrier trapping. It can be shown, however, that Eqs. (1)–(9) can be reduced to Eq. (11) in the adiabatic approximation, which considers the free carriers as a fast-relaxing subsystem. In this case, for the parameters chosen here, the numerical solutions of the approximate system of equations coincide with those of Eqs. (1)–(9).

The solutions of Eqs. (1)–(9) with the parameters in Eq. (10) obtained for steady-state concentrations $n(\infty)$ under red and violet unpolarized illumination agree with the experiment (Fig. 6) in the sense that the spectral dependence of the steady-state concentrations depends on the initial filling of the impurity levels by electrons. More specifically, for $n_i(0) = 0$ ($i = x, y, z$) (reduced sample), we have $n_i(\infty) = 0$ for the red light and $n_i(\infty) \approx 0.06(N/3)$ for the violet light, while for $n_i(0) = 0.4(N/3)$ (oxidized sample), $n_i(\infty)$ practically does not change under illumination.

The experimentally observed absence of alignment and of a noticeable change in the $\mathrm{Fe}^{5+}_{\mathrm{Ta}}$–$V_\mathrm{O}$ concentration is accounted for by the fact that only a small part of these complexes changes their charge state to $\mathrm{Fe}^{4+}_{\mathrm{Ta}}$–$V_\mathrm{O}$. Our estimates of the value of m/M are in agreement with the calculated figure $m/M \approx 0.003$.

Note that the set of parameters in Eq. (10) is not the only one providing a good fit to the experiment. We did not plan determination of the transition parameters by a method so indirect as this one and based on such a simplified model. We intended only to show that our model, which draws on a qualitative analysis of specially designed experiments, is capable of yielding a fairly good quantitative description for some reasonable values of the parameters.

7. OPTICAL ABSORPTION AND PHOTOCONDUCTIVITY

The optical charge-transfer transitions considered above will contribute to the absorption spectrum. The absorption spectrum obtained by us reproduces, in its main features, the one presented in [8]. While the weakly structured spectrum in [8] is divided into three symmetric bands, we would like to focus attention on its long-wavelength edge with a small step occurring exactly at 600 nm (2.05 eV). The absorption coefficient calculated from Eq. (10) is determined primarily by $n(\infty)\sigma_2^{\perp}$ and is found to be less than or of the order of the measured one (the error of calculation is due to that of the determination of the center concentrations). In reduced samples, the absorption coefficient at 455 nm is a few times smaller than that in the oxidized ones, which likewise is in agreement with the values of $n(\infty)$ calculated for different samples.

Note that mutual recharging among centers of *different types* (whose positions in a crystal are hardly correlated) serves in itself as a convincing argument for spatial electron transfer. A more weighty argument, however, is the observation of the contribution of these processes to the photoconductivity.

Photoelectric studies revealed noticeable photoconductivity in $KTaO_3 : Fe$ crystals starting from excitation energies ~1.5 eV, as evident from Fig. 16 displaying photocurrent excitation spectra of an oxidized and a reduced sample. These spectra consist of several broad overlapping bands[6] and a relatively narrow (less than 0.1 eV broad) peak at ~3.6 eV.

A significant feature of the spectra in Fig. 16 is the broad band with a low-energy threshold near 2 eV, which is strong in the spectrum of the reduced sample (note the log scale on the ordinate axis) and can be seen in the spectrum of the oxidized sample. The low-energy threshold of this band is very close to the spectral threshold of the $Fe_K^{2+}–O_i \longrightarrow Fe_K^{3+}–O_i$ light-induced recharging at 2.05 eV, which was found in studies of the light-induced recharging of centers (Fig. 6). Moreover, the substantially higher intensity of this band in the photoconductivity spectrum of the reduced sample correlates well with the ratio of the two charge states, $Fe_K^{2+}–O_i$ and $Fe_K^{3+}–O_i$, in the reduced and oxidized samples.[7] Thus, the EPR results on the $Fe_K^{2+}–O_i \longrightarrow Fe_K^{3+}–O_i$ light-induced recharging find validation in the photocurrent excitation spectra.

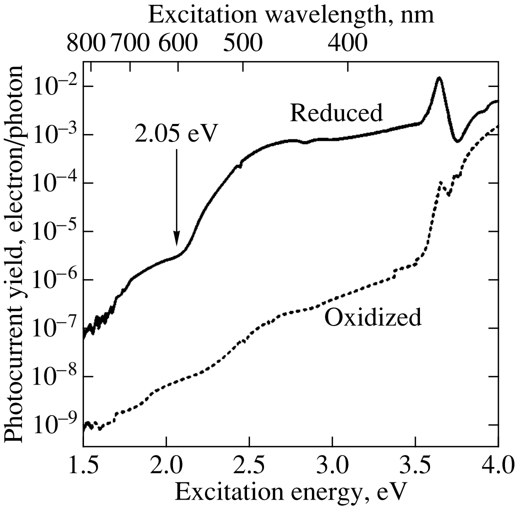

Fig. 16. Photoconductivity spectra of $KTaO_3 : Fe$ for samples of the two types. The photocurrent is normalized to the incident photon flux.

The photoconductivity feature peaking at about 3.6 eV can be due to excitons [20]. In the fairly strong electric field of 10 kV/cm, in which the measurements were carried out, the exciton dissociates [21, 22] and contributes to the photocurrent. As the field is lowered the peak weakens and virtually disappears in fields of ~0.5 kV/cm, which substantiates this interpretation.

8. DISCUSSION OF THE POSSIBLE ROLE OF REAL REORIENTATIONS

As follows from the above, the totality of the experimental observations accumulated thus far allows a self-consistent interpretation based on anisotropic light-induced recharging of axial iron centers in $KTaO_3$, which does not invoke the processes of light-induced center reorientation. Moreover, an explanation of the observed effects which does not include anisotropic light-induced recharging appears to be impossible. As for the possible role of light-induced reorientations in the alignment process, one can speak here only on some manifestations of light-induced reorientation capable of contributing to the effects associated with anisotropic light-induced recharging.[8]

Reorientation of ground-state $Fe_K^{3+}–O_i$ centers for $T > 100$ K in the absence of illumination was reported to occur in a number of publications. This result was obtained in [27] (see also [26]) by measuring the destruction rate of the center alignment in the dark (from observation of the linear dichroism), which was produced preliminarily by polarized light. In [28], the conclusion of thermal center reorientation was drawn

---

[6] At energies above 3.5 eV, the shape of the spectra can be distorted markedly by strong light absorption in samples near the $KTaO_3$ fundamental absorption edge.

[7] Considered in terms of a simple model, the photocurrent is proportional to the concentration ratio of the filled and empty states of the impurity level responsible for the photoconductivity (see, e.g., [18, 19]).

from a comparison of the results obtained by studying the dielectric losses and temperature-induced EPR line broadening of the center in question. Finally, our recent publication [29] reported the orientation of the Fe_K^{3+}–O_i dipole centers by an external electric field. By [27, 28], the activation energy is 0.34 eV and extrapolating the data of [27, 28] to $T = 78$ K yields ~10^{-9} s^{-1} for the reorientation rate, in full agreement with the absence of any changes in the center concentrations at $T = 78$ K in the dark.

When the centers are in the excited state, the barriers can naturally be lower than in the ground state [3]. However, the observed independence of the alignment effect from temperature within the range from 4.2 to 78 K (see Section 4 and [9]) casts doubt on any interpretation of the effect involving temperature-dependent processes (e.g., such as the over-barrier hopping in an excited center discussed in [3]). In addition, the short excited-state lifetime should also constrain very strongly the manifestation of over-barrier hopping in experiments. As for the total absence of any barrier in the excited state, which would give rise to temperature-independent reorientation under optical excitation [3], this situation appears extremely unlikely for centers whose reorientation consists in a change in the position of an interstitial oxygen ion by a few angstroms.

In principle, centers can undergo reorientation in the course of light-induced recharging. An illustration is the Fe_K^{4+}–O_i reorientation in the course of the Fe_K^{3+}–O_i photoionization, as suggested in [25, 26]. In our opinion, reorientation of a center capturing an electron or a hole in the course of nonradiative relaxation, accompanied by an energy release of ~2 eV, is also possible and even preferable.

In all the above models, however, the rate of optically induced reorientation depends strongly on the individual parameters of the center and it can be expected to differ by orders of magnitude for the Fe_K^{3+}–O_i and Fe_K^{4+}–O_i centers differing so markedly in structure. At the same time, the experiment shows that the characteristic alignment rates of these two types of centers are fairly similar (Fig. 9) and, more significantly, that the total concentrations of differently oriented centers vary on the same time scale (Figs. 9, 12, and 14).

The above suggests that an analysis of an additional mechanism, namely, light-induced defect reorientation, besides the undoubtedly operative mechanism of defect alignment involving their anisotropic photoionization, can be accepted as reasonable only if convincing experimental evidence in favor of such a consideration appears.

One of the attempts in this direction was made by us in an experiment in which we looked for the Fe_K^{3+}–O_i orientation in a sample acted upon simultaneously by violet light and a dc electric field $E = 55$ kV/cm at $T = 78$ K. Excitation of the centers by light could, in principle, create favorable conditions for their reorientation. The experiment yielded, however, a negative result, in that no orientation of the centers was detected.

9. CONCLUSION

Thus, the Fe_{Ta}^{4+}–V_O and Fe_K^{3+}–O_i tetragonal centers in $KTaO_3$ acted upon by polarized light undergo orientation-dependent light-induced recharging, as a result of which the distribution of the orientations of the axes of defects in the *given* charge state over the three ⟨100⟩ directions becomes no longer equally probable. This mechanism, which does not include real reorientations of the Fe_{Ta}–V_O and Fe_K–O_i complexes, gives rise, nevertheless, to the alignment of the centers along (or perpendicular) to the light polarization vector.

This mechanism appears to be of a fairly general nature. Indeed, it does not contain any specific microscopic mechanisms inherent in the systems under study here and is based only on light-induced charge transfer between defect centers and the crystal lattice. This transfer inevitably occurs when the incident photon energy exceeds a certain threshold. Generally speaking, anisotropic defects always exhibit an anisotropy in the corresponding absorption cross sections. The magnitude of the effect depends naturally on many microscopic parameters. Nevertheless, we have seen that the possibility of optical alignment of anisotropic defects should never be overlooked when considering any process including light-induced charge transfer.

ACKNOWLEDGMENTS

The authors express their gratitude to Prof. A.A. Kaplyanskiĭ for interest in the work and many fruitful discussions, Prof. S. Kapphan and Prof. V.S. Vikhnin for stimulating criticisms, Dr. H. Hesse for providing the $KTaO_3$: Fe crystals, and to Prof. U. Happek for assistance in photoconductivity measurements in the ultraviolet region of the spectrum.

This work was supported by the Russian Foundation for Basic Research, grant no. 99-02-18319.

---

[8] In [23–26], the dominant role of light-induced reorientations in the alignment of the Fe_K^{3+}–O_i centers is declared. It becomes clear from [26], however, that the equations used in [23–26] describe, as in [9], anisotropic light-induced recharging of the Fe_K–O_i centers involving both electronic bands of $KTaO_3$, complemented by the Fe_K^{4+}–O_i reorientation due to the photoionization of Fe_K^{3+}–O_i. It appears puzzling why this mechanism of alignment was called in [25, 26] "intracenter reorientation accompanied by recharging," whereas, in accordance with the equations presented in [26], the only factor necessary for the alignment to occur is the anisotropy in light-induced recharging, so that under *isotropic* light-induced recharging, no Fe_K^{3+}–O_i alignment should be observed altogether, despite the Fe_K^{4+}–O_i reorientation.

REFERENCES

1. F. Weigert, Z. Phys. B **5** (6), 410 (1921).
2. P. P. Feofilov, *The Physical Basis of Polarized Emission: Polarized Luminescence of Atoms, Molecules, and Crystals* (Fizmatgiz, Moscow, 1959; Consultants Bureau, New York, 1961).
3. F. Lüty, in *Physics of Color Centers,* Ed. by W. B. Fowler (Academic, New York, 1968).
4. R. L. Berney and D. L. Cowan, Phys. Rev. B **23** (1), 37 (1981).
5. I. P. Bykov, M. D. Glinchuk, A. A. Karmazin, and V. V. Laguta, Fiz. Tverd. Tela (Leningrad) **25** (12), 3586 (1983) [Sov. Phys. Solid State **25**, 2063 (1983)].
6. V. V. Laguta, M. D. Glinchuk, I. P. Bykov, *et al.*, Fiz. Tverd. Tela (Leningrad) **29** (8), 2473 (1987) [Sov. Phys. Solid State **29**, 1422 (1987)].
7. D. V. Azamat, S. A. Basun, V. É. Bursian, *et al.*, Fiz. Tverd. Tela (St. Petersburg) **41** (8), 1424 (1999) [Phys. Solid State **41**, 1303 (1999)].
8. H.-J. Reyher, B. Faust, M. Käding, *et al.*, Phys. Rev. B **51**, 6707 (1995); Erratum, Phys. Rev. B **54**, 3662 (1996).
9. S. A. Basun, L. S. Sochava, V. E. Bursian, *et al.*, Mater. Sci. Forum **239–241**, 345 (1997).
10. A. P. Pechenyi, M. D. Glinchuk, T. V. Antimirova, and W. Kleemann, Phys. Status Solidi B **174**, 325 (1992).
11. M. D. Glinchuk, V. V. Laguta, I. P. Bykov, *et al.*, J. Phys.: Condens. Matter **7**, 2605 (1995).
12. H.-J. Reyher, B. Faust, M. Mainwald, and H. Hesse, Appl. Phys. B **B64**, 331 (1996).
13. V. É. Bursian, V. S. Vikhnin, L. S. Sochava, *et al.*, Fiz. Tverd. Tela (St. Petersburg) **39** (4), 626 (1997) [Phys. Solid State **39**, 547 (1997)].
14. M. Born, Verh. Dtsch. Phys. Ges., No. **21/22**, 679 (1919).
15. F. Haber, Verh. Dtsch. Phys. Ges., No. **21/22**, 750 (1919).
16. W. S. Baer, J. Phys. Chem. Solids **28**, 677 (1967).
17. A. Frova and P. J. Boddy, Phys. Rev. **153**, 606 (1967).
18. E. Krätzig, Ferroelectrics **21**, 635 (1978).
19. S. A. Basun, Radiat. Eff. Defects Solids **135** (1–4), 535 (1995).
20. E. F. Gross, A. A. Kaplyanskiĭ, and B. V. Novikov, Dokl. Akad. Nauk SSSR **110** (5), 761 (1956) [Sov. Phys. Dokl. **1**, 582 (1957)].
21. E. F. Gross, A. V. Il’inskiĭ, B. V. Novikov, and N. S. Sokolov, Pis’ma Zh. Éksp. Teor. Fiz. **12** (5), 259 (1970) [JETP Lett. **12**, 177 (1970)].
22. N. S. Sokolov, B. V. Novikov, and S. V. Gastev, Fiz. Tekh. Poluprovodn. (Leningrad) **10** (1), 196 (1976) [Sov. Phys. Semicond. **10**, 118 (1976)].
23. V. S. Vikhnin and S. Kapphan, Ferroelectrics **199**, 83 (1997).
24. V. S. Vikhnin and A. S. Polkovnikov, Ferroelectr. Lett. **23**, 55 (1997).
25. V. S. Vikhnin and A. S. Polkovnikov, Izv. Akad. Nauk, Ser. Fiz. **62** (8), 1502 (1998).
26. V. S. Vikhnin, A. S. Polkovnikov, H.-J. Reyher, *et al.*, J. Korean Phys. Soc. **32**, S486 (1998).
27. H.-J. Reyher, in *Poster of the VI Russian-German Seminar on Point Defects in Insulators and Deep-Level Centres in Semiconductors,* St. Petersburg, 1997.
28. V. V. Laguta, M. D. Glinchuk, I. P. Bykov, *et al.*, Phys. Rev. B **61** (6), 3897 (2000).
29. L. S. Sochava, V. É. Bursian, and A. G. Razdobarin, Fiz. Tverd. Tela (St. Petersburg) **42** (9), 1595 (2000) [Phys. Solid State **42**, 1640 (2000)].

Translated by G. Skrebtsov

Physics of the Solid State, Vol. 43, No. 6, 2001, pp. 1072–1076. Translated from Fizika Tverdogo Tela, Vol. 43, No. 6, 2001, pp. 1037–1040.
Original Russian Text Copyright © 2001 by Yunakova, Miloslavskiĭ, Kovalenko.

SEMICONDUCTORS AND DIELECTRICS

The Absorption Spectrum and Excitons in an Ag_2CdI_4 Ionic Conductor

O. N. Yunakova*, V. K. Miloslavskiĭ*, and E. N. Kovalenko**
**Kharkov State University, Kharkov, 61077 Ukraine*
***Scientific Center of Physics and Technology, the Ministry of Education and National Academy of Sciences of Ukraine, Kharkov, 61145 Ukraine*

Received July 10, 2000; in final form, November 16, 2000

Abstract—The electron absorption spectrum of thin stochiometric Ag_2CdI_4 films produced by thermal vacuum deposition on a quartz substrate in is investigated. The spectrum shape is sensitive to the method of preparation (the substrate temperature and deposition rate). Under optimal preparation conditions, the films are free of AgI and CdI_2 impurities and the fundamental absorption edge is at 3.28 eV. The long-wavelength exciton A band at 3.31 eV (90 K) is associated with the excitation of excitons in the AgI sublattice of the compound. An investigation of the temperature dependence of the spectral position and half-width of the A band in the range 90–430 K revealed that the exciton–phonon interaction makes the major contribution to the broadening of the band at $T \leq 360$ K. At higher temperatures, the contribution associated with the generation of Frenkel defects with activation energy $U_F = 0.200 \pm 0.025$ eV appears. © *2001 MAIK "Nauka/Interperiodica".*

1. INTRODUCTION

At low temperatures, the Ag_2CdI_4 compound is isostructural to the Ag_2HgI_4 compound [1, 2] and has a tetragonal lattice with parameters $a = 0.635$ nm and $c = 1.270$ nm [3, 4]. It has been established that a sharp jump in the conductivity at 50°C and a first-order phase transition with the formation of a cubic lattice with a completely disordered cation sublattice accompany the transition of Ag_2HgI_4 into the superionic state. In contrast to Ag_2HgI_4, the data on the transition of Ag_2CdI_4 into the superionic state are contradictory. For example, according to [3], a smooth increase in the ion conductivity of alloyed Ag_2CdI_4 samples by three orders of magnitude is observed in the range 80–120°C (with a maximum of $\frac{d[\log\sigma(T)]}{dT}$ being near 115°C) and is accompanied by the appearance of the hexagonal phase (β' phase) with $a = 0.896$ nm and $c = 1.462$ nm. However, the authors of [3, 4] do not exclude the appearance of new phases (β-AgI, CdI_2) in this temperature range due to partial decomposition of the compound. At the same time, in accordance with [5] (thin Ag_2CdI_4 films), the transition into a superionic phase occurs at 80°C and is accompanied by a discontinuity in the slope of the dependence of $\log[\sigma(T)T]$ on T^{-1} as the $\frac{d[\log\sigma(T)]}{dT}$ is decreased for $T > 80$°C.

To study the electronic fundamental absorption spectrum, it is appropriate to use thin Ag_2CdI_4 films whose crystal structures have been investigated by x-ray diffractograms [5] and the electron-diffraction method [6, 7]. The results of those studies are also a subject of controversy. For example, according to [5], the crystal lattice of thin Ag_2CdI_4 films does not differ from that of bulk samples, and, at 393 K, the films possess a tetragonal lattice with the aforementioned parameters. More recent investigations [6, 7] indicate that a hexagonal lattice with $a = 0.548$ nm and $c = 0.753$ nm forms in films at 290 K. According to those data, a phase transition into a cubic lattice with $a = 0.505$ nm occurs at 380 K.

The electron absorption spectrum of the Ag_2CdI_4 films was investigated in [5, 6, 8], but the data vary between different authors. According to [5, 6], the fundamental absorption edge of Ag_2CdI_4 is at $\lambda \approx 440$ nm and the longest wavelength band at 423 nm is attributed to the forbidden transition $4d^{10} \longrightarrow 4d^95s$ in the Ag^+ ion of the compound. Contrarily, in films made by diffusion synthesis from multilayer structures consisting of AgI and CdI_2 films, the fundamental absorption edge was at 380 nm [8]; a narrow exciton band at 372 nm was observed at 80 K. Longer wavelength bands have not been found in stochiometric Ag_2CdI_4 films.

The contradictory data on the conductivity, structure, and optical spectra indicate that further investigations of the Ag_2CdI_4 compound are necessary. In the present paper, the optical spectrum of thin stochiometric Ag_2CdI_4 films produced by different methods was studied. The temperature dependence of the spectral position and the half-width of the long-wavelength exciton band were also investigated in the range 80–430 K.

2. PREPARATION TECHNIQUE AND STRUCTURE OF THIN Ag_2CdI_4 FILMS

The 100-nm-thick Ag_2CdI_4 films were produced by vacuum evaporation of a mixture of AgI and CdI_2 powders at a given molar content (2AgI : CdI_2) on quartz substrates heated to 80°C. The choice of the substrate was determined by its transparency in the UV range and by its absorption spectrum over a wide temperature interval (up to 160°C). The phase diagram [3, 4] indicates the existence of the pure Ag_2CdI_4 phase in a narrow range of AgI concentrations (0.63–0.67); this circumstance determined the choice of the mixture content. On heating the evaporator, the powder mixture sublimates without preliminary formation of an alloy. It is established that the films of the pure phase are formed at low deposition rates ($v \approx 100$ nm/min). An increase in the evaporator temperature and in the deposition rate for the same content of the mixture gave rise to the appearance of the excess AgI phase. The optimal value of the substrate temperature ($T_s = 80°C$) is determined by the fact that a noticeable scattering appears in the films at $T \geq 100°C$ and, at $T_s < 80°C$, the exciton bands broaden.

After the preparation of the films, their phase content was determined from absorption spectra and electron-diffraction patterns. The appearance of an additional band at 2.7–3.2 eV, whose edge is at 2.8 eV ($\lambda \approx$ 440 nm), clearly indicates the appearance of the AgI phase. This band corresponds to the diffuse electron band of β-AgI ($\lambda_{max} \approx 423$ nm). At low deposition rates, this band is absent (Figs. 1a, 1b). The electron-diffraction patterns of the films fabricated at low deposition rates confirm the formation of the Ag_2CdI_4 tetragonal structure (the values of the interband distances are in good agreement with those reported in [3, 5]) and indicate the absence of the additional AgI and CdI_2 phases.

3. THE ABSORPTION SPECTRUM OF THIN Ag_2CdI_4 FILMS

The absorption spectrum of the Ag_2CdI_4 films was measured using a SF-46 spectrophotometer in the energy range 2–6 eV at 90–430 K. In general, the electronic fundamental absorption spectrum is similar to the earlier obtained spectra of Ag_2CdI_4 films produced by other methods [8]. The intensive exciton *A*-band lying near the edge of the direct-interband transitions is observed in the spectrum at 3.31 eV. At the liquid-nitrogen temperature, the band splits into two bands (A_0 and A_1 bands, $\Delta E \approx 0.02$ eV), probably because of the thermal stress due to the difference between the linear expansion coefficients of the film and substrate. The spectral position of the *A* band is close to the position of the long-wavelength exciton bands of other triple compounds containing Ag, such as $MeAg_4I_5$ (*Me*: K, Rb, NH_4) [9–11], in which, as in Ag_2CdI_4, the Ag^+ ions

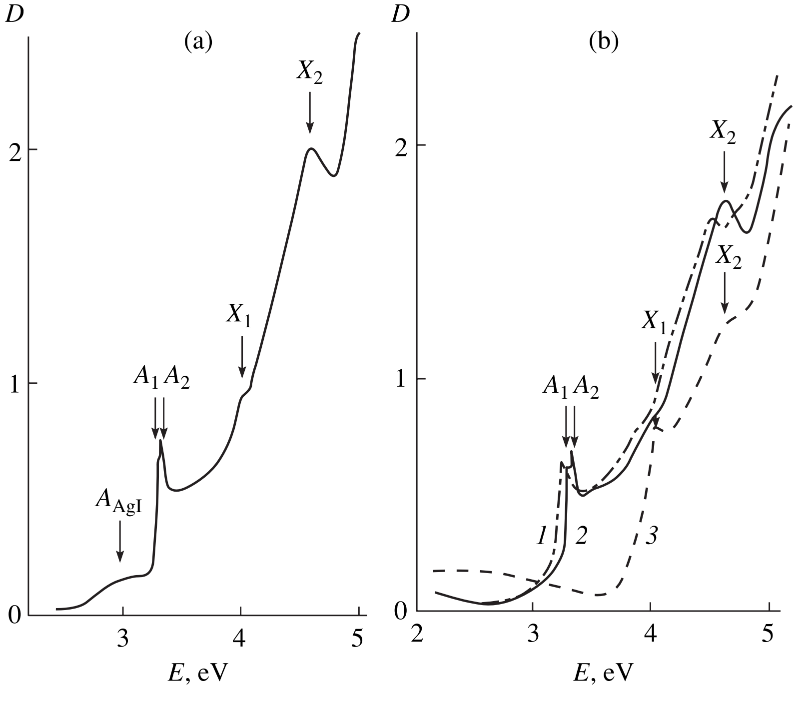

Fig. 1. Absorption spectra (a) of thin Ag_2CdI_4 films containing the AgI phase as an impurity and (b) of stochiometric thin Ag_2CdI_4 films. $T = 293$ (*1*) and 90 K (*2*). Curve *3* is the absorption spectrum of a thin CdI_2 film.

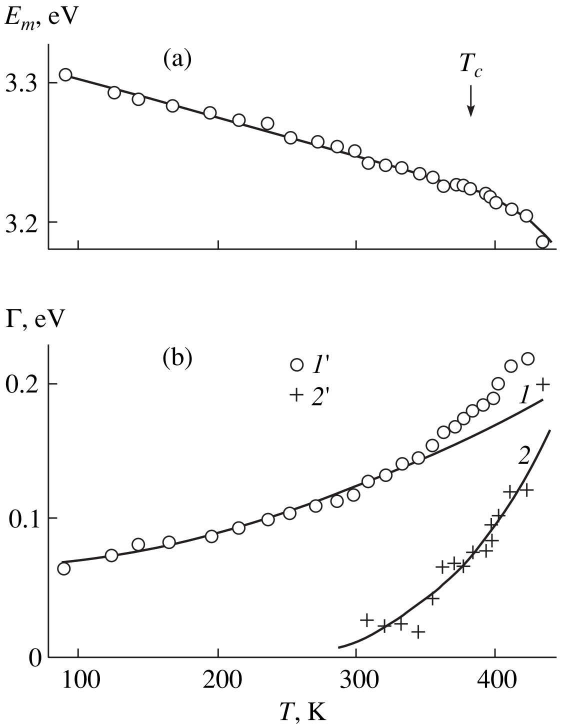

Fig. 2. Temperature dependence of (a) the spectral position $E_m(T)$ and (b) halfwidth $\Gamma(T)$ of the long-wavelength exciton *A* band in Ag_2CdI_4. *1* is the dependence $\Gamma_{ex-ph}(T)$ calculated by Eq. (2); *1'* is the experimental values of $\Gamma(T)$; *2* is Γ_F calculated by Eq. (3) with the value $U_F = 0.2$ eV, and *2'* is the values of Γ_F calculated from Eq. (4).

are situated in the I tetrahedra. For this reason, the *A* band can be attributed to the excitation of excitons in the AgI sublattice of the compound [8]. The aforementioned absence of the band at $\lambda = 423$ nm (2.92 eV) indicates that the absorption spectra of the Ag_2CdI_4 films highly enriched by the β-AgI phase were studied in [5, 6]. In those papers, the intensity of the band at 2.92 eV was found to be approximately equal to the intensity of the *A* band. For this reason, it should be supposed that the hexagonal phase revealed in [6, 7] actually corresponds to β-AgI, rather than to Ag_2CdI_4. The coincidence of the parameters of the "new" phase with those of the β-AgI phase and the phase transition of β-AgI into the cubic α phase with lattice parameters $a = 0.505$ nm [6, 7] also support this conclusion.

The steplike X_1 and X_2 bands are also observed at 4.02 and 4.60 eV, respectively, on the background of the continuous spectrum of the interband absorption, which sharply increases with the photon energy (Figs. 1a, 1b). A comparison with the spectrum of a CdI_2 film of approximately the same thickness (Fig. 1b) indicates that the spectral positions of these bands coincide with those of the X_1 and X_2 bands in CdI_2, despite the fact that electron-diffraction studies do not reveal an excess of the CdI_2 phase in the Ag_2CdI_4 films. The sharp increase in the absorption at 4.0–5.2 eV typical of CdI_2 is also retained. Apparently, the excitation of excitons in the CdI sublattice of the compound leads to the appearance of the X_1 and X_2 bands in the spectrum of Ag_2CdI_4. It should be noted that the complicated structure typical of CdI_2 is partially retained in the tetragonal Ag_2CdI_4 lattice.

4. THE TEMPERATURE DEPENDENCE OF THE PARAMETERS OF THE EXCITON *A* BAND

With increasing temperature, the exciton *A* band broadens and shifts into the low-frequency region and its splitting into components disappears. To determine the temperature dependence of the spectral position E_m and half-width Γ of the band, we separated the *A* band from the edge of the interband absorption using a method [12] that takes into account the multiple reflection and interference in the film. The band was approximated by a mixed symmetric contour composed of Gaussian and Lorentzian components. The band was separated by attaining the best fit of its long-wavelength slope to the calculated dependence. The $E_m(T)$ and $\Gamma(T)$ dependences were determined in the range 90–430 K covering the possible phase transitions reported in [3–5]. At temperatures from 90 to 380 K, the *A* band shifts in proportion to the temperature into the low-frequency region (Fig. 2a):

$$E_m(T) = E_m(T_0) + \frac{dE_m}{dt}(T_0)(T - T_0), \tag{1}$$

where $\frac{dE_m}{dT}(T_0) = -2.8 \times 10^{-4}$ eV/K and $T_0 = 90$ K. The temperature dependence $E_m(T)$ is similar to those for other AgI-type dielectrics and is determined by the exciton–phonon interaction. At $T > 380$ K, the slope of the dependence $E_m(T)$ increases, and, in the range 380–430 K, we have $\frac{dE_m}{dT} = -4.8 \times 10^{-4}$ eV/K. The transition of Ag_2CdI_4 into the hexagonal β' phase, whose appearance at 115°C was pointed out in [3, 4], is a possible cause of the change in the slope. However, this transition is not accompanied by a jump in $E_m(T)$ within the narrow temperature interval typical of $MeAg_4I_5$-like superionic compounds, which, probably, indicates the absence of the first-type phase transition.

With increasing temperature, the half-width of the *A* band grows nonlinearly from 0.065 (90 K) to 0.28 (434 K) [see Fig. 2b]. In ionic crystals and, in particular, in superionic conductors, the temperature dependence of Γ is determined by two factors: by the interaction between the excitons and vibrations of the crystal lattice and by the scattering of the excitons by fluctuations in the internal electric fields arising because of the generation of Frenkel defects [13].

In ionic crystals, the longitudinal optical phonons make the major contribution to the half-width associated with the exciton–phonon interaction. The temperature dependence $\Gamma_{\text{ex–ph}}(T)$ is closely approximated by the dependence [14]

$$\Gamma_{\text{ex–ph}}(T) = \Gamma(0) + An_{\text{ph}}(n_{\text{ph}}+1), \qquad (2)$$

where Γ(0) is the residual broadening determined by the internal stresses in the film and by uncontrollable impurities; the second term in Eq. (2) is due to the exciton scattering by the *LO* phonons; and $n_{\text{ph}} = \left(\exp\frac{\hbar\omega_{LO}}{kT} - 1\right)^{-1}$ is the distribution function of the *LO* phonons. When analyzing the $\Gamma_{\text{ex–ph}}(T)$ dependence, we used the value $\hbar\omega_{LO} = 15.6$ eV found in [15] from the phonon IR spectra of the Ag–I bond, taking into account that the *A* band belongs to the AgI sublattice. The dependence of Γ on $n_{\text{ph}}(n_{\text{ph}} + 1)$ is linear at $T \leq 355$ K. This indicates that $\Gamma_{\text{ex–ph}}$ dominates at low temperatures. Processing the dependence of Γ on $n_{\text{ph}}(n_{\text{ph}} + 1)$ in the range 90–355 K by the method of least squares yields $\Gamma(0) = 65.7 \pm 2.0$ meV and $A = 21.9 \pm 0.8$ meV. At $T \geq 355$ K, a deviation from the dependence in Eq. (2) is observed and it increases with a growth in *T* (Fig. 2b).

We associate the additional contribution to the broadening of the *A* band at $T \geq 355$ K with the generation of Frenkel defects. The concentration of Frenkel defects obeys the Arrhenius law

$$n_{\text{ph}} = n_{\text{F}}(\infty)\exp\left[-\frac{U_{\text{F}}}{kT}\right], \qquad (3)$$

where U_{F} is the activation energy for the defects. Obviously, the contribution of the defects into the half-width, Γ_{F}, is proportional to n_{F}. If the two types of exciton scattering are independent (the Gaussian shape of the *A* band supports this assumption), the half-width of the band is

$$\Gamma = (\Gamma^2_{\text{ex-ph}} + \Gamma^2_{\text{F}})^{1/2}. \qquad (4)$$

The temperature dependence $\Gamma_{\text{F}}(T)$ found from the experimental values of Γ by Eqs. (4) and (2) indicates that, in spite of the large scattering of the dots, $\Gamma_{\text{F}}(T)$ grows exponentially (Fig. 2b). Processing $\Gamma_{\text{F}}(T)$ in the $(\ln\Gamma_{\text{F}}, (1/T))$ coordinates yields $U_{\text{F}} = 0.200 \pm 0.025$ eV. This value of U_{F} is noticeably smaller than the activation energy for the conductivity determined in [5] within the same temperature interval ($U_\sigma = 0.42$ eV). Such a difference is not surprising and is observed in other superionic conductors [11, 16]. It is associated with the temperature dependence of the ion mobility, whose exponential growth is determined by its own activation energy.

Thus, it follows from the measured electron spectrum of Ag_2CdI_4 that a stochiometric compound prepared by different methods can partially decompose into AgI and CdI_2 components. For this reason, there are different interpretations of the absorption spectrum. According to our data, the edge of the electronic fundamental absorption band in Ag_2CdI_4 is at $\hbar\omega \approx 3.28$ eV and is accompanied by a long-wavelength exciton band at 3.31 eV.

In the Ag_2HgI_4 compound, a sharp jump in the conductivity [17] and edge absorption [9, 18], indicating the occurrence of a first-order phase transition, are observed at 50°C. Despite the structure of Ag_2CdI_4 being similar to that of the Ag_2HgI_4 compound, the temperature dependence of σ [3, 5] and the half-width of the exciton *A* band in Ag_2CdI_4 are smoother. These results indicate the absence of the first-order phase transition in the range 90–430 K and are in agreement with the data of [3, 4], indicating that the tetragonal Ag_2CdI_4 lattice is retained up to 120°C. At $T > 360$ K, a noticeable contribution to the broadening of the *A* band is made by the generation of Frenkel defects leading to a significant disorder in the AgI sublattice of the compound. At the temperatures 360–420 K [3], the generation of Frenkel defects in octahedral caverns and the existence of stochiometric tetragonal voids apparently promote a more significant growth in the conductivity of Ag_2CdI_4 in comparison with AgI. The ambiguity concerning the phase transformations in Ag_2CdI_4 requires further investigations of the different physical properties of the compounds above room temperature.

REFERENCES

1. H. G. Le Duc and L. B. Coleman, Phys. Rev. B **31** (2), 933 (1985).
2. K. W. Browall, I. S. Kasper, and H. Wiedemeir, J. Solid State Chem. **10** (1), 20 (1974).
3. I. W. Brightwell, C. N. Buckley, L. S. Miller, and B. Ray, Phys. Status Solidi A **76** (1), 391 (1983).
4. I. W. Brightwell, C. N. Buckley, R. C. Hollyoak, and B. Ray, J. Mater. Sci. Lett. **3**, 443 (1984).
5. R. Sudharsanan, S. Radhakrishna, and K. Hariharan, Solid State Ionics, No. 9/10, 1473 (1983).
6. I. M. Bolesta, I. I. Savitskiĭ, A. V. Futeĭ, and V. I. Kovalisko, Kristallografiya **36** (6), 1542 (1991) [Sov. Phys. Crystallogr. **36**, 873 (1991)].
7. I. M. Bolesta and A. V. Futeĭ, Fiz. Tverd. Tela (St. Petersburg) **34** (9), 2717 (1992) [Sov. Phys. Solid State **34**, 1453 (1992)].
8. O. N. Yunakova, V. K. Miloslavskiĭ, and M. Zhavlangiĭn, Ukr. Fiz. Zh. **35** (10), 1502 (1990).
9. I. Kh. Akopyan, Élektrokhimiya **26** (11), 1495 (1990).

10. V. K. Miloslavski, O. N. Yunakova, and Sung Tsya-Ling, Funct. Mater. **1** (1), 51 (1994).
11. V. K. Miloslavskiĭ and Sung Tsya-Ling, Funkts. Mater. **2b** (4), 438 (1995).
12. V. K. Miloslavskiĭ, O. N. Yunakova, and Sung Tsya-Ling, Opt. Spektrosk. **78** (3), 436 (1995) [Opt. Spectrosc. **78**, 391 (1995)].
13. I. Kh. Akopyan, B. V. Bondarev, D. I. Gromov, *et al.*, Fiz. Tverd. Tela (Leningrad) **29** (8), 2263 (1987) [Sov. Phys. Solid State **29**, 1305 (1987)].
14. V. K. Miloslavskiĭ and O. N. Yunakova, Opt. Spektrosk. **57** (1), 85 (1984) [Opt. Spectrosc. **57**, 51 (1984)].
15. R. Sudharsanan, T. Srinivasan, and S. Radhakrishna, Solid State Ionics **13** (4), 277 (1984).
16. V. K. Miloslavskiĭ, E. N. Kovalenko, and O. N. Yunakova, Fiz. Tverd. Tela (St. Petersburg) **40** (6), 1022 (1998) [Phys. Solid State **40**, 934 (1998)].
17. V. Leute and H. Rusche, J. Phys. Chem. Solids **42** (4), 303 (1981).
18. I. Kh. Akopyan, D. I. Gromov, A. A. Klochikhin, *et al.*, Fiz. Tverd. Tela (Leningrad) **30** (1), 94 (1988) [Sov. Phys. Solid State **30**, 51 (1988)].

Translated by A. Poushnov

Physics of the Solid State, Vol. 43, No. 6, 2001, pp. 1077–1083. Translated from Fizika Tverdogo Tela, Vol. 43, No. 6, 2001, pp. 1041–1047.
Original Russian Text Copyright © 2001 by Sarafanov.

DEFECTS, DISLOCATIONS,
AND PHYSICS OF STRENGTH

The Formation of Quasi-Crystalline Structures in a Dislocation Cluster

G. F. Sarafanov

Nizhni Novgorod State Pedagogical University, Nizhni Novgorod, 603600 Russia

Received August 25, 2000; in final form, November 9, 2000

Abstract—The formation of inhomogeneous dislocation structures is investigated within a model taking into account correlation interaction between screw dislocations. This interaction is found to give rise to an instability of the homogeneous state of the system. It is shown that when the critical nonequilibrium conditions for this instability are attained in a local volume, an inhomogeneous dislocation structure is formed spontaneously. As the degree of instability of the system increases further, this structure is transformed into a cellular quasi-crystalline structure. *© 2001 MAIK "Nauka/Interperiodica".*

1. INTRODUCTION

One of the important problems of physical metallurgy is that of explaining the complicated regularities in the formation and evolution of inhomogeneous dislocation structures which arise during plastic deformation of a material. In spite of advances having been made in the experimental study of the deformation of solids [1, 2], no rigorous quantitative theory that can explain these phenomena adequately has yet been constructed. At the same time, the accumulated data suffice for interpreting the processes of plastic deformation in a unified way, in terms of nonlinear dynamics of a deformed crystal [3–5]. This dynamics was shown to involve complicated processes that proceed at different levels of structural deformation and give rise to the internal self-organization of the crystal [6]. For this reason, current investigations of the behavior of nonequilibrium systems and the processes of their structural rearrangement are based, as a rule, on the synergetic approach [7, 8]. This method allows one to make a universal analysis of systems (differing in nature) that exhibit self-organization properties. The spatially inhomogeneous states (dissipative structures, DSs) arise in these systems because of the homogeneous state becoming unstable (DS instability).

For deformed crystals, this approach to the study of self-organization phenomena in dislocation clusters was first employed in [9, 10]. Further development of this method based on a set of kinetic equations allowed one to disclose and analyze some typical dislocation structures and investigate their evolution (see, e.g., [4, 11–13]). In those investigations, the formation of dissipative dislocation structures was described in terms of a model based on a set of reaction–diffusion equations for the density of dislocations. In the region where the DS instability occurs, these equations are reduced to the universal Swift–Hoenberg equations [7, 14]. Despite the wide range of their possible solutions, these equations fail to describe some classes of dislocation structures. For example, it is known [2, 15] that the experimentally observed dislocation cell structures are not strictly periodic and have no long-range symmetry; rather, they are "quasi-crystalline" and, in some cases, "turbulent." Such structures cannot be described by the Swift–Hoenberg equations [14]. This raises a question concerning the range of applicability of the reaction–diffusion models to describing the evolution of dislocation clusters.

The diffusion processes are known [16, 17] to be controlled by thermal and other fluctuating fields (in the case of dislocations, these fields are primarily the random internal stresses [3]). Fluctuations are usually assumed to be uncorrelated, which is the case if interaction between the particles involved in diffusion is weak [17]. In the case of developed plastic deformation, the dislocation density is high and one has to take into account the elastic interaction of dislocations and, therefore, the dynamics of fluctuations. This leads to correlation interaction between dislocations, which, as is known from the physics of plasmalike media with strong interaction [17], can result in disintegration of the homogeneous state and the formation of cellular structures ("Coulomb crystals") in specific cases [18].

For dislocation clusters, some results on this problem were obtained in [19–21], where the occurrence of an inhomogeneous structure of dislocations was predicted on the basis of some heuristic considerations concerning the dislocation correlation length and the phenomenologically given correlation flux. However, a systematic mathematical analysis of the correlation interaction of dislocations was not made and, therefore, one cannot judge the validity of the findings of the investigations cited above. Such an analysis is intricate, because the relevant correlation fluxes have the form of nonlocal and nonlinear functionals and their direct mathematical treatment shows very little promise.

In this situation, in order to analyze the effects associated with the elastic field of dislocations, the evolution of a model dislocation system was considered in [22, 23] under certain physically justified assumptions which make the problem solvable. The model system was a cluster of rectilinear screw dislocations whose interaction was described by a two-dimensional Coulomb potential. In this case, the problem becomes local in space and time and one can derive self-consistent dynamic equations describing the evolution of the dislocation system with allowance for their correlation interaction.

In this paper, using these equations, we systematically investigate the effect of correlation interaction of dislocations on the formation of dissipative dislocation structures.

2. CORRELATION INSTABILITY

A theoretical investigation of the formation of dislocation structures can be carried out on the basis of a set of nonlinear evolution equations for the density of continuously distributed dislocations $\rho_a(\mathbf{r}, t)$, where index a specifies dislocations by indicating the slip system α to which the dislocations belong and the orientation of the Burgers vector $\mathbf{b}$ relative to the unit vector $\mathbf{l}$ tangent to the dislocation line [4, 24]. Using an isotropic model [22] and taking into account the correlation interaction of dislocations, the evolution equations for the total dislocation density $\rho(\mathbf{r}, t) = \sum_a \rho_a(\mathbf{r}, t)$ can be written in the form [23, 25]

$$\frac{\partial \rho}{\partial t} + \operatorname{div}(\mathbf{J} + \mathbf{J}_{\text{corr}}) = F(\rho), \quad (1)$$

$$\mathbf{J}(\mathbf{r}, t) = -D_f \nabla \rho(\mathbf{r}, t), \quad (2)$$

$$\mathbf{J}_{\text{corr}}(\mathbf{r}, t) = M\rho(\mathbf{r}, t)(A_1 + \Delta A_2 + \dots)\nabla \rho(\mathbf{r}, t). \quad (3)$$

Here, $\mathbf{J}$ is the effective diffusion flux due to relaxation of the dislocation charges caused by elastic interaction of screw dislocations [22], $\mathbf{J}_{\text{corr}}$ is the correlation flux due to interaction between fluctuations of the elastic field of dislocations, $D_f = V^2/MGb^2\rho_0$ is the effective diffusion coefficient, $M = V/\eta b\sigma_{\text{ext}}$ is the mobility of dislocations, σ_{ext} is the flow stress, V is the velocity of steady-state motion of dislocations, $A_1 = Gb^2/4\pi\rho_0$, $A_2 = Gb^2 r_D^2/8\pi\rho_0$, $r_D = \sqrt{T_{\text{ext}}/Gb^2\rho_0}$ is the screening length of the elastic field of dislocations (correlation length), $T_{\text{ext}} = \eta b\sigma_{\text{ext}}\bar{L}$ is the strain energy, $\bar{L}$ is the mean free path of dislocations, $\eta = kT/\Gamma\sigma_{\text{ext}}$ is the thermal-activation parameter, and Γ is the activation volume.

It should be noted that in the isotropic model, when the evolution of dislocation charges is considered, the primary quantity is the vector $\mathbf{J}$ rather than the scalar quantity $I = \sum_a (b_a/b)\rho_a$, which characterizes the excess density of dislocations in the crystal. (A similar situation takes place in the construction of the continuum theory of dislocations, where the primary quantity is the distortion tensor rather than the displacement vector of a point of the medium [24].) In this case, the direction of the vector $\mathbf{J}$ is determined by the direction of the wave vector (or by a combination of wave vectors with corresponding weights) rather than by the dislocation velocity (as is the case with single slipping). This circumstance will be taken into account in what follows.

The set of equations (1)–(3) has a stationary homogeneous solution $\rho = \rho_0$, which can be found by equating the right-hand side of Eq. (1) to zero. For this purpose, we represent the $F(\rho)$ dependence in the most typical form:

$$F(\rho) = \delta\rho - \kappa\rho^2 - c\rho^3, \quad (4)$$

where δ is the coefficient of dislocation multiplied by the double cross slip mechanism, $\kappa \simeq 2hV$ is the dislocation immobilization coefficient ($h = Gb/4\pi\sigma_{\text{ext}}$ is the trapping length of dislocations opposite in sign into dipolar configurations), and $c \simeq h_d/V\kappa\tau_d$ is the coefficient of dislocation locking by screw dipoles (h_d is the trapping length of dislocations by screw dipoles and τ_d is the characteristic annihilation time of dipoles).

The cubic term in Eq. (4) is responsible for triple collisions; it is usually ignored in dislocation dynamics, because this term is assumed to be small and to meet the condition

$$\mu = c\rho_0/\kappa \ll 1. \quad (5)$$

However, this is true only if the dislocation annihilation in the dipoles is intense enough ($\tau_d \ll 1/h_d V\rho_0$). In addition, although the cubic term $c\rho^3$ has an insignificant effect on the evolution of the system, this term is of fundamental importance in forming dislocation structures, as will be shown below. It should be noted that if the possible screw dislocation locking mechanism due to edge dipoles is taken into account (for example, in the kink model [1]), this leads to a renormalization of the coefficient κ. (This mechanism makes a contribution to the term quadratic in ρ, because the density of edge dipoles is $\rho_d \sim \rho$ [1].)

Taking into account the aforesaid, we put $F(\rho) = 0$ and find the stationary homogeneous solution to be

$$\rho_0 = \frac{\sqrt{\kappa^2 + 4c\delta} - \kappa}{2c} \simeq \frac{\delta}{\kappa}. \quad (6)$$

The approximate equality in Eq. (6) is true if $4c\delta/\kappa^2 \ll 1$ (or $\mu \ll 1/4$).

Let us test the equilibrium state in Eq. (6) for stability. Substituting $\mathbf{J}$ and $\mathbf{J}_{\text{corr}}$ into Eq. (1), we find that the variable

$$\varrho(\mathbf{r}, t) = \rho(\mathbf{r}, t) - \rho_0, \quad (7)$$

which characterizes the deviation of the dislocation density from its steady-state value, obeys the nonlinear equation

$$\frac{\partial \varrho}{\partial t} + L(\Delta)\varrho + M\varrho(A_1 + \Delta A_2)\nabla\varrho + \kappa_0\varrho^2 + c\varrho^3 = 0, \quad (8)$$

where $L(\Delta) = A_2M\rho_0\Delta^2 + (A_1M\rho_0 - D_f)D + \tau^{-1}$ is a linear operator, $\tau = (\kappa\rho_0 + 2c\rho_0^2)^{-1}$ is the characteristic relaxation time to the stationary state ρ_0, and $\kappa_0 = \kappa + 3c\rho_0$.

By linearizing Eq. (8) in the vicinity of the homogeneous solution $\varrho(\mathbf{r}) = 0$ and substituting a solution of the form $\varrho \sim \exp(\lambda t + i\mathbf{kr})$ into the linearized equation, we arrive at the dispersion relation

$$\lambda + L(k^2) = 0,$$

from which it follows that the homogeneous solution can become unstable ($\lambda > 0$) if

$$L(k^2) = A_2M\rho_0k^4 - (A_1M\rho_0 - D_f)k^2 + \tau^{-1} < 0. \quad (9)$$

We note that this instability is solely due to correlation interaction of dislocations; indeed, if $A_1 = A_2 = 0$, we always have $L(k^2) > 0$.

An analysis of inequality (9) shows that it is true if the dislocation density ρ_0 exceeds a critical value

$$\rho_0 > \rho_c = \frac{8\pi}{(\sqrt{3}-1)^2b^2}\left(\frac{kT}{\Gamma G}\right)^2. \quad (10)$$

For typical values of the parameters of the system $T = 300$ K, $\Gamma = 40b^3$, $b = 3 \times 10^{-8}$ cm, and $G = 3 \times 10^{10}$ Pa, Eq. (10) gives the critical dislocation density to be $\rho_c \sim 10^9$ cm^{-2}; therefore, above this value, inhomogeneous dislocation structures will arise in a local volume.

From inequality (9), it follows that there is a threshold for DS instability and that this instability occurs in a wave-number range of $|\mathbf{k}| \in (k_1, k_2)$, where

$$k_{1,2}^2 = k_c^2 \pm \sqrt{k_c^4 - (A_2M\rho_0\tau)^{-1}}, \qquad k_c^2 = \frac{A_1M\rho_0 - D_f}{2A_2M\rho_0}. \quad (11)$$

In the vicinity of the bifurcation point ($\rho_0 \sim \rho_c$, $|\mathbf{k}| = k_c$), fluctuations of the dislocation density increase spontaneously in magnitude and their spatial scale is

$$\Lambda_c = \frac{2\pi}{k_c} \simeq \frac{(2\pi)^{3/4}}{4}\sqrt{\bar{L}\bar{r}}. \quad (12)$$

Here, $\bar{L} = \tau V = (h\rho_0)^{-1}$ is the mean free path of dislocations (relaxation length) and $\bar{r} = \rho_0^{-1/2}$ is the mean separation between dislocations. Taking into account that $h = Gb/4\pi\sigma_{\text{ext}}$ and $\sigma_{\text{ext}} \simeq Gb\alpha_f\sqrt{\rho_0}$ [1, 4], we have $h = \bar{r}/4\pi\alpha_f$ and, therefore, Eq. (12) takes the form

$$\Lambda_c = K\rho^{-1/2}, \quad (13)$$

where $K = \sqrt{\alpha_f}(2\pi)^{5/4}$. For typical values of the parameter $\alpha_f = 0.3$–2, we have $K \simeq 6$–15.

Let us compare these results with experimental data. Tensile tests at a constant strain rate for polycrystalline copper showed [26] that the cell size of the dislocation structure was related to the dislocation density by Eq. (13) with $K \simeq 16.7$. In [27], pulse loads were applied to nickel with increasing pulse amplitude (10 to 46 GPa) and the magnitude of K was found to vary in the range of 10–12. Thus, the model under discussion adequately describes these experimental data.

3. CRYSTALLINE AND QUASI-CRYSTALLINE DISLOCATION STRUCTURES

The solution to the linearized problem carries no information on the evolution of a dislocation cluster above the bifurcation point, and one should investigate the original nonlinear equations. We will study the dynamics of a dislocation cluster in the two-dimensional region $\Omega = L_1L_2$ in the case where Eq. (8) is subject to periodic boundary conditions

$$\varrho(\mathbf{r}, t) = \varrho(\mathbf{r} + \mathbf{L}, t), \quad (14)$$

where $\mathbf{L} = L_1\mathbf{e}_x + L_2\mathbf{e}_y$ is a translation vector. It is natural to suppose that L_1 and L_2 are on the order of the grain size for polycrystals and of the size of the sample for single crystals.

Investigations of such systems revealed [7, 8] that if the thermodynamic spectral branch of the system shows bifurcation, then the behavior of the system in the vicinity of the instability point can be described in terms of a set of undamped collective variables (modes) known as order parameters [7]. Therefore, we can represent the solution to Eq. (8) in the form

$$\varrho(\mathbf{r}, t) = \rho(\mathbf{r}, t) - \rho_0 = \sum_{\mathbf{k}}[\xi_{\mathbf{k}}(t)\psi_{\mathbf{k}}(\mathbf{r}) + \text{c.c.}]. \quad (15)$$

In this expansion, the collective variables $\xi_{\mathbf{k}}(t)$ are unknown functions of time; $\psi_{\mathbf{k}}(\mathbf{r}) = \exp(i\mathbf{kr})$ are orthogonal eigenfunctions of the operator $L(\Delta)$; and the wave vector $\mathbf{k}$ takes discrete values [in accordance with the boundary conditions in Eq. (14)]

$$\mathbf{k} = \begin{pmatrix} k_x \\ k_y \end{pmatrix} = 2\pi\begin{pmatrix} n_1/L_1 \\ n_2/L_2 \end{pmatrix}, \quad (16)$$

where n_1 and n_2 are integers.

Using Eq. (15) and taking into account the remarks made above with reference to the evolution of dislocation charges, one can construct an expression for the

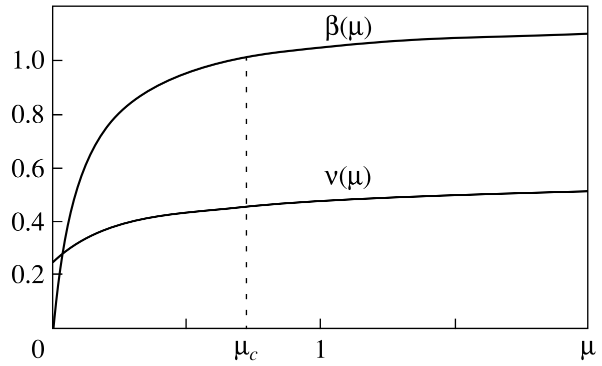

Fig. 1. Dependences of the parameters β(μ) and ν(μ) which are responsible for nonlinear competition of modes. The bifurcation value β = 1 corresponds to the critical value $\mu_c = 0.726$.

excess dislocation density [22]. From Eq. (2), we obtain

$$I(\mathbf{r}, t) = \sum_{\mathbf{k}} I_{\mathbf{k}} = -\frac{D_f}{V}\sum_{\mathbf{k}} |\mathbf{k}|[i\xi_{\mathbf{k}}(t)e^{i\mathbf{kr}} + \text{c.c.}]. \quad (17)$$

Now, we substitute expansion (15) of $\rho(\mathbf{r}, t)$ into Eq. (8) and make use of the orthogonality of the functions $\psi_{\mathbf{k}}(\mathbf{r})$:

$$(\psi_{\mathbf{k}}, \psi_{\mathbf{k}'}) = \frac{1}{\Omega}\int_{\Omega} \psi^*_{\mathbf{k}}(\mathbf{r})\psi_{\mathbf{k}'}(\mathbf{r})dxdy = \delta_{\mathbf{kk}'}. \quad (18)$$

As a result, we obtain resonance equations for the order parameters $\xi_{\mathbf{k}}(t)$. In a region which is slightly above the critical point ($\rho_0 \sim \rho_c$, $|\mathbf{k}| \sim k_c$), these equations have the form

$$\frac{\partial \xi_{\mathbf{k}}}{\partial t} = \lambda_{\mathbf{k}}\xi_{\mathbf{k}} - B_1 \sum_{|\mathbf{k}'| = k_c} \xi_{\mathbf{k}}\left(1 - \frac{\delta_{\mathbf{k},\mathbf{k}'}}{2}\right)|\xi_{\mathbf{k}'}|^2 - B_2\xi^*_{\mathbf{k}}\xi_{2\mathbf{k}} - B_3 \sum_{|\mathbf{k}'|, |\mathbf{k}''| = k_c} \xi_{\mathbf{k}'}\xi_{\mathbf{k}''}\delta_{\mathbf{k},\mathbf{k}'+\mathbf{k}''}, \quad (19)$$

$$\frac{\partial \xi_{2\mathbf{k}}}{\partial t} = \lambda_{2\mathbf{k}}\xi_{2\mathbf{k}} + B_4\xi^2_{\mathbf{k}}. \quad (20)$$

Here, $B_1 = 6c$, $B_2 = 2\kappa_0 + 9(2 - \sqrt{3})/\tau\rho_0$, $B_3 = 2\kappa_0 + \sqrt{3}/\tau\rho_0$, $B_4 = \kappa_0(2\sqrt{3} - 1)$, $\lambda_{\mathbf{k}} = -L/(k) \simeq \varepsilon/\tau - \gamma_0(k^2 - k_c^2)^2$, $\varepsilon = \rho_0/\rho_c - 1$, $\gamma_0 = A_2M\rho_0$, and $\lambda_{2\mathbf{k}} = -L(2k_c) = -9/\tau$. Although $\xi_{2\mathbf{k}}$ are damped variables, they are important for the evolution of the system because, in effect, they stabilize the divergent modes $\xi_{\mathbf{k}}$.

In Eqs. (19) and (20), only the terms quadratic and cubic in $\xi_{\mathbf{k}}$ are taken into account, because these terms determine the behavior of the system at a low supercriticality level and at $B = B_1/2 - B_2B_4/\lambda_{2\mathbf{k}} > 0$ (the latter condition is met in our case); otherwise (at $B < 0$), one has to take into account higher order terms when considering the evolution of other harmonics $\xi_{s\mathbf{k}}$ ($s = 3, 4, 5, \ldots$).

The set of equations (19) and (20) has a wide range of stationary solutions from which one can obtain the corresponding expressions for $\rho(\mathbf{r}, t)$ by using Eq. (15). In what follows, we restrict our consideration to the structures for which the magnitudes of the vectors $\mathbf{k} = \mathbf{k}_n$ are equal to k_c and the angle between the adjacent vectors $\mathbf{k}_n$ and $\mathbf{k}_{n+1}$ is the same and equal to π/N for $N \geq 2$. Here, N is a fixed integer, which determines the number of excited modes ($n = 1, 2, \ldots, 2N$).

The structures described by Eq. (15) with steady-state values of the order parameters involved differ in symmetry depending on N. We consider only the case of $N \leq 5$ in what follows.

The set of equations (19) and (20) is written in dimensionless form by introducing new variables:

$$\xi_{\mathbf{k}_n} = \rho_0 A_n e^{i\varphi_n}, \quad \xi_{2\mathbf{k}_n} = \rho_0 C_n e^{2i\varphi_n}, \quad t' = t/\tau. \quad (21)$$

Here, $A_{n+N} = A_n$, $C_{n+N} = C_n$, $\varphi_{n+N} = -\varphi_n$, and $\mathbf{k}_{n+N} = -\mathbf{k}_n$, with $n = 1, 2, \ldots, N$. Thus, we have

$$\frac{\partial A_n}{\partial t'} = \left[\varepsilon - \gamma_1 A_n^2 - 2\gamma_1\sum_{k \neq n}^{N} A_k^2\right]A_n - \gamma_2 A_n C_n - \delta_{3,N}\gamma_3 A_{N+1}A_{N-1}\cos\Psi_n, \quad (22)$$

$$\frac{\partial C_n}{\partial t'} = -9C_n + \gamma_4 A_n^2, \quad (23)$$

$$A_n\frac{\partial \varphi_n}{\partial t'} = -\delta_{3,N}\gamma_3 A_{n+1}A_{n-1}\sin\Psi_n, \quad (24)$$

where $\Psi_n = \varphi_{n+1} + \varphi_{n-1} - \varphi_n$, $\gamma_1 = 6\mu/(1 + 2\mu)$, $\gamma_2 = 2\gamma + 9(2 - \sqrt{3})$, $\gamma_3 = 2\gamma - \sqrt{3}$, $\gamma_4 = \gamma(2\sqrt{3} - 1)$, $\gamma = (1 + 3\mu)/(1 + 2\mu)$, and $\delta_{3,N}$ is the Kronecker delta.

The set of equations (22)–(24) has a trivial stationary solution $A_n = C_n = 0$, $\varphi_n = \text{const}$, which is unstable at $\varepsilon > 0$, and many other stationary solutions. Their number depends on the value of N, and their stability is controlled by the supercriticality parameter ε and the nonlinear mode–mode coupling parameters

$$\beta = 18\gamma_1/(9\gamma_1 + \gamma_2\gamma_4), \quad \nu = \gamma_3(\gamma_1 + \gamma_2\gamma_4/9)^{-1/2}. \quad (25)$$

The parameters β and ν are uniquely determined by μ. The β = β(μ) and ν = ν(μ) dependences are shown in Fig. 1.

Analysis shows that two types of solutions are stable, namely, the single-mode solution

$$A_1 = \sqrt{\frac{\varepsilon}{\beta_1}}, \quad A_2 = A_3 = \ldots = A_N = 0 \quad (26)$$

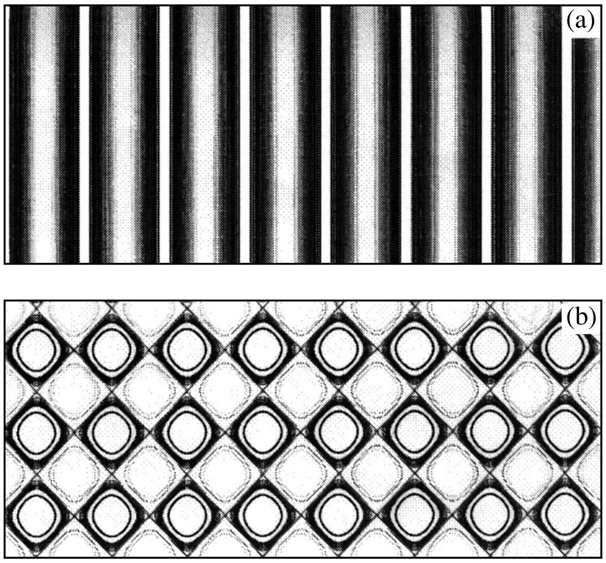

Fig. 2. Small-mode-number structures of the crystal type described by solutions (30) and (31) to Eqs. (1)–(3) and being of the soft-mode type: (a) one-dimensional periodic structure represented by level lines and (b) rhombic structure ($N = 2$).

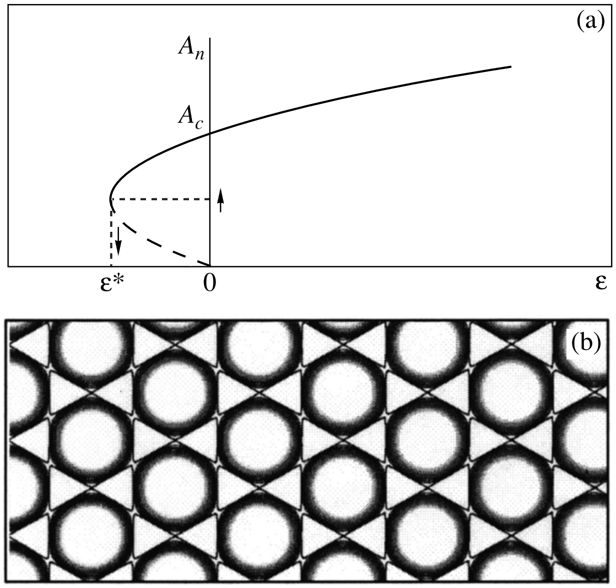

Fig. 3. Hexagonal structure ($N = 3$) of the hard-mode type: (a) bifurcation diagram $A_n = A_n(\varepsilon)$ for the amplitudes of unstable modes (solid line in the stable branch) and (b) the appearance of the structure described by Eqs. (30) and (31).

and the symmetrical multimode configurations

$$A_1 = A_2 = \dots = A_N = \sqrt{\varepsilon/\beta_N}, \quad N \neq 3, \tag{27}$$

$$A_1 = A_2 = A_3 = (-1)^{m+1}\frac{\gamma_3 + \sqrt{\gamma_3^2 + 4\beta_3\varepsilon}}{2\beta_3}, \quad N = 3, \tag{28}$$

where $\beta_N = \gamma_1(2N - 1) + \gamma_2\gamma_4/9$. In all cases, the steady-state values of C_n are expressed in terms of A_n by

$$C_n = \gamma_4 A_n^2/9. \tag{29}$$

In the case of $N = 3$, phase locking takes place and $\Psi_n = \pi m$ (m is an integer). At $N \neq 3$, the phases can have arbitrary values ($\varphi_n = \text{const}$).

The stationary solution in Eq. (26) corresponds to a one-dimensional structure. In the range of DS instability ($\varepsilon > 0$), this structure is stable for any value of the parameters if $N = 1$, but it is stable only at $\beta > 1$ if $N \geq 2$. In the latter case, the other configurations, except the three-mode configuration, are unstable.

At $\beta < 1$, the following multimode cellular structures are stable: rhombic ($N = 2$), hexagonal ($N = 3$), octagonal ($N = 4$), and decagonal ($N = 5$). The total density $\rho(\mathbf{r}, t)$ for these structures is obtained by substituting Eqs. (26)–(29) into Eqs. (21) and (15)

$$\rho(\mathbf{r}) = \rho_0\left\{1 + 2\sum_{n=1}^{N}[A_n\cos(\mathbf{k}_n\mathbf{r} + \varphi_n) + C_n\cos 2(\mathbf{k}_n\mathbf{r} + \varphi_n)]\right\}. \tag{30}$$

The excess dislocation density $I(\mathbf{r}, t)$ for these structures is found from Eq. (17) to be

$$I(\mathbf{r}) = E_{\max} \times \sum_{n=1}^{N}[A_n\sin(\mathbf{k}_n\mathbf{r} + \varphi_n) + C_n\sin 2(\mathbf{k}_n\mathbf{r} + \varphi_n)], \tag{31}$$

where $I_{\max} = 2\rho_0 D_f k_c/V$ is the maximum value of the excess dislocation density.

The structures described by Eqs. (30) and (31) are of the crystal type for $N \leq 3$ (Figs. 2, 3b), while for $N \geq 4$, they are quasi-crystalline structures with elements of local symmetry (Fig. 4).

The excitation mode of all structures, except for the hexagonal one, is soft ($A_n \sim \sqrt{\varepsilon}$). The excitation mode of the hexagonal structure is hard; as the bifurcation point is reached ($\varepsilon = 0$), the amplitude of the three-mode structure increases in a jump to the value $A_c = \nu(1 + 2\beta)/\sqrt{\beta_1}$ (Fig. 3a). In this case, hysteresis takes place; as ε

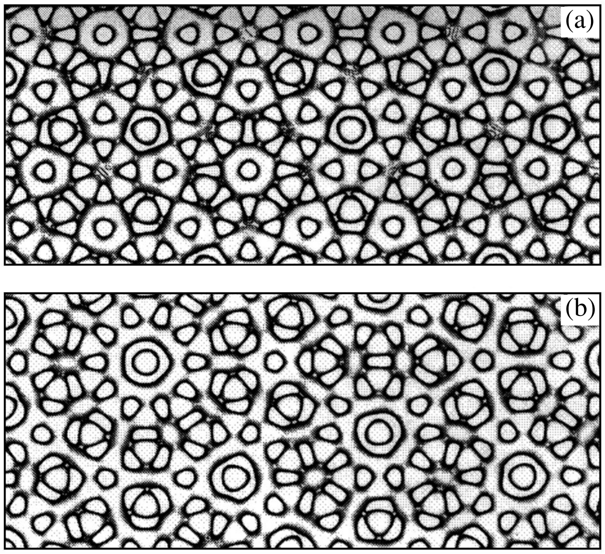

Fig. 4. Quasi-crystalline dislocation structures described by Eqs. (1)–(3): (a) octagonal ($N = 4$) and (b) decagonal ($N = 5$) structures.

decreases, the hexagonal structure remains stable even in a range ($\varepsilon^* < \varepsilon < 0$) of negative values of the parameter ε, where $\varepsilon^* = -\nu^2/4(1 + 2\beta)$. Thus, at $\varepsilon > 0$ and $\beta > 1$, the single-mode and three-mode structures are stable for $N = 3$; these structures correspond to local minima of the Lyapunov function V for the set of equations (22)–(24). Analysis shows that the minimum of V for the hexagonal structure is deeper; therefore, the probability that fluctuations will give rise to the formation of this configuration is higher.

From Eqs. (30) and (31), it follows that at $N = 4$ and 5, a new type of local rotation symmetry appears in addition to long-range symmetry. This local symmetry is incompatible with translational invariance and is the reason why these dislocation structures are quasi-crystalline. The structures with $N > 5$ are not analyzed in this paper. However, investigations of analogous systems [14, 28] showed that the quasi-crystalline character of the structures formed becomes more pronounced with increasing N and the system transforms into a “turbulent crystal” [14] as $N \longrightarrow \infty$.

The quasi-crystalline structures are stable for $\beta < 1$ or $\mu < \mu_c = 0.726$ (Fig. 1). It should be noted that in the reaction–diffusion models that are commonly used in self-organization theory [7, 8], the nonlinear interaction is such that $\beta > 1$ (in the Swift–Hoenberg model, $\beta = 2$ [14]). Therefore, quasi-crystalline (as well as rhombic) structures are unstable and do not appear in those models.

The reason why the parameter β can be less than unity in the model considered in this paper is the presence of nonlinear gradient terms in the original set of equations (1)–(3). These terms are responsible for correlation interaction of dislocations and, mathematically, they decrease the nonlinear interaction coefficients of competing modes, thereby favoring their independent dynamics. This is the reason why the symmetrical cellular structures are stablest for $\beta < 1$.

Thus, the evolution equations taking into account the correlation interaction allow one to explain the formation of various dissipative dislocation structures, including quasi-crystalline ones.

Let us outline the main features of the formation of inhomogeneous dislocation structures investigated in this paper and their possible evolution.

In the initial stage of plastic deformation, when the dislocation density is less than its critical value ($\rho_0 < \rho_c$), the distribution of dislocations is homogeneous. At $\rho_0 = \rho_c$, the DS instability occurs and inhomogeneous dislocation structures arise. Estimates of ρ_c show that the critical value of the dislocation density corresponds to the second stage of plastic deformation ($\rho_c \sim 10^9$ cm^{-2}). The form of dissipative structures arising in the vicinity of the DS instability ($\rho_0 > \rho_c$) depends on the number of excited unstable modes ($2N$) and the parameter $\beta = \beta(\mu)$, which is responsible for the competition of these modes. In the isotropic model considered here, N can have an arbitrary value. In a more realistic anisotropic model, the value of N depends on the number α of active slip systems. Therefore, it is likely that N increases with the amount of deformation. In this situation, two chains of structure transformations with increasing N are possible depending on the value of the parameter β (or μ): one-dimensional periodic ⟶ hexagonal cellular DS (at $\mu > \mu_c$) or one-dimensional ⟶ rhombic ⟶ hexagonal ⟶ octagonal ⟶ decagonal DS (at $\mu < \mu_c$).

It is interesting to note that two transformation chains of dislocation structures with an increasing amount of deformation have been observed experimentally in fcc alloys [15] (although those chains involved other structure types). Physically, the condition $\mu < \mu_c$ [see inequality (5)] implies the smallness of the cubic terms in comparison with the quadratic ones, which is the case, for given mechanisms of local dislocation kinetics, when the lifetime of dipoles of screw dislocations is short. Dislocation annihilation in dipoles typically becomes fast in the third stage of plastic deformation, where the process of cross slip of screw dislocations starts to operate [2]. Therefore, one might expect the formation of quasi-crystalline dislocation structures in this stage of plastic deformation.

The dissipative dislocation structures that arise in the process of plastic deformation are not in equilibrium. When the load is removed, they relax to a homogeneous state. However, their relaxation is not complete, because at the peaks of the spatial dislocation structure (where cell walls are subsequently built up), quasi-equilibrium dipole (or multipole) configurations composed of dislocations opposite in sign are formed and their geometry, on the whole, is a replica of the geometry of the dissipative structure. After the load is removed, such a quasi-equilibrium structure can be only roughly periodic and even unfinished. According to experimental observations, the formation of cells is completed (i.e., their boundaries are closed) by the onset of the third stage of plastic deformation [2, 15]. At the beginning of the third stage, the dislocation charge of dislocation cells is usually increased and subboundaries appear. It is likely that cross slip of screw components of dislocations with jogs causes point defects (vacancies and interstitial atoms) to increase sharply in number, which, in turn, initiate the process of polygonization at the "weakest" sites, namely, at the peaks of the excess dislocation density of the dissipative structure (which is formed, e.g., in the way considered in this paper). As a result, misoriented fragments of equilibrium walls arise inside the dislocation cells; these fragments are "nuclei" of subboundaries.

ACKNOWLEDGMENTS

This work was supported by the Russian Foundation for Basic Research, grant no. 98-02-16976.

REFERENCES

1. B. I. Smirnov, *Dislocation Structure and Hardening of Crystals* (Nauka, Leningrad, 1981).
2. V. I. Trefilov, V. F. Moiseev, É. P. Pechkovskiĭ, *et al.*, *Strain Hardening Deformation and Fracture of Polycrystalline Materials* (Naukova Dumka, Kiev, 1987).
3. *Cooperative Deformation Processes and Localization of Deformation* (Naukova Dumka, Kiev, 1989).
4. G. A. Malygin, Fiz. Tverd. Tela (St. Petersburg) **37** (1), 3 (1995) [Phys. Solid State **37**, 1 (1995)].
5. V. S. Ivanova, A. S. Balankin, I. Zh. Bunin, and A. A. Oksogoev, *Synergetics and Fractals in Material Science* (Nauka, Moscow, 1994).
6. V. E. Panin, V. A. Likhachev, and Yu. V. Grinyaev, *Substructural Levels of Deformation of Solids* (Nauka, Novosibirsk, 1985).
7. H. Haken, *Synergetics: An Introduction* (Springer-Verlag, Berlin, 1977; Mir, Moscow, 1980).
8. G. Nicolis and I. Prigogine, *Self-Organization in Non-Equilibrium Systems* (Wiley, New York, 1977; Mir, Moscow, 1979).
9. E. C. Aifantis, Mater. Sci. Eng. **81**, 563 (1986).
10. D. Walgraef and E. C. Aifantis, J. Appl. Phys. **58** (2), 688 (1985).
11. J. Kratochvil, Rev. Phys. Appl. **23** (4), 419 (1988).
12. G. A. Malygin, Fiz. Tverd. Tela (Leningrad) **31** (1), 175 (1989) [Sov. Phys. Solid State **31**, 96 (1989)].
13. I. L. Maksimov and G. F. Sarafanov, Pis'ma Zh. Éksp. Teor. Fiz. **61** (5), 405 (1995) [JETP Lett. **61**, 411 (1995)].
14. M. I. Rabinovich and A. B. Ezerskiĭ, *Dynamic Theory of Shaping* (Yanus-K, Moscow, 1998).
15. N. A. Koneva and É. V. Kozlov, Izv. Vyssh. Uchebn. Zaved., Fiz., No. 2, 87 (1990).
16. E. M. Lifshitz and L. P. Pitaevskiĭ, *Physical Kinetics* (Nauka, Moscow, 1979; Pergamon, Oxford, 1981).
17. Yu. L. Klimontovich, *Statistical Physics* (Nauka, Moscow, 1982; Harwood Academic, New York, 1986).
18. E. A. Mareev and G. F. Sarafanov, Phys. Plasmas **5** (5), 1563 (1998).
19. D. L. Holt, J. Appl. Phys. **41**, 3197 (1970).
20. Sh. Kh. Khannanov, Fiz. Met. Metalloved., No. 10, 34 (1992).
21. Sh. Kh. Khannanov, Fiz. Met. Metalloved., No. 2, 31 (1994).
22. G. F. Sarafanov and I. L. Maksimov, Fiz. Tverd. Tela (St. Petersburg) **39** (6), 1066 (1997) [Phys. Solid State **39**, 957 (1997)].
23. G. F. Sarafanov, Fiz. Tverd. Tela (St. Petersburg) **39** (9), 1575 (1997) [Phys. Solid State **39**, 1403 (1997)].
24. A. M. Kosevich, *Dislocation in Theory of Elasticity* (Naukova Dumka, Kiev, 1978).
25. G. F. Sarafanov, I. L. Maksimov, and Yu. G. Shondin, in *Abstracts of the XX International IUPAP Conference on Statistical Physics, Paris, 1998*, p. 10.
26. M. R. Staker and D. L. Holt, Acta Metall. Mater. **20**, 576 (1972).
27. *Shock Waves and Phenomena of High-Speed Deformation of Metals* (Metallurgiya, Moscow, 1984).
28. B. A. Malomed, A. A. Nepomnyashchiĭ, and M. I. Tribel'skiĭ, Zh. Éksp. Teor. Fiz. **96** (2), 684 (1989) [Sov. Phys. JETP **69**, 388 (1989)].

Translated by Yu. Epifanov

Physics of the Solid State, Vol. 43, No. 6, 2001, pp. 1084–1088. Translated from Fizika Tverdogo Tela, Vol. 43, No. 6, 2001, pp. 1048–1052.
Original Russian Text Copyright © 2001 by Kardashev, Burenkov, Smirnov, Shpeĭzman, Stepanov, Chernov, Singh, Goretta.

DEFECTS, DISLOCATIONS, AND PHYSICS OF STRENGTH

Elasticity and Inelasticity of Ceramic Samples of Graphitelike Boron Nitride

B. K. Kardashev*, Yu. A. Burenkov*, B. I. Smirnov*, V. V. Shpeĭzman*,
V. A. Stepanov, V. M. Chernov**, D. Singh***, and K. C. Goretta*****
**Ioffe Physicotechnical Institute, Russian Academy of Sciences, Politekhnicheskaya ul. 26, St. Petersburg, 194021 Russia*
***Leĭpunskiĭ Institute of Physics and Power Engineering, pl. Bondarenko 1, Obninsk, 249020 Russia*
****Argonne National Laboratory, Argonne, Illinois 60439, USA*
e-mail: B.Kardashev@pop.ioffe.rssi.ru

Received November 1, 2000

Abstract—This paper reports a study of the effect of temperature and strain amplitude on Young's modulus and ultrasonic damping in ceramic samples of graphitelike boron nitride prepared in the RF and USA by different technologies and using various additions to improve the mechanical properties of the ceramic. It is shown that, in addition to the influence on the effective elasticity modulus, additions improve the sample microplasticity, which apparently increases the strength of the material. *© 2001 MAIK “Nauka/Interperiodica”.*

1. INTRODUCTION

Acoustic properties (the elasticity moduli and ultrasonic damping) are very sensitive to the defect structure of crystals [1]. The acoustic methods developed for the investigation of single and polycrystals are also widely used presently in studies of other solids.

Recent years have witnessed an increased interest in ceramic materials, particularly in connection with the discovery of high-temperature superconductivity (HTSC), as well as because of the use of various ceramics as structural materials capable of withstanding high temperatures.

Development of ceramic materials with a stable structure for use within a broad temperature range is a very complex problem. Studies of HTSCs revealed, for instance, that the structure (the grain size, the presence of pores, etc.), as well as the intragrain defects, can determine the acoustic characteristics of a ceramic to a considerable extent [2–4]. The experience gained in HTSC studies shows that acoustic measurements allow for efficient testing of the quality of ceramic samples.

The first data on the elastic properties of BN ceramics were reported in [5, 6]. This paper presents a more complete body of information on the study of the acoustic properties of ceramic materials based on graphitelike boron nitride. As in [2–5], we used (1) the composite piezoelectric oscillator method and (2) the method of electrostatic excitation of resonance vibrations in rod-shaped samples. Both methods operate in the ultrasonic frequency range. The composite oscillator method is convenient for studying the elastic and microplastic properties of solids at low temperatures, and the electrostatic method is employed to investigate the elastic properties at high temperatures [1].

2. EXPERIMENTAL TECHNIQUE

The studies were carried out on ceramic samples of boron nitride prepared by different technologies. Information on the various methods of ceramic preparation can be found in [7–9]. The table presents data on the composition and some of the properties of the materials studied. The samples prepared in the RF contain 0.3 to 1% B_2O_3. The composition of the samples produced in the USA (Advanced Ceramics Research Company, Tucson, AZ) includes, besides a 2–3% addition of Y_2O_3 and Al_2O_3 in a 3 : 1 ratio, a few percent of a polymer binder. The anneal temperature of all materials was about 1700°C. The RF samples were of a white color, and the US sample was black.

The density of the samples used in the acoustic experiments was determined by hydrostatic weighing to within 0.2%. The manufacturers quote a fairly broad range of material density variation (shown in parentheses).

The last column of the table presents the measured compressive strengths of the samples used in the acoustic measurements. The data on the bending strength were supplied by the manufacturers.

The samples prepared for acoustic measurements were rods of a rectangular cross section 10–20 mm^2 in area and approximately 25 mm long. This length provided a rod resonance frequency close to 100 kHz. We employed two temperature ranges for acoustic measurements under thermal cycling, namely, 100–390 and 290–880 K. The first temperature range was covered by the composite oscillator method, and the second, by electrostatic vibration excitation. The methods employed are discussed in more detail in [1, 10].

Composition and some properties of the materials studied

No.	Material	Manufacturer	BN content	Density, g/cm^3	Bending strength, MPa	Compressive strength, MPa
1	BN	RF	99.0–99.8	1.41 (1.3–1.5)	30–60	21
2	BN : SiC	RF	91.0–93.0	1.68 (1.4–1.7)	70–90	58
3	BN : Al_2O_3, Y_2O_3	USA	93.0–95.0	2.25	–	84

In addition to information on Young's modulus E, the composite oscillator method provides data on ultrasound damping (internal friction) and the inelastic (microplastic) properties of the objects under study. Data on the microplasticity can be obtained from measurements of the E modulus and the decrement δ within a broad range of vibrational strain amplitudes ε, i.e., in the conditions where nonlinear, amplitude-dependent damping sets in at large enough ε values in the sample material. Young's modulus defect $\Delta E/E = [E(\varepsilon) - E_0]/E_0$ can serve as a measure of inelasticity. Here, $E(\varepsilon)$ is the value of the modulus measured at a given amplitude and E_0 is the modulus measured at the smallest value of ε used in the experiment. The elastic-modulus defect is approximately equal to the ratio of the nonlinear inelastic to elastic strain [1]. The decrement δ is also a measure of the inelastic behavior of a material.

3. RESULTS AND DISCUSSION

Figures 1–3 present the temperature dependences of Young's modulus $E(T)$ and of the decrement $\delta(T)$ measured (at $\varepsilon \approx 10^{-6}$) on three materials, BN-1, BN-2, and BN-3 (see the table), under thermal cycling within the range of 100–390 K. These data were obtained by the composite oscillator technique. The measurements were started by heating a sample from room temperature to 390 K, then cooling it to 100 K, with the final measurements again being close to room temperature. The heating and cooling rates were about 2 K/min. As is seen from Figs. 1–3, all the samples exhibit hysteresis in both the elasticity modulus and the decrement. The hysteresis, however, differs from one sample to another; indeed, the hysteresis of BN : SiC is the smallest. Interestingly, the temperature dependences of

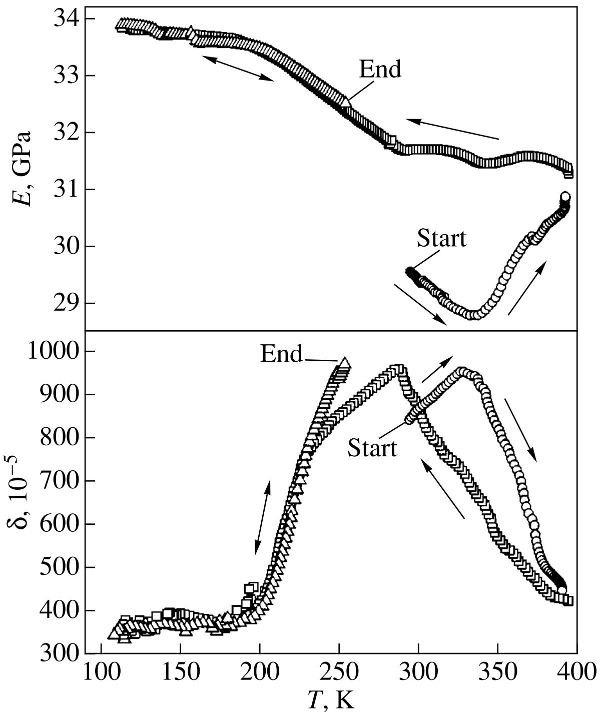

Fig. 1. Young's modulus E and elastic vibration decrement δ of the BN-1 sample measured within the 100–390 K range; the arrows indicate the direction of temperature variation.

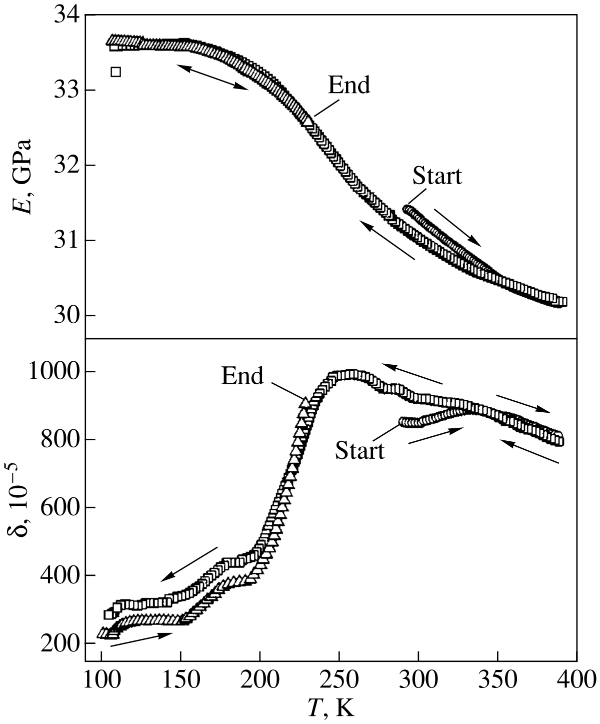

Fig. 2. Young's modulus E and elastic vibration decrement δ of the BN-2 sample measured within the 100–390 K range; the arrows indicate the direction of temperature variation.

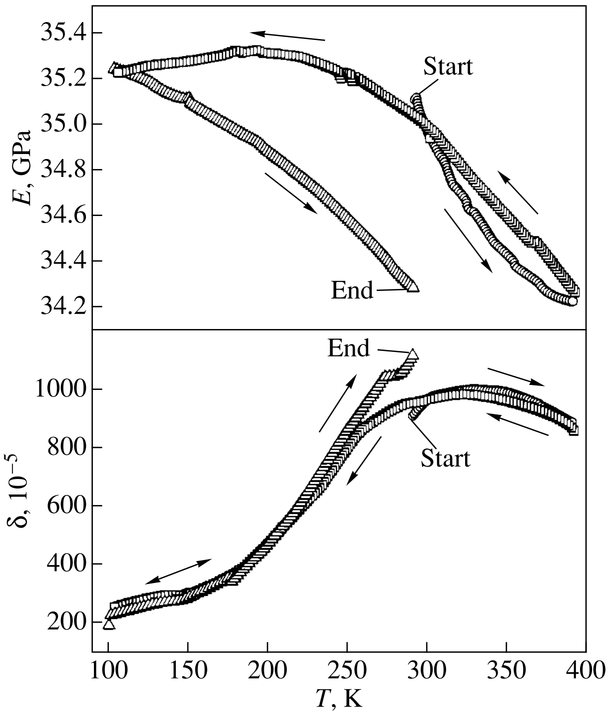

Fig. 3. Young's modulus E and elastic vibration decrement δ of the BN-3 sample measured within the 100–390 K range; the arrows indicate the direction of temperature variation.

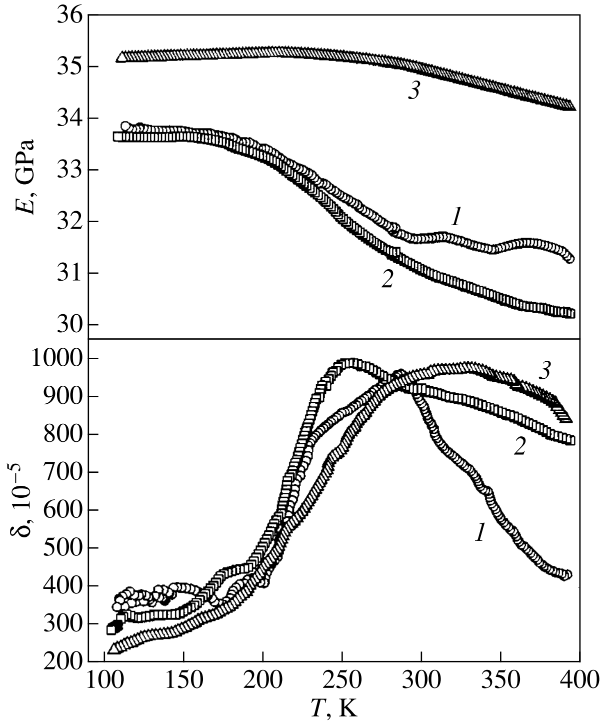

Fig. 4. Young's modulus E and elastic vibration decrement δ of the (*1*) BN-1, (*2*) BN-2, and (*3*) BN-3 samples measured under cooling from 390 to 100 K.

Young's modulus of the BN-1 and BN-2 materials obtained under cooling to 100 K and subsequent heating coincide. Young's modulus of the BN-3 sample exhibits, in the same conditions, a clearly pronounced hysteresis.

Figure 4 compares the absolute values of the modulus and of the decrement for different materials. These data were obtained in the cooling part (390 to 100 K) of the thermal cycle. The BN-3 sample is seen to have the largest modulus (it also has the highest density). At the same time, it exhibits the lowest relative changes in the modulus with temperature (of only approximately 0.3%); by contrast, the moduli of the BN-1 and BN-2 samples change within the same temperature range by approximately 1%. Remarkably, below 200 K, Young's modulus of the BN-3 sample decreases noticeably, whereas that of BN-1 and BN-2 measured in the same temperature range continues to grow under cooling to 100 K, although considerably more slowly than at higher temperatures. As to the internal friction (the δ decrement), we here observed two features, namely, broad maxima or inflection points in the 330–350 and 230–250 K intervals. Interestingly, the BN-1 sample, which did not contain any purposefully introduced additions, exhibits an additional, clearly pronounced peak of internal friction in the room-temperature range.

The behavior of Young's modulus under thermal cycling at higher temperatures (290–880 K) is illustrated in Fig. 5. As at low temperatures, one sees here a temperature hysteresis which acquires different forms

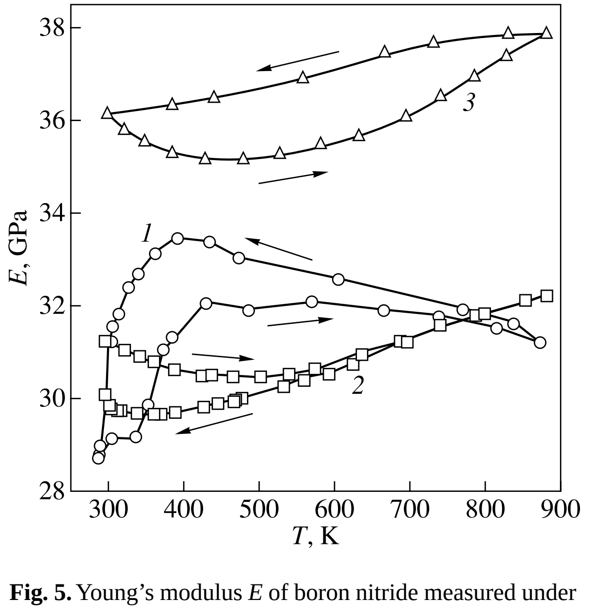

Fig. 5. Young's modulus E of boron nitride measured under thermal cycling within the 290–880 K range on the (*1*) BN-1, (*2*) BN-2, and (*3*) BN-3 samples.

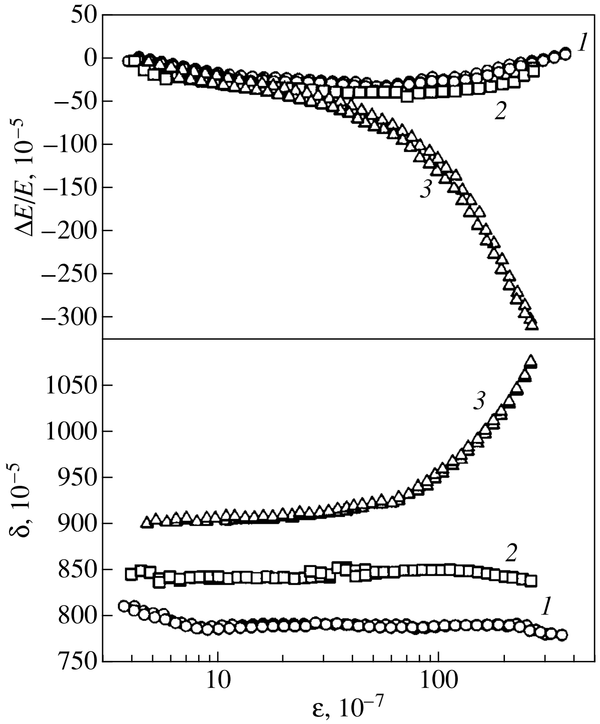

Fig. 6. Young's modulus defect $\Delta E/E$ and elastic vibration decrement δ of the (*1*) BN-1, (*2*) BN-2, and (*3*) BN-3 samples measured at room temperature as functions of the vibration amplitude ε.

in different samples. Here again, BN : SiC exhibits the smallest hysteresis.

The behavior of the elasticity modulus in such complex materials as ceramics is governed primarily by two different factors. First, variation of the temperature changes the atomic bonding forces in the lattice, which should bring about growth in the modulus with decreasing *T*. This effect should operate in all solids. It manifests itself in its purest form in single crystals [1]. Second, a change in the temperature of a ceramic (polycrystalline) sample can create high internal (thermoelastic) stresses in it (because the thermal expansion coefficients in different crystallographic directions are different). This must give rise to noticeable changes in the measured elastic modulus because of the lattice vibration anharmonicity. In the cases where the thermoelastic stresses relax (for instance, through microplastic shear), the measured elastic modulus can also relax.

The various types of temperature hysteresis observed in the samples studied are apparently a consequence of differences in the chemical composition, ceramic preparation technologies, etc. A comparison of the behavior of various samples reveals an interesting point, namely, that the BN-3 boron nitride is very susceptible (compared to BN-1 and BN-2) to microplastic deformation at low temperatures, which is seen particularly clearly if one compares the behavior of the corresponding Young moduli in Figs. 1–3. The different tendency to microplastic shear is also confirmed by measurements of the amplitude dependences of Young's modulus *E* and of the decrement δ, which are displayed graphically in Fig. 6. Interestingly, the amplitude dependences $E(\varepsilon)$ and $\delta(\varepsilon)$ of the BN-3 sample qualitatively resemble the behavior of the modulus and decrement in (metallic and ionic) single crystals containing dislocations [1]. The BN-1 and BN-2 samples exhibited a different behavior; namely, only at low amplitudes did Young's modulus decrease slightly with increasing ε, after which it grew in magnitude, thus implying the disappearance of microplastic deformation at high amplitudes; the decrement fell off slowly with increasing ε in this case. The susceptibility of the BN-3 sample to microplastic deformation is possibly due to the polymer binder used in the preparation of this ceramic. A comparison of the BN-1 and BN-2 samples shows that the BN : SiC sample is softer than the boron nitride without additions. This is indicated by the larger values of the decrement and Young's modulus of BN : SiC. Moreover, the sample with silicon carbide also exhibited a noticeable macroplastic strain when subjected to compressive strength tests.

Thus, the acoustic method employed in this work permits one not only to study the behavior of the elastic modulus, an aspect important from the practical standpoint, but also to predict the behavior of the ceramic strength properties. This is due to the fact that the susceptibility of a ceramic material to microplastic deformation noticeably increases its strength. As for the boron nitride, the manifestation of microplasticity in this material is particularly important, because it is used widely as a binder in fibrous monoliths, in particular, in Si_3N_4/BN [8, 9].

ACKNOWLEDGMENTS

This work was supported by the Russian Foundation for Basic Research, grant no. 00-01-00482; NATO, grant no. PST.GLG.977016; and US DOE, contract no. W-31-109-Eng-38.

REFERENCES

1. S. P. Nikanorov and B. K. Kardashev, *Elasticity and Dislocation Non-elasticity of Crystals* (Nauka, Moscow, 1985).
2. A. B. Lebedev, Yu. A. Burenkov, V. I. Ivanov, *et al.*, Fiz. Tverd. Tela (Leningrad) **31**, 300 (1989) [Sov. Phys. Solid State **31**, 166 (1989)].
3. S. N. Golyandin, B. K. Kardashev, S. B. Kustov, *et al.*, Phys. Status Solidi A **147**, 111 (1995).

4. B. K. Kardashev, S. P. Nikanorov, B. I. Smirnov, *et al.*, Fiz. Tverd. Tela (St. Petersburg) **38**, 3252 (1996) [Phys. Solid State **38**, 1775 (1996)].
5. Yu. A. Burenkov, B. K. Kardashev, V. A. Stepanov, and V. M. Chernov, in *Proceedings of the International Conference-Exhibition "Boron Nitride: Production, Properties, Application," Obninsk, 1993*, p. 20.
6. T. W. Spohnholtz, W. A. Ellingson, and D. Singh, Ceram. Eng. Sci. Proc. **21** (3), 155 (2000).
7. S. A. Perfilov, V. A. Stepanov, L. N. Rusanova, and V. F. Kuznetsova, Poroshk. Metall., No. 2, 73 (1991).
8. S. Baskaran, S. D. Nunn, D. Popovic, and J. W. Halloran, J. Am. Ceram. Soc. **76**, 2209 (1993).
9. D. Kovar, B. H. King, R. W. Trice, and J. W. Halloran, J. Am. Ceram. Soc. **80**, 2471 (1997).
10. Yu. A. Burenkov, S. P. Nikanorov, and A. V. Stepanov, Izv. Akad. Nauk SSSR, Ser. Fiz. **35**, 525 (1971).

Translated by G. Skrebtsov

Physics of the Solid State, Vol. 43, No. 6, 2001, pp. 1089–1092. Translated from Fizika Tverdogo Tela, Vol. 43, No. 6, 2001, pp. 1053–1056.
Original Russian Text Copyright © 2001 by Balaev, Zhukov, Ivanova, Kazak, Ovchinnikov, Popel.

MAGNETISM AND FERROELECTRICITY

On the Two-Phase Magnetic State in a $Cu_xZn_{1-x}Cr_2Se_4$ Cation-Substituted Chalcogenide Spinel

A. D. Balaev, É. G. Zhukov, N. B. Ivanova, N. V. Kazak,
S. G. Ovchinnikov, and E. P. Popel

Kirenskiĭ Institute of Physics, Siberian Division, Russian Academy of Sciences,
Akademgorodok, Krasnoyarsk, 660036 Russia

e-mail: dir@iph.krasnoyarsk.su

Received September 8, 2000

Abstract—The region of the concentration magnetic phase transition in a $Cu_xZn_{1-x}Cr_2Se_4$ chalcogenide spinel in which the substituted ion concentration x smoothly varies from 0.1 to 0.2 with a step of 0.02 is thoroughly investigated. An anomalous behavior of the Curie temperature is observed. This anomaly is associated with the nucleation of ferromagnetically ordered microregions in the vicinity of Cr ions with an intermediate valence and subsequent long-range magnetic ordering at a critical Cu concentration in the range $0.12 < x_c < 0.14$. The possible coexistence of ferro- and antiferromagnetism in the same temperature range is revealed. *© 2001 MAIK “Nauka/Interperiodica”.*

1. INTRODUCTION

Investigation of cation-substituted chalcogenide spinels $Cu_xZn_{1-x}Cr_2Se_4$ has been attracting attention for a long time due to the existence of various types of magnetic ordering in pure samples of $ZnCr_2Se_4$ (helicoidal antiferromagnetism with $T_N \sim 20$ K) and $CuCr_2Se_4$ (ferromagnetism with $T_C \sim 400$ K). This permits one to observe the consequences of competitive exchange interactions in solid solutions with different degrees of substitution [1–4]. Moreover, since the ionic radii of Zn and Cu are very close in magnitude, it is possible to obtain a continuous series of single-phase samples for all x values. Apart from the magnetic properties, the electrical properties are also of interest because the conductivity changes from the semiconductor to the metallic type as Zn atoms are replaced by Cu atoms. Earlier [4], it was shown that ferromagnetism manifests itself in the studied compound at $x \sim 0.2$ and T_C smoothly increases as the copper concentration increases. It was also found that the compounds with $x < 0.1$ are antiferromagnets. However, the mechanism of the transition from noncollinear antiferromagnetism (NCAF) to ferromagnetism (FM) remained unclear. The objective of the present work was to thoroughly investigate the region of the concentration magnetic phase transition. For this purpose, we measured and analyzed the temperature and magnetic-field dependences of the magnetization and magnetic susceptibility of $Cu_xZn_{1-x}Cr_2Se_4$ polycrystalline samples in the concentration range 0.1–0.2 with a step of 0.02.

2. SAMPLE PREPARATION AND EXPERIMENTAL TECHNIQUE

The samples of $Cu_xZn_{1-x}Cr_2Se_4$ solid solutions used were powder polycrystals prepared by solid-phase synthesis in evacuated silica tubes. The synthesis procedure was described in detail in [5]. Samples 1–6 had concentrations in the range $x = 0.1$–0.2 with a step of 0.02. Then, the samples were pressed for resistive measurements.

Measurements of the magnetization M were carried out on a vibrating-coil magnetometer with a superconducting solenoid in the temperature range 4.2–150 K. The real component of the magnetic susceptibility χ' was measured with a phase-sensitive detector by the inductance technique. In the latter case, the sample temperature was maintained and controlled using a flow-type glass cryostat with measuring coils fastened to its outer wall. The coils were exposed to air flow with the aim of reducing spurious temperature drift. Gaseous nitrogen or heated air flow over the sample allowed measurements in the temperature range 80–600 K.

The x-ray diffraction spectra of samples 2 and 3 revealed that these samples have single-phase spinel structures with the same lattice parameter within the limits of experimental error.

3. EXPERIMENTAL RESULTS

The measurements of the temperature dependence of the magnetic susceptibility showed that it is weak for samples 1 and 2 at $T > 80$ K. This is most likely due to

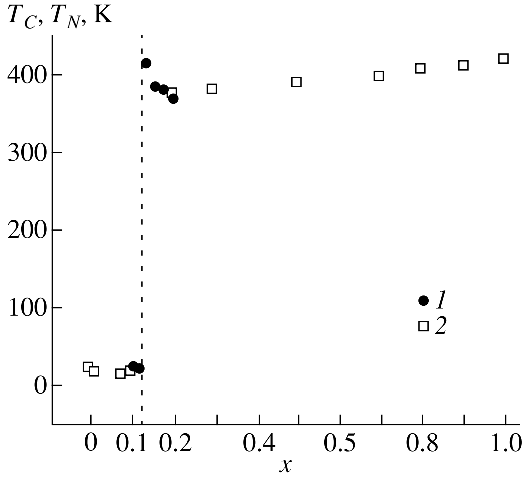

Fig. 1. Concentration dependence of the Curie temperature and Néel temperature: (*1*) our data and (*2*) the data taken from [4].

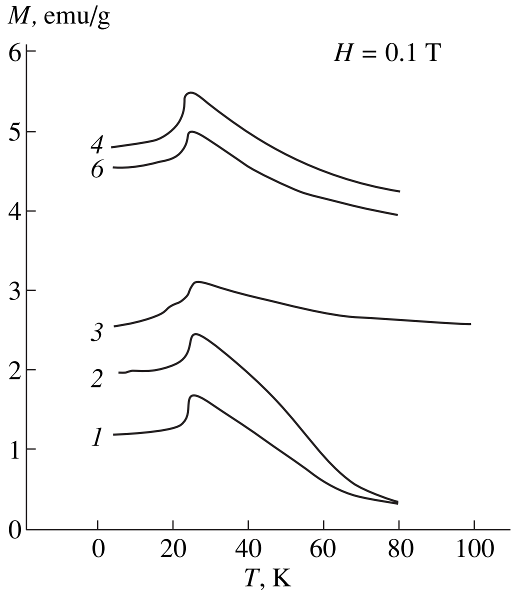

Fig. 2. Temperature dependences of the magnetization. The numerals at the curves correspond to the sample numbers.

the paramagnetic state. However, the measurements of $\chi'(T)$ for samples 3–6 yielded an unexpected result. In contrast to the linear decrease in T_C with a decrease in the copper concentration in the composition range covered, which was observed in [4], it was found that T_C rises nonlinearly and reaches a value of 415 K at x = 0.14 (Fig. 1), which is characteristic of pure $CuCr_2Se_4$.

The low-temperature behavior of the magnetization also exhibits salient features. The measurements of temperature dependences showed that the $M(T)$ curve has a peak at T_N ~ 22 K for all the samples, both with and without magnetic transition at T_C. The essential difference between the $M(T)$ curves for ferromagnetic and nonferromagnetic samples is the following. As is seen from Fig. 2, the magnetization above T_N tends to zero for samples 1 and 2 and to a constant value of M_0 (different for all the samples) for the remaining samples.

Figures 3a–3c display magnetization curves for different temperatures. The character of the $M(H)$ curves at T = 4.2 K is the same for all samples. Only the saturation magnetization is different. For this reason, only the dependence for sample 3 (x = 0.14) is shown. It can be seen from this figure that the $M(H)$ curve has two pronounced features at H ~ 1 T and ~7 T, which correspond to the spin-reorientation transitions. The latter feature was also observed in [4].

Figures 3b and 3c present the magnetization curves for samples 2 and 3, which are similar in composition but drastically differ in their properties. It is seen that, well above T_N, the behavior of sample 2 at 150 K is purely paramagnetic, whereas the curve for sample 3 is of a ferromagnetic character. The shape of the dependences $M(H)$ is intermediate at T = 50 K (Fig. 3b).

4. DISCUSSION

In [2, 4], the magnetic properties of $Cu_xZn_{1-x}Cr_2Se_4$ were interpreted in terms of competitive exchange interactions. The effects observed were explained by the authors of [2, 4] with the use of a complex chain of concentration magnetic phase transformations: simple spiral–FM spiral–spin glass–FM spiral–collinear ferromagnet. The existence of the collinear spin ordering in the pure and cation-substituted $ZnCr_2Se_4$ compounds at certain concentrations and temperatures was confirmed by neutron diffraction data. However, neutron scattering spectra cannot always be interpreted unambiguously [6] and the satellite lines can be attributed not only to the noncollinear magnetic structure of the sample but also to the two-phase state of the sample when it represents a mixture of ferromagnetic and antiferromagnetic regions. Moreover, Nagaev [7] theoretically proved that the NCAF system is less stable than the collinear systems, specifically at high temperatures and low concentrations. In this connection, we cannot say with certainty that it is these noncollinear magnetic structures that are realized in $Cu_xZn_{1-x}Cr_2Se_4$ over a wide range of concentrations and temperatures.

The majority of previously obtained experimental data, as well as that in this work, can easily be explained within the model of the two-phase magnetic state [8]. In this model, the ordered ferromagnetic state coexists with the antiferromagnetic state.

For example, a part of the Cr ions in the state 3+ transforms into the state 4+ as copper atoms are incorporated into pure $ZnCr_2Se_4$. The state with a variable valence is realized. As was shown in [7], individual ferromagnetic microregions can be formed about impurity atoms in this process. This should lead to an increase in the paramagnetic Curie temperature with small variations in T_N, as was actually observed in [4]. As the impurity concentration x increases, the ferromagnetic region becomes simply connected at a certain critical value x_c and the macroscopic ferromagnetic order with the Curie temperature T_C is established. From this point on, the antiferromagnetic regions are present as inclusions in the ferromagnetic matrix. It is presumably this mechanism that is observed in our case when samples 3–6 exhibit T_N and T_C simultaneously, and the antiferromagnetic peak at T_N is seen against the background of the ferromagnetic contribution M_0, whereas the Cr^{4+} concentration in samples 1 and 2 is insufficient for ferromagnetic ordering. According to our data, the critical value x_c for $Cu_xZn_{1-x}Cr_2Se_4$ lies in the concentration range 0.12–0.14.

The two-phase model can also explain the unexpected decrease in T_C in the series of samples 3–6. It is reasonable to assume that, for x close to the critical value, the ferromagnetic “network” which has already been formed should predominantly capture impurity ions; i.e., for the most part, the regions containing copper ions and neighboring chromium atoms should be ferromagnetic. The magnitude and sign of the exchange interaction will be characteristic of pure $CuCr_2Se_4$ with the corresponding T_C value. As the ferromagnetic region increases, a larger number of Zn ions will be captured and the competition between the exchange interactions can lead to a decrease in the T_C temperature, which will then rise again as more and more Zn atoms are replaced with Cu.

The two-phase model is also supported by resistive measurements. Warczewski *et al.* [2] noted a concentration transition from a well-conducting to semiconductor state, which accompanies the disappearance of macroscopic ferromagnetism. Our preliminary measurements of the resistance of pressed samples also showed that samples 1 and 2 have a higher resistance than the others. This also agrees with the predictions of the two-phase model, according to which the samples containing a singly connected ferromagnetic region with an increased carrier concentration should possess a higher conductivity. Thus, almost the whole totality of experimental data for the region of the concentration transition can be described within a unified approach in the model of the two-phase magnetic state, which was proposed in [6–8].

However, a certain part of our data can be interpreted in favor of NCAF ordering. This mainly concerns the indications of two spin-flop transitions in the $M(H)$ dependence at 4.2 K. The first transition presumably takes place when the helicoidally ordered magnetic moment leaves the plane, and the second transition can be attributed to the collinear ferromagnetic ordering. Surprisingly, the former transition was not noted by Krok *et al.* [4], who conducted similar measurements on compositions partly coinciding with

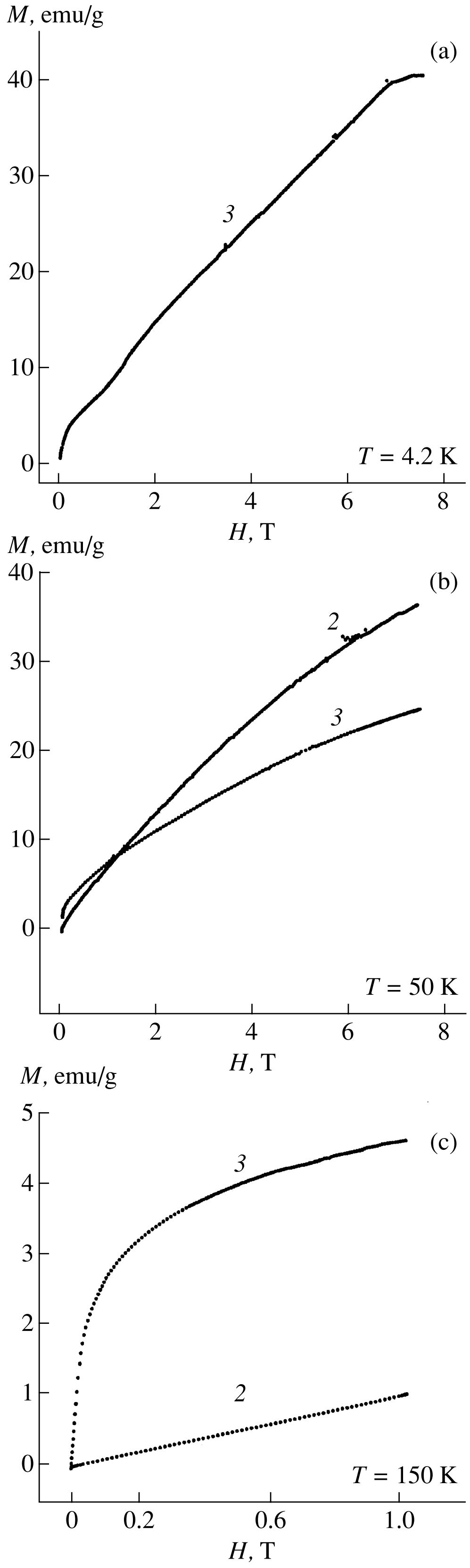

Fig. 3. Magnetization curves at different temperatures *T*, K: (a) 4.2, (b) 50, and (c) 150. The numerals at the curves correspond to the sample numbers.

those used in our work. On the other hand, a similar curve can be obtained by the simple superposition of the ferromagnetic and antiferromagnetic contributions to $M(H)$. In addition, the seemingly “chaotic” jumps of the saturation magnetic moment from sample to sample, which also showed up to some extent in [4], remain unclear.

Thus, it is quite possible that the noncollinear antiferromagnetic ordering is more energetically favorable at low temperatures. Nevertheless, the success of the two-phase model in describing a set of experimental data opens up a field for scientific discussion concerning the boundaries of applicability of one or another model and the ultimate clearing up of the nature of the magnetic phase transition in the cation-substituted chalcogenide spinel $Cu_xZn_{1-x}Cr_2Se_4$.

ACKNOWLEDGMENTS

We are grateful to N. Bulina for performing x-ray measurements.

This work was supported by the Russian Foundation for Basic Research, project no. 99-02-17405.

REFERENCES

1. J. Jendrzejewska, T. Mydlarz, I. Okonska-Kozlowska, and J. Heimann, J. Magn. Magn. Mater. **186** (3), 381 (1998).
2. J. Warczewski, T. Gron, and J. Krok-Kowalski, Phase Transit. B **43** (1–4), 225 (1993).
3. S. Juszczyc and M. Gogolowicz, Physica B (Amsterdam) **192** (4), 338 (1993).
4. J. Krok, J. Spalek, S. Juszczyc, and J. Warczewski, Phys. Rev. B **28** (11), 6499 (1983).
5. É. G. Zhukov, E. S. Polulyak, G. S. Varnakova, and V. A. Fedorov, Zh. Neorg. Khim. **38** (1), 167 (1993).
6. É. L. Nagaev, Usp. Fiz. Nauk **166** (8), 833 (1996) [Phys. Usp. **39**, 781 (1996)].
7. É. A. Nagaev, *Physics of Magnetic Semiconductors* (Nauka, Moscow, 1979).
8. É. L. Nagaev, Pis’ma Zh. Éksp. Teor. Fiz. **6** (1), 484 (1967) [JETP Lett. **6**, 18 (1967)].

Translated by M. Lebedkin

Physics of the Solid State, Vol. 43, No. 6, 2001, pp. 1093–1096. Translated from Fizika Tverdogo Tela, Vol. 43, No. 6, 2001, pp. 1057–1060.
Original Russian Text Copyright © 2001 by Baranov, Gulyaev, Zilberman, Krikunov, Kudryavtsev, Ogrin, Sklizkova, Stepina, Feigin, Heide, Chmil', Elliott.

MAGNETISM AND FERROELECTRICITY

Current Hysteresis in Magnetic Tunnel Junctions

A. M. Baranov, Yu. V. Gulyaev, P. E. Zilberman, A. I. Krikunov, V. V. Kudryavtsev, Yu. F. Ogrin, V. P. Sklizkova, N. D. Stepina, L. A. Feigin, C. Heide, A. I. Chmil', and R. Elliott
Institute of Radio Engineering and Electronics, Russian Academy of Sciences (Fryazino branch),
pl. Vvedenskogo 1, Fryazino, Moscow oblast, 141120 Russia
e-mail: pez253@ire216.msk.ru

Received October 26, 2000

Abstract—A current hysteresis is detected in magnetic tunnel junctions of the ferromagnetic metal–nonmagnetic insulator–ferromagnetic metal type. The hysteresis is manifested in the formation of loops on the curves describing the dependence of the current through the junction on the applied voltage, as well as in the nonreproducibility of this dependence. This effect is caused by the influence of the spin-polarized current on the magnetic state of metallic layers: the current leads to a rearrangement of the domain structure under these conditions. *© 2001 MAIK "Nauka/Interperiodica".*

Two mechanisms of the effect of a spin-polarized current on the magnetic state of metallic films in magnetic tunnel junctions are known. One mechanism is associated with the scattering of the spin of conduction electrons from the boundary surfaces of the junctions. The conservation of angular momentum in such a scattering leads to the rotation of the magnetization vector in the layers [1, 2]. The other mechanism is distinguished by its bulk nature and is associated with the violation of spin balance in the layers (injection of spins) and with the exchange interaction of injected and intrinsic spins of the layers [3].

In experiments, the following phenomena were observed: (1) the "switching" effect, i.e., the magnetization sign inversion in one of the metallic layers for current densities ~10^9 A/cm^2 and for a certain sign of the current [4, 5] and (2) loops in the current–voltage curves [5–7]. In addition, the presence of a magnetic domain structure (DS) varying in an external magnetic field was detected in some experiments [8–11].

The present work is a continuation of our earlier publication [7], in which we reported for the first time on the observation of current hysteresis loops associated with the effect of a current on the magnetic state of the junction. We present additional experimental evidence of the magnetic origin of the loops: they exist irrespective of the type of insulator used in the structure for separating the ferromagnetic metallic layers, but always disappear when the ferromagnetic metallic film is replaced by a film of a normal metal. In addition, we prove that the loops depend on the history of the time variation of the voltage applied to the junction and disappear in strong magnetic fields. It was suggested that the current rearranges the magnetic DS and that hysteresis loops appear because of pinning of the domain walls, which leads to the coercivity effect.

We prepared three-layered magnetic tunnel junctions (MTJ). Nickel films approximately 0.05 μm thick were deposited on substrates made of thermally oxidized silicon by using dc magnetron sputtering in an Ar atmosphere. Insulator films were then deposited on the Ni film surface. The thickness of these insulator films was of the order of 3 to 30 nm, which ensured the possibility of tunnel penetration of electrons. The following two types of insulating films were mainly prepared.

(1) Films of diamond-like carbon (DLC), which were obtained in a plasma excited by a high-frequency discharge. The working gas was C_6H_{12} vapor. The thickness, growth rate, density, and surface roughness of DLC layers were controlled directly in the course of their growth by using *in situ* x-ray monitoring [12].

(2) Organic films on the basis of rigid-chain polyimide, which were obtained in two stages [13]. At the first stage, the film of an amphophilic derivative of polyimidic acid was formed by the Langmuir–Blodgett method. At the second stage, the end product, viz., polyimide (LBP), was obtained as a result of thermal treatment.

A second metallic film, namely, an Fe or $Fe_{91}Zr_9$ film, was deposited on the surface of the insulator film to reduce the magnetic anisotropy. In reference samples, a nonmagnetic Al film was deposited instead of the Fe film. The thickness of the second metallic film was of the same order of magnitude (0.05 μm). The continuity of the insulator film was judged from the resistance of the junction (which amounted to a few gigaohms for currents ~1 nA) and from the shape of the $I(V)$ dependence. The insulator thickness was determined by sputtering technology and was additionally monitored from the capacitance of the junction. The working surface of the junction was ~(60 × 120) μm.

We analyzed the $I(V)$ dependences for a current flowing transversely to the interfaces between the lay-

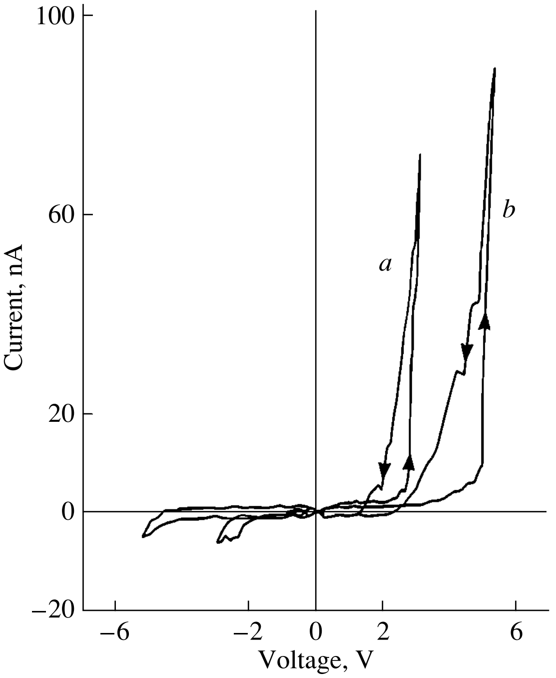

Fig. 1. Loops in the $I(V)$ curves for structures (*a*) of the Ni/LBP/Fe type and (*b*) of the Ni/DLC/Fe type. The arrows indicate the directions of current and voltage variation. The thicknesses of the LBP and DLC films are of the order of 10 nm.

ers in the junction. Figure 1 shows the typical curves obtained for (Ni/Fe) junctions with different insulator layers. It can be seen that the curves have some common features, which are observed for any insulator used. The first peculiarity is that the $I(V)$ curves are irreversible since the current depends on the direction of variation of the voltage. For this reason, when the voltage is varied along a closed path, a loop is formed on the (I, V) plane. A loop appears each time we reverse the direction of V irrespective of the value of the maximum attained voltage V_m. In this respect, these loops basically differ from those described by Pratt *et al.* [6], which were caused by the insulator breakdown and, hence, appeared only for $V_m > V_{\text{th}}$, where V_{th} is the threshold breakdown voltage. The loops in question also differ in their origin from those obtained in [5] when studying the switching effect: in contrast to [5], our loops were observed for any polarity of the current (see Fig. 1). These loops cannot also be associated with the processes occurring in the nanoscopic insulating interlayer since they were observed for any insulator used in the experiments. However, the loops always disappeared when the Fe films were replaced by Al films.

The second feature of the $I(V)$ curves is illustrated best of all in Fig. 2. The figure shows the results of measurements obtained using an *x*–*y* recorder. In Fig. 2a, four consecutive loops are presented. The maximum voltage V_m is chosen to be so large that a considerable increase in current is observed (in the figure, the current is indicated only below the *L*–*L* line). Figure 2b presents two consecutive loops recorded for another (much smaller) value of V_m. It can be seen that the loops are formed for any value of V_m, are nonreproducible, and are arranged at random. The area of the loops has a tendency to increase with V_m.

In our opinion, the very fact of the emergence of loops in the experiments described here and their non-

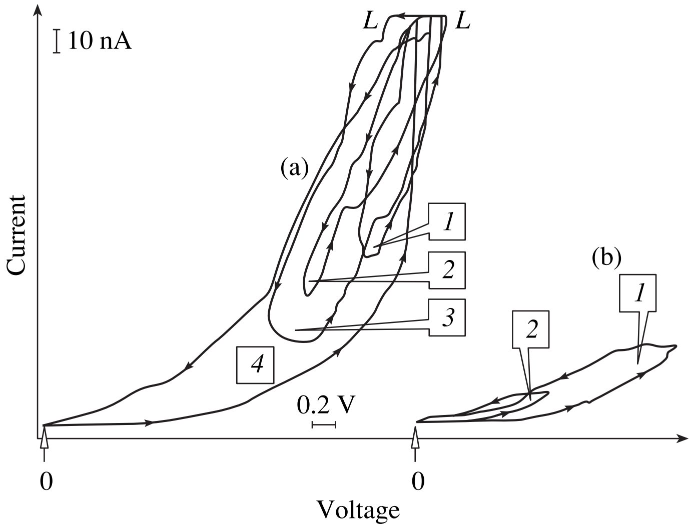

Fig. 2. Dependence of the loops in the $I(V)$ curves on the history of the time variation of the voltage applied to the junction. The arrows indicate the directions of current and voltage variation with time. The numbers label the consecutive loops. The horizontal *L*–*L* line corresponds to ~100 nA and marks the level of the maximum recorded current.

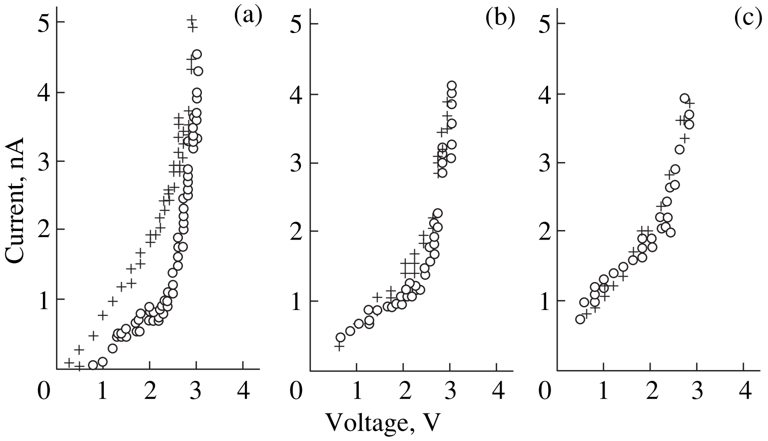

Fig. 3. Effect of the magnetic bias field *H* oriented in the plane of the junction on the form of the *I*(*V*) dependence for an Ni/LBP/Fe sample. *H*, Oe: (a) 0, (b) 40, (c) 150.

reproducibility can be explained by the effect of the current on the magnetic state of the junction. The mechanisms of this effect can be associated with both the surface and the bulk. At the same time, it should be noted that the loops in the *I*(*V*) curves were observed by us for current densities much lower than the threshold current density for observing the switching effect [1, 2, 4, 5]. Even if we assume that the entire current flows through a single channel with the minimum possible linear size of the order of 1 nm, the current density for the total current ≤100 nA (see Fig. 1) will be one to two orders of magnitude lower than the above-mentioned threshold value.

The random distribution of loops in the (*I*, *V*) plane can be due to the presence of an irregular DS in the metallic ferromagnetic film and to its interaction with the spin-polarized current. The results of experiments [14] indicate that any electron can penetrate from a domain in one film to a domain of the other film through the nonmagnetic layer separating the films. We can assume that the known conclusions [15] concerning the dependence of the current on the mutual orientation of the magnetizations remain valid (at least qualitatively) for such a penetration. However, we must now speak of the orientation of magnetizations in the domains: the current will apparently attain its maximum value for the parallel orientation and its minimum value for the antiparallel orientation. Consequently, the current cannot remain uniform over the junction cross section and the paths for easy and hampered passages of current must be formed. In this case, the total current through the junction is the sum of partial currents between the domains.

Similarly, we can assume that the conclusions concerning the effect of the polarized current on the magnetic state of metallic films, which were drawn in [1–3] without taking into account the splitting of films into domains, also remain qualitatively valid. In the presence of a DS, we must obviously speak of the exchange interaction between the spins of electrons injected into domains and the spins of the DS. Such an interaction must result in the rotation of the magnetizations of domains, the motion of domain walls, and, finally, a change in the topology of the entire DS.

The coercivity of magnetic films must lead to the irreversibility and nonreproducibility of the DS rearrangement described above. As a result, the DS will be determined not only by voltage *V* at a given instant *t* but must also considerably depend on the values of *V* at previous instants, i.e., on the history of the formation of the given domain configuration. Since the total current through the junction is determined by the DS (see above), it is clear that the current loops, as well as their irreversibility and nonreproducibility, can be interpreted as a reflection of similar properties of the DS.

This point of view is supported by two additional experiments. In one of them, the memory effect, i.e., the dependence of current *I* on the history of the variation of voltage *V* with time *t*, was investigated. The following remarks explain how it was done. In the experiments discussed by us until now, voltage pulses with a small repetition frequency were used. The voltage in these pulses first increased from zero to V_m and then decreased from V_m to zero at the same rate (equal to approximately 40 mV/s). For instance, the curves in Figs. 1 and 2 were obtained for just such voltage pulses. The current loops in Figs. 1 and 2 were seen clearly; i.e., in compliance with our ideas, the DS had time to change under the effect of the current and the coercivity effect was manifested during the opposite variation of the voltage. Conversely, in the additional experiments, voltage *V* was varied with time at considerably differing rates.

Two series of pulses were used. In the pulses belonging to the first series, the voltage first increased smoothly (at the usual rate of ~40 mV/s) from zero to the maximum value V_m and then abruptly (over milliseconds) dropped to zero. In the pulses of the second series, the voltage first increased jumpwise from zero to V_m and then smoothly decreased to zero at the usual rate. The peculiar feature of the experiment was that the DS rearrangement, which could occur under a smooth variation of voltage, did not affect the $I(V)$ dependence upon a smooth decrease of the voltage. It turned out that these dependences almost coincide and no loops are formed.

In the second additional experiment, the effect of the external magnetic field H was investigated. A strong field H must lead to the saturation of the ferromagnetic metallic layers and to the suppression of the DS. If current loops are formed as a result of the DS rearrangement, they must also be suppressed significantly. The samples of junctions were placed in a field H parallel to the plane of the junction. After the fixation of a certain value of H, the voltage was gradually increased and the current was measured. The voltage was varied slowly to stabilize the conditions for the current flow. For $H = 0$, a loop similar to those shown in Figs. 1 and 2 was observed. For $H = 40$ Oe, the loop became much smaller and vanished altogether for $H = 150$ Oe in the voltage interval $V = 0$ to 3 V (see Fig. 3). The error of measurements amounted to approximately 10% of the value of the current.

It should be noted that if a field H was applied at $V \neq 0$ and $I \neq 0$, its influence on the shape of the $I(V)$ curve was much weaker. In order to eliminate the loop in the $I(V)$ dependence, a field $H \geq 2$ to 4 kOe could be required. This fact apparently indicates that the DS can be rigidly fixed under the conditions of current flow because of the exchange interaction between the ferromagnetic layers through conduction electrons.

Thus, MTJ are characterized by loops in the $I(V)$ curves, which depend on the history of the time variation of voltage V. These observations can be explained by the hysteresis induced by the effect of the current on the magnetic state of the ferromagnetic layers and on the DS in them.

In conclusion, it is appropriate to make the following two remarks. The first feature to note is that the loops formed are quite wide. For a fixed voltage V, the currents in different branches of a loop can differ considerably in accordance with Fig. 2. This might appear as surprising from the viewpoint of the estimates of the magnetoresistance in structures of the (Ni/Fe) type, which were made earlier for relatively weak tunnel currents [15]. It should be emphasized, however, that the current in this case is not weak in the sense that it itself produces magnetization and DS rearrangement in the ferromagnetic layers. For this reason, although the current depends on the orientation of the magnetic moments, the form of this dependence might differ from that observed in familiar experiments on magnetoresistance. For instance, it cannot be ruled out that the tunnel transparency itself becomes a function of the current for the above reason. This question requires special investigation.

The second remark is associated with the fact that the mechanism of conduction through the junction might prove to be not very important for the loop formation unless it leads to a strong depolarization of the current and prevents exchange interaction between the layers. Consequently, it would be expected that a similar effect of current hysteresis could exist in some magnetic junctions with a metallic interlayer.

ACKNOWLEDGMENTS

The authors express their gratitude to A. Vedyaev and A. Granovskiĭ for fruitful discussions and valuable remarks.

This work was supported by the Russian Foundation for Basic Research, project no. 00-02-16384, and NATO, grant no. PST, CLG 975312.

REFERENCES

1. J. C. Slonczewski, J. Magn. Magn. Mater. **159**, L1 (1996).
2. L. Berger, Phys. Rev. B **54** (13), 9353 (1996).
3. C. Heide, R. J. Elliott, and N. S. Wingreen, Phys. Rev. B **59**, 4287 (1999).
4. M. Tsoi, A. G. M. Jansen, J. Bass, *et al.*, Phys. Rev. Lett. **80** (19), 4281 (1998).
5. E. B. Myers, D. C. Ralph, J. A. Katine, *et al.*, Science **285**, 867 (1999).
6. C. L. Pratt, B. Dieny, and A. E. Berkowitz, J. Appl. Phys. **81** (8), 5523 (1997).
7. C. Heide, A. I. Krikunov, Yu. F. Ogrin, *et al.*, J. Appl. Phys. **87** (9), 5221 (2000).
8. T. Miyazaki and N. Tezuka, J. Magn. Magn. Mater. **139**, L231 (1995).
9. V. S. Gornakov, V. I. Nikitenko, L. H. Bennett, *et al.*, J. Appl. Phys. **81** (8), 5215 (1997).
10. X. Portier and A. K. Petford-Long, J. Phys. D **32**, 1 (1999).
11. Yu. Lu, P. L. Trouilloud, D. W. Abraham, *et al.*, J. Appl. Phys. **85** (8), 5267 (1999).
12. A. M. Baranov and I. F. Mikhailov, Thin Solid Films **324** (1–2), 63 (1998).
13. V. P. Sklizkova, V. V. Kudryavtsev, Yu. G. Baklagina, *et al.*, in *Proceedings of the 5th International Conference on Polyimides, Ellenville, 1994,* Nos. 2–4, p. 61.
14. S. J. C. H. Theeuwen, J. Caro, K. P. Wellock, *et al.*, Appl. Phys. Lett. **75** (23), 3677 (1999).
15. M. Julliere, Phys. Lett. A **54**, 225 (1975).

Translated by N. Wadhwa

Physics of the Solid State, Vol. 43, No. 6, 2001, pp. 1097–1102. Translated from Fizika Tverdogo Tela, Vol. 43, No. 6, 2001, pp. 1061–1066.
Original Russian Text Copyright © 2001 by Gan'shina, Bogoroditskiĭ, Kumaritova, Bibikova, Smirnitskaya, Tsidaeva.

MAGNETISM AND FERROELECTRICITY

Magnetooptical Properties of Fe/Pd Multilayer Films

E. A. Gan'shina*, A. A. Bogoroditskiĭ*, R. Yu. Kumaritova*, V. V. Bibikova*,
G. V. Smirnitskaya*, and N. I. Tsidaeva**
**Moscow State University, Vorob'evy gory, Moscow, 119899 Russia*
***North-Osetiya State University, Vladikavkas, Russia*
e-mail: eagan@magn.phys.msu.su

Received November 2, 2000

Abstract—Multilayer films of Fe(x)/Pd(30 Å) ($6 \le x \le 30$ Å) are investigated with the help of the transversal Kerr effect (TKE) with incident light in the energy range 1.3–3.6 eV. Oscillations of the TKE depending on the thickness of the iron layer are revealed. The off-diagonal element of the dielectric tensor ε_2' is calculated using the measured values of the TKE for two incidence angles of light and the optical constants of all samples. It is shown that the quantity $\varepsilon_2'\omega^2$ (where ω is the frequency of incident light), which is proportional to the interband density of states, also oscillates, and its oscillations are similar in character to oscillations of the Kerr effect. The observed oscillatory dependence of the TKE and of the interband density of states are related to the manifestation of quantum confinement effects. © *2001 MAIK "Nauka/Interperiodica".*

1. INTRODUCTION

At the present time, magnetically inhomogeneous low-dimensional materials attract extensive attention in the physics of magnetic phenomena. Such attention is due to the interesting and not completely understood properties of these materials (such as giant magnetoresistance and high magnetooptical activity) and to the perspective of their practical application. Spectral optical and magnetooptical techniques are effective methods of researching magnetically inhomogeneous low-dimensional materials. These techniques allow one to obtain information on the electronic and magnetic structure of samples.

Multilayer Fe/Pd and Fe/Pt films with various thicknesses of paramagnetic and ferromagnetic layers are the most interesting objects of magnetooptical investigations, because the metals of the 4*d* (5*d*) groups have a larger magnitude of the spin-orbital interaction constant and should exert the greatest influence on magnetooptical properties. An analysis of the physical properties of alloys and multilayer films containing palladium shows the following. Palladium, being a paramagnetic element, becomes ferromagnetic in the presence of a ferromagnet [1]. This can be brought about by a number of circumstances, for example, by (1) expansion of the crystalline lattice by 5–10% caused by the introduction of some ions in the Pd matrix and by (2) long-range exchange interaction with ions of transition metals Fe, Co, and Ni [1]. The maximum magnitude of the induced magnetic moment for Pd is equal to $0.4\mu_B$ [2]. In [3], it was shown that, despite a small induced magnetic moment, Pd makes a significant contribution (comparable with the contribution of pure Fe) to the magnetooptical effects in Fe/Pd alloys because of a large spin-orbital splitting of the 4*d* states.

However, the magnetooptical properties observed in ultrathin films ($d < 30$ Å) cannot be explained by the high magnetooptical activity of Pd alone. New size effects (classical and quantum) should appear for such film thicknesses. Such effects cannot be understood with the help of optical and magnetooptical constants of three-dimensional samples.

For example, the oscillatory behavior of magnetooptical effects depending on the thicknesses of ferromagnetic and nonferromagnetic layers ($d < 30$ Å) was experimentally revealed in a number of works [4–6]. The electronic states near the Fermi level in low-dimensional structures of Cu on Co(100) and Ag on Fe(100) were investigated in [4] with the help of inverse photoemission. In that work, the existence of special types of electronic states at the Fermi level was revealed. These so-called "quantum well states" (QWS) arise because of quantization of the magnetic moments of the *s* and *p* electrons caused by the confinement of electron motion in the thin layer in the direction perpendicular to the surface. It was also experimentally shown in [4] that QWS can give rise to oscillations of the exchange interaction in multilayer structures.

Together with the experimental works that considered oscillations of magnetooptical effects in ultrathin films and in which QWS were detected, some works appeared in which the authors attempted to find theoretically the connection between oscillations of the transversal Kerr effect (TKE) and oscillations of the interlayer exchange interaction. For example, a simple model was offered in [7], in which only the transitions from the occupied plane $d_{(x \pm iy)z}\uparrow$ level to the vacant p_z

level were taken into account. It was shown that the oscillations of the TKE can be described in terms of the density of states of electrons, the motion of which is confined owing to the small thickness of the film at hand; therefore, the normal component of the wave vector k_z is quantized. Consequently, the imaginary part of the off-diagonal component of the conductivity tensor σ''_{xy} of a thin film is a sum of δ functions corresponding to certain electron energies. The dependence of σ''_{xy} on the thickness of the layer exhibits oscillations with a decreasing amplitude. It was also shown in [7] that the formula for the oscillation period of the TKE is similar to the formula for the oscillation period of the magnetic interlayer interaction, but the latter oscillation period is inversely proportional to the Fermi wave vector, whereas the oscillation period of the TKE is inversely proportional to the wave vector of a constant-energy surface of the p_z level. Thus, it was theoretically shown in [7] that the confinement of electron motion results in oscillations of the TKE, the period of which can differ from the oscillation period of the magnetic exchange interaction. In order to clarify the nature of oscillations of the TKE in ultrathin films, the interband transitions in Ni in the vicinity of the *L* point of the Brillioun zone were considered in [8]. The very small thickness of a film was taken into account by quantization of the momentum of electrons in the direction perpendicular to the surface of the film. It has been theoretically demonstrated that the period of TKE oscillations depends on the frequency of the incident light.

At present, there is a limited number of works in which the spectral curves of the interband density of states of films were obtained and considered for studying the electronic structure of multilayers. It is necessary to note the detailed investigation of the properties of spin-polarized Pd in Fe/Pd alloys in [3]; however, no study on the magnetooptical properties of multilayers of Fe/Pd has been made to date. In the present work, we attempt to study the electronic structure of Fe/Pd multilayers by investigating the dependence of the spectrum of the interband density of states on the thickness of the magnetic interlayer. In order to calculate the quantity $\varepsilon'_2\omega^2$ (where ε'_2 is the off-diagonal element of the dielectric tensor and ω is the frequency of the incident light), which characterizes the interband density of states, the spectra of the optical and magnetooptical properties of Fe/Pd multilayer films are investigated. The oscillatory dependence of the quantity $\varepsilon'_2\omega^2$ on the thickness of the magnetic interlayer is revealed; such a dependence is a manifestation of quantum confinement effects in Fe/Pd multilayers.

2. EXPERIMENTAL TECHNIQUES

Fe/Pd multilayer films were obtained by deposition on glass substrates in a discharge with oscillating electrons [9]. The low rate of deposition of films allowed us to obtain layers of thickness from a few angstroms up to dozens of angstroms. The number of Fe and Pd layers in the films was approximately equal to 100. The thickness of the Pd layer was the same for all samples and equaled 30 Å, and the thickness of the Fe layer varied from 5.8 to 30 Å. Sputtering was made in Kr inert gas at a pressure of approximately 10 Torr. The investigations of the structure of the obtained films were made on an x-ray diffractometer using monochromatic FeK_α radiation. The results of this structural analysis showed that the Fe/Pd alloy phase was present in films with an iron layer thickness smaller than 30 Å. For films with Fe layers 6–14 Å thick, a layered structure with two phases was observed: the Fe/Pd phase and the fcc-Pd phase; for the Fe layer thickness 17–23 Å, a three-phase structure was observed: the Fe/Pd phase, the fcc-Pd phase, and the bcc-Fe phase; for the Fe layer thickness 30 Å, the Fe/Pd alloy phase disappeared [10].

Optical and magnetooptical investigations were performed in the energy range 1.3–3.6 eV. For the magnetooptical study, we used the TKE, which is a variation of the intensity and the phase shift of linearly polarized light reflected from a sample magnetized in the plane perpendicular to the plane of light incidence [11]. To measure the change in the intensity of linearly polarized light, we used the dynamical method, which consisted in remagnetization of the sample located in the gap of an electromagnet by an alternating magnetic field. The magnitude of this effect is equal to

$$\delta = \frac{1}{2}\frac{I(+\mathbf{M}) - I(-\mathbf{M})}{I(+\mathbf{M}) + I(-\mathbf{M})}, \qquad (1)$$

where **M** is the magnetization vector. The use of the dynamical method of registration of signals allowed us to increase the accuracy of measurements by 2 to 3 orders of magnitude in comparison with the static method and to measure effects as small as 10^{-5}. The amplitude of the ac magnetic field in the gap was sufficiently large to saturate all the samples under investigation (1 kOe). The measurements were performed at room temperature for several angles of light incidence.

The polarimetric Beattie method was used to investigate the optical properties of the films [12]. This method is based on the analysis of the ellipticity arising when linearly polarized light is reflected from the surface of a sample. The diagonal components of the dielectric tensor were calculated from the optical constants of the films obtained to an accuracy of 2%.

In order to obtain additional information on the modification of the electronic structure in the multilayer films of Fe(*x* Å)/Pd(30 Å) from the measured optical and magnetooptical spectra, the off-diagonal elements of the dielectric tensor were calculated. The variation of the intensity of light reflected from a gyroelectric medium in the case of transversal magnetization of the medium can be written as [11]

$$\delta = a\varepsilon'_1 + b\varepsilon'_2, \qquad (2)$$

where

$$a = 2\sin 2\varphi\frac{A_1}{A_1^2 + B_1^2}, \quad b = 2\sin 2\varphi\frac{B_1}{A_1^2 + B_1^2},$$

$$A_1 = \varepsilon_2(2\varepsilon_1\cos^2\varphi - 1),$$

$$B_1 = (\varepsilon_2^2 - \varepsilon_1^2)\cos^2\varphi + \varepsilon_1 - \sin^2\varphi,$$

$$\varepsilon_1 = n^2 - k^2, \quad \varepsilon_2 = 2nk,$$

φ is the angle of light incidence on the sample, n and k are optical constants, and ε'_1 and ε'_2 are the real and imaginary parts of the off-diagonal component of the dielectric tensor, respectively. It follows from Eq. (2) that, in order to determine ε'_1 and ε'_2, it is sufficient to know the diagonal component of the dielectric tensor (ε_1, ε_2) and the magnitude of the TKE (δ_1, δ_2) for the two angles of light incidence φ_1 and φ_2. The corresponding formulas can be obtained from a system of two equations for the angles of light incidence φ_1 and φ_2:

$$\varepsilon'_1 = \frac{\delta_1 b_2 - \delta_2 b_1}{a_1 b_2 - a_2 b_1}, \quad \varepsilon'_2 = \frac{\delta_2 a_1 - \delta_1 a_2}{a_1 b_2 - a_2 b_1}, \tag{3}$$

where coefficients a and b are calculated from Eq. (2).

The obtained formulas are true for magnetooptical effects in an isotropic magnetized medium. However, since the thickness of any layer of the film under investigation is much less than the wavelength of light incident on the film, the given multilayer film can be considered as an effective medium described by an effective dielectric tensor, for which Eqs. (2) and (3) are also true.

It has been shown in [13, 14] that the components of the dielectric tensor in the range of interband transitions can be written as

$$\varepsilon_2\omega^2 \sim \sum_{m>n}\int P_{mn}\delta(\omega - \omega_{mn})d^3k,$$
$$\varepsilon'_2\omega^2 \sim \pm\left\{\sum_{m>n}\int Q_{mn}\delta(\omega - \omega_{mn})d^3k\right\}, \tag{4}$$

where $m(E_m > E_F)$ and $n(E_n < E_F)$ denote the occupied and the vacant electronic states, respectively; P_{mn} and Q_{mn} are the magnitudes of the matrix elements; and the plus and minus signs correspond to various directions of the spins. Thus, the behavior of $\varepsilon_2\omega^2$ and $\varepsilon'_2\omega^2$ is determined by the interband density of states. Consequently, in the first approximation (neglecting the dependence of the matrix elements on the frequency of incident light), the changes in the interband density of states in a system of Fe/Pd films and, therefore, the changes in their electronic energy band structure can be judged from the changes in the frequency dependence of the quantity $\varepsilon'_2\omega^2$.

3. EXPERIMENTAL RESULTS AND DISCUSSION

The spectra of the optical conductivity $\sigma(\hbar\omega) = \dfrac{\varepsilon_2\omega}{4\pi}$ are represented in Fig. 1. It can be seen that the spectra of the optical conductivity of the Fe/Pd films differ from the spectra for the Fe film and that the value of σ varies nonmonotonically with decreasing iron layer thickness. The nonmonotonic dependence on the Fe layer thickness is even in the magnetooptical spectra.

The TKE spectra for the Fe/Pd multilayers and the iron film are displayed in Fig. 2 for two incidence angles, 60° and 73.7°. It follows from Fig. 2 that the magnetooptical spectra of the multilayer films differ considerably from the spectra of the iron film; in addition, the shape of the spectrum and the magnitude of the TKE strongly depend on the thickness of the iron layer for both angles of incidence.

The dependence of the TKE on the iron layer thickness is presented in Fig. 3 for several energies of incident light. It can be seen that the magnitude of the TKE oscillates with increasing thickness of the magnetic layer. The maxima of the effect are observed for the films with an iron layer thickness of 12.4 and 19.3 Å for both angles of light incidence, and the magnitude of the TKE is maximal for the film with an iron layer thickness of 30 Å.

Using the TKE spectra of the Fe/Pd films and the film of pure iron for two angles of incidence of light and also the values of the optical constants, we calculated the off-diagonal elements of the dielectric tensor from Eq. (3). The calculated spectrum of the quantity $\varepsilon'_2\omega^2$ characterizing the interband density of states is presented in Fig. 4a for the Fe/Pd films and the film of pure iron. A comparison of the curves of the interband density of states (as a function of energy) for the Fe/Pd films with the corresponding curves for the iron film and the spin-polarized Pd were obtained in [3] (see Fig. 4b)

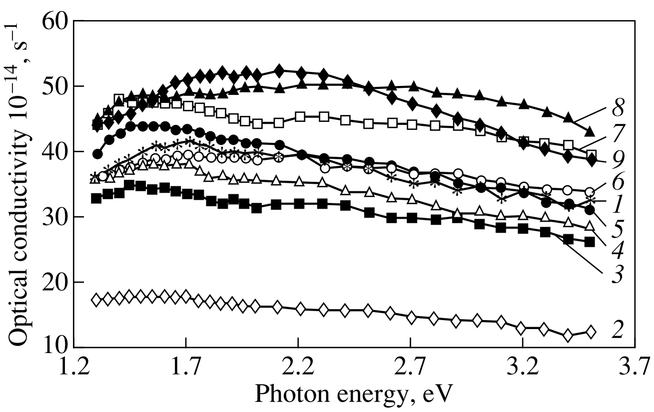

Fig. 1. Spectrum of the optical conductivity of Fe(x Å)/Pd(30 Å) films. x, Å: (*1*) 5.8, (*2*) 9, (*3*) 12.4, (*4*) 14, (*5*) 17, (*6*) 19.3, (*7*) 23, and (*8*) 30; (*9*) a Fe film.

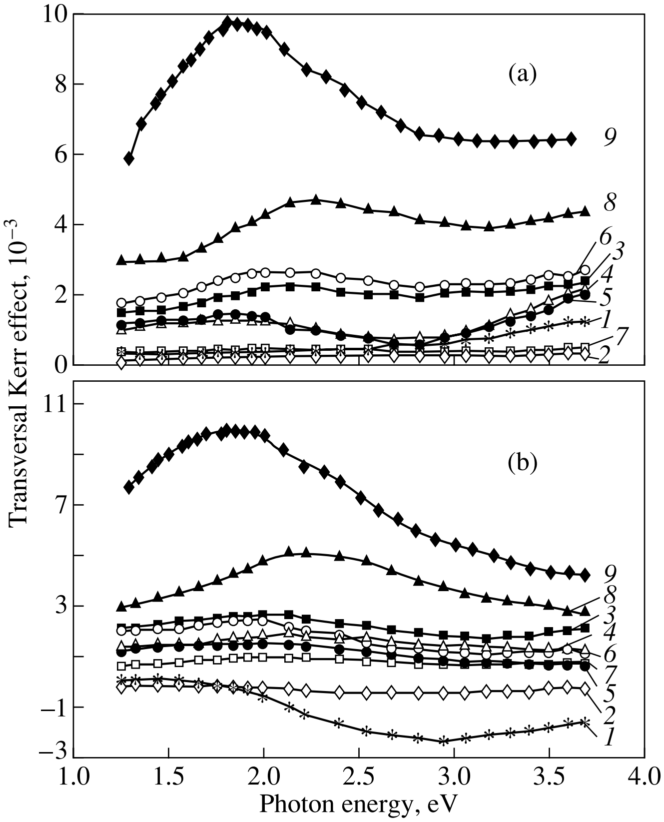

Fig. 2. Spectrum of the TKE for Fe(x Å)/Pd(30 Å) films for incidence angles of (a) 60° and (b) 73.7°. The labels of curves (*1*–*9*) are the same as in Fig. 1.

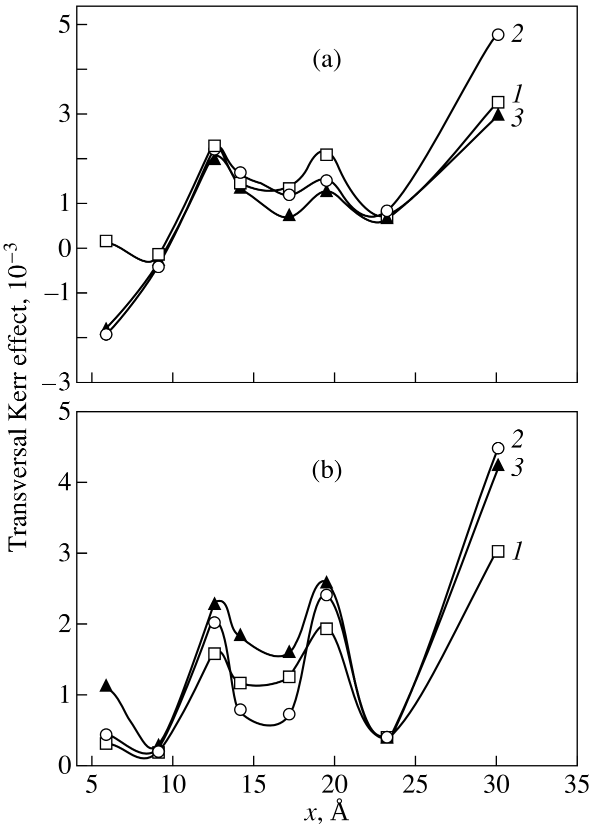

Fig. 3. The TKE for Fe(x Å)/Pd(30 Å) films as a function of the thickness x of magnetic Fe interlayers for various values of the photon energy of incident light and for incidence angles of (a) 60° and (b) 73.7°. E, eV: (*1*) 1.5, (*2*) 2.5, and (*3*) 3.5.

reveals that the curve obtained for the film with a Fe layer thickness of 5.8 Å is similar to the curve for the spin-polarized Pd (Fe_6Pd_{94} alloy). This resemblance is explained by the fact that the multilayer film with an iron layer thickness of 5.8 Å is a two-phase alloy of Pd and Fe/Pd with a Pd concentration of 81 at. % and can be compared to the Fe_6Pd_{94} alloy. For the remaining films ($6 < d < 30$ Å), the behavior of the interband density of states as a function of photon energy cannot be represented as a superposition of the spectra of pure Fe and the spin-polarized Pd (this is indicated by the negative value of $\varepsilon'_2(\hbar\omega)^2$ in the energy range 2.1–3 eV for films with iron layer thicknesses of 14, 17, and 23 Å).

Comparing the spectra of $\varepsilon'_2\omega^2$ for the Fe/Pd films, one can notice the nonmonotonic behavior of these curves as a function of iron layer thickness. For example, only the quantity $\varepsilon'_2\omega^2$ of the film with an iron layer thickness of 5.8 Å is less than $\varepsilon'_2\omega^2$ of the film with an iron layer thickness of 30 Å over the whole spectrum and is less than its values for the film with a thickness of 19.3 Å over magnitudes of the energy range from 1.3 to 2.1 eV. For the films with iron layer thicknesses of

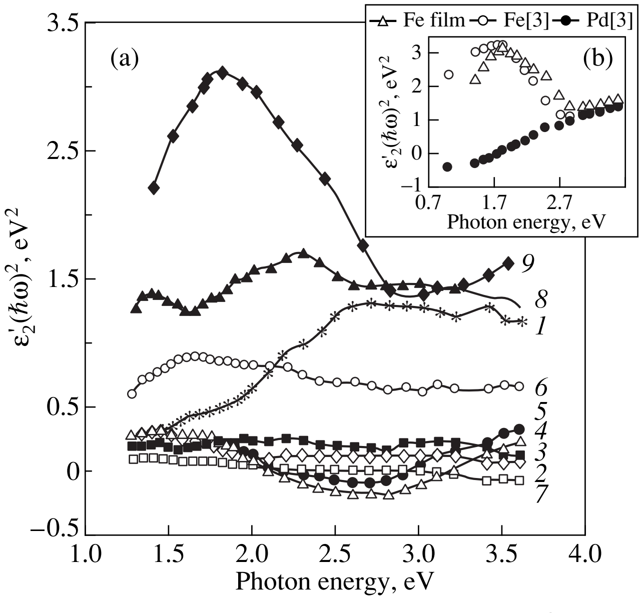

Fig. 4. (a) Spectrum of the quantity $\varepsilon'_2(\hbar\omega)^2$ for Fe(x Å)/Pd(30 Å) films. The labels of curves (*1*–*9*) are the same as in Fig. 1. (b) The spectrum of the quantity $\varepsilon'_2(\hbar\omega)^2$ for the bulk Fe film and the films of spin-polarized Pd and Fe obtained in [3].

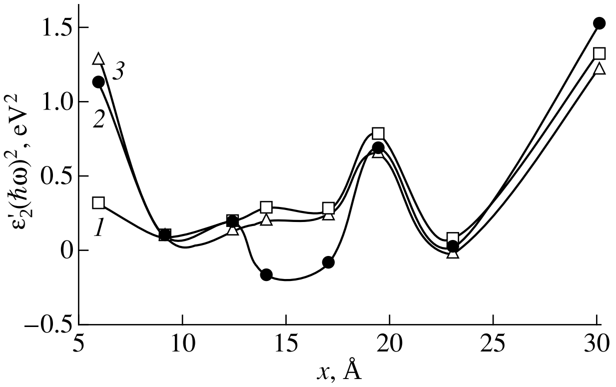

Fig. 5. The quantity $\varepsilon_2'(\hbar\omega)^2$ for Fe(x Å)/Pd(30 Å) films as a function of the thickness x of magnetic Fe interlayers for various values of the photon energy of incident light. E, eV: (*1*) 1.5, (*2*) 2.5, and (*3*) 3.5.

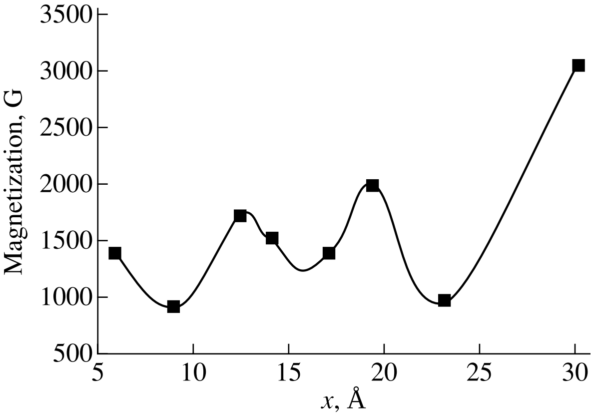

Fig. 6. Saturation Magnetization of Fe(x Å)/Pd(30 Å) films as a function of the thickness x of magnetic Fe interlayers.

14, 17, and 23 Å, the quantity $\varepsilon_2'\omega^2$ changes its sign to negative in the range of energies 2.1–3 eV. In Fig. 5, the quantity $\varepsilon_2'\omega^2$ characterizing the interband density of states is presented as a function of the thickness of the Fe magnetic layer for the photon energies 1.5, 2.5, and 3.5 eV. A comparison of these curves with the TKE plotted as a function of the iron layer thickness for incidence angles of 60° and 73.7° (Fig. 3) reveals that the magnitudes of both the TKE and $\varepsilon_2'\omega^2$ have a local maximum for the film with an iron layer thickness of 19.3 Å for all three values of photon energy magnitudes. For the film with an Fe layer thickness equal to 12.4 Å, the quantity $\varepsilon_2'\omega^2$ is not a local maximum for all values of energy, while the magnitude of the TKE is a local maximum. The magnitude of $\varepsilon_2'\omega^2$ for the film with an iron layer thickness of 30 Å, as well as the magnitudes of the TKE, is maximal.

The similarity of the general shapes of all three curves (the TKE curves for incidence angles of 60° and 73.7° and the dependence of the quantity $\varepsilon_2'\omega^2$ on the iron layer thickness) suggests that the oscillations of the TKE with varying iron layer thickness are the consequence of the corresponding oscillations of $\varepsilon_2'\omega^2$ characterizing the interband density of states.

Theoretically, it was shown [8] that the observed oscillations of the TKE with a varying thickness of the magnetic layer in thin films are due to the oscillations of the off-diagonal component of the dielectric tensor, which in turn, are the result of the quantum confinement in these ($d \ll \lambda$) films, i.e., the result of the QWS formation. The formation of QWS should also result in oscillations of the indirect exchange interaction. Indeed, the saturation magnetization of the multilayers exhibits an oscillatory behavior with varying magnetic layer thickness (Fig. 6). By comparing the oscillations of $\varepsilon_2'\omega^2$ with varying thickness of the iron layer and oscillations of the saturation magnetization of the same films (Fig. 6), one can see that, despite the qualitative similarity of these oscillations, there are also essential differences. The oscillations of the magnetization and $\varepsilon_2'\omega^2$ with varying iron layer thickness are not proportional. For example, the magnetization of the film with an iron layer thickness of 30 Å is three times greater than the magnetization of the film with an iron layer thickness of 23 Å, whereas the respective ratio of the interband density of states is approximately 13 for an energy of 1.5 eV and 30 for an energy of 2.5 eV; furthermore, sign reversal is observed for an energy of 3.5 eV. For the films with Fe thicknesses in the range 12–17 Å, the behavior of the curve of the interband density of states differs qualitatively from the behavior of the curve of magnetization. Thus, the oscillations of $\varepsilon_2'\omega^2$ are not a direct consequence of the oscillations of the indirect exchange interaction. The oscillations in both cases are the manifestation of the quantum confinement in multilayers, which modifies the electronic structure of films with varying magnetic interlayer thickness. However, for the curve of magnetization, the changes at the Fermi level are important, whereas in magneto-optics, the quantum confinement influences all energy structures.

4. CONCLUSIONS

Thus, in this work, we studied the magnetooptical properties of Fe/Pd multilayer films with the help of TKE in the range of photon energies 1.3–3.6 eV for incidence angles of 60° and 73.7° at room temperature.

It is shown that the spectral behavior of the magnitude of the TKE in the energy range at hand for the system of Fe/Pd multilayer films differs essentially from the behavior of the TKE in polycrystalline iron films.

The off-diagonal components of the dielectric tensor are calculated for the system of Fe/Pd films. An oscillatory dependence of $\varepsilon_2^{'}\omega^2$ on the ferromagnetic Fe interlayer thickness is revealed. This dependence is qualitatively similar to the oscillatory dependence of the TKE on the Fe layer thickness.

The observed oscillatory dependences of the TKE and of the interband density of states are the manifestation of quantum confinement.

ACKNOWLEDGMENTS

This work was supported by the Russian Foundation for Basic Research, project no. 99-02-16595.

REFERENCES

1. G. G. Low and T. M. Holden, Proc. Phys. Soc. London **89**, 119 (1966).
2. V. L. Moruzzi and P. M. Marcus, Phys. Rev. B **39**, 471 (1989).
3. D. Weller, W. Reim, and K. Sporl, J. Magn. Magn. Mater. **93**, 183 (1991).
4. J. E. Ortega and E. F. Himpsel, Phys. Rev. Lett. **69**, 844 (1992).
5. W. R. Bennet, W. Schwaracher, and W. F. Egelhoff, Phys. Rev. Lett. **65**, 3169 (1990).
6. T. Katayama, Y. Suzuki, M. Hayashi, and A. Thiaville, J. Magn. Magn. Mater. **126**, 527 (1993).
7. Y. Suzuki and P. Bruno, J. Magn. Magn. Mater. **140–141**, 651 (1995).
8. A. Vedyayev, N. Ryzhanova, S. Young, and B. Dieny, Phys. Lett. A **215**, 317 (1996).
9. É. M. Reĭkhrudel' and G. V. Smirnitskaya, Itogi Nauki Tekh., Ser. Élektron. Ee Primen. **8**, 43 (1976).
10. M. Starkova, E. Likhushina, S. Sveshnikov, and A. Katsnel'son, Vestn. Mosk. Univ., Ser. 3: Fiz., Astron. **6**, 38 (1999).
11. G. S. Krinchik, *Physics of Magnetic Phenomena* (Mosk. Gos. Univ., Moscow, 1976).
12. Y. R. Beatti, Philos. Mag. **460**, 235 (1955).
13. P. N. Argyres, Phys. Rev. **97**, 334 (1955).
14. S. Adler, Phys. Rev. **126**, 413 (1962).

Translated by O. Ivanov

Physics of the Solid State, Vol. 43, No. 6, 2001, pp. 1103–1107. Translated from Fizika Tverdogo Tela, Vol. 43, No. 6, 2001, pp. 1067–1071.
Original Russian Text Copyright © 2001 by Murtazaev, Abdulvagidov, Aliev, Musaev.

MAGNETISM AND FERROELECTRICITY

Heat Capacity of a Cr_2O_3 Antiferromagnet near the Critical Temperature

A. K. Murtazaev, Sh. B. Abdulvagidov, A. M. Aliev, and O. K. Musaev

Institute of Physics, Dagestan Scientific Center, Russian Academy of Sciences,
ul. 26 Bakinskikh Komissarov 94, Makhachkala, 367003 Dagestan, Russia
e-mail: kamilov@datacom.ru

Received August 14, 2000; in final form, November 3, 2000

Abstract—The heat capacity of a Cr_2O_3 antiferromagnet near the critical temperature is precisely measured by ac calorimetry. The critical behavior of the heat capacity is examined. The regularities of variations in the universal critical parameters near the critical point are determined, and their values are calculated. A crossover from the Heisenberg ($n = 3$) to the Ising ($n = 1$) critical behavior is revealed. © *2001 MAIK "Nauka/Interperiodica"*.

1. INTRODUCTION

According to the modern theory of phase transitions and critical phenomena, the critical exponents and critical amplitude ratios which determine the regularities of variations in the equilibrium properties near the critical temperature T_c depend primarily on the lattice dimension d, the number of degrees of freedom of the order parameter n, and the length of the ordering interaction [1–3]. In three-dimensional magnetically ordered crystals, the three universality classes that correspond to the known Heisenberg ($n = 3$), XY ($n = 2$), and Ising ($n = 1$) models are of particular interest.

Experimental investigations of different-type magnetically ordered crystals (ferro-, antiferro-, and ferrimagnets) confirmed the validity of the universality principle and demonstrated that, within the limits of experimental error, numerical values of the critical exponents and critical amplitude ratios are in agreement with the results of the renormalization-group theory and the ε expansion [1–5]. However, elucidation of the critical behavior in a number of magnets involves serious problems. It is interesting that, among these materials are well-known magnets whose critical transition temperatures are especially well suited to experimental investigations, for example, antiferromagnetic Cr_2O_3. As a rule, considerable difficulties emerge when determining the universality class of these magnets. This can be explained by the fact that calculations of the critical parameters do not include the appropriate analysis of the additional interactions disturbing the initial critical behavior [4]. Moreover, the determination of one (singly taken) critical exponent and the absence of the appropriate statistical treatment can give a rather rough account of the critical behavior. In these cases, analysis of the experimental results must be especially careful, because, so far, the theoretical accuracy of the determination of the critical parameters somewhat exceeds the experimental accuracy. It should be mentioned that there are a number of papers reporting on the violation of the universality principle. First of all, this may only mean that, in these experiments, the necessary conditions for establishing a correspondence between the studied crystal and the particular model are absent.

The weakly anisotropic antiferromagnet Cr_2O_3 with a critical temperature $T_N \approx 307$ K belongs to crystals whose statical critical behavior has been the subject of wide current speculation. Analysis of the anisotropic and exchange interactions demonstrates that Cr_2O_3 is an isotropic antiferromagnet (the Heisenberg model), and only at $t = |T - T_c|/T_c < 10^{-3}$, its critical behavior is affected by the uniaxial anisotropy and a crossover from the Heisenberg to the Ising ($n = 1$) critical behavior occurs.

The statical critical behavior of Cr_2O_3 was experimentally investigated in [6–10]. However, all attempts to determine unambiguously the universality class of the statical critical behavior of the Cr_2O_3 antiferromagnet on the basis of these data have failed. In particular, the data available in the literature on the critical behavior of the magnetic susceptibility [6], sublattice magnetization [7], and heat capacity [8–10] provide contradictory accounts of the statical critical behavior of Cr_2O_3.

In the present work, we carried out precise measurements of the heat capacity of a Cr_2O_3 antiferromagnet in the critical region and analyzed their results in the range of reduced temperatures ($1.0 \times 10^{-6} \le t \le 8.0 \times 10^{-3}$).

2. ANTIFERROMAGNETIC Cr_2O_3 AND ITS CRITICAL PROPERTIES

The Cr_2O_3 antiferromagnet has a rhombohedral lattice (the space group D_{3d}^6) with unit cell parameters a = 4.9607 Å and $\alpha = 55°06'$. The unit cell contains two formula units, and the magnetic moments of four Cr^{3+} ions are ordered along the rhombohedral axis. According to [1], in Cr_2O_3, the interactions of each Cr^{3+} ion with all the nearest neighbors ($I_1 < 0$) and the next-nearest neighbors ($I_2 < 0$) play the most important role; the interactions between the more distant neighbors are substantially weaker than the interactions I_1 and I_2. The magnetic moment per ion is equal to $3.8\mu_B$ (where μ_B is the Bohr magneton). The anisotropy of Cr_2O_3 is governed by the single-ion mechanism and dipole–dipole interactions [12, 13]. The anisotropy field H_A is estimated at 7.0×10^2 Oe, and the exchange field is $H_{ch} = 2.45 \times 10^6$ Oe [11–13]. The anisotropy parameter is defined as $g = H_A/H_{ch} = 2.86 \times 10^{-4}$, which allows one to assign Cr_2O_3 to the Heisenberg universality class with the possible crossover to the Ising critical behavior in the immediate vicinity of T_N. The crossover temperature t_{cr} [4] can be calculated by the formula $t_{cr} = g^{1/f}$, where f is the crossover exponent ($f = 1.25$ for the crossover from $n = 3$ to $n = 1$). In our case, $t_{cr} = 1.46 \times 10^{-3}$.

However, the majority of experimental investigations into the critical properties of Cr_2O_3 did not reveal the crossover to the Ising critical behavior [6–9]. Furthermore, the data on the susceptibility χ, which were obtained by the neutron scattering technique [6], indicate the divergence $\chi \sim |t|^{-\gamma}$ with the exponent $\gamma = 1.35 \pm 0.05$, whereas, according to [7], the exponent β is equal to 0.35. These results are in better agreement with the Heisenberg critical behavior. A similar conclusion can be drawn from the data on the heat capacity reported by Bruce and Cannell [9], according to which the Heisenberg critical behavior is observed in the temperature range $2.5 \times 10^{-4} \le t \le 9.0 \times 10^{-3}$, as judged from the critical exponent α of the heat capacity: $\alpha = -0.12 \pm 0.01$. However, the critical amplitude ratios ($A/A' = 0.56$), which were also determined in [9], best satisfy the Ising model. At the same time, as follows from the critical exponents of the heat capacity and the changes in the sound velocity, which, according to the theory, should be equal to each other, $\alpha = 0.14$ [8] and, hence, Cr_2O_3 should be considered the Ising magnet. The data obtained in subsequent measurements of the heat capacity [10], which were processed both with correction for scaling and without regard for this correction, led to $\alpha \approx -0.03$ in most cases. Marinelli *et al.* [10] also gave the value $\alpha \approx -0.12$, which is close to the theoretical estimate for the Heisenberg model. Unfortunately, it is practically impossible to establish the regularities of variations in the critical parameters from the results obtained by these authors, because, in their analysis, they changed all three parameters (t_{max}, t_{min}, and T_N) simultaneously. The same is also true for the values obtained by the authors of [10] for the critical exponent $\alpha = 0.10 \pm 0.02$ and the critical amplitude ratio $A/A' = 0.48 \pm 0.03$, which agree with the Ising model of the critical behavior.

3. EXPERIMENTAL TECHNIQUE

The sample of single-crystal Cr_2O_3 used in our measurements had the form of a disk 3 mm in diameter and 0.253 mm thick.

The heat capacity of a Cr_2O_3 single crystal was measured on a fully automated experimental setup designed for joint precise measurements of the heat capacity and thermal diffusion of thin samples. The experimental setup and measuring technique were described in detail in [14].

The rate of change in the sample temperature near the critical point did not exceed 9 mK/min. Periodic oscillations of the sample temperature at a frequency $f = 2$ Hz were achieved with a luminous flux of an incandescent lamp using a mechanical quartz stabilization chopper.

A junction of the chromel–constantan thermocouple designed for measuring temperature oscillations of the sample was prepared from hammered-out wires 25 mm in diameter and stuck with a BF-2 butvar–phenolic adhesive on the sample side not exposed to light. The amplitude of temperature oscillations did not exceed 5 mK, which is especially important in examining anomalous phenomena in the vicinity of the phase transition temperature.

Computer control of the measurements was performed with the HEAT-MASTER program compiled in Microsoft QuickBASIC [15].

4. RESULTS AND DISCUSSION

Figure 1 shows the temperature dependence of the heat capacity of a Cr_2O_3 single crystal in the vicinity of the phase transition point. These data correspond to the temperature range $T_N \pm 25$ K. As can be seen from this figure, the singular part of the heat capacity virtually coincides with the basis part at temperatures 50 K above or below T_N.

The temperature dependence of the heat capacity of Cr_2O_3 near the critical temperature T_N is depicted in Fig. 2.

The correct determination of the critical temperature is of crucial importance in the study of the critical properties. As a rule, the critical temperature does not coincide with maxima of the heat capacity C and the magnetic susceptibility χ [16]. Moreover, it should be remembered that, for a number of reasons, each specific sample has its own "critical" temperature. As a consequence, the calculations of the critical parameters

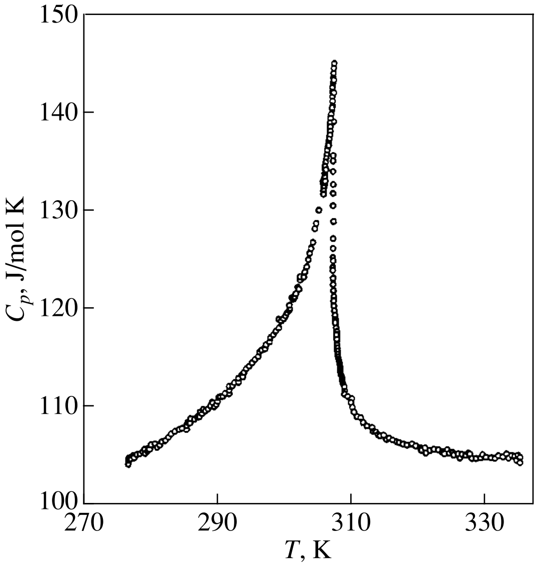

Fig. 1. Temperature dependence of the heat capacity C_p of a Cr_2O_3 antiferromagnet.

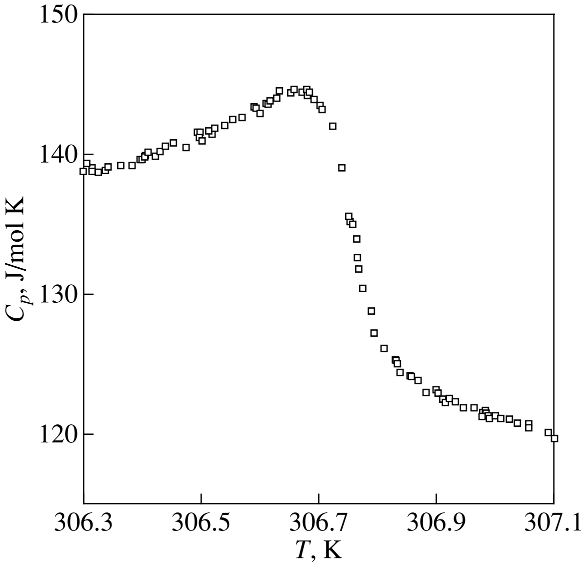

Fig. 2. Temperature dependence of the heat capacity of a Cr_2O_3 antiferromagnet near the critical temperature.

in which the critical temperature T_c (T_N) is determined from the maxima of C and (or) χ can give an incorrect description of the critical behavior.

In our case, the critical temperature T_c was determined relying on the prediction of the statical scaling that $\alpha = \alpha'$. In the approximate relationship, the T_N temperature was chosen near the maximum of the heat capacity in such a way that, at fixed values of $t_{\max}$ and $t_{\min}$, the exponents α and α' coincided with each other at the minimum values of the total root-mean-square deviation R to within the limits of error. The critical behavior of the heat capacity was approximated by the nonlinear least-squares technique. It was assumed that $t_{\max} = 3.0 \times 10^{-3}$ and $t_{\min} = 6 \times 10^{-6}$ and 1.85×10^{-4} at $T > T_N$ and $T < T_N$, respectively. The choice of these parameters was dictated by the fact that, in this case, the numerical value $\alpha = -0.10 \pm 0.02$ was closest to the theoretically predicted estimate $\alpha = -0.12$ [16, 17] for isotropic magnets (see Table 2, approximation 7 (A7)).

The temperature thus obtained, $T = T_N = 306.716$ K, was used as the critical value. In subsequent approximations, we varied only the parameters $t_{\min}$ and $t_{\max}$. It should be noted that both parameters ($t_{\min}$ and $t_{\max}$) were varied simultaneously only in two cases (Table 1, A4; Table 2, A8). This approach makes it possible to reveal the regularities of variations in the calculated parameters, which cannot be said of the results obtained in [9, 10]. Note also that, when approximating

Table 1. Results of the approximation of the heat capacity data without correction for scaling

Approximation	A1	A2	A3	A4
$t_{\max}$	8.0×10^{-3}	5.0×10^{-3}	3.0×10^{-3}	8.0×10^{-4}
$t_{\min}$ ($T < T_N$)	1.85×10^{-4}	1.85×10^{-4}	1.85×10^{-4}	1.85×10^{-4}
$t_{\min}$ ($T > T_N$)	6.5×10^{-6}	6.5×10^{-6}	6.5×10^{-6}	1.0×10^{-6}
T_N, K	306.716	306.716	306.716	306.716
α	-0.02 ± 0.02	-0.04 ± 0.02	-0.14 ± 0.02	0.05 ± 0.02
A', J/mol K	–5.8	–6.45	–5.09	5.41
A, J/mol K	–5.1	–5.39	–8.45	5.69
E, J/mol K	–166.0	154.7	148	149.1
B, J/mol K	197.1	186.3	167	174.6
B', J/mol K	176.3	169.0	163.3	170.2
A/A'	1.13 ± 0.06	1.27 ± 0.06	1.66	0.96
R	142	121	71.78	49.4

Table 2. Results of the approximation of the heat capacity data with correction for scaling

Approximation	A5	A6	A7	A8	A9	A10
$t_{\max}$	8.0×10^{-3}	5.0×10^{-3}	3.0×10^{-3}	1.0×10^{-3}	1.0×10^{-3}	8.0×10^{-4}
$t_{\min}$ $(T < T_N)$	1.85×10^{-4}	1.85×10^{-4}	1.85×10^{-4}	1.85×10^{-4}	1.85×10^{-4}	1.85×10^{-4}
$t_{\min}$ $(T > T_N)$	6.5×10^{-6}	6.5×10^{-6}	6.5×10^{-6}	3.0×10^{-6}	1.0×10^{-6}	1.0×10^{-6}
T_N, K	306.716	306.716	306.716	306.716	306.716	306.716
α	-0.03 ± 0.02	-0.06 ± 0.02	-0.10 ± 0.02	0.02	0.08 ± 0.02	0.09 ± 0.02
A', J/mol K	–2.89	–3.51	–9.19	2.17	5.57	5.68
A, J/mol K	–3.49	–4.43	–10.94	1.72	2.26	2.33
D', J/mol K	49.9	38.2	19.3	–1.3	14.3	19.1
D, J/mol K	2.65	2.36	2.1	–2.3	1.2	1.10
E, J/mol K	127.0	102.7	97.1	57.8	68.1	53.4
B, J/mol K	214.1	228	231.4	244.2	243.3	247.8
A/A'	1.21	1.26 ± 0.06	1.30 ± 0.06	0.79	0.41 ± 0.06	0.41 ± 0.06
R	135.8	105.3	84.0	51.3	53.9	47.3

data on the heat capacity in the vicinity of the critical point which is characterized by various "roundoff" effects (Fig. 2), we ignored points in the range $T_N \pm 30$ mK, because, according to our data, these effects fall in the range of 60 mK near T_N.

In [9, 10], the critical behavior of the heat capacity was approximated by the following relationships:

$$C_p = \frac{A}{\alpha}|t|^{-\alpha} + B + Et, \qquad (1)$$

$$C_p = \frac{A}{\alpha}|t|^{-\alpha}(1 + D|t|^{x}) + B + Et, \qquad (2)$$

where α, A, D, B, and E are fitting parameters at $T > T_N$. The same parameters but with the sign "prime" refer to the case when $T < T_N$. The parameters α, A, and D are the critical exponent of the heat capacity, the critical amplitude, and the amplitude of the correction for scaling, respectively. We used relationships (1) and (2) in data processing of our experiments.

The results of the approximation of experimental data with the use of relationship (1) are presented in Table 1. For the low-temperature phase, we performed the approximation relying on the prediction of the statical scaling that $\alpha = \alpha'$. In the case of relationship (1), we used A, α, B, and E as fitting parameters at $T > T_N$ and assumed that $\alpha = \alpha'$ and $E = E'$ at $T < T_N$. The obtained values of the critical exponent α in the approximations A1, A2, and A3 are negative, which is characteristic of the Heisenberg magnets, even though these exponents disagree in magnitude with the theoretical estimate of the Heisenberg model: $\alpha = -0.126$ [17, 18]. As follows from these data, the α value approaches the theoretical estimate as the upper limit $t_{\max}$ of the approximation interval decreases. The critical amplitude ratio A/A' in the A1 and A2 approximations is also slightly less than the theoretically predicted estimate for the Heisenberg model: $A/A' = 1.52$ [4, 5]. However, at the $t_{\max}$ value used in the A3 approximation, the critical amplitude ratio A/A' already exceeds the theoretical estimate and the critical exponent $\alpha = -0.14 \pm 0.02$ is rather close to the theoretical value $\alpha = -0.126$ [17, 18].

Table 2 presents the results obtained by processing the same data but with the use of relationship (2), i.e., with correction for scaling. In this case, the critical exponents α and critical amplitude ratios A/A' in the same ranges of reduced temperatures (A5, A6, and A7) are somewhat closer to the corresponding theoretical values. Note that the exponent $\alpha = -0.10$ virtually coincides with the theoretical estimate, to within the limits of error. However, the critical amplitude ratios A/A' are slightly less than the theoretical value.

All the approximations considered above, both without correction for scaling (A1, A2, and A3) and with this correction (A5, A6, and A7), demonstrate that any crossover is absent. A crossover from the Heisenberg to the Ising critical behavior for Cr_2O_3 is predicted at $t \approx 1.46 \times 10^{-3}$. However, the crossover exhibits sufficiently pronounced indications in the case when the lower limit $t_{\min}$ of the approximation interval shifts toward T_N or if the entire interval of the approximation is displaced. This can be seen from the data presented in Tables 1 (A4) and 2 (A8, A9, and A10). Note that, when the correction for scaling is disregarded (Table 1, A4) (even though the Ising critical behavior manifests itself), the critical exponent $\alpha = 0.05$ is inconsistent with the theoretically predicted value $\alpha = +0.109$ [17, 18]. The specific features of the initiation and the evolution of the crossover can be revealed from the data listed in Table 2 (A8, A9, and A10). It follows from these data that the crossover occurs when $t_{\min}$ decreases (A8). As the $t_{\min}$ value decreases further, the exponent $\alpha = 0.08$ closely approaches the theoretical estimate (A9). A further decrease in the upper limit $t_{\max}$ of the observation interval to 8.0×10^{-4} leaves the α value virtually unchanged.

It should be noted that such an approach, when among three parameters ($t_{\max}$, $t_{\min}$, and T_N) which can affect the critical parameters two parameters are fixed and one parameter is varied, makes it possible to determine the regularities of variations in the particular quantities.

Note also that the series of experiments performed under variations in the critical temperature in the range $T_N \pm 0.03$ K demonstrated the changes in all the universal critical parameters only within the limits of error which are given in Tables 1 and 2 for the corresponding quantities. The universal critical parameters obtained in this work are in reasonable agreement with the theoretical predictions or coincide with them, to within the limits of error. These results allow one to elucidate the regularities observed in the behavior of the heat capacity of the Cr_2O_3 antiferromagnet—a thermodynamic parameter which is least amenable to study in the critical region. Certain discrepancies can be associated with the experimental error, the inaccuracy in the determination of the critical temperature T_N, and the data processing procedure.

ACKNOWLEDGMENTS

We are grateful to I.K. Kamilov, Kh.K. Aliev[†], and A.B. Batdalov for their aid in performing this study and helpful discussions of the results.

REFERENCES

1. A. Z. Patashinskiĭ and V. L. Pokrovskiĭ, *Fluctuation Theory of Phase Transitions* (Pergamon, Oxford, 1979; Nauka, Moscow, 1982, 2nd ed.).
2. H. E. Stanley, *Introduction to Phase Transitions and Critical Phenomena* (Clarendon Press, Oxford, 1971; Mir, Moscow, 1973).
3. S. Ma, *Modern Theory of Critical Phenomena* (Benjamin, Reading, 1976; Mir, Moscow, 1980).
4. I. K. Kamilov and Kh. K. Aliev, *Statical Critical Phenomena in Magnetically Ordered Crystals* (Dagest. Nauchn. Tsentr Ross. Akad. Nauk, Makhachkala, 1993).
5. A. N. Vasil'ev, *Quantum-Zero Renormalization Group in the Theory of the Critical Behavior in Stochastic Dynamics* (Peterb. Inst. Yad. Fiz., St. Petersburg, 1998).
6. T. Riste and A. Wanic, Phys. Lett. **16**, 231 (1965).
7. E. Fisher, G. Gorodetsky, and S. Shtrikman, J. Phys. (Paris) **32**, C1-650 (1971).
8. A. Bachellerie and C. H. Frenois, J. Phys. (Paris) **35**, 30 (1974).
9. R. H. Bruce and D. S. Cannell, Phys. Rev. B **15** (9), 4451 (1977).
10. M. Marinelli, F. Mercury, U. Zamit, *et al.*, Phys. Rev. B **49** (14), 9523 (1994).
11. E. J. Samuelsen, M. T. Hutchings, and G. Shirane, Physica (Amsterdam) **48** (1), 13 (1970).
12. S. Foner, Phys. Rev. **130** (1), 183 (1963).
13. J. O. Artman, J. C. Murphy, and S. Foner, Phys. Rev. **138** (3A), 912 (1965).
14. Sh. B. Abdulvagidov, G. M. Shakhshaev, and I. K. Kamilov, Prib. Tekh. Éksp., No. 5, 134 (1996).
15. Sh. B. Abdulvagidov, *HEAT-MASTER* (Makhachkala, 1990–1999), Compiled in *Microsoft QuickBASIC*.
16. S. V. Vonsovskiĭ, *Magnetizm* (Nauka, Moscow, 1971; Wiley, New York, 1974).
17. J. J. C. Le Guillou and J. Zinn-Justin, J. Phys. Lett. **46**, L137 (1985).
18. S. A. Antonenko and A. I. Sokolov, Phys. Rev. E **51** (3), 1894 (1995).

Translated by O. Borovik-Romanova

[†] Deceased.

Physics of the Solid State, Vol. 43, No. 6, 2001, pp. 1108–1111. Translated from Fizika Tverdogo Tela, Vol. 43, No. 6, 2001, pp. 1072–1075.
Original Russian Text Copyright © 2001 by Iskhakov, Stolyar, Chekanova, Zhigalov.

Spin-Wave Spectroscopy Study of Spatial Magnetization Fluctuations in Metastable Nanocrystalline Films of Fe-Based Alloys

R. S. Iskhakov*, S. V. Stolyar, L. A. Chekanova*, and V. S. Zhigalov***

**Kirenskiĭ Institute of Physics, Siberian Division, Russian Academy of Sciences,*
Akademgorodok, Krasnoyarsk, 660036 Russia
***Krasnoyarsk State University, Krasnoyarsk, 660041 Russia*
e-mail: rauf@iph.krasnoyarsk.su

Received September 6, 2000; in final form, November 17, 2000

Abstract—The spectrum of standing spin waves is investigated in nanocrystalline Fe films prepared by the pulsed plasma-spraying method. The dispersion relation of these waves is determined in the wave-vector range $(0.2–3.2) \times 10^6$ cm^{-1} and is found to be affected by spatial magnetization fluctuations 100 Å in size. These fluctuations are supported as being due to the inhomogeneous distribution of C atoms in the atomic structure of nanocrystalline Fe films. © *2001 MAIK “Nauka/Interperiodica”.*

1. INTRODUCTION

The objective of this paper is to investigate magnetic inhomogeneities of metastable nanocrystalline films of Fe-based alloys prepared by the pulsed plasma-spraying (PPS) method. This method allows one to produce ferromagnetic supersaturated Fe(C) solid solutions in the form of films with local fcc (hcp) structure [1, 2]. Previously, Mössbauer spectra [^{57}Co(Cr) source] at room temperature were taken for these samples doped with the ^{57}Fe isotope [3]. The spectral lines of an as-prepared film are very broad, which is characteristic of iron in the ultradisperse or amorphous state. After annealing at $T = 470$ K for an hour, the spectral lines become narrower and can be reasonably approximated by two Zeeman sextets with hyperfine fields $H_1 = 211$ kOe and $H_2 = 189$ kOe. Therefore, there are two different environments of Fe atoms in the material under study; that is, the Fe films are magnetically inhomogeneous. It is not easy to investigate inhomogeneous ferromagnets, in particular, to determine which parameter fluctuates [the exchange constant $\alpha(r)$, the saturation magnetization $M(r)$, the anisotropy constant $\beta(r)$, etc.] and to measure the correlation length r^* of the fluctuating parameter. Information on magnetic inhomogenety types and on their space scale can be derived from spin-wave spectra.

Theory predicts (and numerous experiments reveal) that the spectrum of spin waves in ferromagnetic films consists of several separate dispersion curves $\omega(k_n, \chi)$. The dependence of the frequency ω on the wave vector χ for waves propagating in the plane of a film can be examined experimentally by Brillouin scattering. In the case of $\chi = 0$, the spectrum characterizes standing (across the film thickness) spin waves, which can be examined experimentally by the spin-wave resonance (SWR) method. The resonance frequencies for these spin waves are determined both by the average values of the magnetic parameters of the ferromagnetic film at hand and by the fluctuations of these parameters.

At the present time, two types of dispersion curves $\omega(k)$ (associated with two types of magnetic inhomogeneities) have been predicted theoretically and discovered experimentally in thin ferromagnetic films by the SWR method. Inhomogeneities of the first type are those characterized by an isotropic and homogeneous distribution of a fluctuating parameter such as $\alpha(r)$; the $\omega(k)$ curve in this case has a break (change in slope) “due to exchange.” Inhomogeneities of the second type are fluctuations of $M(r)$, and the corresponding $\omega(k)$ curve has a break “due to magnetization.” The dispersion relation for spin waves in such inhomogeneous systems has the form [4, 5]

$$\omega(k) = \omega_0 + \langle \alpha M \rangle g k^2 (1 - \gamma_i^2 J_i(k)), \qquad (1)$$

where ω_0/g is the internal field of the ferromagnet; $i = \alpha, M$; and $\gamma_i^2 = (\Delta_i/i)^2$ is the strength of the fluctuating parameter i. The functions $J_\alpha(k)$ and $J_m(k)$ differ markedly near a characteristic wave vector $k^* = 1/r_i$, which is determined by the correlation length of magnetic inhomogeneities r_i; specifically, in the vicinity of k^*, the function J_α increases sharply (from 1/3 to 5/4), whereas the function J_m sharply decreases (from 1/2 to 0), and only in the region of $k = 2k^*$ does J_m start to increase (from 0 to 5/4). The difference in the behavior of $J_\alpha(k)$ and $J_m(k)$ in the region of $k \sim k^*$ allows one to experimentally reveal the dominant fluctuating parameter of the spin system of an inhomogeneous ferromagnetic alloy (α or M) and to determine the correlation length of this parameter. This experimental identification can be made by spin-wave spectroscopy. Many recent SWR studies have revealed that the spin-wave dispersion relations in ferromagnetic films of amorphous alloys and inhomogeneous supersaturated solid solutions are associated with both α and M fluctuations. It was found that fluctuations of α and M are due to chemical inhomogeneities; these inhomogeneities give rise to spatial fluctuations of the exchange parameter α in inhomogeneous alloys of the transition metal–metalloid type (CoP [6], FeB [7]) and to fluctuations of the magnitude of the magnetization M in transition metal–transition metal alloys (CoZr [8], FeZr [9]).

2. SAMPLES AND EXPERIMENTAL TECHNIQUE

Nanocrystalline films of $Fe_{80}C_{20}$ and $Fe_{74}C_{20}B_6$ alloys are prepared by the PPS method in vacuum with a residual gas pressure of $P_0 = 5.5 \times 10^{-6}$ mm Hg. The substrates are made of glass. The films ranged in thickness from 300 to 3000 Å. The electronic and chemical structures of the films were determined from photoelectron and Auger spectra measured with a photoelectron spectrometer (with Mg anode) at the Institute of Semiconductor Physics (Siberian Division, Russian Academy of Sciences). The SWR spectra of nanocrystalline Fe films were examined with a standard x-band spectrometer (f = 9.2 GHz) at room temperature. These SWR spectra are presented in [2], where the boundary conditions for the magnetization of these films are also discussed. Here, we merely point out that, in the films under study, antisymmetric boundary conditions are realized for which the relation between the mode index of the SWR spectrum and the wave vector **k** of a standing spin wave has the form $k_n = \pi n/d$ (with n = 1, 2, 3, … and d being the film thickness) and the resonance fields of the SWR peaks are given by

$$H_n = \omega/\gamma + 4\pi M - \eta^{\text{eff}} k_n^2. \qquad (2)$$

Using Eq. (2), the effective exchange stiffness η^{eff} ($\eta = \alpha M$) is calculated numerically from the formula

$$\eta^{\text{eff}}(k) = (d/\pi)^2 (H_1 - H_2)/(n^2 - 1). \qquad (3)$$

A correlation is made between the $\eta^{\text{eff}}(k)$ dependence thus found and the theoretical dependence $n^{\text{eff}} = \langle\eta\rangle(1 - \gamma_i^2 J_i(k))$ (see Eq. (1) and [4, 5]) with the aim of determining the dominant fluctuating magnetic parameter i (α or M) and the correlation length r^*.

3. EXPERIMENTAL RESULTS AND DISCUSSION

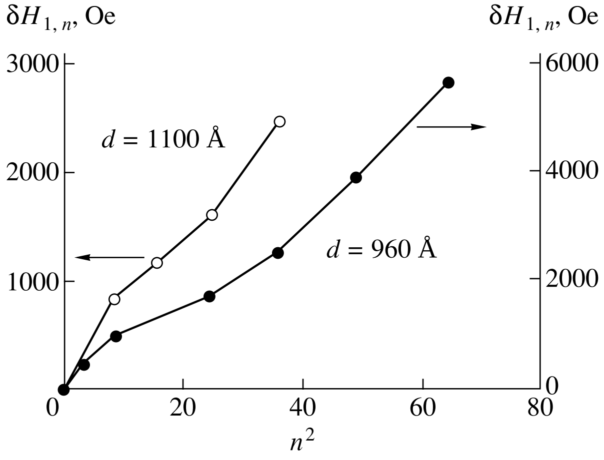

Fig. 1. Difference in the resonance fields of SWR peaks $\delta H_{1,n} = H_1 - H_n$ as a function of n^2 for two $Fe_{74}C_{20}B_6$ alloy films differing in thickness (n is the peak index).

Let us first discuss the experimental SWR spectra of $Fe_{74}C_{20}B_6$ films. Figure 1 shows the experimental dependence of $\delta H_{1,n} = H_1 - H_n$ on n^2 for two films of different thickness, d_1 = 1100 Å and d_2 = 960 Å. It can be seen from Fig. 1 that the $\delta H_{1,n}(n^2) \sim \omega(k^2)$ dispersion curve has a break in the long-wavelength range of the SWR spectrum: the effective exchange stiffness η^{eff} sharply decreases ($\eta_1 > \eta_2$). Therefore, according to the classification introduced in [4], this break is due to exchange. By measuring the coordinate of the break point n_i, one can determine the critical wave vector ($k = \pi n/d$); in this case, we have $k_\alpha = 1.1 \times 10^6$ cm^{-1} for both films. As the wave vector **k** increases further, one more change in the effective exchange stiffness η occurs: this time, η sharply increases ($\eta_2 < \eta_3$) and, therefore, the break is due to magnetization (in the classification of [4]). For the $Fe_{74}C_{20}B_6$ alloy at hand, the corresponding wave vector is $k_m = 1.85 \times 10^6$ cm^{-1}. As indicated above, the $\omega(k)$ dispersion curve affected by fluctuations of M and having a break due to magnetization must have two characteristic features at the wave vectors k_m and $2k_m$. In the case in question, the experimental $\delta H_{1,n}(n^2)$ curve corresponds to the portion of the theoretical $\omega(k^2)$ dispersion curve in the range of $k < 2k_m$, because the boundary wave vector k_b, corresponding to the extreme peak of the SWR spectrum, is $k_b \sim 2.2 \times 10^6$ cm^{-1} and, therefore, $k_b/k_m < 2$.

The observation of breaks of two types (those being due to exchange and to magnetization) in the dispersion curves of films of the $Fe_{74}C_{20}B_6$ alloy under study is a surprising experimental finding. The point is that this alloy belongs to the class of transition metal–metalloid alloys, the dispersion curves of which were observed earlier to show only breaks due to exchange. For instance, in films of alloys CoP [6], FeB [7], etc., the experimental $\delta H_{1,n}(n^2)$ curves obtained by the SWR method are affected only by fluctuations of the exchange constant α. For this reason, we attribute the break due to magnetization observed in the metastable

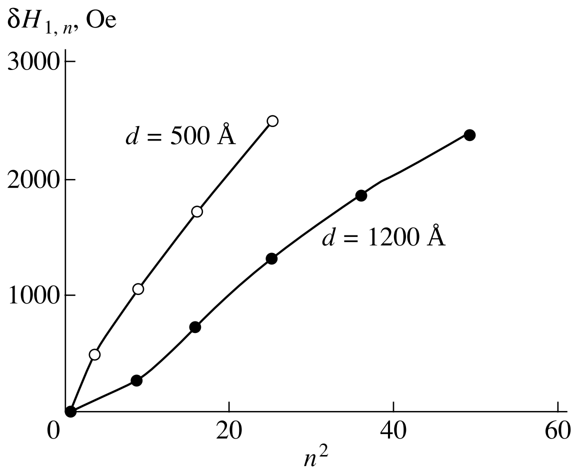

Fig. 2. Difference in the resonance fields of SWR peaks $\delta H_{1,n} = H_1 - H_n$ as a function of n^2 for two $Fe_{80}C_{20}$ alloy films differing in thickness.

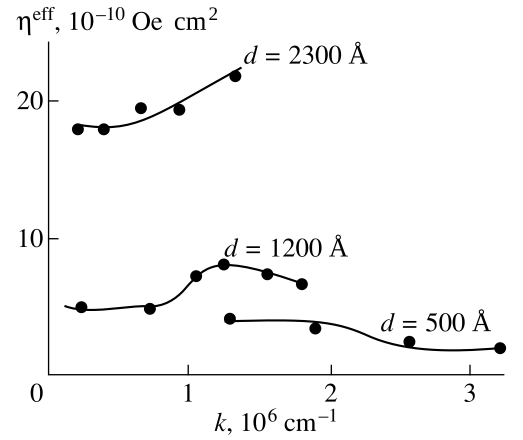

Fig. 3. Effective exchange stiffness η^{eff} as a function of wave vector **k** for $Fe_{80}C_{20}$ alloy films differing in thickness.

$Fe_{74}C_{20}B_6$ alloy to the presence of atoms of another metalloid, carbon, in the alloy. Further investigation provided support for this assumption.

Figure 2 shows the dependences of the resonance fields $\delta H_{1,n}$ on the spin-wave mode index squared n^2 for SWR spectra of two Fe(C) films differing in thickness (d_1 = 1200 Å, d_2 = 500 Å). It can be seen that the $\delta H_{1,n}(n^2) \sim \omega(k^2)$ dispersion curve of the d_1 = 1200 Å thick film has two characteristic features (breaks) at wave vectors $k' = 0.99 \times 10^6$ cm^{-1} and $k'' = 1.6 \times 10^6$ cm^{-1}. The exchange stiffness sharply increases near the characteristic wave vector k' ($\eta_1 < \eta_2$) and sharply decreases near the wave vector k'' ($\eta_2 > \eta_3$). This behavior of the $\delta H_{1,n}(n^2)$ curve suggests that the dispersion relation of spin waves in the d_1 = 1200 Å thick film of Fe(C) is affected by fluctuations of the magnetization M. This conclusion is also supported by the fact that the numerical values of the characteristic wave vectors k' and k'' approximately satisfy the theoretically predicted relation $k'' = 2k'$ (see [4]). The value of the wave vector $k' = k_m$ is determined by the scale of spatial inhomogeneities of the magnetization M in the Fe(C) alloy at hand, $k_m = 1/r_m$, where r_m is the correlation length of fluctuations of M. For films of the Fe(C) alloy, r_m is estimated to be 100 Å. It should be noted that the $\delta H_{1,n}(n^2)$ curve for the thinner (500 Å thick) film exhibits a break which is seemingly due to exchange, but in actual fact, this curve is affected by fluctuations of magnetization in the inhomogeneous Fe(C) alloy. From Fig. 2, it is seen that this $\delta H_{1,n}(n^2)$ curve has a feature near the wave vector $k' = 1.57 \times 10^6$ cm^{-1}; namely, the exchange stiffness sharply decreases in the vicinity of this point ($\eta_1 > \eta_2$). However, the range of observable wave vectors $k_n = \pi n/d$ in the SWR spectrum of the d = 500 Å thick film is such that the wave vector k_m, which characterizes the scale of fluctuations of the magnetization M, satisfies the inequalities $k_1 < k_m < k_2$. Indeed, we have $k_1 = 0.63 \times 10^6$ cm^{-1}, $k_2 = 1.26 \times 10^6$ cm^{-1}, and $k_m = 1 \times 10^6$ cm^{-1}. Therefore, the feature observed in the $\delta H_{1,n}(n^2)$ curve is basically determined by the feature of the $J_m(k)$ function in the vicinity of $2k_m$, which is also supported by the fact that the characteristic wave vector $k' = 1.57 \times 10^6$ cm^{-1} is close to the wave vector k'' at which a break is observed in the dispersion curve for the d_1 = 1200 Å thick film. We note that a similar situation was observed [4] to occur with amorphous $Co_{93}Zr_5P_2$ alloy films differing in thickness. The entire $\omega(k^2)$ dispersion curve affected by fluctuations of M and exhibiting breaks due to magnetization was first observed experimentally for those transition metal–metal alloy films.

Thus, for films of the metastable Fe(C) alloy, which is an interstitial solid solution, the experimental $\delta H_{1,n}(n^2)$ dependence agrees well with the theoretically predicted $\omega(k^2)$ dependence affected by magnetization fluctuations [4, 5]; in particular, the experimental curve exhibits breaks (changes in slope) due to magnetization. We note that the $\omega(k^2)$ curve for this Fe(C) alloy differs in character from those for analogous alloys, substitutional solid solutions, of the transition metal–metalloid system (FeB, CoP, etc.). In those alloys, the dispersion curves exhibited only breaks due to exchange.

Experimental $\delta H_{1,n}(n^2)$ dependences also allow one to calculate some other characteristics of magnetic inhomogeneities, such as the strength of fluctuations γ_m^2 and the average $\langle\eta\rangle$. The effective exchange stiffness $\eta^{eff}(k)$ calculated from the resonance fields $H_n(n^2)$ by Eq. (2) is shown in Fig. 3 for free films differing in thickness (d_1 = 500 Å, d_2 = 1200 Å, d_3 = 2300 Å). The character of the $\eta^{eff}(k)$ dependence suggests that only fluctuations of M are significant in the Fe(C) alloy. The wave vector defined by the relation $r_m = 1/k_m$ is the

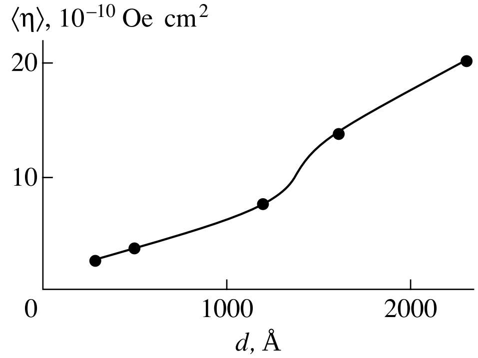

Fig. 4. Average exchange stiffness ⟨η⟩ as a function of the film thickness for an $Fe_{80}C_{20}$ alloy.

same ($k_m = 10^6$ cm^{-1}) for all films of the alloy under study, irrespective of their thickness. From theoretical expressions for the function $J_m(k)$ in Eq. (1) (see [4, 5]), it follows that the effective exchange stiffness $\eta^{\text{eff}}(k)$ measured in the wave-vector range $k_m < k < 2k_m$ is the average exchange stiffness ⟨η⟩ of the film under study. Figure 4 shows ⟨η⟩ calculated in this range of wave vectors **k** as a function of *d* for films of the Fe(C) alloy. From Fig. 4, it is seen that for the films prepared by the method indicated in Section 2, the average ⟨η⟩ depends on the film thickness *d*, which was not observed earlier [6–9]. The reason for this dependence is the following. The kinetics of solidification of an Fe(C) condensate depends on the cooling rate of the condensate, which, in turn, depends on its thickness. Therefore, the phase composition of the Fe films under study (fcc-Fe(C), hcp-Fe(C), cementite Fe_3C [1, 2]) varies with film thickness. This conclusion was supported by the findings of [10], where, by means of Mössbauer spectroscopy based on conversion electrons, it was shown that the phase composition of an Fe(C) film varies across the film. Given the average ⟨η⟩, the strength of magnetization fluctuations can be calculated from Eq. (1); the result is $\gamma_m^2 = 0.6$. It should be noted that, for Fe(C) films, γ_m^2 is independent of the film thickness. Thus, from experimental $\delta H_{1,n}(n^2)$ dependences, we calculated the correlation length r_m and made estimates of the average exchange stiffness ⟨η⟩ and the strength γ_m^2 of fluctuations of *M* in films of metastable Fe(C) alloys. It is found that in films prepared by the PPS method, γ_m^2 and r_m are independent of the thickness of the film, while ⟨η⟩ is thickness dependent. The latter property distinguishes these films from some other films, e.g., from those of CoP [6], in which all three quantities do not depend on the film thickness.

4. CONCLUSION

Thus, in this paper, the dispersion relation of spin waves in films of a nanocrystalline Fe(C) alloy is measured by the SWR method and found to be affected by spatial magnetization fluctuations approximately 100 Å in size. Fluctuations of magnetization *M* are likely to be due to the inhomogeneous distribution of C atoms in the atomic structure of nanocrystalline Fe films. The dispersion relation of the type indicated above distinguishes Fe(C) alloys, which are interstitial solid solutions, from analogous alloys of the transition metal (Fe, Co)–metalloid (B, P, Si) system, which are substitutional solid solutions and in which fluctuations of the exchange constant dominate.

REFERENCES

1. R. S. Iskhakov, S. V. Komogortsev, S. V. Stolyar, *et al.*, Fiz. Met. Metalloved. **88** (3), 56 (1999).
2. R. S. Iskhakov, S. V. Komogortsev, S. V. Stolyar, *et al.*, Pis'ma Zh. Éksp. Teor. Fiz. **70** (11), 727 (1999) [JETP Lett. **70**, 736 (1999)].
3. G. I. Frolov, O. A. Bayukov, V. S. Zhigalov, *et al.*, Pis'ma Zh. Éksp. Teor. Fiz. **61** (1), 61 (1995) [JETP Lett. **61**, 63 (1995)].
4. V. A. Ignatchenko and R. S. Iskhakov, Zh. Éksp. Teor. Fiz. **75** (4), 1438 (1978) [Sov. Phys. JETP **48**, 726 (1978)]; R. S. Iskhakov, L. A. Chekanova, S. Ya. Kiparisov, I. A. Turpanov, I. V. Bogomaz, and A. S. Chekanov, Preprint No. 283F, Inst. Fiziki im. L. V. Kirenskogo Sib. Otd. Akad. Nauk SSSR (Kirenskiĭ Institute of Physics, Siberian Division, Russian Academy of Sciences, Krasnoyarsk, 1984).
5. M. V. Medvedev, Fiz. Met. Metalloved. **67** (5), 876 (1989).
6. V. A. Ignatchenko, R. S. Iskhakov, L. A. Chekanova, and N. S. Chistyakov, Zh. Éksp. Teor. Fiz. **75** (2), 876 (1978) [Sov. Phys. JETP **48**, 328 (1978)].
7. L. J. Maksimowicz and R. Zuberek, J. Magn. Magn. Mater. **58**, 303 (1986).
8. R. S. Iskhakov, M. M. Brushtunov, and A. S. Chekanov, Fiz. Tverd. Tela (Leningrad) **29** (9), 1214 (1987) [Sov. Phys. Solid State **29**, 1553 (1987)].
9. R. S. Iskhakov, M. M. Brushtunov, A. G. Narmonev, and I. A. Turpanov, Fiz. Met. Metalloved. **79** (5), 122 (1995).
10. A. A. Novakova, E. A. Gan'schina, T. Yu. Kiseleva, *et al.*, in *Abstracts of the Moscow International Symposium on Magnetism, Moscow, 1999*, p. 259.

Translated by Yu. Epifanov

Physics of the Solid State, Vol. 43, No. 6, 2001, pp. 1112–1116. Translated from Fizika Tverdogo Tela, Vol. 43, No. 6, 2001, pp. 1076–1079.
Original Russian Text Copyright © 2001 by Korotkov.

MAGNETISM AND FERROELECTRICITY

Proton Ordering and Spontaneous Polarization in Mixed KDP–ADP Crystals

L. N. Korotkov
Voronezh State Technical University, Moskovskiĭ pr. 14, Voronezh, 394026 Russia
e-mail: l_korotkov@mail.ru

Received May 15, 2000; in final form, September 28, 2000

Abstract—Temperature dependences of the transverse permittivity of mixed $K_{1-x}(NH_4)_xH_2PO_4$ crystals ($x \approx 0$, 0.04, 0.09, and 0.19) are experimentally investigated with the aim of determining the parameter P_A that characterizes proton ordering in the region of the ferroelectric phase transition. A comparison of the temperature dependences of the P_A parameter and spontaneous polarization shows that the spontaneous polarization is preceded by a partial ordering of protons in all the compositions studied. It is found that the crystals with a high ammonium content are characterized by a weaker effect of the lattice polarization on the proton ordering. *© 2001 MAIK “Nauka/Interperiodica”.*

Potassium dihydrogen phosphate (KH_2PO_4) is a well-known crystal of the KDP family [1]. In this crystal, a decrease in temperature is accompanied by the ferroelectric phase transition due to proton ordering over the O–H···O hydrogen bonds. It has been conclusively established that, in the vicinity of the transition temperature ($T_C \cong 122$ K), the protons in this crystal predominantly form configurations in which two of them are located either at the top of each PO_4 tetrahedron or at its bottom. In this case, one of the coupled proton–lattice modes becomes unstable, thus giving rise to spontaneous polarization (P_s) along the tetragonal axis *c* of the crystal. The oxygen proton configurations formed upon phase transition correspond to the antiferroelectric-type ordering of dipole moments in the **ab** plane perpendicular to the polar axis. Therefore, the phase transition in potassium dihydrogen phosphate can be considered ferroelectric and antiferroelectric simultaneously [2].

The interaction between the proton subsystem and the soft lattice mode plays an important role in the phase transition. However, discussions of its details persist to date [1, 3, 4]. Certain information on the specific features of this interaction can be obtained from comparison of the temperature dependences of the parameter characterizing proton ordering and the spontaneous polarization P_s, whose magnitude varies linearly with microscopic displacements of “heavy” ions.

Single crystals of $K_{1-x}(NH_4)_xH_2PO_4$ (KDP–ADP) solid solutions are well suited as objects of investigation. This is explained by the fact that, in these structures, protons of the ammonium groups substituting for K^+ ions interact with oxygens of the nearest neighbor PO_4 tetrahedra and, hence, disturb the ordering of “oxygen” protons [5]. As a result, the temperature of the phase transition decreases and the phase transition itself is completely suppressed at a critical concentration $x_c \cong 0.20$ [6, 7]. This circumstance can be used for analyzing the interrelation between the spontaneous polarization and the parameter of proton ordering as a function of the quantity affecting the state of the proton subsystem. This analysis was the primary goal of the present work.

A phenomenological model of an antiferroelectric crystal consisting of two interpenetrating sublattices was described by Kittel [8]. According to this model, each sublattice below the antiferroelectric transition temperature is characterized by dipole moments which have the same magnitude and are aligned in such a way that their total moment is equal to zero. In the case of an order–disorder transition, the polarizations of these sublattices (P_A and P_B, respectively) are proportional to the parameter of proton ordering. The latter quantity is defined as the difference between the probabilities of finding a proton in one of the minima of the double-well potential of the O–H···O bond.

The free energy (A) of the crystal can be represented in the form [8]

$$A = A_0 + f(P_A^2 + P_B^2) + gP_AP_B + h(P_A^4 + P_B^4) + \dots, \tag{1}$$

where A_0 is the free energy component, which does not depend on the sublattice polarization (P_A or P_B), and *f*, *g*, and *h* are the coefficients of the expansion of the crystal free energy into a series.

The relationship between the permittivity (ε) and the polarization of the sublattice can be written in the following form [1, 8]: $[(\varepsilon - 1)\varepsilon_0]^{-1} = \partial^2 A/\partial P_A^2$, where ε_0 is the absolute permittivity. It is generally assumed that the coefficients *g* and *h* vary only slightly with temperature and, in the vicinity of T_C, $f = q + \lambda(T - T_C)$, where q and λ are constants. With this assumption and under the conditions of a weak measuring field, we finally obtain the following relationship:

$$P_A = \sqrt{\frac{1}{12\varepsilon_0 h}\left[\frac{1}{\varepsilon(T) - \varepsilon_\infty} - \frac{1}{C}(\Theta - T)\right]}. \qquad (2)$$

Here, $\Theta = T_C - q/\lambda$ is the Curie–Weiss temperature, $C = 1/\lambda\varepsilon_0$ is the Curie–Weiss constant, and ε_∞ is the ε component, which is independent of the P_A parameter and temperature.

Therefore, the dependence $P_A(T)$ can be determined from the dielectric measurements of the crystals.

Experiments were carried out with KDP–ADP crystals at concentrations $x \approx 0$, 0.04, 0.09, and 0.19. Samples in the form of rectangular plates ~6 × 7 × 0.7 mm in size were cut from the single crystals used earlier in the P_s measurements in [9]. The electrodes located on the sample surfaces perpendicular to the **a** axis were prepared by thermal evaporation of silver under vacuum.

A sample of the nominally pure KDP ($x = 0$) crystals had the form of a rectangular parallelepiped 3 × 3 × 15 mm in size. Electrodes in the form of strips ~1 mm wide were applied on all the four longest faces, which provided simultaneous measurement of the permittivities along the polar and nonpolar directions (ε_{33} and ε_{11}, respectively).

In the course of experiments, the samples were placed in a cryostat in which the temperature ranged from 20 to 300 K and was controlled within an error of no more than ±0.05 K. The real and imaginary components of the permittivity were measured using a capacitance bridge at a frequency of 1.59 kHz and a measuring field amplitude of ~0.5 V/cm under heating (cooling) at a rate of ~1 K/min. Near T_C, the heating rate decreased to ~0.1 K/min; in this case, the calculated nonuniformity of the sample "warming-up" did not exceed ±0.005 K. For simultaneous measurements of the permittivities ε_{33} and ε_{11} of the KDP crystal, we additionally used one more capacitance bridge. For the second bridge, the measuring field amplitude was equal to 0.2 V/cm and the frequency was 3 kHz.

The results of the ε_{11} measurements for compositions with $x \approx 0.04$, 0.09, and 0.19 are shown in Fig. 1. It should be noted that the dependences $\varepsilon_{11}(T)$ measured during heating of the sample virtually coincide with those obtained in the course of its cooling (for this reason, the latter curves are not shown in this figure). Hence, the observed dependences $\varepsilon_{11}(T)$ can be treated as equilibrium curves. At the same time, it is clear that the measurements performed were of a quasi-statical character, because the anomalies in the temperature dependences of the imaginary components of the permittivity that would indicate the ε_{11} dielectric dispersion were not observed in the course of the experiments.

Above T_C, the $\varepsilon_{11}(T)$ dependences follow the Curie–Weiss law over a wide temperature range: $\varepsilon_{11}(T) = \varepsilon_\infty + C/(T - \Theta)$ with the negative Curie–Weiss temperature, as is the case in antiferroelectric ammonium dihydrogen phosphate [11].

The best approximation of the experimental results for compositions with concentrations $x \approx 0.04$, 0.09, and 0.19 was achieved with the following parameters: $\Theta \cong -235$, -240, and -251 K and $C \cong 18770$, 19740, and 19100 K, respectively. For all compositions, $\varepsilon_\infty \cong 8 \pm 2$.

The temperature dependences of the P_A parameter were determined from the results of the ε_{11} measurements according to formula (2). Figure 2 displays the normalized temperature dependences of the P_A parameter and spontaneous polarization (the temperature dependences of the spontaneous polarization were obtained earlier in [9]).

When normalizing the above dependences, we took into account the following reasoning. According to the existing concepts [1], in protonated crystals of the KDP type, the probability of localizing a proton in one of the minima of the double-well potential of the O–H···O bond is universally less than unity due to the tunneling effect. For a deuterated potassium dihydrogen phosphate (DKDP), in which the tunneling effect is noticeably weaker, it can be expected that, at $T \longrightarrow 0$ K, the probability of the particle localization will be close to unity. Hence, the normalization was performed with respect to the spontaneous polarization and the proton ordering parameter (P_s^D and P_A^D, respectively), which

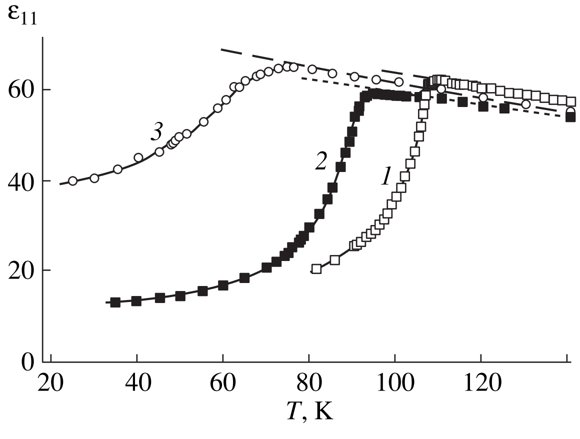

Fig. 1. Temperature dependences of ε_{11} for mixed $K_{1-x}(NH_4)_xH_2PO_4$ crystals with concentrations $x \approx$ (*1*) 0.04, (*2*) 0.09, and (*3*) 0.19. Dashed lines show the approximation of the $\varepsilon_{11}(T)$ dependences according to the Curie–Weiss law.

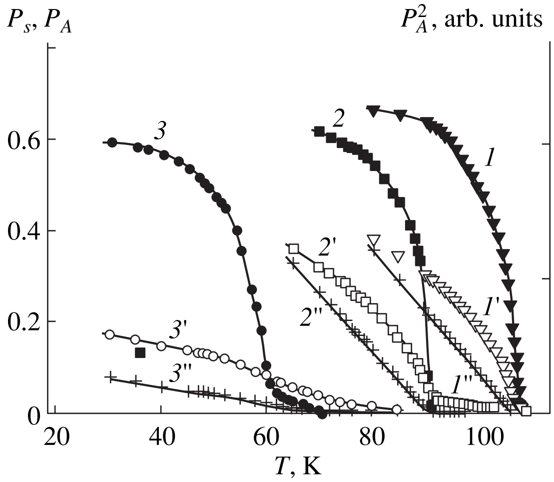

Fig. 2. Temperature dependences of (*1–3*) P_s, (*1'–3'*) P_A, and (*1''–3''*) P_A^2 for $K_{1-x}(NH_4)_xH_2PO_4$ crystals with concentrations $x \approx$ (*1, 1', 1''*) 0.04, (*2, 2', 2''*) 0.09, and (*3, 3', 3''*) 0.19.

were measured for a KDKP crystal in the saturation range of these quantities at temperatures far below T_C.

The numerical value of P_s^D was taken from [1], and P_A^D was calculated by formula (2) taking into account the results of the dielectric measurements [10]. The calculations were carried out under the assumption that the h parameter only slightly depends on the composition.

Note that relationship (1) predicts the temperature dependence of the sublattice polarization in the following form: $P_A \sim (T_C - T)^{1/2}$ [1, 8]; this actually holds for compositions with ammonium concentrations $x \approx 0.04$ and 0.09. This is confirmed by the linear dependences $P_A^2(T)$ (Fig. 2). Thus, formula (2) provides a correct description of the $P_A(T)$ dependence. The deviation of the $P_A(T)$ dependence from the law $(T_C - T)^{1/2}$, which is observed for the crystal with a concentration $x \cong 0.19$, can be explained by the considerable smearing of the phase transition for this composition [11].

It can be seen from Fig. 2 that a certain correlation of the dependences $P_A(T)$ and $P_s(T)$ is observed for all the crystals under investigation. In particular, this correlation manifests itself in the fact that the saturation portions of these curves at $T \ll T_C$ coincide with the portions of "rapid" variations in these dependences near the corresponding phase transition temperatures.

A comparison of P_A and P_s at different compositions in the saturation regions (hereafter, these quantities will be designated as P_A^* and P_s^*, respectively) shows that both P_A^* and P_s^* decrease with an increase in x. It should be mentioned that an increase in the concentration x is accompanied by a more rapid decrease in the P_A^* parameter as compared to P_s^*.

It is worth noting that the relatively large value of P_s^* for the crystal with $x \approx 0.19$ corresponds to a proton ordering parameter which is considerably smaller than that for compositions with $x \approx 0.04$ and 0.09. This implies that the effect of the "lattice" polarization on the proton ordering in the ferroelectric compositions of mixed KDP–ADP crystals becomes weaker when the concentration of the second component increases. This circumstance provides an explanation of the fact that the thermal hysteresis of ε_{11} is absent in the experimental dependences despite the pronounced hystereses in T_C, ε_{33}, and P_s, which were observed under cyclic variations in temperature in the vicinity of the phase transition point for both the objects under investigation in [12, 13] and the ferroelectric compositions of the related system $Rb_{1-x}(NH_4)_xH_2PO_4$ in [14, 15].

It can be assumed that, in the compositions with a concentration $x \longrightarrow x_c$, the stabilization of the ferroelectric phase is achieved primarily through the interactions between dipole moments aligned along the polar axis, which are responsible for the condensation of the soft optical mode, as was predicted in [4].

An increase in the ammonium concentration in mixed crystals is accompanied by a decrease in the slope of the $P_A(T)$ and $P_s(T)$ curves as the phase transition point is approached from below. The influence of the composition on the $P_A(T)$ curves is especially pronounced; in all cases, the P_A parameter becomes nonzero at higher temperatures as compared to those for the corresponding parameter P_s (see Fig. 2).

A possible reason for the existence of a nonzero parameter P_A at $T \gg T_C$ in the KDP–ADP systems could be the deformation of the double-well potential of the O–H···O hydrogen bond under the action of random fields [16], which can be due to nonequivalent substitutions of the ammonium groups for K^+ ions.

For nominally pure potassium dihydrogen phosphate, this reason is absent. At the same time, the proton ordering in KDP crystals, which is identified from the dielectric measurements, is observed at temperatures slightly above the ferroelectric phase transition point that corresponds to the peak of ε_{33}. This can be clearly seen in Fig. 3. This figure demonstrates the dependences $\varepsilon_{11}^0(T)$ and $\varepsilon_{33}^0(T)$, which were measured simultaneously under the aforementioned conditions. (The superscript "0" indicates that these curves slightly differ from the true dependences due to edge effects, which can noticeably manifest themselves for the given shape of the sample.) The measured quantities can be written as $\varepsilon_{11}^0 \cong \varepsilon_{11} + q\varepsilon_{33}$ and $\varepsilon_{33}^0 \cong r\varepsilon_{11} + \varepsilon_{33}$, where $q > 0$ and $r > 0$ are the coefficients specified by the sample geometry and the ratio between ε_{11} and ε_{33}. Since $\varepsilon_{11} \sim 10^2 \ll \varepsilon_{33} \sim 10^5$ for KDP at $T = T_C$ [1], the contri-

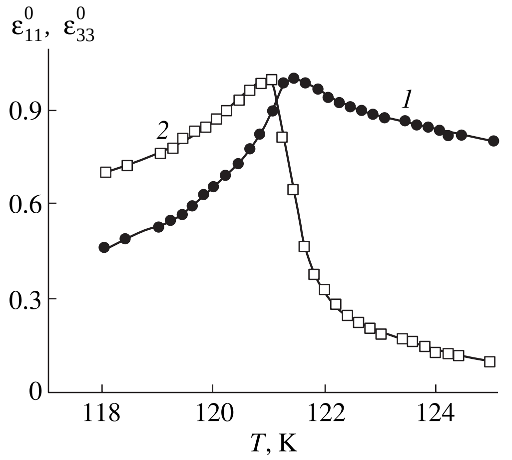

Fig. 3. Temperature dependences of (*1*) ε_{11}^0 and (*2*) ε_{33}^0 for a KH_2PO_4 crystal, normalized to the maximum values of ε_{11}^0 and ε_{33}^0.

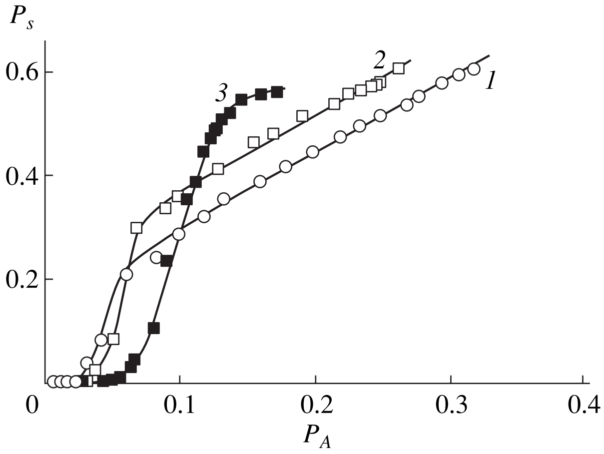

Fig. 4. Dependences of P_s on P_A for $K_{1-x}(NH_4)_xH_2PO_4$ crystals with concentrations $x \approx$ (*1*) 0.04, (*2*) 0.09, and (*3*) 0.19.

bution of ε_{11} to ε_{33}^0 can be ignored. On the other hand, the contribution of ε_{33} to the measured transverse permittivity can result in a distortion of the $\varepsilon_{11}(T)$ dependence in the vicinity of T_C and a shift of its maximum toward the peak of ε_{33}. However, it can be seen (Fig. 3) that the ε_{11}^0 maximum is observed at temperatures of approximately 0.5 K above T_C. This confirms the fact that the ferroelectric phase transition in crystals of the KDP family is preceded by a partial ordering of protons.

Let us now consider the ratio between the parameters P_A and P_s in more detail (Fig. 4). At small parameters of proton ordering ($P_A < 0.02$–0.05 at $T > T_C$), no spontaneous polarization occurs. A further increase in P_A ($T \leq T_C$) is accompanied by a rapid increase in P_s. For compositions with $x \approx 0.19$, the region of rapid increase in the spontaneous polarization is considerably wider than that for the crystals with ammonium concentrations $x \cong 0.04$ and 0.09 in both the P_s–P_A and P_s–T coordinates and the $P_s(P_A)$ dependence attains saturation at smaller P_A parameters.

For crystals with $x \cong 0.04$ and 0.09, a nearly jumpwise increase in P_s is observed in narrow ranges of P_A values ($0.03 \leq P_A \leq 0.07$) and temperatures ($T_C - T \approx 1$ K). At $P_A \approx 0.1$–0.3, which corresponds to the temperature range $T_C - T \approx 15$ K, the spontaneous polarization P_s increases directly with P_A (the proportionality coefficient ≈1.2 ± 0.1).

Note that the results obtained are in agreement with the modern concepts regarding the mechanism of ferroelectric phase transitions in KDP crystals. According to these concepts, the proton ordering serves as a “trigger mechanism” for displacement of heavy atoms. At the same time, it can be seen that, in the immediate vicinity of T_C, the linearity between the spontaneous polarization and the proton ordering parameter, which is postulated in a number of models (see, for example, [1]), is broken.

From the above results, it can be concluded that, in ferroelectric compositions of mixed KDP–ADP crystals, the phase transition is preceded by a partial ordering of the protons which is observed at temperatures slightly above T_C. For crystals with a relatively low ammonium concentration ($x \leq 0.09$), there is a narrow temperature range in the vicinity of T_C in which the spontaneous polarization P_s increases more rapidly than the proton ordering parameter. Below this range, the spontaneous polarization of the crystal varies almost linearly with the proton ordering parameter over a wide range of temperatures. In the crystals with an ammonium concentration close to the critical value, the weakening of the proton–lattice coupling takes place.

ACKNOWLEDGMENTS

The author is grateful to R.M. Fedosyuk for supplying the high-quality KDP–ADP single crystals used in the experiment.

This work was supported by the Russian Foundation for Basic Research, project no. 99-02-17230.

REFERENCES

1. M. E. Lines and A. M. Glass, *Principles and Applications of Ferroelectrics and Related Materials* (Oxford Univ. Press, Oxford, 1977; Mir, Moscow, 1981).
2. S. Havlin, E. Litov, and E. A. Uehling, Phys. Rev. B **9**, 1024 (1974).
3. A. V. Belushkin, Kristallografiya **42** (3), 549 (1997) [Crystallogr. Rep. **42**, 501 (1997)].

4. A. Bussmann-Holder and K. H. Michel, Phys. Rev. Lett. **80** (10), 2173 (1998).
5. E. Courtens, Ferroelectrics **72**, 69 (1987).
6. I. Ono, T. Hikita, and T. Ikeda, J. Phys. Soc. Jpn. **56**, 557 (1987).
7. S. A. Gridnev, L. N. Korotkov, S. P. Rogova, *et al.*, Ferroelectr. Lett. Sect. **13**, 67 (1991).
8. C. Kittel, Phys. Rev. **82**, 729 (1951).
9. S. A. Gridnev, L. N. Korotkov, L. A. Shuvalov, and R. M. Fedosyuk, Kristallografiya **41** (5), 891 (1996) [Crystallogr. Rep. **41**, 848 (1996)].
10. L. A. Shuvalov, I. S. Zheludev, A. V. Mnatsakanyan, *et al.*, Izv. Akad. Nauk SSSR, Ser. Fiz. **31**, 1919 (1967).
11. L. N. Korotkov, S. A. Gridnev, and R. M. Fedosyuk, Kristallografiya **44** (5), 881 (1999) [Crystallogr. Rep. **44**, 821 (1999)].
12. S. A. Gridnev, L. N. Korotkov, and L. A. Shuvalov, Ferroelectrics **175**, 107 (1996).
13. S. A. Gridnev, L. N. Korotkov, L. A. Shuvalov, and R. V. Fedosyuk, Ferroelectrics **144**, 157 (1993).
14. E. Courtens, Helv. Phys. Acta **56**, 705 (1983).
15. S. Amin, R. A. Cowley, and E. Courtens, Z. Phys. B **67**, 229 (1987).
16. R. Blinc, R. Pirc, B. Tadic, and J. Dolinesek, Ferroelectrics **78**, 27 (1988).

Translated by O. Borovik-Romanova

Physics of the Solid State, Vol. 43, No. 6, 2001, pp. 1117–1123. Translated from Fizika Tverdogo Tela, Vol. 43, No. 6, 2001, pp. 1080–1085.
Original Russian Text Copyright © 2001 by Topolov, Turik.

Interphase Boundaries and High Piezoelectric Activity of xPbTiO$_3$–(1 – x)Pb(Zn$_{1/3}$Nb$_{2/3}$)O$_3$ Crystals

V. Yu. Topolov and A. V. Turik
Rostov State University, ul. Zorge 5, Rostov-on-Don, 344090 Russia
e-mail: topolov@phys.md.runnet.ru
e-mail: turik@phys.md.runnet.ru

Received October 9, 2000

Abstract—Model concepts of the interphase boundaries whose displacements are capable of substantially affecting the piezoelectric properties of xPbTiO$_3$–(1 – x)Pb(Zn$_{1/3}$Nb$_{2/3}$)O$_3$ multidomain crystals in the $R3m$–$P4mm$ morphotropic region are developed. The contributions of the interphase boundaries Δd_{33} to the piezoelectric modulus d_{33} are determined, and the factors responsible for the large ratios $\Delta d_{33}/d_{33} \approx 0.5$–$0.9$ are analyzed. *© 2001 MAIK “Nauka/Interperiodica”.*

1. INTRODUCTION

Single- and polycrystal ferroactive solid solutions of the perovskite-type oxides xPbTiO$_3$–(1 – x)Pb(Zn$_{1/3}$Nb$_{2/3}$)O$_3$ (PT–PZN) are characterized by high values of the static permittivity and piezoelectric moduli in the $R3m$–$P4mm$ morphotropic region for $0.08 \lesssim x \lesssim 0.10$ [1–3]. The PT–PZN crystals in the range $0 \le x \le 0.09$ at room temperature (the $R3m$ phase) exhibit a high sensitivity of the piezoelectric, dielectric, and elastic properties to the orientation of the crystallographic axes of the sample [1, 3]. The influence of non-180-degree domain structures and their transformation on the piezoelectric activity of PT–PZN crystals, specifically of samples with a developed (001) face, in an electric field **E** parallel to the [001] direction of a perovskite lattice cell was discussed in experimental works [3–5].[1] However, as far as we know, the role of interphase boundaries in the evolution of the piezoelectric properties of similar crystals during morphotropic transitions has never been investigated theoretically. The purpose of this work was to elaborate model concepts and to analyze quantitatively the effect of interphase boundaries on the piezoelectric modulus d_{33} of PT–PZN crystals in the morphotropic region.

2. EXPERIMENTAL DATA AND MODEL CONCEPTS

According to the experimental data obtained by Park and Shrout [3], the electric field $E = 0.5$–2.0 MV/m, when applied to the polydomain (001) crystals with $x = 0.08$ in the rhombohedral (Rh) phase, brings about their piezoelectric deformation without reorientation of 71° (109°) domains (stage A). The tetragonal (T) phase coexisting with the rhombohedral phase is induced at $E = 2.5$–4.0 MV/m (stage B). A further increase in E leads to the stabilization of the single-domain tetragonal phase to the extent of the electrical breakdown of the crystal at $E \gtrsim 12.0$ MV/m. At the B stage, Park and Shrout [2, 3] measured the very large values of the tensile strain $\xi_{33} > 1\%$ in the [001] direction and the piezoelectric modulus $d_{33,B} \approx 4500$ pC/N, which is one order of magnitude larger than the value of $d_{33,T}$ in the tetragonal phase at $E = 4$–12 MV/m. At the A stage, the rhombohedral PT–PZN (001) crystals with $x = 0.045$ and 0.08 are characterized by sufficiently close values of the piezoelectric moduli $d_{33,A}$ (approximately 2000 and 2500 pC/N, respectively [2, 3]), even though the composition with $x = 0.045$ is almost equidistant from Pb(Zn$_{1/3}$Nb$_{2/3}$)O$_3$ ($x = 0$ and $d_{33} = 1100$ pC/N [2, 3]) and the rhombohedral–tetragonal morphotropic region.

In order to elucidate the role of interphase boundaries in the evolution of the high piezoelectric activity of PT–PZN crystals, we propose a model of a heterophase crystal (Fig. 1) in which the interphase boundary QR parallel to the (001) plane of a perovskite cell is displaced under an external uniform electric field **E** || [001]. It is known that the interface boundary orientation close to (001) can be realized in the morphotropic region of the PT–PZN system [4, 6] at $E = 0$ owing to the small differences between the perovskite unit cell parameters a_T and a_R of the tetragonal and rhombohedral phases, respectively [1, 7]. In this system, the bulk energy density associated with both the elastic displacement of the interphase boundary and the electrostatic interaction between the spontaneous polarization vectors of phase domains and the field **E** is represented as the sum of two competing contributions f_{elas} and f_{el}, respectively. In the approximation of the linear elastic-

---

[1] Hereafter, single- or polydomain crystal samples whose developed faces are parallel to the (001) plane of a perovskite cell will for brevity, be referred to as the (001) crystals.

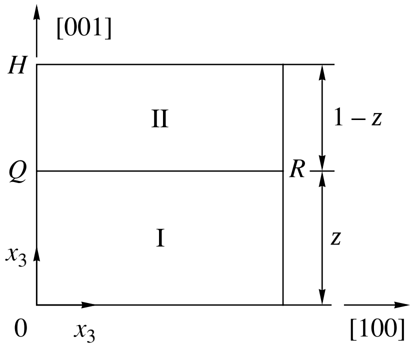

Fig. 1. A schematic drawing of a two-phase crystal with a planar interphase boundary: *z* and 1 – *z* are the volume concentrations of phases I and II, respectively. The crystal can contain two rhombohedral phases (I and II) with close molar concentrations *x* (stage *A*) or the tetragonal (I) and rhombohedral (II) phases coexisting in the course of the phase transition induced by the field **E** (stage *B*).

ity theory [8], an infinitesimal change $d\xi^{\Delta}_{33}$ in the strain of the crystal edge 0*H* (Fig. 1) due to the displacement of the boundary *QR* (i.e., due to the change in the concentration of phase I by *dz*) leads to the differential

$$df_{\text{elas}} = \sigma^{\Delta}_{33} d\xi^{\Delta}_{33} = [c^{\text{I}}_{33} z + c^{\text{II}}_{33}(1-z)]\xi^{\Delta}_{33} d\xi^{\Delta}_{33}, \quad (1)$$

where c^{I}_{33} and c^{II}_{33} are the measured elastic moduli of phases I and II, respectively, along the [001] direction at E = const. According to Bondarenko *et al.* [9], the strain ξ^{Δ}_{33} is defined as $\xi^{\Delta}_{33} = z\delta$, where $\delta = (c_{\text{II}}/c_{\text{I}}) - 1$. Here, c_{I} and c_{II} are the unit cell parameters of single-domain phases I and II along the [001] direction. Integration of relationship (1) over the volume concentrations $0 \le z \le z_{\Delta} < 1$ gives

$$f_{\text{eals}} = \delta^2[\Delta c(z^3_{\Delta}/3) + c^{\text{II}}_{33}(z^2_{\Delta}/2)], \quad (2)$$

where $\Delta c = c^{\text{II}}_{33} - c^{\text{I}}_{33}$.

The bulk energy density for the electrostatic interaction is written as

$$f_{\text{el}} = \mathbf{\Delta P} \cdot \mathbf{\Delta E} z_{\Delta} - \mathbf{P}_{\text{II}} \cdot \mathbf{E}, \quad (3)$$

where $\mathbf{\Delta P} = \mathbf{P}_{\text{II}} - \mathbf{P}_{\text{I}}$ is the difference between the volume-averaged spontaneous polarizations of phases I and II. By minimizing the energy densities $d(f_{\text{elas}} + f_{\text{el}})/dz_{\Delta} = 0$ and $d^2(f_{\text{elas}} + f_{\text{el}})/dz^2_{\Delta} > 0$ with due regard for relationships (2) and (3), we obtain an expression for the volume concentration of phase I in the following form:

$$z_{\Delta} = [-c^{\text{II}}_{33} + ((c^{\text{II}}_{33})^2 + 4\Delta c \mathbf{\Delta P} \cdot \mathbf{E}\delta^{-2})^{1/2}]/(2\Delta c). \quad (4)$$

Taking into account the physical meaning of the relationships $0 < z_{\Delta} < 1$ and $\Delta c < 0$,[2] we obtain that equality (4) holds under the condition

$$0 < \varphi < 1, \quad (5)$$

where $\varphi = \mathbf{\Delta P} \cdot \mathbf{E}/(c^{\text{II}}_{33}\delta^2)$. As a result, the contribution made to the piezoelectric modulus d_{33} of the crystal by the displacement of the interphase boundary is represented as

$$\Delta d_{33} = d\xi^{\Delta}_{33}/dE = \delta dz_{\Delta}/dE. \quad (6)$$

3. RESULTS OF CALCULATIONS AND DISCUSSION

Now, we quantitatively determine the contribution Δd_{33} at the *A* stage. In recent works [4, 5], the 71° (109°) domains were visualized in the rhombohedral phase of the PT–PZN (001) crystals. These domains had the spontaneous polarization vectors $\mathbf{P_{R1}}(P_s; P_s; P_s)$, $\mathbf{P_{R2}}(P_s; -P_s; -P_s)$, $\mathbf{P_{R3}}(P_s; P_s; -P_s)$, and $\mathbf{P_{R4}}(P_s; -P_s; P_s)$ and were separated by domain walls parallel to the (001) plane of the perovskite unit cell. Let us assume that the molar concentration x_d in individual domains differs from the concentration x in the sample as a whole due to composition fluctuations, inhomogeneous distribution of Ti^{4+} ions [6, 12], specific features of the crystal growth, and other factors. In this case, the boundaries between individual domains or domain regions with concentrations x (phase II in Fig. 1) and x_d (phase I) become interfacial and the electric field can induce their motion. For the interaction of these rhombohedral phases, we have $\delta_A = a_{R,\,d}\cos\omega_{R,\,d}(a_R\cos\omega_R)^{-1} - 1$ and $\mathbf{\Delta P} \cdot \mathbf{E} = |P_{R,\,d} - P_R|E/\sqrt{3}$, where a_R and ω_R are the cell parameters of phase II; $a_{R,\,d}$ and $\omega_{R,\,d}$ are the cell parameters of phase I; and $P_{R,\,d}$ and P_R are the magnitudes of the spontaneous polarization vectors of 71° (109°) domains in phases I and II, respectively.

Since the experimental concentration dependences of the electrical parameters for PT–PZN single-domain crystals in the morphotropic region are unavailable, it is necessary to make the estimates from formulas (4)–(6) with the use of the parameters varying within certain ranges. For example, the elastic moduli c^{II}_{33} vary in the range from 1.0×10^{10} to 5.0×10^{9} Pa. These values are approximately equal to the reciprocal of the effective

---

[2] The condition $\Delta c < 0$ corresponds to a decrease in the elastic modulus c^{E}_{33} upon formation of a single-domain structure in BaTiO_3 [10] or PbTiO_3 [11] crystals containing lamellar 90° domains in the tetragonal phase in the field **E**. Data on the change in c^{E}_{33} for polydomain ferroelectric crystals with a perovskite-type structure upon an induced rhombohedral–tetragonal phase transition or the formation of a single-domain rhombohedral phase under the field **E** are unavailable.

compliance s_{33}^{E} measured in [1, 3] for (001) crystals in the vicinity of $x = 0.09$. The difference $\Delta P_A = |P_{R,d} - P_R|$ is taken equal to 0.01–0.03 C/m^3 (which is several dozen times less than the value of P_R for PT–PZN crystals [3]), and the range of variations in the parameter $|\delta_A| = (1.0\text{–}2.5) \times 10^{-3}$ is determined by condition (5). The values of Δc_A are varied so that $\left|\Delta c_A / c_{33,A}^{\mathrm{II}}\right| = 0.01\text{–}0.20$. The calculated data on the volume concentration $z_{\Delta,A}$ and the contribution $\Delta d_{33,A}$ at the A stage are shown in Fig. 2 and Table 1, respectively.

The dependences $z_{\Delta,A}(E)$ (Fig. 2) are determined to a greater degree by the $c_{33,A}^{\mathrm{II}}$ and δ_A parameters as compared to ΔP_A and Δc_A. It seems likely that the aforementioned ranges of variations in these parameters allow us to reveal the main features of the behavior of $z_{\Delta,A}(E)$ in the presence of domains at $x_d \neq x$. The data listed in Table 1 indicate the considerable contribution $\Delta d_{33,A}$ of the interphase boundaries to the piezoelectric modulus $d_{33,A}$, which was measured for the inverse piezoelectric effect. A comparison of the estimates made for $\Delta d_{33,A}$ at different values of Δc_A when the remaining parameters are identical demonstrates that $\Delta d_{33,A}(E)$ is constant to within 1% at small Δc_A under condition (5). Since $\Delta d_{33,A}(E)$ and the piezoelectric modulus $d_{33,A}^{p}(E)$ for a polydomain sample are virtually constant ($d_{33,A}^{p}$ cannot substantially change in sufficiently weak fields), the resulting piezoelectric modulus is given by

$$d_{33,A}(E) = d_{33,A}^{p}(E) + \Delta d_{33,A}(E) \approx \text{const}. \qquad (7)$$

Relationship (7) is in quantitative agreement with the experimental data obtained in [2, 3] for PT–PZN at $x = 0.045$ and 0.08: the field dependences $\xi_{33,A}(E) = d_{33,A}(E)E$ for both compositions exhibit a nearly constant slope at the A stage.

Among the field dependences presented in Fig. 2 and Table 1, the $z_{\Delta,A}(E)$ curves passing through unity in the range $E = 1.5\text{–}2.0$ MV/m are of particular interest. In this case, the interphase boundaries pass throughout the crystal and provide the sufficiently large contribution $\Delta d_{33,A}(E) \approx 1200\text{–}1700$ pC/N (see, for example, the calculations at $|\delta_A| = 2.0 \times 10^{-3}$ and $\Delta P_A = 0.02$ C/m^2 and at $|\delta_A| = 2.5 \times 10^{-3}$ and $\Delta P_A = 0.03$ C/m^2 in group II). A further increase in E leads to a change in the conditions of the Δd_{33} formation. The obtained contributions $\Delta d_{33,A}$ are equal to approximately 50–70% of the $\Delta d_{33,A}$ value measured in [2, 3] for (001) crystals with $x = 0.08$. Note also that the piezoelectric moduli $d_{33,\mathrm{dyn}}$, which were measured by the dynamic method in weak fields ($E \ll 0.5$ MV/m) for (001) crystals, amounted to approximately 1200 pC/N at $x = 0.08$ [3] and 1000–1500 pC/N at $x = 0.09$ [1, 13]. These data for $d_{33,\mathrm{dyn}}$ correlate with the piezoelectric moduli $d_{33,A}^{p}(E)$, which were estimated for the polydomain sample with stationary interface boundaries: according to relationship (7), we have $d_{33,A}^{p} \approx 800\text{–}1300$ pC/N at $x = 0.08$ and $E \gtrsim 0.5$ MV/m.

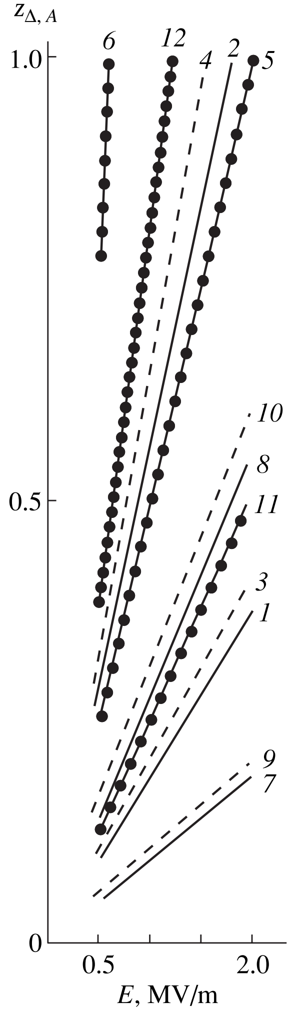

Fig. 2. Field dependences $z_{\Delta,A}(E)$ calculated by formula (4) (stage A). Curves *1–6* and *7–12* correspond to the values of $c_{33,A}^{\mathrm{II}}$ and Δc_A from groups II and I (Table 1), respectively. ΔP_A = (*1, 3, 5, 7, 9, 11*) 0.01 and (*2, 4, 6, 8, 10, 12*) 0.03 C/m^2. $|\delta_A|$ = (*1–4, 7–10*) 2.5×10^{-3} and (*5, 6, 11, 12*) 1.5×10^{-3}. Δc_A = (*1, 2, 5–8, 11, 12*) -5.0×10^7, (*3, 4*) -1.0×10^9, and (*9, 10*) -2.0×10^9 Pa.

At the B stage, it is assumed that the interphase boundary separates the single-domain tetragonal phase I with the spontaneous polarization vector $\mathbf{P}_{\mathbf{I}}(0; 0; P_T)$ and the rhombohedral phase II with the aforementioned orientations of the spontaneous polarization vectors $\mathbf{P}_{\mathbf{Rk}}$ ($k = 1, \ldots, 4$). As follows from our results obtained earlier in [9], for these phases, we have $\delta_B = c_T(a_R \cos\omega_R)^{-1} - 1$ and $\mathbf{\Delta P} \cdot \mathbf{E} = \Delta P_B E$, where c_T is the

Table 1. Calculated contributions $\Delta d_{33,A}$ for 71° (109°) domains in PT–PZN crystals at $x_d \neq x$ (stage A)

E, MV/m	$\lvert\delta_A\rvert$, 10^{-3}	$\Delta d_{33,A}$, pC/N		
		at $\Delta P_A = 0.01$ C/m^2	at $\Delta P_A = 0.02$ C/m^2	at $\Delta P_A = 0.03$ C/m^2
		Group I		
0.5	1.0	580 (610, 660)	1200 (1300, 1600)	1800 (2100, –)
1.0		580 (660, 790)	–	–
1.5		590 (710, –)	–	–
2.0		–	–	–
0.5	1.5	390 (400, 410)	770 (810, 860)	1200 (1300, 1400)
1.0		390 (410, 430)	780 (860, 1000)	1200 (1400, 1900)
1.5		390 (420, 460)	780 (930, 1200)	–
2.0		390 (430, 500)	–	–
0.5	2.0	290 (290, 300)	580 (600, 610)	870 (910, 950)
1.0		290 (300, 310)	580 (610, 660)	870 (950, 1100)
1.5		290 (300, 320)	580 (640, 710)	880 (1000, 1300)
2.0		290 (310, 330)	580 (660, 790)	880 (1100, –)
0.5	2.5	230 (230, 230)	460 (470, 480)	700 (710, 740)
1.0		230 (240, 240)	460 (480, 500)	700 (740, 790)
1.5		230 (240, 250)	460 (490, 520)	700 (760, 850)
2.0		230 (240, 250)	470 (500, 550)	700 (790, 930)
		Group II		
0.5	1.5	770 (810, 860)	1600 (1700, 2000)	2400 (2800, 3700)
1.0		780 (860, 1000)	–	–
1.5		780 (930, 1200)	–	–
2.0		–	–	–
0.5	2.0	580 (600, 610)	1200 (1200, 1300)	1800 (1900, 2100)
1.0		580 (610, 660)	1200 (1300, 1600)	1800 (2100, –)
1.5		580 (640, 710)	1200 (1400, –)	–
2.0		580 (660, 790)	–	–
0.5	2.5	460 (470, 480)	930 (960, 1000)	1400 (1500, 1600)
1.0		460 (480, 500)	930 (1000, 1100)	1400 (1600, 1900)
1.5		460 (490, 520)	930 (1100, 1200)	1400 (1700, –)
2.0		470 (500, 550)	940 (1100, 1400)	–

Note: For the calculated values, $c_{33,A}^{\mathrm{II}} = 1.0$ and $\Delta c_A = -0.01, -0.10$, and -0.20 (in 10^{10}, Pa) (group I) and $c_{33,A}^{\mathrm{II}} = 0.50$ and $\Delta c_A = -0.005$, -0.05, and -0.10 (in 10^{10}, Pa) (group II). The $\Delta d_{33,A}$ values calculated for the last two values of Δc_A in the corresponding group are given in parentheses. Dashes mean that $\Delta d_{33,A}$ at $z_{\Delta,A} > 1$ cannot be determined because of the violation of condition (5).

parameter of the perovskite cell in phase I and $\Delta P_B = P_T - (P_R/\sqrt{3})$. The values of P_T were estimated from the experimental data on d_{33}, the permittivity $\varepsilon_{33}^{\sigma}$, and the electrostriction coefficient Q_{11} of a single-domain crystal with $x = 0.08$ in phase I. A comparison of these estimates with P_R for the same composition in phase II [3] suggests that $\Delta P_B \lesssim 0.30$ C/m^2. The other para-

Table 2. Calculated contributions $\Delta d_{33,B}$ for the $R3m$–$P4mm$ phase transition in PT–PZN crystals (stage B)

E, MV/m	$\lvert\delta_B\rvert$, 10^{-2}	$\Delta d_{33,B}$, pC/N		
		at $\Delta P_B = 0.20$ C/m^2	at $\Delta P_B = 0.25$ C/m^2	at $\Delta P_B = 0.30$ C/m^2
		Group I		
2.5	1.0	2000 (2600, 4100)	2600 (3300, –)	3100 (4200, –)
3.0		2100 (2700, 5000)	2600 (3500, –)	3100 (–, –)
3.5		2100 (2800, –)	2600 (–, –)	–
4.0		2100 (2900, –)	–	–
2.5	1.5	1400 (1600, 2000)	1700 (2000, 2600)	2000 (2400, 3300)
3.0		1400 (1600, 2000)	1700 (2000, 2700)	2000 (2500, 3500)
3.5		1400 (1600, 2100)	1700 (2100, 2900)	2000 (2500, 3900)
4.0		1400 (1600, 2200)	1700 (2100, 3100)	2000 (2600, 4300)
2.5	2.0	1000 (1200, 1400)	1300 (1500, 1700)	1500 (1800, 2100)
3.0		1000 (1200, 1400)	1300 (1500, 1800)	1500 (1800, 2200)
3.5		1000 (1200, 1400)	1300 (1500, 1800)	1500 (1800, 2300)
4.0		1000 (1200, 1400)	1300 (1500, 1900)	1500 (1800, 2400)
		Group II		
2.5	1.5	2700 (3400, 5000)	3400 (4400, 7500)	4100 (5400, –)
3.0		2700 (3500, 5800)	3400 (4500, –)	4100 (5700, –)
3.5		2700 (3600, –)	3400 (4700, –)	4100 (–, –)
4.0		2700 (3700, –)	3400 (–, –)	–
2.5	2.0	2000 (2400, 3000)	2500 (3000, 4000)	3100 (3700, 5100)
3.0		2000 (2400, 3200)	2500 (3100, 4300)	3100 (3800, 5700)
3.5		2000 (2400, 3300)	2600 (3100, 4600)	3100 (3900, 6400)
4.0		2000 (2500, 3500)	2600 (3200, 5100)	3100 (4000, 7500)

Note: For the calculated values, $c^{II}_{33,B} = 0.99$, 0.90, and 0.80 at $\Delta c_B = -0.01$, -0.10, and -0.20 (in 10^{10}, Pa) (group I), respectively; and $c^{II}_{33,B} = 0.495$, 0.45, and 0.40 at $\Delta c_B = -0.005$, -0.05, and -0.10 (in 10^{10}, Pa) (group II), respectively. The $\Delta d_{33,B}$ values calculated for the two last values of Δc_B in the corresponding group are given in parentheses. Dashes mean that $\Delta d_{33,B}$ at $z_{\Delta,B} > 1$ cannot be determined because of the violation of condition (5).

meters used in calculations with formulas (4)–(6) were varied within the same ranges as in the A stage. The results of calculations are presented in Fig. 3 and Table 2.

The "volume concentration $z_{\Delta,B}$–factor φ_B" diagram (Fig. 3) generalizes the data on the influence of the interphase boundaries on the piezoelectric response of PT–PZN crystals at the A and B stages.

Similar to the $z_{\Delta,A}$ concentration at the A stage, the $z_{\Delta,B}$ volume concentration is sufficiently sensitive to changes in $c^{II}_{33,B}$ and δ_B. A variation in ΔP_B at fixed $c^{II}_{33,B}$ and δ_B makes it possible to combine particular portions of the $z_{\Delta,B}(\varphi_B)$ curves into a continuous line with a virtually constant slope. This circumstance plays a decisive role in the formation of the field dependences $\xi_{33,B}(E)$ and the determination of parameters that meet the condition $d_{33,B}(E) = d^{p}_{33,B}(E) + \Delta d_{33,B}(E) \approx \text{const}$, which is similar to relationship (7). As follows from Table 2, in the case when the rhombohedral–tetragonal interphase boundary passes throughout the crystal (i.e., the inequality $z_{\Delta,B}|_{E\to 4.0\ \text{MV/m}} \gtrsim 1$ is fulfilled), the contributions $\Delta d_{33,B}$ lie in the range ≈2600–4100 pC/N and depend only slightly on the field E (at $\left|\Delta c_B/c^{II}_{33,B}\right| \approx 0.01$). Making allowance for the fact that, in the late B stage, $z_{\Delta,B}$ tends to unity and the single-domain tetragonal phase with a piezoelectric modulus $d_{33,T} \approx$

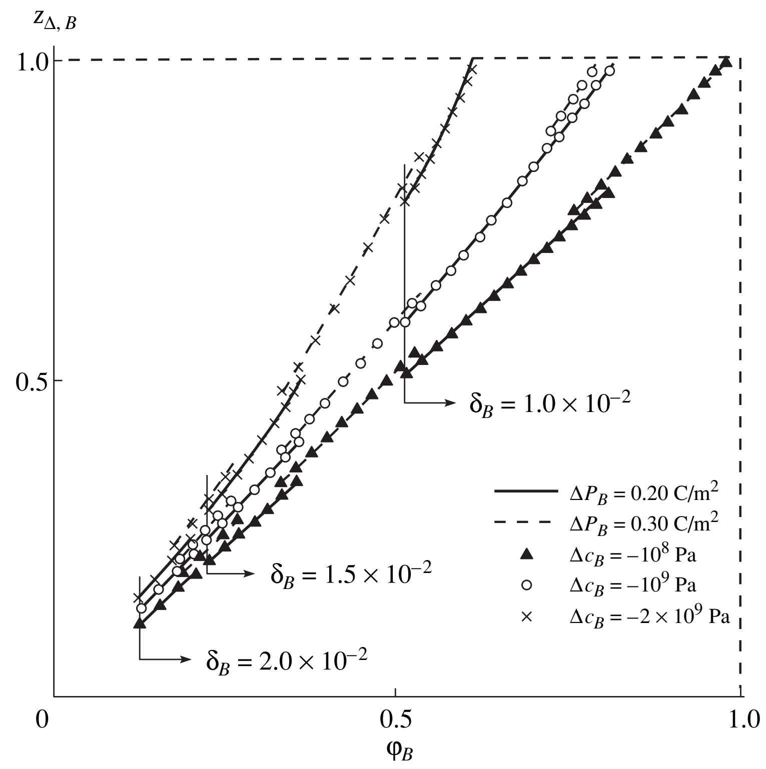

Fig. 3. Diagram relating the volume concentration $z_{\Delta, B}$ and the factor $\varphi_B = \Delta P_B E/(c^{II}_{33, B}\delta_B^2)$ for the induced phase transition (stage *B*). The elastic modulus $c^{II}_{33, B} = 0.99 \times 10^{10}$ Pa corresponds to $\left|\Delta c_A/c^{II}_{33, A}\right| = 0.01$ in group I (stage A).

480 pC/N ($x = 0.08$) [3] predominates, the resulting piezoelectric modulus of the crystal can be estimated as $d_{33, B} \approx d_{33, T} + \Delta d_{33, \mathrm{B}} \approx$ 3000–4600 pC/N. The very large values of $d_{33, B}$ are explained by the considerable contribution $\Delta d_{33, B}/d_{33, B} \approx$ 0.8–0.9 and agree well with the piezoelectric modulus $d_{33, B}(E) \approx 4500$ pC/N ($x = 0.08$) [3], which was measured at the *B* stage.

4. CONCLUSION

The results obtained in the present work can be summarized as follows.

(1) Within a unified model of the heterophase crystal in a uniform electric field **E**, the contributions $\Delta d_{33, A}$ and $\Delta d_{33, B}$ from the displacements of the planar interphase boundaries to the piezoelectric moduli $d_{33, A}$ and $d_{33, B}$ were quantitatively estimated for the first time. It was shown that the interphase boundary motion at the *A* stage can be caused by the 71° (109°) domains in the rhombohedral phase of the xPbTiO$_3$–$(1 - x)$Pb(Zn$_{1/3}$Nb$_{2/3}$)O$_3$ crystals at molar concentrations $x_d \neq x$. The estimated contributions $\Delta d_{33, A}$ account for 70% of the experimental values of the piezoelectric modulus $d_{33, A}$ for the (001) crystals in the morphotropic region.

(2) The volume concentration $z_{\Delta, B}$–factor φ_B diagram was proposed. This diagram quantitatively describes the dependence of the content of the induced tetragonal phase in the xPbTiO$_3$–$(1 - x)$Pb(Zn$_{1/3}$Nb$_{2/3}$)O$_3$ crystals on the electric field *E*, the elastic properties ($c^{II}_{33, B}$ and Δc_B), the difference in the perovskite cell parameters (δ_B), and the difference in the spontaneous polarizations of domains in different phases (ΔP_B). The ranges of variations in the parameters ΔP_B, $c^{II}_{33, B}$, and δ_B, which correspond to the anomalously large contributions $\Delta d_{33, B} > 4000$ pC/N to the piezoelectric modulus $d_{33, B}$ at the *B* stage, were justified analytically.

ACKNOWLEDGMENTS

We are grateful to Dr. Z.-G. Ye (Canada) for his continuing interest in this study and helpful discussions on the problem of the domain and heterophase structures in PT–PZN.

REFERENCES

1. J. Kuwata, K. Uchino, and S. Nomura, Ferroelectrics **37**, 579 (1981).
2. S.-E. Park and T. R. Shrout, Mater. Res. Innovations **1**, 20 (1997).
3. S.-E. Park and T. R. Shrout, J. Appl. Phys. **82**, 1804 (1997).

4. S. Wada, S.-E. Park, L. E. Cross, and T. R. Shrout, Ferroelectrics **221**, 147 (1999).
5. U. Belegunda, X. H. Du, L. E. Cross, and K. Uchino, Ferroelectrics **221**, 67 (1999).
6. V. Yu. Topolov and Z.-G. Ye, in *Abstracts of the Sixth International Symposium on Ferroic Domains and Mesoscopic Structures*, *ISFD-6, Nanjing, China, 2000*, p. 67; Ferroelectrics (2001) (in press).
7. Y. Uesu, Y. Yamada, K. Fujishiro, *et al.*, Ferroelectrics **217**, 319 (1998).
8. T. D. Shermergor, *The Elasticity Theory of Microinhomogeneous Media* (Nauka, Moscow, 1977).
9. E. I. Bondarenko, V. Yu. Topolov, and A. V. Turik, Zh. Tekh. Fiz. **62** (12), 145 (1992) [Sov. Phys. Tech. Phys. **37**, 1206 (1992)].
10. A. V. Turik, Fiz. Tverd. Tela (Leningrad) **12**, 892 (1970) [Sov. Phys. Solid State **12**, 688 (1970)].
11. A. V. Turik, V. Yu. Topolov, and V. I. Aleshin, J. Phys. D **33**, 738 (2000).
12. Z.-G. Ye, M. Dong, and L. Zhang, Ferroelectrics **229**, 223 (1999).
13. G. Robert, D. Damjanovic, and N. Setter, Ferroelectrics **224**, 97 (1999).

Translated by O. Borovik-Romanova

Physics of the Solid State, Vol. 43, No. 6, 2001, pp. 1124–1127. Translated from Fizika Tverdogo Tela, Vol. 43, No. 6, 2001, pp. 1086–1088.
Original Russian Text Copyright © 2001 by Sheleg, Dekola, Tekhanovich.

MAGNETISM AND FERROELECTRICITY

Effect of γ-Irradiation on the Heat Capacity of an $[NH_2(CH_3)_2]_2 \cdot CuCl_4$ Crystal in the Temperature Range 80–300 K

A. U. Sheleg, T. I. Dekola, and N. P. Tekhanovich

Institute of Solid-State and Semiconductor Physics, Belarussian Academy of Sciences,
ul. Brovki 17, Minsk, 220072 Belarus

Received August 11, 2000; in final form, November 9, 2000

Abstract—The heat capacity of $[NH_2(CH_3)_2]_2 \cdot CuCl_4$ crystals prior to and after γ-irradiation with doses of 1, 5, 10, and 50 MR is measured by the calorimetric method in the temperature range 80–300 K. It is found that, as the temperature decreases, the temperature dependence $C_p(T)$ exhibits two anomalies which correspond to phase transitions from the incommensurate to the ferroelectric phase at $T_c = 281$ K and from the ferroelectric to the ferroelastic phase at $T_1 = 255$ K. The nature of the anomalies is typical of a first-order phase transition. In addition, a smeared anomaly in the form of a small increase in the heat capacity of the ferroelectric phase is observed at $T \approx 275$ K. It is demonstrated that when the dose of γ-irradiation increases, the anomalies decrease in magnitude and the phase transition temperatures are displaced: T_c increases and T_1 decreases. © *2001 MAIK “Nauka/Interperiodica”.*

Crystals of dimethylaminochlorocuprate $[NH_2(CH_3)_2]_2 \cdot CuCl_4$ fall into the $[NH_2(CH_3)_2]_2 \cdot MeCl_4$ (Me = Co, Zn, or Cu) group, which belongs to the family of crystals with general formula A_2BX_4. Crystals of the $[NH_2(CH_3)_2]_2 \cdot MeCl_4$ type have been synthesized comparatively recently and are of interest because they undergo a complex sequence of phase transitions which depends on the sort of Me ions involved [1–3]. Bobrova *et al.* [3] demonstrated that two phase transitions in the $[NH_2(CH_3)_2]_2 \cdot CuCl_4$ crystal occur at $T_c = 279.5$ K and $T_1 = 253$ K; between these transitions, it exhibits ferroelectric properties. Investigations into the temperature dependences of the relative linear expansion, heat capacity, and permittivity of $[NH_2(CH_3)_2]_2 \cdot CuCl_4$ crystals [1, 3] have shown that both phase transitions are transitions of the first order. Vlokh *et al.* [4] studied the birefringence and electrooptical properties and made the assumption that the $[NH_2(CH_3)_2]_2 \cdot CuCl_4$ crystal has an incommensurate phase in the temperature range 296–279.5 K. Since the sequence of phase transitions is observed in this crystal, it is of interest to measure the heat capacity in the temperature range where this sequence takes place and to investigate how the γ-irradiation affects the phase transition parameters.

The heat capacity measurements were carried out in a vacuum adiabatic calorimeter with discrete heat supply to the sample ($m = 3.55$ g). The heating rate of the sample was 0.01–0.09 K/min. The measurements of the heat capacity were performed in 0.3–1.9 K intervals with an accuracy of 0.3%. The sample temperature was checked with a platinum resistance thermometer. The sample was irradiated at room temperature on a γ-irradiation facility from a Co^{60} source with a dose rate of ~280 R/s in the irradiation zone. The irradiation dose was accumulated by subsequent exposures of the same sample and amounted to 1, 5, 10, and 50 MR.

The results of the measurements of the heat capacity of the $[NH_2(CH_3)_2]_2 \cdot CuCl_4$ crystal prior to irradiation are presented in Fig. 1. The temperature dependence $C_p(T)$ exhibits two pronounced anomalies in the form of maxima in the temperature ranges that correspond to phase transitions at $T_c = 281$ K and $T_1 = 255$ K. The crystal under study falls into the group of A_2BX_4 ferroelectrics for which the phase transition at T_c is a transition from the incommensurate to the ferroelectric phase and the phase transition at T_1 is a transition from the ferroelectric to the ferroelastic phase. It should be noted that the form of both anomalies corresponds to a first-order phase transition. This is confirmed by the sharp symmetric form of the anomalies and the increase in the time required for establishment of thermal equilibrium in the phase transition region during the experiment. An anomaly in the form of a small smeared maximum is observed in the $C_p(T)$ curve in the range of $T \approx 275$ K. The origin of this anomaly is as yet unknown. We did not reveal any anomalies in the $C_p(T)$ curve in the vicinity of $T_1 = 296$ K, where the authors of work [4] claimed that a transition from the paraphase to the incommensurate phase was evident. The changes in the entropy and enthalpy of the transitions were determined by numerical integration. The calculated values at $T_1 = 255.25$ K are equal to 1.8 J/(K mol) and 50 J/mol, respectively, and at $T_c = 281.23$ K, they are

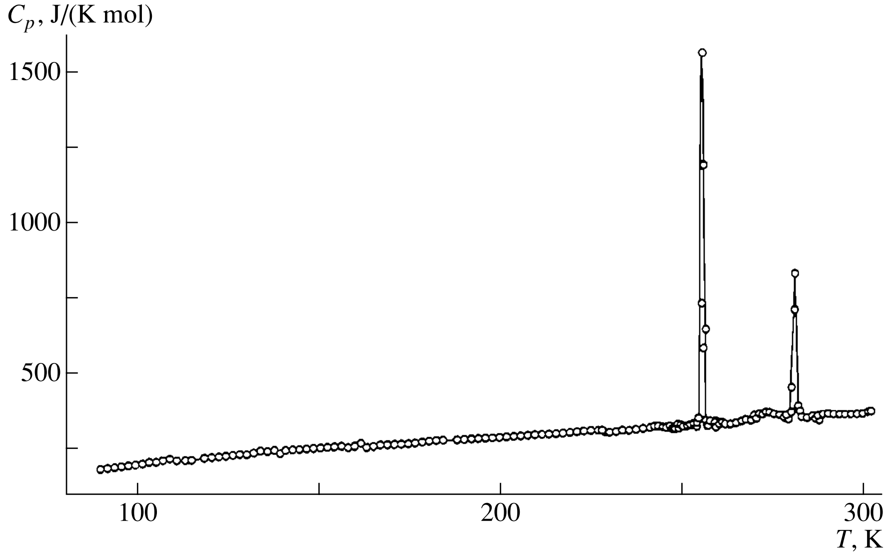

Fig. 1. Temperature dependence of the heat capacity of the $[NH_2(CH_3)_2]_2 \cdot CuCl_4$ crystal.

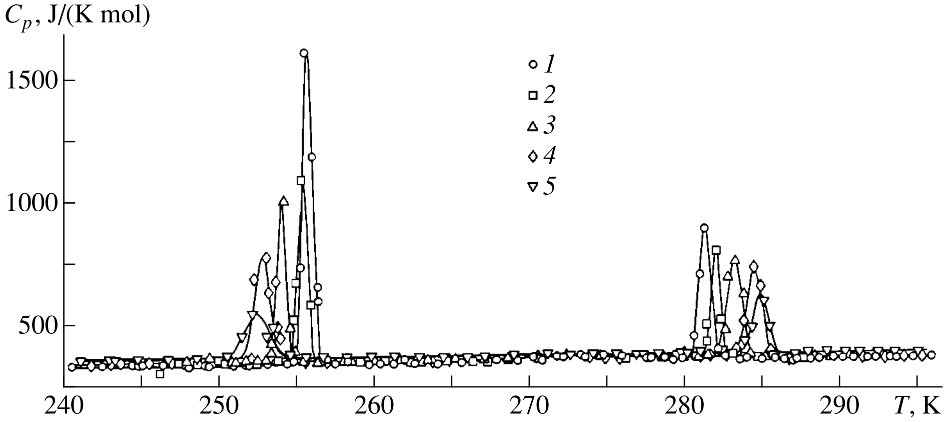

Fig. 2. Temperature dependences of the heat capacity of the $[NH_2(CH_3)_2]_2 \cdot CuCl_4$ crystal exposed to γ-irradiation with doses of (*1*) 0, (*2*) 1, (*3*) 5, (*4*) 10, and (*5*) 50 MR.

4.9 J/(K mol) and 1248 J/mol, respectively. The measured values of the entropy and enthalpy of the anomaly of the transition at $T \approx 275$ K are 0.77 J/(K mol) and 212 J/mol, respectively. The table presents the smoothed values of the heat capacity and the changes in the thermodynamic functions, such as the entropy *S*, the enthalpy *H*, and the Gibbs free energy Φ, which were calculated on their basis.

Figure 2 shows the temperature dependences of the heat capacity of the $[NH_2(CH_3)_2]_2 \cdot CuCl_4$ crystal exposed to different doses of γ-irradiation. It can be seen from this figure that, as the dose of γ-irradiation increases, the anomaly at $T_1 = 255$ K shifts toward the low-temperature range, decreases in height, and becomes smeared. Now, we take into account that the energy change ΔΘ due to the phase transition is determined by the excess heat capacity ΔC_p, i.e., by the area under the anomaly peak, which, according to the thermodynamic theory, can be represented as $\Delta\Theta = \frac{1}{2}\alpha T P_{\max}^2$, where α is the coefficient of proportionality, $P_{\max} = N\mu$ (μ is the unit dipole moment, and *N* is the number of ferroactive dipoles in 1 cm^3). On this basis, it can be inferred that the decrease in the magnitude of the anomaly and its smearing with an increase in the γ-irradiation dose indicate a decrease in the concentration of the ferroactive dipoles that provide the ferroelectric properties [5]. In the region of the incommen-

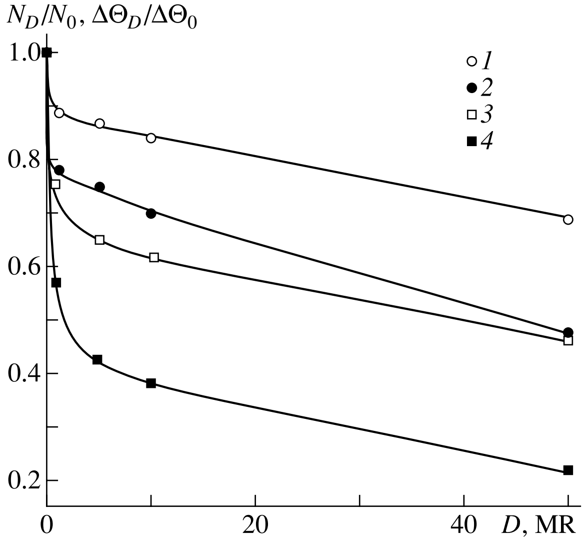

Fig. 3. Dose dependences of the relative excess enthalpy at phase transition temperatures (*2*) T_1 and (*4*) T_c and the concentration of the ferroactive dipoles at (*1*) T_1 and (*3*) T_c.

surate–commensurate ferroelectric phase transition at $T_c = 281$ K, the heat capacity anomaly shifts toward the high-temperature range, the anomaly peak diminishes, and the anomaly itself becomes somewhat smeared. The anomaly at $T \approx 275$ K also becomes smeared and virtually disappears at a dose of 50 MR. The relative change in the excess energy of the phase transition is related to the relative change in the number of ferroelectric dipoles N_D/N_0 in the process of irradiation by the following formula [5]:

$$\frac{N_D}{N_0} = \left(\frac{\Delta Q_D T_0}{\Delta Q_0 T_D}\right)^{1/2},$$

where ΔQ_0 and T_0 are the excess energy and the temperature of the phase transition for the unirradiated crystal, respectively, and ΔQ_D and T_D are the excess energy and the temperature of the phase transition for the irradiated crystal, respectively.

Figure 3 demonstrates the relative changes in the excess energy and in the number of ferroactive dipoles as functions of the irradiation dose in the temperature ranges of the two phase transitions. It is seen that the concentration of the ferroactive dipoles at higher temperatures is considerably less than that at low temperatures with the same irradiation doses. A sharp decrease in the number of active dipoles in the crystal lattice comes with a dose up to 1 MR at a temperature of ≈255 K and with a dose up to 5 MR at a temperature of ≈281 K.

The investigation of the deuterated crystal $[NH_2(CH_3)_2]_2 \cdot CuCl_4$ [6] revealed that when the content of deuterium increases, an inverse effect with respect to γ-irradiation takes place: the T_c temperature decreases and T_1 increases. Deuteration occurs when hydrogen in the polar N–H bonds is replaced by deuterium. It is known that the main mechanism of the phase transition in crystals of the A_2BX_4 family with a β-K_2SO_4 structure is the displacement of the cation which is accompanied by ordering of the tetrahedral groups. It seems likely that the phase transition in $[NH_2(CH_3)_2]_2 \cdot CuCl_4$ are associated with the reorientation of the N–H…Cl–Cu hydrogen bonds. Bobrova and Varikash [6] compared the pressure coefficients of pure and deuterated crystals and showed that when the crystals are deuterated, the role of the ordering of the tetrahedra is increased compared to the displacement of the cations. It can be assumed that the observed displacement of the phase transition points in $[NH_2(CH_3)_2]_2 \cdot CuCl_4$ under irradiation is due to the

Smoothed values of the heat capacity and the change in the thermodynamic functions of the $[NH_2(CH_3)_2]_2 \cdot CuCl_4$ crystal (in J/mol)

T, K	$C_p(T)$	$S(T)–S(80\ K)$	$\Phi(T)–\Phi(80\ K)$	$H(T)–H(80\ K)$
80	181.11	0.000	0.000	0.0
90	193.71	22.08	2.621	1874.1
100	205.65	43.13	6.946	3870.9
110	216.89	63.27	12.41	5983.6
120	227.42	82.60	18.65	8205.2
130	237.28	101.2	25.42	10529
140	246.49	119.1	32.55	12948
150	255.10	136.4	39.93	15455
160	263.17	153.2	47.47	18047
170	270.79	169.4	55.10	20717
180	278.04	185.0	62.78	23461
190	285.02	200.3	70.47	26276
200	291.83	215.1	78.15	29160
210	298.58	229.5	85.81	32112
220	305.39	243.5	93.42	35132
230	312.37	257.3	100.9	38221
240	319.63	270.7	108.5	41381
250	327.29	283.9	115.9	44616
260	335.47	296.9	123.3	47929
270	344.26	309.7	130.6	51328
280	353.78	322.4	137.9	54818
290	364.11	355.0	145.1	58407
300	375.33	347.6	152.2	62105

change in the N–H…Cl–Cu bonds or, more specifically, to the increase in the bond length in $CuCl_4$ tetrahedra.

ACKNOWLEDGMENTS

We are grateful to N.F. Kurilovich for his help in the irradiation of the samples.

This work was supported by the Foundation for Basic Research of Belarus Republic, project no. F 99-043.

REFERENCES

1. Z. A. Bobrova and V. M. Varikash, Dokl. Akad. Nauk Belarusi **30** (6), 510 (1986).
2. V. E. Vasil’ev, V. M. Rudyak, Z. A. Bobrova, and V. M. Varikash, Fiz. Tverd. Tela (Leningrad) **29** (5), 1539 (1987) [Sov. Phys. Solid State **29**, 882 (1987)].
3. Z. A. Bobrova, V. M. Varikash, A. I. Baranov, and L. A. Shuvalov, Kristallografiya **32** (1), 255 (1987) [Sov. Phys. Crystallogr. **32**, 148 (1987)].
4. O. G. Blokh, V. B. Kapustyanyk, and I. I. Polovinko, Izv. Akad. Nauk SSSR, Ser. Fiz. **54** (6), 1143 (1990).
5. S. A. Taraskin, B. A. Strukov, V. A. Fedorikhin, *et al.*, Fiz. Tverd. Tela (Leningrad) **19** (10), 2936 (1977) [Sov. Phys. Solid State **19**, 1721 (1977)].
6. Z. A. Bobrova and V. M. Varikash, Fiz. Tverd. Tela (Leningrad) **30** (9), 2629 (1988) [Sov. Phys. Solid State **30**, 1514 (1988)].

Translated by O. Moskalev

Physics of the Solid State, Vol. 43, No. 6, 2001, pp. 1128–1131. Translated from Fizika Tverdogo Tela, Vol. 43, No. 6, 2001, pp. 1089–1092.
Original Russian Text Copyright © 2001 by Shur, Kozhevnikov, Pelegov, Nikolaeva, Shishkin.

MAGNETISM AND FERROELECTRICITY

Barkhausen Jumps in the Motion of a Single Ferroelectric Domain Wall

V. Ya. Shur, V. L. Kozhevnikov, D. V. Pelegov, E. V. Nikolaeva, and E. I. Shishkin
Institute of Physics and Applied Mathematics, Ural State University, Yekaterinburg, 620083 Russia
e-mail: Vladimir.Shur@usu.ru

Received August 10, 2000; in final form, November 14, 2000

Abstract—It is shown that the motion of a domain wall in the improper ferroelectric–ferroelastic gadolinium molybdate $Gd_2(MoO_4)_3$ demonstrates a self-organized critical behavior under polarization reversal. Barkhausen pulses are measured experimentally during the jumpwise motion of a single plane domain wall in monocrystalline plates with artificial pinning centers of the “field inhomogeneity” type. *© 2001 MAIK “Nauka/Interperiodica”.*

1. INTRODUCTION

The evolution of the domain structure upon polarization reversal is a complex process of nucleation, growth, and coalescence of a large number of individual domains. The analysis of Barkhausen noise (deviation of currents from a monotonic dependence), which is generally attributed to the nucleation, forward growth of individual domains, and pinning (interaction of domain walls with defects), plays a special role in the study of elementary processes of polarization reversal.

Barkhausen’s noise was discovered and studied intensively in ferromagnets, in which it forms a sequence of magnetization jumps [1]. It was proved that the spectrum of this noise in a wide frequency range is proportional to $1/f^b$ [2–4]; i.e., flicker noise takes place. For this reason, an analysis of Barkhausen’s noise in ferromagnets is often carried out using the concept of self-organized critical behavior [2–4] (for explaining the $1/f$ noise). A classical model describing such a self-organized behavior is the “sand pile” model with a critical slope [2, 3]. Elementary excitations in such systems generate responses (avalanches) which have no characteristic size and lifetime. The application of the concept of self-organized criticality is substantiated by the presence of a limited time scaling of the Fourier transform of the noise and a spatial scaling for the Barkhausen jump (BJ) distribution function over the duration, area, and energy [4], as well as the fact that the fractal dimension of Barkhausen’s noise lies in the interval from 1 to 2. We endeavored to use this approach in a statistical analysis of the Barkhausen noise observed during the motion of a single domain wall in ferroelectrics.

2. EXPERIMENT

For our experiments, we chose the improper ferroelectric–ferroelastic $Gd_2(MoO_4)_3$ (GMO) since it displayed Barkhausen pulses in the switching current, which accompanied the nonmonotonic motion of domain walls [5–8]. In addition, the physical properties and domain structure of this material have been studied intensively [9–12]. Plane domain walls (PDW) in ferroelectrics–ferroelastics are stable under a wide range of external actions, which makes them the best model objects for studying elementary polarization switching processes.

The experimental samples were single-crystal rectangular plates (with a typical size of 7 × 2 × 0.39 mm) cut at right angles to the polar axis. The lateral faces of the plates were parallel to a coherently oriented PDW. All faces of the plates were ground and thoroughly polished using diamond pastes. Transparent $In_2O_3 : Sn$ electrodes were deposited on the polar faces by reactive sputtering. A single PDW parallel to the shortest edge of the plate was created mechanically in the sample prior to measurements. The sample was fastened as a cantilever on a substrate.

The electrodes had gaps of a special shape (Fig. 1). Strip gaps on both surfaces limited the range of the PDW displacement and prevented its disappearance. Pinning centers (of the field inhomogeneity type) were created due to a special shape of one of the electrodes, which led to a nonmonotonic motion of the PDW accompanied by Barkhausen’s noise [6, 7].

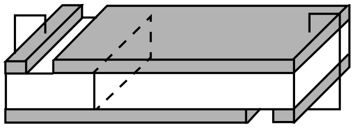

Fig. 1. Schematic diagram of electrodes.

We recorded the switching currents during the cyclic motion of the PDW induced by alternating triangular voltage pulses with an amplitude up to 300 V and a frequency varying from 30 to 100 Hz. The measuring frequency was 300 kHz. The noise component was separated during the subsequent mathematical treatment.

3. BARKHAUSEN NOISE

Figure 2 shows the field (time) dependences of the typical current $j(E(t))$ and the variance $\langle \Delta j^2(E(t)) \rangle$ obtained as a result of statistical treatment of currents measured during 50 successive cycles of the PDW motion.

Proceeding from the value of variance (see Fig. 2b), the current pulse was divided into three segments (see Fig. 2a). On the first segment ($E < 2.15$ kV/cm), the variance was small, indicating a high reproducibility of the PDW motion. On the second segment ($2.15 < E < 3.2$ kV/cm), the variance considerably exceeded the initial level, while on the third segment ($E \geq 3.2$ kV/cm), the variance increased abruptly (see Fig. 2b).

We proved that the current jumps on the second and third segments could be treated as the result of short-term deviations from the uniformly accelerated motion of the PDW, which were caused by the interaction with artificial pinning centers [6, 7] (Fig. 2a). It was noted that only negative Barkhausen jumps were observed on the second segment, while additional positive jumps appeared on the third segment.

4. SPECTRAL ANALYSIS OF BARKHAUSEN NOISE

We used two different methods of the separation of Barkhausen noise $\Delta j(t)$. From individual experimentally measured switching currents $j_i(t)$, we subtracted (a) the mean current $\langle j(t) \rangle$ or (b) its linear approximation. The frequency dependences (in the range from 7 to 80 kHz) of the Barkhausen noise amplitude were analyzed separately on different segments of a current pulse. The Fourier spectra averaged over 50 realizations were approximated by the dependence which is characteristic of flicker noise (see Fig. 3) [2–4]:

$$\Delta j(f) \sim f^{-b}. \tag{1}$$

It is important to note that the form of the dependences does not change qualitatively when different methods of noise measurement are used (cf. Figs. 3a, 3b). On the first segment, the amplitude is independent of frequency; i.e., white noise ($b = 0$) is observed. On the second segment, $b = 0.63$ to 0.94, and on the third segment, b varies from 1.27 to 1.34 (see the table). It should be noted that the typical values of b for the Barkhausen noise observed in ferromagnets vary from 0.8 to 1.0 [13, 14].

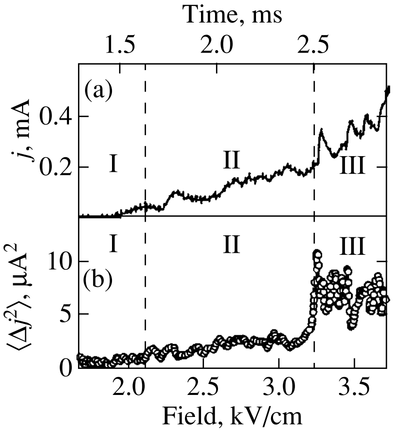

Fig. 2. Field dependences of (a) the switching current j and (b) its variance $\langle \Delta j^2 \rangle$.

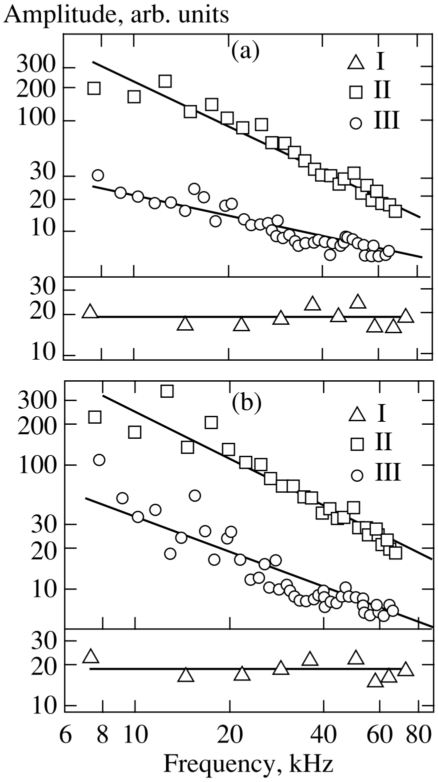

Fig. 3. Frequency dependences of the amplitude of jumps on different segments of a current pulse for the case where (a) the mean current $\langle j(t) \rangle$ or (b) its linear approximation was subtracted from $\langle j(t) \rangle$. Experimental data were fitted by Eq. (1).

The visualization of the PDW during polarization reversal with the help of a polarization microscope with stroboscopic illumination [6–8] allowed us to prove that pinning centers are absent only on the first segment. Consequently, flicker noise appears only as a result of the interaction of the PDW with pinning cen-

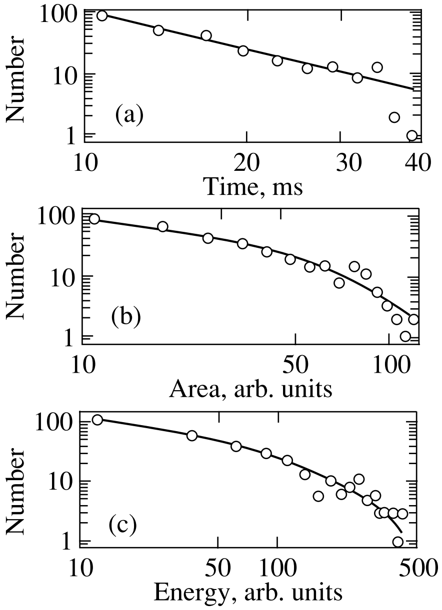

Fig. 4. (a) Duration, (b) area, and (c) energy distribution functions for Barkhausen jumps on the first segment. Experimental data were approximated by the dependence in Eq. (2).

ters. An increase in b upon a transition from the second to the third segment (after the PDW velocity exceeds a certain value) can be attributed to changing the interaction mechanism proposed in [6, 7]. We assumed that the PDW moves only due to the generation of steps at the edge of the sample and their subsequent growth. In a weak field (second segment), the slowing down of the PDW passing through a "defect" (a region with a reduced value of the field), which leads to a decrease in the current (a negative BJ), is due to the cessation of step generation in the defect region. As a result, the number of steps decreases since the annihilation continues at the same rate. During the subsequent motion of the PDW, steps grow in the direction of the defect and bypass it. The emergence of positive BJs in a strong field (third segment) was attributed to the PDW stability loss. When the deviation of the moving PDW from the coherent direction attains its critical value, a wedge-shaped domain is formed [15] and the velocity of a part of the steps increases considerably [16].

Critical exponents and Fourier exponents for different segments of the current pulse: b_1 corresponds to the subtraction of the mean current and b_2 corresponds to the subtraction of a linear approximation

Pulse segment	Critical exponents for BJ			Fourier exponents	
	α_T	α_S	α_E	b_1	b_2
I	1.96	0.26	0.46	~0	~0
II	0	0.41	0.16	0.63	0.94
III	1.46	0.44	0.37	1.27	1.34

It should be noted that the experimental values of the Fourier exponent b on the second segment are close to the results of computer simulation of the evolution of a classical "sand pile" with closed boundaries (b = 0.79) [3].

In order to reveal the peculiarities in the PDW evolution, we used the Hurst exponent $H = b/2$ [17]. It was proved that in the case of a slow motion of the PDW, $H < 1/2$ ($b < 1$), antipersistence (change of tendency) is observed, while for a fast motion, $H > 1/2$ ($b > 1$), persistence (continuation of the tendency) takes place. This is apparently an indication of a rapid restoration of the initial velocity of the PDW after its passage through a defect in the case of a slow motion and a slower restoration of the initial shape of the PDW after its loss of stability (generation of a wedge) in the case of a fast motion [17].

5. STATISTICAL ANALYSIS OF INDIVIDUAL BARKHAUSEN JUMPS

The existence of flicker noise suggests that the motion of a ferroelectric domain wall in a sample with pinning centers may be associated with a self-organized criticality [2–4].

We analyzed individual BJs obtained as a result of statistical treatment of the magnitude of current noise. We determined BJs on the basis of the value of the discrimination level dictated by the amplitude resolution of the current-recording system. Current pulses exceeding the discrimination level were treated as individual BJs and were processed by using the methods proposed in [2–4]. The distribution functions for the BJ duration, area, and energy were plotted for each segment of the current pulse. The BJ areas were determined by integrating the current, while the BJ energies were calculated by integrating the square of the current.

The distribution functions obtained (see Fig. 4) were approximated by universal dependences of the type [2–4]

$$D(x) \sim x^{-\alpha}\exp(-x/\xi), \qquad (2)$$

where x is the duration (T), area (S), or energy (E); α is the critical exponent; and ξ is a constant.

The values of the critical exponents thus obtained (see the table) can be used to classify the type of noise. It can be seen that for the first and second segments, the following theoretical relation is satisfied [2–4]:

$$\alpha_T = 2 - 2b. \qquad (3)$$

The critical exponent of the BJ duration distribution for the first segment corresponds to white noise (α_T = 2), while the noise on the second segment is close to the Brownian noise (α_T = 0), which confirms the conclusions derived from the spectral analysis. For BJs in a strong field (third segment), Eq. (3) does not hold, which can be attributed to a considerable correlation of BJs during the motion of an unstable PDW.

ACKNOWLEDGMENTS

This work was partly supported by the Russian Foundation for Basic Research (grant no. 98-02-17562), the program "Universities of Russia" (grant no. 5563), and the US Civil Research and Development Foundation for the Independent States of the Former Soviet Union (grant no. REC-005).

REFERENCES

1. H. Barkhausen, Z. Phys. **20**, 401 (1919).
2. P. Bak, C. Tang, and K. Wiesenfeld, Phys. Rev. Lett. **59** (4), 381 (1987).
3. P. Bak, C. Tang, and K. Wiesenfeld, Phys. Rev. A **38** (1), 364 (1988).
4. D. Spasojevic, S. Bukvic, S. Milosevic, and H. E. Stanley, Phys. Rev. E **54** (3), 2531 (1996).
5. N. N. Bol'shakova, N. S. Komlyakova, G. M. Nekrasova, *et al.*, Izv. Akad. Nauk SSSR, Ser. Fiz. **45** (9), 1666 (1981).
6. V. Ya. Shur, E. V. Nikolaeva, E. L. Rumyantsev, *et al.*, Ferroelectrics **222**, 323 (1999).
7. V. Ya. Shur, E. L. Rumyantsev, V. P. Kuminov, *et al.*, Fiz. Tverd. Tela (St. Petersburg) **41** (2), 301 (1999) [Phys. Solid State **41**, 269 (1999)].
8. V. Ya. Shur, E. L. Rumyantsev, V. P. Kuminov, *et al.*, Fiz. Tverd. Tela (St. Petersburg) **41** (1), 126 (1999) [Phys. Solid State **41**, 112 (1999)].
9. A. Kumada, Phys. Lett. A **30** (3), 186 (1969).
10. H. J. Borchardt and P. E. Bierstedt, J. Appl. Phys. **38**, 2057 (1967).
11. A. E. Alekseev, M. V. Zlokazov, A. L. Proklov, *et al.*, Izv. Akad. Nauk SSSR, Ser. Fiz. **48** (6), 1123 (1984).
12. V. Ya. Shur, V. V. Letuchev, E. L. Rumyantsev, and T. B. Charikova, Fiz. Tverd. Tela (Leningrad) **28** (9), 2829 (1986) [Sov. Phys. Solid State **28**, 1583 (1986)].
13. H. Bittel, IEEE Trans. Magn. **5** (3), 359 (1969).
14. B. Alessandro, C. Beatrice, G. Bertotti, and A. Montorsi, J. Appl. Phys. **64**, 5355 (1988).
15. A. L. Roytburd, Pis'ma Zh. Éksp. Teor. Fiz. **47** (3), 141 (1988) [JETP Lett. **47**, 171 (1988)].
16. V. Ya. Shur, A. L. Gruverman, V. P. Kuminov, and N. A. Tonkachyova, Ferroelectrics **130**, 341 (1992).
17. J. Feder, *Fractals* (Plenum, New York, 1988; Mir, Moscow, 1991).

Translated by N. Wadhwa

Physics of the Solid State, Vol. 43, No. 6, 2001, pp. 1132–1140. Translated from Fizika Tverdogo Tela, Vol. 43, No. 6, 2001, pp. 1093–1100.
Original Russian Text Copyright © 2001 by Nikiforov, Popov.

Lattice Dynamics of $LaMnO_3$: Coupling of the Lattice and Orbital Degrees of Freedom

A. E. Nikiforov and S. É. Popov
Ural State University, pr. Lenina 51, Yekaterinburg, 620083 Russia
e-mail: popovse@online.ural.ru

Received September 26, 2000

Abstract—The lattice dynamics of regular $LaMnO_3$ is calculated within a shell model with pairwise interionic interaction potentials and with a Jahn–Teller (JT) contribution included into the energy and dynamic matrix of the crystal. A correlation is made between Raman spectral lines and lattice vibrations. The positions of some lines in the Raman spectrum are found to depend heavily on the linear JT coupling constant V_e. The effect of the JT coupling on the phonon density of states of $LaMnO_3$ is investigated. *© 2001 MAIK "Nauka/Interperiodica".*

1. INTRODUCTION

Studies of the properties of manganites $La_{1-x}M_xMnO_3$ (M = Ca, Sr, Ba) are of considerable interest, because these compounds were found to show colossal magnetoresistance [1]. Investigations revealed that the ground state of manganites has a complex character, which is due to coupling between the electronic, spin, and lattice degrees of freedom [2]. A clear manifestation of this coupling is the gigantic isotope shift of the Curie temperature observed in these materials [3].

An important feature of these compounds is the orbital degeneracy of the ground state of the Mn^{3+} ion. Linear electron–vibrational interaction gives rise to distortions of the crystal structure of the lower temperature (O') phase of the regular, i.e., undoped perfect, crystalline $LaMnO_3$ (static Jahn–Teller effect) and plays an important role in the mechanism of colossal magnetoresistance [4]. Undoubtedly, this interaction has to be taken into account when modeling lattice dynamics.

A shell model, which takes into account both the long-range Coulomb interaction of ions and the short-range repulsion due to the Pauli exclusion principle, has proven to be appropriate in describing the physical properties of ionic crystals microscopically (in particular, in calculating the phonon frequencies [5]). However, the applicability of the traditional version of this model to Jahn–Teller (JT) crystals is open to question. For example, when applying the shell model to La_2CuO_4 [6, 7], one has to introduce many additional fitting parameters, the physical meaning of which is unclear; in the case of $LaMnO_3$ [8], one has to assign different charges to oxygen ions occupying different positions despite the fact that the distortions of the perovskite structure are small.

On the other hand, calculations for the JT crystals $KCuF_3$, K_2CuF_4, and $LaMnO_3$ showed [9–11] that, when the JT effect characterized by a single parameter (the linear coupling constant V_e) is explicitly taken into account, the structure and dynamic properties of these crystals can be described without introducing numerous fitting parameters characterizing anisotropic Cu–F, Cu–O, and Mn–O interactions. In the case of $LaMnO_3$ [11], this model allows one to calculate the structure of O^* and O' phases and the elastic moduli of the regular $LaMnO_3$ [11].

In this paper, the pairwise interionic-potential model including the JT contribution to the energy and to the dynamic matrix of the crystal is used to calculate the lattice dynamics of $LaMnO_3$. The results are compared with the experimental data on Raman scattering [12, 13]. The dependence of the Raman spectra on the linear JT coupling constant is investigated.

2. MODEL FOR CALCULATING THE ENERGY AND DYNAMIC MATRIX OF THE CRYSTAL

The energy per primitive cell is the sum of the lattice and JT contributions

$$E = E_{\text{lat}} + E_{\text{JT}}. \tag{1}$$

In the pairwise-potential approximation and the shell model, the lattice energy can be written as

$$E_{\text{lat}} = \frac{1}{2}\sum_i \sum_{k(\neq i)} V_{ik} + \frac{1}{2}\sum_i k_i \delta_i^2, \tag{2}$$

where the index i specifies ions in the primitive cell and the index k enumerates all ions of the crystal. The term $k_i\delta_i^2$ describes the interaction energy between the core of the ith ion and its shell shifted relative to the core by an amount $\boldsymbol{\delta}_i$. The interaction energy of a pair of ions V_{ik} is

$$V_{ik} = \frac{X_iX_k}{\mathbf{r}_{ik}} + \frac{X_iY_k}{|\mathbf{r}_{ik} - \boldsymbol{\delta}_i|} + \frac{Y_iX_k}{|\mathbf{r}_{ik} + \boldsymbol{\delta}_k|} + \frac{Y_iY_k}{|\mathbf{r}_{ik} - \boldsymbol{\delta}_i + \boldsymbol{\delta}_k|} + f_{ik}(r_{ik}) + g_{ik}(|\mathbf{r}_{ik} - \boldsymbol{\delta}_i + \boldsymbol{\delta}_k|), \tag{3}$$

where the term

$$f_{ik}(r) = -A_{ik}\exp(-B_{ik}r)/r \tag{4}$$

describes the screening of the electron densities of the interacting ions and the term

$$g_{ik}(r) = C_{ik}\exp(-D_{ik}r) - \lambda_{ik}/r^6 \tag{5}$$

describes the short-range repulsion between the ion shells (taken in the form of the Born–Mayer potential) and the van der Waals interaction; X_k and Y_k are the charges of the core and shell of the kth ion, respectively ($Q_k = X_k + Y_k$, $Y_k = -6$); and $r_{ik} = |\mathbf{r}_{ik}|$ is the distance between the ion cores. The technique for determining the pairwise potentials is described in detail in [14]. When investigating the structure of the undoped LaMnO$_3$, we used the potentials obtained by fitting to the experimental data on the structure parameters, elastic moduli, permittivities, and the phonon frequencies at the symmetry points of the Brillouin zone of NiO, CaO, SrO, La$_2$NiO$_4$, and MnO crystals [11, 14].

The many-particle JT contribution to the crystal energy is approximated by the sum of expressions for the lower sheets of adiabatic potentials of the [MnO$_6$] clusters

$$E_{\mathrm{JT}} = -\sum_n |V_e|\sqrt{Q_\theta^2(n) + Q_\varepsilon^2(n)}, \tag{6}$$

where the index n specifies the Mn^{3+} ions in the primitive cell, Q_θ and Q_ε are the symmetrized coordinates characterizing e_g distortions of the oxygen octahedra around manganese ions, and V_e is the linear JT coupling constant.

The energy of the LaMnO$_3$ crystal is calculated by Eqs. (1)–(6), and the equilibrium structure is found by minimizing the energy with respect to the parameters involved in it. It is important that the equilibrium structure of the crystal and its dynamic matrix are calculated within the same model.

To calculate the phonon frequencies, one should diagonalize the dynamic matrix of the crystal (for a given wave vector $\mathbf{k}$):

$$\begin{aligned} &D(\mathbf{k}) \\ &= M(F^{cc}(\mathbf{k}) - F^{cs}(\mathbf{k})[F^{ss}(\mathbf{k})]^{-1}F^{sc}(\mathbf{k}) + F^{\mathrm{JT}}(\mathbf{k}))_0, \end{aligned} \tag{7}$$

where $M_{k\alpha,\, n\beta} = \delta_{\alpha\beta}[m_km_n]^{-1/2}$; $F^{cc}(\mathbf{k})$ and $F^{ss}(\mathbf{k})$ are the Fourier transforms of the matrices of the second derivatives of the crystal energy (without the JT contribution) with respect to the displacements of the cores and shells of ions, respectively; $F^{cs}(\mathbf{k})$ and $F^{sc}(\mathbf{k})$ are the Fourier transforms of the matrices of the mixed derivatives of the crystal energy (without the JT contribution) with respect to the displacements of the cores and shells of ions; and $F^{\mathrm{JT}}(\mathbf{k})$ is the Fourier transform of the matrix of the second derivatives of the JT contribution in Eq. (6) with respect to the ion core displacements. In order to find the JT part of the crystal dynamic matrix, one should calculate the projections of the ion displacements onto the directions of local distortions of the e_g symmetry of the oxygenic environment of the manganese ions:

$$\begin{aligned} Q_\varepsilon(n) &= (\mathbf{e}_\varepsilon(n)\mathbf{R}), \\ Q_\theta(n) &= (\mathbf{e}_\theta(n)\mathbf{R}), \end{aligned} \tag{8}$$

where $\mathbf{e}_\varepsilon(n)$ and $\mathbf{e}_\theta(n)$ are the eigenvectors of local ε and θ distortions of the oxygen octahedra around the nth manganese ion (explicit expressions for these eigenvectors can be found, e.g., in [15]) and $\mathbf{R}$ is the vector whose components are the Cartesian coordinates of displacements of all ion cores of the lattice. By substituting Eq. (8) into Eq. (6) and calculating the derivatives with respect to the ion displacements, we find the JT contribution to the dynamic matrix in Eq. (7).

3. RESULTS AND DISCUSSION

3.1. The Equilibrium Crystalline and Orbital Structures of LaMnO$_3$

In order to calculate the phonon spectrum of the crystal consistently, one should investigate the adiabatic potential of the system. For a Jahn–Teller crystal, this potential has a complicated structure with many minima in the ion displacement space and determines the specific features of the crystal dynamics.

LaMnO$_3$ has a slightly distorted perovskite structure. For this reason, we sought stable structures which deviated only slightly from the perfect perovskite structure of symmetry O_h^1. First, we found unstable modes for the lattice part of the adiabatic potential [Eq. (1) with $V_e = 0$].

We calculated the phonon frequencies of LaMnO$_3$ with the perfect perovskite structure O_h^1. For this symmetry group, there is only one parameter, namely, the lattice constant. We determined this parameter by minimizing the crystal energy with the condition that the symmetry group remain O_h^1. Calculations showed that there are several imaginary frequencies (negative eigenvalues of the dynamic matrix), which is indicative of the instability of this crystal structure. The "unstablest" vibrational modes are near points R and M of the Brillouin zone of the crystal (the negative eigenvalues of the dynamic matrix are smallest near these points).

Figure 1 shows the vibration spectrum of LaMnO$_3$ with the undistorted perovskite structure along the Γ–R,

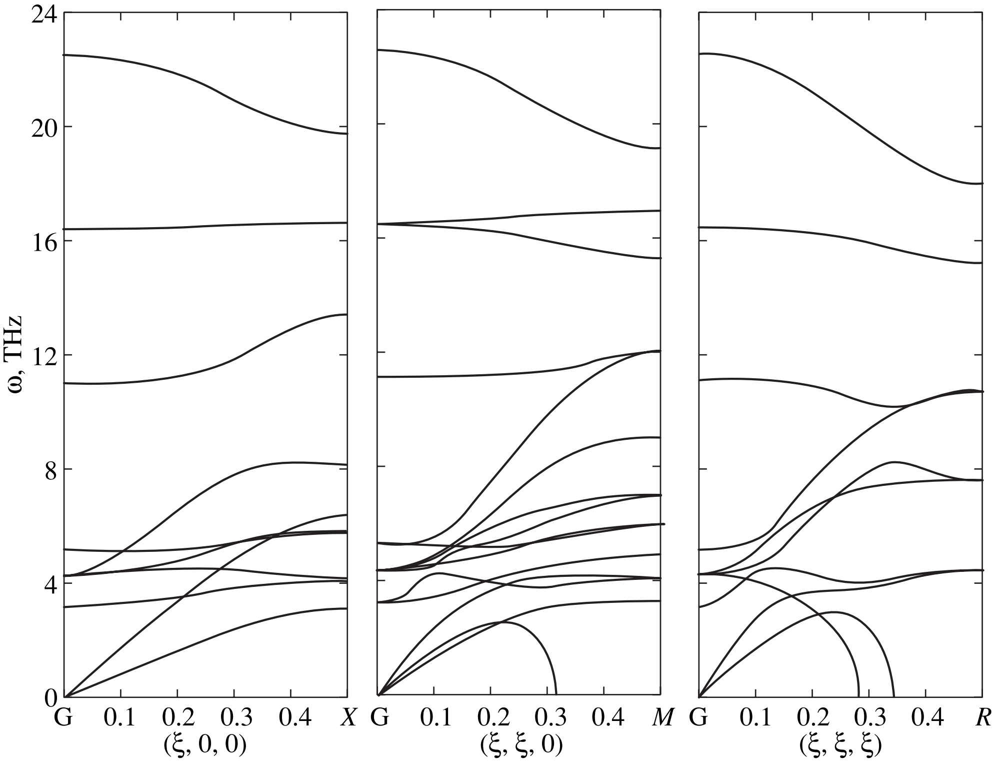

Fig. 1. Dependence of the frequencies of lattice vibrations on the wave vector in units of $(2\pi/a, 2\pi/a, 2\pi/a)$ for the perfect $LaMnO_3$ (symmetry group O_h^1).

Γ–*M*, and Γ–*X* lines of the Brillouin zone. It can be seen that the crystal has three unstable vibrational modes of the τ_9 type along the Γ–*R* line and of the τ_3 type along the Γ–*M* line of the Brillouin zone of the crystal (in these modes, the oxygen octahedra are rotated) and the crystal is stable along the Γ–*X* line. The eigenvalues of the dynamic matrix of the crystal are smallest near points *R* and *M* of the Brillouin zone. As was shown in [11, 16], the lower symmetry structure of the crystalline $LaMnO_3$ can be obtained from the perfect perovskite structure by combining τ_9 and τ_3 distortions at points *R* and *M* of the Brillouin zone of the perfect perovskite, respectively. Along with the D_{2h}^{16} structure, one can also obtain a number of structures corresponding to various combinations of these distortions, namely, a similar structure, but with another orientation of the coordinate axes; or a structure with another combination of the senses of rotation, but belonging to the same symmetry group; or a structure in which the oxygen octahedra are rotated only at point *R* of the Brillouin zone of the perfect perovskite (these last distortions correspond to the D_{3d}^6 group [16]). All these structures, except the last, are stable and differ only in the equilibrium crystal energy. The structure in which the relationship between the distortions of the oxygen octahedra is similar to that in the experimentally observed structure (*Pnma*) has the lowest energy.

An analysis of unstable vibrational modes in $LaMnO_3$ with the perfect perovskite structure revealed that the crystal is unstable only with respect to displacements of the oxygen ions; there is no instability against lanthanum ion displacements. Therefore, it can be inferred that the displacements of the lanthanum ions are induced by the transition to the lower symmetry structure.

The optimum values of the parameters of the structure with its energy not including the JT contribution ($V_e = 0$) are listed in Table 1. These values are close to those for the higher temperature (*O**) phase of the crystal. Therefore, the properties of the *O** phase can be described in terms of the model in which the crystal energy does not contain the JT contribution.

Taking into account the JT contribution to the energy leads solely to a change in the unit-cell parameters, with the symmetry group of the crystal D_{2h}^{16} remaining unchanged. The parameter V_e and the charge of the manganese ion core are refined to give the best fit to the experimental data of the unit-cell parameters in the lower temperature *O*' phase of the crystal. The value of V_e is found to be $V_e = 1.29$ eV/Å, which leads to a large value of the splitting $\Delta E_{JT} = 2|V_e|(Q_\varepsilon^2 + Q_\theta^2)^{1/2} \approx$

Table 1. Lattice parameters of $LaMnO_3$

Lattice parameters		Experiment [17] $T = 14$ K	Experiment [18] $T = 798$ K	Calculation including JT contribution [11]	Calculation without JT contribution [11]
a		5.739	5.583	5.929	5.769
b		7.672	7.889	8.117	8.185
c		5.532	5.581	5.845	5.792
La	x	0.5482	0.5217	0.538	0.522
	y	0.75	0.75	0.75	0.75
	z	–0.0079	–0.0046	–0.004	–0.002
Mn	x	0	0	0	0
	y	0	0	0	0
	z	0	0	0	0
OI	x	–0.0144	–0.011	–0.012	–0.004
	y	0.25	0.25	0.25	0.25
	z	–0.0753	–0.0687	–0.060	–0.046
OII	x	0.3068	0.288	0.304	0.281
	y	–0.0392	–0.033	–0.031	–0.026
	z	0.2252	0.223	0.226	0.219
$Q_\varepsilon(Q_2)$		0.27	0.05	0.26	–0.001
$Q_\theta(Q_3)$		–0.09	–0.001	–0.06	–0.003
φ		12.3	11.0	9.8	7.5
ψ		9.9	6.9	9.5	7.1
Φ		108	*	103	–

Note: The lattice parameters, Q_ε, and Q_θ are given in Å; the coordinates of ions are in fractions of the lattice parameters; and the angles are in degrees.

* At small JT distortions, it would make no sense to introduce the orbital-structure angle.

0.68 eV. Thus, the orthorhombic distortions of the perfect perovskite lattice are as follows [11].

(1) The R type of distortion is a rotation of the oxygen octahedra about the [101] axis of the perfect perovskite and the doubling of the unit-cell dimensions along each of the three axes ($\{k_{13}\}\tau_9(C_1\ 0\ C_1)$ in Kovalev's notation [19] or ($\varphi\ 0\ \varphi$) in the notation of [20]).

(2) The M type of distortion is a rotation of the oxygen octahedra about the b axis and the doubling of the unit-cell dimensions along two axes ($\{k_{11}\}\ \tau_3(0\ C_2\ 0)$ in the notation of [19] or ($0\ \psi\ 0$) in the notation of [20]).

(3) The ε type (Q_2) of distortion is an e-type distortion of an oxygen octahedron and the doubling of the unit cell along two axes ($\{k_{11}\}\ \tau_5$ in the notation of [19], with the choice of the $[\frac{1}{2}\ 0\ \frac{1}{2}]$ ray).

The basic distortions are accompanied by lattice relaxation. In the O^* phase, there is no ε distortion, but rotational distortions are retained.

In the equilibrium structure, local e_g-symmetry distortions of an oxygen octahedron Q_θ and Q_ε (Q_3, Q_2) are expressed in terms of the lattice parameters a, b, and c and the displacement parameters of the oxygen sublattice V_X and V_Z [11]:

$$\begin{aligned} Q_\theta &= \frac{1}{\sqrt{12}}\left[\left(b - \frac{1}{\sqrt{2}}\right)(a + c)\right], \\ Q_\varepsilon &= \sqrt{2}(V_X a + V_Z c). \end{aligned} \qquad (9)$$

A calculation shows that this structure is stable; the dynamic matrix of the crystal calculated for the *Pnma* structure with the lattice parameters and ion displacements corresponding to a minimum of the energy of the crystal with this structure has no negative eigenvalues. In addition, the matrix of elastic moduli must be positively definite.

The minimum found is separated from the adjacent minima corresponding to other combinations of the senses of low-symmetry distortions. For the structures differing only in the sense of the $Q_\varepsilon(Q_2)$ distortion, the height of the energy barrier separating them (per formula unit) is $\Delta \approx 320$ cm^{-1}. Therefore, the phonon spectrum at low temperatures can be calculated using Eqs. (7) and (8).

The local e_g-symmetry distortions significantly affect the orbital structure. In the strong JT effect

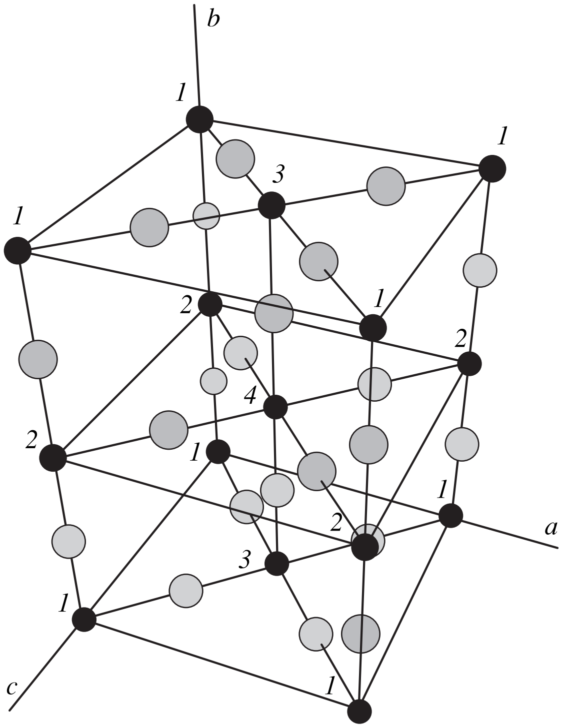

Fig. 2. Different positions of Mn^{3+} ions in the primitive cell of $LaMnO_3$. Only O^{2-} (open circles) and Mn^{3+} ions (filled circles) are shown; manganese ions are labeled *1* to *4*.

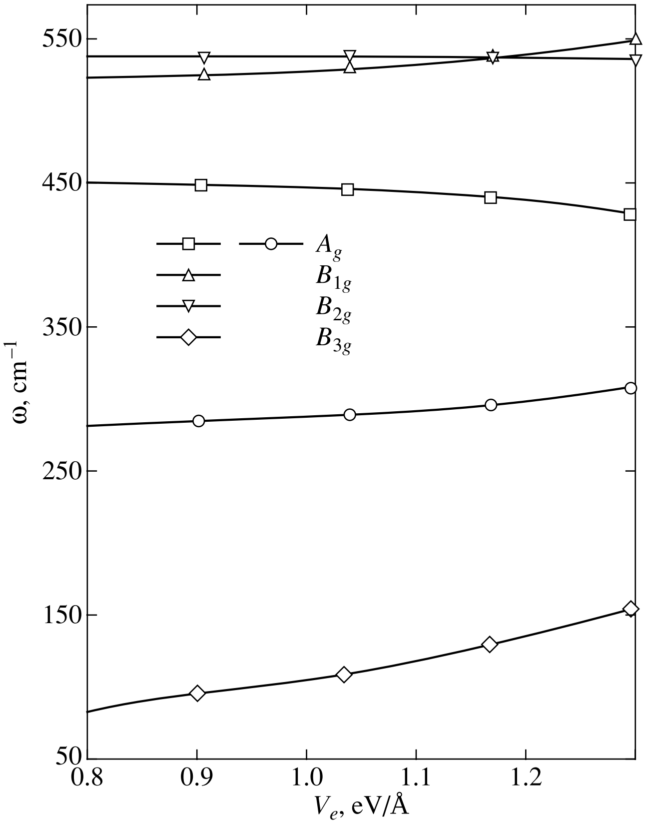

Fig. 3. Dependence of the frequencies of Raman-active vibrational modes on the linear JT coupling constant V_e.

approximation, the wave function of the ground state of the *n*th Mn^{3+} ion can be written in the form (for $V_e < 0$)

$$\psi_n = \sin(\Phi_n/2)\varphi_{n\theta} + \cos(\Phi_n/2)\varphi_{n\varepsilon}, \tag{10}$$

where Φ_n is the angle of the orbital structure and $\varphi_{n\theta}$ and $\varphi_{n\varepsilon}$ are the orbital wave functions of the ^5E state. The orbital-structure angle is considered to mean one-half the angle in space of the orbital wave functions that transform according to the *E* representation; that is, this angle defines the ground state in the basis of local orbital *E* functions.

The orbital-structure angles are given by

$$\sin\Phi = \frac{Q_\varepsilon + B_\varepsilon/V_e}{\sqrt{(V_eQ_\varepsilon + B_\varepsilon)^2 + (V_eQ_\theta + B_\theta)^2}} \approx \frac{Q_\varepsilon}{\sqrt{Q_\varepsilon^2 + Q_\theta^2}},$$
$$\cos\Phi = \frac{Q_\theta + B_\theta/V_e}{\sqrt{(V_eQ_\varepsilon + B_\varepsilon)^2 + (V_eQ_\theta + B_\theta)^2}} \approx \frac{Q_\theta}{\sqrt{Q_\varepsilon^2 + Q_\theta^2}}, \tag{11}$$

where B_ε and B_θ describe the contribution from the crystalline field of the whole crystal.

A calculation shows that the contribution from the crystalline field to Φ is small for $LaMnO_3$ (for the experimentally observed structure [17], we have $|B_\varepsilon| = 4.5 \times 10^{-3}$ eV, $|B_\theta| = 2.5 \times 10^{-3}$ eV). Therefore, we can assume that the orbital-structure angle Φ is determined by the local distortions of the oxygenic environment of the manganese ion. Thus, the orbital structure of the regular $LaMnO_3$ is characterized by the relation between the orbital-structure angles of the manganese ion sublattices (see Fig. 2):

$$\Phi_1 = \Phi_2 = -\Phi_3 = -\Phi_4 = \Phi. \tag{12}$$

The orbital and crystal structures of the $LaMnO_3$ crystal are found self-consistently; the anisotropic charge distribution over the Mn^{3+} ion causes the surrounding ions to shift, which produces a change in the crystalline field acting on the manganese ion and, therefore, in the orbital structure. According to the experimental data [17], Φ = 107° in the equilibrium structure of $LaMnO_3$ (Table 1).

3.2. The Influence of the JT Contribution on the Phonon Frequencies in the Regular $LaMnO_3$

The JT contribution to the crystal energy increases the orthorhombicity of the crystal and leads to the appearance of a $Q_\varepsilon(Q_2)$ distortion (see Table 1); it is also of importance in calculating the dynamic matrix of the crystal.

We calculated the frequencies of lattice vibrational modes active in Raman scattering (see Table 2). A comparison between the Raman scattering spectrum and the experimental data of [12, 13] shows that the strongest lines in the spectrum correspond to the vibrational modes in which the $Q_\varepsilon(Q_2)$ distortion of the crystal lat-

Table 2. Frequencies of vibrational modes active in Raman scattering

Symmetry of modes	Mode frequency			Mode	Involvement in the JT effect
	experiment [12]	experiment [13]	calculation		
A_g	–	96	89	La(x)	
A_g	140	142	154	$A_g(6)$	
A_g	198	210	193	$A_g(5)$	
A_g	257	260	225	$A_g(4)$	
A_g	284	291	309	$A_g(3)$	JT
A_g	–	333	349	$A_g(2)$	
A_g	493	493	430	$A_g(1)$	JT
B_{1g}	184	–	167	$B_{1g}(5)$	JT
B_{1g}	–	–	207	$B_{1g}(4)$	
B_{1g}	–	–	312	$B_{1g}(3)$	JT
B_{1g}	–	–	405	$B_{1g}(2)$	JT
B_{1g}	–	–	551	$B_{1g}(1)$	JT
B_{2g}	109	–	101	La(z)	
B_{2g}	170	149	165	La(x)	
B_{2g}	–	–	195	$B_{2g}(5)$	
B_{2g}	308	309	283	$B_{2g}(4)$	
B_{2g}	–	450	342	$B_{2g}(3)$	
B_{2g}	481	484	394	$B_{2g}(2)$	
B_{2g}	611	609	539	$B_{2g}(1)$	JT
B_{3g}	–	–	156	La(y)	JT
B_{3g}	–	–	182	$B_{3g}(4)$	JT
B_{3g}	–	–	266	$B_{3g}(3)$	
B_{3g}	320	–	360	$B_{3g}(2)$	
B_{3g}	–	–	570	$B_{3g}(1)$	

Note: In [13], the choice of the axes is different from that for the *Pnma* group and, therefore, the notation for vibrational modes in [13] is different from that used in this paper and in [12]. The frequencies of the modes from [13] are presented in the notation of [12] for the crystal axes corresponding to the *Pnma* group.

tice is varied. The JT contributions to the energy and dynamic matrix of the crystal give rise to significant changes in the frequencies of the modes that are involved in the JT effect. For example, the calculated frequencies of the $B_{3g}(1)$ and $B_{3g}(4)$ vibrational modes (see Table 2) are 570 and 182 $\mathrm{cm^{-1}}$, respectively; if the JT contribution and the corresponding lattice relaxation are not taken into account, these frequencies are calculated to be 574 and 451 $\mathrm{cm^{-1}}$, respectively.

Bivalent-ion doping of $\mathrm{LaMnO_3}$ significantly affects the structure and lattice dynamics of this compound [13]. Basically, this doping gives rise to an effective change in the ionic radius and charge of the rare-earth ion, to a change in the effective charge and effective linear JT coupling constant V_e of the manganese ion, and to the appearance of charge carriers in the system. Because of these and many other effects, the structure and the lattice dynamics of the manganites are changed. The model of a crystal lattice constructed in this paper enables one to investigate the influence of a change in the linear JT coupling constant on the Raman scattering spectrum of $\mathrm{LaMnO_3}$. We calculated the dependence of the frequencies of the Raman-active vibrational modes on the linear JT coupling constant V_e. Our calculation revealed that the frequency of the $B_{3g}(5)$ mode is affected significantly, whereas the frequencies of the A_g, B_{1g}, and B_{2g} modes are changed only slightly (see Fig. 3).

In $\mathrm{LaMnO_3}$ lightly doped with strontium ions, according to the data of [13], the frequency shifts of high-frequency vibrational modes are close to the calculated shifts due to the decrease in the JT coupling constant. Therefore, the frequency of the high-frequency $A_g(1)$ mode can be used for revealing the presence of a JT distortion in the crystal.

A crystal with the perfect perovskite structure has no mode active in the first-order Raman scattering.

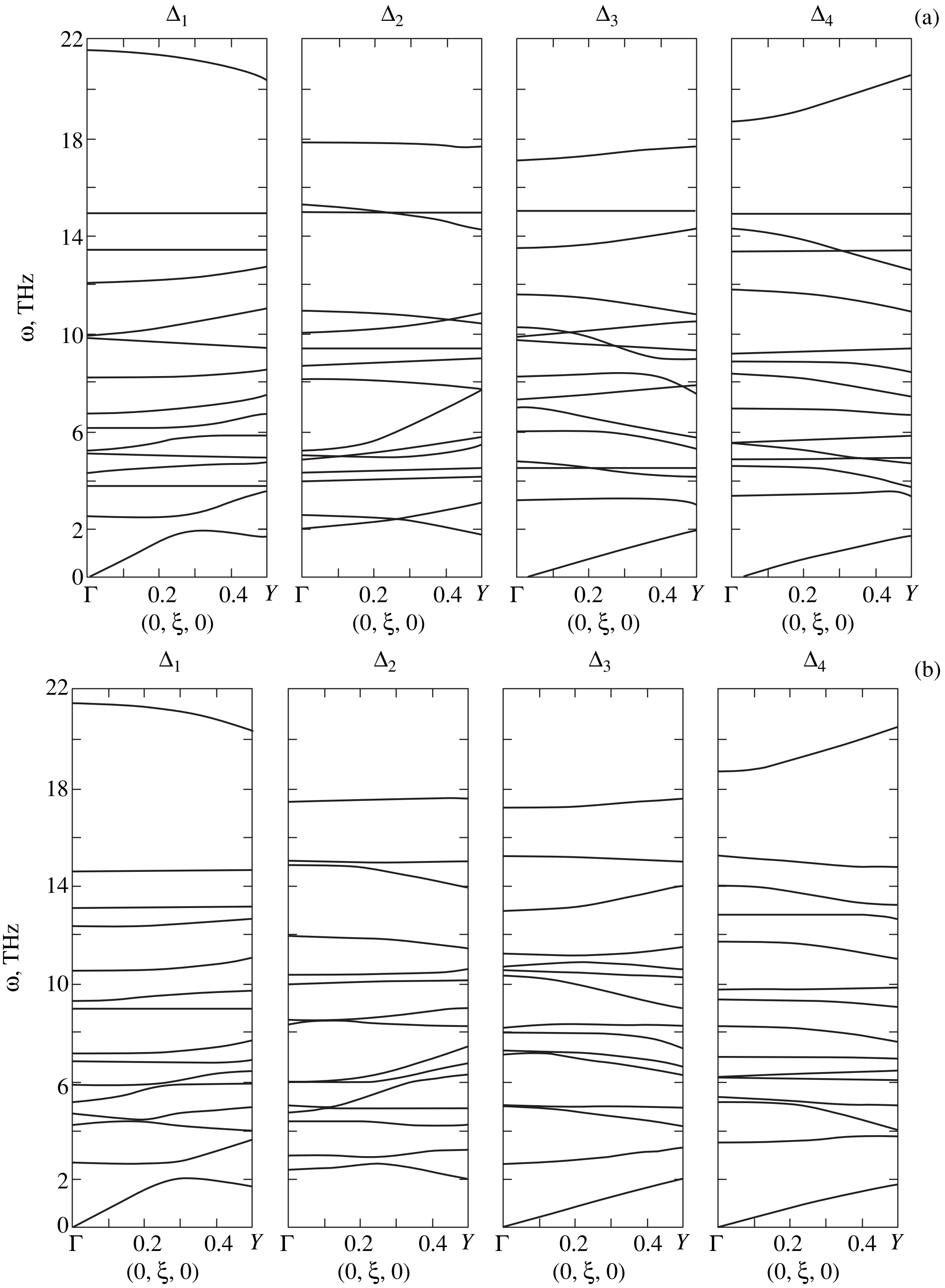

Fig. 4. Dependence of the frequencies of lattice vibrations on the wave vector in units of ($2\pi/a$, $2\pi/b$, $2\pi/c$) along the Δ line of the Brillouin zone of $LaMnO_3$, calculated (a) without and (b) with regard to the JT contribution.

Structural distortions produced by the rotation of the oxygen octahedra affect the crystal symmetry insignificantly and, therefore, cannot give rise to a noticeable increase in the Raman scattering intensity. When V_e is taken to be zero, the structure of $LaMnO_3$ becomes quasi-cubic but its low-symmetry distortions do not disappear; however, the experiment shows [13] that they are substantially decreased. Therefore, it may be inferred that the Raman spectrum of $LaMnO_3$ is determined fundamentally by the JT distortions.

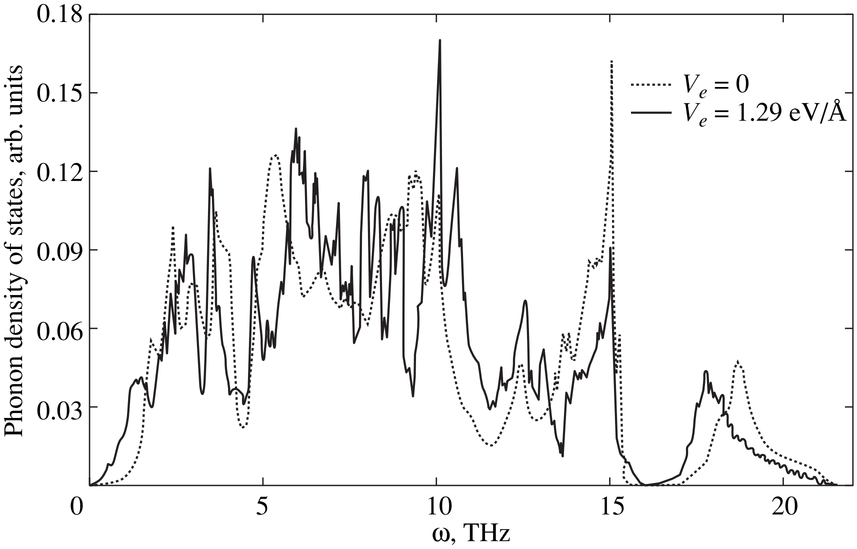

Fig. 5. Phonon density of states calculated with and without regard to the JT contribution to the energy and to the dynamic matrix of the crystal.

We calculated the dispersion of the phonon frequencies in the undoped $LaMnO_3$ in the Δ directions with and without regard to the JT contribution to the dynamic matrix of the crystal. In both cases, the structure corresponding to the energy minimum is used. A comparison of the calculated dispersion relations shows that, when the JT contribution is taken into account, the dispersion curves are "pushed apart" to a greater extent (see Fig. 4). The effect of the JT contribution is demonstrated most clearly by comparing the phonon densities of states calculated for both phases (with and without regard to this contribution) (see Fig. 5); it can be seen that the JT contribution gives rise to a shift (to lower frequencies) of the peaks that are fundamentally determined by the modes involved in the JT effect and by the acoustic modes.

4. CONCLUSION

Thus, the JT contributions to the energy and to the dynamic matrix of the crystal should be taken into account when describing the properties of JT dielectrics. It is found that the pairwise interionic interaction potential approximation adequately describes the structure, lattice dynamics, and the Raman scattering spectrum of JT crystals if the JT contribution is explicitly taken into account. A comparison between the calculations and the experimental data showed that the strongest lines in the Raman spectrum correspond to the modes that are involved in the JT effect.

Using the model developed in this paper, the frequencies of lattice vibrations are calculated for $LaMnO_3$ with the perfect perovskite structure. It is found that the vibrational modes in which oxygen octahedra are rotated are unstable, whereas the modes involving the rare-earth ions are stable.

With the pairwise-potential parameters and the charges of the lattice ions that have been determined previously, we calculated the phonon spectra in the entire Brillouin zone of the crystal with and without regard to the JT contribution. In contrast to a widely used approach, the structure corresponding to the minimum energy of the crystal was used in both cases.

ACKNOWLEDGMENTS

The authors are grateful to S.Yu. Shashkin for discussing this work with them.

This study was supported in part by CRDF, grant no. REc-005.

REFERENCES

1. A. Urushibara, Y. Morimoto, T. Arima, *et al.*, Phys. Rev. B **51** (20), 14103 (1995).
2. M. Yamada, A. Fujimori, and Y. Tokura, Rev. Mod. Phys. **70** (4), 1040 (1998).
3. G. M. Zhao, K. Conder, H. Keller, and K. A. Müller, Nature **381**, 676 (1996).
4. A. J. Millis, Phys. Rev. B **53** (13), 8434 (1996).
5. C. R. A. Catlow and W. C. Mackrodt, *Computer Simulation of Solids* (Berlin, 1982).
6. L. Pintschovius, J. M. Bassat, P. Odier, *et al.*, Phys. Rev. B **40** (4), 2229 (1989).
7. P. Koval, R. Migoni, and H. Bonadeo, J. Phys.: Condens. Matter **4** (4), 4759 (1992).
8. I. S. Smirnova, Physica B (Amsterdam) **262** (3), 247 (1999).
9. A. E. Nikiforov and S. Yu. Shashkin, Fiz. Tverd. Tela (St. Petersburg) **37** (5), 1325 (1995) [Phys. Solid State **37**, 719 (1995)].

10. A. E. Nikiforov and S. Yu. Shashkin, Fiz. Tverd. Tela (St. Petersburg) **38** (11), 3446 (1996) [Phys. Solid State **38**, 1880 (1996)].
11. A. E. Nikiforov, S. É. Popov, and S. Yu. Shashkin, Fiz. Met. Metalloved. **87** (2), 14 (1999).
12. M. N. Iliev, M. V. Abrashev, H.-G. Lee, *et al.*, Phys. Rev. B **57** (5), 2872 (1998).
13. V. B. Podobedov, A. Weber, D. B. Romero, *et al.*, Phys. Rev. B **58** (1), 43 (1998).
14. A. E. Nikiforov and S. Yu. Shashkin, Fiz. Tverd. Tela (St. Petersburg) **39** (6), 1094 (1997) [Phys. Solid State **39**, 981 (1997)].
15. I. B. Bersuker and V. Z. Polinger, *Vibronic Interactions in Molecules and Crystals* (Nauka, Moscow, 1983; Springer-Verlag, New York, 1989).
16. V. E. Naĭsh, Fiz. Met. Metalloved. **85** (6), 5 (1998).
17. Q. Huang, A. Santoro, J. W. Lynn, *et al.*, Phys. Rev. B **55** (22), 14987 (1997).
18. J. Rodríguez-Carvajal, M. Hennion, F. Moussa, *et al.*, Phys. Rev. B **57** (6), R3189 (1998).
19. O. V. Kovalev, *Irreducible and Induced Representation and Corepresentation of Fedorov Groups* (Nauka, Moscow, 1986).
20. K. S. Aleksandrov, A. T. Anistratov, B. V. Beznosikov, and N. V. Fedoseeva, *Phase Transition in Crystals of Halogen Compounds* (Nauka, Novosibirsk, 1981).

Translated by Yu. Epifanov

Physics of the Solid State, Vol. 43, No. 6, 2001, pp. 1141–1151. Translated from Fizika Tverdogo Tela, Vol. 43, No. 6, 2001, pp. 1101–1109.
Original Russian Text Copyright © 2001 by Slezov, Schmelzer.

LATTICE DYNAMICS AND PHASE TRANSITIONS

Decomposition Kinetics of a Solid Solution with the Formation of a New Phase of Complex Stoichiometric Composition

V. V. Slezov* and J. Schmelzer**
** Kharkov Institute of Physics and Technology, National Scientific Center, ul. Akademicheskaya 1, Kharkov, 61108 Ukraine*
*** Rostock University, Rostock, Germany*
e-mail: slt@mail.vl.net.ua

Received November 9, 2000

Abstract—The evolution of a metastable solid solution containing impurities of different sorts is investigated at the nucleation and transient stages upon precipitation of new-phase particles of a stoichiometric composition. The flux of new-phase particles in the size space, their maximum number, and the size distribution are determined. *© 2001 MAIK "Nauka/Interperiodica".*

1. INTRODUCTION

As is known, particles of a new phase can precipitate in solid solutions involving impurity atoms of different sorts. These particles consist of complex stoichiometric compounds, which can considerably affect all properties of materials.

A large number of works, including monographs, are devoted to the kinetics of first-order phase transformations [1–10]. However, for the most part, these works have been concerned with single-component systems and calculations of the flux of new-phase nuclei in the size space. As far as we know, the evolution of the number of new-phase nuclei and their distribution function over the entire size range with time virtually have never been studied for particles with a complex stoichiometric composition.

At the nucleation and transient stages, solid solutions are characterized by a rather high metastability with respect to the formation of different phases. Under these conditions, different phases precipitate independently of each other, because the amount of the material in solutions is sufficient for the formation of each phase. The competition begins at the late stage of decomposition (Ostwald ripening or coalescence) when the material amount has already proved insufficient for all the phases and, as in the nucleation stage, the excess surface energy plays a dominant role. This stage was considered in a number of works [11–13] and was generalized in [14].

In the present work, we investigated the nucleation and transient stages.

2. THE BASIC SYSTEM OF EQUATIONS

In consideration of the kinetics of first-order phase transformations in condensed media with the formation of a new stoichiometric phase, it is believed that its surface interfacial energy remains constant, because the atomic composition of a precipitated phase does not change in the course of growth. This is explained by the fact that the growth or dissolution of this phase occurs through structural units (groups of atoms that simultaneously add or split out) with a constant composition for a particular stoichiometric compound. Therefore, the volume of a new phase is determined by the number of structural units that comprise a particle of this phase.

The kinetics of phase transformations is described by a system of equations for the distribution function $f(n, t)$ of the number of structural units per lattice site:

$$\frac{\partial f}{\partial t} = -\frac{\partial I(n,t)}{\partial n},$$

$$f(n,t)|_{n\to 0} \longrightarrow \prod_i c_i^{\nu_i}; \quad f(n,t)|_{t=0,\, n>1} \longrightarrow 0, \tag{1}$$

$$c_{0i} = c_i(t) + \nu_i \int_0^{\infty} f(n,t)\, n\, dn;$$

$$I(n,t) = -\nu_{n,n+1}\left(\frac{\partial f}{\partial n} + \frac{1}{T}\frac{\delta \Delta\Phi}{\delta n}\right),$$

where n is the number of structural units, $V = n \times \omega_s$ is the volume, $\omega_s = \sum_i \nu_i \omega_i$ is the volume per structural unit, ω_i are the volumes per atom in the composition of a structural unit in the solid solution, ν_i are the corresponding stoichiometric coefficients of the compound, $I(n, t)$ is the flux in the space of structural units, c_{0i} are the initial concentrations of the ith atoms per matrix lattice site, and $c_i = c_i(t)$ is the conservation law for impurity atoms in the absence of sources and sinks [15, 16].

The initial conditions disregard small fluctuations that occur prior to the transformation of the system into a metastable state. The boundary condition in the course of homogeneous nucleation determines the min-

1063-7834/01/4306-1141$21.00 © 2001 MAIK "Nauka/Interperiodica"

imum (one structural unit) aggregate of atoms that form a new-phase nucleus per matrix site.

In order to obtain this system of equations (1), it is necessary to derive $I(n, t)$.

As was shown in our earlier works [15, 17], the relationship for the change in the number n of structural units has the form

$$\frac{dn}{dt} = -\nu_{n,\,n+1}\frac{\delta\Delta\Phi}{\delta n}, \qquad (2)$$

where $\frac{\delta\Delta\Phi}{\delta n}$ is the change in the thermodynamic potential of the system “new-phase particle (containing n units)–solid solution” upon transfer of one structural unit from a solution to a particle. Each subsystem is in equilibrium by itself, but an equilibrium between subsystems is absent. In the general case, $\nu_{n,\,n+1}$ is the probability of the transfer of one structural unit from a medium to a new-phase particle in a unit time.

Relationship (2) can be deduced by introducing a virtual medium into the closed system “new-phase particle–medium” in such a way that the virtual medium is in equilibrium with this particle [15, 17]. By construction, the kinetic coefficient for the transfer from the virtual medium is equal to the kinetic coefficient for the transfer of one structural unit from the medium to the new-phase particle [15, 17].

Thus, the ratio between the probability $\nu_{n,\,n+1}$ of the transfer of a structural unit from an actual medium to a new-phase particle in a unit time and the probability of the transfer from a virtual medium (which, owing to the equilibrium, is equal to the probability of the transfer of a structural unit from a new-phase particle to an actual medium in a unit time) is equal to the ratio $W/\tilde{W}$ between favorable configurations in these media.

By using the microcanonical distribution, after the appropriate integration, we obtain the probabilities of favorable configurations for the transfer of one structural unit from an actual medium W and a virtual medium $\tilde{W}$:

$$\tilde{W}(E, N, \tilde{E}, \tilde{N}-1, E_p, N_p+1) = \mathrm{const}\exp[S(E, N)$$
$$+ S(\tilde{E}, \tilde{N}-1) + S(E_p, N_p+1)] = B\exp(-\Delta\tilde{S}),$$
$$W(E, N-1, \tilde{E}, \tilde{N}, E_p, N_p+1) = B\exp(-\Delta S),$$
$$\Delta S = S(E, N) - S(E, N-1),$$

where

$$\Delta\tilde{S} = S(\tilde{E}, \tilde{N}) - S(\tilde{E}, \tilde{N}-1),$$

$$B = \mathrm{const}\exp[S(E, N) + S(\tilde{E}, \tilde{N}) + S(E_p, N_P+1)],$$

and N, $\tilde{N}$, N_p, E, $\tilde{E}$, and E_p are the mean thermodynamic numbers of particles in subsystems and the corresponding energies. The quantities without a tilde, with a tilde, and with the subscript p refer to an actual medium, a virtual medium, and a new-phase particle, respectively.

As a result, we have

$$\frac{\nu_{n+1,\,n}}{\nu_{n,\,n+1}} = \frac{\tilde{\nu}_{n+1,\,n}}{\nu_{n,\,n+1}} = \frac{\tilde{W}_{n+1,\,n}}{W_{n,\,n+1}}$$
$$= \exp[\Delta S - \Delta\tilde{S}] = \exp\Delta S_n,$$

where ΔS_n is the change in the total entropy of the closed system, which consists of the actual subsystem (ΔS) and the virtual subsystem ($\Delta\tilde{S}$). In the general case, these subsystems are not in equilibrium with each other.

The expression for the deficit of the total entropy ΔS_n upon transfer of one structural unit from a new-phase particle or, what is the same, from a virtual medium to an actual medium and in the opposite direction is derived from the general relationships obtained in [15, 17], that is,

$$\Delta S_n = -\frac{|\Delta S_n|}{\Delta E}R_{\min} = -\frac{1}{T}R_{\min}.$$

This relationship is applicable to the case when the entropy deficit increases ($\Delta S_n < 0$) as compared to the equilibrium entropy under the given conditions. Here, $R_{\min}$ is the minimum work that should be done to increase the energy of the system by $\Delta E > 0$ and, thus, to increase the deficit of the total entropy with respect to the initial total entropy of a metastable system (composed of two equilibrium subsystems) by $\Delta S_n < 0$ at its constant value.

If the conditions of the transfer are such that the entropy deficit decreases by $\Delta S_n > 0$ as compared to the equilibrium entropy under the given conditions, we obtain

$$\Delta S_n = \frac{\Delta S_n}{|\Delta E|}|R_{\max}| = \frac{1}{T}R_{\max}.$$

Here, by definition, $|R_{\max}| > 0$ is the maximum work which can be done by the metastable system to decrease its energy by $\Delta E > 0$ and, thus, to decrease the deficit of the total entropy with respect to the equilibrium entropy by $\Delta S_n > 0$ at its constant value. Formally, both formulas can be written as

$$\Delta S_n = -\frac{1}{T}R_{\min}. \qquad (3)$$

For the formal condition $R_{\min} < 0$, it is known that $|R_{\max}| = |R_{\min}| = -R_{\min}$.

By applying these relationships of the discrete approach [15, 17] to the evolution of a new-phase particle with time, we obtain formula (2). The expression for the $\nu_{n,\,n+1}$ coefficient can be found from consideration of the process near the surface of small nuclei at the nucleation stage. At the transient stage, when new-phase particles are sufficiently large and diffusion clouds of impurities are formed around them, $\nu_{n,\, n+1}$ is determined from the solution of the corresponding diffusion equation.

First, we calculate the change $\frac{\delta\Delta\Phi}{\delta n}$ in the thermodynamic potential upon the transfer of one structural unit from a solution to a new-phase particle:

$$\Delta\Phi = n\mu^s - \sum_i n_i\mu_i + 4\pi n a_s^2\sigma n^{2/3}, \tag{4}$$

where $\Delta\Phi$ is the change in the thermodynamic potential upon the formation of new-phase particles from n structural units and the transfer of n_i atoms of each component from a solution. Then,

$$\frac{\delta\Delta\Phi}{T\delta n} = \frac{1}{T}\left(\mu^s - \sum_i \nu_i\mu_i\right) + \beta n^{-1/3}, \quad \beta = \frac{8\pi}{3}\frac{\sigma a_s^2}{T}, \tag{5}$$

where μ^s is the chemical potential of the structural unit in a particle of a new stoichiometric phase, ν_i is the stoichiometric coefficient for atoms of the ith sort in the composition of the structural unit in the new-phase particle, μ_i is the chemical potential of an impurity of the ith sort in the solid solution, $\omega_s = 4\pi a_s^3/3$ is the volume per structural unit, σ is the surface energy of the new-phase particle in the solid solution, and T is the temperature in energy units.

Let us consider a new-phase particle that has the critical size n_c and is in equilibrium with the solid solution of a given composition. From the condition $\frac{\delta\Delta\Phi}{\delta n} = 0$ and taking into account that $\frac{\delta n_i}{\delta n} = \nu_i$ for stoichiometric compounds, we have

$$n_c^{1/3} = \frac{\beta}{\Sigma_i\nu_i\mu_i - \mu^s}. \tag{6}$$

For a diluted solution, when $\mu_i = \psi_i + T\ln c_i$, we obtain

$$r_c = n_c^{1/3} = \frac{\beta}{\ln\left(\frac{\Pi_i c^{\nu_i}}{K_\infty}\right)}, \tag{7}$$

where $K_\infty = \exp\left(\frac{\mu_s - \Sigma_i\nu_i\psi_i}{T}\right)$ is the chemical equilibrium constant.

At arbitrary n, from relationship (5) with due regard for formula (6) or (7), we find

$$\frac{\delta\Delta\Phi}{T\delta n} = \beta(n^{-1/3} - n_c^{-1/3}),$$

$$\frac{\Delta\Phi(n)}{T} = -\frac{\beta n}{n_c^{1/3}} + \frac{3}{2}\beta n^{2/3},$$

$$-\frac{1}{2T}\frac{\delta^2\Delta\Phi}{\delta n^2} = \frac{\beta}{6n^{4/3}} = \frac{1}{\delta n^2}, \tag{8}$$

$$\frac{\Delta\Phi(n_c)}{T} = \frac{\beta}{2}n_c^{2/3}, \quad \Delta\Phi(8n_c) = -2\beta n_c^{2/3},$$

$$\delta n = \sqrt{\frac{6m^{4/3}}{\beta}}.$$

This expression in terms of n_c is applicable to any solution. Let us also write $\frac{\delta^2\Delta\Phi}{\delta n^2}$ in the form

$$\frac{1}{2T}\frac{\delta^2\Delta\Phi(n)}{\delta n^2}\bigg|_{n = n_c} = -\frac{1}{\delta n_c^2} = -\frac{\beta}{6}n_c^{-4/3}. \tag{9}$$

Now, we determine the growth rate of a new-phase particle in terms of the number of structural units $n(V = \omega_s n)$, where ω_s is the volume per structural unit in a new phase. By ignoring the difference in the volumes per atom and, correspondingly, elastic stresses arising near a particle, we have $\omega_s = \Sigma_i\nu_i\omega_i$, where ω_i is the volume per atom in the solid solution.

The distribution function in the size space depends on the number of structural units in new-phase particles and the time. Earlier [18–24], it was shown that, for the growth or dissolution of a new-phase particle with a stoichiometric composition, the stoichiometry conditions should be met for all sorts of atoms entering into the particle composition, that is,

$$\frac{j_i}{\nu_i} = \frac{j_k}{\nu_k} = \dots. \tag{10}$$

For the flux j_i, we can write the following relationship [21]:

$$\begin{aligned} 4\pi R^2 j_i &= -\nu_{n_i,\, n_i+1}\frac{1}{T}\frac{\delta\Delta\Phi^s}{\delta n_i} \\ &= \frac{3\alpha_i D_i\tilde{c}_i n^{2/3}}{a_m^2 T}\left(\frac{\omega_s}{\omega_m}\right)^{2/3}(\mu_i(\tilde{c}_i) - \mu_i(c_{ni})). \end{aligned} \tag{11}$$

Here, $\Delta\Phi^s = \Sigma_i n_i[\mu_i(c_{ni}) - m_i(\tilde{c})]$, $\mu^s = \Sigma_i n_i\mu(c_{ni})$ is the chemical potential of a structural unit in a new-phase particle in equilibrium, $\mu_i(c_{ni})$ is the chemical potential of atoms of the ith sort that are in equilibrium with a new-phase particle of size n, $\mu_i(\tilde{c}_i)$ is the chemical potential of atoms of the ith sort near the particle surface, $\tilde{c}_i$ is the concentration of atoms of the ith sort near the particle surface, c_{ni} is the set of atomic concentrations in a particle (being in equilibrium with the new phase) of size n upon formation and decomposition of structural units of the particle,

$$\frac{\delta\Delta\Phi^s}{\delta n_i} = -\frac{1}{T}(\mu_i(\tilde{c}) - \mu_i(c_{ni})),$$

$$\nu_{n_i, n_i+1} = \frac{3\alpha_i D_i}{a_m^2}\tilde{c}_i\left(\frac{\omega_s}{\omega_m}\right)^{2/3} n^{2/3},$$

ν_{n_i, n_i+1} is the frequency of attachment of one atom of the ith sort, α_i is the sticking coefficient ($0 \le \alpha_i \le 1$), D_i is the diffusion coefficient for atoms of the ith sort, a_m is the lattice parameter of the matrix, $n = 4\pi R^3/(3\omega_s)$, $\omega_m = 4\pi a_m^3/3$, and $\omega_s = 4\pi a_s^3/3$.

By using formula (10) and the equality $\omega^s = \Sigma_i \nu_i \omega_i$, the growth rate can be represented as

$$\frac{dn}{d\tau} = \frac{4\pi R^2}{\omega^s}\sum_i \omega_i j_i = 4\pi R^2 \frac{j_i}{\nu_i}. \tag{12}$$

Let us now substitute expression (11) into formula (12). Then, we rearrange the multiplier ahead of $[\mu(\tilde{c}_i) - \mu_i(c_{ni})]$ to the left side, multiply the equation by ν_i, sum over i, and finally obtain the convenient relationship

$$\frac{dn}{dt} = \frac{3D^*}{a_m^2}\left(\frac{\omega_s}{\omega_m}\right)^{3/2} n^{2/3}\sum_i \nu_i(\mu_i(\tilde{c}_i) - \mu_i(c_{ni})),$$
$$D^{*-1} = \sum_i \frac{\nu_i^2}{\alpha_i D_i \tilde{c}_i}. \tag{13}$$

For a diluted solution, we have

$$\frac{dn}{dt} = \frac{3D^*}{a_m^2}\left(\frac{\omega_s}{\omega_m}\right)^{3/2} n^{2/3}\ln\frac{\Pi_i c^{\nu_i}}{K_n} = -\nu_{n, n+1}\frac{\delta\Delta\Phi}{\delta n}$$
$$= \frac{3D^*}{a_m^2}\left(\frac{\omega_s}{\omega_m}\right)^{2/3} n^{2/3}\beta(n_c^{-1/3} - n^{-1/3}), \tag{14}$$

where

$$\Delta\Phi = -n\ln\left(\frac{\Pi_i(c_i)^{\nu_i}}{k_n}\right) + 4\pi\sigma a_s^2 n^{2/3},$$

$$k_n = \Pi_i(c_{in})^{\nu_i} = k_\infty e^{\beta/n^{1/3}},$$

$$k_\infty = \exp((\mu_s - \Sigma_i \nu_i \psi_i)/T),$$

$$\frac{\delta\Delta\Phi}{\delta n} = -\ln\left(\frac{\Pi_i(c_i)^{\nu_i}}{k_n}\right), \quad \nu_{n, n+1} = \frac{3D^*}{a_m^2}\left(\frac{\omega_s}{\omega_m}\right)^{2/3} n^{2/3}.$$

Formula (14) describes the flux incident on a new-phase particle from the immediate vicinity of its surface, where $\tilde{c}_i$ is determined by the transfer of atoms from the bulk of the solid solution to the neighborhood of a particle. In order to find $\tilde{c}_i$, it is necessary to solve the corresponding diffusion problem [14, 22] and to match the solutions in the neighborhood of a particle.

When the impurity concentrations in a new phase and the solid solution differ considerably, the quasi-stationary solution of the diffusion equation can be used with a sufficient accuracy and the velocity of the particle surface motion can be ignored (the accuracy is of the order of $c_i/c_i^s \ll 1$) [14, 19]. Then,

$$\frac{dn}{dt} = 4\pi R^2 \frac{j_i}{\nu_i} = 3\left(\frac{\omega_s}{\omega_m}\right)^{2/3} D_i a_m^{-2}\frac{c_i - \tilde{c}_i}{\nu_i} n^{1/3}. \tag{15}$$

By matching expressions (11) and (15), we derive the equations for the determination of $\tilde{c}_i$ in the case of a diluted solution, that is,

$$\ln\left(\frac{\tilde{c}_i}{c_{in}}\right) = \frac{1}{\alpha_i n^{1/3}}\frac{c_i - \tilde{c}}{\tilde{c}_i}. \tag{16}$$

The stoichiometry equations (10) and (16) and the equilibrium condition at the boundary of a new-phase particle completely determine all the quantities $\tilde{c}_i$ and c_{in} at the nucleation stage. At $\alpha_i n^{1/3} \le 1$, we have $\tilde{c}_i \simeq c_i$ and it is more convenient to use relationship (14) for dn/dt, where $\tilde{c}_i \longrightarrow c_i$, $\ln\frac{\tilde{c}_i}{c_i n} \cong \ln\frac{c_i}{c_{in}}$.

At the transient stage, when particles with large n play a considerable role, we have $\alpha_i n^{1/3} \gg 1$. Then, as can be seen from expression (16), $\tilde{c}_i \simeq c_{in}$ and relationship (15) with due regard for condition (10) should be used for dn/dt, because the growth rate in this case is governed by the transfer of a material from the bulk of the solid solution.

Therefore, the system of Eqs. (1) and (11) [or Eq. (14) for a diluted solution] form the complete set of equations that describe the initial stage of new-phase nucleation. For the transient stage, as is seen from relationship (15), the equation for dn/dt can be somewhat rearranged.

The kinetics of new-phase nucleation is substantially simplified when the quasi-stationary flux of new-phase particles is attained in the size space $0 \le n \le n_c$ (where n_c is the critical size) [15, 22]. This is explained by the fact that, after a short time interval of attaining the quasi-stationary flux, a simpler equation can be used directly for the flux $I(n, \tau)$ [as compared to that for the distribution function $f(n, \tau)$] during the remaining time interval of the nucleation stage τ_N ($\tau \le \tau_N$). The distribution function itself is expressed through the flux in the size space. The boundary conditions for the flux $0 \le n \le n_c$ are expressed in terms of the boundary conditions for the distribution function. The time required for attaining the quasi-stationary flux can be estimated in the same manner as in [23, 25, 26]. As a result, we obtain

$$t_r = \frac{5}{3}\frac{a_m^2}{D^*}\left(\frac{\omega_s}{\omega_m}\right)^{-2/3}\frac{n_c^{2/3}}{\beta}. \tag{17}$$

3. NUCLEATION STAGE OF NEW-PHASE PARTICLES

After the attainment of the quasi-stationary flux, it is convenient to change over to the equation for $I(n, \tau)$ with a time measured from the time required to attain the quasi-stationary state ($\tau - \tau_r \longrightarrow \tau$) [15, 23, 25, 26]:

$$\frac{\partial I(n, t)}{\partial t} = \nu_{n, n+1}\left\{\frac{\partial^2 I}{\partial n^2} + \frac{1}{T}\frac{\delta \Delta\Phi}{\delta n}\frac{\delta I}{\delta n}\right\} \tag{18}$$

with the boundary condition $I(n, t)|_{n = n_c} = I(n_c)$. Here, small terms of the order of $c^{-1}cI\left(\frac{\partial I}{\partial t}\right)^{-1} \simeq \frac{\tau_N}{\tau_c} \ll 1$ (where τ_c is the time of change in the concentration) are dropped.

As will be shown below, the change in the concentration for the time τ_N is small at $n_c|_{t=0} \gg 1$. Relationship (18) is valid at $\tau \le \tau_N$ or when $I(n, \tau)$ is everywhere larger than 0. Correspondingly, the number of new-phase nuclei increases in this time interval. At $\tau > \tau_N$, $I(n_c) \simeq 0$ and the nucleation of new-phase particles is virtually completed. At this transient stage, the number of new-phase particles remains constant at $\tau_f > \tau_N$, where τ_f is the time of the onset of the late stage (Ostwald ripening) when the number of new-phase particles begins to decrease.

At the nucleation stage ($\tau < \tau_N$), $f(n, \tau)$ is conveniently expressed in terms of $I(n, \tau)$ [15, 23, 26]:

$$f(n, t) = \exp\left[-\frac{\Delta\Phi(n)}{T}\right]\int\limits_n^\infty \exp\left(\frac{\Delta\Phi(n')}{T}\right)\frac{I(n', \tau)}{\nu_{n', n'+1}}dn', \tag{19}$$

where $\nu_{n, n+1}$ and $\Delta\Phi$ for a diluted solution are determined by expression (14). Taking into consideration that the condition $I(n, \tau) = I(n_c)$ (where $0 \le n \le n_c + \delta n$) is fulfilled at $\tau > \tau_r$, we find $I(n_c)$ from the boundary condition for f at $n \longrightarrow 0$, that is,

$$\prod_i c_i^{\nu_i} = \int\limits_0^\infty \exp\left(\frac{\Delta\Phi(n')}{T}\right)\frac{I(n', \tau)}{\nu_{n, n+1}}dn', \quad \Delta\Phi(0) = 0.$$

Since $\Delta\Phi(n)$ at the point n_c exhibits a very sharp maximum ($\Delta\Phi(n) = \Delta\Phi(n_c) - (n - n_c)^2\delta n_c^{-2} \gg 1$), by using formula (9), we obtain

$$I(n_c) = \sqrt{\frac{3\beta}{2\pi}}\frac{D^*}{a_m^2}\left(\frac{\omega_s}{\omega_m}\right)^{2/3}\prod_i c_i^{\nu_i}\exp\left[-\frac{\Delta\Phi(n_c)}{T}\right]. \tag{20}$$

It is evident that relationship (20) in the case of a single-component compound can be recast into the known result [26].

At $n < n_c$, there is a maximum at $\Delta\Phi I(n, \tau) = I(n_c)$ and, for $f(n, \tau)$ [see expression (19)], we have

$$\begin{aligned} f(n, \tau)|_{n < n_c} &= \prod_i c_i^{\nu_i}\exp\left[-\frac{\Delta\Phi(n)}{T}\right] \\ &\times \frac{1}{2}\left[1 - \operatorname{erf}\left(\frac{n - n_c}{\delta n_c}\right)\right], \end{aligned} \tag{21}$$

where $\operatorname{erf}(x) = -\operatorname{erf}(-x)$ is the error function. At equilibrium, $n_c \longrightarrow \infty$ and, hence, we obtain an equilibrium distribution—heterophase fluctuations.

As was noted above, at the nucleation stage, $I(n, \tau) > 0$ and the values of $I(n, \tau)$ at given n are determined by $n' < n$ in distinction to the late stage when $I(n, \tau) < 0$ at $n < n_c$ and $I(n, \tau) > 0$ at $n > n_c$.

This means that, in different intervals of n, we can use sufficiently accurate approximate equations by matching them at the left boundaries of intervals. Let us introduce the dimensionless time $\tau = t/T$, where $T^{-1} = D^* a_m^{-2}(\omega_s/\omega_m)^{2/3}$. Note that the quantity $A = 3[(n/n_c)^{1/3} + (n/n_c)^{-1/3} + 1]^{-1}$ varies from 1 to 6/7 in the range $1 \le \frac{n}{n_c} \le 8$ [26]. Then, in this range, it is possible to set $3n^{2/3}(n^{-1/3} - n_c^{-1/3}) = -(n - n_c)n_c^{-2/3}A \cong -(n - n_c)n_c^{-2/3}$ and the equation for $I(n, \tau) = IT$ in a unit of dimensionless time takes the form

$$\begin{gathered} \frac{\partial I}{\partial \tau} = -\frac{\beta}{n_c^{2/3}}(n - n_c)\frac{\partial I}{\partial n} + 3n_c^{2/3}\frac{\partial^2 I}{\partial n^2}, \\ I|_{n = n_c} = I(n_c) = I_0 T; \quad I(n, \tau)|_{n > n_c, \tau = 0} = 0. \end{gathered} \tag{22}$$

The replacement $n^{2/3} \longrightarrow n_c^{2/3}$ in the coefficient of the second term leads to a decrease in the diffusion term of the flux at $n > n_c$, but the diffusion term itself in this range is small [26]. However, in the range of $n \simeq n_c$, in which the diffusion term plays a considerable role, this is a sufficiently good approximation. The time is reckoned from the instant of the relaxation completion τ_r, i.e., after the attainment of the quasi-stationary state in the range $0 \le n \le n_c$. Now, we make the change $I(n, \tau) \longrightarrow I(\psi(x, \tau), t(\tau))$ in such a way as to obtain the simplest equation in terms of the ψ and t variables:

$$\psi = (n - n_c)\exp(-\delta\tau), \quad \delta = \beta n_c^{-2/3},$$

$$t(\tau) = \frac{3n_c^{2/3}}{2\delta}(1 - e^{-2\delta\tau}).$$

As a result, we have

$$\frac{\partial I}{\partial t} = \frac{\partial^2 I}{\partial \psi^2}, \quad I|_{n = n_c} = I(n_c), \qquad (23)$$
$$I(n, \tau)|_{n > n_c, \tau = 0} = 0.$$

The solution of this equation is given by

$$I = I(n_c)\left(1 - \operatorname{erf}\frac{\psi}{2\sqrt{t}}\right) = I(n_c)\left(1 - \operatorname{erf}\frac{e^{-\delta\tau}(n - n_c)}{2\sqrt{t(\tau)}}\right).$$

Hence, it follows that, after the time $\tau \simeq \frac{1}{\delta} \simeq \tau_r$, the quasi-stationary state $I = I(n_c)$ at $n = g = 8n_c$ is also attained in the range $n_c \le n \le g = 8n_c$ for the time $\tau \simeq \tau_p$, i.e., for the time equal in the order of magnitude to the time of attaining the quasi-stationary state in the range of subcritical nuclei $0 \le n \le n_c$. The distribution function in the range $n_c \le n \le g \le 8n_c$ can be deduced from relationship (19) by expanding $\Delta\Phi(n)$ about the point n, that is,

$$f(n, \tau) = \frac{I_0}{\nu_{n, n+1}}\int_n^\infty e^{-\frac{1}{T}(\Delta\Phi(n) - \Delta\Phi(n'))} dn'$$

$$= \frac{I_0}{2\nu_{n, n+1}}\sqrt{\frac{\pi}{b}}\left(1 - \operatorname{erf}\left(\frac{a}{2b}\right)\right)e^{a^2/(4b^2)}, \qquad (24)$$

$$a = -\frac{1}{T}\frac{\delta\Delta\Phi}{\delta n} \ge 0, \quad b = -\frac{1}{2T}\frac{\delta^2\Delta\Phi}{\delta n^2} > 0, \quad n \ge n_c.$$

Functions (24) and (21) are smoothly matched at the point n_c. Consequently, after $\tau \simeq 2\tau_r$, the boundary conditions for $I(n, \tau) = I(n_c)$ in the range $n \ge g$ can be specified at the point $g = 8n_c$. In the range $n \ge g$, a simpler equation that can be solved exactly is also available for $I(n, \tau)$. In this case, the time interval τ_N during which new-phase particles are nucleated at a high rate should be calculated with allowance made for a decrease in the metastability of the system.

In the range $n \ge g \ge 8n_c$, for a diluted solution, we obtain

$$\frac{\Delta\Phi(n_c)}{T} = \frac{\Delta\Phi(n_c(0))}{T} + n_c(0)\varphi,$$

where $\varphi(\tau) = -\ln\prod_i\left(\frac{c_i(\tau)}{c_i(0)}\right)^{\nu_i}$ and $c_i(0) = c_{i0}$ is the initial concentration of atoms of the ith sort ($c_{i0} \ge c_i$). Correspondingly, the boundary conditions at $n = g$ are represented as

$$I(n_c) = I(n_c(0))\exp(-n_c(0)\varphi(\tau)). \qquad (25)$$

As follows from relationship (25), at $n_c(0) \gg 1$, φ varies with time by the small quantity $\varphi \simeq n_c^{-1}$ [$\varphi(0) = 0$]. The nucleation is completed, and $\varphi(\tau_n) = \frac{1}{n_c(0)}$ determines the time interval τ_N of the high-rate nucleation. The equation for I in this range takes an especially simple form in terms of the variables $r = n^{1/3}$ [26]:

$$\frac{\partial I}{\partial \tau} = -\frac{\beta}{r_c}\frac{\partial I}{\partial r} + \frac{1}{3r_c^2}\frac{\partial^2 I}{\partial r^2} \qquad (26)$$

with the boundary condition (25).

In expression (26), we dropped the terms $2r^{-3}/3\partial I/\partial r$ and $\beta/r\partial I/\partial r$ ($\beta > 1$) (small compared to $\frac{\beta}{2r_c}\frac{\delta I}{\delta r}$) and made the change $3r^{-2} \longrightarrow 3r_c^{-2}$, because $r > 2r_c$ in the range under consideration. This approximation sufficiently well describes the spectrum of “viable” new-phase particles upon their nucleation. These particles make the main contribution to the conservation law for the total number of atoms but lead to a certain increase in the spreading of the front of new-phase particle motion in the size space [26]. Substitution of $I = \exp\left(\frac{3}{2}\beta r r_c\right)\exp\left(-\frac{3}{4}\beta^2\tau\right)p(r, \tau)$ (where $r = n^{1/3} - g^{1/3}$ is measured from $r_g = g^{1/3}$) into relationship (26) gives the equation for $p(r, \tau)$,

$$\frac{\partial p}{\partial \tau} = (3r_c^2)^{-1}\frac{\partial p^2}{\partial r^2}. \qquad (27)$$

By solving Eq. (26) with the boundary conditions (25), we have

$$I = I(n_c(0))e^{3\beta r r_c/2}\frac{r}{2}\left(\frac{\pi}{3r_c}\right)^{-1/2}$$
$$\times\int_0^\tau e^{-n_c(0)\varphi(\tau') - 3\beta^2(\tau - \tau')/4 - 3r^2r_c^2/(4(\tau - \tau'))}\frac{d\tau'}{(\tau - \tau')^{3/2}}.$$

Now, we introduce the variable $z = rr_c\left(\frac{4}{3}(\tau - \tau')\right)^{-1/2}$ and rewrite I in the convenient form

$$I = I(n_c(0))\frac{2}{\sqrt{\pi}}\int_{rr_c(4\tau/3)^{-1/2}}^\infty \exp[-n_c\varphi(\tau - 3r^2r_c^2z^{-2}/4)]$$

$$\times \exp[-(3\beta r r_c z^{-1}/4 - z)^2]dz$$
$$= I(n_c(0))\frac{2}{\sqrt{\pi}}\exp[-n_c\varphi(\tau - r r_c\beta^{-1})] \qquad (28)$$

$$\times \int\limits_{z(\tau' = 0)}^{\infty} \exp[-(3\beta r r_c z^{-1}/4 - z)^2]dz.$$

Here, we took into account that the second multiplier in the first relationship exhibits a sharp maxima at the point $z = z_0$ [$f^2(z) = \left(\frac{3}{4}\frac{\beta r r_c}{z} - z\right)^2 \simeq 4(z - z_0)^2$ near $z = z_0$, $z_0 = \sqrt{\left(\frac{3}{4}\beta r r_c\right)}$]. Let us designate $\xi = 2(z - z_0)$. Then,

$$I(n, \tau) = I(n_c(0))\exp[-n_c\varphi(\tau_0(n, \tau))]$$
$$\times \frac{2}{\sqrt{\pi}}\int\limits_{\xi}^{\infty}\exp -\xi'^2 d\xi', \qquad (29)$$

where $\xi = 2(z(\tau' = 0) - z_0) = 2\left(\frac{r r_c}{\sqrt{4\tau/3}} - z_0\right)$, $\tau_0(n, \tau) = \tau - r r_c\beta^{-1} = \tau - (r - r_g)r_c/\beta$, $\tau_0(r_{\max}, \tau) = 0$, $\tau_0(g^{1/3}, \tau) = \tau$, and $r_{\max}(\tau) = r_g + \beta r_c^{-1}\tau$. Here, we used that $r = n^{1/3}$ is reckoned from $g^{1/3} = r_g$ ($r \longrightarrow r - r_g$) and $r_{\max}(t)$ is the time dependence of the center of the weakly spread front of new-phase particle motion that travels along the size axis according to Eq. (26). The front spreading is represented by the integral in expression (29). This integral is virtually equal to unity at $\xi \le 0$ and zero at $\xi \ge 0$. Therefore, without regard for the spreading, we have

$$I(n, \tau) = I(n_c(0))$$
$$\times \exp[-n_c(0)\varphi(\tau_0(n, \tau))]\Theta(r_{\max}(t) - r), \qquad (30)$$

where

$$r_{\max}(t) = r_g + \frac{\beta\tau}{r_c} = r_g + \ln\left(\prod_i \frac{c_i^{\nu_i}}{K_\infty}\right)\frac{t}{T},$$

$$\Theta(x) = 1(x > 0), \quad \Theta(x) = 0(x < 0).$$

Since the spreading of the particle front is small, expression (30) can be substituted into the integral relationship for the atom conservation laws with a good accuracy. We now write the atom conservation laws taken from [1]:

$$\varphi = -\ln\prod_i\left(\frac{c_i}{c_{i0}}\right)^{\nu_i} = \sum_i \nu_i \ln\frac{c_{i0}}{c_i},$$

$$c_{i0} = c_i + \nu_i\int\limits_0^{\infty} n f(n, \tau)dn,$$
$$\dot{c}_i = -\nu_i\int\limits_0^{\infty} n\frac{\partial f}{\partial n}dn = -\nu_i\left(I(\tau)g - \int\limits_0^{\tau} I(\tau_0)\frac{\partial n}{\partial \tau_0}d\tau_0\right). \qquad (31)$$

From the definition of $\tau_0(n, \tau)$ with due regard for formula (29), it follows that

$$n(\tau - \tau_0) = \left[r_g + \ln\prod_i\left(\frac{c_i^{\nu_i}}{c_{i0}}\right)(\tau - \tau_0)\right]^3. \qquad (32)$$

Taking into account expression (32), we changed over from the variable n to the variable $\tau_0(n, t)$ in the integral term in expression (31). Actually,

$$\int\limits_g^{\infty} I(\tau_0(n, \tau))dn = \int\limits_g^{n_{\max}} I(\tau_0)dn$$
$$= \int\limits_{\tau_0(g, \tau) = \tau}^{\tau_0(n_{\max}, \tau) = 0} I(\tau_0)\frac{dn}{d\tau_0}d\tau_0 = -\int\limits_0^{\tau} I(\tau_0)\frac{dn}{d\tau_0}d\tau_0,$$

where $dn/d\tau = -dn/\tau_0$ is the growth rate of new-phase particles (arisen at the point g at the instant τ_0) at the instant τ, $n|_{\tau = \tau_0} = g$, and $r|_{\tau = \tau_0} = r_g$. Thus, for φ, we have the equation

$$\frac{d\varphi}{d\tau} = -\sum_i \frac{\nu_i}{c_i}\frac{dc_i}{d\tau} = \left(\sum \frac{\nu_i^2}{c_i}\right)\left(I_g - \int\limits_0^{\tau} I(\tau_0)\frac{dn}{d\tau_0}d\tau_0\right). \qquad (33)$$

Equation (33), as in [26], has the simple physical meaning. A decrease in the metastability φ is determined by an increase in the number of new-phase particles (the first term on the right-hand side) and an increase in the volume of already existing new-phase particles (the second term on the right-hand side).

By taking the integral in relationship (33) by parts and using expressions (30) and (32), we obtain

$$\frac{d\varphi}{d\tau} = \left(\sum \frac{\nu_i^2}{c_i}\right)I_0 n(\tau), \quad I_0 = I(n_c(0)), \qquad (34)$$

where $I(n_c(0))$ is calculated by formula (20), $n(\tau) = n(\tau - \tau_0)|_{\tau_0 = 0} = (r_g + a\tau)^3 = r_{\max}^3(\tau)$, $a = \ln(\prod_i c_i^{\nu_i}/K_\infty)$, $\tau = tT^{-1} = D^* a_m^{-2}(\omega_s/\omega_m)^{2/3}t$, and $r_{\max}(\tau) = r_g + a\tau$.

In formula (34), we omitted the small term of the second order in the flux per lattice site $I_0 \ll 1$. Since $d\varphi/d\tau_0 \simeq I_0$,

$$-n_c\int\limits_0^{\tau} I_0 e^{-n_c\varphi(\tau_0)}\frac{d\varphi}{d\tau_0}n(\tau - \tau_0)d\tau_0 \simeq I_0^2.$$

Furthermore, in the multiplier in expression (34), the condition $c_i \simeq c_{i0}$ is met because of the small change in the concentration at the nucleation stage. The integration of Eq. (34) with the initial condition $\varphi|_{\tau = 0} = 0$ results in

$$\varphi = \left(\sum \frac{\nu_i^2}{c_{i0}}\right)\frac{I_0}{4a}[(r_g + a\tau)^4 - r_g^4], \quad (35)$$
$$\varphi(\tau_N) \simeq n_c^{-1}, \quad 0 \le \tau \le \tau_N.$$

As can be seen, τ_N depends only slightly on n_c^{-1}, that is,

$$\tau_N^4 = \left[\left(\sum \frac{\nu_i^2}{c_i}\right)I_0\frac{a^3}{4}\right]^{-1}\frac{1}{n_c}.$$

Substituting n_c and a into expression (34) at $a\tau_N \gg r_0$ gives

$$\tau_N = \frac{t_N}{T} = 4^{1/4}\beta^{-3/4}\left(\sum_i \frac{\nu_i^2}{c_{i0}}\right)^{-1/4} I_0^{-1/4}. \quad (36)$$

In order to obtain the distribution function $f(r, \tau)$ at $r \ge g^{1/3} = 2r_c$, the flux $I(r, t)$ defined by expression (30) should be derived in an explicit form. For this purpose, we determine $n_c\varphi(\tau_0(r, \tau))$ with the use of relationship (35):

$$n_c(\varphi[\tau_0(r, \tau)]) = \frac{\varphi(\tau_0(r, \tau))}{\varphi(\tau_N)} \simeq \left(\frac{\tau_0(r, \tau)}{\tau_N}\right)^4 \quad (37)$$
$$= \left(\frac{r_{\max}(\tau) - r}{r_{\max}(\tau_N) - r_g}\right)^4.$$

From expression (37), it is seen that this quantity throughout the nucleation stage at $\tau = \tau_N$ is considerably less than unity for the main part of the size distribution of nuclei $[r \le r_{\max}(\tau_N)]$ that make a dominant contribution to the integral characteristics. This means that the flux I is constant over the entire range of nucleus sizes at this stage, that is,

$$I = I_0\Theta(r_{\max}(\tau) - r), \quad (38)$$
$$\Theta(x) = 1(x > 0), \quad \Theta(x) = 0(x < 0).$$

In the range $r > r_g$, the surface energy of particles and the diffusion term in the flux at $n_c \gg 1$ can already be ignored. Then, from relationship (24), at $-T^{-1}(\delta\Delta\Phi/\delta n) \gg -0.5T^{-1}(\delta^2\Delta\Phi/\delta n^2)$ $(n = 8n_c = r_g^3)$, we obtain

$$f(r, \tau)|_{r \ge r_g} = I\left(\frac{dr}{dt}\right)^{-1} \quad (39)$$
$$= \frac{I_0}{a}\Theta(r_{\max}(\tau) - r)\Theta(r - r_g),$$

where $\frac{dr}{dt} = a$ at $r_g = 2r_c$ according to formula (14). Here, we took into account that $f(r, \tau) = f(n, \tau)3n^{2/3}$. Thus, the particle size distribution function at the nucleation stage is determined by relationships (21) and (24) at $0 \le r \le r_g$ and relationship (39) at $r_{\max} \ge r > r_g$ (a “plateau” in the size space at $\tau_N > \tau > 2\tau_r$).

The number of viable new-phase particles per matrix lattice site with due regard for relationships (38) and (39) and $r_{\max} = a\tau$ at $r \gg r_g$ is given by

$$N = \int_0^{\tau} I(g, \tau')d\tau' = \int_{r_g}^{r_{\max}(\tau)} f(n, \tau)dn = I_0\tau.$$

Correspondingly, the maximum number of particles is as follows:

$$N_{\max} = I_0\tau_N = 4^{1/4}\beta^{-3/4}I_0^{3/4}\left(\sum_i \nu_i^2/c_{i0}\right)^{1/4}. \quad (40)$$

The maximum size that is achieved by new-phase particles at the nucleation stage is represented as

$$n_{\max}^{1/3} = r_{\max} = a\tau_N = \ln\left(\frac{\Pi_i c_{i0}^{\nu_i}}{K_\infty}\right)\tau_N. \quad (41)$$

The amount of the material (structural elements) at $a\tau_N = r_{\max} \gg r_g$ is defined by

$$J = \int_{g^{1/3}}^{r_{\max}} f(r, \tau)r^3 dr = \frac{I_0 r_{\max}^4}{4a} = \frac{1}{n_c}\left(\sum \frac{\nu_i^2}{c_{i0}}\right)^{-1},$$

$$\frac{\Delta c}{c_{i0}} = \frac{c_{i0} - c_i(\tau_N)}{c_{i0}} = \frac{\nu_{i0}}{c_{i0}}J \quad (42)$$
$$= \frac{1}{n_c}\frac{\nu_{i0}}{c_{i0}}\left(\sum \frac{\nu_i^2}{c_{i0}}\right)^{-1} < n_c^{-1} \ll 1.$$

Therefore, at $n_c(0) \gg 1$, the nucleation stage is actually completed when the change in concentrations of components forming new-phase particles is relatively small.

Physically, this is quite evident, because, as is seen from formula (30), the flux described by the large parameter $n_c(0)$ in the exponent decreases exponentially fast.

This also implies that all the quantities ahead of the exponent at the nucleation stage can be replaced by their initial values.

4. TRANSIENT STAGE

The transient stage begins at $\tau \ge \tau_N$ when the stage of the high-rate nucleation of new-phase particles is completed. The distribution of new-phase particles at the nucleation stage is the initial ($\tau \le \tau_N$) distribution for the transient stage.

The possibility of disregarding the diffusion term in the size space owing to the substantial smoothness of the distribution function after the completion of the nucleation stage is of importance in considering the transient and late stages.

Moreover, as will be shown below, the surface tension can also be ignored in the range $r > r_g = 2r_c$, which corresponds to the main amount of an excess material. Consequently, at the transient and late stages, we have

$$\frac{\partial f}{\partial \tau} + \frac{\partial}{\partial r}\left(\frac{dr}{dt}\right) f(r, t) = 0, \quad r = n^{1/3},$$

$$f(r, \tau)|_{\tau = \tau_N} = f_H(r, \tau_N)\Theta(r_g - r) + f_H(r, \tau_N) \quad (43)$$

$$\times \Theta(r - r_g)\Theta(r_{\max}(\tau_N) - t),$$

where $f_H(r_0, \tau_N)$ is defined by formulas (21) and (24) at $r \le r_g$ and by formula (39) at $r \ge r_g$ and dr/dt is given by relationship (14).

The solution of Eq. (43) in the general form is represented as

$$f(r, \tau) = f(r_0, 0)\frac{\partial r_0}{\partial \tau} = [f_H(r_0, \tau_N)\Theta(r_g - r_0)$$

$$+ f_H(r_0, \tau_N)\Theta(r_0 - r_g)\Theta(r_{\max}(\tau_N) - r_0)]\frac{\partial r_0}{\partial r}, \quad (44)$$

where $r_0 = r_0(r, \tau)$ is the characteristic of Eqs. (43) and is determined by relationship (14). The time τ is measured from the time τ_N of the onset of the transient stage.

The characteristic r_0 can be found from the system consisting of Eq. (15) and the conservation laws (1):

$$\frac{dr^2}{dt} = 2\left(\frac{\omega_s}{\omega_m}\right)^{2/3} a_m^{-2} B_{in}, \quad r|_{r=0} = r_0,$$

$$B_{in} = \frac{D_i}{\nu_i}(c_i - c_{in}) = B_{jn} = \ldots = B, \quad (45)$$

$$\prod (c_{in})^{\nu_i} = K_\infty \exp\frac{\beta}{n^{1/3}}, \quad (46)$$

$$c_{i0} = c_i + \nu_i J, \quad J = \int_0^\infty f n dn. \quad (47)$$

At the transient stage, for $n > n_c$, we can replace $\beta_{in} \longrightarrow \beta_{i\infty}$ or $c_{in} \longrightarrow c_{i\infty}$ and $K_\infty \exp(\beta n^{-1/3}) \longrightarrow K_\infty$.

For $n \le n_c$, the characteristic is described by an equation that cannot be solved in the general case at arbitrary $c_i(\tau)$. However, this range of n is of no importance at the transient stage. The metastability of the system decreases owing to the growth of large-sized new-phase particles at $n \gg n_c(0)$. Small-sized particles at $n \le n_c$ that exist at the initial instant will disappear and make a small contribution to the supersaturation of the system.

With an increase in $n_c(t)$ with time, the region with $n \le n_c(t)$ will include dissolving large-sized particles with $n \gg n_c(0)$ that occur at the initial instant $\tau \ge \tau_N$ after the completion of the high-rate nucleation stage. From relationships (45)–(47), we have

$$c_{in} = c_{i0} - \nu_i J - \frac{\nu_i}{D_i A}\frac{dr^2}{dt}, \quad A = \left(\frac{\omega_s}{\omega_m}\right)^{2/3} a_m^{-2}, \quad (48)$$

$$\prod_i (c_{i0} - \nu_i J)^{\nu_i} \prod_i \left(1 - \frac{\nu_i}{D_i A(c_{i0} - \nu_i J)}\frac{dr^2}{dt}\right)^{\nu_i} = K_\infty e^{\beta/r}. \quad (49)$$

The time of the transient stage corresponds to $dt^2/dt \longrightarrow 0$, $r \gg \beta$, and $J \le J_{\max}$, where $J_{\max}$ is the maximum (under the given conditions) amount (volume) of a material per site of the new-phase lattice. This is especially true with regard to a sufficiently high initial metastability ($\Pi_i c_{i0}^{\nu_i} \gg K_\infty$ for a diluted solution) when new-phase particles at the transient stage are sufficiently large and the surface tension can be ignored but the metastability remains rather high. At the late stage, the metastability is very low and the surface tension cannot be ignored [11, 14]. It is this inclusion of the surface tension that forms the universal distribution function determined by the mass transfer mechanism at the late stage [11, 14]. On this basis, by expanding the expression in the second parentheses in the left-hand side of Eq. (49) at small $dr^2/dt \longrightarrow 0$, we obtain the approximate but sufficiently exact equation

$$\frac{dr^2}{dt} = \left[1 - \frac{K_\infty}{\Pi_i(c_{i0} - \nu_i J)^{\nu_i}}\right]\left[\sum_i \frac{\nu_i^2}{D_i}\frac{1}{A(c_{i0} - \nu_i J)}\right]^{-1}. \quad (50)$$

At $J \le J_{\max}$, Eq. (50) can be rewritten in the form

$$\frac{dr^2}{dt} = -D_{\text{eff}} A(J - J_{\max}), \quad t_N \le t \le t_f, \quad (51)$$

where

$$D_{\text{eff}} A = \left[\sum_i \frac{\nu_i^2}{D_i}\frac{1}{A(c_{i0} - \nu_i J_{\max})}\right]^{-1}\left[\sum_i \frac{\nu_i^2}{(c_{i0} - \nu_i J_{\max})}\right],$$

$$\prod_i (c_{i0} - \nu_i J_{\max})^{\nu_i} = K_\infty,$$

and t_f is the time taken to complete the transient stage. Note that, for a single-component system, the exact expression for dr^2/dt in relationship (48) can be obtained from Eq. (51) at $r \gg \beta$. The same equation holds when a precipitated compound contains a component for which the diffusion coefficient is less than or of the order of the diffusion coefficients for the other components and the initial concentration is considerably less than the concentrations of the other components.

In this case, the growth rate of new-phase particles is determined by the motion of this component. The other components are adjusted to this component, and their characteristics can be found from the conservation laws. The difference from a single-component compound lies in the fact that, when an atom of this component is attached, the volume of the particle changes by the volume of the structural unit.

As is seen from formula (44), the number of new-phase particles does not change and is given by relationship (40), that is,

$$N = \int_0^{\infty} f(r_0, r)\frac{\partial r_0}{\partial r}dr \simeq \int_{r_c}^{r_{\max}(\tau_N)} f(r_0, 0)dr_0 = N_{\max},$$

$$J = \int_0^{\infty} f(r_0, 0)\frac{\partial r_0}{\partial r}r^3(r_0, \tau)dr \qquad (52)$$

$$\simeq \int_{r_c}^{r_{\max}(\tau_N)} f(r_0, 0)r^3(r_0, \tau)dr_0 = N_{\max}r^3.$$

Here, we took into consideration that, at the transient stage, the inequality $r \gg r_{\max}(t_N)$ is fulfilled in the main range and, hence, r^3 is virtually independent of r_0. The explicit form of Eq. (51) follows from relationship (52), that is,

$$\frac{dr^2}{dt} = -D_{\text{eff}}AN_{\max}(r^3 - r_{\max}^3),$$
$$r|_{t = t_N} = r_0, \quad t_N \le t \le t_f, \qquad (53)$$

where $r_{\max} = (J_{\max}/N_{\max})^{1/3} = n_{\max}^{1/3}$ and $J_{\max}$ is defined by Eq. (51).

The variables are separated in Eq. (53), and its solution in an implicit form is represented by

$$\int_{y_0}^{y} \frac{ydy}{1 - y^3} = \frac{1}{3}\left[\ln\frac{1 - y_0}{1 - y} + \frac{1}{2}\ln\frac{y^2 + y + 1}{y_0^2 + y_0 + 1} - \sqrt{3}\right.$$
$$\left.\times\left(\arctan\frac{2}{\sqrt{3}}(y + 1/2)\right] - \arctan\frac{2}{\sqrt{3}}(y_0 + 1/2)\right) = \frac{t}{t_0}, \qquad (54)$$

$$y_0 \le y = \frac{r}{r_{\max}} \le 1, \; y_0 = \frac{r_0}{r_{\max}} \ll 1, \; t_0^{-1} = \frac{D_{\text{eff}}}{2}ANr_{\max}.$$

Substitution of A and introduction of the distance between new-phase particles $l = a_m N^{-1/3}$ gives t_0^{-1} = $D_{\text{eff}} l^{-2}(\omega_s/\omega_m)^{2/3} J_{\max}^{1/3}$. Here, N is determined from expression (40) and $J_{\max}$ is defined by Eq. (51).

From relationships (54), it is seen that y^3 in the denominator can be ignored in the main part of the spectrum of r ($y < 1$). It is natural that the same result is obtained by expanding the first part of relationship (54) in terms of $y \ll 1$. Then, we have

$$y^2 = y_0^2 + 2\frac{t}{t_0}, \quad t_0 = t_f. \qquad (55)$$

In the range $y \le 1$, y tends to 1 exponentially fast. Therefore, a population of new-phase particles is formed for the time $t_N \le t \le t_0$. In this population, the Ostwald ripening (coalescence) begins after the completion of the transient stage at $t_f \simeq t_0$ [11, 12, 14]. The size distribution function for the transient stage is defined by Eq. (44) with r_0 determined from relationship (54):

$$f = \frac{I_0 r_0}{ar}\Theta(r_{\max}(\tau_N) - r_0)\Theta(r_0 - r_g), \qquad (56)$$

where a is derived from expression (34).

As follows from relationship (55), the size range of new-phase particles that make the main contribution to the atom conservation laws at the transient stage is substantially less than the corresponding size range $r_{\max}(\tau_N) - r_g = \Delta r_0$ at its preceding nucleation stage, that is,

$$\Delta = \frac{r_0 \Delta r_0}{\sqrt{2r_{\max}^2 t/t_0}} \simeq \frac{r(\tau_N)}{r_{\max}}\Delta r_0 \ll \Delta r_0, \quad (t \ge t_0), \qquad (57)$$

where $r_{\max}$ at the transient stage is determined from relationship (53). In other words, the size range at the transient stage decreases by a factor equal to the ratio between the maximum sizes at the nucleation [$r(\tau_N)$] and transient stages.

Note that the distribution function (56) is the initial function for the late stage. At the transient stage, the right and left fronts of the distribution function along the size axis are steep. At the late stage, as a rule, the right front remains steep and the left front becomes smeared, which is associated with a considerable increase in the critical size with time [11, 12, 14].

5. CONCLUSION

The above approach can be applied for describing the formation of new-phase particles with a nonstoichiometric composition and drops in liquids with an arbitrary composition of impurities. Since the nucleation and transient stages are relatively short, their experimental investigation is rather difficult. For this reason, well-studied systems at these stages in condensed media are virtually absent. A detailed experimental investigation of these stages and a comparison with the theory can provide additional information on the parameters of the studied systems.

REFERENCES

1. M. Volmer, *Kinetik der Phasenbildung* (Th. Steinkopf, Dresden, 1933).
2. R. Becker and W. Doring, Ann. Phys. (Leipzig) **24**, 719 (1935).
3. R. Kaischew and I. Stranski, J. Phys. Chem. A **170**, 295 (1934).
4. K. Binder and D. Stauffer, Adv. Phys. **25**, 343 (1976).
5. H. Trinkaus and H. Yoo, Philos. Mag. A **55**, 269 (1987).
6. H. Wiedersich and J. Katz, Adv. Colloid Interface Sci. **10**, 33 (1979).
7. F. M. Kuni and A. P. Grinin, Kolloidn. Zh. **46** (3), 460 (1984).
8. F. M. Kuni and A. P. Grinin, Teor. Mat. Fiz. **80** (3), 418 (1989).
9. J. Katz and M. Donohue, Adv. Chem. Phys. **40**, 137 (1979).
10. I. Gutzow and J. Schmelzer, *The Vitreous State: Thermodynamics, Structure, Rheology, and Crystalization* (Springer-Verlag, Berlin, 1995).
11. I. M. Lifshits and V. V. Slezov, Zh. Éksp. Teor. Fiz. **35**, 475 (1958) [Sov. Phys. JETP **8**, 327 (1959)].
12. I. M. Lifshits and V. V. Slezov, Fiz. Tverd. Tela (Leningrad) **1**, 1401 (1959) [Sov. Phys. Solid State **1**, 1285 (1960)].
13. I. M. Lifshitz and V. V. Slezov, J. Phys. Chem. Solids **19**, 35 (1961).
14. V. V. Slezov, *Theory of Diffusive Decomposition of Solids Solution* (Moscow, 1995); Sov. Sci. Rev. **117** (1995).
15. V. V. Slezov and J. Schmelzer, Fiz. Tverd. Tela (St. Petersburg) **36**, 353 (1994) [Phys. Solid State **36**, 193 (1994)].
16. V. V. Slezov and J. Schmelzer, J. Phys. Chem. Solids **55**, 243 (1994).
17. V. V. Slezov, J. Schmelzer, and Ya. Yu. Tkach, Fiz. Tverd. Tela (St. Petersburg) **37**, 3212 (1995) [Phys. Solid State **37**, 1767 (1995)].
18. V. V. Slezov, Fiz. Tverd. Tela (St. Petersburg) **37**, 2879 (1995) [Phys. Solid State **37**, 1589 (1995)].
19. V. V. Slezov, Fiz. Tverd. Tela (St. Petersburg) **38**, 433 (1996) [Phys. Solid State **38**, 239 (1996)].
20. V. V. Slezov and V. V. Sagalovich, Fiz. Tverd. Tela (Leningrad) **17**, 1497 (1975) [Sov. Phys. Solid State **17**, 974 (1975)].
21. V. V. Slezov, J. Phys. Chem. Solids **39**, 367 (1978).
22. V. V. Slezov and V. V. Sagalovich, J. Phys. Chem. Solids **38**, 943 (1977).
23. L. M. Tanatarov and V. V. Slezov, Metallofizika **10**, 199 (1988).
24. V. V. Slezov and V. V. Sagalovich, Usp. Fiz. Nauk **151**, 67 (1987) [Sov. Phys. Usp. **30**, 23 (1987)].
25. V. V. Slezov, Fiz. Tverd. Tela (St. Petersburg) **42** (4), 733 (2000) [Phys. Solid State **42**, 751 (2000)].
26. V. V. Slezov and J. Schmelzer, Fiz. Tverd. Tela (St. Petersburg) **39** (12), 2210 (1997) [Phys. Solid State **39**, 1971 (1997)].

Translated by O. Borovik-Romanova

Physics of the Solid State, Vol. 43, No. 6, 2001, pp. 1152–1158. Translated from Fizika Tverdogo Tela, Vol. 43, No. 6, 2001, pp. 1110–1116.
Original Russian Text Copyright © 2001 by Burdov.

LOW-DIMENSIONAL SYSTEMS AND SURFACE PHYSICS

Two-Electron States in a Double Quantum Dot in a Constant Electric Field

V. A. Burdov
Lobachevskiĭ State University, pr. Gagarina 23, Nizhni Novgorod, 603600 Russia
e-mail: burdov@phys.unn.runnet.ru

Received June 22, 2000; in final form, September 4, 2000

Abstract—The wave functions of stationary states and the spectrum of two-electron system are analytically determined in a symmetric double quantum dot. It is shown that in the ground state when the external electric field is absent, electrons cannot reside in the same quantum dot due to the Coulomb blockade. This situation changes in an external electric field. At a critical field strength, the probability of finding both electrons in the same quantum dot jumpwise increases from zero to unity. *© 2001 MAIK “Nauka/Interperiodica”.*

1. INTRODUCTION

Heterostructures involving semiconductor quantum dots are promising materials for modern optoelectronics and nanoelectronics. Their optical and transport properties have been extensively investigated in recent years. The tendency to a decrease in the size of various semiconductor components dictates the necessity of producing and studying quantum dots with sizes as small as possible, for example, several nanometers [1–5].

Since heterostructures with quantum dots have attracted considerable attention as luminescence sources [6–8], the electronic spectra for quantum dots are calculated in many theoretical works (see, for example, [4, 5]). Note that the radiation accompanying transitions between size quantization levels, as a rule, was observed in experiments. In the present work, we demonstrated that the structure composed of two tunnel-coupled quantum dots (double quantum dot) with two electrons is characterized by quite different quantum transitions associated with the Coulomb electron–electron interaction. In this case, the frequency of photon radiation induced by these transitions noticeably differs not only in magnitude but also in the character of the dependence on the quantum dot size.

Moreover, the particular interest expressed in heterostructures with a double quantum dot is explained by the fact that the electron density in these systems can be transferred in a controllable way, for example, from one quantum dot to an adjacent dot, which gives grounds to consider the possibility of using a double quantum dot as a base element in quantum calculations [9]. At the same time, it is known that the Coulomb interaction in quantum dots can be quite significant. Hence, it is interesting to calculate the electron density in a double quantum dot with due regard for the electron–electron interaction (in the case when the number of electrons is larger than one) and also to evaluate the change in the charge density in response to an external electric field.

Earlier, the electronic spectra for double quantum dots were calculated in the absence of external fields [10] and in the presence of constant magnetic [11] and transverse electric [12] fields. The two-electron spectrum in the longitudinal electric field was calculated only numerically for large quantum dots with a rectangular shape [13].

In the present work, we considered a system comprised of two identical, tunnel-coupled, spherical quantum dots of radius R with two electrons in a constant electric field that is characterized by the strength $\mathbf{E}$ and is aligned with the structure axis. The two-electron spectrum and the charge distribution in dots were analytically calculated as functions of the external field strength.

2. ENERGY SPECTRUM AND ELECTRON DISTRIBUTION

It seems likely that the two-electron spectrum and the wave functions for a double quantum dot can be rigorously calculated only in a numerical way. Therefore, in order to obtain more informative analytical results, we will use certain simplifying assumptions. In particular, let us assume that the potential barrier between the quantum dots is sufficiently high (for example, the barrier height for a Si/SiO$_2$ junction is equal to 3.2 eV [2, 4]). Consequently, since the tunnel coupling between the quantum dots is weak, the level splitting energy Δ turns out to be exponentially small over the height and the thickness of the barrier. According to estimates, the value of Δ can be equal to 10^{-2} eV when the distance $2L$ between the centers of quantum dots does not exceed twice the dot diameter.

At the same time, the characteristic transition energy due to the size quantization is of the order of

1 eV at quantum dot sizes of the order of 2 nm. This is substantially larger than the splitting energy Δ, as well as the Coulomb energy and the thermal energy at room temperature. For this reason, we can restrict our consideration to the two-level approximation under the assumption that higher-lying levels are not involved in electron dynamics.

The Hamiltonian of the two-electron system can be written as

$$\hat{H} = \hat{H}_0(\mathbf{r}_1) + \hat{H}_0(\mathbf{r}_2) + V(\mathbf{r}_1) + V(\mathbf{r}_2) + V_{\text{int}}(\mathbf{r}_1, \mathbf{r}_2),$$

where $\hat{H}_0(\mathbf{r})$ is the one-particle Hamiltonian for the double quantum dot with the eigenfunctions $\chi_{0,1}(\mathbf{r})$ and the eigenvalues $E_{0,1}$, $V(\mathbf{r})$ is the potential energy of an electron in an external field, and $V_{\text{int}}(\mathbf{r}_1, \mathbf{r}_2)$ is the electron–electron interaction $V_{\text{int}}(\mathbf{r}_1, \mathbf{r}_2) = V_{\text{int}}(\mathbf{r}_2, \mathbf{r}_1)$.

Within the two-level approximation, the two-electron wave function will be sought in the form

$$\Psi(\mathbf{r}_1, \mathbf{r}_2) = \sum_{i,j=0}^{1} C_{ij}\chi_i(\mathbf{r}_1)\chi_j(\mathbf{r}_2),$$

where C_{ij} are the constant expansion coefficients. Since the magnetic field is absent in the problem under consideration, the spin part of the wave function will be omitted.

The standard procedure [14] of solving the equation for the eigenfunctions $\Psi(\mathbf{r}_1, \mathbf{r}_2)$ and the eigenvalues $\mathcal{E}$ of the Hamiltonian $\hat{H}$ results in the following equation for the C_{ij} expansion coefficients:

$$\begin{aligned} &C_{ij}(\mathcal{E} - E_i - E_j) \\ &= \sum_{n=0}^{1} C_{nj}V_{in} + \sum_{n=0}^{1} C_{in}V_{jn} + \sum_{n,m=0}^{1} C_{nm}V_{in}^{jm} \end{aligned} \tag{1}$$

with the matrix elements

$$V_{in} = \langle \chi_i(\mathbf{r})|V(\mathbf{r})|\chi_n(\mathbf{r})\rangle,$$

$$V_{in}^{jm} = \langle \chi_i(\mathbf{r}_1)\chi_j(\mathbf{r}_2)|V_{\text{int}}(\mathbf{r}_1, \mathbf{r}_2)|\chi_n(\mathbf{r}_1)\chi_m(\mathbf{r}_2)\rangle.$$

Without specifying the form of the functions $V(\mathbf{r})$ and $V_{\text{int}}(\mathbf{r}_1, \mathbf{r}_2)$, it is, however, possible to make certain conclusions about the matrix elements on the basis of symmetry properties for the interaction energy $V_{\text{int}}(\mathbf{r}_1, \mathbf{r}_2)$ with respect to permutations of particles and the symmetry of the one-particle wave functions $\chi_j(\mathbf{r})$ with respect to the reflections $z \longrightarrow -z$.

In particular, it is easy to show that the one-particle diagonal matrix elements within the infinitely high barrier approximation are identical: $V_{00} = V_{11} \equiv X$. The same is also true for the off-diagonal elements: $V_{01} = V_{10} \equiv W$. Out of sixteen matrix elements that correspond to the pair interaction, eight elements appear to be nonzero and each of the four elements of these pairs are the same: $V_{00}^{00} = V_{11}^{11} = V_{11}^{00} = V_{00}^{11} \equiv U$ and $V_{01}^{01} = V_{01}^{10} = V_{10}^{01} = V_{10}^{10} \equiv V$. The specific relationships for X, W, U, and V will be derived below. Substitution of the V_{ij} and V_{in}^{jm} matrix elements into relationship (1) leads to the system of four equations for the C_{ij} coefficients. The condition for the existence of nontrivial solutions of this system is written as

$$\begin{aligned} &(\varepsilon + V)[(\varepsilon + V)(\varepsilon - V)^2 \\ &- 4W^2(\varepsilon + V) - (\varepsilon - V)\Delta^2] = 0, \end{aligned} \tag{2}$$

where $\varepsilon = \mathcal{E} - U - 2X - \hbar^2\pi^2/mR^2$ (hereafter, the infinitely deep potential well approximation will be used for simplifying the calculations).

One out of four energies,

$$\varepsilon_1 = -V, \tag{3}$$

corresponds universally to the first excited state. The wave function of this state is antisymmetric with respect to permutations of particles and does not depend on the applied external field strength, that is,

$$\Psi_1(\mathbf{r}_1, \mathbf{r}_2) = \frac{\Psi_L(\mathbf{r}_1)\Psi_R(\mathbf{r}_2) - \Psi_R(\mathbf{r}_1)\Psi_L(\mathbf{r}_2)}{\sqrt{2}}. \tag{4}$$

Here, $\Psi_{L,R}(\mathbf{r})$ are the ground-state one-electron wave functions for the left and right quantum dots. The energies of the other three states are determined by solving the third-order equation that is derived from Eq. (2). The wave functions of these states are symmetric with respect to permutations of particles and are described by the following general expression:

$$\begin{aligned} \Psi_j(\mathbf{r}_1, \mathbf{r}_2) = {} & \frac{(\varepsilon_j + V)[(\varepsilon_j - V - 2W)\Psi_L(\mathbf{r}_1)\Psi_L(\mathbf{r}_2) + (\varepsilon_j - V + 2W)\Psi_R(\mathbf{r}_1)\Psi_R(\mathbf{r}_2)]}{\sqrt{2}\sqrt{(\varepsilon_j^2 - V^2)^2 + \Delta^2(\varepsilon_j - V)^2 + 4W^2(\varepsilon_j + V)^2}} \\ & - \frac{\Delta(\varepsilon_j - V)[\Psi_L(\mathbf{r}_1)\Psi_R(\mathrm{r}_2) + \Psi_R(\mathbf{r}_1)\Psi_L(\mathbf{r}_2)]}{\sqrt{2}\sqrt{(\varepsilon_j^2 - V^2)^2 + \Delta^2(\varepsilon_j - V)^2 + 4W^2(\varepsilon_j + V)^2}}, \\ & j = 0, 2, 3. \end{aligned} \tag{5}$$

Let us examine in more detail the solutions of Eq. (2) and the electron density distribution in the quantum dots.

We start with the case of zero external field. Then, $W = 0$ and Eq. (2) is easily solved. As a result, we have

$$\varepsilon_0 = -\sqrt{V^2+\Delta^2}, \quad \varepsilon_2 = V, \quad \varepsilon_3 = \sqrt{V^2+\Delta^2}. \tag{6}$$

The energy ε_1 is given above [see expression (3)]. It is seen that, owing to the Coulomb interaction, the energy levels as a whole are shifted by the energy $U + 2X$ [relative to which the pairs of the levels lie symmetrically (above and below)] and the degeneracy of the third level is removed.

As was noted above, the Coulomb interaction between particles gives rise to new quantum transitions. Most likely, these are the three transitions $0 \longleftrightarrow 2$, $0 \longleftrightarrow 3$, and $2 \longleftrightarrow 3$. Because of the antisymmetry with respect to permutations of particles, the first excited state can not be related through an external electric field (the operator for the interaction of particles with an external field is exactly symmetric) to any of the symmetric states described by relationship (5). Therefore, no transitions to the first state or from the first state occur.

In addition, it should be taken into account that the Coulomb matrix element V can be estimated in order of magnitude at $e^2/\epsilon R$, where ϵ is the permittivity [more exact formulas (12) and (14) will be obtained below], which is approximately equal to 0.1 eV. The energy splitting Δ, at the minimum, is less by an order of magnitude, and, hence, the energy of the transition between the second and third levels in the absence of an electric field is less than 10^{-3} eV, which does not exceed the characteristic broadening of levels ($\gtrsim 10^{-3}$ eV). Consequently, the transition $2 \longleftrightarrow 3$ most likely also cannot be observed in a real experiment.

At the same time, the energy of the transitions from two high-lying levels to the ground state is approximately equal to $2V$ (~0.1 eV), which is considerably larger (approximately by two orders of magnitude) than the broadening of levels. Therefore, when the temperature is sufficiently low and phonons are virtually absent, it is possible to obtain radiation with the frequency $2V/\hbar$. This frequency turns out to be approximately one order of magnitude less than the frequency of transitions between the size quantization levels for quantum dot sizes of several nanometers. It should also be noted that the frequencies of transitions between the Coulomb levels (6) and between the size quantization levels depend differently on the quantum dot radii (as R^{-1} and R^{-2}, respectively). As a consequence, a decrease in the quantum dot size will bring about a larger difference in the transition frequencies and vice versa. These frequencies will approach each other with an increase in the quantum dot size.

The wave functions of stationary states, except for the first excited state, can be determined from relationship (5) by setting the matrix element W equal to zero. By using expressions (4) and (5) at $W = 0$, we can derive the two-particle probabilities of the symmetric ($P_S^{(j)}$) or antisymmetric ($P_A^{(j)}$) location of electrons in the double quantum dot when they reside in different dots or in the same dot, respectively.

For the ground state, we have

$$\begin{aligned} P_S^{(0)} &= \frac{1}{2}\left(1 + \frac{V}{\sqrt{V^2+\Delta^2}}\right), \\ P_A^{(0)} &= \frac{1}{2}\left(1 - \frac{V}{\sqrt{V^2+\Delta^2}}\right). \end{aligned} \tag{7}$$

In the case when the Coulomb interaction is sufficiently strong ($V \gg \Delta$), which, according to estimates, is true for our problem, the probability that both electrons reside in the same dot is small and approximately equal to $(\Delta/2V)^2$, whereas the probability of finding electrons in different dots is close to unity.

In the first excited state, two electrons cannot be together in the same quantum dot at all. With the probability equal to unity, electrons come apart as much as possible to different dots owing to the Coulomb interaction.

The opposite situation occurs in the second excited state. Electrons reside in the same dot with a probability equal to unity and cannot be found in different dots.

Finally, in the last case, i.e., in the third excited state, we obtain $P_A^{(3)} = P_S^{(0)}$ and $P_S^{(3)} = P_A^{(0)}$. Then, with a good accuracy, we can state that electrons reside in the same quantum dot.

The location of electrons in different quantum dots in the ground state is naturally explained by the Coulomb repulsion. In this case, it can be said that the electron tunneling from one dot to another dot that already has the electron is forbidden to some extent—this phenomenon is referred to as the Coulomb blockade of tunneling [15, 16]. In order to overcome the Coulomb blockade, it is necessary to apply a certain additional external action, for example, a constant electric field along the axis of the double quantum dot. Let us calculate the spectrum and the distribution of electrons in the quantum dots in the presence of a constant electric field.

The energies of the ground state and the second and third excited states obey the third-order equation deduced from Eq. (2). Its exact solution is possible only in an implicit (the so-called trigonometric) form [17] and is rather cumbersome. Therefore, in the subsequent calculations, we will use the approximate solution of Eq. (2) with due regard for the smallness of the energy Δ compared to the Coulomb energy V.

By specifying small deviations from the solutions obtained for Eq. (2) in the zeroth approximation (i.e., at $\Delta = 0$) and ignoring the terms containing these small deviations to the third power in Eq. (2), we find

$$\varepsilon_0 = \begin{cases} -\dfrac{V^2 + W^2 + \sqrt{(V^2 - W^2)^2 + 2V^2\Delta^2}}{2V}, & |W| \le V \\ -|W| - \sqrt{(V - |W|)^2 + \Delta^2/2}, & |W| \ge V, \end{cases} \quad (8)$$

$$\varepsilon_2 = \begin{cases} V + \dfrac{4W^2 + \Delta^2/4 - \sqrt{4W^2(V - |W|)^2 + (\Delta^2/4)^2 + 2W^2\Delta^2}}{V - 3|W|}, & |W| \le V \\ \dfrac{\sqrt{(V^2 - W^2 - \Delta^2/4)^2 + 2V^2\Delta V^2 - V^2 - W^2 - \Delta^2/4}}{2V}, & |W| \ge V, \end{cases} \quad (9)$$

$$\varepsilon_3 = V + \Delta^2/4V + \sqrt{4W^2 + (\Delta^2/4V)^2}. \quad (10)$$

The exact energy of the first excited state was obtained above [see relationship (3)].

The functional dependences $\varepsilon_j(W)$ calculated by formulas (3) and (8)–(10) are depicted in Fig. 1 (numerals near the curves correspond to the numbers of the stationary states). Owing to the complete spatial symmetry of the double quantum dot, the energy spectrum is independent of the field direction and depends only on the field strength. Therefore, the curves shown in Fig. 1 are exactly symmetric.

Now, we determine the two-electron probabilities and analyze their dependence on the external field strength. Note that, unlike the case of zero field, instead of the probability $P_A^{(j)}$, it is expedient to introduce the probabilities $P_{LL}^{(j)}$ and $P_{RR}^{(j)}$ of finding both electrons in the left and right quantum dots, respectively. These probabilities are not equal to each other, because the electric field breaks the symmetry of the system.

For the first excited state, all the probabilities remain identical to those deduced in the absence of the field; i.e., $P_{LL}^{(1)} = P_{RR}^{(1)} = 0$ and $P_S^{(1)} = 1$. For the other three states, we easily obtain

$$P_{LL}^{(j)} = \frac{1}{2} \times \frac{(\varepsilon_j^2 - V^2)^2 + 4W^2(\varepsilon_j + V)^2 - 4W(\varepsilon_j + V)(\varepsilon_j^2 - V^2)}{(\varepsilon_j^2 - V^2)^2 + \Delta^2(\varepsilon_j - V)^2 + 4W^2(\varepsilon_j + V)^2},$$

$$P_S^{(j)} = \frac{(\varepsilon_j - V)^2\Delta^2}{(\varepsilon_j^2 - V^2)^2 + \Delta^2(\varepsilon_j - V)^2 + 4W^2(\varepsilon_j + V)^2}, \quad (11)$$

$$P_{RR}^{(j)} = \frac{1}{2} \times \frac{(\varepsilon_j^2 - V^2)^2 + 4W^2(\varepsilon_j + V)^2 + 4W(\varepsilon_j + V)(\varepsilon_j^2 - V^2)}{(\varepsilon_j^2 - V^2)^2 + \Delta^2(\varepsilon_j - V)^2 + 4W^2(\varepsilon_j + V)^2}.$$

It is worth noting that, according to formulas (11), the probabilities $P_S^{(j)}$ are symmetric functions of W and the probabilities $P_{RR}^{(j)}$ and $P_{LL}^{(j)}$ transform into each other when W changes its sign.

The dependences of the probabilities defined by relationships (11) are displayed in Fig. 2. As can be seen, the two-particle probabilities for the states that are symmetric with respect to the permutations of particles sharply change when passing through the anticrossing points $W = V$ or $W = 0$ and vary only slightly in the other range of W. It should also be noted that there is a correlation between the behavior of the electron density in the quantum dots (i.e., in actual fact, the two-particle probabilities) and the dependence of the energies of stationary states on the external field. It is easy to see that the matrix elements W in horizontal portions (or portions asymptotically approaching horizontal lines) of the $\varepsilon_j(W)$ dependence always correspond to the symmetric charge distribution in the quantum dots. By contrast, the portions in which the energy varies in a monotonic (and nearly linear) way with a change in the electric field correspond to the most asymmetric spatial distribution of the electron density. The change in the modes occurs at the anticrossing

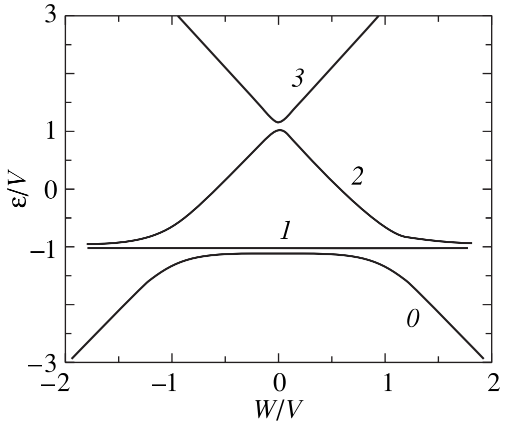

Fig. 1. Energy spectrum of the system at $\Delta/V = 0.5$.

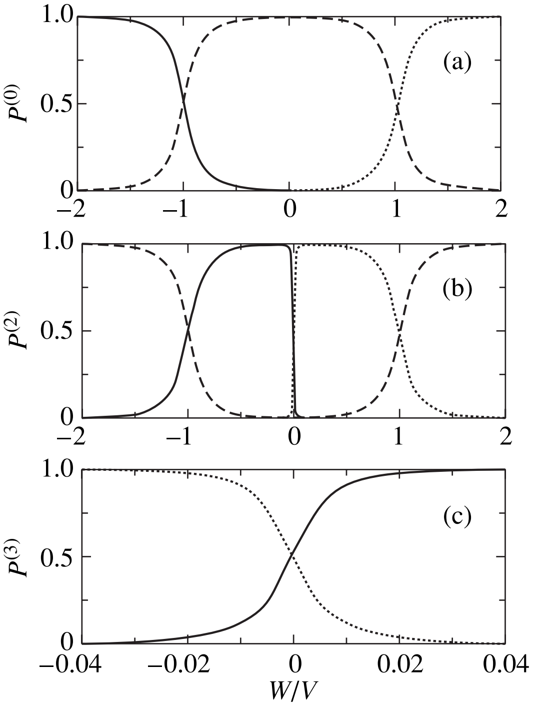

Fig. 2. Two-particle probabilities (a) $P^{(0)}$, (b) $P^{(2)}$, and (c) $P^{(3)}$, calculated by formula (11): $P_{RR}^{(j)}$ (solid lines), $P_{LL}^{(j)}$ (dotted lines), and $P_S^{(j)}$ (dashed lines). $\Delta/V = 0.25$.

points: $W = 0$ for the second and third excited states and $W = \pm V$ for the ground and second excited states.

This correlation is easily explainable. Specifically, for the ground state at $|W| < V$, the electrons reside in different quantum dots, and, hence, their potential energies in the external field have opposite signs and compensate for each other, which manifests itself in the nearly horizontal portion in the $\varepsilon_0(W)$ dependence (Fig. 1). When passing through the anticrossing point $W = V$ for the ground state, both electrons appear to be in the left dot. In this case, the potential energies of electrons in the external electric field have the same sign and are added, the result of which causes the energy of the ground state to vary proportionally to the field. Similar explanations can also be offered for the other stationary states.

Evidently, the described regularities are sufficiently universal and should not strongly depend on the specific shape of the quantum dots. This is confirmed by the results obtained by Bryant [13], who numerically calculated the two-electron spectra that exhibited the aforementioned characteristic features for an asymmetric rectangular quantum dot. In particular, the dependences of the energy on the applied voltage show pronounced inflections that indicate that the Coulomb blockade is overcome (or, by contrast, arises).

It is clear that the potential energy of electrons and, hence, the matrix elements should considerably depend on the dielectric polarization properties of materials that form both the quantum dots themselves and the surrounding medium. Let us discuss two limiting cases: the contact of two materials with close permittivities (for example, two semiconductors with close properties) and the contact of two materials with strongly differing dielectric properties (for example, a semiconductor and a dielectric).

3. QUANTUM DOTS IN A SEMICONDUCTOR

We now consider the first limiting case—the contact of two semiconductors. Let ϵ_s be the permittivity of both materials. By ignoring insignificant disturbances of the electric field near the quantum dot boundaries, we assume that the permittivity is constant throughout the volume.

In this case, the potential energy of the pair interaction between two electrons is written in the standard form $V_{\text{int}}(\mathbf{r}_1, \mathbf{r}_2) = e^2/\epsilon_s|\mathbf{r}_1 - \mathbf{r}_2|$. The potential energy of each electron in the external electric field is described by the relationship $V(\mathbf{r}) = e\mathbf{E}\mathbf{r} = eEz$ (where $-e$ is the electron charge) if the potential energy is reckoned from the midpoint between the dots. Here, E is the projection of the electric field vector onto the z axis in the semiconductor.

The matrix elements V_{ij} are calculated easily. Note that, owing to the symmetry of the problem, the diagonal matrix elements X are identically equal to zero and the off-diagonal elements appear to be nonzero $W = eEL$. It is clear that the value of W corresponds to the potential energy of an electron at the center of the right quantum dot in the constant electric field $\mathbf{E}$.

For the pair interaction matrix elements V_{int}^{jm}, we obtain

$$\begin{aligned} U &= \frac{e^2}{\epsilon_s R}\left(1 - \frac{\operatorname{Si}(2\pi)}{2\pi} + \frac{\operatorname{Si}(4\pi)}{4\pi}\right) \\ &\quad + \frac{e^2}{4\epsilon_s L} \approx \frac{0.893 e^2}{\epsilon_s R} + \frac{e^2}{4\epsilon_s L}, \\ V &= \frac{e^2}{\epsilon_s R}\left(1 - \frac{\operatorname{Si}(2\pi)}{2\pi} + \frac{\operatorname{Si}(4\pi)}{4\pi}\right) \\ &\quad - \frac{e^2}{4\epsilon_s L} \approx \frac{0.893 e^2}{\epsilon_s R} - \frac{e^2}{4\epsilon_s L}, \end{aligned} \tag{12}$$

where $\operatorname{Si}(x)$ is the sine integral function of the argument x. It can be shown that the sum $U + V$ has the meaning of the energy of interaction between the space densities of two charges at the center of the same quantum dot. The difference $U - V$ can be interpreted as the energy of interaction between the electrons at the centers of different quantum dots.

It is obvious that inclusion of the Coulomb repulsion between electrons should lead to an increase in the energy of the system. In the absence of the interaction, the energies of the stationary states (without external field) are as follows: $\hbar^2\pi^2/m - \Delta$ for the ground state, $\hbar^2\pi^2/m + \Delta$ for the third excited state, and $\hbar^2\pi^2/m$ for the first and second excited states. Consequently, reasoning from formulas (3), (6), and (12), the energies of the ground and first excited states increase approximately (without regard for the small transition energy Δ) by $e^2/2\epsilon_s L$ and the energies of the second and third excited states increase by $1.786e^2/\epsilon_s R$. The calculated two-particle probabilities demonstrate that the electrons reside in different quantum dots for the ground and first excited states and in the same dot for the second and third excited states. This explains the obtained shifts in the energy levels due to the Coulomb repulsion.

Now, the condition $|W| = V$ specifying the anticrossing points can be rewritten in the form

$$\frac{1.786e^2}{\epsilon_s R} - \frac{e^2}{2\epsilon_s L} = 2e|E|L. \tag{13}$$

Note that this condition represents the energy conservation law: the left-hand side of the relationship is the difference between the energies of the interaction of electrons in the same and different quantum dots, and the right-hand side is the work done by the electric field on a charge to move it from one quantum dot to another quantum dot. Relationship (13) determines a critical electric field strength E at which the Coulomb blockade can be overcome. At strengths less than the critical value, the electric field cannot do the work required to overcome the repulsion forces and the electrons remain in different quantum dots. According to numerical estimates, the critical electric field strength can exceed 10^5 V/cm, which corresponds to a dot-to-dot potential difference of several tens of mV.

4. QUANTUM DOTS IN A DIELECTRIC

Let us dwell on the other limiting case—the contact of two materials with strongly differing dielectric properties, for example, a semiconductor and a dielectric. In this case, the dependence $V_{\text{int}}(\mathbf{r}_1, \mathbf{r}_2)$ substantially differs from the usual Coulomb law and $V(\mathbf{r})$ is not equal to $e\mathbf{Er}$, because the fields produced by each electron appreciably differ from those in a homogeneous medium.

The total potential energy of electrons should be written taking into account the energy of interaction of each electron with the image fields (polarization fields). Note that the energy of interaction of an electron with its own image field makes the contribution to the function $V(\mathbf{r})$, and the energy of interaction with the field of another electron contributes to $V_{\text{int}}(\mathbf{r}_1, \mathbf{r}_2)$. It is rather difficult to derive the exact relationships for $V(\mathbf{r})$ and $V_{\text{int}}(\mathbf{r}_1, \mathbf{r}_2)$, and, hence, we will use certain assumptions.

In particular, we will ignore the effect of the polarization fields induced by one quantum dot on the electron in another quantum dot. Furthermore, we assume that the permittivity ϵ_s of a semiconductor is considerably larger than the permittivity ϵ_d of a dielectric (for example, $\epsilon_s \approx 12$ for silicon and $\epsilon_d \approx 4$ for silicon dioxide). This allows us to ignore anisotropic terms and to retain only the zeroth-order expansion terms in relationships for the electric field potential, which are traditionally represented in the form of Legendre polynomial expansions (see, for example, [4]).

Generally speaking, the first condition can be rigorously justified only at a sufficiently large distance between the dots, which is not true for our problem. However, as follows from the calculations, the allowance made for the mutual influence of quantum dots leads to corrections that are of the order of $(R/2L)^4$ compared to the retained terms in the energy of electron–electron interaction and $(R/2L)^3$ in the potential energy of electrons in the external electric field. Since the ratio $R/2L$ is, at least, smaller than 1/2, these corrections most likely do not exceed 10%.

With due regard for the above assumptions, the expression for the energy of interaction between a charge and its own image field can be represented as $e^2/2\epsilon_d R$. When both charges are on the same quantum dot, the energy of their interaction involves the usual Coulomb term $e^2/\epsilon_s|\mathbf{r}_1 - \mathbf{r}_2|$ and the energies of interaction of each electron with the image field of another electron, which add up to $e^2/2\epsilon_d R$. If charges are on different dots, the total energy of their interaction can be written as $e^2/2\epsilon_d L$. Within the same approximation, the potential energies of electrons in the external electric field for the right and left quantum dots are equal to eEL and $-eEL$, respectively. Therefore, at $\epsilon_d \ll \epsilon_s$, we obtain $X = e^2/2\epsilon_d R$ and $W = eEL$, where E, as before, is the electric field strength directly in the medium (in our case, in the dielectric). The matrix element X has the meaning of the characteristic energy of an electron in the external field—its own image field. Unlike the preceding case of a homogeneous medium, the appearance of the additional potential energy of an electron results in the fact that all energy levels of the stationary states are additionally shifted by e^2/ϵ_dR.

For the pair interaction matrix elements, we have

$$U = \frac{e^2}{2\epsilon_d}\left(\frac{1}{R} + \frac{1}{2L}\right), \quad V = \frac{e^2}{2\epsilon_d}\left(\frac{1}{R} - \frac{1}{2L}\right). \tag{14}$$

As in the first case (a homogeneous medium), the combinations of the matrix elements $U + V$ and $U - V$ are interpreted as the energies of interactions of the electrons in the same dot and different quantum dots, respectively. However, now, the largest contribution to these energies is made by the interaction of electrons with the polarizations fields of each other rather than by the direct Coulomb repulsion.

Let us consider the condition for overcoming the Coulomb blockade of electron tunneling. As was shown above, this occurs when the matrix elements W and V are equal to each other. As for the contact of two semiconductors with close properties, this equality has the meaning of the energy conservation law for the electron transfer from one quantum dot to another quantum dot. From relationship (14), we can also derive the critical field

$$E^* = \frac{e}{2\epsilon_d L}\left(\frac{1}{R} - \frac{1}{2L}\right),$$

which is sufficient to overcome the repulsion forces. The numerical values of the critical electric field strength and the corresponding potential difference for the semiconductor quantum dots in the dielectric are of the same order of magnitude as in the case of the contact between two semiconductors with close polarization properties.

5. CONCLUSION

Thus, at relatively low electric fields $|E| < E^*$, the configuration with electrons in different quantum dots corresponds to the potential energy minimum of the system. The stronger electric field that exceeds the critical value E^* gives rise to the new two-electron configuration corresponding to the potential energy minimum in which both electrons reside in the same left or right (depending on the field vector direction) quantum dot. Consequently, the change in the external electric field can lead to the transfer of electrons from one quantum dot to another dot and, thus, provides a way of controlling their population. Note that the transition between the stable configurations occurs abruptly with such a change in an electric field strength that is approximately one order of magnitude less than the value of E^*.

ACKNOWLEDGMENTS

This work was supported by the Russian Foundation for Basic Research, project no. 00-02-17488.

REFERENCES

1. M. A. Olshavsky, A. N. Goldstein, and A. P. Alivisatos, J. Am. Chem. Soc. **112** (25), 9438 (1990).
2. Q. Ye, R. Tsu, and E. H. Nicolian, Phys. Rev. B **44** (4), 1806 (1991).
3. A. D. Andreev and A. A. Lipovskii, Phys. Rev. B **59** (23), 15402 (1999).
4. D. Babic, R. Tsu, and R. F. Greene, Phys. Rev. B **45** (24), 14150 (1992).
5. J.-L. Zhu, Z.-Q. Li, J.-Z. Yu, *et al.*, Phys. Rev. B **55** (23), 15819 (1997).
6. K. Kim, Phys. Rev. B **57** (20), 13072 (1998).
7. M. Lannoo, C. Delerue, and G. Allan, J. Lumin. **70**, 170 (1996).
8. D. I. Tetel’baum, O. N. Gorshkov, S. A. Trushin, *et al.*, in *Proceedings of the Conference “Nanophotonics,” Nizhni Novgorod, 1999*, p. 246.
9. L. E. Fedichkin, M. V. Yanchenko, and K. A. Valiev, in *Proceedings of the 4th Russia Conference on Physics of Semiconductors, Novosibirsk, 1999*, p. 233.
10. J. Q. You and H.-Z. Zheng, Phys. Rev. B **60** (12), 8727 (1999).
11. H. Imamura, P. A. Maksym, and H. Aoki, Phys. Rev. B **59** (8), 5817 (1999).
12. S. Nagaraja, J.-P. Leburton, and R. M. Martin, Phys. Rev. B **60** (12), 8759 (1999).
13. G. W. Bryant, Phys. Rev. B **48** (11), 8024 (1993).
14. L. D. Landau and E. M. Lifshitz, *Course of Theoretical Physics*, Vol. 3: *Quantum Mechanics: Non-Relativistic Theory* (Pergamon, New York, 1977, 3rd ed.; Nauka, Moscow, 1989, 4th ed.).
15. A. A. Galkin and O. M. Ignat’ev, Pis’ma Zh. Éksp. Teor. Fiz. **9** (12), 657 (1969) [JETP Lett. **9**, 407 (1969)].
16. I. O. Kulik and R. I. Shekhter, Zh. Éksp. Teor. Fiz. **68** (2), 623 (1975) [Sov. Phys. JETP **41**, 308 (1975)].
17. G. A. Korn and T. M. Korn, *Mathematical Handbook for Scientists and Engineers* (McGraw-Hill, New York, 1961; Nauka, Moscow, 1974).

Translated by O. Borovik-Romanova

Physics of the Solid State, Vol. 43, No. 6, 2001, pp. 1159–1168. Translated from Fizika Tverdogo Tela, Vol. 43, No. 6, 2001, pp. 1117–1125.
Original Russian Text Copyright © 2001 by Lang, Korovin, Contreras-Solorio, Pavlov.

LOW-DIMENSIONAL SYSTEMS AND SURFACE PHYSICS

Reflection and Absorption of Light by a Quantum Well in a Strong Magnetic Field under Pulsed Irradiation

I. G. Lang[1], L. I. Korovin[1], D. A. Contreras-Solorio[2], and S. T. Pavlov[2, 3]
[1]*Ioffe Physicotechnical Institute, Russian Academy of Sciences, Politekhnicheskaya ul. 26, St. Petersburg, 194021 Russia*
[2]*Escuela de Física de la UAZ, Apartado Postal c-580, 98060 Zacatecas, México*
[3]*Lebedev Institute of Physics, Russian Academy of Sciences, Leninskiĭ pr. 53, Moscow, 117924 Russia*
e-mail: ilang@dor.ioffe.rssi.ru
e-mail: pavlov@ahobon.reduaz.mx

Received October 17, 2000

Abstract—The interaction between a quantum well with a large number of equidistant excited electron energy levels and light is investigated. It is shown that nonsinusoidal oscillations occur in the transmitted, reflected, and absorbed energy fluxes under exposure of the quantum well to irradiation with light pulses. For long pulses whose length γ_l^{-1} is one order of magnitude longer than the time $\hbar/\Delta E$ (where ΔE is the energy level spacing), the oscillation amplitude is small. In the case of narrow pulses when $\gamma_l^{-1} \le \hbar/\Delta E$, the oscillation amplitude is comparable to the flux magnitudes. For very narrow pulses with $\gamma_l^{-1} \ll \hbar/\Delta E$, the decaying echo of exciting pulse should be observed at the time intervals $2\pi\hbar/\Delta E$. Symmetric and asymmetric pulses are considered. The theory is applicable to narrow quantum wells in a strong magnetic field when the equidistant levels correspond to electron–hole pairs with different Landau quantum numbers. *© 2001 MAIK "Nauka/Interperiodica".*

1. INTRODUCTION

In the last decade, considerable attention has been focused on the investigation of the response of various systems to irradiation with light pulses [1–4]. The use of short pulse techniques and commercial light sources has made it possible to examine coherent phenomena in processes of interaction between light and elementary excitations in different systems, which provided new useful information on the excitation spectra and relaxation mechanisms.

A number of theoretical and experimental works are devoted to the investigation of the Wannier–Mott excitons in bulk crystals and semiconductor quantum wells by the time-resolved scattering technique, because the most interesting results obtained by this method are associated with the occurrence of discrete energy levels. It is well known that a pair of closely spaced energy levels is responsible for a new effect—sinusoidal beats in reflected and transmitted pulses at the frequency corresponding to the energy gap between the levels (see, for example, [1]).

The present work is devoted to the theoretical investigation of the reflection and absorption of light pulses in semiconductor quantum wells in a strong magnetic field. In the case when the magnetic field is aligned perpendicularly to the *xy* plane of the quantum well (it is this case that will be considered in our work), excitations in the well can be characterized by the quasi-momentum $\mathbf{K}_\perp$ in the *xy* plane, because the system in this plane is homogeneous. If the motion along the *z* axis is finite, the other indices describing excitations are discrete. In the case when the excitations in the quantum well are induced by light, the condition $\mathbf{K}_\perp = \kappa_\perp$ (where $\kappa_\perp$ is the projection of the light wave vector onto the *xy* plane) is met. We will investigate the normal irradiation of a quantum well when $\mathbf{K}_\perp = \kappa_\perp = 0$. In this case and with finite motion along the *z* axis, the excitation spectrum is always discrete [5].

If the carrier frequency ω_l of an exciting light pulse is slightly larger than the band gap E_g of a semiconductor (material of the well), the excitations induced by light are electron–hole pairs, which can be characterized by the indices

$$n_e = n_h = n, l_e, l_h,$$

where n_e (n_h) are the Landau quantum numbers of electrons (holes) and l_e (l_h) are the quantum numbers of the size quantization of electrons (holes) along the *z* axis. In the case of an infinitely deep quantum well, only the pairs with $l_e = l_h$ are formed; however, we will not restrict ourselves to this approximation. The excitation energy reckoned from the ground-state energy is given by

$$E_{\xi_0} = E_g + \varepsilon^e_{l_e} + \varepsilon^h_{l_h} + \left(n + \frac{1}{2}\right)\hbar\Omega_\mu, \qquad (1)$$

where ξ_0 is the set of the indices; $\mathbf{K}_\perp = 0$, n, l_e, and l_h; $\varepsilon^e_{l_e}$ ($\varepsilon^h_{l_h}$) is the energy of an electron (a hole) in the size quantization level l (see, for example, [6]); $\Omega_\mu = |e|H/\mu c$; $\mu = m_e m_h/(m_e + m_h)$; and m_e (m_h) is the effective electron (hole) mass. From relationship (1), it follows that the excited energy levels at the fixed numbers l_e and l_h are equidistant. Generally speaking, the equidistance of levels is disturbed when the influence of the Coulomb interaction between an electron and a hole, i.e., the exciton effect, is taken into account. However, as was shown by Lerner and Lozovik [7], the Coulomb interaction is a weak perturbation under the conditions

$$d \ll a, \quad a_H \ll a,$$

where d is the quantum well width, a is the Wannier–Mott exciton radius at zero magnetic field, and $a_H = (c\hbar/|e|H)^{1/2}$ is the magnetic length; this leads only to small shifts in the energy levels defined by expression (1). Let us assume that quantum wells are sufficiently narrow and magnetic fields are strong enough for the exciton effects to be ignored. The equidistance disturbance can also be associated with the nonparabolic shape of bands in a semiconductor; however, we will assume that this effect is weakly pronounced in the electron and hole energy range under consideration near the extrema of the conduction and valence bands.

We assume that the quantum well with a system of equidistant (not necessarily) excited energy levels is irradiated by a light pulse with a carrier frequency ω_l. Let the carrier frequency ω_l be close to the resonance with one of the energy levels. Then, there are two possible variants: either the influence of all the other levels can be neglected or it is necessary to account for the effect of a certain number of adjacent levels. The choice between these two variants depends on the shape and duration of the pulse, i.e., on the frequency spectrum corresponding to the pulse. Lang *et al.* [8, 9] predicted a ladder structure of the reflected and transmitted pulses formed under irradiation of the quantum well in a strong magnetic field by sharply asymmetric pulses with a steep front, which corresponds to the second variant. The first variant can be realized, for example, in the case of a symmetric pulse at $\gamma_l \ll \Delta\omega$, where $\Delta\omega$ is the spacing between adjacent levels, γ_l^{-1} is the characteristic pulse duration, and γ_l is the frequency spread.

Many theoretical works have dealt with the investigation of the response of an electronic system of the quantum well in the case of two or one excited levels. It should be emphasized that, for quasi-two-dimensional systems, the breaking of the translational invariance in a direction perpendicular to the plane of the quantum well results in the radiative broadening γ_r of energy levels [10, 11]. For high-quality wells, radiative broadening can be comparable to the contributions from other relaxation mechanisms and can even exceed them. This physical situation requires an adequate theoretical description in which higher-order terms in the interaction between electrons and the electromagnetic field should be taken into account [8–21].

These works are concerned with quantum wells with one or two excited levels, which are responsible for the absorption and reflection of light by the well. In the case when

$$\gamma_r \ll \gamma, \tag{2}$$

where γ is the reciprocal nonradiative lifetime of the electron excitations, the response to a monochromatic or pulsed irradiation can be studied within the perturbation theory and it is sufficient to take into account the lowest-order term in the interaction of electrons with the electromagnetic field.[1]

Under condition (2), the fields induced on the left and right of the quantum well are smaller than the exciting fields. For a monochromatic irradiation, the coefficients of the reflection $\mathcal{R}$ and the absorption $\mathcal{A}$ of light are small in comparison with unity and the transmitted pulse only slightly differs in shape from the exciting pulse. However, interesting experimental results were obtained in this case too: “pulling” of a short pulse is found in the transmitted light for times of the order of γ^{-1} and sinusoidal beats at the frequencies $\Delta E\hbar$ (where ΔE is the level spacing) are observed for two closely spaced levels (see, for example, [1]).

In the opposite case,

$$\gamma_r \geq \gamma, \tag{3}$$

the induced fields are comparable in magnitude to the exciting fields, the $\mathcal{R}$ coefficient can be close to unity, and the $\mathcal{A}$ coefficient can be close to 1/2. The irradiation of the quantum well by monochromatic light under condition (3) was studied for one excited level in [10–13, 18] and for two excited levels in [19]. In our earlier works [17, 21], we determined the shape of the reflected and transmitted pulses near the resonance of the carrier frequency with the sole level in the quantum well. It was demonstrated that the shape of the transmitted pulse under condition (3) can strongly differ from that of the exciting pulse. The radiative lifetimes of electron–hole pairs in the quantum well in a strong magnetic field were calculated in [8, 19].

In the present work, we studied the response of a multilevel system of excitations in a quantum well in a strong magnetic field upon exposure to a symmetric pulse and compared the obtained data with the results for an asymmetric pulse with a steep front.

---

[1] In the case of pulsed irradiation, the lowest-order approximation of the interaction between electrons and the electromagnetic field under condition (2) is applicable only for times $t \ll \gamma_r^{-1}$, because the intensity of the transmitted and reflected light for $t \geq \gamma_r^{-1}$ decays according to the law $\exp(-\gamma_r t)$.

2. ELECTRIC FIELDS TO THE RIGHT AND THE LEFT OF A QUANTUM WELL UNDER PULSED IRRADIATION

Let us assume that a time-limited light pulse falls on a solitary quantum well normal to its plane from the left and the electric field corresponding to this pulse has the form

$$\mathbf{E}_0(z, t) = E_0\mathbf{e}_l e^{-i\omega_l p}\{\Theta(p)e^{-\gamma_{l1}p/2} + [1-\Theta(p)]e^{\gamma_{l2}p/2}\} + \text{c.c.}, \tag{4}$$

where E_0 is the real amplitude, $\mathbf{e}_l$ is the polarization vector, ω_l is the carrier frequency,

$$p = t - zn/c, \tag{5}$$

n is the refractive index of the medium outside the quantum well, and $\Theta(p)$ is the Heaviside function. The pulse defined by relationship (4) is described by the Poynting vector

$$\mathbf{S}(z, t) = \mathbf{S}_0 P(p), \quad \mathbf{S}_0 = \frac{\mathbf{e}_z c}{2\pi n}E_0^2, \tag{6}$$

$$P(p) = \Theta(p)e^{-\gamma_{l1}p} + [1-\Theta(p)]e^{\gamma_{l2}p}, \tag{7}$$

where $\mathbf{e}_z$ is a unit vector along the z axis. We carry out the Fourier transformation of expression (4) in the form

$$\mathbf{E}_0(z, t) = E_0\mathbf{e}_l\int_{-\infty}^{\infty} d\omega e^{-i\omega p}D_0(\omega) + \text{c.c.}, \tag{8}$$

$$D_0(\omega) = \frac{i}{2\pi}\left[\left(\omega - \omega_l + \frac{i\gamma_{l1}}{2}\right)^{-1} - \left(\omega - \omega_l - \frac{i\gamma_{l2}}{2}\right)^{-1}\right]. \tag{9}$$

In the case when

$$\gamma_{l1} = \gamma_{l2} = \gamma_l, \tag{10}$$

the pulse is symmetric. For $\gamma_l \longrightarrow 0$, this pulse transforms into a monochromatic light wave with a frequency ω_l and the function $D_0(\omega)$ is modified into the Dirac function $\delta(\omega - \omega_l)$.

In [8, 9, 17], a strongly asymmetric pulse with a steep front was used, for which $\gamma_{l2} \longrightarrow \infty$ and the second terms in the curly brackets in relationship (4) and in the square brackets in expression (9) vanish.

The pulse in the form defined by relationship (4) is convenient for computations. Its drawback is the sharp shape of the peak at $t - zn/c = 0$, i.e., the discontinuity of the derivative of the function $P(p)$ at $p = 0$, but all of the qualitative theoretical conclusions that will be drawn below remain valid after the change-over to pulses with smoothed shapes.

Now, we assume that the incident waves have circular polarization, that is,

$$\mathbf{e}_l = \frac{1}{\sqrt{2}}(\mathbf{e}_x \pm i\mathbf{e}_y), \tag{11}$$

where $\mathbf{e}_x$ and $\mathbf{e}_y$ are unit vectors along the x and y axes, respectively.

Let us consider quantum wells whose width d is considerably smaller than the wavelength $c/n\omega_l$ of the light waves. In this case, the electric fields $\mathbf{E}_{\mathrm{l(r)}}$ on the left (right) of the quantum well are given by [17]

$$\mathbf{E}_{\mathrm{l(r)}}(z, t) = \mathbf{E}_0(z, t) + \Delta\mathbf{E}_{\mathrm{l(r)}}(z, t), \tag{12}$$

$$\Delta\mathbf{E}_{\mathrm{l(r)}}(z, t) = E_0\mathbf{e}_l\int_{-\infty}^{\infty} d\omega e^{-i\omega(t \pm zn/c)}D(\omega) + \text{c.c.}, \tag{13}$$

where the upper (lower) sign corresponds to the subscript l(r).

The frequency distribution $D(\omega)$ is defined as

$$\mathcal{D}(\omega) = -\frac{4\pi\chi(\omega)\mathcal{D}_0(\omega)}{1 + 4\pi\chi(\omega)}, \tag{14}$$

$$\chi(\omega) = \frac{i}{4\pi}\sum_{\rho}\frac{\gamma_{r\rho}}{2}[(\omega - \omega_\rho + i\gamma_\rho/2)^{-1} + (\omega + \omega_\rho + i\gamma_\rho/2)^{-1}] + \frac{Q(\omega)}{4\pi} - i\frac{I(\omega),}{4\pi} \tag{15}$$

where the index ρ designates the number of the excited state, $\hbar\omega_\rho$ is the excitation energy measured from the ground-state energy, $\gamma_{r\rho}(\gamma_\rho)$ is the reciprocal radiative (nonradiative) lifetime of the excitation with the index ρ, and $Q(\omega)$ and $I(\omega)$ are the contributions to the real and imaginary parts of the quantity $\chi(\omega)$ due to ignored electron excitations (for example, excitations from levels deeper than the valence band) and lattice excitations. By analogy with [8–21], we assume that the absorption and reflection of light by the quantum well is determined by a finite number of discrete levels, that is,

$$Q(\omega) \simeq 0, \quad I(\omega) \simeq 0. \tag{16}$$

Furthermore, we omit the second nonresonant term in the square brackets in expression (15).[2] Thus, we write

$$\chi(\omega) \simeq \frac{i}{4\pi}\sum_{\rho}\frac{\gamma_{r\rho}}{2}(\omega - \omega_\rho + i\gamma_\rho/2)^{-1}. \tag{17}$$

Substitution of formula (17) into expression (14) leads to

$$D(\omega) = -\frac{i\sum_{\rho}(\gamma_{r\rho}/2)(\omega - \omega_\rho + i\gamma_\rho/2)^{-1}D_0(\omega)}{1 + i\sum_{\rho}(\gamma_{r\rho}/2)(\omega - \omega_\rho + i\gamma_\rho/2)^{-1}}. \tag{18}$$

---

[2] Relationships (13)–(15) at $Q(\omega) \simeq 0$ and $I(\omega) \simeq 0$ are applicable when one of two circular polarizations corresponds to the excitation of one of two types of electron–hole pairs with identical energies from the ground state.

By substituting relationship (18) into expression (13), we can represent the induced field as the sum of two terms:

$$\Delta\mathbf{E}_r(z,t) = \Delta\mathbf{E}_1(p) + \Delta\mathbf{E}_2(p). \qquad (19)$$

The first term is determined by the contribution from the poles of the function $D_0(\omega)$. By using formulas (9) and (13), it is easy to show that this term is given by

$$\Delta\mathbf{E}_1(p) = -iE_0\mathbf{e}_l e^{-i\omega_l p}\left\{\Theta(p)e^{-\gamma_{l1}p/2} \times \frac{\sum_\rho \gamma_{r\rho}[\omega_l - \omega_\rho + i(\gamma_\rho - \gamma_{l1})/2]^{-1}}{2 + \sum_\rho \gamma_{r\rho}[\omega_l - \omega_\rho + i(\gamma_\rho - \gamma_{l1})/2]^{-1}} + [1-\Theta(p)]e^{\gamma_{l2}p/2} \times \frac{\sum_\rho \gamma_{r\rho}[\omega_l - \omega_\rho + i(\gamma_\rho - \gamma_{l2})/2]^{-1}}{2 + \sum_\rho \gamma_{r\rho}[\omega_l - \omega_\rho + i(\gamma_\rho - \gamma_{l2})/2]^{-1}}\right\} + \text{c.c.} \qquad (20)$$

The second term $\Delta\mathbf{E}_2(p)$ is the contribution from the poles of the function

$$-\frac{i\sum_\rho \gamma_{r\rho}(\omega - \omega_\rho + i\gamma_\rho/2)^{-1}}{2 + i\sum_\rho \gamma_{r\rho}(\omega - \omega_\rho + i\gamma_\rho/2)^{-1}}.$$

For one excited level, we have one pole $\omega_0 - i(\gamma + \gamma_r)/2$. In the case of two levels, there are two poles, which are easily determined. However, even for three levels, the determination of poles is complicated, because this requires the solution of a third-order equation. Therefore, for a large number of levels in the quantum well, we have to calculate $\Delta\mathbf{E}_2(p)$ under the assumption that it is applicable only at small values of $\gamma_{r\rho}$. By using only the lowest-order contribution to the interaction of electrons with light and setting

$$D(\omega) \simeq 4\pi\chi(\omega)D_0(\omega), \qquad (21)$$

we obtain the following approximate relationship for $\Delta\mathbf{E}_2(p)$:

$$\Delta\mathbf{E}_2(p) \simeq -iE_0\mathbf{e}_l\Theta(p)\sum_\rho \frac{\gamma_{r\rho}}{2}\exp(-i\omega_\rho p - \gamma_\rho p/2) \times \{[\omega_l - \omega_\rho + i(\gamma_\rho - \gamma_{l1})/2]^{-1} - [\omega_l - \omega_\rho + i(\gamma_\rho + \gamma_{l2})/2]^{-1}\} + \text{c.c.} \qquad (22)$$

Expression (20) involves sums of the type

$$S = \sum_\rho \frac{\gamma_{r\rho}}{2}(\omega_l - \omega_\rho + i\bar{\gamma}_\rho/2)^{-1},$$

where $\bar{\gamma}_\rho = \gamma_\rho - \gamma_{l1}$ or $\gamma_\rho + \gamma_{l2}$. The real parts of these sums diverge when the quantities $\gamma_{r\rho}$ are considered to be independent of the index ρ. In the case of equidistant levels, this divergence is logarithmic. Actually, this divergence is undoubtedly cut off, but the cutoff mechanism is difficult to elucidate. Therefore, we proceed as follows. Let us write the sum S in the form

$$S = \sum_\rho{}' \frac{\gamma_{r\rho}}{2}(\omega_l - \omega_\rho + i\bar{\gamma}_\rho/2)^{-1} - J(\omega_l), \qquad (23)$$

where the sign (') on the sum over ρ indicates summation over a limited number of levels. The dimensionless quantity $J(\omega_l)$ weakly depends on ω_l if the set of the frequencies defined by expression (9) is at resonance with the group of the levels included in the first term of sum (23). Expression (23) should be compared with relationship (15). The quantity $J(\omega_l) \simeq J$ is added to the constant $I(\omega) \simeq I$. So, the quantity J is unknown, but, in any case, $J \ll 1$ or ≥ 1 and, as follows from relationship (20), the contribution $\Delta\mathbf{E}_1(p)$ decays for a time of the order of γ_l^{-1}.

The problem of divergences that can arise in relationship (22) will be considered in Section 6. We will see that the divergences do not arise in the case of a symmetric exciting pulse. The expressions for the induced field $\Delta\mathbf{E}_1(z, t)$ on the left of the quantum well differ from relationships (19)–(22) only in the substitution of the variable $s = t + zn/c$ for the variable $p = t - zn/c$.

3. CALCULATION OF THE TRANSMITTED, REFLECTED, AND ABSORBED ENERGY FLUXES

For brevity, we will refer to the Poynting vectors as the energy fluxes. The transmitted flux, i.e., the flux on the right of the well, is given by

$$\mathbf{S}_r(z,t) = \frac{e_z c}{4\pi n}|\mathbf{E}_r(z,t)|^2, \qquad (24)$$

and the flux on the left of the well is written as

$$\mathbf{S}_1(z,t) = \mathbf{S}(z,t) + \mathbf{S}_{\text{ref}}(z,t), \qquad (25)$$

where $\mathbf{S}(z, t)$ is the flux of the exciting pulse [defined by relationship (6)] and $\mathbf{S}_{\text{ref}}(z, t)$ is the reflected flux determined as

$$\mathbf{S}_{\text{ref}}(z,t) = -\frac{\mathbf{e}_z c}{4\pi n}|\Delta\mathbf{E}_1(z,t)|^2. \qquad (26)$$

The absorbed energy flux is represented as

$$\mathbf{S}_{\text{abs}}(t) = \mathbf{S}_1(z=0,t) - \mathbf{S}_r(z=0,t) \qquad (27)$$

and is equal to

$$\mathbf{S}_{\text{abs}} = -\frac{\mathbf{e}_z c}{2\pi n}\mathbf{E}_{\text{r}}(z=0,t)\Delta\mathbf{E}(z=0,t), \tag{28}$$

where

$$\Delta\mathbf{E}(z=0,t) = \Delta\mathbf{E}_1(z=0,t) = \Delta\mathbf{E}_{\text{r}}(z=0,t). \tag{29}$$

We introduce the dimensionless functions $\mathcal{R}(t)$, $\mathcal{A}(t)$, and $\mathcal{T}(t)$, defining them by the relationships

$$\begin{aligned}\mathbf{S}_{\text{ref}}(z,t) &= -\mathbf{S}_0\mathcal{R}(s),\\ \mathbf{S}_{\text{abs}}(t) &= \mathbf{S}_0\mathcal{A}(t),\\ \mathbf{S}_{\text{r}}(z,t) &= \mathbf{S}_0\mathcal{T}(p).\end{aligned} \tag{30}$$

It follows from expression (27) that the relationship

$$\mathcal{R}(t) + \mathcal{A}(t) + \mathcal{T}(t) = P(t) \tag{31}$$

always holds true. The quantities $\mathcal{R}(t)$ and $\mathcal{T}(t)$ are always positive, whereas the absorption $\mathcal{A}(t)$ can be positive or negative.

Let us consider a system with an arbitrary number of levels under exposure to pulse (4). In the calculation of contribution (22), we used the condition according to which the parameters $\gamma_{r\rho}$ are least among all the parameters in the problem and the times $p \ll \gamma_{r\rho}^{-1}$ and $s \ll \gamma_{r\rho}^{-1}$ are treated. Now, we apply the additional condition for a narrow pulse

$$\gamma_\rho \ll \gamma_l \tag{32}$$

and will consider the times

$$p \gg \gamma_l^{-1}, \quad s \gg \gamma_l^{-1}. \tag{33}$$

Evidently, in this case, only the contribution $\Delta\mathbf{E}_2(p)$, which, according to formula (22), involves $\exp(-\gamma_\rho p/2)$, is retained in relationship (19), because the contribution $\Delta\mathbf{E}_1(p)$ defined by formula (20) and the exciting field $\mathbf{E}_0(z, t)$ contain the multiplier $\exp(-\gamma_l p/2)$ and, consequently, are exponentially small in magnitude. Thus, under conditions (32) and (33), we obtain

$$\begin{aligned}\mathbf{E}_{\text{r}}(z,t) &\simeq \Delta\mathbf{E}_2(p),\\ \mathbf{E}_1(z,t) &\simeq \Delta\mathbf{E}_2(s).\end{aligned} \tag{34}$$

Hence, it follows that the transmitted and reflected fluxes are equal in magnitude, that is,

$$\mathcal{R}(t) \simeq \mathcal{T}(t). \tag{35}$$

Since, at times determined by condition (33), the exciting flux

$$P(t) \simeq 0,$$

from expression (31), we have

$$\mathcal{A}(t) = -2\mathcal{R}(t). \tag{36}$$

The negative absorption equal in magnitude to twice the reflection indicates that the quantum well gives away the accumulated energy and radiates it symmetrically, i.e., through two fluxes toward the right and left. The energy was accumulated in the form of excitations generated by light during the transmission of the pulse.

4. RESPONSE FOR AN EQUIDISTANT SYSTEM OF LEVELS IN A QUANTUM WELL IN A STRONG MAGNETIC FIELD

Under conditions (32) and (33), from relationships (34) and (22), we obtain

$$\begin{aligned}\mathbf{E}_{\text{r}}^s(z,t) \simeq{}& iE_0\mathbf{e}_l\Theta(s)\sum_\rho \frac{\gamma_{r\rho}}{2}\exp(-i\omega_\rho p - \gamma_\rho p/2)\\ &\times\{[\omega_l - \omega_\rho + i(\gamma_\rho - \gamma_l)/2]^{-1}\\ &\times[\omega_l - \omega_\rho + i(\gamma_\rho + \gamma_l)/2]^{-1}\}\end{aligned} \tag{37}$$

for a symmetric pulse and similar expression without a second term in the curly brackets for an asymmetric pulse with a steep front [8, 9, 17]. It is easy to see that the sum over ρ in formula (37) does not diverge at large values of ρ at any values of the variable p. However, this divergence can arise in the case of an asymmetric pulse.

Relationship (37) can be simplified by assuming that the reciprocal lifetimes $\gamma_{r\rho}$ and γ_ρ are identical for all levels, that is,

$$\gamma_{r\rho} \simeq \gamma_r, \quad \gamma_\rho \simeq \gamma, \tag{38}$$

and by ignoring the quantities γ that are small as compared to γ_l in the square brackets. Then, with the use of expression (26), the reflected flux for a symmetric pulse is written as

$$\begin{aligned}\mathcal{R}^s(s) \simeq{}& \frac{\gamma_r^2\gamma_l^2}{4}e^{-\gamma s}\sum_{\rho\rho'}\left[(\omega_l - \omega_\rho)^2 + \frac{\gamma_l^2}{4}\right]^{-1}\\ &\times\left[(\omega_l - \omega_{\rho'})^2 + \frac{\gamma_l^2}{4}\right]^{-1}\cos[(\omega_\rho - \omega_{\rho'})s].\end{aligned} \tag{39}$$

The reflected flux for an asymmetric pulse has the form

$$\begin{aligned}\mathcal{R}^{\text{as}}(s) \simeq{}& e^{-\gamma s}\sum_{\rho,\rho'}\left[(\omega_l - \omega_\rho)^2 + \frac{\gamma_l^2}{4}\right]^{-1}\\ &\times\left[(\omega_l - \omega_{\rho'})^2 + \frac{\gamma_l^2}{4}\right]^{-1}\left\{\frac{\gamma_l}{2}(\omega_\rho - \omega_{\rho'})\sin[(\omega_\rho - \omega_{\rho'})s]\right.\\ &\left.+\left[(\omega_l - \omega_\rho)(\omega_l - \omega_{\rho'})^2 + \frac{\gamma_l^2}{4}\right]\cos[(\omega_\rho - \omega_{\rho'})s]\right\}.\end{aligned} \tag{40}$$

We now apply relationships (39) and (40) to the case of Landau equidistant levels corresponding to formula (1) for the energy of electron–hole pairs at the fixed numbers l_e and l_h of the size quantization of electrons and holes. The frequencies ω_ρ and ω_l in expressions (39) and (40) will be reckoned from the level

$$\frac{E_g}{\hbar} + \varepsilon^e_{l_e} + \varepsilon^h_{l_h} + \frac{\Omega_\mu}{2}.$$

Then,

$$\omega_\rho = n\Omega_\mu, \quad n = 0, 1, 2\ldots \tag{41}$$

Let us justify assumption (38) for electron–hole pairs in the quantum well in a strong magnetic field. In our earlier work [19], we calculated the radiative lifetime of electron–hole pairs within the band model that is applicable to heavy holes in GaAs. There exist pairs of two sorts denoted by indices I and II. The pairs of these sorts differ in the interband matrix elements $\mathbf{p}_{cv}$ of a momentum; that is,

$$\begin{aligned} \mathbf{p}^I_{cv} &= \frac{1}{\sqrt{2}}p_{cv}(\mathbf{e}_x - i\mathbf{e}_y), \\ \mathbf{p}^{II}_{cv} &= \frac{1}{\sqrt{2}}p_{cv}(\mathbf{e}_x + i\mathbf{e}_y). \end{aligned} \tag{42}$$

With the use of the circular polarizations (11), each polarization is rigidly associated with a particular sort (I or II) of electron–hole pairs, because the interaction of a pair with light is proportional to the scalar product $\mathbf{e}_l\mathbf{p}_{cv}$ (see Footnote 2). In [19], it was shown that the reciprocal radiative time of a pair of any sort (I or II) at $\mathbf{K}_\perp = 0$ is given by

$$\gamma_{r\xi_0} = 2\frac{e^2}{c\hbar}\frac{\Omega_0}{n}\frac{p^2_{cv}}{m_0 E_{\xi_0}}\pi^2_{l_e, l_h}, \tag{43}$$

where $\Omega_0 = |e|H/m_0c$ is the cyclotron frequency for the bare electron mass m_0, the E_{ξ_0} energy is defined by formula (1), n is the refractive index,

$$\pi_{l_e, l_h} = \int\limits_{-\infty}^{\infty} dz\varphi_{cl_e}(z)\varphi_{vl_h}(z), \tag{44}$$

$\varphi_{cl}(z)$ and $\varphi_{vl}(z)$ are the real functions corresponding to the quantum number l of the size quantization for the quantum well with a finite depth (see, for example, [6]), and $c(v)$ is the subscript designating the conduction (valence) band.

From expression (43), it follows that the reciprocal time $\gamma_{r\xi_0}$ is proportional to the magnetic field strength H. The dependence on the index n and the strength H due to the multiplier E_{ξ_0} in the denominator is very weak, because the band gap is considerably greater than the energy $(n + 1/2)\hbar\Omega_\mu$ in formula (1).

As regards the quantities γ_ρ, it can be only argued that there are most likely no reasons for their strong dependence on the integer n.

By using relationship (39), the reflected flux can be represented as

$$\mathcal{R}^s(s) = 4\left(\frac{\gamma_r}{\gamma_l}\right)^2 e^{-\gamma s}Y^s_{\Omega_l, G_l}(S). \tag{45}$$

Here,

$$\begin{aligned} Y^s_{\Omega_l, G_l}(S) = \frac{G_l^4}{16}&\left\{\left[\sum_{n=0}^{\infty}\frac{\cos(nS)}{(\Omega_l - n)^2 + G_l^2/4}\right]^2\right. \\ &+ \left.\left[\sum_{n=1}^{\infty}\frac{\sin(nS)}{(\Omega_l - n)^2 + G_l^2/4}\right]^2\right\} \end{aligned} \tag{46}$$

and we introduced the dimensionless variable $S = \Omega_\mu s$ and the dimensionless quantities

$$\Omega_l = \frac{\omega_l}{\Omega_\mu}, \quad G_l = \frac{\gamma_l}{\Omega_\mu}. \tag{47}$$

Function (46) is periodic with a period of 2π and is symmetric with respect to the replacement of S by $2\pi - S$.

In the case of irradiation by an asymmetric pulse, instead of expression (46), we obtain a relationship that is conveniently written in the form

$$\begin{aligned} Y^{\text{as}}_{\Omega_l, G_l}(S) &= \frac{G_l^2}{16}[(\sigma_{c0}\Omega_l - \sigma_{c1})^2 + (\sigma_{s0}\Omega_l - \sigma_{s1})^2] \\ &+ \frac{G_l^3}{16}(\sigma_{s1}\sigma_{c0} - \sigma_{s0}\sigma_{c1}) + \frac{G_l^4}{64}(\sigma^2_{c0} + \sigma^2_{s0}), \end{aligned} \tag{48}$$

where

$$\begin{aligned} \sigma_{c0} &= \sum_{n=0}^{\infty}\frac{\cos(nS)}{(\Omega_l - n)^2 + G_l^2/4}, \\ \sigma_{c1} &= \sum_{n=0}^{\infty}\frac{n\cos(nS)}{(\Omega_l - n)^2 + G_l^2/4}, \\ \sigma_{s0} &= \sum_{n=0}^{\infty}\frac{\sin(nS)}{(\Omega_l - n)^2 + G_l^2/4}, \\ \sigma_{s1} &= \sum_{n=0}^{\infty}\frac{n\sin(nS)}{(\Omega_l - n)^2 + G_l^2/4}. \end{aligned} \tag{49}$$

5. ENERGY FLUXES IN THE CASE OF SYMMETRIC EXCITING PULSE: THE ECHO OF AN EXCITING PULSE IN TRANSMITTED AND REFLECTED FLUXES

When the frequency ω_l is at resonance with one of the Landau levels, i.e., at

$$\Omega_l = n_0, \quad n_0 = 0, 1, 2, \ldots, \tag{50}$$

from formula (46), we have

$$Y^s(S) = \frac{G_l^4}{16}\left\{\left[\sum_{n=0}^{\infty}\frac{\cos(nS)}{n^2+G_l^2/4} + \sum_{n=1}^{n_0}\frac{\cos(nS)}{n^2+G_l^2/4}\right]^2 + \left[\sum_{n=n_0+1}^{\infty}\frac{\sin(nS)}{n^2+G_l^2/4}\right]^2\right\}. \tag{51}$$

In the limiting case,

$$\Omega_l = n_0, \quad G_l \ll 1, \tag{52}$$

and expression (51) transforms into the relationship

$$Y^s(S) \simeq 1 + \frac{G_l^2}{2}\left[F_s(S) + \sum_{n=1}^{n_0}\frac{\cos(nS)}{n^2}\right], \tag{53}$$

where

$$F_s(S) = \sum_{n=1}^{\infty}\frac{\cos(nS)}{n^2} = \frac{(\pi-S)^2}{4} - \frac{\pi^2}{16} \tag{54}$$

is defined in the range from 0 to 2π. At $G_l \longrightarrow 0$, we obtain

$$Y^s = 1$$

and, according to formula (45),

$$\mathcal{R}^s(s) \simeq \left(\frac{2\gamma_r}{\gamma_l}\right)^2 e^{-\gamma s},$$

which corresponds to the contribution of the sole Landau level that is at resonance with the frequency ω_l.

Let us consider the case when the frequency ω_l is at resonance with one of the high-lying Landau level with n_0, that is,

$$\Omega_l = n_0, \quad n_0 \gg 1, \tag{55}$$

and the value of G_l is arbitrary. Then, from expression (51), we immediately have

$$Y^s(S) \simeq \frac{G_l^4}{16}\left(\frac{4}{G_l^2} + 2\sum_{n=1}^{\infty}\frac{\cos(nS)}{n^2+G_l^2/4}\right)^2. \tag{56}$$

The sum in relationship (56) is calculated exactly, as a result of which we find

$$Y^s(S) \simeq \frac{G_l^2}{4}\pi^2\cosh^2\left[(\pi-S)\frac{G_l}{2}\right]\operatorname{cosech}^2\left(\frac{\pi G_l}{2}\right). \tag{57}$$

At $G_l \ll 1$, formula (57) leads to

$$Y^s(S) \simeq 1 + G_l^2 F_s(S), \tag{58}$$

which agrees with relationship (53) in the limit $n_0 \longrightarrow \infty$.

Under the condition

$$G_l \gg 1, \tag{59}$$

it follows from expression (57) that

$$Y_s(S) \simeq \frac{\pi^2 G_l^2}{4}\begin{cases}\exp(-SG_l), & S \ll 1\\ \exp[-(2\pi-S)G_l], & 2\pi - S \ll 1.\end{cases} \tag{60}$$

The curves described by formula (46) at different parameters Ω_l and G_l are depicted in Figs. 1–4. The $Y^s_{\Omega_l,G_l}(S)$ functions are periodic with a period of 2π (one period is shown).

Figure 1 corresponds to the small value of $G_l = 0.1$ and $\Omega_l = 0$, 0.05, and 0.1. At $\Omega_l = 0$, the frequency ω_l is at resonance with the low-lying Landau level for electron–hole pairs. The values of $\Omega_l = 0.05$ and 0.1 correspond to a small deviation from this resonance. Curves *a* and *b* are calculated using the exact formula (46) and the approximate formula (53), respectively. Figure 1 allows us to conclude that, when the frequency ω_l is at exact resonance with one of the Landau levels, the periodic oscillations of the reflected and transmitted energy fluxes at small G_l values are very small in amplitude and the results obtained with the approximate formula (53) are very close to the exact data. A small deviation of the frequency ω_l from the resonance leads to a sharp decrease in the energy fluxes.

Similar results obtained at the larger value of G_l = 0.5 are displayed in Fig. 2. Compared to Fig. 1, the amplitude of periodic beats increases considerably, the approximate formula (53) works poorly, and small deviations of the frequency ω_l from the resonance do

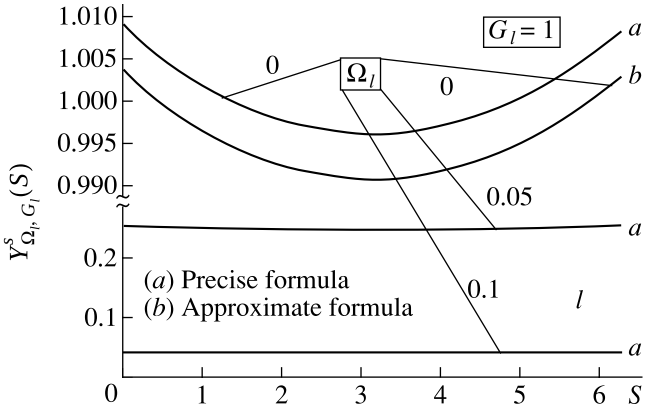

Fig. 1. Functions $Y^s_{\Omega_l,G_l}(S)$ corresponding to the periodic multiplier in the expression for the reflected energy flux under irradiation of the quantum well by a symmetric exciting pulse. The values of parameters are given in the figure. The pulse duration γ_l^{-1} is one order of magnitude longer than the time Ω_μ^{-1}.

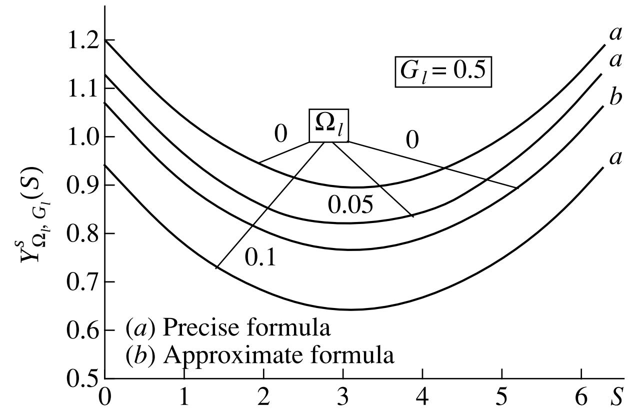

Fig. 2. The same as in Fig. 1. The pulse duration γ_l^{-1} is twice as long as Ω_μ^{-1}.

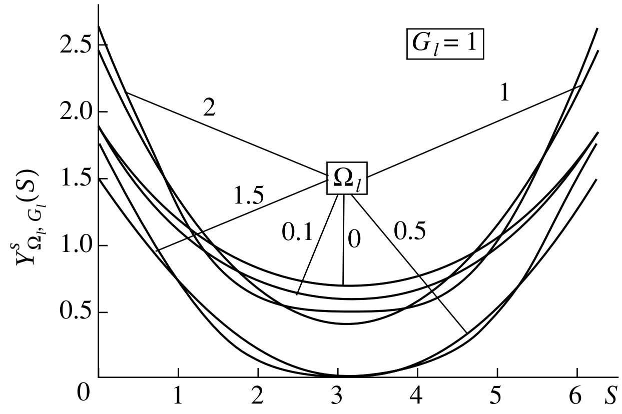

Fig. 3. The same as in Fig. 1 for the pulse duration $\gamma_l^{-1} = \Omega_\mu^{-1}$.

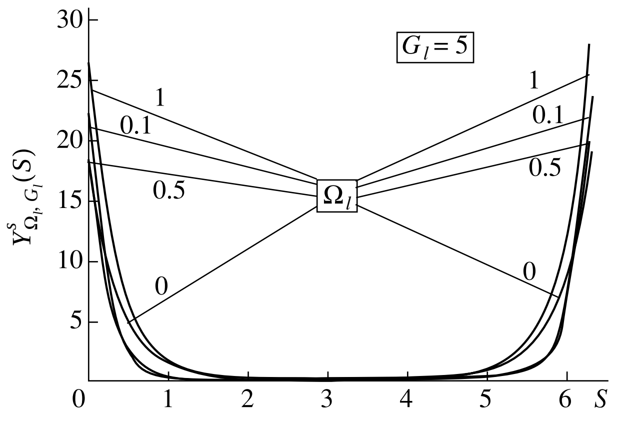

Fig. 4. The same as in Fig. 1 for the very short pulse duration γ_l^{-1} when the echo of an exciting pulse is observed.

not bring about such a sharp decrease in the energy fluxes.

The results of calculations for the parameters $G_l = 1$ and $\Omega_l = 0, 0.1, 0.5, 1, 1.5$, and 2 are shown in Fig. 3. In this case, the amplitude of periodic oscillations of the dimensionless multiplier $Y^s(S)$ is as much as 1.5–2.0. At $\Omega_l = 0.5$ and 1.5, i.e., when the frequencies ω_l lie between the Landau levels with $n = 0$ and 1 and with $n = 1$ and 2, respectively, the curves at the point $S = \pi$ touch the abscissa axis, which means that the fluxes tend to zero.

Finally, the data obtained for the large value of $G_l = 5$ and the parameters $\Omega_l = 0, 0.1, 0.5$, and 1 are represented in Fig. 4. The values of the $Y^s(S)$ multiplier at the points $S = 0$ and 2π sharply increase (to 30) as compared to the corresponding values in Figs. 1–3, but become very small in the ranges $S \gg G_l^{-1}$ and $(2\pi - S) \gg G_l^{-1}$. Thus, the periodic function $Y^s(S)$ is a series of sequential short pulses, which have durations of the order of G_l^{-1} and arise at intervals of 2π. By using expression (45), we find that at $\gamma_l \gg \Omega_\mu$, the exciting-pulse echo decaying as $e^{-\gamma s}$ is observed in the reflected energy flux at intervals $2\pi/\Omega_\mu$. According to relationship (35), the echo should also be observed in the transmitted energy flux. In the range of Ω_l from zero to several units, i.e., at the frequency ω_l close to low-lying Landau levels, the shape of the generated pulses is distorted. When the frequency ω_l is at resonance with one of the high-lying Landau levels with $n_0 \gg 1$, from expressions (35) and (60), we obtain that the shape of the generated pulses (echo) coincides with that of the exciting pulse. However, the amplitude of these pulses is substantially less, because it involves the small multiplier $\pi^2(\gamma_r/\Omega_\mu)^2\exp(-\gamma s)$.

6. ASYMMETRIC EXCITING PULSE

Analysis of relationship (48) shows that this function becomes infinite at the points $S = 2\pi m$, since the sum σ_{c1} given by formulas (49) diverges. This implies that infinite values of $Y^{as}(S)$ would be observed for an asymmetric exciting pulse at the points $S = 0$ and 2π in figures similar to Figs. 1–4. Undeniably, this result is invalid, because the quantities $\mathcal{R}$, $\mathcal{A}$, and $\mathcal{T}$ defined by expressions (30) cannot be larger than unity. In actual fact, the infinite values of functions are cut off, but the dominant cutoff mechanism is hard to reveal. The approximation according to which $\Delta\mathbf{E}_2(p)$ in formula (19) is calculated using only the lowest-order contribution to the interaction of electrons with light [i.e., using relationship (21)] is inapplicable near the points $S = 2\pi m$.

In this respect, we consider here only the results for the resonance of the frequency ω_l with one of the high-

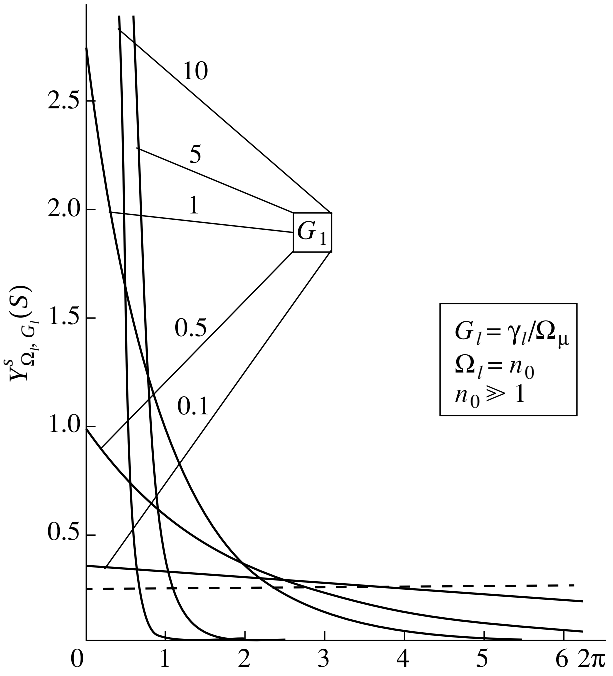

Fig. 5. Functions $Y^{\mathrm{as}}(S)$ [formula (62)] for an asymmetric exciting pulse with a steep front at resonance of the frequency ω_l with one of the high-lying Landau levels. The values of the parameter $G_l = \gamma_l/\Omega_\mu$ are given in the figure.

lying Landau levels when divergences do not occur. At $\Omega_l = n_0$ ($n_0 \gg 1$), from expression (48), we obtain

$$Y^{\mathrm{as}}(S) = \frac{G_l^2}{16}\left[\sum_{n=-\infty}^{\infty}\frac{n\sin(nS)}{n^2+G_l^2/4} + \frac{G_l}{2}\sum_{n=-\infty}^{\infty}\frac{n\cos(nS)}{n^2+G_l^2/4}\right]^2. \quad (61)$$

The sums in relationship (61) are calculated exactly, and we have

$$Y^{\mathrm{as}}(S) = \frac{\pi^2 G_l^2}{16}\operatorname{cosech}^2\left(\frac{\pi G_l}{2}\right)\exp[(\pi - S)G_l]. \quad (62)$$

At $G_l \ll 1$, formula (62) transforms into the expression

$$Y^{\mathrm{as}}(S) \simeq \frac{1}{4}[1 + 2G_l F(S)],$$
$$F(S) = \sum_{n=1}^{\infty}\frac{\sin(nS)}{n} = \frac{\pi - S}{2}. \quad (63)$$

For $G_l = 0$, we obtain the relationship

$$Y^{\mathrm{as}}(S) \simeq \frac{1}{4}, \quad \mathcal{R}^{\mathrm{as}}(s) = \left(\frac{\gamma_r}{\gamma_l}\right)^2\exp(-\gamma s), \quad (64)$$

which corresponds to the resonance of the frequency ω_l with the sole level in the quantum well. At $G_l \gg 1$, we find

$$Y^{\mathrm{as}}(S) \simeq \frac{\pi^2}{4}G_l^2\exp(-SG_l). \quad (65)$$

The last expression suggests that the echo of the exciting pulse arises in the case of an asymmetric pulse at $\gamma_l \gg \Omega_\mu$, i.e., for very short pulses. At $n_0 \gg 1$, the shape of the generated pulses coincides with that of the exciting pulse. However, as for a symmetric pulse, the amplitude of the echo pulse contains the small multiplier $\pi^2(\gamma_r/\Omega_\mu)^2\exp(-\gamma s)$.

The $Y^{\mathrm{as}}(S)$ functions defined by formula (62) at $\Omega_l = n_0$ ($n_0 \gg 1$) for $G_l = 0.1$, 0.5, 1, 5, and 10 are plotted in Fig. 5. This function is sawtooth at $G_l = 0.1$ and follows the shape of the exciting pulse at $G_l = 10$.

7. CONCLUSION

Thus, we investigated the time dependences of the transmitted, reflected, and absorbed energy fluxes formed under exposure of the quantum well in a strong magnetic field to normal irradiation with an exciting pulse. It was assumed that the system of excited electron levels in the quantum well is equidistant with the spacing $\hbar\Omega_\mu$. Results were obtained for symmetric and asymmetric exciting pulses. Analysis was carried out for specific relationships between the parameters,

$$\gamma_r \ll \gamma, \quad \gamma \ll \gamma_l, \quad \gamma \ll \Omega_\mu, \quad (66)$$

and at an arbitrary ratio between γ_l and Ω_μ.

The fluxes were examined at times

$$t \gg \gamma_l^{-1}, \quad t \ll \gamma_r^{-1}, \quad (67)$$

when the exciting pulse already decayed, the transmitted and reflected fluxes are equal in magnitude, and the absorbed flux is negative and equal in magnitude to twice the transmitted (or reflected) flux.

The relationship for the reflected flux includes the multiplier $\exp(-\gamma s)$, which determines its decay. Moreover, this relationship contains the multiplier Y that is periodic in s with the period $2\pi\Omega_\mu^{-1}$. These oscillations at any conditions are not sinusoidal, which is characteristic only of two closely spaced excited levels. At $\gamma_l \ll \Omega_\mu$, i.e., for relatively long pulses whose duration exceeds the time Ω_μ^{-1}, the oscillation amplitude is small. In the limit $\gamma_l/\Omega_\mu = 0$, when the frequency ω_l is at resonance with one of the levels, the obtained results corresponds to the presence of this sole level. For $\gamma_l \geq \Omega_\mu$, the oscillation amplitude becomes large. Finally, in the case when $\gamma_l \gg \Omega_\mu$, i.e., the pulse duration is considerably less than the time Ω_μ^{-1}, the decaying echo of the exciting pulse arises at the time intervals $2\pi\Omega_\mu^{-1}$.

ACKNOWLEDGMENTS

We are grateful to A. D'Amore for helpful remarks.

This work was supported by the Russian Foundation for Basic Research (project no. 00-02-16904) and the

International Scientific and Technical Program "Physics of Solid-State Nanostructures" (project no. 97-1099). S.T. Pavlov acknowledges the support and the hospitality of Zacatecas University and the Mexican CONACyT. D.A. Contreras-Solorio acknowledges the support of the CONACyT (27736-E).

REFERENCES

1. H. Stolz, *Time-Resolved Light Scattering from Excitons* (Springer-Verlag, Berlin, 1994).
2. J. Shah, *Ultrafast Spectroscopy of Semiconductors and Semiconductor Nanostructures* (Springer-Verlag, Berlin, 1996).
3. H. Hang and S. W. Koch, *Quantum Theory of the Optical and Electronic Properties of Semiconductors* (World Scientific, Singapore, 1993).
4. S. Mukamel, *Principles of Nonlinear Optical Spectroscopy* (Oxford Univ. Press, Oxford, 1995).
5. L. I. Korovin, I. G. Lang, and S. T. Pavlov, Zh. Éksp. Teor. Fiz. **118** (2), 388 (2000) [JETP **91**, 338 (2000)]; cond-mat/0004373.
6. I. G. Lang, V. I. Belitsky, A. Cantarero, *et al.*, Phys. Rev. B **54** (24), 17768 (1996).
7. I. V. Lerner and Yu. E. Lozovik, Zh. Éksp. Teor. Fiz. **78** (3), 1167 (1980) [Sov. Phys. JETP **51**, 588 (1980)].
8. I. G. Lang, V. I. Belitsky, and M. Cardona, Phys. Status Solidi A **164** (1), 307 (1997).
9. I. G. Lang and V. I. Belitsky, Phys. Lett. A **245** (3–4), 329 (1998).
10. L. C. Andreani, F. Tassone, and F. Bassani, Solid State Commun. **77** (11), 641 (1991).
11. L. C. Andreani, in *Confined Electrons and Photons*, Ed. by E. Burstein and C. Weisbuch (Plenum, New York, 1995), p. 57.
12. E. L. Ivchenko, Fiz. Tverd. Tela (Leningrad) **33** (8), 2388 (1991) [Sov. Phys. Solid State **33**, 1344 (1991)].
13. F. Tassone, F. Bassani, and L. C. Andreani, Phys. Rev. B **45** (11), 6023 (1992).
14. T. Stroucken, A. Knorr, C. Anthony, *et al.*, Phys. Rev. Lett. **74** (13), 2391 (1995).
15. T. Stroucken, A. Knorr, P. Thomas, and S. W. Koch, Phys. Rev. B **53** (4), 2026 (1996).
16. M. Hübner, J. Kuhl, S. Haas, *et al.*, Solid State Commun. **105** (2), 105 (1998).
17. I. G. Lang and V. I. Belitsky, Solid State Commun. **107** (10), 577 (1998).
18. L. C. Andreani, G. Panzarini, A. V. Kavokin, and M. R. Vladimirova, Phys. Rev. B **57** (8), 4670 (1998).
19. I. G. Lang, L. I. Korovin, D. A. Contreras-Solorio, and S. T. Pavlov, cond-mat/0001248.
20. D. A. Contreras-Solorio, S. T. Pavlov, L. I. Korovin, and I. G. Lang, cond-mat/0002229.
21. L. I. Korovin, I. G. Lang, D. A. Contreras-Solorio, and S. T. Pavlov, Fiz. Tverd. Tela (St. Petersburg) **42** (12), 2230 (2000) [Phys. Solid State **42**, 2300 (2000)]; cond-mat/0006364.

Translated by O. Borovik-Romanova

Physics of the Solid State, Vol. 43, No. 6, 2001, pp. 1169–1171. Translated from Fizika Tverdogo Tela, Vol. 43, No. 6, 2001, pp. 1126–1128.
Original Russian Text Copyright © 2001 by Karpov, Muzafarova, Yastrebova.

LOW-DIMENSIONAL SYSTEMS AND SURFACE PHYSICS

Quantum Confinement Effect in the Vibrational Spectrum of CdS_xSe_{1-x} Quantum Dots in a Fluorophosphate Glass Matrix

S. V. Karpov, G. K. Muzafarova, and M. A. Yastrebova
Research Institute of Physics, St. Petersburg State University, Ul'yanovskaya ul. 1, Petrodvorets, 198904 Russia
e-mail: karpov@snoopy.niif.spb.ru

Received July 14, 2000; in final form, October 31, 2000

Abstract—The vibrational spectra of mixed cadmium sulfoselenide nanocrystals in a fluorophosphate glass matrix are investigated by Raman spectroscopy. The asymmetry of the lines of the fundamental modes of nanocrystals is experimentally observed in the region of lattice vibrations, which is interpreted as a quantum confinement effect. In the framework of the model of confined phonons, the contribution of the band states to the Raman scattering spectrum is calculated and the size of nanocrystalline regions is estimated. The results obtained are in good agreement with the data on the low-frequency Raman scattering in these objects. *© 2001 MAIK "Nauka/Interperiodica".*

It is known that, in addition to direct electron microscopy and small-angle x-ray scattering, the size of nanocrystalline regions (quantum dots) in glass matrices is often determined from the magnitude of the quantum confinement effect in the exciton region of the spectrum. The magnitude of the blue shift of the fundamental absorption edge of a nanocrystal and observation of discrete quantum confinement states near the edge allow one to estimate the quantum dot size in the range from 100 to 30 Å [1, 2]. An alternative method for determining the nanocrystal size is the observation of the additional low-frequency peak in the Raman scattering spectrum at a frequency determined by the nanocrystal size D [3]. This spectral feature at a frequency $\omega_{\min} = V/Dc$ (where V is the velocity of sound in the crystal and c is the velocity of light) actually indicates that the spectrum of the finite-size object lies in the range from the lowest frequency $\omega_{\min}$ to the Debye frequency $\omega_{\max} \approx V/ac$, where a is the lattice parameter. The exact value of the additional peak frequency in nanocrystals depends on the ratio of the velocities of the longitudinal and transverse acoustic vibrations, the type of frequency spectrum of the matrix, and the type of nanoparticle interface [4]. However, a decrease in the crystal size leads not only to a rise in the boundary of low-frequency vibrations of the crystal but also to a change in the spectrum of the crystal in the region of fundamental modes. In this case, the description of the vibrational excitations (phonons) is usually based on the *a priori* specified type of spatial damping of the phonon wave function in the constrained crystal [5]. A small volume of the crystal structure leads to a clearly pronounced quantization of vibrational states in the Brillouin zone, whereas a small size of nanocrystals is the factor responsible for violation of the quasi-momentum selection rule. For this reason, the individual vibrational modes of the wide-band lattice vibrations can be observed experimentally.

In this connection, we investigated the Raman spectra of cadmium sulfoselenide nanocrystals ($CdS_{0.3}Se_{0.7}$) in a fluorophosphate matrix in which the content of the crystalline phase may be as much as 1.5 wt %. We examined the frequency range of optical modes for CdS (near 300 cm^{-1}) and CdSe (near 200 cm^{-1}) and analyzed the contours of the lines considered. The Raman spectra of the samples under investigation were recorded at room temperature in a 180° scattering geometry under excitation with the 4880 Å line of an ion argon laser. Experimental details of the setup were described elsewhere [6]. The low-frequency region of the Raman scattering spectrum of the fluorophosphate glass sample containing mixed $CdS_{0.3}Se_{0.7}$ nanocrystals is shown in Fig. 1. It is seen that the contour of the lines of the mode for CdS and CdSe in the mixed crystal is substantially asymmetric.

As is known, the phonon confinement effect can manifest itself in both the shift and the asymmetric broadening of the fundamental mode, depending on the size and the type of nanoregions [7, 8]. This is explained by the fact that only phonons with the wave vector $\mathbf{k} = 0$ (at the center of the Brillouin zone) can contribute to the Raman scattering in a perfect bulk crystal. By contrast, a nanocrystal in which the phonons are spatially confined by a small volume of the periodic structure is characterized by an uncertain value of the wave vector $\mathbf{k}$; hence, the phonons from all points of the Brillouin zone can manifest themselves in the Raman spectrum. The proper choice of the particular model of the spatial phonon confinement [8] makes

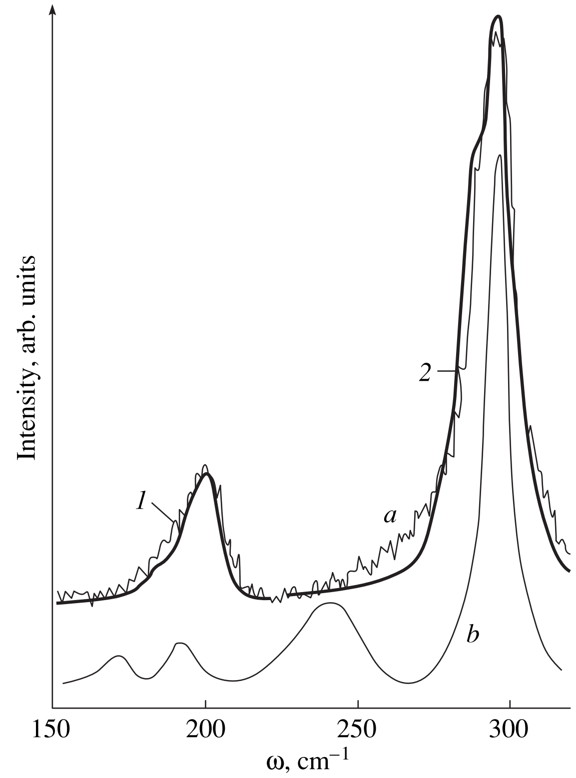

Fig. 1. Raman spectra of (*a*) the fluorophosphate glass doped with a mixed cadmium sulfoselenide semiconductor and (*b*) the $CdS_{0.75}Se_{0.25}$ bulk crystal in the polarization $x(zz)x$ upon excitation by the 488.0-μm line of an argon laser. Solid curves *1* and *2* are the calculated contours for the fundamental frequencies of cadmium selenide and cadmium sulfide at the following parameters (frequency ω_0, band width Δ, and oscillator damping Γ_0), cm^{-1}: (*1*) 209, 45, and 5.2 and (*2*) 297, 48, and 5.1.

it possible to determine the modes responsible for the phonon confinement state in the nanometer-size object and to calculate their power.

In order to describe the frequency shift and the shape of the lines attributed to scattering from nanoregions whose size is equal to N lattice parameters a, we used the model of the Gaussian spatial confinement of a phonon in a sphere of diameter $D = 2R = aN$. This model is specified by the function $\exp(-\alpha r^2/R^2)$, so that the amplitude of mechanical displacements at the microcrystal interface decays by a factor of e^{α} compared to the vibration amplitude at the center. The coefficient α, which was obtained from the analysis of the Raman contours for a series of nanocrystalline semiconductors, is equal to approximately $4\pi^2$ [8]. Note that the introduction of this multiplier is actually equivalent to the change in the nanocrystal size. The model under consideration describes the quantum confinement state by a set of harmonics with different wave vectors **k** and a power distributed according to the Gaussian law $\exp(-k^2R^2/4\alpha)$. The choice of the Gaussian confinement of excitation in the nanocrystal is explained not only by the mathematical simplicity of the description. There is also a physical reason to assume that this form of confinement is realized, because it accounts, to some extent, for the nanoparticle size distribution. However, it is necessary to keep in mind that the microcrystal size D, which is introduced in this fashion, corresponds only approximately to the sizes obtained from the x-ray diffraction data.

Thus, in the approximation of the spherical Brillouin zone, the contour of the observed line of the fundamental mode is described by the superposition of separate lines (Lorentzians in the simplest case) at discrete frequencies of the optical branch $\omega = \omega(k)$ with weighting factors which are specified by the type of the phonon confinement in the region of size D.

$$I(\omega) = \frac{1}{A}\int_0^1 \frac{4\pi k^2 e^{-k^2R^2/4\alpha}}{(\omega-\omega(k))^2+\Gamma_0^2}dk,$$

$$A = \int_0^1 4\pi k^2 e^{-k^2R^2/4\alpha}dk.$$

Here, integration is carried out with respect to the quasi-continuous wave vector **k** in the reciprocal space to the Brillouin zone boundary, which is normalized to unity. It is assumed that the Brillouin zone is spherical, whereas the phonon dispersion dependence $\omega(k)$ is isotropic. This assumption is valid, because only the vibrations with the wave vectors in the vicinity of the Brillouin zone center contribute to light scattering; i.e., they are centered with respect to the point Γ. However, for a small-size crystal, it is necessary to take into account that the wave vector in this expression takes discrete values $k = (\pi/aN)p$ (where a is the lattice parameter and $p = 1, 2, \ldots, N$ are integer numbers) so that the integral is replaced by the sum for small N. In this case, we can expect N lines at discrete frequencies of the vibrational spectrum, which are determined by the dispersion of the corresponding optical branch.

$$I(\omega) = \frac{1}{A}\sum_{p=1}^{N}\frac{4\pi p^2 e^{-\left(\frac{\pi p}{4}\right)^2\frac{1}{\alpha}}}{(\omega-\omega(k))^2-\Gamma_0^2},$$

$$A = \sum_{p=1}^{N} 4\pi p^2 e^{-\left(\frac{\pi p}{4}\right)^2\frac{1}{\alpha}}.$$

The aforesaid can be illustrated in Fig. 2, in which the Fourier harmonic amplitude distribution is given in the graph of the dispersion dependence and the formation of the discrete structure of the wide-band vibration is shown for a concrete branch $\omega = \omega(k)$.

Taking into account the dispersion dependence of the optical branch for the cadmium sulfoselenide crystal [9], which is approximated by the dependence

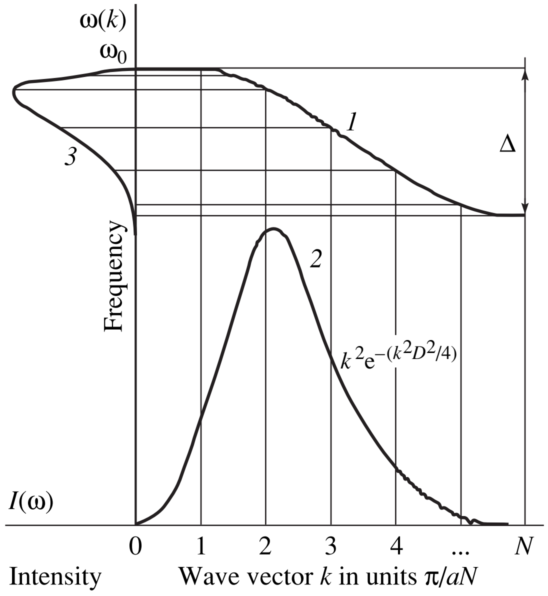

Fig. 2. A scheme illustrating the formation of the asymmetric contour of the lines of fundamental modes for a nanocrystalline object with a specified type of phonon confinement: (*1*) the dispersion dependence of the wide-band vibration, approximated by the function $\omega(k) = \omega_0 - \Delta/2(1 - \cos ka)$; (*2*) the Gaussian distribution of the Fourier harmonics of the function of phonon confinement in a constrained crystal; and (*3*) the asymmetric contour of the spectrum observed, which consists of a finite number of discrete lines.

$\omega(k) = \omega_0 - \Delta/2\cos(1 - \cos ka)$, we allowed for the contributions of the vibration band width Δ and the damping magnitude Γ_0 of a separate oscillator to the Raman spectrum in the vicinity of the lines of fundamental modes for different nanocrystal sizes $D = aN$ and carried out a comparison with the experiment. This makes it possible to estimate the size of cadmium sulfoselenide nanocrystals in a fluorophosphate glass matrix at a certain annealing time and to determine the degree of damping α for the amplitude of mechanical vibrations at the nanocrystal interface as compared to the amplitude at the center. The calculated contours of the lines of the fundamental mode for CdS and CdSe in this model are shown in Fig. 1. The calculation was carried out for different values of the vibration band width Δ, the damping magnitude Γ_0, and the parameter α. The vibration band width for both cadmium selenide and cadmium sulfide crystals was equal to approximately 40 cm^{-1}, and the damping magnitude was ~5 cm^{-1}. The best results of the optimization of the observed asymmetric contour of the line and the calculated contour were obtained when the magnitude of the damping α of the phonon amplitude at the boundary was equal to approximately $\pi^2/4$. This result differs essentially from the value $\alpha = 4\pi^2$, which was obtained in [8]. However, in this case, the quantum dot size was equal to 8–9 lattice constants, i.e., about 30 Å, which is in satisfactory agreement with the values obtained from the low-frequency Raman spectra [6]. It is worth noting that for this α value, the harmonic with the number p close to unity ($p = 2$) has the maximum power, regardless of the number of lattice constants of the nanocrystal. The wave vector of this harmonic corresponds to the mode with a wavelength approximately equal to the nanocrystal size ($k = 2\pi/aN$, $\lambda = aN$). It is possible that the difference between the α coefficient and the values obtained in [8] is related to the substantially nonspherical nanocrystals of the mixed semiconductor in the fluorophosphate glass matrix [10].

REFERENCES

1. A. I. Ekimov, F. Hache, M. C. Shanne-Klein, *et al.*, J. Opt. Soc. Am. B **10**, 100 (1993).
2. D. J. Norris and M. J. Bavendi, J. Chem. Phys. **103**, 5260 (1995).
3. E. Duval, A. Boukenter, and B. Champagnon, Phys. Rev. Lett. **56**, 2052 (1986).
4. B. Champagnon, B. Andrianasolo, A. Ramos, *et al.*, J. Appl. Phys. **73** (6), 2775 (1993).
5. V. S. Gorelik, A. V. Igo, and S. N. Minkov, Zh. Éksp. Teor. Fiz. **109** (6), 2141 (1996) [JETP **82**, 1154 (1996)].
6. E. P. Denisov, S. V. Karpov, E. V. Kolobkova, *et al.*, Fiz. Tverd. Tela (St. Petersburg) **41** (7), 1306 (1999) [Phys. Solid State **41**, 1194 (1999)].
7. H. Richter, Z. P. Wang, and L. Ley, Solid State Commun. **39**, 625 (1981).
8. I. H. Campbell and P. M. Fauchet, Solid State Commun. **58**, 739 (1986).
9. R. Purlys and J. Jakimavicius, Sov. Phys. Collect. **25** (3), 40 (1985).
5. E. V. Kolobkova, A. A. Lipovskii, N. V. Nikonorov, and A. A. Sitnikova, Phys. Status Solidi A **147**, K65 (1995).

Translated by N. Korovin

Physics of the Solid State, Vol. 43, No. 6, 2001, pp. 1172–1177. Translated from Fizika Tverdogo Tela, Vol. 43, No. 6, 2001, pp. 1129–1134.

LOW-DIMENSIONAL SYSTEMS AND SURFACE PHYSICS

Kinetics of Desorption from Adsorbed Layers Formed by Two-Dimensional Islands and by a Two-Dimensional Gas

V. B. Bondarenko, M. V. Kuz'min, and M. A. Mittsev

Ioffe Physicotechnical Institute, Russian Academy of Sciences, Politekhnicheskaya ul. 26, St. Petersburg, 194021 Russia

Received October 17, 2000

Abstract—The kinetics of desorption from the adsorbed layers formed by two-dimensional (2D) islands and by a 2D gas of single atoms is considered for the case when the flux of adsorbate atoms from the gaseous phase reaches the surface. The effect of this flux on the desorption kinetics is analyzed. It is shown that this effect can be disregarded when the islands are in equilibrium with the surrounding 2D gas. The possibilities of determining the energy required for the removal of atoms from 2D islands to a vacuum are considered for the case of the absence of equilibrium in adsorbed layers. The conditions under which such a determination is possible are formulated, and the corresponding recommendations for experimental studies are worked out. *© 2001 MAIK "Nauka/Interperiodica".*

1. INTRODUCTION

The kinetics of desorption from adsorbed submonolayer films formed by two-dimensional (2D) islands and by a 2D gas of single atoms has been investigated by many authors [1–17]. In these publications, it has been shown that the evaporation of such islands into a vacuum mainly occurs through the 2D gas and that the order of desorption kinetics in such systems is determined by the relation between the diffusion length X_S of adatoms and the mean distance between the islands, which is equal to $\rho^{-1/2}$ (ρ is the density of the islands). The theory [4, 8] predicts that, for $X_S \gg \rho^{-1/2}$, i.e., in the case when the islands are in equilibrium with the 2D gas, the desorption rate is described by a zero-order kinetic equation and the desorption activation energy appearing in this equation is equal to the energy E_0 required for the removal of an edge atom of an island into a vacuum. Another situation is observed in the absence of such an equilibrium. According to Kern *et al.* [4, 8], the order of desorption kinetics for $X_S < \rho^{-2}/8$ is equal to 1/2 and the desorption activation energy decreases by an amount equal to the energy of the removal of a delocalized adatom, diffusing over the surface, into a vacuum.

However, the existing theory has several serious drawbacks. For one, the case when adsorbate atoms arrive at the surface from the gaseous phase has not been analyzed in the framework of this theory [1–14]. Consequently, it cannot predict the form of the dependence of the desorption kinetic parameters (desorption rate, order, etc.) on the intensity of the incident flux. Another limitation of the theory is that it can be used to determine the energy E_0 only in the particular case when the islands are in equilibrium with the 2D gas, i.e., when this quantity is equal to the desorption activation energy. However, the latter value can easily be determined in experiments. If this equilibrium is violated (e.g., for $X_S \sim \rho^{-1/2}$), the desorption activation energy does not have a definite physical meaning. The methods of determining the value of E_0 were not indicated in the above-mentioned works for such cases.

In the present work, an attempt is made to overcome these difficulties. We propose a more universal model of desorption kinetics in the system "2D islands + 2D gas." The evolution of this model has made it possible, in particular, to develop a method of determining the value of energy E_0 for an arbitrary relation between the quantities X_S and $\rho^{-1/2}$ from the experimental results obtained with the help of isothermal desorption spectroscopy [15].

2. MODEL

The model considered here is based on the concepts concerning the kinetics of desorption processes occurring in the system "2D islands + 2D gas," which were formulated by Arthur and Cho [1], as well as by Kern *et al.* [4, 5, 7, 8]. The diagram illustrating this kinetics is presented in Fig. 1. As in the above-mentioned publications, we assume that the major part of adsorbed particles are concentrated at the surface of a substrate in 2D disk-shaped islands. The concentration of such particles is N. The least bound atoms in the islands are located at the edges (adsorption centers in position $i = 0$). Consequently, we assume that only these atoms can go over to the 2D gas or evaporate directly into a vacuum. The number of edge atoms in the islands per unit surface area is equal to $2N^{1/2}\sqrt{\pi\rho}$.

We also assume that the islands are surrounded by a 2D gas of single atoms. The latter can be located on the clean surface of the substrate (in the first atomic layer) or on the surface of an island (in the second layer). The

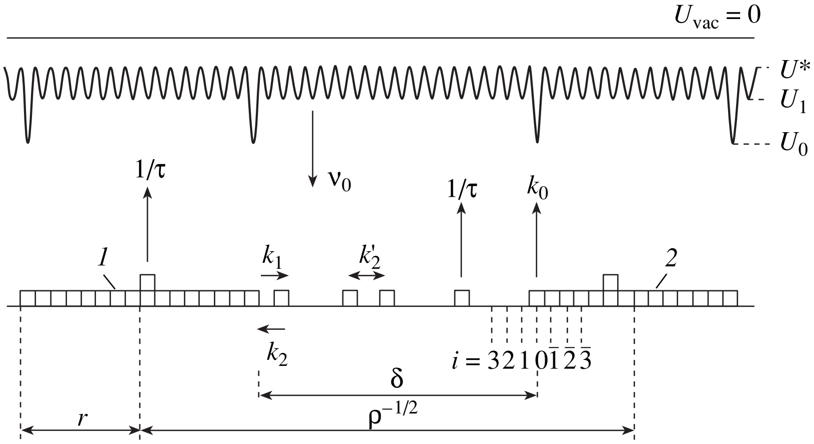

Fig. 1. Diagram illustrating the model of the kinetics of adsorption–desorption processes in the system “2D islands + 2D gas”: *1*, *2* are two-dimensional islands; U_0 is the potential energy of atoms at the edges of the islands; U_1 is a similar quantity for solitary atoms of the 2D gas, localized at adsorption centers in the first and second layers; and U^* is the same for single adsorbed atoms migrating over the surface of the substrate between the islands and over their surface. The values of U_0, U_1, and U^* are measured from the level U_{vac} corresponding to the potential energy of an atom which is at rest at a large distance from the surface. The value of U_{vac} is assumed to be zero; k_0, k_1, k_2, and k_2' are the rate constants of the processes indicated by arrows.

concentration of single atoms is n. In order to simplify the model, we will use the assumption made by Kern *et al.* [4, 8], according to which the parameters such as the binding energy and lifetime are identical for single atoms in the first and second layers. We will also assume that an isotropic and constant-in-time atomic flux whose intensity is ν_0 is incident on the surface.

The equation describing the variation of the particle concentration in the islands (i.e., at adsorption sites $i = 0$) can be written in the form

$$\frac{dN}{dt} + \dot{N} = -k_0 N^{1/2} - 2k_1(1-\theta_1)N^{1/2} + 2k_2\theta_1 N^{1/2} + \frac{2N^{1/2}\sqrt{\pi\rho}}{a^{-2}}\nu_0, \qquad (1)$$

where a is the lattice constant of the substrate and of a 2D island (the diffusion length for a single adatom migrating over the surface) and θ_1 is the probability that the adsorption center $i = \pm 1$ is occupied (the quantities θ_i for other values of i have the same meaning). The first term on the right-hand side of Eq. (1) describes the rate of direct desorption of edge atoms from islands into a vacuum. The rate constant of this process is given by

$$k_0 = 2\sqrt{\pi\rho}\,\frac{f^*}{f_0}\frac{kT}{h}\exp\left(-\frac{E_0}{kT}\right), \qquad (2)$$

where f^* and f_0 are the partition functions of atoms desorbed from 2D islands in the activated complex and in the initial state, respectively; $E_0 = -U_0$ is the energy required for the removal of an edge atom from an island into a vacuum (Fig. 1); k is Boltzmann’s constant; T is the temperature; and h is Planck’s constant.

The second and third terms on the right-hand side of Eq. (1) describe the rates of opposite processes on the surface, namely, the transition of atoms into the 2D gas to adjacent adsorption centers $i = \pm 1$ and the implantation of individual atoms into islands. The rate constants k_1 and k_2 of these processes have the form

$$k_1 = 2\sqrt{\pi\rho}\,\frac{f_1^*}{f_0}\frac{kT}{h}\exp\left(-\frac{E_0 - E^*}{kT}\right), \qquad (3)$$

$$k_2 = 2\sqrt{\pi\rho}\,\frac{f_1^*}{f_1}\frac{kT}{h}\exp\left(-\frac{E_1 - E^*}{kT}\right), \qquad (4)$$

where f_1^* and f_1 are the partition functions for an adatom in the activated complex and in the initial state, respectively; $E_1 = -U_1$ is the energy required for the removal of a single atom of the 2D gas localized at an adsorption center into the vacuum; and $E^* = -U^*$ is the energy required for the removal of a delocalized adatom migrating over the surface into the vacuum (see Fig. 1). The last term on the right-hand side of Eq. (1) is the flux of adsorbate atoms incoming to islands from the gaseous phase.

We express θ_1 from Eq. (1). Its value is approximately equal to

$$\theta_1 \simeq \frac{\dot{N} + 2N^{1/2}\left(k_1 - \frac{\sqrt{\pi\rho}}{a^{-2}}\nu_0\right)}{2k_2N^{1/2}}. \qquad (5)$$

This expression can easily be derived taking into account the fact that, in accordance with Fig. 1, $E_0 > E_1 > E^*$ and, hence, $k_0 \ll k_1 \ll k_2$.

Let us now go over to the balance equation for particles of the 2D gas. The variation of their concentration (n_i is the concentration of single atoms occupying the ith adsorption centers) for all values of $|i| \geq 2$ can be presented as

$$\frac{dn_i}{dt} = \dot{n}_i = -\frac{n_i}{\tau} + k_2'(n_{i+1} - 2n_i + n_{i-1}) + \nu_0. \quad (6)$$

In this equation, τ and k_2' are the lifetime and the diffusion rate constant for a single atom on the surface, respectively. These quantities are given by

$$\tau = \frac{h}{kT}\frac{f_1}{f_1^*}\exp\left(\frac{E_1}{kT}\right), \quad (7)$$

$$k_2' = \frac{f_1^*}{f_1}\frac{kT}{h}\exp\left(-\frac{E_1 - E^*}{kT}\right). \quad (8)$$

In order to simplify Eq. (6), we will use the Arthur–Cho hypothesis [1], according to which the atomic concentration of the 2D gas attains its stationary value quite rapidly, and assume that $\dot{n}_i = 0$. Under this assumption, the balance equation has the form

$$n_{i+1} - 2n_i + n_{i-1} - \frac{n_i}{k_2'\tau} = -\frac{\nu_0}{k_2'}. \quad (9)$$

Considering that the diffusion coefficient D and the square of diffusion length X_S^2 of single atoms are given by

$$D = k_2'a^2, \quad (10)$$

$$X_S^2 = D\tau = a^2\exp\left(\frac{E^*}{kT}\right) \quad (11)$$

and that, as a rule, the diffusion length $X_S \gg a$, we can go over from the difference Eq. (9) to the differential equation

$$\frac{d^2n(x)}{dx^2} - \frac{1}{X_S^2}n(x) = -\frac{\nu_0}{D}, \quad (12)$$

in which x is the coordinate measured from the midpoint between the boundaries of two islands (for solitary atoms in the first layer, i.e., for $i \geq 2$) or from the center of an island (for solitary atoms in the second layer, i.e., for $i \leq -2$). The solutions of this equation for the first $n^{(1)}(x)$ and second $n^{(2)}(x)$ layers have the form

$$n^{(1)}(x) = (n_2 - \nu_0\tau)\frac{\cosh(x/X_S)}{\cosh((\delta/2 - 2a)/X_S)} + \nu_0\tau, \quad (13)$$

$$n^{(2)}(x) = (n_2 - \nu_0\tau)\frac{\cosh(x/X_S)}{\cosh((r - 2a)/X_S)} + \nu_0\tau, \quad (14)$$

where n_2 is the concentration of particles in the 2D gas at centers $|i| = 2$, δ is the mean distance between the boundaries of adjacent islands, and r is the radius of an island (see Fig. 1). The values of δ and r, as a rule, are much larger than the lattice constant a. In addition, the functions $n^{(1)}(x)$ and $n^{(2)}(x)$ are smooth and continuous. Consequently, we can assume, to a high degree of accuracy, that the concentration n_2 in Eqs. (13) and (14) is $n_2 \simeq n_1 \equiv n_\infty$, where n_∞ is the equilibrium concentration of atoms in the 2D gas at centers $|i| = 1$ adjacent to the islands. Taking into account the latter circumstance, as well as the fact that the equilibrium flux ν_∞ is equal to n_∞/τ, we can write Eqs. (13) and (14) in the form

$$n^{(1)}(x)/n_\infty = \left(1 - \frac{\nu_0}{\nu_\infty}\right)\frac{\cosh(x/X_S)}{\cosh(\delta/2X_S)} + \frac{\nu_0}{\nu_\infty}, \quad (15)$$

$$n^{(2)}(x)/n_\infty = \left(1 - \frac{\nu_0}{\nu_\infty}\right)\frac{\cosh(x/X_S)}{\cosh(r/X_S)} + \frac{\nu_0}{\nu_\infty}. \quad (16)$$

3. THE DISTRIBUTION OF 2D-GAS ATOMS OVER THE SURFACE

It was noted above that the desorption of atoms from the adsorbed layer formed by 2D islands and by a 2D gas occurs mainly from the states of single atoms. For this reason, a detailed analysis of the distributions (or concentration profiles) of 2D-gas particles on the surface is essential for understanding the kinetics of desorption from the adsorbed films under investigation. Here, we present the results of such an analysis carried out on the basis of Eqs. (15) and (16) for the following two cases: (1) $\nu_0 = 0$ and (2) $\nu_0 > 0$.

(1) $\nu_0 = 0$ (evaporation from the islands). In this case, Eqs. (15) and (16) assume a simpler form:

$$n^{(10)}(x)/n_\infty = \frac{\cosh(x/X_S)}{\cosh(\delta/2X_S)}, \quad (17)$$

$$n^{(20)}(x)/n_\infty = \frac{\cosh(x/X_S)}{\cosh(r/X_S)}. \quad (18)$$

Figure 2 shows the functions $n^{(10)}(x)/n_\infty$ and $n^{(20)}(x)/n_\infty$ plotted for various values of $\delta/2X_S$ and r/X_S. It can be seen from Fig. 2 that, as the adatom diffusion length increases, the surface distribution of 2D-gas particles becomes more and more uniform. In the limiting cases when $X_S \gg r$ or $X_S \gg \delta/2$, the concentration of single atoms is independent of coordinate x and is equal to n_∞. This corresponds to the equilibrium between the 2D gas and the islands.

(2) $\nu_0 > 0$. The curves describing the functions in Eqs. (15) and (16) are presented in Fig. 3. In the case when r/X_S or $\delta/2X_S = 10$, i.e., in the absence of equilibrium between the islands and the 2D gas (Fig. 3a), the concentration of single atoms depends on the flux ν_0 (it increases considerably with the flux). It is also worth noting that the concentration remains virtually unchanged and equal to $\nu_0\tau$ in a wide range of variation

of concentration x except in narrow regions near the boundaries of the islands. This means that the influence of the islands on the 2D gas is manifested only at small distances from their edges, while solitary atoms located at large distances from the islands virtually do not "perceive" them.

A qualitatively different pattern is observed when the 2D gas is in equilibrium with the islands or close to this state. As an example, the case when r/X_S (or $\delta/2X_S$) = 0.5 is considered in Fig. 3b. A characteristic difference from the case depicted in Fig. 3a is a much less pronounced dependence of the concentration of single atoms on the flux ν_0. In the limiting case, when these ratios are much smaller than unity, the concentration of 2D-gas particles is completely independent of the flux.

4. DESORPTION RATE

The desorption flux ν from the adsorbed film formed by two-dimensional islands and by a 2D gas is the sum of two components. The first of them is due to the evaporation of atoms from the boundaries of the islands, and the second is associated with the desorption of atoms from the 2D gas. For this reason, the expression for the flux from the surface can be presented in the form

$$\nu = k_0 N^{1/2} + \frac{1}{\tau\rho^{-1/2}}\left(\int_{-\delta/2}^{\delta/2} n^{(1)}(x)dx + \int_{-r}^{r} n^{(2)}(x)dx\right). \quad (19)$$

Obviously, the value of flux ν depends on the flux ν_0 of particles from the gaseous phase to the surface. In this connection, it is necessary to consider two cases: (1) when $\nu_0 \neq 0$, $\nu \equiv \nu_1$ and (2) when $\nu_0 = 0$, $\nu \equiv \nu_2$. The second case was analyzed in [1–14], while the first case has not as yet been discussed. We will analyze both cases.

(1) Substituting Eqs. (15) and (16) into Eq. (19) and integrating, we obtain the expression

$$\nu_1 = k_0 N^{1/2} + \frac{2\rho^{1/2} X_S f \theta_1}{\tau a^2} + \nu_0(1 - 2\rho^{1/2} X_S f), \quad (20)$$

where $f = \tanh\frac{\delta/2}{X_S} + \tanh\frac{r}{X_S}$. Equation (20) can be transformed by substituting Eq. (5) into it and taking into account the fact that $\dot{N} = \nu_0 - \nu_1$ under steady-state conditions ($\dot{n} = 0$) and that the equality $\tau a^2 k_2 = 2\sqrt{\pi\rho}X_S^2$ holds. This leads to a quite general equation for the desorption from the adsorbed layer formed by

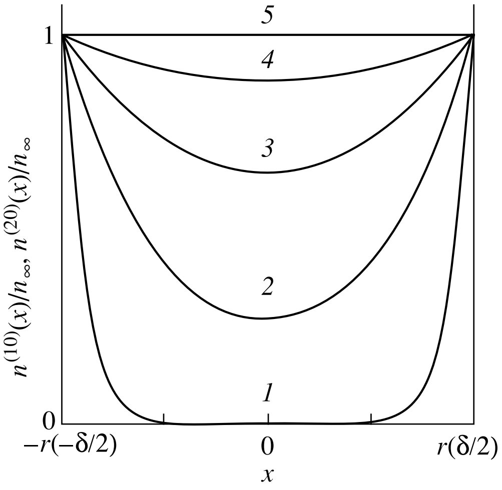

Fig. 2. Distribution of 2D-gas atoms over the surface for $\nu_0 = 0$, $r/X_S = \delta/2X_S$ = 10 (*1*), 2 (*2*), 1 (*3*), 0.5 (*4*), and 0.1 (*5*).

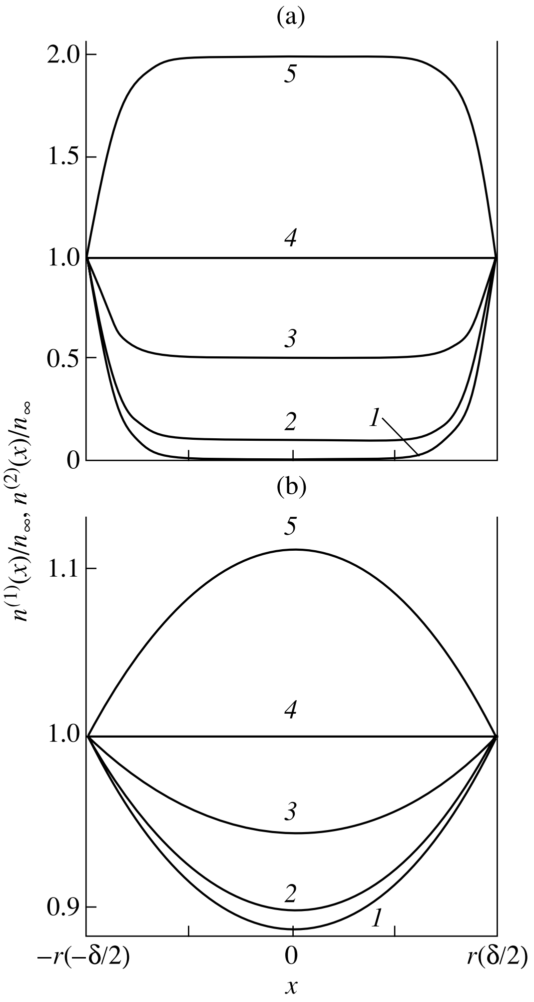

Fig. 3. Distribution of 2D-gas atoms over the surface for $\nu_0 \geq 0$, $r/X_S = \delta/2X_S$ = 10 (a) and 0.5 (b). The ratio ν_0/ν_∞ is equal to 0 (*1*), 0.1 (*2*), 0.5 (*3*), 1 (*4*), and 2 (*5*).

2D islands and the 2D gas:

$$\nu_1 \simeq \frac{2k_1 N^{1/2}}{1 + 2\sqrt{\pi} f^{-1} X_S N^{1/2}} + \nu_0\left(1 - \frac{4\sqrt{\pi\rho} X_S^2 N^{1/2}}{1 + 2\sqrt{\pi} f^{-1} X_S N^{1/2}}\right). \tag{21}$$

This equation describes, among other things, the dependence of the desorption rate on the flux of adsorbate atoms from the gaseous phase to the surface and on the concentration N. The latter dependence is especially complex. It can be seen that in the general case it cannot be reduced to a simple kinetic equation of the form $\nu = KN^m$, where K is the desorption rate constant and m is the exponent having an integer or fractional value which is independent of the concentration N.

However, when the equilibrium condition $X_S \gg \rho^{-1/2}$ is satisfied in the adsorbed layer, Eq. (21) is simplified considerably. Indeed, under these conditions, the quantity $f \simeq \rho^{-1/2}/2X_S$ and the term $2\sqrt{\pi} f^{-1} X_S N^{1/2}$ in the denominators on the right-hand side of this equation is much greater than unity. If we neglect unity, the second term on the right-hand side of Eq. (21) vanishes and the first term is simplified considerably. This gives

$$\nu_1 = \frac{f_1^*}{f_0}\frac{kT}{h} a^{-2} \exp\left(-\frac{E_0}{kT}\right). \tag{22}$$

The obtained expression describes the zero-order desorption kinetics. Its exponential factor is determined by the energy E_0 required for the removal of edge atoms from the surface into the vacuum.

(2) For $\nu_0 = 0$, the general expression for flux ν_2 has the form

$$\nu_2 = \frac{2k_1 N^{1/2}}{1 + 2\sqrt{\pi} f^{-1} X_S N^{1/2}}. \tag{23}$$

It follows that the dependence of the quantity ν_2 on the concentration N is quite complex in this case. However, under certain conditions, it is simplified considerably or disappears altogether. The latter takes place under the equilibrium conditions, when Eq. (23) is transformed into Eq. (22) (zero-order desorption kinetics).

If, however, there is no equilibrium between the islands and the 2D gas and the condition $X_S < \rho^{-1/2}/8$ holds, the second term in the denominator of Eq. (23) can be neglected as compared to unity (see [4, 8]). The obtained equation describes the desorption kinetics of the order 1/2; i.e., it has the form $\nu_2 = KN^{1/2}$. A detailed analysis shows, however, that the condition $X_S N^{1/2} \ll 1$ must be satisfied in this case, which is observed only for very low concentrations N. It can easily be verified that, strictly speaking, the half-order desorption kinetics is not realized even for $N \sim 10^{13}$ cm^{-2}.

5. DETERMINATION OF ENERGY E_0

It follows from what has been said above that when the two-dimensional islands are in equilibrium with the 2D gas, the value of E_0 can easily be determined from experiments by using Eq. (22) for the desorption rate both for $\nu_0 = 0$ and for $\nu_0 \neq 0$. In actual practice, however, we are often dealing with adsorption systems in which such an equilibrium is not observed. Consequently, for experimental investigations, one needs, first, a method for establishing whether or not the equilibrium on the surface exists and, second, a method which makes it possible to determine the value of E_0 under equilibrium, as well as nonequilibrium, conditions. In this section, various versions of these methods are considered, which are applicable when the concentrations ρ of islands for $\nu_0 = 0$ and $\nu_0 \neq 0$ are identical. The essence of these methods follows logically from the results of the analysis carried out in the previous sections. For example, it follows from these results that a comparison of the fluxes ν_1 and ν_2 from the surface makes it possible to immediately establish whether or not the given adsorption system is in equilibrium. Indeed, using Eqs. (21) and (22), we can write

$$\Delta\nu \equiv \nu_1 - \nu_2 \simeq \nu_0\left(1 - \frac{4\sqrt{\pi\rho} X_S^2 N^{1/2}}{1 + 2\sqrt{\pi} f^{-1} X_S N^{1/2}}\right). \tag{24}$$

As was noted in Section 4 that under the equilibrium conditions, the factor in the parentheses on the right-hand side of Eq. (24) is equal to zero. It follows that, under these conditions, fluxes ν_1 and ν_2 are equal. However, as the value of X_S decreases (e.g., upon a change in temperature), and, hence, as the equilibrium is violated, this factor increases together with the difference between the fluxes ν_1 and ν_2.

As regards the value of E_0, a detailed analysis of Eqs. (21) and (23) for the desorption rate indicates that it can be determined experimentally not only when two-dimensional islands are in equilibrium with the 2D gas but also in the absence of such an equilibrium. This conclusion is based on the fact that, in accordance with these equations, the equilibrium rate of evaporation of the form of Eq. (22) in the general case is equal to $\nu_0\nu_2/(\nu_0 - \Delta\nu)$; i.e.,

$$\nu_0\nu_2/(\nu_0 - \Delta\nu) = \frac{f_1^*}{f_0}\frac{kT}{h} a^{-2} \exp\left(-\frac{E_0}{kT}\right). \tag{25}$$

It follows from this equation that, in the absence of equilibrium at the surface, the value of E_0 can be determined if the three easily measurable fluxes ν_0, ν_1, and ν_2 are known.

The methods considered in this section were tested in the study of the thin-film Eu–Si(111) system [17]. Using these methods, a detailed analysis of the experimental results was carried out and energy E_0 was determined in the case when the conditions at the surface cannot be regarded as equilibrium even approximately.

ACKNOWLEDGMENTS

This work was supported by the State Program of the Ministry of Science "Surface Atomic Structures," project no. 2.5.99.

REFERENCES

1. J. R. Arthur and A. Y. Cho, Surf. Sci. **36** (2), 641 (1973).
2. J. A. Venables and M. Bienfait, Surf. Sci. **61** (2), 667 (1976).
3. M. Bienfait and J. A. Venables, Surf. Sci. **64** (2), 425 (1977).
4. R. Kern and G. LeLay, J. Phys. (Paris) **38** (10), C4-155 (1977).
5. G. LeLay, M. Manneville, and R. Kern, Surf. Sci. **65** (1), 261 (1977).
6. R. G. Jones and D. L. Perry, Surf. Sci. **71** (1), 59 (1978).
7. G. LeLay, M. Manneville, and R. Kern, Surf. Sci. **72** (2), 405 (1978).
8. R. Kern, G. LeLay, and J. J. Metois, Curr. Top. Mater. Sci. **3**, 131 (1979).
9. K. Christmann, G. Ertl, and H. Shimizu, J. Catal. **61** (2), 397 (1980).
10. R. Opila and R. Gomer, Surf. Sci. **112** (1/2), 1 (1981).
11. H. Asada, J. Res. Inst. Catal., Hokkaido Univ. **30** (1), 55 (1982).
12. J. J. Metois and G. LeLay, Surf. Sci. **133** (2/3), 422 (1983).
13. K. Nagai, T. Shibanuma, and M. Hashimoto, Surf. Sci. **145** (1), L459 (1984).
14. J. W. He, Chem. Phys. Lett. **151** (1/2), 27 (1988).
15. T. V. Krachino, M. V. Kuz'min, M. V. Loginov, and M. A. Mittsev, Fiz. Tverd. Tela (St. Petersburg) **39** (2), 256 (1997) [Phys. Solid State **39**, 224 (1997)].
16. T. V. Krachino, M. V. Kuz'min, M. V. Loginov, and M. A. Mittsev, Fiz. Tverd. Tela (St. Petersburg) **40** (2), 371 (1998) [Phys. Solid State **40**, 341 (1998)].
17. T. V. Krachino, M. V. Kuz'min, M. V. Loginov, and M. A. Mittsev, Fiz. Tverd. Tela (St. Petersburg) **42** (3), 553 (2000) [Phys. Solid State **42**, 566 (2000)].

Translated by N. Wadhwa

Physics of the Solid State, Vol. 43, No. 6, 2001, pp. 1178–1181. Translated from Fizika Tverdogo Tela, Vol. 43, No. 6, 2001, pp. 1135–1138.
Original Russian Text Copyright © 2001 by Venger, Goncharenko, Zavadskiĭ.

LOW-DIMENSIONAL SYSTEMS AND SURFACE PHYSICS

Dielectric Response of a Crystal with a Damaged Surface Layer in the Longitudinal–Transverse Splitting Region

E. F. Venger, A. V. Goncharenko, and S. N. Zavadskiĭ
Institute of Semiconductor Physics, National Academy of Sciences of Ukraine, pr. Nauki 45, Kiev, 03028 Ukraine
e-mail: avg@isp.kiev.ua

Received July 21, 2000; in final form, November 2, 2000

Abstract—A model of the dielectric function of a surface layer formed under the mechanical treatment of the crystal surface is considered in the range of the lattice optical vibrations. An approach is proposed based on the continuous distribution of the dipole-active modes in order to take into account the dislocation effect. It is demonstrated that the model used allows one to describe satisfactorily the decrease in the reflectivity of polished SiC6*H* samples in the vicinity of the frequency of the transverse optical phonon. *© 2001 MAIK “Nauka/Interperiodica”.*

1. INTRODUCTION

At present, the optical properties of crystals with a disordered layer near the surface are attracting considerable interest. These systems can manifest unusual properties, for example, the Anderson localization and its associated effects [1, 2], the surface amplification of Raman scattering [3], and the generation of surface polaritons by s-polarized light [4]. The present work is dedicated to a problem of practical significance, in particular, associated with the method of the optical control of damaged surface layers of the semiconductor wafers formed under mechanical treatment.

2. MATHEMATICAL MODEL

It is well known that the abrasive treatment of crystal structures brings about the formation of defects, i.e., sources of local stresses, both in the bulk and on the surface. It is believed that the main mechanisms of irreversible plastic deformation are the dislocation mechanisms of slipping and twinning [5]. When the density of defects in a damaged surface layer is very high, even continuous fields of elastic stresses can be generated as a result of the superposition of the local fields of these stresses. Note that the formation of dislocation networks under mechanical treatment is proved by electron microscopy.

A number of approaches to the description of amorphous materials are based on dislocation models (see, for example, [6–8]). Indeed, the introduction of dislocations into an ideal crystal leads to a disturbance of the long-range order. It is assumed that if dislocations are introduced in sufficiently large amounts, the lattice can deform in such a manner that only the short-range order will remain, whereas the long-range order will completely disappear.

In our work, we proceed from the concept of a damaged layer as a partially disordered (amorphizated) structure, which was formed under mechanical treatment. One of the features of noncrystalline materials is that the classical notions of the transverse and longitudinal normal vibrations become hard to define due to the absence of the long-range order. However, in this case, the possibility exists of describing the vibrational properties in terms of the density of vibrational states $g(\omega)$. The so-called method of the equations of motion [9] can be set off from the known methods of calculating the $g(\omega)$ function and IR and Raman spectra of amorphous semiconductors [10]. In particular, the following relationship for the $g(\omega)$ function was obtained by this method: $g(\omega) \sim \Sigma_s[\Delta(\omega + \omega_s) + \Delta(\omega - \omega_s)]$, where ω_s is the frequency of the sth normal mode, $\Delta(\omega) = \int_0^\tau \exp(-\lambda t^2)\cos(\omega t)dt$, and τ and λ are the phenomenological parameters of the model. At $\tau \longrightarrow \infty$ and $\lambda \longrightarrow +0$, $\Delta(\omega)$ degenerates into the δ function; when τ and λ are finite, $\Delta(\omega)$ is the Gaussian function with a half-width proportional to τ^{-1}.

A simple and handy approach to the description of the dielectric function of amorphous materials was proposed in [11]. It is based on an idea of the continuous (Gaussian) frequency distribution of oscillators (dipole–active oscillatory resonances). According to [11], the dielectric function of a disordered crystal can be represented in the form

$$\varepsilon(\omega) = \varepsilon_\infty + \sum_j \frac{s_j}{\sqrt{2\pi}\sigma_j} \int_{-\infty}^{+\infty} \frac{\exp[-(x-\omega)^2/2\sigma_j^2]}{x^2 - \omega^2 - i\omega\Gamma_j} dx, \quad (1)$$

where ε_∞ is the background (high-frequency) permittivity; s_j and Γ_j are the oscillator strength and damping constant of the jth oscillator, respectively; and σ_j are the parameters of the Gaussian distribution function.

A similar approach was proposed in [12], but with a uniform (step-function) frequency distribution of oscillators. In this case, instead of formula (1), the resulting expression for ε(ω) takes the form

$$\varepsilon(\omega) = \varepsilon_\infty + \sum_j \frac{s_j}{\sigma_j} \int\limits_{\omega_T - \sigma/2}^{\omega_T + \sigma/2} \frac{dx}{x^2 - \omega^2 - i\omega\Gamma}, \qquad (2)$$

where the parameter σ has the meaning of the width of the distribution function (of the step). However, let us note that when σ is sufficiently small, the form of the aforementioned distribution function should not significantly affect the results. We will use formula (1) in the following numerical calculations, because it seems more justified from the physical point of view. On the other hand, formula (2) allows one to perform the integration and to obtain the analytical result for ε(ω) in an explicit form. For example, if we restrict ourselves to a single oscillator ($j = 1$) in expression (2), after integration, it is an easy matter to obtain the relationship

$$\varepsilon(\omega) = \varepsilon_\infty + \frac{s}{\omega_T^2 - (\sigma/2 + \sqrt{\omega^2 + i\omega\Gamma})^2}. \qquad (3)$$

Assuming that $\sigma \ll \omega_T$, we have

$$\varepsilon(\omega) \approx \varepsilon^0(1 + \Delta), \qquad (4)$$

where

$$\varepsilon^0 = \varepsilon(\omega, \sigma = 0),$$

$$\Delta = \frac{\sigma s}{\varepsilon^0} \frac{\sqrt{\omega^2 + i\omega\Gamma}}{(\omega_T^2 - \omega^2 - i\omega\Gamma)^2}, \quad |\Delta| \ll 1.$$

Let us now analyze how the weak variation in ε(ω) affects the reflectivity. For this purpose, we will use relationship (4) and expand the expression for the reflectivity in the case of normal incidence,

$$R = \left|\frac{\sqrt{\varepsilon^0(1 + \Delta)} - 1}{\sqrt{\varepsilon^0(1 + \Delta)} + 1}\right|^2, \qquad (5)$$

in a power series, keeping only the term linear with respect to Δ. It is easy to verify that the result can be represented in the form

$$R = R_0 + \sigma F, \qquad (6)$$

where

$$R_0 = |r_0|^2 = \left|\frac{\varepsilon^0 - 1}{\varepsilon^0 + 1}\right|^2,$$

$$F = \mathrm{Re}(\gamma)\mathrm{Re}(r_0) + \mathrm{Im}(\gamma)\mathrm{Im}(r_0),$$

$$\gamma = \frac{\Delta}{\sigma} \frac{1}{\varepsilon^0 + \sqrt{\varepsilon^0}}.$$

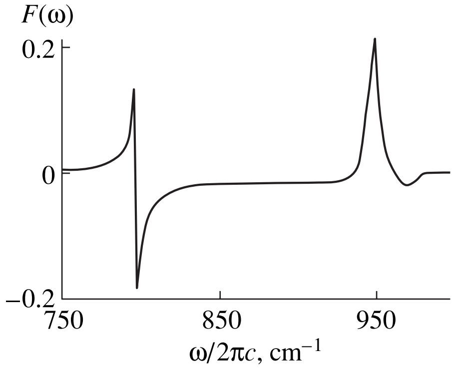

Fig. 1. The form of the $F(\omega)$ function for silicon carbide in the region of the longitudinal–transverse splitting (calculation).

As an illustration, Fig. 1 shows the form of the $F(\omega)$ function for silicon carbide in the region of the longitudinal–transverse splitting (of the residual rays). It can be seen that this function has two singularities at frequencies which approximately correspond to the frequencies of the transverse and longitudinal optical phonons. Moreover, it is negative virtually throughout the entire region of residual rays, which corresponds to a decrease in the reflectivity of the crystal. Function F is close to zero at some distance from the region of the residual rays.

3. EXPERIMENT

The energy depth of light penetration into the material in the case of the normal incidence is given by

$$l = \frac{1}{2\mathrm{Im}(k)} = \frac{c}{2\omega\mathrm{Im}\sqrt{\varepsilon}}, \qquad (7)$$

where c is the velocity of light and $k = \omega/c\sqrt{\varepsilon}$ is the magnitude of the wave vector in the medium. It is clear that if the characteristic thickness of the damaged surface layer is $d \ll l$, the change in the reflectivity cannot be observed. It is rather difficult to achieve sizable values of d in actual practice, because the act of interaction of an abrasive grain with a local microvolume (and, consequently, both its stressed state and heating) lasts a very short period of time and dislocations do not manage to penetrate deeply into the bulk of the crystal. (The activation energy of the dislocation displacement at room temperature is usually much greater than the energy of the lattice thermal vibrations [13].) It seems likely that the possibility of achieving a small value of l is more reasonable. Indeed, if $\mathrm{Im}\sqrt{\varepsilon}$ is sufficiently large, the necessary condition $d > l$ can be met. This situation becomes possible at corresponding frequencies in crystals in which transverse optical phonons possess a large oscillator strength and a weak attenuation. Thus,

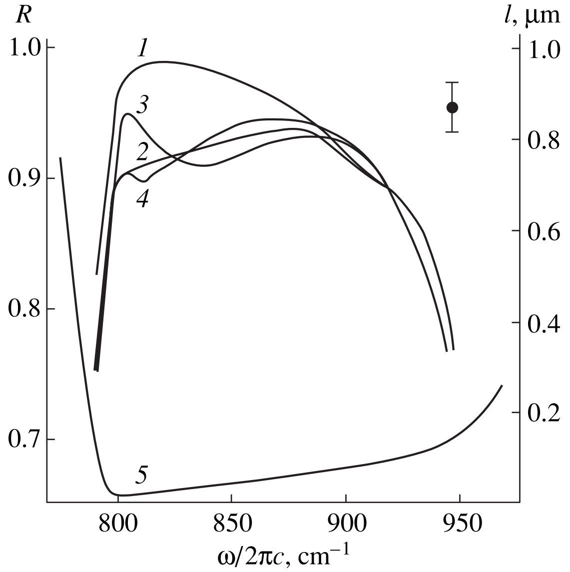

Fig. 2. Spectra of the normal reflectivity of silicon carbide: (*1*) before mechanical treatment, (*2*) after the treatment, and (*3*, *4*) the results of the fitting with the step and exponential models for the damaged layer, respectively. Curve *5* shows the depth of the light penetration into the crystal (calculation).

for an initial crystal ($\sigma = 0$), when $\omega = \omega_T$, it follows from expressions (1) and (6) that

$$l \approx \frac{c}{2}\sqrt{\frac{\Gamma}{s}}\omega_T^{-\frac{3}{2}}, \tag{8}$$

which actually corresponds to the minimum of the penetration depth.

The experiment was carried out for crystals of weakly doped silicon carbide SiC6*H* which were subjected to prolonged polishing with a fine-grained abrasive of boron carbide BC-3. Polytype SiC6*H* is characterized by weak optical anisotropy, a large oscillator strength at the frequency $\omega_T/2\pi c = 797$ cm^{-1}, and the low phenomenological constant of the phonon attenuation $\Gamma/2\pi c \approx 3$ cm^{-1} [14, 15]. The experimental reflectivity spectrum and the depth of light penetration for the initial crystal are shown in Fig. 2 by curves *1* and *5*, respectively. The parameters of the Lorentz dielectric function and the parameters of the semiconductor plasma were determined from curve *1* by analysis of the variance. These parameters are as follows: $\varepsilon_\infty = 6.5$, $s/\omega_T^2 = 3.1$, $\Gamma = 3$ cm^{-1}, $\omega_p = 295$ cm^{-1}, and $\omega_p\tau = 0.3$ (here, ω_p and τ are the frequency of natural vibrations and the relaxation time of the semiconductor plasma, respectively). Note that the contribution of the plasma subsystem to the dielectric function is disregarded in expression (1), but, according to our estimates, its effect on $\varepsilon(\omega)$ in the actual region of the resonance variation of the latter was very modest. However, in the subsequent calculations, we took into account the contribution of the semiconductor plasma to the dielectric function through the known additive Helmholtz–Kettler formula

$$\varepsilon^*(\omega) = \varepsilon(\omega) - \frac{\varepsilon_\infty\omega_p^2}{\omega^2 + i\omega/\tau}. \tag{9}$$

The experimental reflectivity spectrum of the sample after mechanical treatment is shown by curve *2*. It can be seen that it differs from the reflectivity spectrum of the initial crystal only in the range 800–880 cm^{-1}, where the depth of light penetration into the crystal is small. Here, the decrease in the reflectivity is observed in accordance with the above considerations. The depth of the light penetration into the crystal is large outside of the aforementioned range, and here, the reflectivity is determined by the volume parameters of the material. In this case, almost total correspondence of the reflectivity of samples outside of the aforementioned range can be proof that the diffuse light scattering by the surface of the polished sample is quite insignificant. Another circumstance which allows one to ignore the diffusion component of the scattering is that the reflectivities of both the initial sample and the sample after the treatment are virtually independent of the angular aperture of the spectral instrument [16].

Considering the reflectivity in the system consisting of a damaged layer (of thickness *d*) and the initial crystal (substrate), we carried out the optimization of the deviation of the experimental reflectivity curve *2* from the calculated curve with the use of relationships (1) and (9) (curve *3*). The fitted values of the variable parameters were as follows: $d = 0.1$ μm, $\sigma = 22$ cm^{-1}, and the root-mean square-deviation with respect to the spectrum $\langle\Delta R\rangle$ was 0.03.

It can be assumed that the parameter σ, which specifies the degree of plastic deformation of the surface layer, varies exponentially with respect to the wafer depth (similarly to the density distribution function of cracks [5]):

$$\sigma(z) = \sigma_0\exp(-z/z_0). \tag{10}$$

In this case, the problem of determination of the quantities σ and *d* is replaced by the determination of the parameters σ_0 and z_0 of the $\sigma(z)$ function. It is evident that the z_0 parameter in some way specifies the depth of the damaged layer. The result of the optimization of the experimental reflectivity spectrum with the use of the model approximations (1) and (10) is curve *4*, to which correspond the fitting parameters $\sigma_0 = 35$ cm^{-1} and $z_0 = 0.04$ μm. It can be seen that model (10) describes our experimental results essentially better than the preceding (single-layer) model, without an increase in the number of variable parameters. Thus, the reflectivity spectrum turned out to be sensitive to the state of the damaged layer at the depth of light penetration $l \le 0.1$ μm, which seems to be sufficiently reasonable.

ACKNOWLEDGMENTS

We are grateful to Yu.A. Pasechnik, who kindly put the samples for measurements at our disposal.

REFERENCES

1. A. R. McGurn, Surf. Sci. Rep. **33**, 357 (1990).
2. A. R. McGurn and A. A. Maradudin, Proc. SPIE **2117** (2), 12 (1994).
3. M. Moskovits, Rev. Mod. Phys. **57**, 783 (1985).
4. E. F. Venger, A. V. Goncharenko, and Yu. A. Pasechnik, Pis'ma Zh. Tekh. Fiz. **18** (3), 63 (1992) [Sov. Tech. Phys. Lett. **18**, 84 (1992)].
5. A. I. Tatarenkov, K. L. Enisherlova, T. F. Rusak, and V. N. Gridnev, *Control Methods of Damaged Layers during Mechanical Treatment of Single Crystals* (Moscow, 1978).
6. M. F. Ashby and J. Logan, Scr. Metall. **7**, 513 (1973).
7. G. C. M. Li, *Frontiers in Materials Science* (New York, 1976).
8. K. Suzuki, H. Fuzimori, and K. Hasimoto, *Amorphous Metals* (Omsya, Tokyo, 1982).
9. D. Beeman and R. Alben, Adv. Phys. **26**, 339 (1977).
10. H. Böttger, *Principles of the Theory of Lattice Dynamics* (Physik-Verlag, Weinheim, 1983; Mir, Moscow, 1986).
11. Yu. I. Kopilevich and E. G. Makarova, Opt. Spektrosk. **63**, 147 (1987) [Opt. Spectrosc. **63**, 86 (1987)].
12. D. K. Lynch, Astrophys. J. **467**, 894 (1996).
13. Yu. A. Kontsevoĭ, Yu. M. Litvinov, and Yu. A. Fattakhov, *Plasticity and Strength of Semiconductor Materials and Structures* (Moscow, 1982).
14. W. G. Spitzer, D. Kleinman, and D. Walsh, Phys. Rev. **113**, 127 (1959).
15. Yu. A. Pasechnik, O. V. Snitko, and A. G. Bychkov, Fiz. Tverd. Tela (Leningrad) **16**, 719 (1974) [Sov. Phys. Solid State **16**, 470 (1974)].
16. H. E. Bennett and J. M. Bennett, *Physics of Thin Films: Advances in Research and Development*, Ed. by G. Hass and R. Thun (New York, 1967; Mir, Moscow, 1970), Vol. 4.

Translated by O. Moskalev

Physics of the Solid State, Vol. 43, No. 6, 2001, pp. 1182–1187. Translated from Fizika Tverdogo Tela, Vol. 43, No. 6, 2001, pp. 1139–1144.
Original Russian Text Copyright © 2001 by Ivina, Orlov.

Effect of Surface Segregation on the Sharpness of Heteroboundaries in Multilayered Si(Ge)/Si$_{1-x}$Ge$_x$ Structures Grown from Atomic Beams in Vacuum

N. L. Ivina and L. K. Orlov

Nizhni Novgorod State University, pr. Gagarina 23, Nizhni Novgorod, 603600 Russia
Institute for Physics of Microstructures, Russian Academy of Sciences, Nizhni Novgorod, 603600 Russia

Received November 13, 2000

Abstract—The main reasons for composition intermixing in the vicinity of heteroboundaries in an Si(Ge)/Si$_{1-x}$Ge$_x$ heterosystem grown by the molecular beam epitaxy method are considered. The proposed model explains all the experimentally observed peculiarities, such as the clearly manifested asymmetry of the solid solution profile in layers, and demonstrates the noticeable erosion of the composition profile at the boundaries even in the absence of the surface segregation effect. It is shown that the surface segregation in the Ge/Si$_{1-x}$Ge$_x$ system may play a positive role, leading to an increase in the profile steepness of the Si$_{1-x}$Ge$_x$ layer near the boundaries. *© 2001 MAIK “Nauka/Interperiodica”.*

The properties of two-dimensional charge carriers in the transport channels of heterosystems formed on the basis of elementary semiconductors (Si, Ge) and their solid solution have been widely discussed in recent years. However, the observation of many unique physical phenomena in such systems often encounters considerable difficulties due to the structural imperfection of the layers forming transport channels, as well as of the interfaces forming these layers. This problem becomes especially serious in the study of composite materials with ultrathin (1 to 3 nm) layers, as well as Si–Ge superlattices (Si$_m$Ge$_n$), in which the perfection of interfaces becomes the decisive factor limiting the mobility of charge carriers along the plane of the layers in the structure [1] and the possibility of observing various fine physical effects predicted by the theory.

While the mechanisms leading to a deviation from the planarity of heteroboundaries are quite clear, the reasons behind the deterioration of the interface sharpness and erosion (intermixing) of the solid solution composition in the direction perpendicular to the plane of the layer virtually have not been discussed. This is primarily due to the difficulties encountered when the width of transition regions in the vicinity of interfaces in heterosystems with nanometer-thick layers is measured directly. However, experimental data on the width of transition regions determined by objective factors only (i.e., not associated with the imperfection of the technological process) have been reported recently. The following peculiarities in the distribution of the solid solution composition at the boundaries of the Si$_{1-x}$Ge$_x$ layer implanted in the silicon matrix have been established experimentally: (1) the extent and form of the erosion of the upper and lower boundaries of the Si$_{1-x}$Ge$_x$ layer are not identical [2, 3], and (2) the emergence of a tail in the distribution of the solid solution composition at the upper boundary may be caused by several factors, which is manifested as a difference between the rates of the decrease [3] in the concentration of one species of atoms in the transition region. The emergence of a transition region is mainly attributed to the effect of surface segregation of Ge, although this effect is not typical of the temperature range below 500°C, which is used most often for growing the structures.

In the present work, an attempt is made to compare the various reasons (including those connected with segregation [4]) behind the blurring of the concentration profile for Si and Ge atoms in the vicinity of heteroboundaries, to explain the observed singularities in the composition distribution in a thin Si$_{1-x}$Ge$_x$ layer by theoretically analyzing the transient processes on the surface of the growing layer, and to estimate the effective width of interfaces in the Si/Si$_{1-x}$Ge$_x$ heterosystems grown by the molecular beam epitaxy (MBE) technique.

We will analyze the reasons for and the type of erosion of the heteroboundaries in the multilayered structure of Si/Si$_{1-x}$Ge$_x$ grown by the traditional MBE method by studying the transient processes on the growth surface, which can be described by a system of kinetic equations for θ_i, viz., the dimensionless mean surface concentrations of Si and Ge atoms:

$$d\theta_i/dt = (F_i/n_s)\theta_{\mathrm{fr}} - (\nu_i + r_i)\theta_i. \quad (1)$$

Here, F_i is the *i*th atomic flux density, with $i = 1, 2$ for Ge and Si, respectively; $\nu_{\mathrm{Ge(Si)}}$ is the desorption frequency; $r_{\mathrm{Ge(Si)}}$ is the crystallization rate for Ge(Si) atoms; θ_{fr} is the concentration of surface dangling bonds; and $n_s = 6.78 \times 10^{14}$ cm^{-2} is the concentration of adsorption centers on the growth surface.

For adsorbed atoms, the following condition is assumed to be satisfied:

$$\theta_{\mathrm{Si}} + \theta_{\mathrm{Ge}} + \theta_{\mathrm{fr}} = 1. \tag{2}$$

Relations (1) and (2) form a system of equations for determining θ_i. Given θ_i, we can easily calculate the growth rate V_{gr} for the film and the concentration of Ge atoms in the epitaxial layer:

$$V_{\mathrm{gr}} = (r_{\mathrm{Si}}\theta_{\mathrm{Si}} + r_{\mathrm{Ge}}\theta_{\mathrm{Ge}})n_s/n_0, \tag{3}$$

$$x = r_{\mathrm{Ge}}\theta_{\mathrm{Ge}}/(r_{\mathrm{Si}}\theta_{\mathrm{Si}} + r_{\mathrm{Ge}}\theta_{\mathrm{Ge}}). \tag{4}$$

Here, $n_0 = 5.0 \times 10^{22}$ cm^{-3} is the volume concentration of atoms in the crystal.

Let us consider the peculiarities of the formation of the concentration profile in a Si$_{1-x}$Ge$_x$ layer grown in a silicon (germanium) matrix by the MBE method. We will study the kinetics of the surface concentrations of Si and Ge atoms in films grown from atomic beams of germanium and silicon by analyzing the second-order differential equations with constant coefficients, which follow from the system of equations (1):

$$(d\theta_{1,2}^2/dt^2) + \alpha(d\theta_{1,2}/dt) + \beta\theta_{1,2} + \gamma_{1,2} = 0, \tag{5}$$

where the coefficients α, β, and $\gamma_{1,2}$ are given by

$$\alpha = \sum_{i=1,2}\alpha_i = \sum_{i=1,2}(F_i/n_s + \nu_i + r_i), \tag{5a}$$

$$\beta = \alpha_1\alpha_2 - F_1F_2/n_s^2, \tag{5b}$$

$$\gamma_{1,2} = (F_{1,2}/n_s)(F_{2,1}/n_s - \alpha_{2,1}). \tag{5c}$$

We consider the case of a constant flux of Si(Ge) atoms and an atomic flux of Ge(Si) superimposed on it during the time interval $t = t_0 - t_1$. In this case, the general expression for the dimensionless surface concentrations of silicon and germanium adatoms as a function of time has the form

$$\begin{aligned}\theta_i(t) &= \theta'_{0i} + C_i^+\exp(-k^+(t-t_0))\\ &\quad + C_i^-\exp(-k^-(t-t_0)),\end{aligned} \tag{6}$$

where

$$C_1^+ = \{(F_{\mathrm{Ge}}/n_s + \nu_{\mathrm{Ge}} + r_{\mathrm{Ge}} - k^-)\theta'_{01} - (F_{\mathrm{Ge}}/n_s)(\theta_{02} - \theta'_{02})\}/(k^+ - k^-),$$

$$C_2^+ = (F_{\mathrm{Ge}}/n_s + \nu_{\mathrm{Ge}} + r_{\mathrm{Ge}} - k^+) \times \{(F_{\mathrm{Ge}}/n_s + \nu_{\mathrm{Ge}} + r_{\mathrm{Ge}} - k^-)\theta'_{01} - (F_{\mathrm{Ge}}/n_s)(\theta_{02} - \theta'_{02})\}/(F_{\mathrm{Ge}}/n_s)(k^- - k^+),$$

$$C_1^- = -\theta_{01} - C_1^+, \quad C_2^- = \theta_{02} - \theta'_{02} - C_2^+,$$

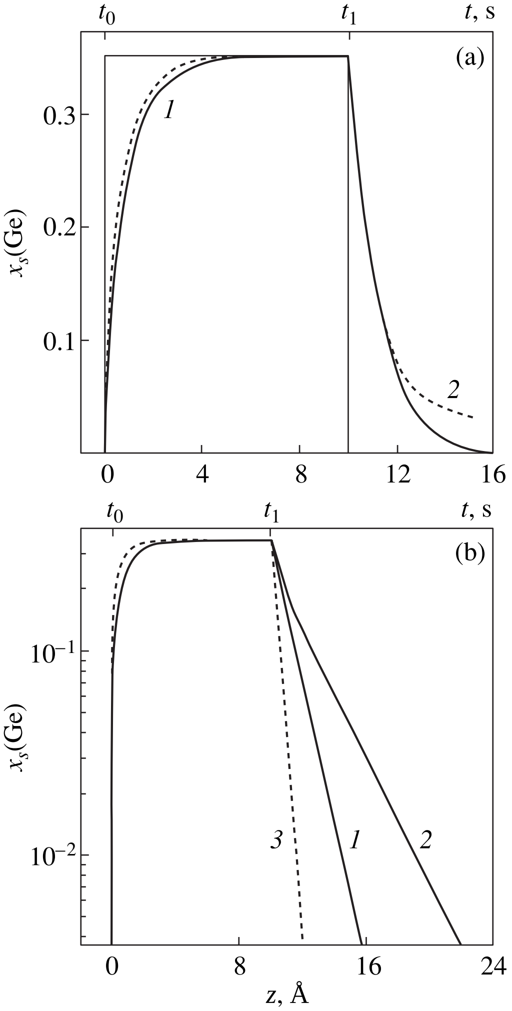

Fig. 1. Profile of the Ge distribution in the Si$_{1-x}$Ge$_x$ layer ($x = 0.35$) calculated for a rectangular flux pulse of Ge atoms for $V_{\mathrm{gr}} \approx 4$ Å/s, $\nu_{\mathrm{Ge}} = \nu_{\mathrm{Si}} = 0.01$, $r_{\mathrm{Si}} = 3.1$, and for various ratios of the rates of implantation of Si and Ge atoms into the lattice of the solid solution: $r_{\mathrm{Ge}} = r_{\mathrm{Si}}$ (curves *1* in (a) and (b)), $r_{\mathrm{Ge}} = r_{\mathrm{Si}}\,f(\theta_{\mathrm{Ge}})$ (curve *2* in (a)), $r_{\mathrm{Ge}} = 0.31r_{\mathrm{Si}}$ (curve *2* in (b)), and $3.1r_{\mathrm{Si}}$ (curve *3* in (b)). (b) Demonstrates the exponential nature of variation of the composition profile for the alloy in the vicinity of the layer boundary.

in the vicinity of the left (lower) boundary ($t = t_0$) and

$$\begin{aligned}\theta_i(t) &= C_i + C_i^+\exp(-k^+(t-t_1))\\ &\quad + C_i^-\exp(-k^-(t-t_1)),\end{aligned} \tag{7}$$

where

$$C_1 = 0, \quad C_2 = \theta_{02}, \quad C_1^+ = 0, \quad C_1^- = \theta'_{01},$$

$$C_2^+ = \theta'_{02} - \theta_{02} - (F_{\mathrm{Si}}/n_s)\theta'_{01}/(k^- - k^+), \tag{8}$$

$$C_2^- = (F_{\mathrm{Si}}/n_s)\theta'_{01}/(k^- - k^+),$$

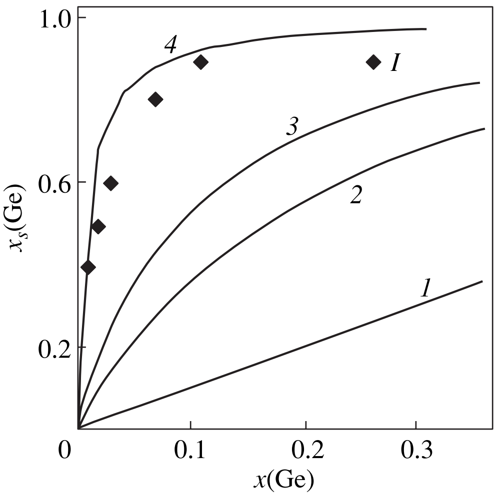

Fig. 2. Dependence of the surface concentration x_s(Ge) of Ge atoms on their concentration x(Ge) in the bulk of the $Si_{1-x}Ge_x$ layer for various values of ratio $k = r_{Si}/r_{Ge}$: 1 (*1*), 5 (*2*), 10 (*3*), and 100 (*4*). Dots (*I*) are describes the experimental values borrowed from [4] for $T_{gr} = 700$°C.

in the vicinity of the right (upper) boundary ($t = t_1$) of the flux pulse of germanium atoms (see Fig. 1). In our calculations, we assumed that the time of the growth of $Si_{1-x}Ge_x$(Si) layers is much longer than the time of stabilization of relaxation processes in the system with steady-state values of the surface concentrations θ_{0i}, which are given by

$$\theta_{01} = 0, \quad \theta_{02} = (F_{Si}/n_s)/(F_{Si}/n_s + \nu_{Si} + r_{Si})$$

at instants $t < t_0$ and $t \gg t_1$ and

$$\theta'_{0i} = (F_i/n_s)(\nu_i + r_i)/\{(F_{Ge}/n_s + \nu_{Ge} + r_{Ge})$$
$$\times (F_{Si}/n_s + \nu_{Si} + r_{Si}) - (F_{Ge}/n_s)(F_{Si}/n_s)\}$$

at instants $t_0 \ll t < t_1$. The exponents in the exponentials, determined by the determinant of the homogeneous equation (5) for the corresponding time intervals ($t_0 < t < t_1$ ($F_1 \neq 0$) and $t > t_1$ ($F_1 = 0$)), are given by

$$k^{+(-)} = \alpha/2 \pm (\alpha^2/4 - \beta)^{1/2}.$$

The exponent has the simplest form when the atomic flux densities of silicon and germanium are equal and when the rates of desorption and crystallization coincide ($F_{Ge} = F_{Si} = F$, $\nu_{Ge} = \nu_{Si} = \nu$, $r_{Ge} = r_{Si} = r$). Expressions for the concentration of germanium atoms on the film surface in this case have the form

$$\theta_1(t) = \theta'_{01} + C_1^+ \exp(-(\nu + r)(t - t_0))$$
$$\times [\exp(-(2F/n_s)(t - t_0)) + C_1^-/C_1^+],$$

$$C_1^+ = (1/2)\{\theta'_{01} - \theta_{02} - \theta'_{02}\},$$

$$C_1^- = (1/2)\{-3\theta'_{01} + \theta_{02} + \theta'_{02}\}$$

at the lower ($z > z_0$) boundary of the $Si_{1-x}Ge_x$ layer and

$$\theta_1(t) = \theta'_{01} \exp(-(\nu + r)(t - t_1))$$

at the upper boundary. It can be seen that even in the absence of surface segregation associated with the different rates of implantation of silicon and germanium atoms into the growing layer, i.e., for $r_{Ge} = r_{Si}$, the widths of the regions of composition blurring at the upper and lower boundaries of the $Si_{1-x}Ge_x$ layer have different values (see Fig. 1), which leads to asymmetry of the composition profile and, hence, of the potential in the structure. Here and below, we chose for our calculations values of the parameters which are close, to the maximum possible extent, to the experimental results obtained by Baribeau *et al.* [2] and correspond to the growth of $Si_{1-x}Ge_x$ films with $x = 0.35$ at a rate of ~4 Å/s at $T = 500$°C. At the initial stage of the transient process ($t \geq t_{0,\,1}$), the conditions for the implantation of Ge atoms into the growing layer at its upper and lower boundaries are not identical due to the difference in their surface densities for $t \geq t_0$ and $t \geq t_1$. In the former case, atoms are accumulated due to the activation of the additional flow of Ge atoms (the rate of the process at the initial stage is proportional to $\exp[-(2F/n_s)(t - t_0)]$). In the latter case, because of the absence of the corresponding flow of atoms to the substrate, only their relaxation associated with the finite time of embedding atoms into the crystal lattice of the adsorbed atoms remaining at the surface takes place (the decrease in the concentration of Ge atoms for $t > (t - t_1)$ is proportional to $\exp[-(\nu + r)(t - t_1)]$). It is just in the vicinity of this boundary that the effect of segregation of Ge atoms is manifested most strongly.

Let us consider the influence of segregation on the boundary blurring in greater detail. The segregation effects in the Ge–Si system, which are associated with the inequality of the rates of embedding of Si and Ge atoms into the crystal lattice, are manifested most markedly in the growth temperature range $600 < T < 800$°C. In this range, the r_{Si}/r_{Ge} ratio can vary from 10 to 100. This is confirmed by Fig. 2, which shows, along with the theoretical curves calculated by using the simplest formula $x_s = f(x)$ connecting the surface concentration $x_s = \theta_{Ge}/(\theta_{Ge} + \theta_{Si})$ of germanium atoms with their concentration $x = r_{Ge}\theta_{Ge}/(r_{Ge}\theta_{Ge} + r_{Si}\theta_{Si})$ in the bulk of the $Si_{1-x}Ge_x$ alloy, the experimental data (*I*) obtained in [4] for the growth temperature $T_{gr} = 700$°C. According to the available experimental data, outside this temperature interval, the surface segregation effects are usually manifested weakly.

The effect of the difference in the crystallization rates r_{Ge} and r_{Si} is demonstrated in Fig. 1b, which shows that in the case of the $Ge_{1-x}Si_x$/Si system, this effect ($r_{Ge} < r_{Si}$) enhances the boundary blurring (curve *2*). Obviously, the same condition ($r_{Ge} < r_{Si}$) for a less abundant system $Ge_{1-x}Si_x$/Ge (in this case, index 1 corresponds to Si and 2 to Ge) leads to the opposite effect, namely, to an increase in the steepness of the composition distribution profile at the upper heteroboundary. This formally corresponds to curve *3* in Fig. 1b (see also Figs. 3b, 3c) calculated for the $Ge_{1-x}Si_x$/Si interface for $r_{Ge}/r_{Si} > 1$. The difference in the crystallization rates for the $Ge_{1-x}Si_x$/Ge system produces a positive effect, leading to sharper composition profiles in the vicinity of the heteroboundary.

Figure 3a shows the effective blurring (light symbols) of the upper film boundary [defined as the distance $L1$ at which the concentration of one of the components (germanium in our case) decreases by two orders of magnitude] as a function of the rate of embedding of atoms into the growing layer in the absence of the surface segregation effect, which corresponds to the condition $r_{Ge} = r_{Si}$. In accordance with the calculations made in [5], the value of r_{Si} for a given flux of silicon atoms can vary by several orders of magnitude depending on the growth temperature and the surface coverage with adsorbed atoms. The value of r_{Si} becomes larger the higher the surface coverage with Si atoms and the higher the growth temperature. According to Fig. 3a, an order-of-magnitude change in r_{Si} for small values of the flux of Si atoms can considerably decrease the boundary blurring. In other words, the growth of films at higher temperatures (but in the interval where the segregation effects are weakly pronounced) may turn out to be preferable. At a high coverage of the surface with adsorbed atoms, this effect is much less pronounced, but an increase in the fluxes does not lead to a strong increase in the boundary blurring as a result of the opposite effect emerging due to the simultaneous increase in the values of r_{Si} and r_{Ge}.

An analysis of the curves in Figs. 3a–3c shows that under the experimental conditions used in [2], a width of ~6 Å (*I* in Figs. 3a–3c) of the region of composition mixing is attained if we assume the absence of segregation in a narrow range of the atomic fluxes, which corresponds to an extremely high degree of surface coverage with adsorbed atoms of the substance ($\theta_{Si} \approx (0.7–0.9)n_s$). For the lower levels of atomic fluxes traditionally used in experiments and corresponding to the coverage of the surface $\theta_{Si} \approx (0.1–0.2)n_s$ the width of the boundaries of the $Si_{1-x}Ge_x$ layer measured in [2] cannot be attributed only to the finite rate of implantation of atoms into the growing layer in the case of equality of r_{Si} to r_{Ge}. In this case, we must assume that the surface segregation effects play a noticeable role in the growth temperature range under investigation.

The influence of segregation (which is manifested for $r_{Ge} < r_{Si}$) on the interface blurring width is demonstrated in Figs. 3b and 3c, which clearly show that the effective blurring of a heteroboundary for a given growth rate (~4 Å/s in our case) varies by several angstroms depending on the effectiveness of the implantation of Ge atoms into the growing layer. The curves presented in Figs. 1 and 3 show that for a small ratio r_{Si}/r_{Ge},

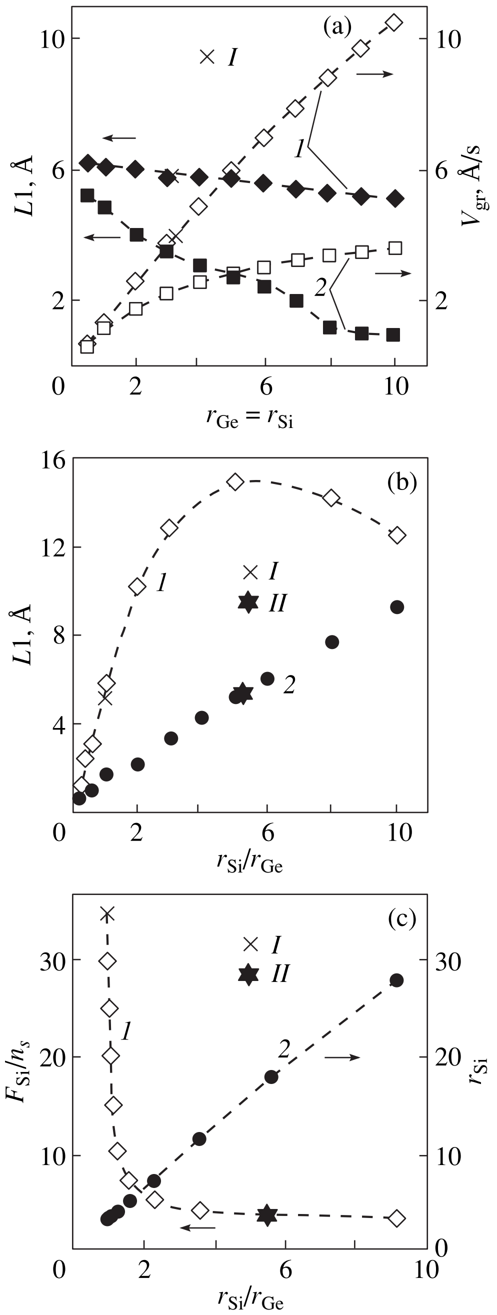

Fig. 3. Effective width ($L1$) of the composition blurring at the upper boundary of the $Si_{1-x}Ge_x$ layer ($x_{max} = 0.35$) and the values of growth (V_{gr}, r_{Si}) and technological (F_{Si}) parameters as functions of the implantation rate of Ge atoms into the lattice of the solid solution: (a) $L1(r_{Ge})$ (dark symbols) and $V_{gr}(r_{Ge})$ (light symbols) for $r_{Ge} = r_{Si}$, F_{Si}/n_s = 35 (*1*) and 3.5 (*2*); (b) $L1(r_{Si}/r_{Ge})$ for $V_{gr} \approx 4$ Å/s, F_{Si}/n_s = 35, $r_{Si} = 3.1$ (*1*) and $F_{Si}/n_s = 3.5$, $r_{Si} = 18$ (*2*); and (c) the curves corresponding to given values of $L1 = 5.8$ Å (*1*) and $V_{gr} \approx 4$ Å/s (*2*) on the planes (F_{Si}/n_s, r_{Si}/r_{Ge}) and (r_{Si}, r_{Si}/r_{Ge}). Symbols *I* ($r_{Si}/r_{Ge} = 1$) and *II* ($r_{Si}/r_{Ge} = 5.5$) on the curves correspond to the experimental situations considered in [4]: $V_{gr} \approx 4$ Å/s and $L1 = 5.8$ Å for r_{Si}/r_{Ge} = 1 and 5.5, respectively.

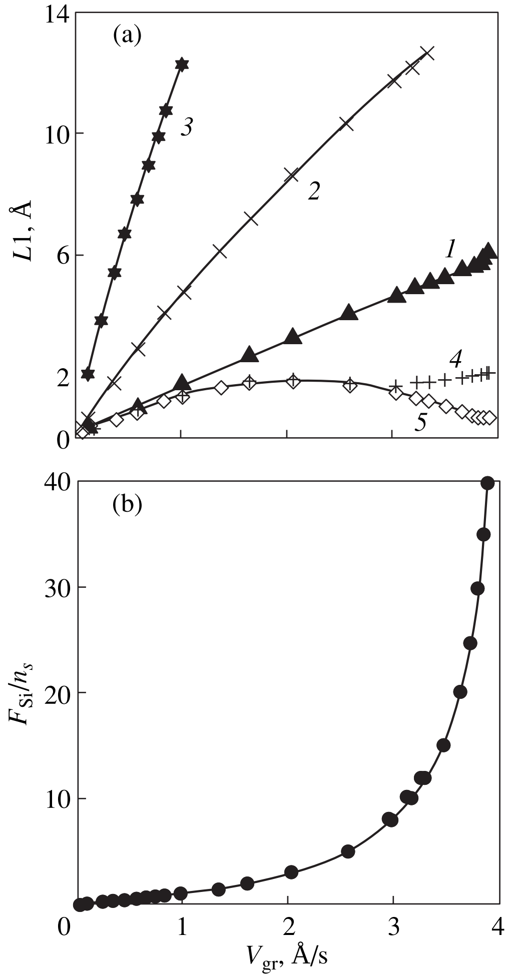

Fig. 4. (a) Effective blurring of the right boundary of the $Si_{1-x}Ge_x$ layer ($x = 0.35$) as a function of the growth rate of the films for a constant value of coefficient $r_{Si} = 3.1$, $\nu_{Ge} = \nu_{Si} = 0.01$, r_{Ge}: 3.1 (*1*), 1 (*2*), 0.31 (*3*), 10 (*4*), and 31 (*5*). (b) Atomic fluxes of silicon in the setup corresponding to the range of the film growth rates presented in (a) for the above values of parameters r_{Si}, ν_{Ge}, and ν_{Si} (the shape of the $F_{Si}(V_{gr})$ curve does not depend on r_{Ge}).

the effect of surface segregation of Ge atoms proper is not dominant in the formation of the heteroboundary profile. Along with segregation, a comparable contribution to the heteroboundary blurring comes from the surface diffusion processes determining the time of embedding of adsorbed atoms from the surface into the growing layer. It should be noted that for a given growth rate, the same blurring of the layer boundary corresponding to $L1 = 5.8$ Å (*II* in Figs. 3b, 3c) in the presence of segregation (for $k = r_{Si}/r_{Ge} = 5.5$) can be attained at the level of atomic flux to the substrate that is an order of magnitude lower than in the absence of segregation (for $k = 1$). The indeterminacy is due to the fact that the boundary blurring is directly connected with the growth rate, while the latter is determined, on the one hand, by the intensity of atomic fluxes of the substance to the substrate and, on the other hand, by the rate of implantation of atoms into the growing layer. The atomic flow rates can easily be determined in each specific experiment, but their values are not given in the literature cited. This leads to a certain ambiguity in the theoretical analysis of the experimental results presented in those publications. For example, it can be seen from Fig. 3c that for a given growth rate of the layer, the same width of the interface ($L1 = 5.8$ Å) can be obtained, depending on the value of k, in a wide range of values (curve *1*) of the fluxes of Si atoms from the source to the substrate. The range of the parameters to the right of this curve corresponds to values $L1 > 5.8$ Å; to the left of this curve, to values of $L1 < 5.8$ Å. The value of k and, hence, the segregation coefficient for a specific system can be determined directly from Fig. 3c if the values of atomic fluxes in the setup, along with information on the growth rate of the film, are obtained in the course of the experiments.

In the above analysis of the composition distribution profile in the vicinity of heteroboundaries, we disregarded the dependence of the rate of implantation of Ge atoms into the Si lattice on its surface concentration. It was proved by us earlier [5] that in the general case, the $r_{Ge}(\theta_{Ge})$ dependence takes place and the range of variation of r_i for various temperatures and concentrations of atoms at the surface can be quite wide. According to [5], the lowering of the surface concentration level for germanium after the removal of the corresponding atomic flow will also reduce the value of r_{Ge}. In the growth temperature range 500 to 600°C, an order-of-magnitude decrease in the surface concentration of germanium reduces r_{Ge} by several times for a virtually unchanged value of r_{Si}, thus ensuring the increasing role of segregation effects in the system and enlarging the width of the transition region at the upper heteroboundary. The corresponding curve calculated for $r_{Ge} = f(\theta_{Ge})r_{Si}$ is presented by the dashed curve in Fig. 1a. As θ_{Ge} decreases from the maximum value equal to the dimensionless surface concentration of Ge atoms on the surface of the $Si_{1-x}Ge_x$ layers ($x = 0.35$) to its minimum value corresponding to an alloy composition with $x_{min} = 0.01x$, the function $f(\theta_{Ge})$ varies from 1 to 0.1 in accordance with a linear law.

Analysis of the dependence of the transition region width on the Si atomic flux (Fig. 4) shows that the sharpness of heteroboundaries can considerably be improved by using lower growth rates for epitaxial layers.

In conclusion, we will formulate the main results of this work. The kinetic model of the growth of $Si_{1-x}Ge_x$ layers used in our calculations correctly describes the available experimental data [2, 3]. This model makes it possible to calculate the width of the transition regions at the upper and lower boundaries of the epitaxial layer for various growth conditions and explains the clearly manifested asymmetry in the composition distribution over the layer. It has been proved by us here that the formation of the upper boundary of the layer is mainly determined by relaxation mechanisms, while the higher sharpness of the lower heteroboundary of the $Si_{1-x}Ge_x$ layer is mainly due to the high rate of the flow of the substance to the surface of the growing film. If the segregation effects are insignificant (the region of low growth temperatures), the dominating factor of heteroboundary blurring is the finite time of implantation of Ge atoms into the growing layer, which is determined, in all probability, by the rate of atomic diffusion over the surface. It is shown for the first time that the surface segregation effects, leading to additional blurring of boundaries in the $Si/Si_{1-x}Ge_x$ system, can facilitate an increase in the steepness of the potential profile in the $Ge/Si_{1-x}Ge_x$ system.

ACKNOWLEDGMENTS

The authors thank E.S. Demidov, as well as A.V. Potapov and V.I. Vdovin, for fruitful discussions in the course of the investigations and for valuable remarks.

This work was supported by the Russian Federation programs “Universities of Russia,” grant no. 992849, and “Physics of Solid-State Nanostructures,” grant no. 7(00)P.

REFERENCES

1. P. Waltereit, J. M. Fernandes, S. Kaya, and T. J. Thornton, Appl. Phys. Lett. **72**, 2262 (1998).
2. J. M. Baribeau, D. J. Loskwood, and R. L. Headrick, J. Electron. Mater. **24**, 341 (1995).
3. V. I. Vdovin and K. D. Shcherbachev, in *Proceedings of the All-Russia Conference “Nanostructures Based on Silicon and Germanium,” IFM RAN, Nizhni Novgorod, 1998*, p. 168.
4. Y. J. Zheng, A. M. Lam, and J. R. Engstrom, Appl. Phys. Lett. **75**, 817 (1999).
5. A. V. Potapov, L. K. Orlov, and C. V. Ivin, Thin Solid Films **336**, 191 (1998).

Translated by N. Wadhwa

Physics of the Solid State, Vol. 43, No. 6, 2001, pp. 1188–1194. Translated from Fizika Tverdogo Tela, Vol. 43, No. 6, 2001, pp. 1145–1151.

POLYMERS
AND LIQUID CRYSTALS

Features of the Magnetic and Dielectric Behavior of Mesophases of Chromium (III) Complexes with Azacyclic Ligands

N. E. Domracheva*, I. V. Ovchinnikov*, A. Turanov*, G. Lattermann, and A. Facher****
**Kazan Physicotechnical Institute, Russian Academy of Sciences, Kazan, 420029 Tatarstan, Russia*
***Universität Bayreuth, D-95440 Bayreuth, Germany*
e-mail: domracheva@mail.knc.ru
Received October 17, 2000

Abstract—Two paramagnetic (**1**, **2**) chromium metallomesogens were studied by the EPR, magnetic-susceptibility, and dielectric-spectroscopy methods. These mesogens possess columnar liquid-crystal phase polymorphism. For mesogen **1** in the columnar $\mathrm{Col_{xd}}$ phase, an irreversible structural phase transition was detected by the EPR method. An anomalous nonlinear temperature dependence of the resonance fields of the EPR line positions and of the fine-structure parameter D in the mesophases of compound **1** was observed. It was shown that this anomaly is associated with the soft mode of crystal lattice. The dielectric spectroscopy data provide support for the existence of the soft mode, which is probably due to the transition of the system from a paraelectric to a dipole-ordered state. The structure of the hexagonal columnar plastic phase of mesogen **2** is formed by a single type of paramagnetic monomer chromium center and does not exhibit any specific features. *© 2001 MAIK "Nauka/Interperiodica".*

1. The creation of mesogen molecules containing metallic atoms (metallomesogens) [1–3] has considerably enriched the physical (optical, magnetic, and electrical) properties of liquid crystals. In particular, paramagnetic mesophases with a large magnetic anisotropy [4] have been obtained. Searches for polar achiral liquid-crystal systems [5] are in progress.

Two paramagnetic chromium (III) metallomesogens, namely, **L1** $\mathrm{CrCl_3}$ (**1**) and **L2** $\mathrm{CrCl_3}$ (**2**), were studied by the EPR method. These mesogens include the azacyclic ligands 1,4,7-tri(3,4-didecyloxybenzyl)-1,4,7-triazacyclononan **L1** and 1,3,5-tri(3,4-didecyloxybenzyl) hexahydro-1,3,5-triazine **L2**, which have similar arrangements of ligand atoms (Fig. 1a) but exhibit radically different physical properties.

An unusual polymorphism of the columnar liquid-crystal phases is observed for the **L1** $\mathrm{CrCl_3}$ mesogen (the phase transition temperatures are shown in °C): K 42.0 $\mathrm{Col_{xd}}$ 68.5 $\mathrm{Col_{hd}}$ 167 $\mathrm{Col_{rd}}$ 223.5 **I**, where K is a crystalline phase; $\mathrm{Col_{xd}}$ is a nonidentified columnar mesophase, $\mathrm{Col_{hd}}$ is a hexagonal columnar mesophase, and $\mathrm{Col_{rd}}$ is a rectangular columnar mesophase; and **I** is an isotropic phase. The **L2** $\mathrm{CrCl_3}$ complex has only one stable mesophase ($\mathrm{Col_{hp}}$), namely, the columnar hexagonal plastic phase K36 $\mathrm{Col_{hp}}$233.5 **I**.

To elucidate the differences in the electronic structure of metallomesogens **1** and **2**, the EPR technique was used. This is one of the most sensitive methods for studying the electronic structure of a substance and the local crystalline fields changing at the phase transitions.

The X- and Q-band EPR spectra were measured for the crystalline, isotropic, and different mesomorphic phases, as well as for a vitrified anisotropic solvent, such as a eutectic mixture of nematic liquid crystals MBBA + EBBA. In the last case, an anisotropic solution was preliminarily oriented by a magnetic field and then sharply cooled to the glassy state. The EPR spectra were recorded on a Bruker ER 200E-SRC spectrometer (X band) in the temperature range from –130 to 240°C and on a Varian (E-line) spectrometer (Q band) at room temperature.

2. The EPR spectrum (X band) of compound **2** (**L2** $\mathrm{CrCl_3}$) in the whole interval of existence of the columnar plastic phase and in the vitrified anisotropic solvent (the eutectic MBBA + EBBA mixture) had identical shapes and consisted of two lines with effective g factors $g_{\mathrm{eff}} \approx 2$ and 4 (see Fig. 1b). The type of the observed spectrum, similar to that observed in a powder (the case of strong crystalline fields), has been well studied in the literature; in particular, it is identical to the spectrum of the tris-chelate acetyl-acetonate complex of chromium $\mathrm{Cr(acac)_3}$ [6]. The detected lines of the fine structure are due to the $1/2 \longrightarrow -1/2$ transition for parallel ($g_{\mathrm{eff}} \approx 2$) and perpendicular ($g_{\mathrm{eff}} \approx 4$) orientations of the magnetic field with respect to the particular molecular axis C_3 of the complex. The EPR spectra of the chromium ions are described by the spin Hamiltonian with $S = 3/2$

$$H = g_{\parallel}\beta H_Z S_Z + g_{\perp}\beta(H_X S_X + H_Y S_Y) + D[S_Z^2 - S(S+1)/3] + E(S_X^2 - S_Y^2), \qquad (1)$$

where D and E are the fine-structure parameters which characterize the axial and rhombic distortions, respectively, in the octahedron environment of the Cr^{3+} ion. In the Q band ($\nu = 36.5$ GHz), the shift of the line corresponding to the perpendicular orientation allowed us to determine the fine-structure parameters: $D = 0.6$ cm^{-1}, $E = 0.008$ cm^{-1}, and $g = 1.98$, where $g = (g_{\parallel} + 2g_{\perp})/3$. The orientation of compound **2** in an anisotropic liquid-crystal matrix (eutectic MBBA + EBBA mixture) showed that the character of the orientation of the **L2** $CrCl_3$ complex is also analogous to that of $Cr(acac)_3$ [6] in the same matrix (Fig. 1b); namely, the C_3 axis was along the director. For this orientation, the parallel component of the EPR spectrum, with $g_{\text{eff}} \approx 2$, has a maximum intensity for $\gamma = 0°$, where γ is the angle between an external magnetic field and the director.

Therefore, the structure of the column plastic phase of compound **2** is formed by a single type of paramagnetic monomer chromium center. The principal molecular axis in these centers is the C_3 axis (the magnetic axis z of the D tensor is oriented along this axis), so that the octahedral configuration of the Cr^{3+} environment has quite strong axial ($D = 0.6$ cm^{-1}) and insignificant rhombic ($E = 0.008$ cm^{-1}) distortions.

3. Several types of the EPR spectra of the mesogen complex **1** are observed for different polymorphic states of the substance. The EPR spectra for the crystalline phase at room temperature for the X and Q bands are presented in Fig. 2 (solid lines). A rough estimation of the parameter D in the crystalline phase of compound **1** (without a calculation of the spectrum) can be obtained in the Q-band spectrum from the position of the extra absorption peak (EP), which corresponds to the intermediate orientation lines in the Q band. The EPR spectrum of the Q range consists of the line with $g_{\text{eff}} \approx 2$, corresponding to the $1/2 \longrightarrow -1/2$ transition [7]. The resonance values of the fields $H_{\parallel}$ and $H_{\perp}$ for this transition are close to each other; the EP peak is situated a little bit apart from them (at a higher field). The anisotropic splitting for the EP peak, Δ, equals [7]

$$\Delta = H_{\text{EP}} - H_{\parallel} \approx (D^2[4S(S+1) - 3] \times 7)/(64(g\beta)^2 H_0). \qquad (2)$$

Substituting the value of the resonance field of the EP peak into Eq. (2), we obtain a rough estimation of the parameter D to be 0.2 cm^{-1}. A computer simulation of the spectra in the X and Q bands (dashed lines in Fig. 2) by using the spin Hamiltonian (1) gives the following values of the fine-structure parameters: $D = 0.17$ cm^{-1}, $E = 0.03$ cm^{-1}, and $g = 1.99$.

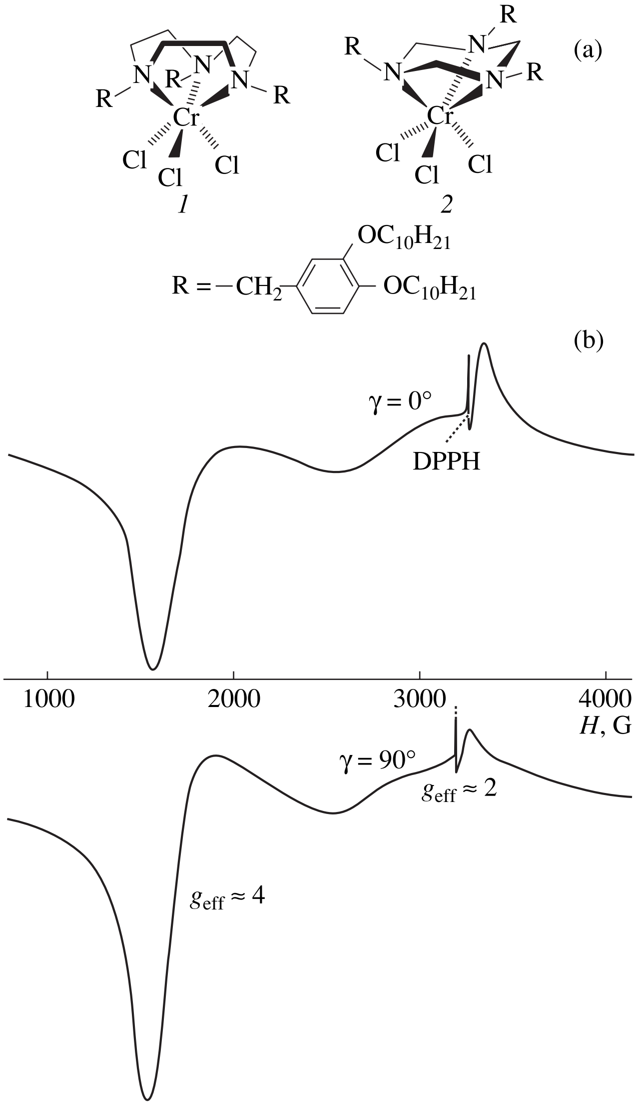

Fig. 1. (a) Structural formulas of metallomesogens **1** and **2** and (b) the EPR spectrum of compound **2**, oriented in a mixture of nematic liquid crystals at $\gamma = 0°$ and 90°.

Thus, the crystalline phase of compound **1** is formed only by a single type of the chromium (III) paramagnetic complexes (which will be referred to as the A type). This type is characterized by a higher symmetry of the local crystalline field at the site of the chromium ion than in compound **2**.

4. To compare the metal–ligand covalent-bond strengths in compounds **1** and **2**, let us use an approximate relation for the g factors [8]:

$$g = 2.0023 - \alpha_\sigma^2 \alpha_\pi^2 8\lambda/10D^*q. \qquad (3)$$

In this case, the ratio of the covalence parameters α for complexes **1** and **2** is $\alpha_\sigma^2(1)\alpha_\pi^2(1)/\alpha_\sigma^2(2)\alpha_\pi^2(2) \approx 0.6$, where the values of $10D^*q$ obtained from the optical studies [9] are equal to 15700 and 14300 cm^{-1} for com-

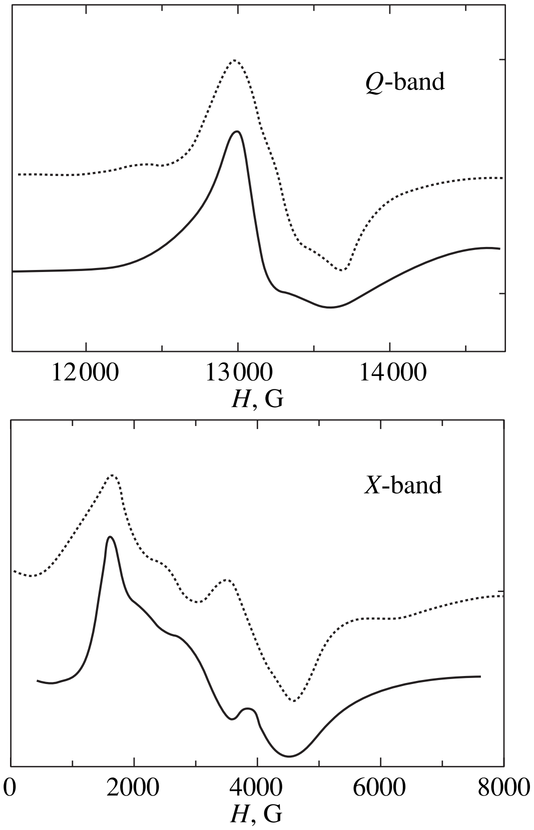

Fig. 2. Experimental and theoretical EPR spectra of compound **1** in the crystalline phase.

pounds **1** and **2**, respectively. Hence, the metal–ligand bonds in mesogen **1** are considerably more covalent than in mesogen **2**. This correlates well with the pulse IR spectroscopy data (the frequencies of CrN_3 covalent vibrations are higher in compound **1** than in **2** by approximately 100 cm^{-1} [9]). It is likely that the higher flexibility of the azacyclic ligand in mesogen **1** and, therefore, its stronger covalent bond determine the differences in the behavior of mesophases of complexes **1** and **2**.

We have not succeeded in determining the orientation of complex **1** in an anisotropic matrix (eutectic MBBA + EBBA mixture) because of the presence of two types (*A* and *B*) of paramagnetic centers in it. The *B*-type centers will be discussed below. However, the similar geometric structure of compounds **1** and **2** allows one to suppose that the directions of the principal magnetic and molecular axes in these substances are identical.

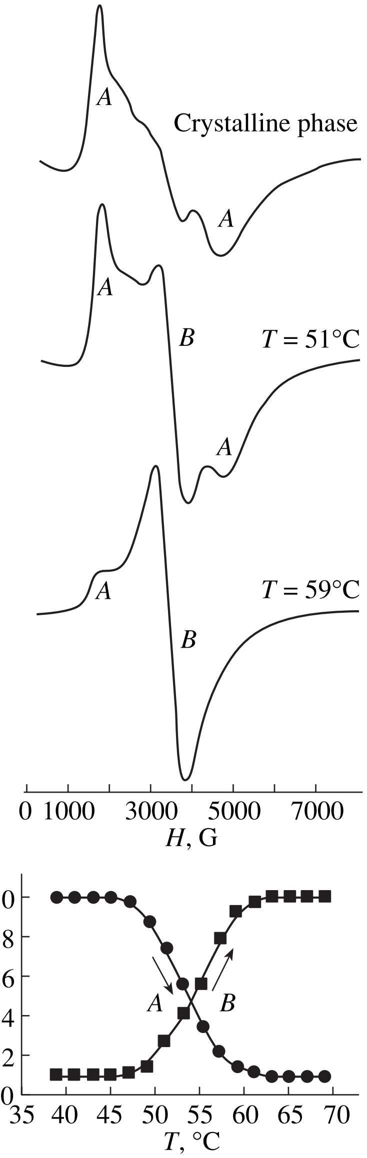

Fig. 3. Transformation of the EPR spectrum the $A \longrightarrow B$ phase transition in compound **1**.

5. Let us now consider EPR (*X* band) of compound **1** in different columnar mesophases. The transformation of the sample from the crystalline phase to the nonidentified columnar mesophase in the process of the first heating is accompanied by an irreversible structural phase transition (see Fig. 3). At this transformation, the symmetry of the nearest neighbor surrounding of the chromium ion is changed abruptly and the *A*-type paramagnetic centers are transformed to new (marked as *B*-type) paramagnetic centers.

The EPR spectrum of the *B*-type paramagnetic centers is an almost symmetrical line (crosses in Fig. 4a) with the effective *g* factor $g_{\text{eff}} = 2.08$ and the experimentally measured (peak-to-peak) line width of 680 G. A calculation of the spectrum for the *B*-type centers after the $K \longrightarrow Col_{xd}$ transition (solid curve in Fig. 4a) by using the spin Hamiltonian (1) gives the following values of the parameters: $D = 0.05$ cm^{-1}, $E = 0$, and $g = 2.08$ for an individual Lorentzian-shaped line with $\Delta H_{\parallel} = 500$ and $\Delta H_{\perp} = 450$ G for the parallel and perpendicular orientations of the external magnetic field relative to the C_3 axis, respectively. The temperature depen-

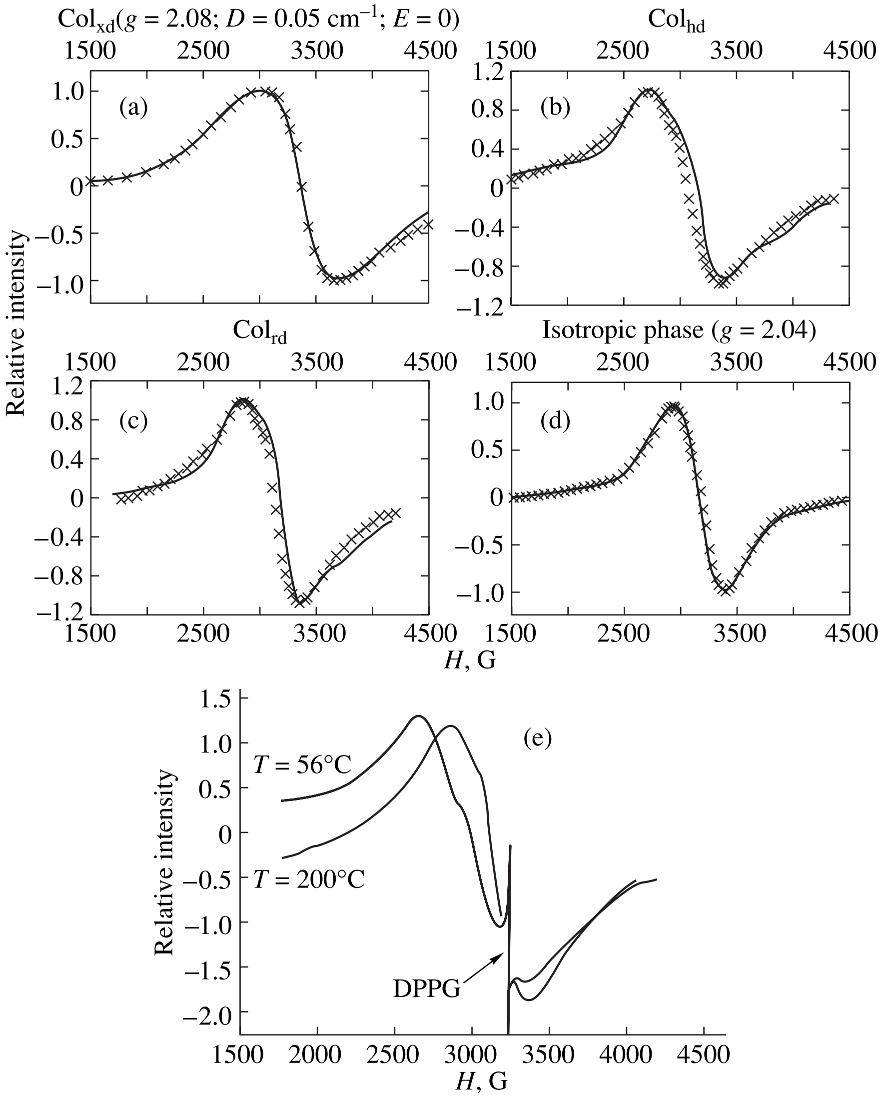

Fig. 4. Experimental and calculated EPR spectra of the metallomesogen **1** in (a) Col$_{xd}$, (b) Col$_{hd}$, (c) Col$_{rd}$, and (d) isotropic phases. (e) The temperature shift of the 3/2 ⟶ 1/2 transition EPR line.

dence of the changes in the normalized integral intensities of the spectra for the A- and B-type paramagnetic centers at the structural phase transition is shown Fig. 3. The rate of temperature change in the vicinity of the transition was of the order of 1° per minute. Note that about 90% of the transition from one spectrum to the other occurs in the temperature range 47–63°C. However, the traces of both spectra are visible at temperatures below and above this range. The characteristic value of the structural phase transition temperature (i.e., the temperature at which the A- and B-type spectrum intensities are equal) is 54°C. The temperature width of the phase transition, characterized by the temperature interval over which the intensity is changed by 90%, is equal to 18–20°C. The phase transition exhibited no hysteresis since only the higher temperature B phase was being frozen on cooling the sample.

The determined values of the fine-structure parameters at the $A \longrightarrow B$ structural phase transition allow one to conclude that the octahedral configuration surrounding the chromium (III) ion is changed from an axially elongated (along the C_3 axis) octahedron with a rhombic distortion to a weakly distorted octahedral configuration. On further heating (cooling), the columnar mesophases are formed exclusively by the B-type paramagnetic centers.

The columnar mesophases (Col$_{rd}$, Col$_{hd}$, Col$_{xd}$) were studied at slow cooling of compound **1** from the isotropic phase, because, according to the polarization microscopy data, the phase textures are most pronounced in this case. The EPR spectrum in the isotropic phase represents a single symmetrical line (see Fig. 4d) with the g factor equal to 2.04. The EPR lines in the columnar mesophases become asymmetrical (see Figs. 4b, 4c), and the line corresponding to the 3/2 ⟶ 1/2 transition

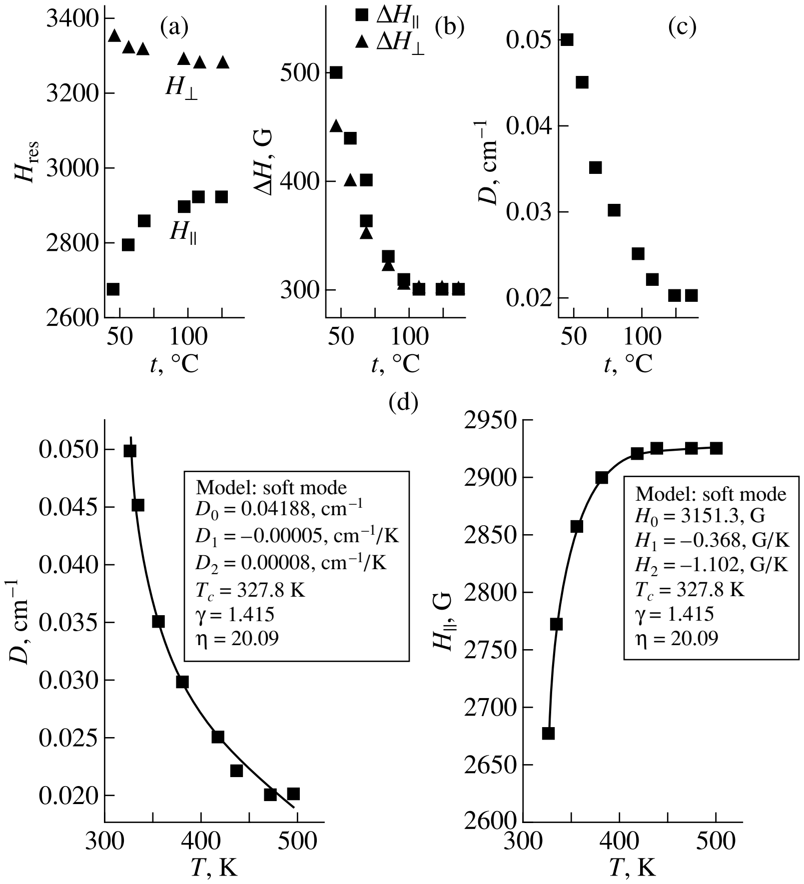

Fig. 5. Temperature dependence of (a) the resonance fields, (b) the line widths, and (c) the parameter *D* in the column phases of mesogen **1**. (d) The approximation, according to Eqs. (7) and (8), of the temperature dependence of the fine-structure parameter and of the position of $H_\parallel$. The approximation parameters are listed in the insets.

is observed in the fine structure of the spectrum. When the temperature is decreased, the left wing of the asymmetrical line (the 3/2 ⟶ 1/2 transition) is displaced by ~250 G (in the 185°C interval) to lower fields relative to the central transition ±1/2 (Fig. 4e). When the (Col_{xd} ⟶ K) phase transition point is approached, the EPR line is considerably broadened, becoming again symmetrical, and is described by the same parameters *g*, *D*, *E*, and ΔH as at first heating (for the phase transition K ⟶ Col_{xd}).

The EPR spectra for different types of the columnar phases were simulated with the spin Hamiltonian in Eq. (1). The microwave resonance fields H_{res}, the individual line widths ΔH (for the parallel $\{H \parallel z(C_3)\}$ and perpendicular orientations of the external magnetic field relative to the C_3 axis), and the fine-structure parameter *D* were calculated. The temperature dependences of these values are presented in Figs. 5a–5c, respectively. As is clear from Fig. 5a, the behavior of the microwave resonance fields for parallel and perpendicular orientations in the region of existence of the column phases is different. Moreover, the temperature dependences of the resonance field $H_\parallel$, the line widths, and the parameter *D* during the transition from the Col_{rd} and Col_{hd} phases to the columnar Col_{xd} phase are nonlinear.

The behavior of the resonance field shifts and the line widths is analogous to the behavior of these parameters in anisotropic ferromagnets [10] and antiferromagnets [11] above the critical point, where such a behavior is due to the growth of the spin correlation effects [10].

To clarify the nature of these anomalies, we carried out measurements of the magnetic susceptibility, the dielectric permittivity and the relaxation time for compound **1** in standard temperature regimes (cooling, heating) of the sample.

The magnetic susceptibility (Fig. 6a) is described by the Curie–Weiss law, $\chi = C/(T - \Theta) + \chi_{dia}$, in the temperature interval 4.2–400 K with the constant *C* corresponding to the spin value $S = 3/2$, $\chi_{dia} = -1023$ cm^3/mol, and $\Theta = 0.65$ K. This is evidence of the weak ferromagnetic exchange interactions ($J/k = 0.13$ K) between the chromium (III) ions. Such value of the exchange integral is too small to lead to the anomalous changes in the resonance field $H_\parallel$ position and in

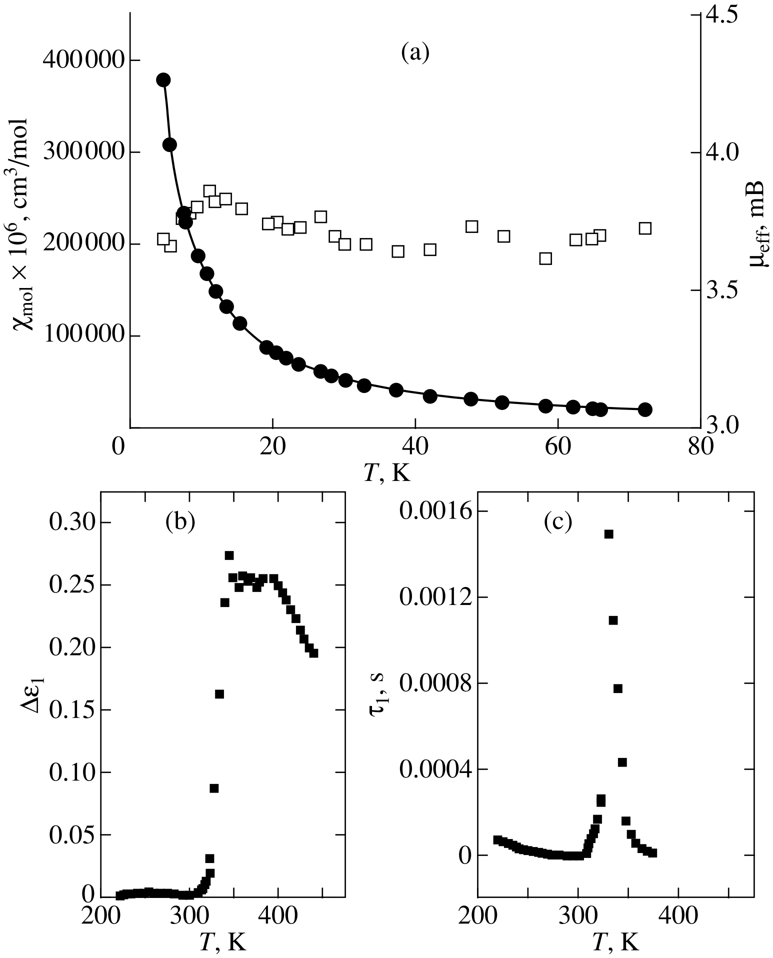

Fig. 6. Temperature dependences (a) of the molar magnetic susceptibility and the magnetic moment of compound **1**, (b) of the change in the real part of the dielectric permittivity, and (c) of the relaxation time of the Col$_{xd}$ phase.

the fine-structure parameter D detected in the higher temperature columnar phases to be explained by the magnetic ordering.

The nature of the EPR-registered anomalies is, probably, associated with the internal electric field acting on the chromium atom. To test this assumption, dielectric measurements were carried out by Feldman and coworkers. At $T_c = 54.8°C$ (327.9 K), a phase transition (Figs. 6b, 6c) from the paraelectric state to the dipole-ordered state was observed. This transition was connected with the dynamical contribution from the soft mode.

It was shown in [12–14] that the nonlinear temperature dependence of the EPR line positions and of the fine-structure parameter D can be due to the contribution from the soft mode (the optical branch of the crystalline lattice vibration spectrum, the frequency of which vanishes at the phase transition temperature T_c at some point of the Brillouin zone).

The dependence of the soft mode frequency upon the temperature, the wave vector, and the propagation direction is expressed by the formula [12, 13]

$$\omega_q^2 = \alpha^2\left(\frac{T - T_c}{T_c}\right)^{\gamma} + \beta^2 q^2 + q^2\lambda^2\cos^2\theta, \qquad (4)$$

where θ is the angle between the direction of the spontaneous polarization and the phonon propagation direction.

Let us express the contribution of the soft mode as a displacement of the Cr^{3+} ion $U(t)$ relative to the surrounding lattice (as in [12]):

$$D(t) = D^0 + \Delta D(U(t)), \qquad (5)$$

where D^0 is the term connected with the static contribution of the surrounding ions. Expanding ΔD in powers of the displacement $U(t)$ for small $U(t)$ and taking time average of $D(t)$, we get

$$\langle D(t)\rangle = D^0 + \sum (K^2 d/\omega_q)(2n_q + 1), \qquad (6)$$

where d is the expansion coefficient of $U(t)^2$ in $D(U(t))$, n_q is the number operator of phonons, K is a constant, and ω_q is the frequency of the soft mode with the wave vector q.

When the temperature approaches T_c, we have $\omega_q \longrightarrow 0$; the contribution from the soft mode increases; and, according to Eq. (6), the parameter D grows considerably. Equation (6) was integrated in [12, 13] with respect to q and θ over the Brillouin zone, taking into account Eq. (4) and the high-temperature approximation

$$D(T) = D_0 + D_1 T + D_2 T \times\left[1 - \frac{|T-T_c|^{\gamma/2}}{\eta}\arctan\left(\frac{\eta}{|T-T_c|^{\gamma/2}}\right)\right], \quad (7)$$

where $\eta = (\beta q_m/\alpha)$ and q_m is the maximum value of the wave vector q.

The anomalous shifts of the resonance fields are closely related to the change in the D tensor. Taking into account the linear relation between the position of the EPR line and the value of D [14, 15], one gets an expression for $H(T)$ in the paraelectric phases.

$$H(T) = H_0 + H_1 T + H_2 T \times\left[1 - \frac{|T-T_c|^{\gamma/2}}{\eta}\arctan\left(\frac{\eta}{|T-T_c|^{\gamma/2}}\right)\right]. \quad (8)$$

The temperature dependences of $H_{\parallel}$ and D were approximated using Eqs. (7) and (8) (see Fig. 5d). As is clear from Fig. 5d, this approximation describes the experimental data adequately. This proves the effect of the soft mode on the EPR spectra of the chromium ions of compound **1** in the paraelectric phase. The values of the critical exponent γ and η are typical of the ferroelectric phase transitions, detected by EPR [13, 14].

Thus, the anomalous temperature dependences of the parameter D and the resonance field $H_{\parallel}$ position for compound **1** in the paraelectric phase are due to soft mode vibrations.

The appearance of the soft-mode in the EPR spectra of the chromium mesophases is due to the dynamic process of the dipole ordering in the system. The specific structure leading to a double-well-potential model, which is necessary to understand the dynamic process mentioned above, as well as the unusual value of the g factor for the chromium (III) compounds, will be discussed in a separate work.

The obtained result, independently of the concrete structural model explaining it, is of interest in connection with the problem of searching for liquid crystalline supramolecular structures with collective ferroelectric properties.

ACKNOWLEDGMENTS

The authors are grateful to Yu. Feldman and É. Galstyan (Jerusalem University) for carrying out the dielectric measurements, to Marc Nilgels from the Illinois Center of EPR Studies (USA) for supplying us with the program for calculating “powder-like” EPR spectra, and to Prof. B.Z. Malkin for fruitful discussions of the results.

This work was supported by the Russian Foundation for Basic Research, grant no. 99-03-32716.

REFERENCES

1. A. M. Giroud-Godquin and P. M. Maitlis, Angew. Chem. Int. Ed. Eng. **30**, 375 (1991).
2. S. A. Hudson and P. M. Maitlis, Chem. Rev. **93** (3), 861 (1993).
3. *Metallomesogens: Synthesis, Properties and Applications*, Ed. by J. L. Serrano (VCH, Weinheim, 1996).
4. Y. Galyametdinov, G. Ivanova, I. Ovchinnikov, *et al.*, Liq. Cryst. **20** (6), 831 (1996).
5. L. M. Blinov, Liq. Cryst. **24** (2), 143 (1998).
6. I. G. Bikchantaev and I. V. Ovchinnikov, Fiz. Tverd. Tela (Leningrad) **18** (5), 1479 (1976) [Sov. Phys. Solid State **18**, 861 (1976)].
7. N. M. Zhidomirov, Ya. S. Lebedev, S. N. Dobryakov, M. Ya. Shteĭnshneĭder, A. K. Chirkov, and V. A. Gubanov, *Interpretation of Complex Spectra of Electron Spin Resonance* (Nauka, Moscow, 1975).
8. B. R. McGarvey, J. Chem. Phys. **41** (12), 3743 (1964).
9. A. Facher, Dissertation (Universität Bayreuth, 2000).
10. D. L. Huber and M. S. Seehra, Phys. Status Solidi B **74** (1), 145 (1976).
11. Y. Yokozawa, J. Phys. Soc. Jpn. **31** (5), 1590 (1971).
12. K. Tzuchida and R. Abe, J. Phys. Soc. Jpn. **46** (4), 1225 (1979).
13. D. Barb, N. M. Grecu, V. V. Grecu, and F. F. Popescu, Chem. Phys. Lett. **56** (2), 355 (1978).
14. G. V. Mamin and V. N. Efimov, Ferroelectrics **233** (1–2), 111 (1999).
15. G. Burns, J. Appl. Phys. **32** (9), 2048 (1961).

Translated by A. Sonin

Physics of the Solid State, Vol. 43, No. 6, 2001, pp. 993–996. Translated from Fizika Tverdogo Tela, Vol. 43, No. 6, 2001, pp. 961–964.
Original Russian Text Copyright © 2001 by Sevast'yanova, Yalovega, Mansour, Marchelli, Soldatov.

METALS AND SUPERCONDUCTORS

The Local and Electronic Structures of $Al_{90}Fe_xCe_{10-x}$ Alloys ($x = 3, 5, 7$): XANES Analysis

T. I. Sevast'yanova, G. É. Yalovega, A. Mansour, A. Marchelli, and A. V. Soldatov
Rostov State University, pr. Stachki 194, Rostov-on Don, 344006 Russia

Received September 26, 2000; in final form, November 3, 2000

Abstract—The x-ray absorption near-edge structure (XANES) of $Al_{90}Fe_xCe_{10-x}$ ($x = 3, 5, 7$) is measured above the Fe *K* edge and analyzed theoretically by the multiple scattering method. By comparing the experimental data with the theoretical findings, the most adequate model for describing the neighbor environment of Fe atoms is chosen. Since the dipole transition matrix element is a smoothly varying function of energy near the Fe *K* edge, the x-ray absorption fine structure in this energy range characterizes the density of free *p* states of Fe in the conduction band of $Al_{90}Fe_xCe_{10-x}$ alloys. © *2001 MAIK "Nauka/Interperiodica".*

1. INTRODUCTION

$Al_{90}Fe_xCe_{10-x}$ ($x = 3, 5, 7$) show metallic properties and have a glasslike structure [1]. These compounds possess many interesting mechanical [2] and magnetic properties [3]: they have high strength and ductility, low density, and high corrosion resistance. A study of their local structure provides important information that provides insight into the nature of the properties of these compounds. Their geometrical structure has been studied by x-ray diffraction [4], neutron and x-ray scattering [1], and extended x-ray absorption fine structure (EXAFS) spectroscopy [5].

The electronic structure of the Al–Fe–Ce system has been investigated by XANES [6] and angle-resolved x-ray photoelectron spectroscopy [7]. The unoccupied states near the bottom of the conduction band in these alloys significantly affect their physical properties. However, these states have not been adequately studied.

In this work, we performed XANES measurements near the Fe *K* edge. The data obtained are analyzed theoretically within the multiple-scattering approximation. The objective of this study was to elucidate the local structure of the $Al_{90}Fe_xCe_{10-x}$ system and the features of their electronic structure by using x-ray absorption fine structure data. Earlier, the multiple-scattering method was employed to study the properties of various materials [8]; in particular, it was successfully applied to ordered alloys Ni_3Al and Al_3Ni [9].

2. EXPERIMENT AND CALCULATION TECHNIQUE

The x-ray absorption spectra of iron in the alloys under study were measured in transmission geometry at the Stanford Synchrotron Center. The experimental energy resolution in the energy range covered was 1.0 eV. The spectra are recorded in steps of 0.3 eV by using an ionization chamber. The iron foil spectrum is used to calibrate the photon energy. Thin film specimens are prepared based on an x-ray transparent kapron ribbon. The ribbon is folded in two to make the specimens more homogeneous. The recorded spectra are corrected for the beam-current function in the storage ring.

Table 1. The parameters of the neighbor environment of an absorbing Fe atom in five inequivalent positions in the $FeAl_3$ model

Shell	Number of atoms in the shell	Average shell radius, Å
	Fe1	
1	4	2.32435
2	4	2.63015
3	3	2.80345
	Fe2	
1	6	2.53195
2	4	2.73690
3	6	4.18040
	Fe3	
1	4	2.35330
2	4	2.55860
3	3	2.82335
	Fe4	
1	8	2.51825
2	2	2.75160
3	1	3.00520
	Fe5	
1	3	2.38900
2	5	2.57810
3	3	3.32765

1063-7834/01/4306-0993$21.00 © 2001 MAIK "Nauka/Interperiodica"

Table 2. The parameters of the neighbor environment of an absorbing Fe atom in the $FeAl_6$ model with interatomic distances decreased by 4%

Shell	Number of atoms in the shell	Average shell radius, Å
1	10	2.42905
2	10	4.07390
3	6	4.35495

The calculational multiple-scattering technique used in this work was described in [10]. The neighbor environment of an Fe atom in an $Al_{90}Fe_xCe_{10-x}$ alloy is considered using model compounds $FeAl_6$ [11] and $FeAl_3$ [12]. The parameters of several shells of Fe atom neighbors are listed in Table 1 for the $FeAl_3$ model alloy and in Table 2 for the $FeAl_6$. For the latter model alloy, the original interatomic spacings are decreased by 4%. The phase shifts are calculated using a muffin-tin (MT) potential with contacting MT spheres. The MT radii and MT parameters are determined following the MT constructing procedure described in [10]. The crystal potential is constructed using the Mattheiss scheme with an exchange parameter equal to 1.0. The atomic charge densities are calculated by the Dirac–Slater self-consistent method. The phase shifts for orbital angular momentum values up to 3 are taken into account.

When comparing the experimental and theoretical spectra, we took account of the experimental spectrum broadening due to the finite lifetime of the core hole and the finite mean free path of the photoelectron, as well as the experimental error. The width of the *K* energy level is taken to be 1.25 eV [13]. The energy dependence of the mean free path was calculated in [12]. The experimental energy resolution is 1.0 eV. All these factors are taken into account in the imaginary part of the complex potential.

3. RESULTS AND DISCUSSION

Figure 1 shows the experimental x-ray absorption spectra above the iron *K* edge in an amorphous and a crystalline $Al_{90}Fe_3Ce_7$ alloy. It is seen that the spectra in these two cases differ in the region of the fundamental absorption edge and they also differ in the position of the higher energy peak. In this work, we analyzed the spectrum of the amorphous $Al_{90}Fe_3Ce_7$ alloy.

We considered two models. One of them is an $FeAl_3$ alloy [12]. In its crystalline structure, there are five inequivalent positions of Fe atoms. The theoretical spectra calculated for these positions and the average spectrum characterizing the alloy as a whole are presented in Fig. 2. Since the neighbor environments for these five Fe-atom positions are different, the shape of the partial spectra also varies with the Fe position. However, the agreement between the overall spectrum

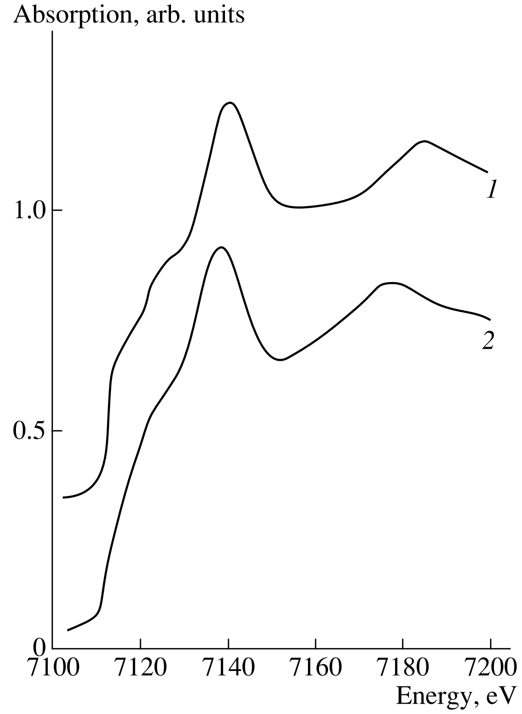

Fig. 1. Experimental x-ray absorption spectra near the Fe *K* edge of (*1*) an amorphous and (*2*) a crystalline $Al_{90}Fe_3Ce_7$ alloy.

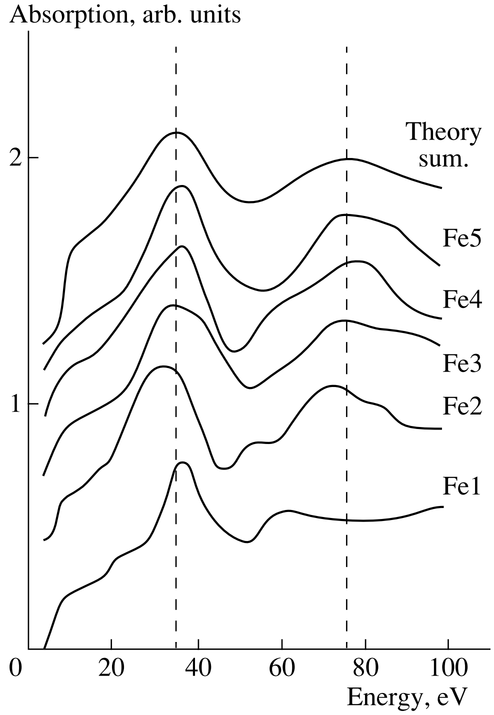

Fig. 2. Theoretical x-ray absorption spectra near the Fe *K* edge for an Fe atom in five inequivalent positions and the average spectrum of the $FeAl_3$ model alloy.

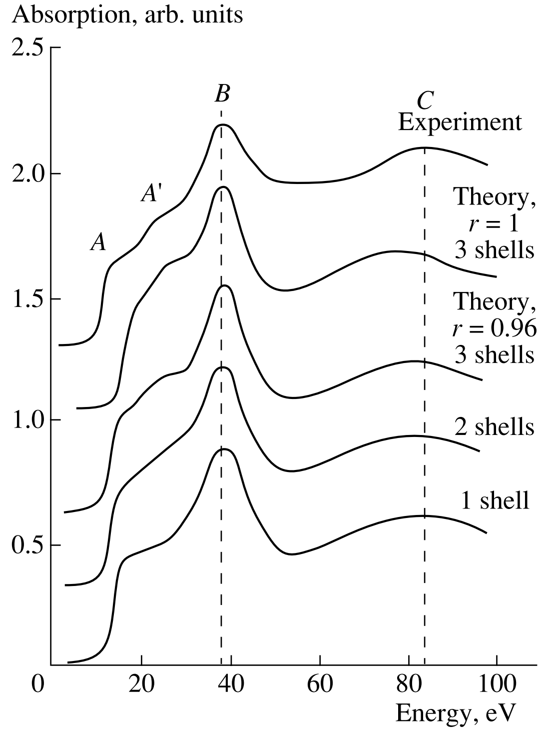

Fig. 3. Theoretical x-ray absorption spectrum near the Fe *K* edge of the $FeAl_6$ model alloy. The lower three curves show the dependence of the shape of the spectrum on the cluster size.

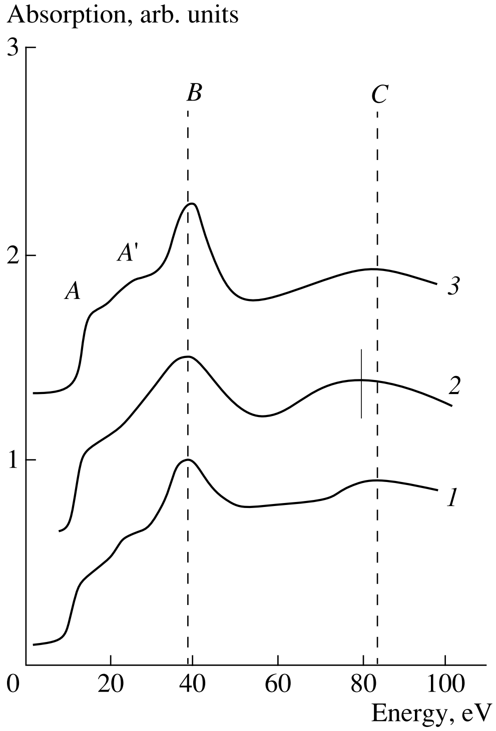

Fig. 4. X-ray absorption spectra near the Fe *K* edge: (*1*) experimental spectrum of an amorphous $Al_{90}Fe_3Ce_7$ alloy and theoretical spectra of (*2*) the $FeAl_3$ and (*3*) $FeAl_6$ model alloys.

calculated for this model alloy and the experimental spectrum is poor. The other model alloy is $FeAl_6$ [11]. Figure 3 shows the theoretical spectra for this alloy. The lower three curves in Fig. 3 show the dependence of the shape of the spectrum on the number of atoms in the cluster taken for the calculation. It can be seen that the main characteristic features (*A*, *B*, *C*) of the spectrum are reproduced even in the case of a small cluster that contains only the first shell of neighbors (11 atoms, curve “1 shell”). However, as a larger number of atoms (up to 27) is taken into consideration, some finer features appear in the spectrum (feature *A*' near *A*) and the agreement between the theoretical and experimental spectra becomes better (curve “3 shells”). A comparison of the spectra of the $FeAl_6$ alloy calculated for the two values of the interatomic distance that differ by 4% (r = 0.96 and 1.0) shows that the energy position of peak *C* is in better agreement with the experiment for the smaller interatomic distance.

Figure 4 compares the experimental iron *K*-edge x-ray absorption spectrum of $Al_{90}Fe_3Ce_7$ and the theoretical Fe *K*-edge absorption spectra of the $FeAl_3$ and $FeAl_6$ model alloys (Tables 1, 2). For $FeAl_6$, the original interatomic distances are decreased by 4% (Table 2). It can be seen that both models reproduce the specific shape of the experimental XANES spectrum. However, the energy position of peak *C* and the doublet structure below the absorption edge (*A*–*A*') are described better by the $FeAl_6$ model. This is also the case with the spectra of other alloys ($Al_{90}Fe_5Ce_5$, $Al_{90}Fe_7Ce_3$), which are not presented in this paper. Thus, it may be concluded that the neighbor environment of Fe atoms in $Al_{90}Fe_xCe_{10-x}$ alloys (x = 3, 5, 7) is similar to that in the $FeAl_6$ model alloy but with the interatomic distance being decreased by 4%.

The fine structure of the x-ray absorption spectrum is determined not only by the phase shifts and the structure of the neighbor environment, but also by the transition matrix element [given by Eq. (2)], which affects the relative intensity.

As is known, in the dipole approximation, the iron *K*-edge x-ray absorption coefficient $\alpha(E)$ is proportional to the density of unoccupied Fe *p* states and to the transition matrix element; that is,

$$\alpha(E) \sim |m_L(E)|^2 N_p^{\mathrm{Fe}}(E). \quad (1)$$

Here, $N_p^{\mathrm{Fe}}(E)$ is the partial density of unoccupied Fe *p* states and the normalized dipole transition matrix element is given by

$$m_L(E) = \frac{\int dr \Phi_l(r, E)\Delta(r)\Psi_c(r)}{\left[\int dr \Phi_l^2(r, E)\right]^{1/2}}, \quad (2)$$

where $\Phi_l(r, E)$ is the solution of the radial Schrödinger equation with an MT potential characterized by energy E, $\Delta(r)$ is the electron–photon interaction operator, and $\Psi_c(r)$ is the K-level wave function.

Since the dipole matrix element depends only slightly on the energy in the range 30 eV higher than the fundamental absorption edge, the Fe K-edge absorption in the compounds in question can be used to investigate the density of unoccupied Fe p states in the conduction band.

4. CONCLUSION

Thus, analysis of the theoretical XANES spectra above the Fe K edge allowed us to choose an adequate model for the neighbor environment of Fe atoms. It is shown that the $FeAl_6$ model with its interatomic distance decreased by 4% agrees better with the experimental data. The experimental iron XANES spectra can be used to investigate the partial density of unoccupied Fe p states in the conduction band of $Al_{90}Fe_xCe_{10-x}$ alloys ($x = 3, 5, 7$).

REFERENCES

1. H. Y. Hsieh, B. H. Toby, T. Egami, *et al.*, J. Mater. Res. **5**, 2807 (1990).
2. G. J. Shiflet, Y. He, and S. J. Poon, J. Appl. Phys. **64**, 6863 (1988).
3. J. L. Wagner, K. M. Wong, F. S. Pierce, and S. J. Poon, Phys. Rev. B **39**, 5500 (1989).
4. H. Y. Hsieh, T. Egami, Y. He, *et al.*, J. Non-Cryst. Solids **135**, 248 (1991).
5. A. N. Mansour, C.-P. Wong, and R. A. Brizzolara, Phys. Rev. B **50**, 12401 (1994).
6. A. N. Mansour and C. A. Meledres, J. Electrochem. Soc. **142** (6), 1961 (1995).
7. A. N. Mansour, C. A. Meledres, S. J. Poon, *et al.*, J. Electrochem. Soc. **143** (2), 614 (1996).
8. P. J. Durham, *X-ray Absorption: Principles, Applications, Techniques of EXAFS, SEXAFS, and XANES*, Ed. by D. C. Koningsberger and R. Prins (Wiley, New York, 1988), pp. 53–84.
9. A. N. Mansour, A. Dmitrienko, and A. V. Soldatov, Phys. Rev. B **55**, 15531 (1997).
10. S. Della Longa, A. V. Soldatov, M. Pompa, and A. Bianconi, Comput. Mater. Sci. **4**, 199 (1995).
11. P. Villars and L. D. Calvert, *Pearson's Handbook of Crystallographic Data for Intermetallic Phases. American Society for Metals* (Metals Park, 1985), Vol. 2, pp. 920, 972.
12. P. J. Black, Acta Crystallogr. **8**, 43 (1955); **8**, 175 (1955).
13. J. C. Fuggle and J. E. Inglesfield, *Unoccupied Electronic States* (Springer-Verlag, Berlin, 1992).

Translated by Yu. Epifanov

Physics of the Solid State, Vol. 43, No. 6, 2001, pp. 997–1000. Translated from Fizika Tverdogo Tela, Vol. 43, No. 6, 2001, pp. 965–967.

Oscillations of the Density of Atoms in the Vicinity of Symmetrical Grain Boundaries in Metals

E. I. Lugovskaya, T. I. Mazilova, and I. M. Mikhaĭlovskiĭ

"Kharkov Physicotechnical Institute" Research Center, Kharkov, 61108 Ukraine

e-mail: astr@ktts.kharkov.ua

Received August 11, 2000; in final form, November 9, 2000

Abstract—Oscillatory atomic relaxation in symmetrical grain boundaries in metals is investigated by molecular-dynamics methods. It is found that the density of atoms varies nonmonotonically in various metastable grain boundaries and that the amplitude, period, and character of damping of the oscillations are virtually the same in these boundaries. A continuum model is proposed for surface layer deformation produced by linear distributed forces and is shown to adequately describe oscillatory grain-boundary relaxation. *© 2001 MAIK "Nauka/Interperiodica".*

In [1, 2], by high-resolution field ion microscopy and computer simulation, it has been shown that, in symmetrical special (commensurate) grain boundaries, collective grain-boundary relaxation occurs in addition to mutual translational displacements of the lattices of adjacent crystallites [3]; this relaxation consists in translations of atomic planes parallel to the plane of the boundary. Translational zone shifts of individual atomic planes in the core of a boundary can be as large as the spacing between atomic planes and, therefore, must be taken into account when calculating lattice sums in models of rigid-grain-boundary relaxation. Taking zone shifts of atomic planes into consideration allows one to fully describe the atomic structure of commensurate boundaries in terms of a limited number of parameters characterizing the state of near-boundary atomic planes.

Of special interest are translational zone shifts of atomic planes that cause the density of atoms to oscillate in the vicinity of grain boundaries. These oscillations are observed not only in metals, but also in covalent and ionic crystals [1, 3]. It is obvious that they significantly affect the kinetics of formation and migration of point defects and can be the reason for the difference between the structural and diffusion widths of grain boundaries [4] and for the oscillatory interaction between lattice dislocations and symmetrical commensurate boundaries [5].

The character of oscillations of the density of atoms is determined by many macroscopic and microscopic parameters which characterize the structure and microtopography of grain boundaries [3]. This circumstance severely hampers the elucidation of the physical nature of this phenomenon. In this paper, we investigate the oscillatory behavior of the density in the vicinity of the same boundary in different structural states. The atomic structure and the field of dilatation of a 38.9° [110] tilt boundary in bcc metals are investigated by using computer simulation techniques. Previous investigations of this boundary [6] have revealed several metastable configurations of cores corresponding to different translational shifts of the lattices of adjacent grains.

In our calculations, a bicrystal is taken to consist of 1350 atoms forming 40 atomic planes {114}. Computer simulations are performed by the molecular-dynamics method in the pairwise-potential approximation, following a procedure described in [5, 6]. The lattices of the adjacent grains are translated in the plane of the tilt boundary along the x axis parallel to the $[\bar{2}21]$ direction. The y axis is taken to be parallel to the tilt axis [110], and the z axis is normal to the plane of the boundary. A special (commensurate) symmetrical $(1\bar{1}4)$ boundary with its tilt axis parallel to [110] and the tilt angle 38.9° is investigated; for this boundary, the inverse density of sites of the coincidence lattice Σ is equal to 9.

Figure 1 shows the atomic structure of a $(1\bar{1}4)$ 38.9°[110] tilt boundary in a tungsten bicrystal as projected onto the (110) plane. This configuration occurs after the lattices of the adjacent grains undergo translations along the $[\bar{2}21]$ direction by a distance of 0.258 nm followed by atomic relaxation of the bicrystal. In Fig. 1, the atoms situated in the core of the boundary and having a higher excess energy are enclosed in circles. The maximum excess energy in the core is 0.70 eV/atom. A translation by 0.206 nm takes the boundary to the metastable state described in [2, 5]. The core configurations of the $\Sigma 9$ $(1\bar{1}4)$ 38.9°[110] grain boundary in these two states differ drastically; after the 0.258-nm shift, the two $(1\bar{1}4)$ planes coa-

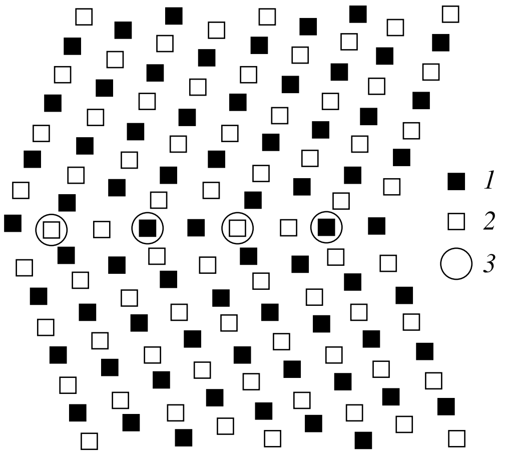

Fig. 1. Arrangement of atoms in the vicinity of the $\Sigma 9$ $(1\bar{1}4)38.9°[110]$ tilt boundary. *1* and *2* are atoms in two adjacent (110) planes, and *3* are atoms with an excess repulsion energy.

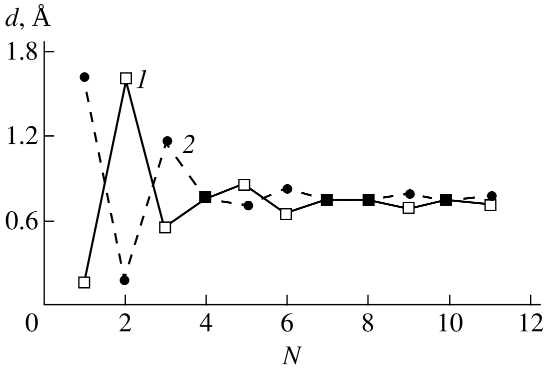

Fig. 2. Oscillations of interplanar spacings in the vicinity of grain boundaries in the metastable states caused by a translation of the adjacent grains by (*1*) 0.258 and (*2*) 0.206 nm. N is the number of the atomic $(1\bar{1}4)$ plane.

lesced completely at the core center (Fig. 1), whereas after a shift of 0.206 nm, two pairs of atomic planes parallel to the plane of the boundary coalesced partly at the core [2]. However, the gross features of the grain boundary relaxation in these two structural states are similar. Figure 2 illustrates the oscillatory behavior of atomic relaxation in the vicinity of grain boundaries in the metastable states characterized by translational shifts 0.258 (curve *1*) and 0.206 nm (curve *2*). It can be seen from Fig. 2 that the amplitudes, periods, and character of damping of oscillations in these two metastable states are virtually the same; only the oscillation phases of interplanar spacings are different.

The reason for the spatial oscillations of the spacings between atomic planes in the vicinity of grain boundaries is widely believed to be associated with the curving of atomic planes near the cores of grain-boundary edge dislocations [3]. The formation of structural grain-boundary dislocations is due to cohesion forces acting between adjacent crystallites and producing a relaxing displacement field. This model allows one to qualitatively describe density oscillations and coalescence of grain-boundary atomic planes. However, the $\Sigma 9(1\bar{1}4)38.9°[110]$ tilt boundary considered in this paper, as well as other symmetrical commensurate grain boundaries with a high density of coincident sites, has no structural grain-boundary dislocations. Since the oscillatory character of variations in the density of atoms in the near-boundary region virtually does not depend on the atomic structure of the core (Fig. 2), it is not unreasonable to analyze the grain-boundary relaxation phenomenologically in the framework of the linear elasticity theory. This analysis is presented below.

A crystallographic and geometrical analysis of the symmetrical commensurate grain boundary in question [6] reveals that this tilt boundary can be considered as a dislocation-free staircase-like vicinal surface with terraces being parallel to the singular {112} faces. The spacing between grain-boundary steps is $(a/2)[\bar{2}21]$ (the half-period of the lattice in the direction perpendicular to the tilt axis). At these dislocation-free steps, repulsive short-range forces operate because of the interaction between the adjacent grains. Using the computer simulation data, we calculated the local stresses by the method described in [3]. It is found that in the vicinity of atoms with a higher excess energy in the boundary with a translational shift of 0.258 nm (Fig. 1), the compression stress component σ_{zz}, normal to the surface, is equal to 31 GPa; i.e., it is of the order of $0.1E$, where E is Young's modulus. The repulsive short-range forces operating mainly in the vicinity of relatively close-packed $\langle 110\rangle$ chains of atoms (enclosed in circles in Fig. 1) produce a grain-boundary dilatation, the limiting value of which is determined by the work of the attractive long-range forces acting between the atoms of the adjacent grains. Taking into account that the basic characteristics of atomic-density oscillations (period and damping) depend only slightly on the atomic structure of the boundary core with a change in the structural state of the boundary, we replace the complex pattern of interaction between adjacent crystallites by the interaction between periodic arrays of parallel lines. Linear distributed forces are assumed to be localized near close-packed atomic chains on the grain boundary, which are characterized by an excess energy (Fig. 1). Each of the crystallites is considered as an elastic continuum bounded by a plane surface. The distance L along the x axis between the lines to which the forces are applied is equal to the half-period of the lattice in the direction perpendicular to the tilt axis. The forces P_z, uniformly distributed over the tilt axis y, are directed along the z axis, normal to the plane surface bounding the elastic half-space.

The linear distributed force P_z acting on the plane surface bounding the elastic half-space produces a strain field [7]

$$e_{xx} = \frac{2P_z(1+\sigma)}{\pi E}\frac{z}{x^2+z^2}\left(\sigma - \frac{x^2}{x^2+z^2}\right), \tag{1a}$$

$$e_{zz} = \frac{2P_z(1+\sigma)}{\pi E}\frac{z}{x^2+z^2}\left(\sigma - \frac{z^2}{x^2+z^2}\right), \tag{1b}$$

$$e_{yy} = 0, \tag{1c}$$

where P_z is the applied force per unit length and σ is the Poisson ratio.

At $z \gg L$, the infinite array of parallel linear distributed forces produces a homogeneous compression of the crystallite. At the same time, as follows from the computer simulation data, all components of the stress tensor vanish at such distances. In order to meet the requirement of the strains being equal to zero at large distances from the surface, one should subtract the strain produced by the long-range stress field. The strain field produced by the system of parallel linear forces can be calculated from Eqs. (1a)–(1c) in the same manner as the strain field of an array of lattice dislocations in [8]. The result is

$$U_z = \frac{P_z(1+\sigma)}{2\pi E}\left\{Z\left[\frac{\sinh(Z)}{\cosh(Z)-\cos(X)} - 2\sigma + 1\right] - 2(1-\sigma)\ln[\cosh(Z)-\cos(X)]\right\}, \tag{2}$$

where $X = 2\pi x/L$ and $Z = 2\pi z/L$.

The relaxing shifts can be found if the atomic displacements in adjacent planes parallel to the tilt boundary are given. For the $\Sigma 9\ (1\bar{1}4)\ 38.9°[110]$ tilt boundary at hand, the displacements of atoms in the ith $(1\bar{1}4)$ plane can be written as [2]

$$\mathbf{x}_i - \mathbf{x} = (2i/9)[\bar{2}21]. \tag{3}$$

Figure 3 shows the relative relaxing shift of the $(1\bar{1}4)$ planes calculated within the continuum model as a function of the distance from the $\Sigma 9\ (1\bar{1}4)\ 38.9°[110]$ tilt boundary (curve *2*). The local values of the spacing between atomic layers i and $(i+1)$ are determined from Eqs. (2) and (3) as $d_i = d + (U_{i+1} - U_i)$. For comparison, Fig. 3 also shows the calculations by the molecular-dynamics method (curve *1*). Since the linear distributed forces cannot be found in the framework of the elasticity theory, we used those values of P_z that gave the best fit of the calculated data to the experimental curve. It follows from Fig. 3 that the continuum model in which the interaction between the atoms of the adjacent crystallites is replaced by the interaction between periodic arrays of lines at which linear distributed forces act in the direction normal to the surface of each crystallite describes the oscillatory atomic grain-boundary relaxation adequately (except for a thin layer, one to two interplanar-spacing thick, to which the linear elasticity theory is certain to be inapplicable).

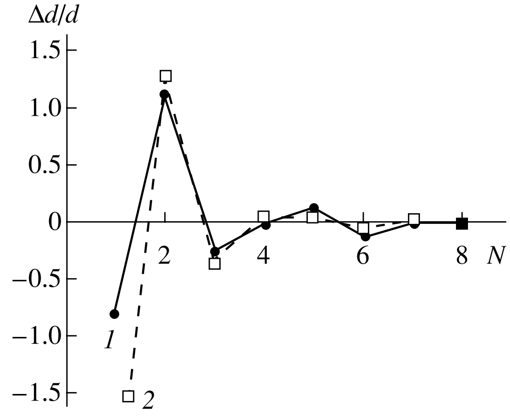

Fig. 3. Relative changes in the interplanar spacing in the grain-boundary region as calculated (*1*) by the molecular-dynamics method and (*2*) within the continuum model.

It should be noted that an analogous model was proposed by Marchenko and Parshin [9] for the free surface of a crystal. By considering the relaxation of the surface layers as their response to the action of linear distributed forces, many subtle morphological effects that occur in the surface layers of solids (from cryocrystals [10] to refractory metals [11]) can be described quantitatively. It is interesting to note that the continuum approximation adequately describes relaxation processes in grain-boundary (Fig. 3) and free-surface regions [8] even in the cases where the local deformation in the direction normal to the boundary far exceeds the limiting amount of macroscopic deformation for the linear elasticity theory to be applicable. The adequacy of the continuum approximation for describing the oscillatory grain-boundary and surface relaxation is likely to be due to the fact that, when the spacing between vicinal (loosely packed) sheets of atoms varies nonmonotonically, the relative change in the distance between the nearest neighbor atoms is small enough for the linear elasticity theory to be applicable.

REFERENCES

1. P. A. Bereznyak, O. A. Velikodnaya, T. I. Mazilova, and I. M. Mikhaĭlovskiĭ, Pis'ma Zh. Éksp. Teor. Fiz. **59** (8), 515 (1994) [JETP Lett. **59**, 542 (1994)].
2. T. I. Mazilova and I. M. Mikhaĭlovskiĭ, Kristallografiya **42** (5), 796 (1997) [Crystallogr. Rep. **42**, 729 (1997)].
3. A. P. Sutton and R. W. Ballufi, *Interfaces in Crystalline Materials* (Clarendon Press, Oxford, 1995).

4. I. M. Mikhailovskij, V. B. Rabukhin, and O. A. Velikodnaya, Phys. Status Solidi A **125** (2), K65 (1991).
5. B. C. Boĭko and I. N. Sidorenko, Fiz. Met. Metalloved. **67** (3), 444 (1989).
6. T. I. Mazilova and I. M. Mikhaĭlovskiĭ, Fiz. Tverd. Tela (St. Petersburg) **37** (1), 206 (1995) [Phys. Solid State **37**, 113 (1995)].
7. L. D. Landau and E. M. Lifshitz, *Course of Theoretical Physics*, Vol. 7: *Theory of Elasticity* (Nauka, Moscow, 1965; Pergamon, New York, 1986).
8. D. J. Sroloviz and J. P. Hirth, Surf. Sci. **255** (1), 111 (1991).
9. V. I. Marchenko and A. Ya. Parshin, Zh. Éksp. Teor. Fiz. **79** (1), 257 (1980) [Sov. Phys. JETP **52**, 129 (1980)].
10. V. I. Marchenko, Zh. Éksp. Teor. Fiz. **81** (3), 1140 (1981) [Sov. Phys. JETP **54**, 605 (1981)].
11. K. Swamy, E. Bertel, and I. Vilfan, Surf. Sci. Lett. **425** (2), L369 (1999).

Translated by Yu. Epifanov